STATE OF CALIFORNIA DEPARTMENT OF TRANSPORTATION

TECHNICAL REPORT DOCUMENTATION PAGE

TR0003 (REV. 10/98)

ADA Notice
For individuals with sensory disabilities, this document is available in alternate formats. For alternate format information, contact the Forms Management Unit at (916) 445-1233, TTY 711, or write to Records and Forms Management, 1120 N Street, MS-89, Sacramento, CA 95814.

1. REPORT NUMBER	2. GOVERNMENT ASSOCIATION NUMBER	3. RECIPIENT'S CATALOG NUMBER
CA14-2176		

4. TITLE AND SUBTITLE	5. REPORT DATE
Next Generation of Bridge Columns for Accelerated Bridge Construction in High Seismic Zones	August 2014
	6. PERFORMING ORGANIZATION CODE UNR
7. AUTHOR(S) Mostafa Tazarv and M. Saiid Saiidi	8. PERFORMING ORGANIZATION REPORT NO. UNR/CCEER 14-06
9. PERFORMING ORGANIZATION NAME AND ADDRESS Department of Civil and Environmental Engineering University of Nevada, Reno Reno, Nevada 89557-0258	10. WORK UNIT NUMBER 11. CONTRACT OR GRANT NUMBER 65A0372
12. SPONSORING AGENCY AND ADDRESS California Department of Transportation Engineering Service Center 1801 30th Street, MS 9-2/5i Sacramento, California 95816 California Department of Transportation Division of Research, Innovation, and System Information P.O. Box 942873 Sacramento, CA 95814	13. TYPE OF REPORT AND PERIOD COVERED Final Report 08/01/2010 to 08/29/2014 14. SPONSORING AGENCY CODE 913

15. SUPPLEMENTAL NOTES

16. ABSTRACT

Accelerated bridge construction (ABC) utilizes advanced planning, new construction techniques, and innovative detailing to facilitate construction. ABC offers many advantages over conventional construction, the most important of which is the reduction of onsite construction time. Even though ABC has been widely used in low seismic regions of the country mostly in superstructure, application of ABC in seismic areas has been limited due to the lack of seismic performance data regarding substructure connections. The main objective of this study was to develop new ABC connections for bridge columns using novel detailing and advanced materials. Three low-damage materials were incorporated: ultra-high performance concrete (UHPC), Nickel-Titanium shape memory alloy (NiTi SMA), and engineered cementitious composite (ECC). Furthermore, two types of mechanical bar splices, grouted coupler and headed bar coupler, were utilized. UHPC-filled duct connections were developed and evaluated through 14 pullout tests. A new detailing was proposed for grouted coupler column end connections to enhance the drift capacity. Three half-scale precast column models were tested under slow reversed cyclic loading, each with a new precast element connection or low-damage plastic hinge. A material model was developed for reinforcing superelastic NiTi SMA bars. Furthermore, new simple methods were developed to account for bond-slip effects and bar debonding effects in analytical models of reinforced concrete members. It was found that bar bond strength in UHPC is eight times higher than that in conventional concrete. UHPC-filled duct connections exhibited no damage even under 12% drift ratio cycles. The displacement capacity and displacement ductility capacity for the grouted coupler column were respectively increased by 47 and 56% compared to grouted coupler column models investigated previously. Longitudinal bar debonding allowed spread of yielding and prevented premature failure of reinforcements in UHPC-filled duct connections and grouted coupler column pedestal. The SMA-reinforced ECC column showed superior seismic performance compared to a conventional column in which the plastic hinge damage was limited to only ECC cover spalling even under 12% drift ratio cycles. The column residual displacements were 79% lower than CIP residual displacements on average due to the superelastic NiTi SMA longitudinal reinforcement, and higher base shear capacity and higher displacement capacity were observed. The analytical modeling methods were simple and sufficiently accurate for general design and analyses of precast components proposed in the present study. The proposed symmetrical material model for reinforcing NiTi superelastic SMA was found to be a viable alternative to the more complex asymmetrical model. Extensive experimental and analytical investigations performed in the present study led to a new generation of ABC bridge columns in which columns can be built in relatively short time but the seismic performance of these columns is equal or better than columns that are built cast-in-place with conventional materials.

17. KEY WORDS	18. DISTRIBUTION STATEMENT	
Accelerated Bridge Construction, Precast Columns, Connections, low-damage materials, UHPC, ECC, SMA, Mechanical Bar Splices, High Seismic Zones	No restrictions. This document is available to the public through the National Technical Information Service, Springfield, VA 22161	
19. SECURITY CLASSIFICATION (of this report) Unclassified	20. NUMBER OF PAGES 400	21. PRICE

Reproduction of completed page authorized

Disclaimer Statement

This document is disseminated in the interest of information exchange. The contents of this report reflect the views of the authors who are responsible for the facts and accuracy of the data presented herein. The contents do not necessarily reflect the official views or policies of the State of California or the Federal Highway Administration. This publication does not constitute a standard, specification or regulation. This report does not constitute an endorsement by the Department of any product described herein.

For individuals with sensory disabilities, this document is available in Braille, large print, audiocassette, or compact disk. To obtain a copy of this document in one of these alternate formats, please contact: the Division of Research and Innovation, MS-83, California Department of Transportation, P.O. Box 942873, Sacramento, CA 94273-0001.

Report No. CA14-2176, CCEER 14-06

NEXT GENERATION OF BRIDGE COLUMNS FOR ACCELERATED BRIDGE CONSTRUCTION IN HIGH SEISMIC ZONES

Mostafa Tazarv
M. Saiid Saiidi

A draft report submitted to the California Department of Transportation
Contract Number 65-A0372

Center for Civil Engineering Earthquake Research

University of Nevada, Reno
Department of Civil and Environmental Engineering, MS 258
1664 N. Virginia St.
Reno, NV 89557

August 2014

Abstract

Accelerated bridge construction (ABC) utilizes advanced planning, new construction techniques, and innovative detailing to facilitate construction. ABC offers many advantages over conventional construction, the most important of which is the reduction of onsite construction time. Even though ABC has been widely used in low seismic regions of the country mostly in superstructure, application of ABC in seismic areas has been limited due to the lack of seismic performance data regarding substructure connections. The main objective of this study was to develop new ABC connections for bridge columns using novel detailing and advanced materials.

Three low-damage materials were incorporated: ultra-high performance concrete (UHPC), Nickel-Titanium shape memory alloy (NiTi SMA), and engineered cementitious composite (ECC). Furthermore, two types of mechanical bar splices, grouted coupler and headed bar coupler, were utilized. UHPC-filled duct connections were developed and evaluated through 14 pullout tests.

A new detailing was proposed for grouted coupler column end connections to enhance the drift capacity. Three half-scale precast column models were tested under slow reversed cyclic loading, each with a new precast element connection or low-damage plastic hinge. A material model was developed for reinforcing superelastic NiTi SMA bars. Furthermore, new simple methods were developed to account for bond-slip effects and bar debonding effects in analytical models of reinforced concrete members.

It was found that bar bond strength in UHPC is eight times higher than that in conventional concrete. UHPC-filled duct connections exhibited no damage even under 12% drift ratio cycles. The displacement capacity and displacement ductility capacity for the grouted coupler column were respectively increased by 47 and 56% compared to grouted coupler column models investigated previously. Longitudinal bar debonding allowed spread of yielding and prevented premature failure of reinforcements in UHPC-filled duct connections and grouted coupler column pedestal. The SMA-reinforced ECC column showed superior seismic performance compared to a conventional column in which the plastic hinge damage was limited to only ECC cover spalling even under 12% drift ratio cycles. The column residual displacements were 79% lower than CIP residual displacements on average due to the superelastic NiTi SMA longitudinal reinforcement, and higher base shear capacity and higher displacement capacity were observed. The analytical modeling methods were simple and sufficiently accurate for general design and analyses of precast components proposed in the present study. The proposed symmetrical material model for reinforcing NiTi superelastic SMA was found to be a viable alternative to the more complex asymmetrical model.

Extensive experimental and analytical investigations performed in the present study led to a new generation of ABC bridge columns in which columns can be built in relatively short time but the seismic performance of these columns is equal or better than columns that are built cast-in-place with conventional materials.

Acknowledgements

The research presented in this document was funded by the California Department of Transportation (Caltrans) through contract No. 65-A0372. However, the statements and findings presented in this document are those of the author and do not necessary represent the views of Caltrans. Special thanks are due Dr. Saad El-Azazy and Dr. Charles Sikorsky, the Caltrans Research Program Managers for their support and advice. The interest and comments of Messrs. Mike Keever, Mark Mahan, and Ron Bromenschenkel are also much appreciated.

The research team is indebted to Messrs. Christian Dahl and Joseph Morente of Headed Reinforcement Corp. (HRC), and Messrs. Frank Sczerzenie, Giorgio Vergani, and Rich LaFond of SAES Smart Materials for generously donating materials and providing advice. The advice and comments of Dr. Darel Hodgson of Nitinol Technology, Inc. are highly appreciated. The authors would like thank Mr. Vic Perry, vice-president and general manager of Lafarge North America Inc. for donating the UHPC material. The assistance of Mr. Peter Seibert and Mr. Kyle Nachuk of Lafarge North America Inc. for mixing and casting of UHPC is also highly appreciated. Mr. Toshikazu Yamanishi of Splice Sleeve North America, and Mr. Jim Schroder of Schroder & Associates, LLC are thanked for donating material and technical input. The authors are indebted to Dr. Patrick Laplace, Mr. Mark Lattin, Mr. Robert Nelson, and Mr. Chad Lyttle of UNR for their assistance in execution of the tests. Mr. Ali Mehrsoroush, Mr. Mehrdad Mehraein, Mr. Brian Nakashoji, and Dr. Zachary Haber are thanked for their assistance in experimental parts of this study.

This report is based on a PhD dissertation by the first author supervised by the second author.

Executive Summary

1. Introduction

Accelerated bridge construction (ABC) utilizes advanced planning, new construction techniques, and possibly innovative detailing to facilitate construction. ABC offers many advantages over conventional construction, the most important of which is the reduction of onsite construction time. Even though ABC has been widely used in low seismic regions of the country mostly in superstructure, application of ABC in seismic areas has been limited due to the lack of seismic performance data regarding substructure connections.

1.1. Objectives

The main objective of the present study was to develop a new generation of bridge columns that can be built in a relatively short time than conventional construction with seismic performance that is equal to or exceeds conventional column performance. New ABC connections were developed to facilitate construction and low-damage materials such as ultra-high performance concrete (UHPC), shape memory alloy (SMA), and engineered cementitious composite (ECC) were incorporated in the connections and critical areas to reduce the damage.

Fourteen pullout models were developed and tested to identify reliable UHPC-filled duct connections and to develop methods to estimate the bond strength and deformation of these connections. Tensile tests were carried out to optimize reinforcing SMA bar performance connected to reinforcing steel bars with mechanical headed bar splices. Three half-scale column models each with either an innovative ABC connection or low-damage materials were constructed and tested at the Large Scale Structural Laboratory at the University of Nevada, Reno (UNR). In two models, precast columns were connected to footings using UHPC-filled duct connections. Mechanical grouted sleeve bar splices were incorporated in the last column model as a ABC connection. ECC and SMA were utilized in plastic hinge of one of two columns with UHPC-filled duct connections to reduce the damage and improve the overall performance.

Analytical investigation for each column model and pullout tests was performed using a finite element computer program. New methods were developed to include bond-slip effects and bar debonding effects in analytical modeling of reinforced concrete members. A design specification was proposed for reinforcing NiTi superelastic SMA bars. A parametric study was also performed to determine which mechanical properties of reinforcing SMA bars have the most effect on the overall seismic performance of SMA-reinforced bridge columns. Design recommendations were developed for a new generation of precast bridge columns. Highlights of different aspects of the study and

important findings are presented in the "Executive Summary." The proposed design recommendations are presented in Appendix D and are not repeated herein.

1.2. Low-Damage Materials

Application of engineered materials such as concrete and steel in civil engineering structures dates back to a century ago. Concrete has negligible tensile strength with low compressive and tensile ductility, and steel exhibits large permanent deformations upon yielding and is susceptible to fatigue and corrosion. Despite these deficiencies, concrete and steel are the main construction materials and can be found almost in all civil structures. New materials are emerging to overcome these shortcomings of steel and concrete and enhance the overall performance of structures under different environmental conditions and loading. Three advanced materials that exhibit low-damage behavior even under large loads are of interest in this study: (1) UHPC, (2) ECC, and (3) SMA.

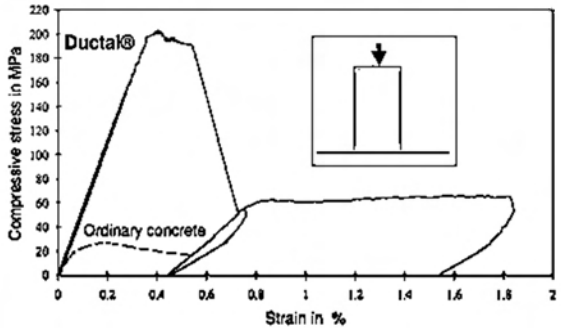

(a) UHPC Complete Compressive Stress-Strain Relationship (Lafarge.com)

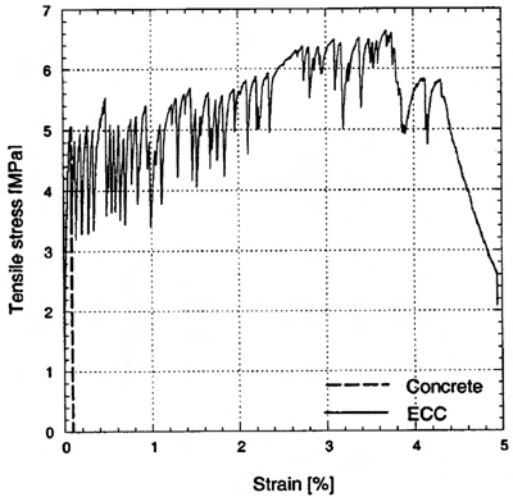

(b) ECC Tensile Stress-Strain (Li and Fischer, 2003)

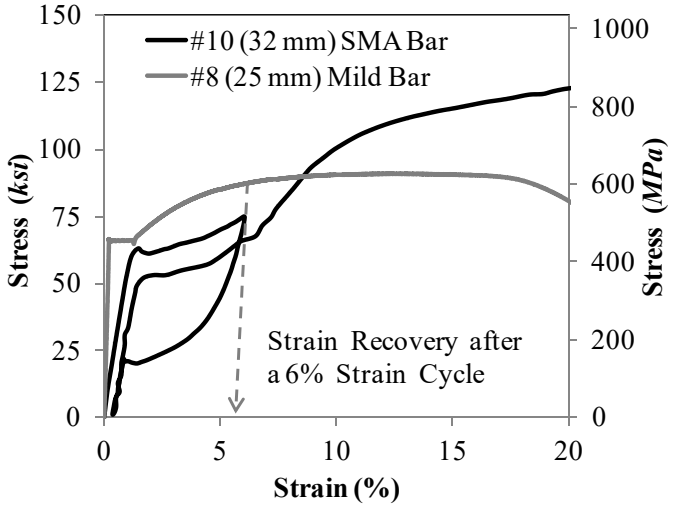

(c) Measured Tensile Stress-Strain for NiTi SMA and Steel Bars (Tazarv and Saiidi, 2014)

Figure ES.1- Measured Stress-Strain of UHPC, ECC, and SMA

UHPC is a class of fiber reinforced concrete with a specified strength of 22000 *psi* (150 *MPa*), which is significantly higher than conventional concrete. Figure ES.1a shows the measured compressive stress-strain of UHPC. Furthermore, UHPC exhibits improved tensile and compressive ductility and durability over conventional concrete. Similar to UHPC, ECC is another class of high performance fiber reinforced concrete with a significant tensile ductility (4% strain) (Fig. ES.1b). Both UHPC and ECC are made with very fine aggregates and fibers with usually 2% volumetric ratio. SMA is a class of metallic materials with an ability to recover its original shape upon unloading (superelastic effect) or heating (shape memory effect). Figure ES.1c shows a typical stress-strain relationship for a Nickel-Titanium (NiTi) superelastic #10 (Ø32 *mm*) reinforcing SMA bar as well as a #8 (Ø25 *mm*) reinforcing steel bar. It can be seen that the SMA exhibited slightly lower yield strength but higher ultimate strength compared to the reinforcing steel. Furthermore, the SMA bar showed negligible residual strain even under 6% strain cycle. Steel bars exhibit large permanent strains after yielding.

1.3. Mechanical Bar Splices

Bar couplers are to provide a shorter splice length over conventional splices but with a proper detailing they may be used in ABC to connect precast segments or members. Several types of mechanical bar splices are available in the market. Figure ES.2 shows two types of these splices that were used in the present study: grouted sleeve coupler and headed bar coupler. Both products satisfy minimum limitations that were set by current US design specifications.

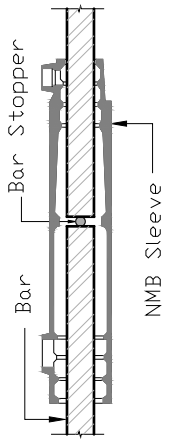

(a) Grouted Sleeve Coupler

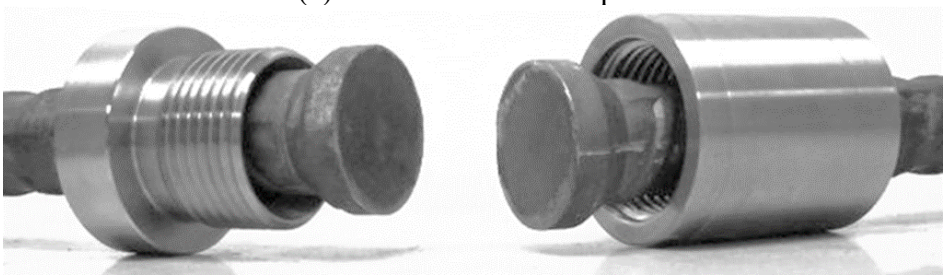

(b) Headed Bar Coupler

Figure ES.2- Mechanical Bar Splices

2. Experimental Studies

2.1. UHPC-Filled Duct Connections

Cap beams are usually sufficiently deep to accommodate column longitudinal bars in grout-filled ducts. However, to connect precast columns to shallow cap beams or footings, an alternative method is required. UHPC was proposed as duct filler instead of conventional gout to reduce embedment length.

Seismic performance of UHPC-filled duct connections was investigated at UNR in two phases. In the first phase, 14 large-scale specimens were tested under tensile loading to determine bond strength of UHPC-filled duct systems. In the second phase, two half-scale RC bridge columns incorporating these type of connections were tested under slow cyclic loads. In this section, bond testing and results of the phase one of the tests are presented.

The test parameters were embedment length, bar size, duct diameter, number of ducts, and bundling of bars. Straight #8 (Ø25 *mm*) and #11 (Ø36 *mm*) bars were used with embedment lengths of $3d_b$, $5d_b$, $8d_b$ and $12d_b$ where d_b is bar diameter. Ducts with nominal size of 3 *in*. (75 *mm*), 4 *in*. (100 *mm*) and 5 *in*. (125 *mm*) were used. The inner diameter of duct (d_d) was used in analyses of data. Corrugated galvanized strip metal ducts conforming to ASTM A653 with 26-gauge (0.018 *in*. or 0.46 *mm*) wall thickness were used. Bundled bars consisting of two #8 (Ø25 *mm*) bars were used in three of the specimens. The effect of using double ducts spaced at clear distance of 3 *in*. (76 *mm*), each with single bar, was investigated in two specimens. Test specimens were designed in two groups to find the duct bond strength in group I (10 specimens) and the bar bond strength in group II (4 specimens). Figure ES.3 shows schematic view of specimens. Both groups had similar geometries but a large portion of the bars were debonded using 3/8-*in*. (9.5-*mm*) thick pipe insulation foams in group II. With this detail the entire length of the duct was mobilized in transferring the loads, and duct pullout was avoided.

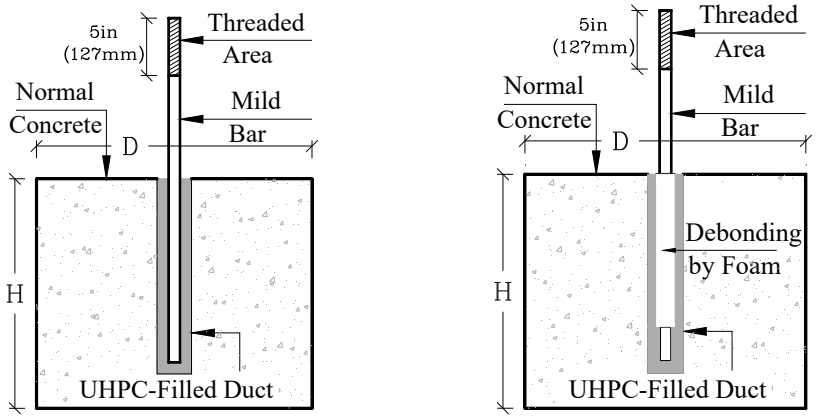

(a) Group I Specimens (b) Group II Specimens

Figure ES.3- Schematic View of Pullout Tests Specimens (Tazarv and Saiidi, 2014)

There are several test configurations with different bar sizes, multi ducts, and bundled bars. To accommodate these different configurations, a self-reacting pullout test setup was designed and built at UNR with pull force capacity of 300 *kips* (1335 *kN*).

For two specimens in group I, SP4 and SP11, the ducts pulled out with severe damage of surrounding concrete and conical failure of concrete at a depth of 3.5 *in*. (89 *mm*). No damage was observed in UPHC. Only in one specimen in group II with $3d_b$ embedment length, SP6, bundled bars pulled out with no visible concrete or UHPC damage. To understand the failure, the specimen was vertically cut in half. It was observed that both plastic deformation of ribs and crushing of surrounding UHPC next to the ribs are the causes of the bars pull out. Note that only four ribs were engaged with UHPC in this specimen. In other specimens, bar ruptured at the threads.

It was found that the effect of bar bundling, bar size, and multiple duct was negligible on the bond performance but duct size had significant effects on bond strength. Table ES.1 presents the test variables and the test results. The duct bond strengths (u_d) were normalized to the square root of test day compressive strength of normal concrete. The average normalized duct bond strength for all tests in group I was 7.27 $psi^{0.5}$ (0.60 $MPa^{0.5}$) with a standard deviation of 1.33 $psi^{0.5}$ (0.11 $MPa^{0.5}$). The bar bond strengths (u_b) were normalized to the square root of test day compressive strength of UHPC. The average normalized bar bond strength for all tests in group II was 33.4 $psi^{0.5}$ (2.77 $MPa^{0.5}$) with a standard deviation of 6.44 $psi^{0.5}$ (0.53 $MPa^{0.5}$).

Table ES.1- Duct/Bar Bond Strength for Group I & II of Pullout Tests

SP. No.	Bar Size	Test Group No.	Embed. Length, *in*. (*mm*)	Duct Diam., d_d *in*. (*mm*)	Force, *kips* (*kN*)	Duct Bond Strength, u_d, *psi* (*MPa*)	Bar Bond Strength, u_b, *psi* (*MPa*)
1	#8 (Ø25)	I	8 (203)	3.12 (79)	56.4 (388.9)	720* (4.96)	N/A
2	#8 (Ø25)	I	12 (305)	3.12 (79)	55.0 (379.2)	467* (3.22)	N/A
3	#8 (Ø25)	II	3 (76)	3.12 (79)	56.2 (387.5)	N/A	5967* (41.14)
4	2#8 (2Ø25)	I	8 (203)	4 (102)	67.5 (465.4)	671 (4.63)	N/A
5	2#8 (2Ø25)	I	12 (305)	4 (102)	107.7 (742.6)	712* (4.90)	N/A
6	2#8 (2Ø25)	II	3 (76)	4 (102)	78.4 (540.6)	N/A	4162 (28.70)
7	#8 (Ø25)	I	8 (203)	4 (102)	54.7 (377.1)	544* (3.75)	N/A
8	#8 (Ø25)	II	5 (127)	3.12 (79)	56.0 (386.1)	N/A	3568* (24.60)
9	2#8 (2Ø25)	I	8 (203)	3.12 (79)	109.8 (757.0)	700* (4.83)	N/A
10	2#8 (2Ø25)	I	12 (305)	3.12 (79)	102.4 (706.0)	435* (3.00)	N/A
11	#11 (Ø36)	I	11.28 (286)	4 (102)	93.9 (647.4)	662 (4.29)	N/A
12	#11 (Ø36)	I	16.92 (430)	4 (102)	106.4 (733.6)	500* (3.45)	N/A
13	#11 (Ø36)	II	4.23 (107)	4 (102)	110.8 (763.9)	N/A	5920* (40.82)
14	#11 (Ø36)	I	11.28 (286)	5.26 (134)	110.9 (764.6)	595* (4.10)	N/A

d_b is nominal diameter of bar; d_d is inner diameter of duct; * Lower bound bond strength

It was found that bond strength of bar in UHPC was eight time stronger than that in conventional concrete. Based on the normalized test data, design equations were proposed for bar embedment length in UHPC-filled duct connections as follows:

$$L_d = \max\left(L_{d,duct}, L_{d,bar}\right)$$

US Customary Units	SI Units	
$L_{d,duc\varepsilon} = \frac{{}_b \cdot f_s}{27\ {}_d \cdot \sqrt{f'_c}}$	$L_{d,duc\varepsilon} = \frac{{}_b \cdot f_s}{2.24\ {}_d \cdot \sqrt{f'_c}}$	(ES-1)
$L_{d,bar} = \frac{{}_b \cdot f_s}{120\sqrt{f'_{UHPC}}}$	$L_{d,bar} = \frac{{}_b \cdot f_s}{9.96\sqrt{f'_{UHPC}}}$	(ES-2)

where

L_d: Development length for un-hooked deformed bar in UHPC-filled duct connections (*in, mm*)

$L_{d,duc\varepsilon}$: Bar development length based on duct bond strength (*in, mm*)

$L_{d,bar}$: Bar development length based on bar bond strength (*in, mm*)

${}_b$: Nominal diameter of bar (*in, mm*)

${}_d$: Inner diameter of duct (*in, mm*)

f_s: Bar stress (*psi, MPa*); 1.5f_y or f_u whichever is greater

f'_c: Compressive strength of concrete surrounding the duct (*psi, MPa*)

f'_{UHPC}: Compressive strength of UHPC in the duct (*psi, MPa*)

2.2. Column Test Models

2.2.1. Geometry and Detailing

Four half-scale precast bridge column models incorporating new types of column-to-footing connections suitable for ABC in high seismic zones were previously designed and tested at UNR by Haber et al. (2013). Models had similar geometries and bar arrangements but different types of column base connections were investigated. Grouted couplers were utilized in plastic hinge of two of the models. Headed bar couplers were incorporated in two other models. A 12-inch (305-mm) high pedestal was used in two precast models to investigate the effect of lower moment demand over coupler location on the seismic performance of the columns. A cast-in-place (CIP) column was also tested to serve as a benchmark model. It was found that headed bar coupler columns were emulative to CIP. Even though grouted coupler columns showed similar base shear and stiffness to CIP, the displacement capacity and displacement ductility capacity of these columns were 40% lower than CIP.

Three new half-scale precast column models each with new connection detailing or low-damage plastic hinge were tested in the present study (Fig. ES.4). UHPC-filled duct connections were incorporated in two of three large-scale column models, “PNC” and “HCS”, to connect the precast columns to footings. Connection of the third precast column, “GCDP”, to the footing was provided using a modified grouted coupler connection in which longitudinal bars were debonded in a cast-in-place pedestal. This

was done to spread bar yielding and potentially overcome the shortcoming of the previously tested grouted coupler columns, low displacement capacity. SMA and ECC were incorporated in the plastic hinge of one of the UHPC-filled-duct columns, "HCS", to improve the overall seismic performance of the column and to enhance its post-earthquake serviceability. Headed bar couplers were utilized to connect SMA bars to steel bars. Column height and diameter for all models were 9 *ft* (2.74 *m*) and 24 *in*. (609 *mm*), respectively.

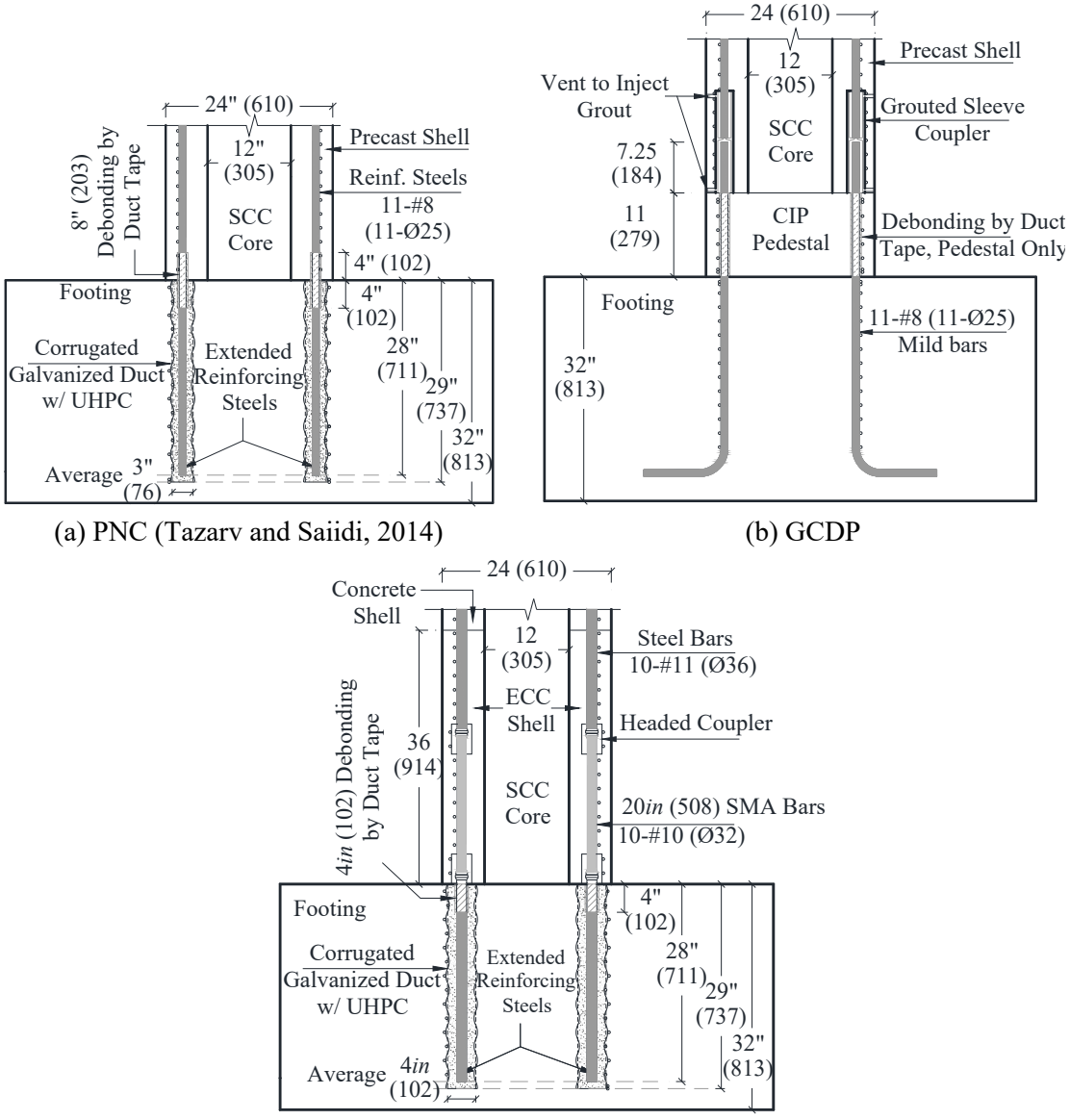

(a) PNC (Tazarv and Saiidi, 2014) (b) GCDP

(c) HCS

Figure ES.4- Proposed Base Connection Details for Precast Columns, unit: *in*. (*mm*)

2.2.2. Key Column Test Results

Mode of failure in all column models was bar fracture. Reinforcing steel bars buckled before fracture in columns with conventional materials (CIP, PNC, and GCDP).

However, no reinforcing SMA bar buckling was observed in HCS. Figure ES.5 shows column plastic hinge damage at 10% drift ratio. PNC plastic hinge damage was similar to CIP damage in which a few bars fractured and core concrete was crushed. Most of the damage of GCDP was concentrated in the pedestal. The plastic hinge damage of HCS was substantially lower than the other models because of using ECC and SMA. HCS damage in plastic hinge area was limited to cover ECC spalling with no spiral exposure even after 12% drift cycles.

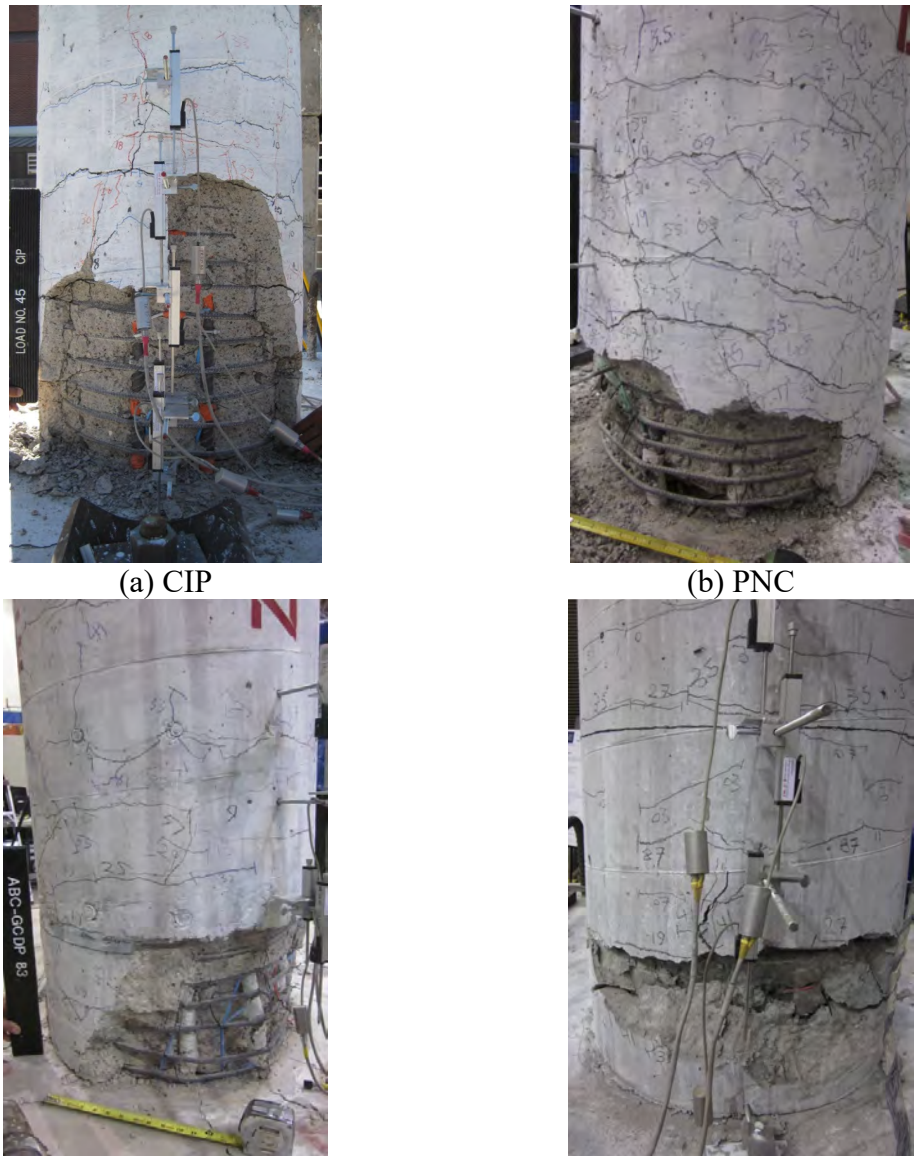

(a) CIP (b) PNC

(c) GCDP (d) HCS

Figure ES.5- Column Plastic Hinge Damage at 10% Drift Ratio

The measured lateral force-drift hysteretic curves for PNC, GCDP, and HCS are shown in Fig. ES.6. Both PNC and GCDP showed wide and stable hysteresis with no strength degradation up to their first longitudinal bar fracture. Similar behavior was observed in CIP. Base shear capacity in each cycle for HCS was comparable to CIP but

HSC showed flag-shape behavior with minimal residual displacements because of using SMA. Residual displacements of HCS was 79% lower than those of CIP on average.

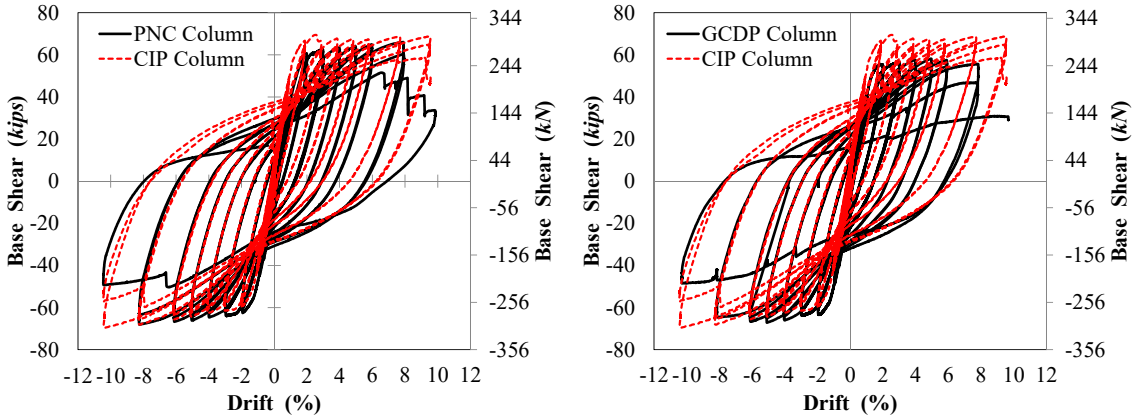

(a) PNC (b) GCDP

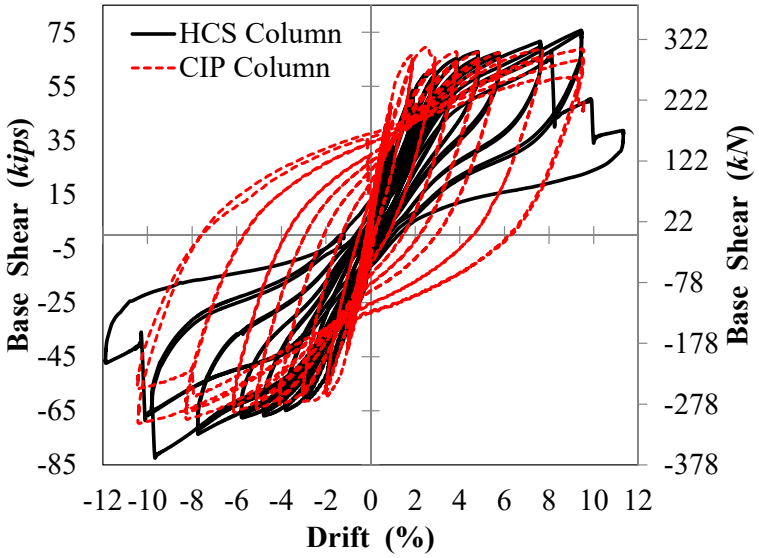

(c) HCS

Figure ES.6- Measured Force-Drift Hysteresis for Precast Columns

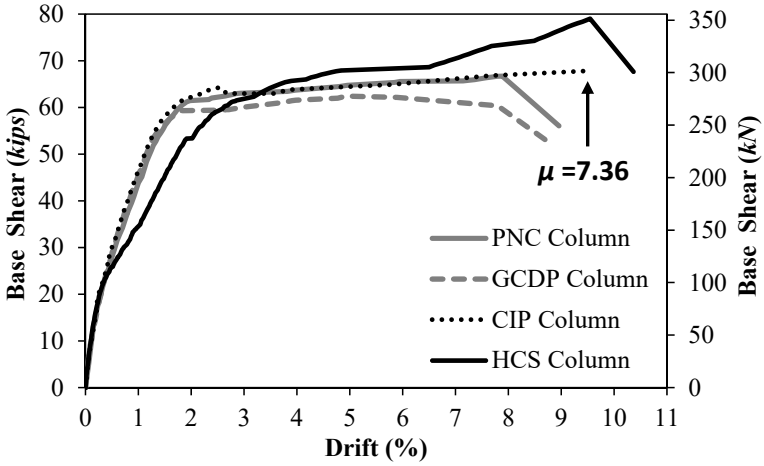

Figure ES.7- PNC, GCDP, HCS, and CIP Column Average Push/Pull Force-Drift Envelopes

The average force-drift push and pull envelopes for precast columns as well as CIP are shown in Fig. ES.7. PNC and GCDP showed slightly lower displacement capacity compared to CIP because of 1100 *psi* (7.58 *MPa*) lower compressive strength of their shell concrete, which reduced column resistance against bar buckling. Design displacement ductility was seven for CIP column. PNC showed 10% lower ductility than the design target, GCDP showed 1% higher displacement ductility capacity than target, and displacement capacity of HCS was slightly higher than that measured in CIP. Compared to the previous grouted coupler columns, GCDP showed 47 and 56% higher displacement capacity and displacement ductility capacity, respectively. Figure ES.8 shows the columns residual displacements. It can be seen that residual displacements of HCS, the column with reinforcing SMA bars, was substantially lower than steel-reinforced columns. After four SMA bar rupture, residual drift of HCS was approximately 1%. This will ensure post-earthquake functionally of bridges built with SMA-reinforced columns after severe ground shaking.

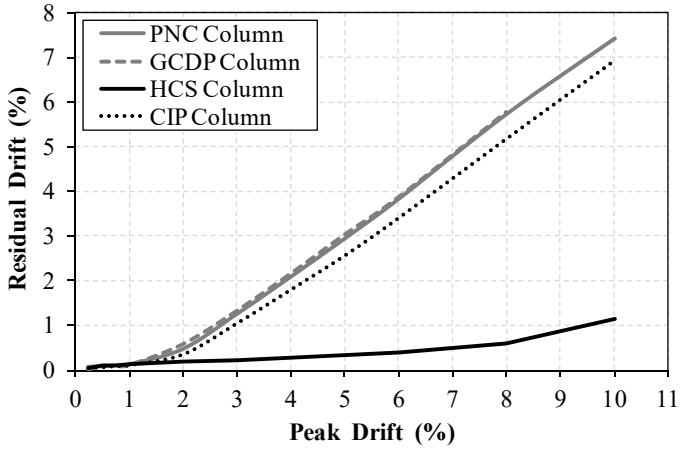

Figure ES.8- PNC, GCDP, HCS, and CIP Column Residual Displacements

Figure ES.9 shows large plasticity distribution of column longitudinal bars, which was defined as measured strains greater than 1%. It can be seen that large bar yielding was well distributed along the height of all precast columns resulting in high displacement capacity. Debonding of longitudinal bars using two layers of duct tape was found to be a successful technique to spread bar yielding and to avoid premature failure of bars due to strain concentration either in UHPC or under the coupler regions.

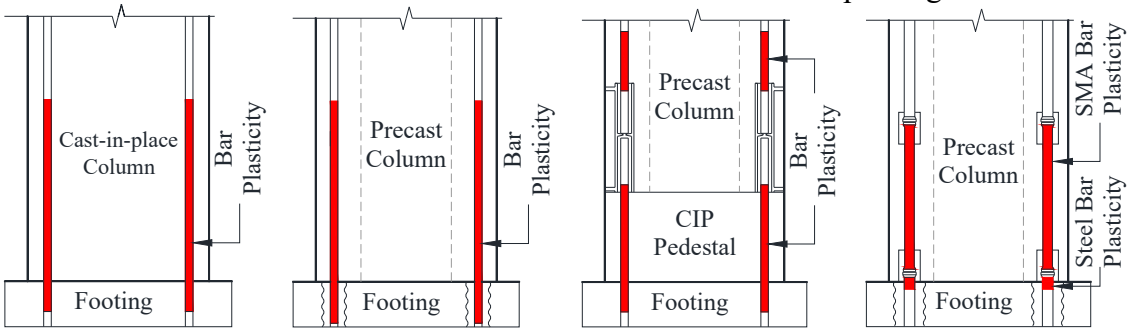

(a) CIP (b) PNC (c) GCDP (d) HCS

Figure ES.9- Distribution of Bar Large Plasticity in Columns

2.2.3. Overall Evaluation of Column Performance

The UHPC-filled duct connection incorporated in PNC was emulative of the conventional connection since:

1. The ultimate capacities of the column were developed and high drift ratios were achieved,
2. No connection damage such as bar pullout, duct pullout, or conical failure of the footing was observed in the PNC column base connection,
3. Mode of failure, base-shear capacity, and strength and stiffness degradation of PNC was nearly the same as those of CIP. However, PNC showed slightly higher energy dissipation due to the debonding of longitudinal bars above and below the column-footing interface.

Overall, UHPC-filled duct connections are proposed as alternative to cast-in-place connections in high seismic regions to connect precast columns to shallow cap beams and footings. When the footing or the cap beam depth is sufficient, high-strength grouts may be used in lieu of UHPC.

The seismic performance of the grouted coupler column with pedestal presented in this study, GCDP, was emulative of CIP since:

1. Mode of failure and strain distribution in the plastic hinge of GCDP was similar to those of CIP. GCDP dissipated more energy than CIP because of the longitudinal bar debonding in the pedestal,
2. The displacement ductility capacity of GCDP was only 4% lower than that of CIP,
3. GCDP reached its ultimate capacities without any connection damage or premature failure of the reinforcements.

In summary, the mechanical grouted sleeve splice connection presented in this study is proposed as a suitable ABC column-to-footing connection in high seismic zones even though most design specifications prohibit utilizing mechanical bar splices in plastic hinge of reinforced concrete members.

The precast SMA-reinforced ECC bridge column presented in this study, HCS, exhibited improved seismic performance over CIP since:

1. The displacement capacity of HCS was higher than that of CIP,
2. The plastic hinge damage of HCS was limited only to the cover concrete while the damage penetrated into the CIP core concrete,
3. HCS reached its ultimate capacities without any connection damage,
4. Residual displacement of HCS was substantially lower than that of CIP ensuring post-earthquake functionality of the bridge.

In summary, ABC columns with connection and details similar to HCS are expected to perform better than conventional columns in seismic zones.

3. Analytical Studies

3.1. SMA Material Model

A comprehensive literature review was carried out and series of tensile tests were performed by the authors or SMA manufacturer to define mechanical properties of NiTi superelastic SMA bars from structural engineering viewpoints, to develop SMA material model, and to propose design specifications for these types of reinforcements. Figure ES.10 shows the proposed material model. Key mechanical properties of reinforcing SMA were defined as:

- Observed yield strength (f_{yo}) is the stress at the initiation of nonlinearity on the first cycle of loading to the upper plateau.
- Austenite modulus (k_1) is the average slope between 15 to 70% of f_{yo}.
- Post yield stiffness (k_2) is the average slope of curve between 2.5% and 3.5% of strain on the upper plateau of the first cycle of loading to 6% strain.
- Austenite yield strength (f_y) is the stress at intersection of line passing through origin with slope of k_1 and line passing through stress at 3% strain with slope of k_2.
- Lower plateau inflection strength (f_i) is the stress at the inflection point of lower plateau during unloading from the first cycle to 6% strain.
- Lower plateau stress factor, $\beta = 1 - (f_i/f_y)$.
- Residual strain (ε_{res}) is the tensile strain after one cycle to 6% and unloading to 1 *ksi* (7 *Mpa*).
- Recoverable superelastic strain (ε_r) is maximum strain with at least 90% strain recovery capacity. Using the ASTM standard for tensile testing, $\varepsilon_r \leq 6\%$.
- Martensite modulus (k_3) is the slope of the curve between 8 to 9% strain, subsequent to one cycle of loading to 6% strain, unloading to 1 *ksi* (7 *MPa*) and reloading to the ultimate stress.
- Secondary post-yield stiffness ratio, $\alpha = k_3/k_1$.
- Ultimate strain (ε_u) is strain at failure.

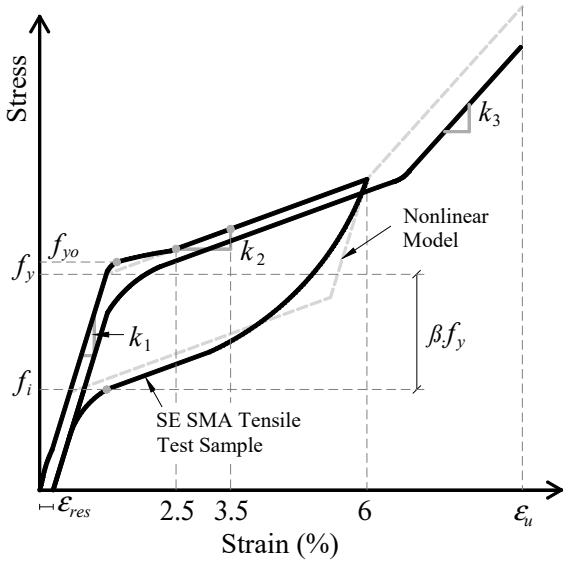

Figure ES.10 - NiTi SE SMA Nonlinear Model (Tazarv and Saiidi, 2014)

Using the proposed model, mechanical properties of reinforcing NiTi SMA were extracted from all available test data and design specifications were proposed as presented in Table ES.2. The average of test data was proposed as expected mechanical properties to be used in seismic design of SMA-reinforced concrete members. However, minimum mechanical properties were specified to be used in SMA material production.

Table ES.2- Minimum and Expected Reinforcing NiTi SE SMA Mechanical Properties (Tazarv and Saiidi, 2014)

Parameter	Tensile		Compressive, Expected[(b)]
	Minimum[(a)]	Expected[(b)]	
Austenite modulus, k_1	4500 *ksi* (31025 *MPa*)	5500 *ksi* (37900 *MPa*)	8900 *ksi* (61365 *MPa*)
Post yield stiffness, k_2	--	250 *ksi* (1725 *MPa*)	1400 *ksi* (9650 *MPa*)
Austenite yield strength, f_y	45 *ksi* (310 *MPa*)	55 *ksi* (380 *MPa*)	70 *ksi* (480 *MPa*)
Lower plateau stress factor, β	0.45	0.65	0.65
Recoverable superelastic strain, $_r$	6%	6%	3%
Secondary post-yield stiffness ratio, α	--	0.3	0.45
Ultimate strain, $_u$	10%	10%	10%

(a) To be used in reinforcing SMA production
(b) To be used in seismic design of SMA-reinforced concrete members

A parametric study was performed to investigate the effect of each mechanical property of SMA material model on moment-curvature, pushover, cyclic, and dynamic responses of SMA-reinforced bridge columns. It was found that variation of each mechanical property had individually minor effect on the seismic responses. Among the parameters, the response was generally more sensitive to the tensile properties. The cyclic and dynamic analyses showed that the austenite modulus (k_1), the austenite yield strength (f_y), and the lower plateau stress factor (β) are the more dominant properties of the reinforcing SMA model in controlling the calculated seismic response of SMA-reinforced columns. That is the reason for specifying the minimum mechanical properties for these parameters to ensure functionality of SMA-reinforced members under severe ground motions.

Even though including the compressive mechanical properties of the reinforcing SMA bars (asymmetric stress-strain model) resulted in better agreement between the calculated and measured responses, a symmetric stress-strain SMA model based on only the "expected tensile properties" (Table ES.2) is proposed for general analysis and design of SMA-reinforced concrete members because it is sufficiently accurate and it simplifies the analysis. Using a simple model for SMA is proposed to facilitate adoption of SMA in civil engineering applications.

3.2. Bond-Slip Modeling

Longitudinal bars slippage relative to the surrounding concrete when stressed under tensile forces is known as the bond-slip effect. The slippage usually affects the local and global response of RC members. In the present study, an efficient simple method was

developed using a modified stress-strain relationship for reinforcing steel fibers to implicitly include the bond-slip effect in response analysis. The method does not require additional elements or pre-nonlinear analysis and can be used in fiber-section analysis of RC members.

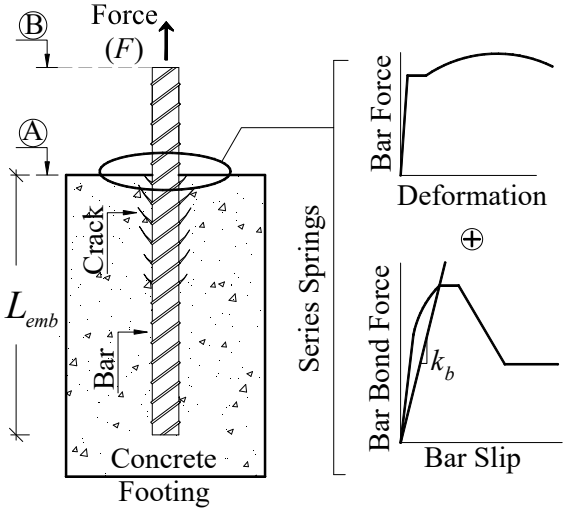

Figure ES.11- Bond-Slip Effect on Bar Stress-Strain in Conventional Connections

Figure ES.11 shows a schematic view of a single bar anchored in a conventional concrete connection. The effective strain of the bar at the surface of concrete (level A) can be calculated based on the combined deformation of the bar force-deformation spring and the bar bond force-slip spring in series. The modified strain of the bar (ε_s') is:

$$\varepsilon_s' = \varepsilon_s + (\frac{F}{k_b})/L \qquad \text{(Eq. ES.3)}$$

$$k_b = 78.5 d_d . L_{emd} . u \qquad \text{(Eq. ES.4)}$$

$$u = \begin{cases} \dfrac{9.5\sqrt{f'_c}}{d_b} \le 800\ psi, & for\ \#11\ bars\ and\ smaller \\ 6\sqrt{f'_c} & for\ \#14\ and\ \#18\ bars \end{cases} \qquad \text{(Eq. ES.5)}$$

$$L = \frac{F}{\pi . d_b . u} = \frac{f_s . d_b}{4u} \le L_{emb} \qquad \text{(Eq. ES.6)}$$

where ε_s is the strain of the bar (*in./in.*), F is the bar force (*lbs*), k_b is the bond force-slip stiffness (*lbs/in.*), d_b is the diameter of the bar (*in.*), L_{emd} is the embedment length of the bar in the connection (*in.*), u is the bond strength of the bar (*psi*), f'_c is the compressive strength of concrete (*psi*), L is the effective development length (*in.*), and f_s is the bar stress (*psi*). In the present study it is proposed to modify the modulus of elasticity of the bar to account for the softening effect of bond-slip on the overall bar stiffness:

$$E_s' = f_y / \varepsilon_y' \qquad \text{(Eq. ES.7)}$$

where f_y is the yield strength of the bar and ε_y' is the modified yield strain.

The proposed method may be used to account for the bond-slip effect in any reinforcing steel model. However, note that only strain-related parameters are modified. Figure ES.12 shows an example of original and modified reinforcing steel models using the proposed method for GCDP. It can be seen that the modified steel fiber stress-strain behavior including the bond-slip effect is softer than that of the original model with no bond-slip effect, as expected. The modified stress-strain steel material model may be used only in the fiber sections located at connections, and the original steel fibers may be used elsewhere. No extra fiber section or elements is needed and no preliminary analysis is required. Overall, it is recommended to use the proposed method in analytical modeling of RC members at which the bond-slip effect is significant because of its simplicity, generality, and ease of modeling.

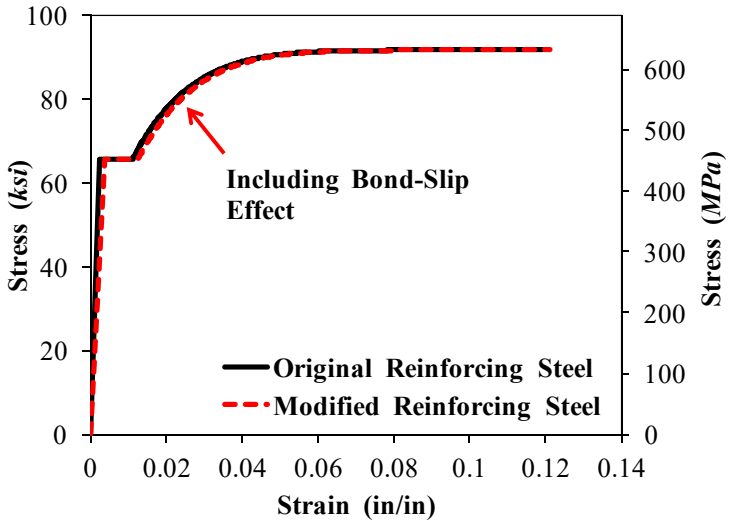

Figure ES.12- Bond-Slip Effects on Steel Fibers Used in GCDP Model

3.3. Bar Debonding Modeling

To help spread plasticity, the longitudinal bars were debonded at the connection region in the three column models investigated in this study. Debonding tends to soften the connection and hence should be included in analyses especially for the GCDP column model in which the debonded length was relatively long.

When a bar is debonded from concrete, the strain compatibility assumption between the bar and the surrounding concrete is not valid, thus making analytical modeling of debonded bars very complex. No study regarding modeling of debonded reinforcements in RC members was found in the literature. Therefore, a method was developed in the present study to include the bar debonding effect in response analysis of RC members using a modified stress-strain behavior for reinforcement.

Experimental studies have shown that the bond strength of plain bars is less than 30% of that of deformed bars (Mo and Chan, 1996; Verderame et al., 2009). A European design code recommends a plain bar bond strength of only 10% of the deformed bar bond strength (CEB-Fib Model Code, 1993). It was therefore decided to ignore the bond strength of plain bars in the present study. The bond behavior of debonded deformed

bars was assumed to be the same as the plain bar bond behavior with negligible bond strength. Thus, it can be assumed that behavior of a debonded bar embedded in concrete is similar to behavior of a bar that is not connected on its side surface to concrete. Level B shown in Fig. ES.11 illustrates this condition at which the bar is debonded from level A to B (or is free from level A to B). The modified strain of the debonded bar at level B is calculated based on cumulative displacements at this level, which consists of: (1) the bar deformation at level B assuming full bond (original bar force-deformation relationship), (2) displacement caused by the slippage of the bar at level A due to bond slip, and (3) the bar elongation at level A. The modified strain of the debonded bar (ε_s') at level B is:

$$\varepsilon_s' = \varepsilon_s + (\frac{F}{k_b}) / L + \varepsilon_{elong} \quad \text{(Eq. ES.8)}$$

where ε_{elong} can be found using Wehbe's method (Wehbe et al., 1997) as follows:

$$\varepsilon_{elong} = \begin{cases} \dfrac{\varepsilon_s}{2} & f_s \le f_y \\ \dfrac{\varepsilon_y}{2} + \dfrac{\varepsilon_s . L_1}{2L} & f_s > f_y \end{cases} \quad \text{(Eq. ES.9)}$$

$$L_1 = \frac{(f_s - f_y) d_b}{4u} \le L \quad \text{(Eq. ES.10)}$$

All parameters were defined in the previous section. The first two terms of Eq. ES.8 are the same as Eq. ES.3 terms. The third term in this equation is the additional strain at level B caused by the bar elongation at level A (Fig. ES.11).

Formulations regarding modeling of bond-slip and bar debonding effects in UHPC-filled duct connections were presented in Chapter 7.

3.4. Simulation of Pullout Tests

A one-dimensional finite element model was developed to simulate the pullout tests responses (Fig. ES.13). Three portions of the bar were modeled. "Stee02" material was used to model the steel bar in all segments. The embedded portion of the bar was divided into 99 elements attached to a series of nonlinear bar and duct bond-slip springs. This was done to determine the stress and strain distribution along the height of the bar. However, if global responses such as duct or bar force-slip are desired, only one bar element working in series with one bar bond-slip spring and one duct bond-slip spring is sufficient. "MultiLinear" material model was used in OpenSees (2013) to model the bar and duct bond-slip springs.

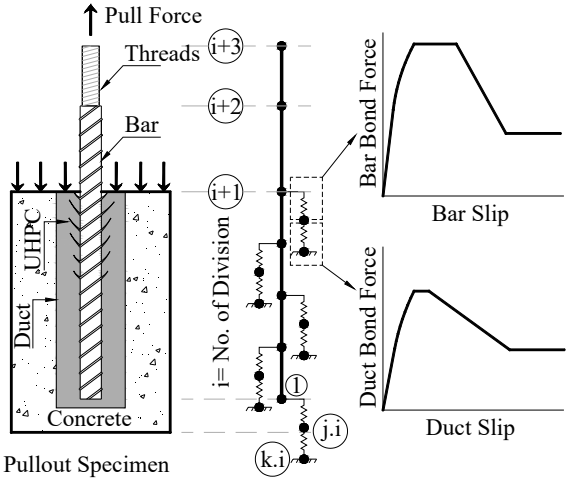

Figure ES.13- Finite Element Model for Pullout Tests (Tazarv and Saiidi, 2014)

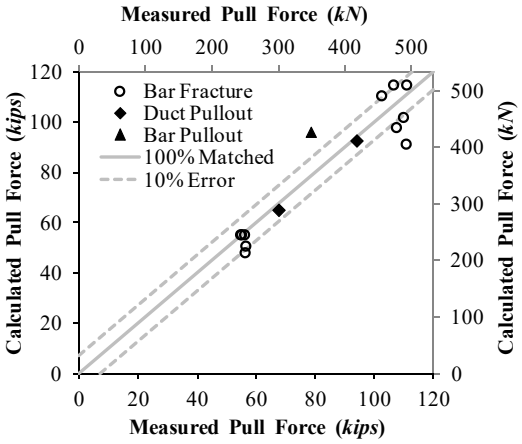

Figure ES.14- Measured and Calculated Pull Forces for Pullout Tests (Tazarv and Saiidi, 2014)

All 14 specimens were analyzed using the modeling method presented in the previous sections. The test day compressive strength of conventional concrete and UHPC, and the measured yield and ultimate strength of bars were used in analyses. Figure ES.14 shows the measured and calculated pull forces with a ±10% error band. Only in three specimens (group II specimens in which the bar bond behavior was investigated) the calculated pull force showed more than 10% error. The error between the measured and calculated pull forces was 7.7% on average with a standard deviation of 6.7%.

In summary, the proposed finite element model may be used for analyses of UHPC-filled duct connections for further bond study or seismic analysis of elements incorporating these types of connections.

3.5. Simulation of Column Tests

Three-dimensional finite element fiber-section models were constructed in OpenSees for all column models. Footings and column heads were modeled using elastic elements each with a stiffness calculated based on the test day compressive strength of concrete. Column elements were modeled with a force-based element, "forceBeamColumn", with at least five integration points. The test day compressive strength of column concrete was used for the unconfined concrete fibers. The Mander's model was utilized to determine the confined concrete model parameters. The peak axial load measured during each test was applied to each model, and the P-Δ effect was included. Reinforcing steel stress-strain relationship was modified in the first integration point located at the column base for all models to include bond-slip effects. Furthermore, modified behavior of reinforcements were incorporated in the second integration point of the GCDP and HCS analytical models to include bar debonding effects.

Figure ES.15 shows the measured and calculated pushover curves for all column models. Good correlation was observed for all models.

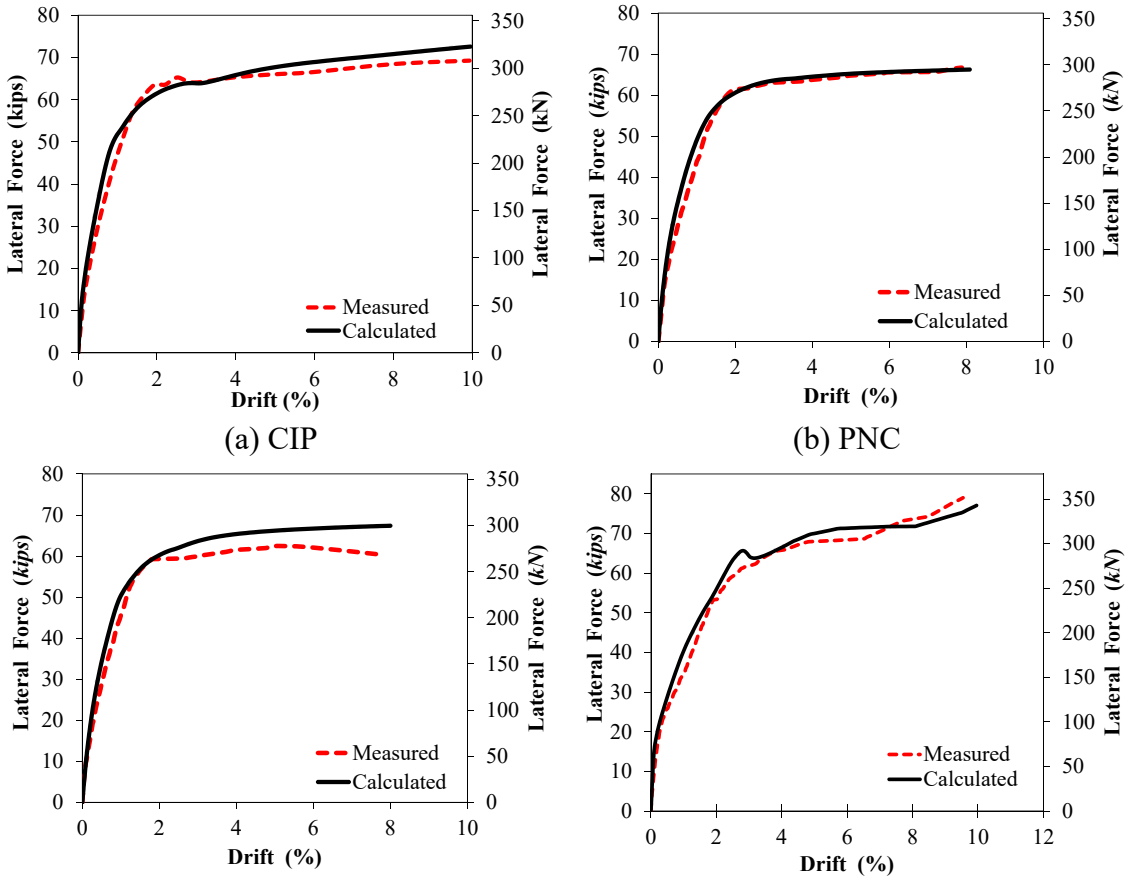

Figure ES.15- Measured and Calculated Pushover Curves for all Columns

4. Concluding Remarks

Findings from experimental and analytical studies on precast bridge column connections and low-damage materials used in critical areas of precast members led to the following conclusions:

1. Bond strength of deformed bars in UHPC is eight times higher than that in conventional concrete. This results in relatively low bar embedment length in UHPC-filled duct connections compared to conventional or grouted duct connections.
2. Duct bond strength, which was introduced in the present study, was found to control the UHPC-filled duct connection behavior and the required bar embedment length in these systems.
3. UHPC-filled duct connections incorporated in column-to-footing connections of two column model tests exhibited no damage even under 12% drift cycles.
4. Column model tests confirmed that UHPC-filled duct connections are emulative of conventional connections in which precast columns can be designed in accordance to current bridge codes with no limitations.

5. Detailing proposed in the present study for grouted coupler columns by shifting the couplers and debonding longitudinal bars in the plastic hinge ("GCDP" column details), improved the seismic performance compared to detailing investigated previously (Haber et al. 2013). The displacement capacity and displacement ductility capacity were increased by 47 and 56%, respectively. GCDP column displacement ductility was only 4% lower than the reference cast-in-place (CIP) column ductility.
6. Debonding was a successful technique to spread bar yielding and prevent premature failure of reinforcements in UHPC-filled duct connections and grouted coupler column pedestal.
7. The SMA-reinforced ECC column ("HCS") showed improved seismic performance over CIP. The plastic hinge exhibited substantially less damage than steel-reinforced concrete hinges. ECC damage was limited only to cover ECC even under 12% drift cycles. HCS column residual displacements were 79% lower than CIP residual displacements on average due to using NiTi superelastic SMA longitudinal reinforcement.
8. HCS column model test confirmed the feasibility of a new generation of precast columns in which columns can be built in a shorter time with better seismic performance and less post-event repair costs compared to conventional cast-in-place columns.
9. Analytical models presented for pullout tests and column model tests were found to be simple and sufficiently accurate. The models may be used for general design or analysis of these members and systems.
10. The proposed simple methods for taking into account bond-slip and bar debonding effects improved analytical model accuracy in the simulation of both global and local responses of column models.
11. The proposed reinforcing SMA material model used in the HCS column simulation resulted in good agreements between the calculated and the measured global and local responses. Parametric studies showed that a symmetrical stress-strain model based on the expected tensile mechanical properties is a viable alternative to the more realistic but complicated asymmetrical model.
12. It was found from parametric studies that the austenite modulus (k_1), the austenite yield strength (f_y), and the lower plateau stress factor (β) of the reinforcing SMA material model were the more dominant properties in controlling the calculated seismic response of SMA-reinforced columns. The response was more sensitive to the SMA tensile mechanical properties compared to compressive properties.

Overall, precast column connections proposed in the present study utilizing UHPC-filled duct connections and grouted coupler connections, as well as the low-damage plastic hinges were found to be viable alternatives to conventional connections or plastic hinges because they led to equal or improved seismic performance compared to conventional construction. UHPC-filled duct connections fully comply with current bridge codes. Even though using mechanical bar splices is prohibited in plastic hinge of reinforced members according to the most bridge seismic design codes, experimental findings from the present study showed that this limitation should be revisited and reevaluated in light of recent research data.

Table of Contents

List of Tables

List of Figures

Chapter 1: Introduction

1.1. Introduction

Both cast-in-place and precast construction techniques are utilized in bridges. Cast-in-place bridge construction has more than a century history in the United States. The first reinforced concrete bridge in the USA, Alvord Lake Bridge, was built in 1889 in San Francisco Golden Gate Park (Fig. 1.1) with a length of 29 *ft* (8.8 *m*) (Alvord Lake Bridge, 2014). More than half a century later, the first prestressed concrete bridge in the USA, Walnut Lane Memorial Bridge, was built (1951) in Philadelphia (Fig. 1.2), which had a span length of 160 *ft* (49 *m*) (Walnut Lane Memorial Bridge, 2014). Cast-in-place construction method is still popular in the USA (Fig. 1.3). Prefabricated bridge construction, in contrast, utilizes precast components that generally requires more rigorous planning, new technology, and improved construction methods because of tighter required tolerance.

Accelerated bridge construction (ABC) makes extensive use of prefabricated components and offers many advantages over conventional construction: reduction of onsite construction time, reduction of total project delivery time, potential reduction of total cost, improvement of safety of highway workers and public traffic, and improvement of quality of component materials (Culmo, 2011).

Many bridges constructed in the past were built in low-populated, low-traffic, and even open areas with minimum traffic impact. However, rehabilitation, replacement, and even construction of new bridges inevitably interrupt traffic and adversely affect the economy of the region mainly because of traffic congestion and the potential need for detours. According to the Federal Highway Administration (FHWA), approximately one-fourth of 600,000 bridges in the USA require rehabilitation, repair, or total replacement. That has led to FHWA-initiated programs such as Every Day Counts (EDC) and Highways for LIFE (HfL) to make longer-lasting bridges in a shorter time. Many state transportation agencies have also initiated their own ABC programs.

Five components of ABC were recognized by FHWA: (1) foundation and wall elements, (2) rapid embankment construction, (3) prefabricating bridge elements and systems (PBES), (4) structural placement methods, and (5) fast tracked constructing (Culmo, 2011). Among those, only PBES is focused in the present study.

PBES is the most common form of ABC and has been implemented in bridge construction since 1951, when the first prestressed bridge in the USA (Fig. 1.2) was built. PBES has been widely used in non- and low-seismic regions in super- and sub-structures. However, application of ABC in high seismic areas, especially for substructure elements, has been scarce due to uncertainly in seismic performance of precast member connections. Thirty-six states have at least some parts that are considered to be moderate

and high seismic zones (Marsh et al., 2011). Exploring new ABC connections suitable for high-seismic zones is appealing not only for seismic prone states but also for moderate-seismic states because of the many advantages of ABC.

1.2. Previous Studies and Applications

Many bridge substructure and superstructure components can be built precast. Connections of those components in seismic areas, however, are critical for ABC applications since those connections should allow for large deformations of adjoining members while resisting ultimate loads of the members. This is even more challenging for bridge columns since these elements are allowed by the most design specifications to undergo high nonlinearity. Because ABC for bridge columns is the focus of the present study, a summary of laboratory investigations and field applications on the topic is presented in this section.

Seismic performance of seven types of precast column connections in moderate and high seismic regions was evaluated by Marsh et al. (2011): (1) bar couplers, (2) grouted ducts, (3) pocket connections, (4) member socket connections, (5) hybrid connections, (6) integral connections, and (7) emerging technology.

1.2.1. Bar Coupler Connections

Bar couplers are to provide a shorter splice length over conventional splices but with a proper detailing they may be used in ABC to connect precast segments or members. Several types of mechanical bar splices are available in the market. The most common types are illustrated in Fig. 1.4. Many of these products satisfy minimum limitations that were set by current US design specifications.

Grouted bar couplers are more common than the other types in the bridge industry. The Utah Department of Transportation (UDOT) has developed a ABC design manual for substructure incorporating these couplers (Utah DOT Precast Substructure Elements Manual, 2010). Furthermore, these couplers were incorporated in precast column to cap beam connections of the Edison bridge (Fig. 1.5) in Florida (Culmo, 2009).

A comprehensive literature review on the performance of bar couplers was conducted by Haber et al. (2013). Two types of couplers, headed bar couplers and grouted sleeve couplers, were selected for further investigations by performing monotonic and cyclic tensile tests. Both coupler types showed satisfactory performance. Then, these couples were incorporated in half-scale column models to connect precast columns to footings. Two column models were built with each coupler type (Fig. 1.6). The bar coupler connection was shifted using a precast pedestal in two column models to reduce moment over the coupler region. Slow reversed cyclic tests on the precast columns as well as a reference cast-in-place column (CIP) showed that the headed bar coupler columns were emulative of CIP, which exhibited a 10% drift ratio capacity and a displacement ductility capacity of seven. Emulative is defined as a feature that utilizes conventional design with

no additional considerations at the design stage and leads to performance that is the same or nearly the same as that of cast-in-place. Even though the strength capacity of the grouted coupler column models was the same as the CIP strength, the drift capacity of these columns was 6% due to strain concentration outside the couplers or the precast pedestal.

Ameli et al. (2014) tested four precast half-scale columns connected to footings or cap beams incorporating grouted couplers connections. Couplers were utilized either in column plastic hinge immediately above the column to adjoining member interface or inside the adjoining member. Normal grouted couplers (Fig. 1.4e left) were used in two column-to-footing connections in which bars were grouted at both coupler ends. Modified grouted couplers were incorporated in two column-to-cap beam connections in which one end of couplers was threaded to reduce coupler size (Fig. 1.4f). These columns exhibited displacement ductility from 4.4 to 6.1 in cyclic tests. Columns with modified grouted couplers showed lower displacement ductility than columns with normal couplers by 5 to 26%. Columns with couplers embedded in adjoining members showed higher displacement ductility compared to columns with couplers inside the plastic hinge. The ductility increase was 3% for normal coupler columns but 32% for the column with modified couplers.

1.2.2. Grouted Duct Connections

Precast members can be connected with grouted duct systems in which member longitudinal reinforcements are anchored in ducts placed in an adjoining member then the ducts are filled with grout. A comprehensive literature review regarding bond strength and seismic performance of these types of connections is presented in the next chapter. Grouted duct systems were incorporated in a few bridges in Texas (Brenes et al., 2006) and Washington (Khaleghi et al., 2012) to connect columns to cap beams (Fig. 1.7).

1.2.3. Pocket Connections

In pocket connections, precast member longitudinal reinforcements are anchored in a single pocket placed in an adjoining member, then the pocket is grouted. Bond performance of bars in pocket systems was investigated by Matsumoto et al. (2001). After observing satisfactory performance, they incorporated pocket systems in two column-to-cap beam connections and tested. Similar strength and ductility capacity compared to a cast-in-place model was observed. Seismic performance of a 42%-scale bridge column model connected to a cap beam using a pocket connection (Fig. 1.8) was experimentally investigated by Restrepo et al. (2011). Under cyclic loading, the specimen showed a displacement ductility capacity of eight, which was 20% lower than a reference cast-in-place model.

Motaref et al. (2011) tested a two-column bent at the University of Nevada, Reno (UNR) in which each column was connected to the footing using pocket connections (Fig. 1.9). Engineered cementitious composite (ECC) was incorporated in the plastic

hinge of one of the columns and another column was built with a fiber reinforced polymer (FRP) tube filled with concrete. Both columns were embedded in the footing with a length of 1.5 column diameter. The embedded part of the column with ECC was constructed using conventional concrete. The precast bent showed large displacement capacity under shake table testing, and no connection damage was observed. Other cyclic and shake table studies at the University of Nevada, Reno (UNR) on precast members with pocket connections confirmed that full moment response can be expected from these connections making them suitable for high seismic regions (Kavianipour and Saiidi, 2013; Mehrsoroush and Saiidi, 2014).

1.2.4. Member "Socket" Connections

A length of a precast member is anchored in an adjoining member in socket connections. Connections are completed by either grouting the socket or casting the adjoining member in-place. It is obvious that the precast member embedment length is a key parameter in the performance of these types of connections.

Matsumoto et al. (2001) and Restrepo et al. (2011) performed similar experimental studies as described in the previous section on this type of connections. Similar bond and seismic performance compare to conventional connections was reported. Haraldsson et al. (2012) tested three large-scale columns connected to spread footings using this type of connections. In the first two models, the footing depth (or column embedment length) was approximately equal to the column diameter but the footing depth in the third model was one-half the column diameter. The column side surface under the column-footing interface was roughened in a sawtooth pattern in all three models. The cyclic tests showed the connection might be considered to be emulative if the column embedment length is at least one column diameter. To demonstrate feasibility in the field, a bridge was built in the State of Washington using this connection type (Fig. 1.10). The column embedment length in the bridge was 1.2 time the column diameter. In this project, columns were secured then the footing was cast.

1.2.5. Hybrid Connections

Connection of two members or sections in hybrid systems is provided by prestressing tendons as well as mild steel reinforcements. Hybrid denotes incorporation of two reinforcing materials in the system, tendon and mild steel. Tendons provide stability of the structure and increase self-centering tendency. Reinforcements are added to these connections to increase the overall energy dissipation of the system by yielding. Flag-shape hysteretic responses with small residual displacements are usually observed in these systems. High performance materials may also be incorporated at rocking joints to minimize the damage.

Seismic performance of precast columns incorporating these connections was experimentally investigated in a few studies. Billington and Yoon tested seven 1/6-scale precast segmental columns with hybrid configurations, six of which had ECC plastic

hinges. Cyclic tests showed that pretensioning tendons yielded at 9% drift ratio. ECC increased the energy dissipation of the systems compared to conventional concrete precast model and minimized the plastic hinge damage. Marriott et al. (2006) tested three 1/3-scale hybrid bridge columns. Steel plates were used at the rocking interface to minimize concrete damage. Minimal residual displacements and minimal plastic hinge damage were observed in cyclic and dynamic testing. Similar behavior was found in other experimental studies performed by Wang et al. (2008) and Motaref et al. (2011).

1.2.6. Integral Connections

Precast members are connected in an integral connection with no joint or articulation to form a moment-resistant connection. Integral connections are usually cast-in-place but a portion of the connections may be precast to facilitate construction. For example, a cap beam can be built in two lower and upper segments (Fig. 1.11). The lower segment can be connected to precast columns with one of the abovementioned ABC connections and the upper segment can be cast after securing the precast beams and deck systems on the lower segment of the cap.

1.2.7. Emerging Technology

Novel, advanced, or low-damage materials may be used in precast member connections to facilitate construction, minimize damage, improve serviceability of structure after an event, and reduce repair costs. At the time of this writing, only two experimental studies conducted at UNR are found as emerging technology connections suitable for ABC. Motaref et al. (2011) tested a 1/3-scale precast segmental column in which elastomeric rubber pad was incorporated in the plastic hinge instead of concrete (Fig. 1.12). The drift capacity of this column was 14% in shake table testing under 150% Sylmar ground motion recorded in 1994 Northridge earthquake. Higher displacement capacity, higher strength, and lower damage were observed compared to a reference segmental column cast with conventional concrete.

A futuristic study is underway at UNR in which bridge columns can be fully detached after an event or end of the useful life of the bridge. The components then can be recycled in other bridges (Varela and Saiidi, 2013). Columns were built in two segments: (1) plastic hinge segment, and (2) elastic segment (Fig. 1.13). The plastic hinge is made with either elastomeric rubber or ECC pad element with holes to accommodate longitudinal reinforcements. Two types of shape memory alloys (SMAs) were used as reinforcements in plastic hinges. Reinforcing SMA bars were connected to the footing using threaded couplers and the plastic hinge was then secured before SMA bars were tightened at the top. Finally, the elastic segment, which is made with FRP tube filled with conventional concrete, was connected to a steel plate that was connected to the pad with shear studs. Shake table testing of large-scale columns built with this configuration proved that this innovative technique can be used as an alternative to conventional construction with improved seismic behaviors.

1.3. Low-Damage Materials

Application of engineered materials such as concrete and steel in civil engineering structures dates back to a century ago. Concrete has negligible tensile strength with low compressive and tensile ductility, and steel exhibits large permanent deformations upon yielding and is susceptible to fatigue and corrosion. Despite these deficiencies, concrete and steel are the main construction materials and can be found almost in all civil structures. New materials are emerging to overcome these shortcomings of steel and concrete and enhance the overall performance of structures under different environmental conditions and loading. Three advanced materials that exhibit low-damage behavior even under large loads are of interest in this study: (1) ultra-high performance concrete (UHPC), (2) ECC, and (3) SMA. A summary on development and application of these materials is presented.

1.3.1. Ultra-High Performance Concrete (UHPC)

UHPC was defined as a concrete with discontinuous fibers that has a minimum specified compressive strength of 22000 *psi* (150 *MPa*) with specified durability, tensile ductility and toughness requirements (ACI Committee 239, 2012). UHPC is made of very fine aggregates, a range from micron to less than one millimeter (0.04 inch), steel fibers usually with a dose of 2-2.5% by volume (Fig. 1.14), and a low water to cement ratio (0.22 for Ductal®). Ductal® is the most common type of UHPC being used in North America.

The measured compressive stress-strain curves for unconfined field-cast UHPC are shown in Fig. 1.15a for different ages. It can be seen that the rate of gaining strength in the first few days for UHPC is high. The UHPC compressive strength after 48 hours of casting is more than 8000 *psi* (60 *MPa*), which is higher than the ultimate strength of conventional concrete. A sample of measured UHPC complete compressive stress-strain relationship is illustrated in Fig. 1.15b. The graph shows that the ultimate compressive strain of UHPC is significantly higher than that of conventional concrete (approximately 3.5 times) due to confining effect of internal steel fibers. The tensile strength for the field-cast UHPC is usually 900 *psi* (6.2 *MPa*), which is sustained over a wide tensile strain range from the concrete first cracking to 0.8% (Graybeal, 2006; Gowripalan and Gilbert, 2000). Figure 1.16 illustrates the measured and an idealized tensile stress-strain curves for UHPC. It can be seen that UHPC exhibits a relatively large tensile ductility. A state-of-the-art literature review on the development, properties, and worldwide applications of UHPC was conducted by Russell and Graybeal (2013). Table 1.1 presents a range for each UHPC material property as well as design equations that were extracted from the report. The properties presented in the table are mainly for Ductal®.

UHPC has been incorporated in many structures worldwide, two examples of which are shown in Fig. 1.17. UHPC in the commercial form has been available in the USA since 2000. UHPC has been incorporated in more than 50 bridges in the North America, mainly in bridge superstructure elements such as precast deck-to-deck connections.

Three design guidelines and construction recommendations are available at the time of this writing for UHPC: (1) Design Guidelines for Ductal Prestressed Concrete Beams (Australia) (Gowripalan and Gilbert, 2000), (2) Recommendations for Design and Construction of Ultra High Strength Fiber Reinforced Concrete Structures by the Japan Society of Civil Engineers (Russell and Graybeal, 2013), and (3) Ultra High Performance Fiber-Reinforced Concretes, Interim Recommendations prepared by AFGC (French Association of Civil Engineers) and SETRA (French Road and Traffic Government Agency (SETRA-AFGC, 2002). The later document was revised to conform to the latest version of the Euro Code and was published in 2013 as design recommendations for UHPC.

1.3.2. Engineered Cementitious Composite (ECC)

Similar to UHPC, ECC is another class of high performance fiber reinforced concrete with significant tensile ductility. There is no coarse aggregate in the ECC matrix and polyvinyl alcohol (PVA) fibers with 2% volumetric ratio are usually used in ECC mix design. What makes ECC different form UHPC is its fiber functionality and tensile ductility. High strength fibers are added to UHPC matrix to provide ductility for the densified matrix and increase both tensile and compressive strength. Fibers in ECC are to maximize the tensile ductility by developing multiple microcracks (Li, 2008). This is achieved by coating the fiber in which surface coating allows the fiber to slip partially when it is over loaded thus preventing fiber fracture and leading to hairline cracks instead of wide cracks.

Typical compressive and tensile stress-strain curves for ECC are shown in Fig. 1.18 (Li and Fischer, 2003). A significant tensile ductility (4% strain) and a larger compressive ductility than conventional concrete can be observed in ECC. A range for ECC major mechanical properties are presented in Table 1.2. Motaref et al. (2011) developed a constitutive stress-strain model for confined ECC (Fig. 1.19).

Li (2008) presented a summary of experimental studies investigating the seismic performance of ECC structural components. Performance of ECC bridge columns was investigated in a few studies (Saiidi and Wang, 2006; Saiidi et al., 2009; Motaref et al., 2011; Cruz and Saiidi, 2012; Nakashoji et al., 2013; Varela and Saiidi, 2013; Mehrsoroush and Saiidi, 2014). All studies showed low damage with minimal post-event repair need for ECC. Regarding the field application of ECC, Washington Department of Transportation has designed and plans to construct the first SMA-ECC bridge in the world in Seattle at the time of this writing (SR99 SMA-ECC Bridge, 2014). The Japan Society of Civil Engineers has developed design recommendations for ECC (JSCE Concrete Library 127, 2008).

1.3.3. Shape Memory Alloy (SMA)

SMA is a class of metallic materials with an ability to recover its original shape upon unloading (superelastic effect) or heating (shape memory effect). Solid-solid

transformations between two material phases, martensite and austenite, give these unique properties to SMA (Otsuka and Wayman, 1998). SMA is usually in one of the stable martensite or austenite phases. The martensite phase is seen when the temperature is low. When heated, SMA transforms to the austenite phase. This phase transformation is illustrated in Fig. 1.20 (Wilson and Wesolowsky, 2005). A three-dimensional stress-strain-temperature relationship for SMA is shown in Fig. 1.21 (McCormick, 2006). It can be seen that SMA exhibits large permanent deformations at low temperature. However, superelastic behavior is dominant at and above the austenite finish temperature (A_f). In superelastic stage, SMA usually exhibits a flag-shape behavior with negligible residual strains.

SMA in the present form was developed by Buehler and Wiley (1961) at the Naval Ordnance Laboratory. Since this SMA was composed of Nickel and Titanium (NiTi) alloys, it has been frequently referred to as Nitinol, an acronym for Nickel Titanium Naval Ordnance Laboratory (DesRoches and Smith, 2003). Since then several other SMA alloys have been developed such as Ag-Cd, Au-Cd, Cu-Zn, Cu-Zn-Al, Cu-Al-Ni, Fe-Mn, Mn-Cu, Fe-Pd, Cu-Zn-Al-Mn-Zr, Cu-Al-Be, Ti-Ni-Cu, Ti-Ni-Hf, and Ni-Ti-Fe, Research is underway to explore new alloys such as Ferrous Polycrystalline and Cu-Al-Mn SMAs. Alam et al. (2007) presented chemical compositions and mechanical properties of some of the abovementioned SMA alloys. Among those alloys, NiTi SMA has gained more attention since it exhibits a large superelastic strain recovery, high energy dissipation, excellent low- and high-cycle fatigue properties, and excellent corrosion resistance (DesRoches and Delemont, 2002). Because of these properties, only NiTi SMA was considered in the present study.

SMA has been widely used in medical, aerospace, and industrial applications (Machado and Savi, 2003; Tarnita et al., 2009, Wu and Schetky, 2000). Figures 1.22 and 1.23 illustrate some of those applications. SMA has also been implemented in structural applications in recent years. Reviews of SMA structural implementations were presented in DesRoches and Smith (2003), Wilson and Wesolowsky (2005), Song et al. (2006), Alam et al. (2007), and Dong et al. (2011). SMA has been utilized in a few studies as reinforcements in concrete members. The first of such studies was on beams by Ayoub et al. (2003) and Saiidi et al. (2007). Saiidi and Wang (2006), Youssef et al. (2008), and Saiidi et al. (2009) subsequently showed that reinforcing SMA can substantially reduce other concrete member residual displacements even under large deformations.

Many parameters affect stress-strain behavior of SMA: (1) temperature, (2) loading type, (3) number of loading cycles, and (4) strain rate. Chapter 6 of the present study is dedicated to SMA material behavior, analytical model, and design specifications for reinforcing SMA bars.

Figure 1.24 shows a typical stress-strain relationship for a NiTi superelastic #10 (Ø32 *mm*) reinforcing SMA bar as well as a #8 (Ø25 *mm*) reinforcing steel bar. It can be seen that the SMA exhibited slightly lower yield strength but higher ultimate strength compared to the reinforcing steel. Furthermore, the SMA bar showed negligible residual strain even under 6% strain cycle. Steel bars exhibit large permanent strains after yielding (Tazarv and Saiidi, 2014).

NiTi SMA shows an excellent corrosion resistance which is due to the formation of a passive Titanium Oxide layer, which limits surface diffusion over time (DesRoches and Delemont, 2002). Galvanic corrosion tests of NiTi SMA showed that SMA is the anode. In general, metal at the anode corrodes first preventing corrosion of metal at the cathode. Tests on NiTi SMA (as anode) and gold (as cathode) couple showed no evidence of corrosion in either metals (Carroll and Kelly, 2003). Therefore, corrosion of neither NiTi SMA nor steel is expected when SMA and steel bars are coupled as reinforcements.

Welding process is difficult for NiTi SMA since SMA may become brittle by reacting to oxygen, nitrogen, and hydrogen at high temperature. Figure 1.25 illustrates stress-strain relationship of a NiTi SMA base specimen and a laser-welded specimen (Schlossmacher et al., 1997). It can be seen that both strength and strain capacities of the SMA specimen were adversely affected by welding. Even though laser and other types of welding such as plasma and Tungsten inert gas (TIG) have been used in SMA industry, welding of reinforcing SMA to reinforcing SMA or welding of other materials to reinforcing SMA such as steel spirals is not recommended in structural engineering applications.

1.4. Objectives and Scope

The main objective of the present study was to develop a new generation of bridge columns that can be built in a relatively short time than conventional construction with seismic performance that is equal to or exceeds conventional column performance. New ABC connections were developed to facilitate construction and low-damage materials were incorporated in the connections and critical areas to reduce the damage.

A series of fourteen pullout tests was performed to develop reliable UHPC-filled duct connections and develop methods to estimate the bond strength and deformation of these connections. Tensile tests was carried out to optimize reinforcing SMA bar performance connected to reinforcing steel bars with mechanical headed bar splices. Three half-scale column models each with either an innovative ABC connection or low-damage materials were constructed and tested at the Large Scale Structural Laboratory at the University of Nevada, Reno (UNR). In two models, precast columns were connected to footings using UHPC-filled duct connections. Mechanical grouted sleeve bar splices were incorporated in the last column model as a ABC connection. ECC and SMA were utilized in plastic hinge of one of two columns with UHPC-filled duct connections to reduce the damage and improve the overall performance.

Analytical investigation for each column model and pullout tests was performed using a finite element computer program. New methods were developed to include bond-slip effects and bar debonding effects in analytical modeling of reinforced concrete members. A design specification was proposed for reinforcing NiTi superelastic SMA bars. A parametric study was also performed to determine which mechanical properties of reinforcing SMA bars have the most effect on the overall seismic performance of SMA-reinforced bridge columns. Design recommendations were developed for a new generation of precast bridge columns.

1.5. Document Outline

The document starts with an introduction to accelerated bridge construction techniques and performance of low-damage materials. Bond behavior for UHPC-filled duct connections is presented in Chapter 2 in addition to the design equations and bond-slip models that are developed for these connections. Design procedure, structural detailing, testing protocols for all three bridge column models as well as reinforcing SMA bar tensile tests are described in Chapter 3. Column test results for each individual model are presented in Chapter 4. Evaluation of column model performance by comparing the seismic behavior with a reference cast-in-place column model is presented in Chapter 5. Reinforcing SMA mechanical properties are defined in Chapter 6, and design specifications were proposed for SMA bars. Analytical modeling of pullout tests and column model tests are included in Chapter 7. New methods to include bond-slip effects and bar debonding effects in analyses of reinforced concrete members are described in this chapter. A parametric study on the performance of SMA-reinforced bridge columns using moment-curvature, pushover, cyclic, and dynamic analyses is described in Chapter 8. Chapter 9 includes design considerations for a new generation of bridge columns to facilitate their applications in actual bridges. A summary of findings and conclusions are presented in Chapter 10.

Chapter 2: Bond Study of UHPC-Filled Duct Connections

2.1. Introduction

The main advantages of accelerated bridge construction (ABC) were mentioned in the previous chapter. Prefabricated elements are the essence of ABC. Connections of the prefabricated elements to adjacent members are challenging, especially column connections are more critical since they should undergo severe nonlinear actions under seismic loads while maintaining structural integrity. Seven possible types of precast RC bridge column connections suitable in moderate and high seismic zones were introduced in the Chapter 1. One of those is grouted duct system that has been experimentally tested and deployed in column-cap beam connection in actual bridges. Cap beams are usually sufficiently deep to accommodate column longitudinal bars in grout-filled ducts. However, to connect precast columns to shallow cap beams or footings, an alternative method is required.

Seismic performance of ultra-high performance concrete (UHPC) filled duct connection was investigated at the University of Nevada, Reno (UNR) in two phases. In the first phase, fourteen specimens were tested under tensile loading to determine bond strength of UHPC-filled duct system. In the second phase, a half-scale RC bridge column incorporating this type of connection was tested under slow cyclic loads. In this chapter, bond testing and results of phase one are presented. The column details and test results are presented in the following chapters.

2.2. Previous Studies

2.2.1. Bond Strength

Bond between reinforcing bar and concrete controls performance of reinforced concrete structures. Loads can be transferred between deformed bar and concrete through three mechanisms: (1) chemical adhesion, (2) frictional force arising from the roughness of the interface, and (3) mechanical anchorage or bearing of the ribs against the concrete surface (ACI408R-03, 2003). Figure 2.1 shows the bond force transfer mechanism of deformed bars in concrete. When bar is stressed, adhesion force is lost by slippage while frictional force on the ribs and barrel of the bar are reacting. As slip increases, principal load carrying mechanism is bearing of ribs against the concrete surface. Reaction of the bar forces is also resisted by the surrounding concrete (Fig. 2.2). The reacting tensile and compressive forces on the concrete around the ribs cause cracking.

Bond stress along the member is nonlinear even under pure tensile loads. One source of nonlinearity is the local concrete cracking at areas around the ribs. In Fig. 2.3, stress distribution of a well-anchored bar as well as bond stress along the embedment length of well-confined specimens are illustrated. It can be seen that bond stress also varies along the length of member. Theoretically, it can be shown that under pure tensile loads, bond stress is related to the rate of change of the stress in the reinforcement (Abrishami and Mitchell, 1992). But for design purpose, it is more practical to assume uniform bond stress (u) along the embedment length that is defined as ratio of force to surface area of the embedded bar (Fig. 2.3). In ACI 318-63, bond strength is calculated as follows:

$$u = 9.5\frac{\sqrt{f'_c}}{d_b} < 800\ psi \tag{2-1}$$

$$u = 20\frac{\sqrt{f'_c}}{d_b} < 5.52\ MPa \tag{2-1 SI}$$

where f'_c (*psi* or *MPa*) is compressive strength of concrete and d_b (*in*. or *mm*) is bar diameter.

2.2.2. Grouted Duct Connections

Grouted duct column-cap beam connection has been experimentally tested and deployed in actual bridges in the United States. Eight pullout tests were carried out at the University of Texas, Austin to determine bond strength of grout-filled duct system (Matsumoto et al., 2001). Epoxy-coated #11 (Ø36 *mm*) bars were embedded in 4-*in*. (102-*mm*) diameter corrugated steel ducts filled with standard grout. Two of those bars were headed. Effect of embedment length, grout brand, and bar anchorage (straight or headed bars) was investigated on the bond behavior. Figure 2.4 shows photographs of the connection. Table 2.1 presents the test matrix and summary of the results. The measured bond strengths, u, are also included in the table.

The bars with 12-*in*. (305-*mm*) embedment length exhibited pullout failure, characterized by development of splitting cracks in the surrounding concrete and pullout of the bar-grout mass from the duct. The bar in VD04 that had the minimum compressive grout strength was also pulled out. In other specimens, the maximum tensile force was restricted by either test setup limitation or bar fracture. The average bond strength of straight bars in the grout-filled duct connection was 1264 *psi* (8.7 *MPa*) with a standard deviation of 220 *psi* (1.5 *MPa*). Normalized bond strength is defined as ratio of the bond strength to the square root of compressive strength of concrete. The normalized mean bond strength for straight bars was 17 $psi^{0.5}$ (1.41 $MPa^{0.5}$) with a standard deviation of 3 $psi^{0.5}$ (0.25 $MPa^{0.5}$). Note that compared to the Eq. 2-1 for #11(Ø36 *mm*) bar, the normalized bond strength of grout-filled duct system is 2.5 times stronger than conventional connections.

In the next step, a full-scale precast cap beam was connected to a column incorporating the grout-filled duct system (Fig. 2.5). The column was reinforced longitudinally with 4 epoxy-coated #9 (Ø29 *mm*) bars and transversely with #3 (Ø10 *mm*) spiral spaced at 4 *in*. (102-*mm*) resulting in longitudinal and transverse steel ratio of 0.57% and 0.46%, respectively. The column diameter and clear height were 30 *in*. (762

mm) and 2 *ft* (610 *mm*), respectively. The embedment length was 15 *in*. (381 *mm*). Two vertical and one horizontal rams were used to obtain load-deflection of connection at service and failure levels under different moment demands. Test results showed that the grout-filled duct connection exhibited similar load-deflection relationship to the cast-in-place model with expected strength, ductility, and bar anchorage. Only minor distress developed in the connection.

Another 32 pullout tests were carried out by Brenes et al. (2006) at the University of Texas, Austin. The test specimens were similar to the specimens in the aforementioned pullout study but embedment length, duct material, number of ducts, bar coating, and bar eccentricity in the ducts were investigated. Three types of 4-*in*. (102-*mm*) diameter ducts were used: corrugated galvanized strip metal duct, corrugated high-density polyethylene (PE) duct, and corrugated polypropylene (PP) duct. Three embedment lengths, $8d_b$, $12d_b$, and $16d_b$, were used where d_b is bar diameter. Grade 60 uncoated and epoxy-coated deformed #11 (Ø36 *mm*) bars conforming to ASTM A615 were used. Normal strength grout, 5800 *psi* (40 *MPa*) in 28 days, was used to fill the ducts.

All of the 32 specimens failed due to the bar pullout. Test results showed that initial stiffness of bond-slip curves and ultimate bond strength of galvanized steel duct (GS) was greater than those of the plastic ducts (PE and PP) with the same embedment length. An example of bond-slip relationship of different ducts with $8d_b$ embedment length is shown in Fig. 2.6. The embedment length had minor effect on the initial stiffness of the system. Substantial reduction of the bond strength was observed in multiple duct tests while the initial stiffness exhibited minor variations. For example, 25% reduction of bond strength was observed in double-GS-duct system compared to single-GS-duct connection. Test results also confirmed that the duct spacing in multiple duct connections had minor effect on the bond-slip relationship. The clear duct distances were $1d_d$ and $2d_d$ where d_d is duct diameter. Bar eccentricity had minor effect on the initial stiffness but reduced the bond strength by 17%. The other test variables had negligible effect on the bond strength of grout-filled duct system.

Test result of the galvanized steel duct connections showed that for almost all the tests the grout fractured before duct seams opened 3 *in*. (76 *mm*) or more below the surface. Example of this type of failure is shown in Fig. 2.7. The lack of sufficient tensile strength of grout can be the cause of the failure. In the plastic ducts, other types of failure such as slippage of grout relative to the duct, bar pullout with partial grout pullout, and bar pullout with complete grout pullout were also observed.

The authors proposed a design equation for embedment length (l_d) of bar in the grout-filled duct connection as follows:

$$l_d = \max\left(8d_b, 12\ in., \frac{\beta f_y d_b}{180\gamma\sqrt{f'_c}}, \frac{\beta f_{s,cr} d_b}{45\gamma\sqrt{f'_c}}\right) \quad (2\text{-}2)$$

$$l_d = \max\left(8d_b, 305\ mm, \frac{\beta f_y d_b}{14.95\gamma\sqrt{f'_c}}, \frac{\beta f_{s,cr} d_b}{3.74\gamma\sqrt{f'_c}}\right) \quad (2\text{-}2\ SI)$$

where d_b (*in*. or *mm*) is bar diameter, f_y (*psi* or *MPa*) is specified yield stress of bar, $f_{s,cr}$ (*psi* or *MPa*) is the calculated tensile stress in bar corresponding to the critical load combination, f'_c (*psi* or *MPa*) is the specified compressive strength of concrete, β is a

modification factor for duct material taken as 1.0 for galvanized steel duct and 1.3 for plastic duct, and γ is a modification factor to account for group effects, calculated based on the number of ducts subjected to simultaneous tension under the design load combination.

Restrepo et al. (2011) carried out a series of 42%-scale column-cap beam connection tests incorporating different ABC techniques suitable for seismic zones (Fig. 2.8). One of those specimens utilized grout-filled duct (GD) system. In the GD specimen, closely spaced 1.75-*in* (45-*mm*) diameter, 22-gage (0.028 *in*. or 0.71 *mm*) corrugated ducts were used in the bent cap filled with high-strength, non-shrink, cementitious grout to anchor the column longitudinal reinforcement. The column diameter was 20 *in*. (508 *mm*). The column was reinforced longitudinally with 16-#5 (Ø16 *mm*) bars (ρ_l=1.58%) and transversely with #3 (Ø10 *mm*) hoops spaced at 1.5 *in*. (38 *mm*) (ρ_s=1.73%). The column height was 45 *in*. (1.14 *m*). Test results of cyclic loading showed that the GD model is emulative of a cast-in-place model with stable hysteretic behavior without appreciable strength degradation. A displacement ductility capacity of 8 was achieved in the GD model that was 80% of that of the cast-in-place model.

Seventeen pullout tests of large-diameter bars embedded in the grout-filled pipes/ducts (Fig. 2.9) were carried out by Steuck et al. (2008). The bar size ranged from #8 (Ø25 *mm*) to #18 (Ø57 *mm*). The effects of embedment length (ranged from 2 to 14 bar diameter), bar size, grout type (conventional and fiber-reinforced), and specimen scaling were investigated in the tests. Eight-inch (203-*mm*) nominal diameter corrugated steel pipes were used in fifteen specimens with #10 (Ø32 *mm*), #14 (Ø43 *mm*), and #18 (Ø57 *mm*) bars. The pipe wall thickness was 0.068 *in*. (1.7 *mm*), which was three times thicker than 4-*in*. (102-*mm*) diameter corrugated steel ducts used for the two specimens with #8 (Ø25 *mm*) bar. A thicker pipe was used to provide more confinement for grout and to enhance the bond behavior. The bars were A706 Grade 60 steel. The test day strength of grout was 7500 *psi* (51.7 *MPa*) to 8500 *psi* (58.6 *MPa*). Also, the test day strength of concrete was approximately 7400 *psi* (51.0 *MPa*). The fiber added to the grout was Fibermesh 150 polypropylene with dosage of 3 lb/yr^3 (1.77 kg/m^3).

Test results showed that bars pulled out from pipes with some grout attached in specimens with short embedment length. Either grout or bar failure was observed in specimens with longer embedment length. The results also showed that adding fibers to the grout had minor effect on the bond behavior. The bar size had insignificant effect on bond behavior. The bond strength of scaled specimens was similar to the bond strength of full scale specimens. It was reported that the embedment length of $6d_b$ in the grout-filled pipe connection is sufficient to yield large-diameter bars and that $14d_b$ embedment length is sufficient to fully anchor the bar to fracture. The average bond strength of all the tests was 2290 *psi* (15.79 *MPa*) with a standard deviation of 700 *psi* (4.83 *MPa*).

Steuck et al. (2009) proposed a design equation for embedment length, l_d (*in*. or *mm*), of large-diameter bar in grout-filled pipe connections as follows:

$$l_d = \frac{f_y d_b}{130.\sqrt{f'_g}} + \left(\frac{d_{duct} - d_b}{2}\right) \qquad (2\text{-}3)$$

$$l_d = \frac{f_y d_b}{(10.8).\sqrt{f'_g}} + (\frac{d_{duct} - d_b}{2}) \quad \text{(2-3 SI)}$$

where f_y (*psi* or *MPa*) is bar yield stress, d_b (*in*. or *mm*) is bar diameter, f'_g (*psi* or *MPa*) is grout compressive strength, and d_{duct} (*in*. or *mm*) is duct diameter. The second term in the equation presents length of cone in the conical pullout failure mode. If partial cone failure is prevented by thick pipe or sleeve, this term should be taken as zero.

Pang et al. (2008) utilized grout-filled pipe connections in 40%-scale column to cap beam connections to investigate their seismic performance (Fig. 2.10). A cast-in-place model was also tested. The cast-in-place column was reinforced with 16-#5 (Ø16 *mm*) bars whereas the columns in the precast models were reinforced with 6-#8 (Ø25 *mm*) bars. The column diameter and height were 20 *in*. (508 *mm*) and 60 *in*. (1.5 *m*), respectively. Transverse reinforcement consisted of 0.244-*in*. (6-*mm*) diameter, smooth wire spirals spaced at 1.25 *in*. (32 *mm*) on center. The column longitudinal bars were developed in 4-*in*. (102-*mm*) diameter corrugated metal ducts filled with grout that had a compressive strength of 8500 *psi* (58.6 *MPa*) at 5 days. The axial load was approximately 8% of the compressive strength times the cross-sectional area of the column. Cyclic loads were applied to the column to failure.

Test results showed that behavior of the precast connection was similar to a typical cast-in-place connection. Bars buckled then ruptured in the both columns. The majority of deformation of the precast system was concentrated at one large crack at the interface of the beam-column joint while in the cast-in-place reinforced concrete connection deformations were distributed over the column height.

2.2.3. Code Development Length

In this section, development length of straight deformed bars in tension for some of the United States design specifications is presented. ACI 318-11 requires that deformed bar or wire to be anchored with a minimum length l_d (*in*. or *mm*) that is:

$$l_d = \frac{3}{40}\frac{f_y}{\lambda\sqrt{f'_c}}\frac{\psi_t\psi_e\psi_s}{\left(\frac{C_b + K_{tr}}{d_b}\right)}d_b \quad \text{(2-4)}$$

$$l_d = \frac{f_y}{1.1\lambda\sqrt{f'_c}}\frac{\psi_t\psi_e\psi_s}{\left(\frac{C_b + K_{tr}}{d_b}\right)}d_b \quad \text{(2-4 SI)}$$

where f_y (*psi* or *MPa*) is specified yield strength of reinforcement, d_b (*in*. or *mm*) is nominal diameter of bar, f'_c (*psi* or *MPa*) is specified compressive strength of concrete, ψ_t is reinforcement location factor, ψ_e is reinforcement coating factor, ψ_s is reinforcement size factor, λ is lightweight concrete factor, C_b is smaller of (a) the distance from center of a bar or wire to nearest concrete surface, and (b) one-half the center-to-center spacing of bars or wires being developed (*in*. or *mm*) and

$$K_{tr} = \frac{40A_{tr}}{sn} \tag{2-5}$$

where n is the number of bars or wires being spliced or developed along the plane of splitting, s (*in*. or *mm*) is center-to-center spacing of longitudinal reinforcement, transverse reinforcement, prestressing tendons, wires, or anchors, and A_{tr} (in^2 or mm^2) is the total cross-sectional area of all transverse reinforcement within spacing s that crosses the potential plane of splitting through the reinforcement being developed.

The AASHTO LRFD Bridge Design Specification (2010) requires another development length, l_d (*in*. or *mm*), equation for deformed bar that shall not be less than the product of the basic tension development length, l_{db} (*in*. or *mm*), and the modification factors as follows:

$$l_{db} = \begin{cases} \text{For bar \#11 (Ø36 } mm\text{) and smaller} & \dfrac{1.25A_b f_y}{\sqrt{f'_c}} > 0.4 d_b f_y \\ \text{For bar \#14 (Ø43 } mm\text{)} & \dfrac{2.7 f_y}{\sqrt{f'_c}} \\ \text{For bar \#18 (Ø57 } mm\text{)} & \dfrac{3.5 f_y}{\sqrt{f'_c}} \\ \text{For deformed wire} & \dfrac{0.95 d_b f_y}{\sqrt{f'_c}} \end{cases} \tag{2-6}$$

where A_b is area of bar or wire ($in.^2$), f_y (*ksi*) is specified yield strength of reinforcing bar, f'_c (*ksi*) is specified compressive strength of concrete at 28 days, and d_b (*in*.) is diameter of bar or wire. Modification factors are applied depending on the aggregate type, epoxy coating of the bars, etc.

The Caltrans Seismic Design Criteria (SDC) (2010) require that the minimum column bar development length in the cap beam (l_{ac}) providing special joint shear reinforcement detailing, minimum bar spacing, and minimum transverse reinforcement to be

$$l_{ac} = 24 d_{bl} \tag{2-7}$$

where d_{bl} (*in*. or *mm*) is nominal bar diameter of longitudinal column reinforcement.

2.3. Test Parameters and Test Matrix

In two test groups, several parameters were investigated by testing fourteen pullout specimens with UHPC-filled duct connections. The parameters were:

- Embedment length
- Bar size
- Duct diameter
- Number of ducts
- Bundling of bars

The test matrix is presented in Table 2.2. Straight #8 (Ø25 *mm*) and #11 (Ø36 *mm*) bars were used with embedment lengths of $3d_b$, $5d_b$, $8d_b$ and $12d_b$ where d_b is bar diameter. Ducts with nominal size of 3 *in*. (75 *mm*), 4 *in*. (100 *mm*) and 5 *in*. (125 *mm*) were used. Table 2.3 presents the nominal and actual diameters of the duct used in this study. The inner diameter of duct (d_d) was used in analyses of data. Corrugated galvanized strip metal ducts conforming to ASTM A653 with 26-gauge (0.018 *in*. or 0.46 *mm*) wall thickness were used. Bundled bars consisting of two #8 (Ø25 *mm*) bars were used in three of the specimens. The effect of using double ducts spaced at clear distance of 3 *in*. (76 *mm*), each with single bar, was investigated in two specimens.

Several modes of failure are possible in grout-filled duct connections: (1) bar fracture, (2) bar pullout caused by bond failure, (3) grout pullout from the duct , and (4) duct pullout by either failure of bond between concrete surrounding the duct and the duct or conical failure of concrete (Fig. 2.11). It is obvious that there are two critical bond surfaces in this type of connections. One is the bar-grout interface and the other is the grout-duct-concrete interface. The former was used in all the previous bond studies to obtain "bar bond strength" determined as the ratio of the peak tensile force to the surface area of bar. This approach does not address directly the duct-concrete interface failure. Therefore, a new term was needed to account for bond failure at the interface between the duct and concrete. In this study, "duct bond strength" is introduced as the ratio of the peak tensile force to the surface area of duct.

Tests specimens were designed in two groups to find the duct bond strength in group I (10 specimens) and bar bond strength in group II (4 specimens). Figure 2.12 shows schematic view of specimens. Both groups had similar geometries but a large portion of the bars were debonded using 3/8-*in*. (9.5-*mm*) thick pipe insulation foams in group II. With this detail the entire length of the duct was mobilized in transferring the loads, and duct pullout was avoided.

2.4. Specimen Design and Fabrication

The study by Brenes et al. (2006) on the grout-filled duct connection showed that projected failure surface of a single bar in tension can be idealized as a square with sides equal to $15d_b$ (Figure 2.13). In the present study, specimen diameter (D) was designed as sum of $15d_b$, spacing of ducts, if any, and 5 *in*. (127 *mm*) tolerance for concrete cover and lifting bolts. For construction purposes, two diameters were considered for specimens: 24 *in*. (610 *mm*) and 30 *in*. (762 *mm*). The height of specimens (H) was assumed to be equal to the embedment length plus 5 *in*. (127-*mm*). Three heights were used: 16 *in*. (406 *mm*), 20 *in*. (508 *mm*) and 28 *in*. (711 *mm*). The dimensions of specimens are also presented in the Table 2.2. Details of some of the specimens with different test parameters are shown in Fig. 2.14.

All specimens were lightly reinforced longitudinally with 6-#3 (Ø10 *mm*) bars and transversely with #3 (Ø10 *mm*) spiral at 2-*in*. (51-*mm*) pitch (Fig. 2.15). The longitudinal and transverse steel ratios of specimens were 0.09-0.15% and 0.79-1.0%, respectively. Those two values are for specimens with 30-*in*. (762-*mm*) and 24-*in*. (610-*mm*)

diameters, respectively. Clear cover was 1 *in*. (25 *mm*) in all specimens. Specimen lifting bolts anchor is also shown in Fig. 2.15.

Bottom end of the ducts were plugged by duct tape. Figure 2.16 shows formwork for two of the specimens. Pencil rod at the bottom end of duct and plywood at the top end were used to hold the ducts in position. After casting and curing the concrete, the ducts were vacuumed and wiped with a wet cloth before casting UHPC.

Gravity tremie-tube method was used to fill the ducts to avoid air trapping (Fig. 2.17). In this method, a PVC pipe was inserted into the duct then UHPC was continuously poured from top passing through a funnel. At the same time, pipe was slowly pulled out, thus allowing the material to fill the duct by its own weight. Note that static and dynamic flow table tests of UHPC mix were 8.5 *in*. (216 *mm*) and 9.25 *in*. (235 *mm*), respectively. After filling the ducts with UHPC, mild bars were inserted into the ducts then covered for curing. Examples of two frames to fix the bars at the center of the ducts are shown in Fig. 2.18.

2.5. Pullout Test Setup

There are several test configurations with different bar sizes, multi ducts, and bundled bars. To accommodate these different configurations, a self-reacting pullout test setup was designed and built at UNR with pull force capacity of 300 *kips* (1335 *kN*). Figure 2.19 shows the details of test setup and Fig. 2.20 shows photographs of the setup.

Threaded pull out bar (or bars) of the specimen was bolted to the bottom plate of system. ANSI/ASME thread sizes 7/8-9 and 1 ¼ -7 were used for #8 (Ø25 *mm*) and #11 (Ø36 *mm*) bars, respectively. Four 1 1/8-*in*. (28-*mm*) diameter high-strength bolts connected the bottom plate with thickness of either 1.5 or 2 *in*. (38 or 51 *mm*) to top plate with thickness of 1.5 *in*. (38 *mm*). High-strength 2-*in*. (51-*mm*) diameter threaded rod attached the top plate to a 200 *kips* (889.6 *kN*) ram. The ram was placed on the top flange of a load spreader beam and was controlled manually by an oil pump with slow pumping rate resulting in force rate of 1000 *lbs/sec* (4500 *N/sec*) on average. The ram force was measured based on oil pressure of the system.

2.6. Measured Materials Properties

2.6.1. Concrete

Plastic cylinders with 6-*in*. (152-*mm*) diameter and 12-*in*. (305-*mm*) height were used for concrete sampling. The measured strength history of the concrete is shown in Fig. 2.21 and test day compressive strength of concrete for each specimen is presented in Table 2.4. At least three samples were used for compressive tests but only the average of test data was reported.

2.6.2. UHPC

A previous study showed that 3-*in*. (76-*mm*) cylinder specimen is an acceptable alternative to the standard 4-*in*. (102-*mm*) cylinder specimen for compressive testing of UHPC with strength ranged from 11.6 *ksi* (80 *MPa*) to 29 *ksi* (200 *MPa*) (Graybeal and Davis, 2008). In this study, plastic cylinders with 3-*in*. (76-*mm*) diameter and 6-*in*. (152-*mm*) height were used for UHPC sampling. There were two mixes for UHPC, one for group I and another for group II. In Fig. 2.22, strength history of both mixes is shown and test day strength of UHPC for each specimen in presented in the Table 2.4. At least three samples were used for compressive tests but only the average of test data was reported. Details regarding sample end preparation, and compressive mode of failure are presented in chapter 4.

2.6.3. Reinforcement

Grade 60 ASTM A615 bars with three sizes were used in the pullout specimens. Specimens were reinforced longitudinally and transversely with #3 (Ø10 *mm*) bars. Reinforcing bars that were anchored in the UHPC-filled ducts were #8 (Ø25 *mm*) and #11 (Ø36 *mm*) bars. Table 2.5 presents average mechanical properties of the bars and Fig. 2.23 shows measured stress-strain of the anchored bars. No yielding plateau was observed for #3 (Ø10 *mm*) bars. Therefore, the yield point was calculated using 2% offset method. The full stress-strain curve for #11 (Ø36 *mm*) bar could not be obtained due to bar slippage in grips of the UNR tensile test machine.

2.6.4. Duct

Corrugated galvanized strip metal ducts conforming to ASTM A653 were used with minimum specified yield strength of 33 *ksi* (227.5 *MPa*). Note that strength of ducts is controlled by the seams as they open before yielding of duct base material in tension.

2.7. Instrumentation

Strain gauges were installed on opposite faces of bars and ducts at depth of $6d_b$ from surface of the group I specimens where d_b is bar diameter. Since embedment length was very short in group II specimens, strain gauges were only installed on ducts. However, two strain gauges were installed on all bars at the height of $6d_b$ from specimen surface to measure strain of the free bars. Slippage of ducts was measured by four position transducers, of which two were installed on the concrete and two on UHPC. The average measured displacements are reported in subsequent sections. Photographs of the instrumentation are shown in Fig. 2.24.

2.8. Test Results

Mode of failure and observed damage in the pullout tests are summarized in Table 2.6. For two specimens in group I, SP4 and SP11, the ducts pulled out with severe

damage of surrounding concrete and conical failure of concrete at a depth of 3.5 *in*. (89 *mm*) (Fig. 2.25). No damage was observed in UPHC. Only in one specimen in group II with $3d_b$ embedment length, SP6, bundled bars pulled out with no visible concrete or UHPC damage. To understand the failure, the specimen was vertically cut in half (Fig. 2.26). It was observed that both plastic deformation of ribs and crushing of surrounding UHPC next to the ribs are the causes of the bars pull out. Note that only four ribs were engaged with UHPC in this specimen. In other specimens, bar ruptured at the threads.

As mentioned before, for most of the tests bar ruptured at the thread instead of bar or duct pullout. Therefore, full bond-slip relationship of the system could not be well established. However, the initial stiffness of the system can be investigated. Force versus duct slippage of all specimens is shown in Fig. 2.27.

Bar slippage can be measured indirectly by subtracting the bottom plate displacement, bar elongation, and duct slippage assuming that the bar above the surface remains elastic. Only in SP6, this assumption was valid for the entire of the test. Force-slippage relationship of bars of SP6 is shown in Fig. 2.28.

In the previous section, duct (u_d) and bar (u_b) bond strengths were defined as the ratio of peak force to the surface area of duct and bar, respectively presented as:

$$u_d = \frac{force}{surface\ area} = \frac{F}{n_d.\ \pi.\ d_d.\ L_{emb}} \tag{2-8}$$

$$u_b = \frac{force}{surface\ area} = \frac{F}{n_b.\ \pi.\ d_b.\ L_{emb}} \tag{2-9}$$

where d_b is the nominal diameter of bar (*in*. or *mm*), d_d is the inner diameter of duct (*in*. or *mm*), n_d is number of ducts in multiple duct system, n_b is number of bars in bundled bar system, and L_{emb} is embedment length (*in*. or *mm*). Table 2.7 summarizes the duct and bar bond strengths for the pullout tests. Note that in the majority of tests, bar fractured at the threads instead of bar/duct pullout, thus the values that are listed are the lower bound bond strength marked with an asterisk in the table.

Some of specimens with the lower bound bond strength are excluded from further analyses since similar specimens with shorter embedment length had the same mode of failure of bar fracture at the thread. These specimens are SP2, SP7, SP8 and SP10. For instance, the bar in SP1 with $8d_b$ embedment length ruptured at a force of 56.4 *kips* (388.9 *kN*) resulting in bond strength of 720 *psi* (4.96 *MPa*). Similarly, the bar in SP2 with $12d_b$ embedment length ruptured at a force of 55.0 *kips* (379.2 *kN*) resulting in bond strength of 467 *psi* (3.22 *MPa*). Noting that both specimens are similar but with different embedment lengths, there is no need to include lower bound bond strength of SP2 in analyses.

The duct bond strengths (u_d) were normalized to the square root of test day compressive strength of normal concrete ($\sqrt{f'_c}$) (Fig. 2.29). The average normalized duct bond strength for all tests in group I is 7.27 $psi^{0.5}$ (0.60 $MPa^{0.5}$) with a standard deviation of 1.33 $psi^{0.5}$ (0.11 $MPa^{0.5}$). The bar bond strengths (u_b) were normalized to the square root of test day compressive strength of UHPC ($\sqrt{f'_{UHPC}}$). The average normalized bar bond strength for all tests in group II is 33.4 $psi^{0.5}$ (2.77 $MPa^{0.5}$) with a standard deviation of 6.44 $psi^{0.5}$ (0.53 $MPa^{0.5}$).

Note that the average bar bond strength of group II specimens excluding SP8 is 5350 *psi* (36.9 *MPa*), which is approximately eight times stronger than that of conventional concrete based on Eq. 2-1.

The effect of bar bundling on the duct bond strength was investigated by comparing the normalized duct bond-slip curves of SP1 and SP4 (Fig.2.30a). It can be inferred that the effect of bundling is minor on the duct bond behavior. The effect of bar size on the duct bond behavior is shown in Fig. 2.30b, which indicates the effect is negligible. Multiple duct effect could not be determined since bar fractured at small slippage (Fig. 2.30c). The duct slippage was divided to the duct diameter to determine the effect of duct size (Fig. 2.30d). Duct size had minor effect on the initial duct bond behavior. However, it should be noted that duct diameter is in the denominator of duct bond strength thus it has a significant effect on the bond strength. For example, even though pull force capacity of SP11 was only 85% of that of SP14, the normalized duct bond strength of SP11 was 13% higher than SP14 due to 24% smaller duct diameter. In other words, the larger the duct diameter, the lower the duct bond strength. Similar behavior exists in conventional bar bond strength (Fig. 2.31) in which the bar bond strength decreases as the bar size increases (Soroushian and Choi, 1989).

Figure 2.32 shows strain profiles of the bar and duct for specimens in which either the bar ruptured or the duct pulled out. Note that absolute strains are plotted. The measured strains were tensile for bars and compressive for ducts. Zero height denotes the surface of specimen and negative values are the embedment lengths. It can be seen that the bar strains are slightly higher in specimens with bar fracture. Also, the duct experienced higher strains in specimens in which the duct pulled out.

2.9. Design Equation for UHPC-Filled Duct Connections

2.9.1. Embedment Length Based on Duct/Bar Bond Strength

As mentioned earlier, there are two types of bond strengths in the UHPC-filled duct connections, one for the bar and the other for the duct. In this section, design equations were developed based on the findings from the pullout tests.

Normalized duct and bar bond strengths were defined in the previous section. The average normalized duct bond strength for group I specimens, excluding SP2, SP7 and SP10, was 7.88 $psi^{0.5}$ (0.65 $MPa^{0.5}$) with a standard deviation of 1.02 $psi^{0.5}$ (0.085 $MPa^{0.5}$) (Fig. 2.33). The design duct bond strength ($\bar{u}_{d,design}$) was defined as average strength less one standard deviation, which was 6.86 $psi^{0.5}$ (0.57 $MPa^{0.5}$). For the sake of simplicity, the coefficient was rounded down to 6.75 $psi^{0.5}$ (0.56 $MPa^{0.5}$). By substituting u_d of Eq. 2.8 with $\bar{u}_{d,design}$ and rearranging the equation for embedment length, bar development length based on the duct bond strength is:

$$L_{d,duct} = \frac{F}{\bar{u}_{d,design}.\pi.d_d.\sqrt{f'_c}} = \frac{A_s.f_s}{\bar{u}_{d,design}.\pi.d_d.\sqrt{f'_c}} = \frac{d_b^2.f_s}{4\bar{u}_{d,design}.d_d.\sqrt{f'_c}} \qquad (2\text{-}10)$$

where f_s is bar stress, which is recommended to be $1.5f_y$ or f_u, whichever is greater. Other parameters were defined before.

For the bar bond strength, there were only three acceptable test data. To enrich the database, three pullout tests of bars anchored in UHPC cylinders [diameter of 15.74 *in.* (400 *mm*) and height of 7.87 *in.* (200 *mm*)] carried out by FHWA were also used in deriving the design equation that are presented in Table 2.8, even though these data were not for duct-field UHPC. The normalized bar bond strength from six tests is shown in Fig. 2.34 with an average of 34.9 $psi^{0.5}$ (2.89 $MPa^{0.5}$) and a standard deviation of 5.56 $psi^{0.5}$ (0.46 $MPa^{0.5}$). Similar to the recommended design duct bond strength, the design bar bond strength ($\bar{u}_{b,design}$) was recommended to be the average less one standard deviation. The coefficient was rounded to 30 $psi^{0.5}$ (2.49 $MPa^{0.5}$). The design equation for embedment length of bar based on the bar bond strength is as follows:

$$L_{d,bar} = \frac{F}{\bar{u}_{b,design}.\pi.d_b.\sqrt{f'_{UHPC}}} = \frac{A_s.f_s}{\bar{u}_{b,design}.\pi.d_b.\sqrt{f'_{UHPC}}} = \frac{d_b.f_s}{4\bar{u}_{b,design}.\sqrt{f'_{UHPC}}} \quad (2\text{-}11)$$

The recommended bar embedment length in the UHPC-filled duct connections is the larger of the lengths calculated using equations 2-10 and 2-11.

2.9.2. Summary of Design Equations

The proposed design equations are summarized as follows:

L_d = max ($L_{d,duct}$, $L_{d,bar}$)

US Customary Units	SI Units	
$L_{d,duct} = \frac{d_b^2.f_s}{27d_d.\sqrt{f'_c}}$	$L_{d,duct} = \frac{d_b^2.f_s}{2.24d_d.\sqrt{f'_c}}$	(2-12)
$L_{d,bar} = \frac{d_b.f_s}{120\sqrt{f'_{UHPC}}}$	$L_{d,bar} = \frac{d_b.f_s}{9.96\sqrt{f'_{UHPC}}}$	(2-13)

where

L_d: Development length for un-hooked deformed bar in UHPC-filled duct connections (*in, mm*)
$L_{d,duct}$: Bar development length based on duct bond strength (*in, mm*)
$L_{d,bar}$: Bar development length based on bar bond strength (*in, mm*)
d_b: Nominal diameter of bar (*in, mm*)
d_d: Inner diameter of duct (*in, mm*)
f_s: Bar stress (*psi, MPa*); 1.5f_y or f_u whichever is greater
f'_c: Compressive strength of concrete surrounding the duct (*psi, MPa*)
f'_{UHPC}: Compressive strength of UHPC in the duct (*psi, MPa*)

It is expected that the duct bond strength controls the embedment length in most cases (Eq. 2-12) due to lower bond strength compared to the bar bond strength. Note that Eq. 2-13 can also be used as a stand-alone equation to determine the embedment length of un-hooked deformed bars in UHPC blocks such as UHPC-footing.

The embedment length can be substantially reduced in the UHPC-filled duct connections. Figure 2.35 shows bar stress versus development length for different design

equations presented in previous sections. Bar assumed to be #8 (Ø25 *mm*) with ultimate strength of 110 *ksi* (758 *MPa*). Compressive strength of concrete and UHPC are 5000 *psi* (34.5 *MPa*) and 20000 *psi* (137.9 *MPa*), respectively. All ACI development length factors are assumed to be one. For Eq. 2.12, three graphs are shown that are for different duct to bar diameter ratios of 2.83, 3.12 and 4.0.

To fracture the bar in a 4-*in*. (101-*mm*) diameter duct, bar needs to be embedded 15 *in*. (381 *mm*) in the UHPC-filled duct connection, whereas the bar development length in the grout-filled duct and conventional construction connections are 35 *in*. (889 *mm*) and 47 *in*. (1194 *mm*), respectively. Therefore, more than 50% reduction of embedment length can be achieved in the UHPC-field duct connection compared to other anchorage systems. Note that the other equations are independent of the duct diameter.

It can be seen in Fig. 2.35 that minimum bar embedment length based on Steuck et al., 2009 is $12d_b$. However, it should be noted that the grout-filled pipe system design equation, Eq. 2-3, was based on mostly pullout tests in which thick corrugated steel pipes rather than thin corrugated ducts, had been used. An UHPC-filled duct system with an 8-*in*. (200-*mm*) diameter duct would results in an embedment length of $7d_b$.

It is worth noting that designers should extend the ducts to extreme layer of reinforcements in cap or footing even though the design embedment length is shorter than the depth of connecting element. This is necessary to develop a strut-and-tie mechanism to transfer connection forces. However, depth of footing or cap beam can be reduced to fully anchor the bars.

2.10. Bond-Slip Models

Constitutive bar and duct bond-slip models were developed for the UHPC-filled duct connections. A bar bond-slip model (Fig. 2.36) developed by Eligehausen et al. (1982) has been widely used in previous studies:

$$u = u_1\left(\frac{s}{s_1}\right)^{\propto} \qquad 0 < s \le s_1 \qquad \text{(2-14a)}$$

$$u = u_{max} \qquad s_1 < s \le s_2 \qquad \text{(2-14b)}$$

$$u = \frac{u_3 - u_1}{s_3 - s_2}(s - s_2) + u_1 \qquad s_2 < s \le s_3 \qquad \text{(2-14c)}$$

$$u = u_3 \qquad s > s_3 \qquad \text{(2-14d)}$$

where s_1=0.04 *in*. (1.0 *mm*), s_2=0.12 *in*. (3.0 *mm*), s_3=0.43 *in*. (11.0 *mm*), u_1=1958 *psi* (13.5 *MPa*), u_3=725 *psi* (5.0 *MPa*), and $\propto$=0.4. In the present study, bond-slip models for duct and bar were formulated similar to Eligehausen's model but the strengths and slippage were revised. Other significant difference is that the bond strengths and slippages are normalized in this study to account for the effect of the material strength and embedment length which were not included in the original model.

Figure 2.37 shows the normalized duct bond stress versus normalized duct slip, which is the ratio of the duct slip (s_d) to the bar embedment length (L_{emb}) of the specimen. The constitutive duct bond-slip model (Fig. 2.37) is proposed in the US customary units (*psi, in.*) as:

$$\frac{u_d}{\sqrt{f'_c}} = \bar{u}_{d,max}\left(\frac{s_d}{0.004L_{emb}}\right)^{0.4} \qquad 0 < \frac{s_d}{L_{emb}} \le 0.004 \qquad \text{(2-15a)}$$

$$\frac{u_d}{\sqrt{f'_c}} = \bar{u}_{d,max} \qquad 0.004 < \frac{s_d}{L_{emb}} \le 0.0065 \qquad \text{(2-15b)}$$

$$\frac{u_d}{\sqrt{f'_c}} = \frac{3.5 - \bar{u}_{d,max}}{0.0185}\left(\frac{s_d}{L_{emb}} - 0.0065\right) + \bar{u}_{d,max} \qquad 0.0065 < \frac{s_d}{L_{emb}} \le 0.025 \qquad \text{(2-15c)}$$

$$\frac{u_d}{\sqrt{f'_c}} = 3.5 \qquad \frac{s_d}{L_{emb}} > 0.025 \qquad \text{(2-15d)}$$

The bond-slip models need to be representative of actual behavior of connections. Therefore, $\bar{u}_{d,max}$, is proposed to be the average normalized duct bond strength, 7.88 $psi^{0.5}$ (0.65 $MPa^{0.5}$), instead of the design duct bond strength. The initial slope of duct bond-slip curve is 3600 $psi^{0.5}$ (300 $MPa^{0.5}$) that can be used as stiffness of a linear duct bond-slip spring in well-anchored UHPC-filled duct connections. The model in SI units (*MPa*, *mm*) is the same as this model but the value of 3.5 $psi^{0.5}$ should be replaced with 0.3 $MPa^{0.5}$ in Eq. 2-15c and Eq. 2-15d.

Figure 2.38 shows the normalized bar bond stress versus normalized bar slip, which is the ratio of the bar slip (s_b) to the bar embedment length (L_{emb}). As mentioned before, complete bar bond-slip relationship was only established for SP6 since only in this specimen the bars pulled out without yielding. However, bond-slip relationships of six other specimens were also included in the figure up to the yielding of the threaded portion of the bar and were used to establish initial bond-slip relationship. Maximum normalized bar bond strengths for SP3, SP11, and FHWA UHPC pullout tests are also shown. The constitutive bar bond-slip model (Fig. 2.38) was proposed in the US customary units (*psi, in.*) as:

$$\frac{u_b}{\sqrt{f'_{UHPC}}} = \bar{u}_{b,max}\left(\frac{s_b}{0.06L_{emb}}\right)^{0.4} \qquad 0 < \frac{s_b}{L_{emb}} \le 0.06 \qquad \text{(2-16a)}$$

$$\frac{u_b}{\sqrt{f'_{UHPC}}} = \bar{u}_{b,max} \qquad 0.06 < \frac{s_b}{L_{emb}} \le 0.1 \qquad \text{(2-16b)}$$

$$\frac{u_b}{\sqrt{f'_{UHPC}}} = \frac{12 - \bar{u}_{b,max}}{0.3}\left(\frac{s_b}{L_{emb}} - 0.1\right) + \bar{u}_{b,max} \qquad 0.1 < \frac{s_b}{L_{emb}} \le 0.4 \qquad \text{(2-16c)}$$

$$\frac{u_b}{\sqrt{f'_{UHPC}}} = 12 \qquad \frac{s_b}{L_{emb}} > 0.4 \qquad \text{(2-16d)}$$

Similar to the duct bond-slip model, the maximum normalized bar bond strength, $\bar{u}_{b,max}$, is proposed to be the average normalized bar bond strength that is 34.9 $psi^{0.5}$ (2.89 $MPa^{0.5}$). The initial slope of the curve is 930 $psi^{0.5}$ (77 $MPa^{0.5}$). Due to limited test data, the secondary branches of the model were obtained from Eligehausen's model. Further

study is necessary to establish the full bar bond-slip model of UHPC-filled duct connections.

2.11. Concluding Remarks

To be able to deploy grouted duct connections in shallow cap beams and footings, it is proposed to use UHPC instead of conventional grout. In phase one of the performance evaluation of the UHPC-filled duct connection, fourteen pullout tests were carried out at UNR to determine the bond behavior of the connection. A summary of the findings of the pullout tests are as follows:

- The average normalized bar bond strength was 34.9 $psi^{0.5}$ (2.89 $MPa^{0.5}$).
- The bond strength of UHPC is approximately 8 times stronger than of conventional concrete.
- The average normalized duct bond strength was 7.88 $psi^{0.5}$ (0.65 $MPa^{0.5}$).
- The bar size had minor effect on the duct bond behavior.
- Bundling of bars had negligible effect on the duct bond strength.
- The duct size had minor effect on the initial bond behavior.
- Duct bond strength is reduced when duct size increases.
- The critical bond surface is typically UHPC-duct-concrete surface.
- Using UHPC-filled duct connection results in at least 50% reduction in the required embedment length compared to conventional construction.
- Duct and bar bond-slip models were proposed to be used in analytical modeling of UHPC-filled duct connections.

Test results confirm that it is feasible to incorporate the UHPC-filled duct system to connect precast column to shallow cap beams or footings.

Chapter 3: Column Test Models

3.1. Introduction

Bridge columns are allowed to undergo inelastic deformations under seismic loads while maintaining integrity of the bridge. In other words, the columns are the most important elements of the bridge in terms of performance during severe events, safety and serviceability after the event. In ABC, connections of the columns to adjacent members are challenging since connections should be able to transfer forces while undergoing large inelastic cyclic deformations.

Five half-scale bridge column models incorporating new types of column-to-footing connections suitable for ABC in high seismic zones were previously designed and tested at the University of Nevada, Reno (UNR) (Table 3.1). Grouted couplers (GC) were utilized in plastic hinge of two of those models. Headed bar couplers (HC) were incorporated in two other models. The first model was a cast-in-place (CIP) standard column to serve as a benchmark model (Haber, 2013). The models had similar geometries and bar arrangements but different types of column base connections were investigated. A 12-inch (305-*mm*) high pedestal was used in two precast models to investigate the effect of lower moment demand over coupler location on the seismic performance of the columns.

The displacement ductility capacity of CIP was 7.36 (equal to 10% drift capacity) with no strength degradation before bar fracture at 10% drift ratio. The force-displacement relationship (Fig 3.1) and energy dissipation of the precast models were similar to those of the CIP model, indicating emulative behavior. However, the average displacement ductility capacity and drift ratio capacity of the GC models were 4.52 and 6%, respectively, which are approximately 60% of those of the CIP model. The average displacement ductility capacity of the HC models was 6.78 with 10% drift ratio capacity. In the present study, 3 half-scale precast column models were designed and tested at UNR. These models incorporated either couplers or advanced materials in the plastic hinge (Table 3.1).

Bond studies of the UHPC-filled duct connection were presented in the previous chapter. The results showed that it is feasible to incorporate this type of connection in bridge columns. Therefore, a precast column model labeled “PNC” was designed and tested utilizing UHPC-filled duct connection at the column base.

The main shortcoming of the GC models found in the previous UNR study was the relatively low displacement ductility as mentioned before. The grouted couplers behaved the same as large diameter reinforcements resulting in a stronger section. The precast pedestal in the GC models was made using grout-filled corrugated ducts. The higher compressive strength of the grout as well as the high level of confinement provided by the ducts made the precast pedestal stronger than the rest of the columns. Therefore,

damage was shifted away from the coupler region and precast pedestal and limited the displacement ductility capacity. Some of the column longitudinal bars fractured 4 *in*. (102 *mm*) below the column-footing interface in the GC models. To overcome this shortcoming, a new model (GCDP) was designed with unbonded longitudinal bars in a cast-in-place pedestal. Debonding allows spreading of yielding in the bar and avoids strain concentration.

Eight different materials, conventional and advanced, were incorporated in the third column model (HCS) tested in the present study. In this column superelastic shape memory alloy (SE SMA) and engineered cementitious composite (ECC) were used in addition to UHPC-filled duct connection at the footing. The objective of using novel materials in the column was to enhance seismic performance of the column compared to the conventional reinforced concrete. SE SMA is known to substantially reduce residual displacements and ECC is known to minimize damage even under large rotations.

Previous studies on the SMA-mild bar connections were presented in chapter 1. However, to connect the SMA bar to the mild bar, an extensive research was carried out at UNR to make a new SMA-mild bar connection with headed couplers. Four #4 (Ø13 *mm*) SMA bars and 8 #10 (Ø32 *mm*) SMA bars each with 20 to 40 *in*. (508 to1016 *mm*) length were headed at either one end or both ends then connected to the same or one size larger headed mild bar/s using HRC coupler/s. Figure 3.2 shows photographs of a SMA-mild bar connection for #10 (Ø32 *mm*) bars.

Design, construction, and test setup of the new column models, PNC, GCDP, and HCS, are presented in this chapter. A short review of the benchmark CIP model is also presented. In addition, information regarding the SMA-mild bar connection tests is provided.

3.2. Design and Construction of Column Models

The cross section of all the column models was circular with a diameter of 24 *in*. (610 *mm*) and the height of all the models was 9 *ft*. (2.74 *m*) from the top of the footing to the axis of the hydraulic actuator used to apply lateral loads.

3.2.1. CIP Column Model

A half-scale conventional cast-in-place column model (CIP) was designed based on Caltrans Seismic Design Criteria (SDC) version 1.4 (2006) with an aspect ratio of 4.5. The CIP model was a standard bridge column but with a thicker clear cover (Table 3.2) to account for the size of coupler in the other models. The CIP model served as a reference column to be compared with the precast models.

The column was reinforced longitudinally with 11-#8 (11-Ø25 *mm*) bars and transversely with #3 (Ø10 *mm*) spiral at a 2-*in*. (51-*mm*) pitch resulting in longitudinal and transverse steel ratios of 1.92% and 1.05%, respectively. The axial load index, which is the ratio of the axial load to the product of column gross section area and the compressive strength of column concrete, was 10%. The expected compressive strength

of concrete and the expected yield strength of reinforcements were 5000 *psi* (34.5 *MPa*) and 68 *ksi* (468.8 *MPa*), respectively. Column was initially designed for a minimum displacement ductility capacity of 5 but with final detailing (Fig. 3.3), the calculated displacement ductility capacity of the column was 7.

3.2.2. PNC Column Model

Feasibility of using the UHPC-filled duct connection at the base of precast columns was investigated in the duct system bond study presented in the previous chapter. To accomplish the second phase of investigation of seismic performance of the connection, a half-scale precast column model labeled "PNC" was constructed incorporating the UHPC-filled duct connection. The precast model had a similar geometry, bar size, and bar arrangement (Table 3.2) to CIP thus its performance was assumed to be emulative of the conventional construction. There was no additional design limitation for PNC with respect to CIP.

Figure 3.4 shows PNC and Fig. 3.5 shows the base connection in detail. The clear cover was 1.5 *in*. (38 *mm*) in the column. Corrugated galvanized steel ducts with a nominal 3-*in*. (75-*mm*) diameter were used in the footing to be filled with UHPC (Fig. 3.6). The confinement of the duct cage was similar to the column and was provided by #3 (Ø10 *mm*) spiral spaced at a 2-*in*. (51-*mm*) pitch. The column longitudinal bars were extended 28 *in*. (711 *mm*) at the base for insertion into the ducts. However, the required embedment length was only 19 *in*. (483 *mm*) based on the design equations presented in chapter 2 assuming the concrete compressive strength is 5000 *psi* (34.5 *MPa*), the UHPC compressive strength is 20000 *psi* (137.9*MPa*), and #8 (Ø25 *mm*) bars had an ultimate strength of 110 *ksi* (758.4 *MPa*). The duct length was 1 *in*. (25 *mm*) longer than the extended bar as a construction tolerance. The bottom end of the ducts was plugged with thin plywood attached to the duct with a duct tape.

It was found that the bond strength of UHPC is 8 times stronger than the normal concrete. Therefore, strain concentration could occur a short distance below the column-footing interface, possibly limiting the overall column ductility. To help spread bar yielding, 4 *in*. (102 *mm*) of the column longitudinal bars were debonded above and below the column-footing interface (Fig. 3.5). Therefore, the effective bar embedment length in the UHPC-filled duct connection of PNC was 24 *in*. (610 *mm*), only 5 *in*. (127 *mm*) longer than the required development length.

To minimize the precast column weight for transportation, hollow core circular section with a 6-*in*. (152-*mm*) wall thickness was used at initial stage of construction. After installing the column, the column core was filled with self-consolidating concrete (SCC). Construction stages of PNC were as follows (Fig. 3.7):

- Casting the footing with ducts (Fig. 3.8)
- Casting the hollow column with extended longitudinal bars at the column base (Fig. 3.9)

- Filling the ducts with UHPC using a tremie tube method (Fig. 3.10) then erecting and installing the precast column (Fig. 3.11)
- Filling the core and casting the head, both with SCC

The average static and dynamic flow table test results for UHPC mix were 8.75 *in*. (222 *mm*) and 9.25 *in*. (235 *mm*), respectively. Two mix control tests were performed for SCC: (1) Slump flow test according to ASTM C1611-09b, and (2) static segregation test according to ASTM C1610-10. Acceptance criteria were based on the Standard Specification for the State of California (2010) presented in Table 3.3. The SCC and UHPC mix designs used in this study are presented in Tables 3.4 and 3.5.

The slump flow of the SCC mix was 19.9 *in*. (505 *mm*) only 0.5% lower than the minimum requirement of 20 *in*. (508 *mm*). Furthermore, it took 2.6 *sec* for the SCC to spread 20 *in*. (508 *mm*) (T_{50}=2.6). This time is also within the acceptable range of 2-7 *sec*. Visual stability index (VSI) was evaluated as 1.0, which indicates the SCC mix is stable (Fig. 3.12). The static segregation of the core SCC was 14.9%, which is less than 15%. Overall, the SCC mix was accepted for casting based on the tests results.

3.2.3. GCDP Column Model

It was mentioned that the previous GC column models showed emulative behavior compared to CIP but the drift ratio capacity and displacement ductility capacity of those models were limited to approximately 60% of those of CIP. It was also found that in GCPP the 12-*in*. (305-*mm*) precast pedestal did not improve the displacement capacity. This was contrary to the expectation. The lack of improvement is attributed to the grouted ducts inhibiting yielding of the bars. In both GC models, longitudinal bar ruptured at approximately 4 *in*. (102 *mm*) below the column-footing interface.

To spread yielding and avoid strain concentration, debonding of longitudinal bars in a cast-in-place pedestal was proposed in the new GC column model labeled "GCDP" (Fig. 3.13). GCDP had similar properties as those of CIP, therefore emulative behavior was expected. The key design parameters of GCDP are presented in the Table 3.2. Figure 3.14 shows the details of connection.

The clear cover for the section with couplers was 1 *in*. (25 *mm*) and for the sections away from the couplers was 1.75 *in*. (44 *mm*). The intended height of the pedestal was 12 *in.* (305 *mm*). However, due to a minor construction error the actual pedestal height was 11 *in*. (279 *mm*). Approximately 0.5 *in*. (13 *mm*) was added to the pedestal height after closure of pedestal-column gap (Fig. 3.21). The longitudinal bars were debonded only in the pedestal using two layers of duct tape. Similar to PNC, the hollow core column was filled with SCC after the column installation. The SCC mix properties and tests results were similar to those of PNC presented in the previous section (Fig. 3.12).

The grout-filled mechanical bar coupler was NMB Splice Sleeve (Fig. 3.15). The sleeve material properties conform to ASTM A536-85. The sleeves were filled with non-shrink high-early-strength grout labeled "SS Mortar" with a minimum 28-day compressive strength of 11000 *psi* (75.8 *MPa*).

Construction stages of GCDP were as follows (Fig. 3.16):

- Casting the footing with extended bars (Fig. 3.17)
- Casting the pedestal with debonded longitudinal bars
- Casting the hollow column with embedded couplers (Fig. 3.18)
- Erecting and installing the hallow column (Fig. 3.19)
- Injecting the SS-Mortar to the sleeves (Fig. 3.20)
- Filling the gap between the pedestal and the column (Fig. 3.21)
- Filling the core and casting the head, both with SCC

The construction gap between the pedestal and the precast column was filled with non-shrink, high-strength grout by dry packing technique.

3.2.4. HCS Column Model

Conventional materials were used in plastic hinges of the seven column models that were designed and tested at UNR to develop new column-to-footing connections for ABC in high seismic zones. In chapter 1, new materials such as SMA and ECC were discussed. The seismic performance of a half-scale bridge column model labeled "HCS" incorporating those materials in the plastic hinge was investigated. Similar to the other seven models, HCS was a precast column but was connected to the footing using a UHPC-filled duct connection. Totally, 8 different materials were used in HCS: conventional concrete, reinforcing steel bars, corrugated galvanized steel ducts, UHPC, reinforcing SMA bars, ECC, head reinforcement couplers, and SCC.

The geometry of the model was similar to the CIP geometry but bar arrangement was modified since the mechanical properties of SMA bars are different from steel bars. Nickel-Titanium (NiTi or Nitinol) superelastic SMA bars with approximate austenite finish temperature (A_f) of 32^oF (0^oC) were used. SMA remains superelastic at any temperature above A_f. HCS was designed such that its flexural strength was the same as the CIP flexural strength.

A comprehensive study of mechanical properties of reinforcing SMA and analytical model is presented in chapter 6. The properties of the reinforcing SMA used in the HCS model were extracted from tensile test data for #10 (Ø32 *mm*) SMA bars provided by the SMA manufacturer. Figure 3.22 illustrates the backbone curve of reinforcing SMA model used in the analyses. The modulus of elasticity and yield strength of the SMA were 5400 *ksi* (37231.7 *MPa*) and 55.6 *ksi* (383.3 *MPa*), respectively. The post-yield stiffness and secondary post-yield stiffness were 355 *ksi* (2447.6 *MPa*) and 1620 *ksi* (11169.5 *MPa*), respectively. The maximum superelastic strain was assumed to be 6% with an ultimate strain of 10%. The confined and unconfined properties of ECC were assumed to be similar to those of conventional concrete in CIP. The test day concrete compressive strength of CIP was used in the analyses instead of the design strength.

Moment-curvature analyses were carried out using OpenSees (2013) to determine the SMA bar arrangement (Fig. 3.23). The analyses showed that a model, with 10-#10 (Ø32

mm) SMA bars (ρ_l=2.8%) exhibits the same flexural capacity as the CIP model, which had 11-#8 (Ø25 *mm*) steel bars.

Since SMA bars are costly (approximately $80-$100 per pound), it was decided not to incorporate them over the entire length of the column but only in the plastic hinge zone with a 20-*in*. (508-*mm*) length. The SMA bars are connected to adjacent #11 (Ø36 *mm*) mild bars with headed couplers as described before. Nonlinearity in the reinforcing steel is expected to be minor since the reinforcing steel is one size larger than the reinforcing SMA with higher yield strength. The transverse reinforcement was similar to the CIP transverse reinforcement. Table 3.2 summarizes the key design parameters of HCS.

Figure 3.24 shows HCS in detail. The column base detail is shown in Fig. 3.25. Four-inch (102-*mm*) diameter corrugated galvanized metal ducts were used in the footing and later were filled with UHPC. Note that using the design equation presented in the previous chapter and the basic material strength as assumed for PNC, an embedment length of 28.5 *in*. (724 *mm*) is required to fully anchor the #11 (Ø36 *mm*) steel bars in the UHPC-filled duct system. However, the reinforcing SMA bars in HCS fails before the reinforcing steel bars since they are softer and one size smaller than the steel bars thus a shorter embedment length is expected. As mentioned before, the bond strength of bars in UHPC is substantially higher than that of conventional concrete. Therefore, 4 *in*. (102 *mm*) of the longitudinal steel bars were debonded below the coupler level to avoid localized failure because minor nonlinearity could still occur in the mild bars. The effective embedment length in HCS was 24 *in*. (610 *mm*). The SMA bars were connected to headed mild bars at the ends using HRC couplers. The coupler material properties conform to ASTM A576-06 Grade 1141. The shear reinforcement (ρ_s=1.04%) of HCS was similar to the other column models. Thirty six inches (914 *mm*) of the height of the shell (1.5 times of the column diameter) was cast using ECC with a 28-day design compressive strength of 4500 *psi* (31.0 *MPa*). The remainder of the shell was cast with conventional concrete with the same design compressive strength. A minimum clear cover of 1.31 *in*. (33 *mm*) was used in the sections with the couplers. However, the clear cover was 1.62 *in*. (41 *mm*) elsewhere. HCS was initially hollow, but the core was filled with SCC after column installation.

The construction stages of HCS were as follows:

- Casting the footing with embedded ducts (Fig. 3.26)
- Connecting SMA bars to mild bars then assembling the bar cage (Fig. 3.27)
- Casting ECC portion of the shell (Fig. 3.28)
- Casting conventional concrete for remainder of the shell
- Erecting and positioning precast column (Fig. 3.29)
- Filling the ducts with UHPC (Fig. 3.30)
- Column shell Installation (Fig. 3.31)
- Filling the column core and casting the head, both with SCC

The ends of the ducts were plugged with galvanized steel duct caps (Fig. 3.32). A rectangular 2 *in*. (51 *mm*) by 3 *in*. (76 *mm*) plastic gutter was used to cast ECC from top of the column to avoid fiber segregation. The length of the gutter was sufficient to reach

the column plastic hinge from top. The UHPC material for the footing ducts were placed from the top using a scoop.

SCC, UHPC, and ECC mix designs used in this study are presented in Tables 3.4 to 3.6. The quality of UHPC and SCC mixes were evaluated before casting. The average static and dynamic flow table test results for UHPC were 7.44 *in*. (189 *mm*) and 8.75 *in*. (222 *mm*), respectively. The slump flow of the SCC mix was 20 *in*. (508 *mm*), which was more than the minimum required (Table 3.3). T_{50} was 2.0 *sec*, which is within the acceptable range of 2-7 *sec*. Visual stability index (VSI) was evaluated as 0.0, which indicates the SCC mix is stable (Fig. 3.33). The static segregation of SCC was 10.3%, which is less than 15%. Overall, the UHPC and SCC mixes met all the requirements.

3.3. Instrumentation

Local and global responses of the column models were measured by a large number of transducers. Strains of the reinforcements were measured by strain gauges installed at different levels. Figures 3.34 to 3.37 show the location of strain gauges. Photographs of the strain gauge installed on the bar, duct, and grouted coupler are shown in Fig. 3.38. Rotations and curvatures of the columns at plastic hinges were measured by vertical displacement transducers placed at opposite faces of the columns in the loading plane (Fig. 3.39). Columns lateral displacements were measured by three displacement transducers (string pots) installed on the column heads. Column lateral forces were measured by the actuator load-cell.

As mentioned before, performance of new SMA-mild bar connection was investigated by tensile tests. To measure mechanical properties of SMA bars connected to mild bars using headed couplers, four strain gauges were installed at the mid-height of the SMA bars for each test sample (Fig. 3.40). Two to four strain gauges were also installed a few inches away from coupler on each mild bar. Strain of the SMA bar was also measured by a laser extensometer, which was used as input of controller of the tensile test machine. At least one extensometer was used to measure slippage of the coupler. The axial force was measured by the load-cell in the tensile test machine.

3.4. Test Setup

A single cantilever configuration test setup was used for column tests (Fig. 3.41). Support for actuator was provided by mounting and prestressing four 4 *ft* ×4 *ft* ×8 *ft* (1.22 *m* ×1.22 *m* ×2.44 *m*) concrete blocks on the strong floor. A 220-*kip* (978-*kN*) servo-hydraulic actuator was used to apply loads to the column models. Axial load was applied to the columns using two 200-*kip* (890-*kN*) hollow core jacks installed on a spreader beam perpendicular to the loading direction.

A self-reacting high-force servo-hydraulic test system was used to test SMA-mild bar connections (Fig. 3.42). The machine has static and dynamic test capabilities with different types of control mechanisms.

3.5. Loading Protocol

The column models were subjected to slow cyclic loads using displacement-control loading. The drift ratio is the ratio of the lateral displacement to the height of the column measured from the top of the footing to the center line of the horizontal actuator. Figure 3.43 shows the drift loading protocol for the column tests. Two full cycles were completed at each drift level. Two displacement rates of 1 *in/min* (25 *mm/min*) and 5 *in/min* (127 *mm/min*) were used in the tests. The former rate was used to capture yielding, which was expected from 0.25% to 3.0% drift ratio. The latter rate was to measure post-yield strength of models from 3% drift ratio to failure. The rates are based on ASTM limits for strain rates of bar tests.

The performance of SMA-mild bar connection was investigated by applying strain-control half-cycle loads (Fig. 3.44). A strain rate of 0.02 %/*sec* (1.2 %/*min*) was applied in all coupler connection tests.

Chapter 4: Column Test Results

4.1. Introduction

The key configuration and novelty of the eight precast column models were presented in the previous chapter. The seismic performance of five of those was evaluated by Haber (2013). In this study, the seismic performance of three other column models, PNC, GCDP, and HCS, was investigated.

In this chapter, the measured strength of materials and the test results for the latter three column models are presented. The test results include observed damage, force-displacement relationships, strain profiles, moment-rotation relationships, and energy dissipation.

4.2. Measured Materials Properties

Several types of materials were used in construction of the column models: conventional concrete, SCC, ECC, UHPC, reinforcing steel, reinforcing SMA, corrugated galvanized steel ducts, and two types of mechanical bar splices. The measured or the ASTM minimum required strength of those materials is presented in this section.

4.2.1. Conventional Concrete

Conventional concrete was used in the footing of all models, the column and the head of CIP, the full-height in the shell of PNC and GCDP, and a partial-height in the shell of HCS. For the compressive testing, 6-*in*. (152-*mm*) by 12-*in*. (305-*mm*) cylinders were used. Table 4.1 presents the measured compressive concrete strength for the conventional concrete at 7-day, 28-day, and the column test-day for each model. At least three samples were tested according to ASTM C39/C39M-12 but only the average of the test data is reported.

4.2.2. SCC

SCC was used in the core and the head of all the precast hollow columns. The measured compressive strength of SCC is presented in Table 4.1. The sample size and the test procedure were similar to the conventional concrete samples.

4.2.3. ECC

ECC was used only in the shell plastic hinge zone of HCS over a 3-*ft* (914-*mm* or 1.5 the column diameter) height from the column-footing interface. The compressive test samples were 4-*in*. (102-*mm*) by 8-*in*. (203-*mm*) cylinders. The compressive test procedure was the same as the conventional concrete. The summary of the compressive test results is presented in Table 4.1.

4.2.4. UHPC

In two column models, PNC and HCS, UHPC was used to fill the corrugated ducts placed in the footings. As mentioned in chapter 2, 3-*in*. (76-*mm*) by 6-*in*. (152-*mm*) cylinders were used for the UHPC compressive test sampling instead of the standard molds. The UHPC manufacturer established its own sample preparation and compressive test method that consists of: sample end saw cutting (Fig. 4.1a), sample end grinding (Fig. 4.1b), and testing at a compressive stress rate of 145 *psi/sec* (1 *MPa/sec*) to failure. To avoid point loading on the sample during the compressive tests, the angle from the center of the sample to any point at the sample end face was not more than 0.5^{o}. No cap was used during the tests since the strength of UHPC is usually higher than any caps. Photographs of the mode of failure of UHPC are shown in Fig. 4.2. At least three samples were used for the UHPC compressive testing but only the average of the test data is presented in Table 4.1.

4.2.5. Mortar and Grout

A non-shrink high-early-strength grout, SS-Mortar, was injected into the grouted couplers used in GCDP. A high strength non-shrink grout was used to fill the construction pedestal-column gap of GCDP using the dry packing technique. For sampling of the both materials, 2-*in*. (51-*mm*) cube molds were used. The compressive test was according to ASTM C109/C109M-11b. The average compressive test results are summarized in Table 4.1.

4.2.6. Reinforcing Steel

Two types of reinforcing steel bars conforming to ASTM A615 and ASTM A706 were used in the models as longitudinal and transverse steels (Table 4.2). #3 (Ø10 *mm*) bars were used for spirals. #6 (Ø19 *mm*) bars were used for the footing and the column head reinforcements. #8 (Ø25 *mm*) and #11 (Ø36 *mm*) bars were used as the column longitudinal reinforcement. The tensile test procedure of reinforcing steel was according to ASTM E8. Figure 4.3 shows the measured stress-strain curves of the longitudinal and transverse steel bars.

4.2.7. Reinforcing SMA

Twenty-*in*. (508-*mm*) long #10 (Ø32 *mm*) SMA bars were used in the plastic hinge of HCS. To date, NiTi superelastic SMA (SE SMA) related ASTM standards are either to explain the material terminologies or how to perform a tensile test suitable for medical applications. However, there is no standard to determine the mechanical properties of reinforcing SMA from structural engineering viewpoints. Definition of those properties as well as a method to measure them from tensile tests is presented in Chapter 6. A summary of the measured mechanical properties of NiTi SE reinforcing SMA used in HCS is presented in Table 4.3. Figure 4.4 shows the measured stress-strain curves of the SE SMA bars used in this study. The second tensile test SMA sample was fractured at the head during the first cycle of 2% strain. Therefore, only the austenite modulus of elasticity was determined and other mechanical properties could not be established for this SMA bar sample. The SMA bars had an austenite finish temperature (A_f) less than 0^oC (32^oF). SMA remains superelastic at any temperature above A_f.

4.2.8. Galvanized Steel Ducts and Couplers

Corrugated galvanized steel ducts were used in the footing of PNC and HCS. Headed reinforcement couplers and grouted couplers were used in the plastic hinge of HCS and GCDP, respectively. In this study, no coupon test was performed on the base material of the ducts and couplers. However, the manufacturers have used standard materials in their products that the properties of which are presented in Table 4.4.

4.3. PNC Column Model

PNC, the column with a UHPC-filled duct connection at the column base, was tested according to the slow reversed cyclic loading protocol presented in Chapter 3. The performance of PNC is presented in this section.

4.3.1. Observed Damage

The PNC cross-section orientation was shown in Fig. 3.4. The column longitudinal bars were labeled as shown in Fig. 3.4. The column was loaded in the North-South direction. The push load was defined as the loading from North to South and the pull load was designated to the loading from South to North (Fig. 3.41). Table 4.5 presents the detailed observed damage for each push/pull load at different drift levels for PNC. Figures 4.5 to 4.22 show the PNC plastic hinge damage in the second cycle of various drift levels.

Flexural cracks were observed during the first cycle of 0.25% drift ratio. Shear cracks were observed during the first cycle of 0.5% drift ratio (Fig. 4.5-4.6). A crack was formed at the column-footing interface during the second cycle of 0.5% drift ratio. The column experienced its first yielding in the pull direction at bar B7 at 0.79% drift ratio of

1% drift cycle under a 41.2-*kip* (183.3-*kN*) force (Fig. 4.8). Concrete spalling was observed on the South-East side of the column during the 3% drift cycle (Fig. 4.11-4.12). Bar B7 was exposed during the second cycle of 5% drift ratio (Fig. 4.16) then buckled during 8% drift cycle (Fig. 4.19-4.20). Finally, four longitudinal bars fractured during 10% drift cycle, three on the North-side and one on the South-side (Fig. 4.21-4.22).

The PNC column mode of failure was longitudinal bar buckling followed by bar fracture above the column-footing interface during 10% drift cycles. No damage of the UHPC-filled duct connection such as bar pullout, duct pullout, or conical failure of the footing concrete was observed.

4.3.2. Force-Displacement Relationship

The measured lateral force-drift hysteretic and envelope responses of PNC are shown in Fig. 4.23. The envelope is shown up to 85% of the push/pull base shear capacity. PNC exhibited no strength degradation up to 8% drift ratio neither in the push nor in the pull direction. However, substantial strength and stiffness loss was observed during the following cycles due to the bar rupture. The column was slightly stronger and more ductile in the pull direction than the push due to the uneven number of longitudinal reinforcements as well as a 7^{o} rotation of the bar cage from North to the East in the column test setup plan view (Fig. 3.4 and 3.41). The longitudinal bar yielded in the push direction at 1.02% drift ratio under a 39.2-*kip* (174.5-*kN*) force. The bar yielded in the pull direction at -0.79% drift ratio under a -41.2-*kip* (183.3-*kN*) force.

The average push and pull envelope is shown in Fig. 4.24. The average yield drift ratio and the average yield lateral force of PNC were 0.89% and 40.3 *kips* (179.4 *kN*), respectively. Failure of a reinforced concrete column is usually considered at the point that the column lateral load resistance drops to 85% of its peak strength due to either bar rupture or the column core concrete crushing. According to this criterion, the drift capacity (or the ultimate drift) of PNC was 8.96%. Displacement ductility is defined as the ratio of the ultimate displacement to the effective yield displacement, which can be calculated using a bilinear curve in which the area under the bilinear curve from the yield displacement to the ultimate displacement is equal to that of the actual column force-displacement relationship from the yield to the ultimate point. Example of the bilinear curve is shown in Fig. 4.24 for PNC. The effective yield drift ratio and the effective lateral force were 1.42% and 63.7 *kips* (283.4 *kN*), respectively. The displacement ductility capacity of PNC was 6.30.

4.3.3. Strain Profiles

PNC reinforcing steel bars were instrumented with 71 strain gauges installed at nine levels of the column. Figures 4.25 to 4.29 show the maximum measured tensile strain of bars B1, B2, B6, B7, and B11 versus the height of the column.

Strain profile was uniform along the column height prior to bar yielding. However, strain was larger in the plastic hinge of the column at and above 2% drift ratio at which strains exceeded the yield strain significantly. Debonding of the longitudinal bars was a successful technique to spread the strain in the footing and above the column-footing interface, which resulted in prevention of strain concentration in UHPC. Outside the debonded region in the footing, the longitudinal bars experienced a higher stress. For example, Fig. 4.30 shows the measured force-strain of strain gauges SG18 and SG12 installed on Bar B1, which were only 1 *in*. (25 *mm*) apart, but former was in the debonded region 4 *in*. (25 *mm*) below the column-footing interface and the latter was outside the debonded region and deeper in the footing. It is obvious that the strain of the bar outside the debonded region was higher than the strain measured inside the unbounded area confirming the effectiveness of debonding in preventing localized failure.

The measured strains in the spirals in the compressive zone for PNC are shown in Fig. 4.31 at different levels. The spirals remained elastic almost in all drift levels. The spirals strain in the compression zone was well distributed above 12 *in*. (305 *mm* or half of the column diameter) from the column-footing interface but was slightly higher at the column base. Due to limitation of data acquisition system at the time of testing, five of the strain gauges installed on the spirals in the East and West sides of the column were not connected. Therefore, the data in the shear cracking zone was not obtained. Nonetheless, the measured data of the remaining gauges showed that the spirals did not yield during the entire test.

4.3.4. Measured Rotation and Curvature

The vertical displacement transducers (DT) installed in the loading plane measured relative displacements that were converted to rotations and curvatures in the plastic hinge. Figure 4.32 shows displacement instrumentation plan for PNC. Figure 4.33 shows a schematic view of a set of DTs installed on a column as well as parameters that are required in rotation (θ) and curvature (φ) calculations:

$$\theta = \frac{\Delta L_L - \Delta L_R}{D + d_L + d_R} \tag{4-1}$$

$$\varphi = \frac{\theta}{h_{ave}} \tag{4-2}$$

where ΔL_L and ΔL_R (*in*. or *mm*) are respectively the measured relative displacements at the left and right sides of the column in the loading direction, D (*in*. or *mm*) is the diameter of the column, d_L and d_R (*in*. or *mm*) are the distances of the left and right DTs from the column faces, respectively. Since the instruments installed on the two sides of the column may not have always the same gage length due to slight variation during installation, the average height (h_{ave}) was used. In PNC, the rotations and curvatures were measured at five levels at the plastic hinge zone.

The measured base moment-rotation (closest level to the footing) of PNC is shown in Fig. 4.34. The column curvature profile, the column height versus the peak curvature, is

shown in Fig. 4.35. The base rotation and curvature were always the highest among the five levels mainly because of the cracking and bar slip at the column-footing interface. Prior to the bar yielding (approximately 1% drift ratio), the column curvature was almost uniform along the height but it was more concentrated at the base at the larger drift levels.

4.3.5. Energy Dissipation

Dissipated energy is defined as area under the force-displacement hysteretic loops. Figure 4.36 shows the cumulative dissipated energy for PNC at different drift levels. The dissipated energy of the column was negligible up to 1% drift ratio prior to reinforcements yielding. However, after the bars yielding in higher drifts, the hysteretic loops became wider resulted in higher energy dissipation.

4.4. GCDP Column Model

The seismic performance of the grouted coupler column, GCDP, is presented in this section.

4.4.1. Observed Damage

The cross-section orientation of GCDP was shown in Fig. 3.13. The loading protocol, loading direction, and push/pull definition are the same as those of the PNC column test presented in the previous section. Detailed description of the observed damage of GCDP at different drift levels is presented in Table 4.6. The strain gauge instrumentation plan is shown in Fig. 3.36.

Figures 4.37 to 4.54 show the GCDP column plastic hinge damage at the end of the second cycle of various drift levels. Cracking at the column base was observed during the second pull of 0.5% drift ratio (Fig. 4.37-4.38). The first longitudinal bar yielded at bar B7 at a 0.83% drift ratio during the first 1% drift ratio cycle under a 35.7-*kip* (158.9-*kN*) force. Spalling of concrete was observed during the first cycle of 2% drift ratio (Fig. 4.41-4.42). During the 3% drift ratio cycle, a small portion of the footing concrete failed in a conical shape at the North-side of the column (Fig. 4.43), which may be attributed to a higher water/cement ratio near the footing surface. The spiral was exposed on the South-side of the column during the first cycle of 4% drift ratio. Bars B11 and B7 were exposed on the South-side of the column during the first push cycle of 6% drift ratio. Bars B6 and B7 buckled during the second push cycle of 6% drift ratio (Fig. 4.49). A spiral fractured during the second push cycle of 8% drift ratio (Fig. 4.51). Bar B6 fractured during the second pull cycle of 8% drift ratio (Fig. 4.52). Then, the column was pulled from 8 to 10% drift ratio with no more bar fracture. Finally, two more bars fractured during the push cycle of 10% drift ratio (Fig. 4.54).

It can be seen in the figures that most of the column damage was concentrated in the pedestal. The reason is that the bulky grouted couplers behaved as large size reinforcements, which made the column stronger in the coupler area and shifted the damage to the weaker region. Minor cracks were observed in and above the coupler region. The GCDP column mode of failure was bar fracture during the second pull cycle of 8% drift ratio.

4.4.2. Force-Displacement Relationship

The measured lateral force-drift hysteretic and envelope responses of the GCDP column are shown in Fig. 4.55. Similar to PNC, the end point of the envelope curves are taken at a point where the lateral force has dropped to 85% of the peak measured base shear. No strength degradation was observed up to 5% drift ratio with minimal strength degradation up to 8% drift ratio. Significant strength degradation occurred when the longitudinal bars ruptured. The column exhibited 9 *kips* (40 *kN*) higher base shear capacity and 0.9% higher drift capacity in the pull direction compared to the push direction. The reason for those differences could not be determined. The first longitudinal bar yielded in the push direction at 0.83% drift ratio with a 35.7-*kip* (158.9-*kN*) force. The first pull yielding was occurred at 0.79% drift ratio with a 43.1-*kip* (191.6-*kN*) force.

Figure 4.56 shows the average of the measured push and pull envelope as well as the idealized curve for GCDP to be used in the displacement ductility calculation. The column average yield drift ratio and the average yield lateral force were 0.81% and 39.4 *kips* (175.3 *kN*), respectively. The effective yield drift ratio and the effective lateral force were 1.23% and 59.9 *kips* (266.6 *kN*), respectively. The ultimate drift capacity of GCDP was 8.73%. The displacement ductility capacity of the column was 7.07.

4.4.3. Strain Profiles

Similar to PNC, five longitudinal bars of GCDP were instrumented with strain gauges at different levels. Figures 4.57 to 4.61 show the strain profiles of the column. No bars were instrumented inside the sleeves but the sleeves were instrumented on the outer surface at their mid-length. The sleeve strains are also shown in the figures. It can be seen that the strain was well distributed along the height of the pedestal due to debonding of the bars. As an example, Fig. 4.62 shows the measured lateral force-strain hysteretic curves of two strain gauges, SG18 and SG23, which were both installed in the debonded region of bar B11 but 5.5 *in*. (140 *mm*) apart. It is obvious that the strains at two levels of the column are similar due to the debonding. The measured strains of the sleeves were significantly lower than those of the longitudinal bars due to larger size of the sleeves.

4.4.4. Measured Rotation and Curvature

Figure 4.63 shows the displacement transducers in the GCDP column plastic hinge zone. The rotation and curvatures were measured at six levels. Figure 4.64 shows the column base moment-rotation curve. The curvature profile is shown in Fig. 4.65. It can be seen that the curvature at the bottom of the couplers (level 4) was higher than the reminder of the coupler region mainly because of the gap opening at the end of pedestal as well as the coupler bond-slip effect. The curvature of the column at the base (level 1) was the highest because of the longitudinal bar slip.

4.4.5. Energy Dissipation

Figure 4.66 shows the cumulative dissipated energy of GCDP at different drift levels. Similar to PNC, the dissipated energy was negligible up to 1% drift ratio because of the elastic behavior of the system. However, the longitudinal bar yielding in the higher cycles resulted in higher energy dissipation.

4.5. HCS Column Model

Both conventional and advanced materials were used in HCS. In this section, the seismic performance of HCS is presented.

4.5.1. Observed Damage

The cross-section orientation of HCS was shown in Fig. 3.24. The loading protocol, loading direction, and push/pull definition are the same as those defined for the other two columns as presented in the previous sections. Detailed description of the observed damage of HCS at different drift levels is presented in Table 4.7. The strain gauge instrumentation plan was shown in Fig. 3.37. Figures 4.67 to 4.86 show the HCS column plastic hinge damage at the end of the second cycle of various drift levels.

Due to using ECC and SMA, plastic hinge damage of HCS was relatively minor even under large drifts (Fig. 4.81 to 4.86). Cracking at the column base was observed during the first push of 0.75% drift ratio. The longitudinal SMA bar yielded at bar B10 at 1.44% drift ratio during the first 2% drift ratio cycle under a 44.6-*kip* (198.3-*kN*) force. At 3% drift level, spalling of the cover concrete was initiated (Fig. 4.73-4.74). However, no spiral was exposed during the entire of the test. A major crack was developed on both sides of the column approximately at a 10-*in*. (254-*mm*) high above the column-footing interface in which the SMA bars were visible under large drifts (Fig. 4.75 to 4.86). The average width of crack was 1.31 *in*. (33 *mm*) at 8% drift level (Fig. 4.81-4.82). No longitudinal bar was exposed at zero-force at any of the drift levels, which indicates that the plastic hinge damage of HCS was limited to only the cover concrete damage. The column withstood one full cycle of 10% drift ratio without any bar fracture. However, the first bar rupture was observed exactly at the end of the first pull cycle of 10% drift

ratio. No more bar fracture occurred during the second cycle of 10% drift ratio. Two more bars ruptured during the first push cycle of 12% drift ratio (Fig. 4.85) and one more bar fractured during the first pull cycle of 12% drift ratio (Fig. 4.86).

It can be seen that most of the damage was concentrated in a major crack, which was nearly closed by SMA restoring forces even under large drifts after removing the lateral force (Fig. 4.87 to 4.93). The HCS column mode of failure was bar fracture at the end of one full cycle of 10% drift ratio.

4.5.2. Force-Displacement Relationship

The measured lateral force-drift hysteretic and envelope responses of HCS are shown in Fig. 4.94. As described for the previous models, the end points of the envelopes are assumed where the lateral force drops to 85% of the maximum base shear. No strength degradation was observed up to 10% drift ratio prior to the longitudinal bars fracture. The column behavior was almost symmetric in push and pull directions. The first longitudinal bar yielded in the push direction at 1.44% drift ratio under a 44.6-*kip* (198.3-*kN*) force. The first pull yielding was occurred at 1.15% drift ratio under a 37.5-*kip* (166.7-*kN*) force.

Figure 4.95 shows the average of the measured push and pull envelope of HCS. The column average yield drift ratio and the average yield lateral force were 1.29% and 41.0 *kips* (182.5 *kN*), respectively. The effective yield drift ratio and the effective lateral force were 2.16% and 68.29 *kips* (303.8 *kN*), respectively. The displacement ductility capacity of the column was 4.80. However, it should be noted that the displacement ductility is not a good representative of ductility of SMA-reinforced structures since the yield strain of reinforcing SMA is approximately 5 times of reinforcing steel yield strain resulting in a higher effective yield displacement and very small ductility. For example, the displacement ductility capacity of HCS was only 65% of that of CIP. However, the drift capacity of both columns was 10%.

4.5.3. Strain Profiles

Six longitudinal bars of HCS were instrumented with strain gauges at different levels. On each longitudinal bar, two strain gauges were installed on the SMA part and four strain gauges were installed on the steel parts. Figures 4.96 to 4.101 show the longitudinal bar strain profiles. As mentioned before, a major crack was developed on both sides of the column approximately at 10 *in*. (254 *mm*) above the column-footing interface (mid-length of the SMA bars). It can be seen that the highest strains were measured in the vicinity of this crack on the SMA bars. The peak measured strain of the steel bars was only four times higher than the yield strain of steel indicating a minor plasticity in the steel bars. Note that the ultimate strain of a steel bar is usually 50 times of its yield strain. Similar to the other two columns, the strain distribution was uniform in the debonded area below the column-footing interface.

The measured strains of the spirals in the compressive zone and the shear cracking zone of HCS are shown in Fig. 4.102 and 4.103, respectively. It can be seen that the spirals were yielded in both zones. However, the spiral strains were higher leading to yielding earlier in the column compression zone compared to the shear cracking zone. The spirals yielded at 4% drift ratio due to the confinement effect in the compression zone. The shear cracks were observed in the first cycle of 5% drift ratio (Table 4.7), but spirals did not yield in the shear crack zone until the column reached 8% drift ratio.

4.5.4. Measured Rotation and Curvature

The as-built displacement transducer installation plan is shown in Fig. 4.104. The rotation and curvatures were measured at five levels. Figure 4.105 shows the column base moment-rotation curve. The curvature profile is shown in Fig. 4.106. It can be seen that the curvature in the vicinity of the major crack was the highest almost under all drift levels.

4.5.5. Energy Dissipation

The cumulative dissipated energy of HCS is shown in Fig. 4.107 at different drift levels. The dissipated energy was negligible up to 1% drift ratio. However, after initiation of phase transformation in the SMA bars under the higher drifts, the energy dissipation was increased.

4.6. Summary of Column Test Results

Three half-scale columns, PNC, GCDP, and HCS, incorporating novel column-to-footing connections and advanced materials were tested under slow cyclic loading to failure. The summary of the experimental findings is as follows:

- The mode of failure of all three specimens was the longitudinal bar rupture.
- The drift ratio capacity of PNC, GCDP, and HCS was 8, 8, and 10%, respectively.
- The damage was well distributed in the plastic hinge of PNC. The GCDP column plastic hinge damage was concentrated in the 12-*in*. (305-*mm*) pedestal. The plastic hinge damage of HCS was minor and limited only to the cover concrete due to using the high performance reinforced concrete, ECC.
- No column-to-footing connection damage was observed in any of the three column models.
- Debonding was a successful technique to spread the strain in the plastic hinge and to avoid strain concentration.

Chapter 5: Evaluation of Column Performance

5.1. Introduction

The test results of three new precast column models, PNC, GCDP, and HCS, were individually presented in the previous chapter. In this chapter, the seismic performance of those columns is compared with a reference cast-in-place column (CIP) as well as other counterpart precast models that were tested by Haber (2013).

5.2. PNC and CIP Column Models

5.2.1. Mode of Failure

PNC was a precast column model that did not incorporate any couplers. The column bars in PNC extended into UHPC-filled ducts placed in the footing. The longitudinal bar buckling followed by bar fracture was the failure mode of both CIP and PNC columns (Table 5.1). PNC withstood two full cycles of 8% drift ratio without any strength degradation. Buckling of the bars was observed in this drift level. However, four longitudinal bars fractured during the following loading to 10% drift. Three of those bars were located above the column-footing interface. The location of the fourth bar fracture could not be identified, and it is suspected that it occurred inside the footing. The first bar buckling in CIP was observed during the second push cycle of 10% drift ratio followed by bar fracture during the second pull cycle of 10% drift ratio. Two more bars fractured in the following cycle. All the fractured bars located above the column-footing interface. The drift capacity of the PNC and CIP columns was 8 and 10%, respectively.

5.2.2. Plastic Hinge Damage

The plastic hinge damage in PNC and CIP is shown in Fig. 5.1 to 5.7 for selected drift levels. The PNC and CIP column plastic hinge damage for all drift levels can be found in Appendix A. The damage in PNC was similar to CIP damage nearly at all drift levels. However, the cover concrete deterioration was slightly more extensive in PNC mainly because of 1150 *psi* (7.93 *MPa*) lower concrete compressive strength compared to that in CIP. For example, the first longitudinal bar in PNC was exposed during 5% drift cycle while the longitudinal bar was first exposed during 6% drift cycle in CIP. A small portion of the footing around the CIP column failed in a conical shape, which is attributed to either poor quality of concrete above the top layer reinforcements of the footing or strain penetration into the footing. However, no damage of the UHPC-filled duct

connection such as bar pullout, duct pullout, or conical failure of the footing was observed in PNC.

5.2.3. Force-Displacement Relationship

The lateral force-drift hysteretic curves for PNC and CIP are shown in Fig. 5.8. The CIP column exhibited minor strength degradation at 2.5% drift ratio but maintained its strength after 3% drift ratio to the second cycle of 10% drift ratio when some of the longitudinal bars fractured. The PNC model showed wider hysteretic loops than the CIP model in the push direction indicating higher energy dissipation. The CIP model was stronger than the PNC model in the push direction up to the 5% drift ratio but exhibited the same capacity in the following cycles. However, the PNC model was slightly stronger than the CIP model in the pull direction. These minor strength differences are because of the difference in the materials strength as well as variations in the actual bar locations in the models.

Figure 5.9 shows the average push and pull force-drift envelopes for PNC and CIP. The envelope of PNC is essentially the same as CIP envelope up to 8% drift ratio. The displacement ductility capacity of PNC and CIP using the idealized curves were 6.30 and 7.36, respectively. The lower displacement ductility capacity of PNC (14%) was because of 1150 *psi* (7.93 *MPa*) lower concrete compressive strength of the shell compared to the CIP column concrete, which reduced the column resistance against bar buckling. The first longitudinal bar was exposed in PNC at 5% drift ratio while the first CIP bar exposure was at 6% drift ratio. Consequently, the first longitudinal bar buckling in PNC occurred at 8% drift ratio while the first bar buckling in CIP was observed at 10% drift ratio. It is clear that the premature loss of the cover concrete due to the lower compressive strength in PNC is the cause of the lower displacement capacity compared to CIP.

5.2.4. Strain Profiles

The peak tensile strain profiles of extreme bars B1, B2, B6, and B7 (Fig. 3.4 and 3.24) measured in the plastic hinge region of PNC and CIP are shown in Fig. 5.10 at 2, 4, and 5% drift ratios. Note that the measured yield strain was 2270 $\mu\varepsilon$. The strains for higher drift ratios are not shown because the data were not reliable for some of the strain gauges. The strain was well distributed along the height of the PNC column similar to the strain profile in CIP. Debonding of the bars in PNC resulted in an approximately uniform strain distribution in the debonded area. Furthermore, the debonding of the bars below the footing surface led to shifting of higher strains to a higher depth into the footing. No yielding of the transverse reinforcements was observed even at 10% drift ratio in the columns.

5.2.5. Measured Rotation and Curvature

The base moment-rotation hysteretic curves of PNC and CIP are shown in Fig. 5.11. Both columns showed the same moment-rotation behavior in the push direction up to 8% drift ratio. However, PNC exhibited higher rotations than CIP in the pull direction even in low drift levels. Generally PNC rotations were higher because of the debonded bars at the column-footing interface. The maximum measured curvature profile for PNC and CIP at each drift level versus the column height is shown in Fig. 5.12. The curvature in PNC was approximately the same as the CIP curvature except for that at the column base where the curvature in CIP was slightly higher under various drift levels.

5.2.6. Energy Dissipation

The cumulative dissipated energy of PNC and CIP are shown in Fig. 5.13 at different drift levels. The end point of the curve is the largest drift level at which the column withstood at least one full cycle without any bar fracture. It can be seen that the energy dissipation was comparable in the two columns with slightly larger energy dissipation in PNC. The higher energy dissipation in PNC is more visible under larger drift ratios and it is attributed to the debonding of the longitudinal bars that spread the longitudinal bar yielding over a larger portion of these bars.

5.3. GCDP, CIP, and GCPP Column Models

Two grouted coupler column models were tested by Haber (2013), one with a partial precast pedestal at the column base (GCPP) and the other with no pedestal (GCNP). Both columns showed 40% lower drift and displacement ductility capacities than those of CIP mainly because of the strain concentration below the column-footing interface. The shifting of the grouted couplers above the pedestal by one-half of the column diameter did not improve the drift capacity in GCPP. This was because the ducts in the pedestal confined the grout and the combination of the bars and ducts behaved similarly to large size reinforcements with little yielding, thus shifting the nonlinearity to the footing.

In the present study, the longitudinal bars in the pedestal were debonded in GCDP to improve the displacement capacity. The seismic performance of GCDP is compared with CIP and GCPP in detail in this section. The global response of GCNP is also included.

5.3.1. Mode of Failure

Failure in all column models with grouted couplers was due to fracture of the longitudinal bars (Table 5.1). GCDP withstood a full cycle of 8% drift ratio but five of its longitudinal bars fractured in the following cycles. Only two of those were visible, located 4 *in*. (102 *mm*) above the column-footing interface. The first bar fracture in the CIP column was observed during the second cycle of 10% drift ratio followed by two more bar fracture in the following cycle, all located above the column-footing interface.

In summary, the drift capacity of GCDP and CIP were 8 and 10%, respectively. The drift capacity of GCPP was 6% with two fractured longitudinal bars located approximately 4.94 *in*. (125 *mm*) below the column-footing interface on average. The drift capacity and the location of the bar fracture for GCNP was the same as those of GCPP.

5.3.2. Plastic Hinge Damage

The plastic hinge damage of GCDP, CIP, and GCPP are shown in Fig. 5.14 to 5.19 for selected drift levels. The plastic hinge damage of those columns for all drift levels is presented in Appendix B. In CIP, the damage was well distributed along the plastic hinge. However, the damage was concentrated in the pedestal of GCDP and GCPP with minor flexural and shear cracks in and above the coupler region. The reason is that the bulky grouted sleeves behaved as large size reinforcements resulting in stronger section with minor damage.

5.3.3. Force-Displacement Relationship

The lateral force-drift hysteretic curves of GCDP, GCPP, and CIP are shown in Fig. 5.20. All three models showed wide and stable hysteretic loops with minimal strength degradation up to the first longitudinal bar rupture. The lateral load capacity of GCDP was approximately 18% less than CIP and GCPP base shear capacity in the push direction but it was almost the same as the CIP and GCPP base shear capacity in the pull direction. The reason for the force difference in push and pull directions could not be clearly identified.

The average push and pull lateral force-drift envelope for all the grouted coupler columns as well as CIP is shown in Fig. 5.21. GCDP showed 56% higher displacement ductility capacity with respect to the previous grouted coupler models (GCPP and GCNP) and only 4% less displacement ductility capacity compared to CIP. As mentioned before, the lower drift capacity of GCDP (8% drift ratio) compared to CIP (10% drift ratio) was because of 1235 *psi* (8.51 *MPa*) lower concrete compressive strength of the shell compared to CIP, which reduced the column resistance against bar buckling.

5.3.4. Strain Profiles

The peak tensile strain profiles for GCDP, GCPP, and CIP are shown in Fig. 5.22 at different drift levels for extreme bars B2, B6, B7, and B11. The couplers strains measured on the outer face of the sleeves are also shown at 20 *in*. (508 *mm*) from the column-footing interface. It can be seen that in GCPP, most of the bar large plasticity was concentrated in the bottom half of the pedestal while the strain was well distributed in the plastic hinge of GCDP due to debonding of the longitudinal bars in the pedestal. The strain was also well distributed in the plastic hinge of CIP. The longitudinal reinforcements of GCDP experienced the largest strains among all columns.

5.3.5. Measured Rotation and Curvature

The moment-rotation hysteretic curve for GCDP, GCPP, and CIP are shown in Fig. 5.23. The rotation at the end of the first cycle of 6% drift ratio is marked in the figure. The rotation at the base of GCDP was large and similar to the CIP column rotation. However, the base rotation of GCPP was less than the other columns base rotations due to the presence of the pedestal with grouted ducts. The grouted ducts incorporated in the precast pedestal increased the stiffness and strength of the section resulted in a lower section ductility.

The curvature profile for GCDP, GCPP, and CIP are shown in Fig. 5.24 at different drift levels. It can be seen that GCPP exhibited lower curvature than the other models. The curvature profile of GCDP was similar to the CIP column.

5.3.6. Energy Dissipation

The cumulative dissipated energy versus drift level is shown in Fig. 5.25 for the grouted coupler models as well as CIP. GCDP dissipated higher energy than the other columns because of the distribution of the bar plasticity in the debonded region. Compared to CIP, GCDP exhibited 17% higher dissipated energy, an average from 2 to 8% drift ratio. The GCPP and GCNP columns exhibited similar energy dissipation to CIP up to 5% drift ratio. However, GCNP dissipated 10% higher energy than the CIP and GCPP columns at 6% drift ratio.

5.4. HCS, CIP, and HCNP Column Models

Eight different materials, conventional and advanced, were incorporated in the HCS column. The seismic performance of HCS is compared with that of CIP as well as HCNP (the headed coupler column with no pedestal) performance since the headed reinforcement couplers were utilized in both HCS and HCNP. The global responses of HCPP (the headed coupler column with partial pedestal) are also included.

5.4.1. Mode of Failure

The failure mode of all four columns was the longitudinal bar fracture (Table 5.1). All four columns withstood at least one full cycle of 10% drift ratio without any bar fracture. No evidence of the reinforcing SMA bar buckling was observed in HCS.

5.4.2. Plastic Hinge Damage

The plastic hinge damage of HCS, CIP, and HCNP are shown in Fig. 5.26 to 5.33 for selected drift levels. The plastic hinge damage of the columns for all drift levels is

presented in Appendix C. It is clear that the plastic hinge damage of HCS was minimal and significantly less than CIP and HCNP plastic hinge damage due to utilizing the high performance fiber reinforced concrete, ECC. In CIP and HCNP, the damage was distributed along the plastic hinge in which the longitudinal bars were exposed and the core concrete was crushed. However, in HCS, no significant spalling occurred until 8% drift and only the cover concrete spalled with no longitudinal bar exposure even after 12% drift cycle. A major crack was developed on both sides of HCS approximately at 10-*in*. (254-*mm*) high (mid-length of the SMA bars) from the column-footing interface. However, the crack was almost completely closed after removing the lateral forces even at large drifts because of the SMA bars self-centering forces (Fig. 4-87 to 4.93).

5.4.3. Force-Displacement Relationship

The lateral force-drift hysteretic curves of HCS, CIP, and HCNP are shown in Fig. 5.34. CIP and HCNP showed wide and stable hysteretic loops with minimal strength degradation up to the first longitudinal bar rupture. However, the hysteretic loops of HCS were significantly different than the other columns with a flag-shape behavior due to utilizing superelastic reinforcing SMA bars in the plastic hinge. Not only the lateral load capacity was maintained with no degradation in HCS, but also the rate of gaining strength was increased after 6% drift ratio due to phase transformation of SMA bars, which is not seen in conventional RC columns.

The average push and pull lateral force-drift envelope for all the headed bar coupler columns as well as CIP is shown in Fig. 5.35. In low drift cycles, the initial stiffness of HCS was the same as the other columns stiffness due to the elastic behavior. However, after the concrete cracking under higher drifts in which the reinforcement effect is dominant, the stiffness of HSC was lower than the other columns stiffness since the modulus of elasticity of reinforcing SMA is only 20% of that of reinforcing steel. It is evident that the displacement capacity of the precast columns was equal or better than the cast-in-place column. The lateral load capacity of HCS was 12% higher than that of CIP, HCNP, and HCPP on average.

5.4.4. Strain Profiles

The peak tensile strain profiles for HCS, CIP, and HCNP are shown in Fig. 5.36 at different drift levels. Note that due to using a different bar arrangement in HCS compared to the other columns, strains of bars B5 and B10 of HCS were compared with those of CIP (and HCNP) bars B6 and B11, respectively. It can be seen that the strain was well distributed in the plastic hinge of CIP and HCNP. However, high strains were measured in HCS in the vicinity of the single crack near to the mid-length of SMA bars.

5.4.5. Measured Rotation and Curvature

The moment-rotation hysteresis for HCS, CIP, and HCNP is shown in Fig. 5.37. The rotation at the end of the first cycle of 8% drift ratio is also illustrated in the figure. It can be seen that the base rotations of HCS and HCNP were less than those of CIP because of presence of the headed bar couplers at or above the column-footing interface. In addition, #11 (Ø36 *mm*) reinforcing steel bars were used in the footing of HCS while #8 (Ø25 *mm*) reinforcing steel bars were used in CIP and HCNP footing, which caused smaller rotations in HCS compared to the other columns.

The curvature profiles for HCS, HCNP, and CIP are shown in Fig. 5.38 at different drift levels. It can be seen that the HCS base curvature was the smallest among the other columns base curvature. HCS exhibited higher curvature than the other models approximately at the mid-length of SMA bars due to a concentrated crack that was developed on both sides of the column approximately at 10 *in*. (254 *mm*) from the footing surface.

5.4.6. Energy Dissipation

Figure 5.39 shows the cumulative dissipated energy versus drift levels for the headed bar coupler models as well as CIP. The energy dissipation in HCS was lower than the other columns since the SMA flag-shape behavior controlled the force-drift hysteretic curves in HCS resulting in narrower loops with less enclosed area. Note that the lower energy dissipation of HCS is not necessarily a concern since the column showed higher strength and displacement capacity than the conventional column, satisfying all design specification limitations. Furthermore, the lower cracked stiffness of HCS compared to other columns results in longer vibration period and generally smaller seismic forces, which could reduce energy dissipation demand.

5.4.7. Residual Displacements

In cyclic responses, residual displacement is the displacement at the intersection of the unloading curves with the abscissa. Figure 5.40 shows the HCS, HCNP, and CIP columns residual drift versus the peak drift. The residual drift is the ratio of the residual displacement to the column height, which was 108 *in*. (2.74 *m*) for all column models. It is evident that the residual displacements of the SMA-reinforced column, HCS, were substantially lower than those of HCNP and CIP, which were reinforced with steel bars. For example, the residual displacement of HCS was on average 79% smaller than that of CIP for drift ratios of 2 to 10%, a range with significant residual displacements for CIP.

5.5. Summary and Overall Evaluation

A summary of the seismic performance of the precast columns with emphasis on PNC, GCDP, and HCS is presented in this section. The performance parameters that were considered are: mode of failure, displacement capacity, distribution of plasticity, dissipated energy, and residual displacements.

5.5.1. Mode of Failure

The longitudinal bar fracture was the failure mode in all eight columns. Table 5.1 presents the failure mode of the columns, the number, and the location of the ruptured bars. Note that a reinforced concrete column is considered to have failed when either longitudinal bars fracture or the core concrete fails in compression, whichever happens earlier resulting in 15% reduction of the lateral load resistance of the system. Table 5.2 presents the percent reduction of the lateral load strength at each drift level (the ratio of the peak base shear measured in the second cycle of each drift level to the first cycle peak base shear at that drift level). It is clear that 15% reduction in the base shear occurred at drift levels during which the first longitudinal bar ruptured. The transverse reinforcement fracture and confined concrete failure at the core edge were observed in some of the column models but they were not considered to constitute failure since the lateral load strength dropped only by a small amount (a maximum of 6%).

5.5.2. Displacement Capacity

The displacement capacity and displacement ductility capacity of the ABC columns are presented in Table 5.3. Figure 5.41 shows the measured average push and pull envelope of PNC, GCDP, HCS, and CIP hysteretic curves. The displacement capacity (the displacement at the point where the lateral load capacity has dropped by 15%) of PNC was 9.67 *in*. (246 *mm*), which was 10% lower than that of CIP, 10.7 *in*. (272 *mm*). Note that in the previous sections, the drift capacity of PNC and CIP was reported as 8 and 10%, respectively, which was the drift level of the cycle in which the first longitudinal bar fractured. The displacement capacity of GCDP was 9.43 *in*. (240 *mm*), 12% lower than that of CIP. It was pointed out before that the lower displacement capacity of PNC and GCDP compared to CIP was because of the lower compressive strength of the column shell. Compared to the previous grouted coupler columns, GCPP and GCNP, the displacement capacity of GCDP was 47% higher on average. The displacement capacity of HCS was 11.19 *in*. (284 *mm*), 5% larger than that of CIP.

In terms of displacement ductility capacity, PNC and GCDP showed 14 and 4% lower ductility than CIP, respectively. The displacement ductility evaluation is not recommended for SMA-reinforced structures since the yield strain of SMA is approximately 5 times the steel yield strain resulting in smaller apparent displacement ductility, a misleading number when compared to ductility of conventional RC members.

5.5.3. Distribution of Plasticity

Based on the measured strains, the location of longitudinal bar large plasticity (strains greater than four times the steel bar yielding, approximately 10,000 $\mu\varepsilon$) was identified for each column model. Figure 5.42 illustrates the PNC and CIP bar large nonlinearity in the plastic hinge. It can be seen that the bar plasticity pattern for PNC was similar to that of CIP. The bar large plasticity for grouted coupler column models as well as CIP is shown

in Fig. 5.43. It can be seen that only in GCDP, the bar nonlinearity pattern is comparable with that of CIP, which was because of the bar debonding in the pedestal resulting in 56% higher displacement ductility capacity compared to GCNP and GCPP. In HCS, the large plasticity was observed in the 20-*in*. (508-*mm*) long SMA bars and small portion of the steel bars under the footing surface (Fig. 5.44) and the plasticity pattern was comparable to that of CIP.

5.5.4. Dissipated Energy

The cumulative dissipated energy for PNC, GCDP, HCS, and CIP are shown in Fig. 5.45. It can be seen that PNC and GCDP dissipated 13 and 17% more energy than CIP (on average for 2 to 8% drift ratio), respectively mainly because of the bar debonding. The dissipated energy of HCS was 44% lower than that of CIP (on average for 2 to 10% drift ratio) due to the flag-shape behavior of the reinforcing SMA bars.

5.5.5. Residual Displacements

Figure 4.46 shows residual drift versus peak drift for PNC, GCDP, HCS, and CIP. It can be seen that the residual displacements of the SMA-reinforced column, HCS, were substantially smaller than those of steel-reinforced columns, which ensures post-earthquake serviceability of SMA-reinforced bridges even after severe ground shaking.

5.5.6. Overall Evaluation

In this section, overall seismic performance of the precast column models of the present study in contrast with cast-in-place column model is presented.

The UHPC-filled duct connection incorporated in PNC was emulative of the conventional connection since:

1. The ultimate capacities of the column were developed and high drift ratios were achieved,
2. No connection damage such as bar pullout, duct pullout, or conical failure of the footing was observed in the PNC column base connection,
3. Mode of failure, base-shear capacity, and strength and stiffness degradation of PNC was nearly the same as those of CIP. However, PNC showed slightly higher energy dissipation due to the debonding of longitudinal bars above and below the column-footing interface.

Overall, UHPC-filled duct connections are proposed as alternative to cast-in-place connections in high seismic regions to connect precast columns to shallow cap beams and footings. When the footing or the cap beam depth is sufficient, high-strength grouts may be used in lieu of UHPC.

The seismic performance of the grouted coupler column with pedestal presented in this study, GCDP, was emulative of CIP since:

1. Mode of failure and strain distribution in the plastic hinge of GCDP was similar to those of CIP. GCDP dissipated more energy than CIP because of the longitudinal bar debonding in the pedestal,
2. The displacement ductility capacity of GCDP was only 4% lower than that of CIP,
3. GCDP reached its ultimate capacities without any connection damage or premature failure of the reinforcements.

In summary, the mechanical grouted sleeve splice connection presented in this study is proposed as a suitable ABC column-to-footing connection in high seismic zones even though most design specifications prohibit utilizing mechanical bar splices in plastic hinge of reinforced concrete members.

The ABC SMA-reinforced concrete bridge column presented in this study, HCS, exhibited improved seismic performance over CIP since:

1. The displacement capacity of HCS was higher than that of CIP,
2. The plastic hinge damage of HCS was limited only to the cover concrete while the damage penetrated into the CIP core concrete,
3. HCS reached its ultimate capacities without any connection damage,
4. Residual displacement of HCS was substantially lower than that of CIP ensuring post-earthquake functionality of the bridge.

In summary, ABC columns with connection and details similar to HCS are expected to perform better than conventional columns in seismic zones.

Chapter 6: NiTi Superelastic SMA Reinforcements for Concrete Structures

6.1. Introduction

Shape memory alloy (SMA) is an advanced material with large strain recovery and high energy dissipation capacity that may be used as an alternative to conventional reinforcing steel in civil engineering structures. Previous studies regarding general applications of superelastic SMA in civil engineering were presented in chapter 1. In this chapter, behavior of SE SMA as reinforcement is described in detail. There are several constitutive models for stress-strain behavior and design of SMA in different austenite and martensite phases. However, they are based on very limited test data. A lack of well-established procedure to determine key points (e.g. yield point) of the stress-strain curves from uniaxial tests is another shortcoming of previous models.

In this chapter, first behavior of SMA is illustrated. Large strains in SMA can be recovered by either heating known as shape memory effect or unloading known as superelastic (SE) effect (Otsuka and Wayman, 1998). Only Nickel-Titanium (NiTi or Nitinol) SE SMA is the interest of this research because of its many advantages such as high strength capacity, high ductility capacity, high strain recovery, and high corrosion resistance. Previous studies regarding simple SE SMA constitutive models are then briefly presented. A standard tensile test method for NiTi SE SMA bars and wires is described. The key points of the model from structural engineering viewpoints are identified, and a procedure is proposed to determine these key points from test data. Finally, a structural design specification is proposed for NiTi SE SMA reinforcements with either minimum acceptable or expected mechanical properties.

6.2. Previous Studies

6.2.1. NiTi SMA Stress-Strain Behavior

The behavior of SMA is generally affected by: (1) temperature changes, (2) whether SMA is under tension or compression, (3) the number of loading cycles, and (4) loading rate. The effect of these factors on the hysteretic behavior is presented in this section.

Strnadel et al. (1995) tested a dog-bone NiTi SMA specimen at different temperatures under tensile loading (Fig. 6.1). Austenite finish temperature (A_f) was 44^oC (111^oF) for this specimen. Note that SMA remains superelastic at any temperature above A_f. The cross section of the specimen was rectangular at the middle portion with a dimension of 0.04 *in*. (1 *mm*) by 0.157 *in*. (4 *mm*). The strain rate was $4\times10^{-4}\ s^{-1}$. It can be seen in Fig. 6.1 that the strength and stiffness of SMA increase when temperature rises. SMA

behaves similarly to conventional reinforcing steel at temperature below A_f but superelastic behavior is dominant above this temperature.

Limited test data is available regarding stress-strain behavior of SE SMA under compressive loads. Plietsch and Ehrich (1997) performed uniaxial tensile and compressive tests on an hourglass NiTi SE SMA specimen machined from wire at a strain rate of 0.01 s^{-1}. The diameter of specimen was 0.12 *in*. (3 *mm*) at the neck of the specimen. Figure 6.2 shows the measured full-cycle stress-strain relationships. It can be seen that the compressive strength and stiffness are higher than of those in tension.

Frick et al. (2004) tested hot-rolled and cold-drawn NiTi SE SMA specimens under tensile and compressive loads (Fig. 6.3). Tensile flat dog-bone shape specimen had a length of 1 *in*. (25 *mm*) and a 0.12-*in*. × 0.04-*in*. (3-*mm* ×1-*mm*) rectangular cross section. The compressive specimen was also a rectangular section with dimensions of 0.16*in.* × 0.16*in.* × 0.31*in.* (4*mm* × 4*mm* × 8*mm*). Similar to the previously described study, higher stiffness and strength were observed for SE SMA under the compressive loads compared to tensile loads.

Miyazaki et al. (1986) investigated cyclic behavior of NiTi SE SMA wires at different temperatures (Fig. 6.4). Increasing number of cycles resulted in lower strength at inducing martensite (first yield) and higher residual displacements. For example, under 100 cycles of loading at a temperature of 298.5^oK (25.3^oC or 77.5^oF), the first yield strength dropped by approximately 20% and the residual strain increased by approximately 0.006 *in*./*in*. (*mm*/*mm*).

Strain rate effect on NiTi SE SMA was investigated by McCormick (2006). Figure 6.5 shows the SE SMA stress-strain behavior of a dog-bone shaped bar at loading rate of 0.025 *Hz* (static loading), 0.5 *Hz*, and 1.0 *Hz* (approximate earthquake loading). The diameter of the reduced section of the bar was 0.5 *in*. (12.7 *mm*). A loading frequency of 1.0 *Hz* made the hysteretic loops narrower with an approximately 20% increase in the yield strength. Equivalent viscous damping deceased from 3.9% for the static loading to 2.4% and 1.8% for the 0.5 and 1 *Hz* loading frequencies, respectively. The residual strain was insensitive to the loading rate.

It is clear that there are several parameters affecting the stress-strain behavior of SE SMA. To facilitate adoption of SMA in civil engineering structures, a simple constitutive model was used in this study to reproduce the actual behavior with minor acceptable discrepancies. There are some supporting facts that even simple approximate models are sufficiently accurate to estimate seismic performance of SMA-reinforced members. First, reinforcing SMA is not subjected to severe temperature variations since it is embedded in concrete. Figure 6.6 shows temperature profiles for a circular column with a diameter of 11.8 *in*. (300 *mm*) exposed to fire loading (EVN 1992-1-2, 1996). Only one quarter of the section is shown. Noting that the minimum column cover is 2 *in*. (50.8 *mm*) based on AASHTO LRFD 2010, at least 50% reduction of temperature is expected at the reinforcement layer compared to the ambient temperature. For example, if the column ambient temperature rises to 1000^oC (1800^oF), the reinforcements only experience 500^oC (900^oF), in the worst-case scenario. For the lower temperature rises such as weather temperature changes, the reduction factor is expected to be even higher. Second,

asymmetric behavior may be included in the simple models. Third, a structure may experience only a few large cycles but many small ones during an earthquake. Therefore, the strength and stiffness degradation due to the multi-cycle loading is minor.

6.2.2. Atanackovic's Model

Moment-curvature relationships for a rectangular beam made of superelastic SMA were parametrically investigated by Atanackovic and Achenbach (1989) using the stress-strain model shown in Fig. 6.7. They stated that the yield in loading starts at the point (σ_2, ε_2) and ends at (σ_2, ε_4). The lines OB and RR^{II} are assumed to be parallel with a slope of E_1. The constitutive model was presented with parameters as shown but the key points were not quantified and no procedure was presented to determine the points in the model from tests.

6.2.3. Graesser's Model

Graesser and Cozzarelli (1991) proposed another simple model for SMA under uniaxial loads (Fig. 6.8). The model is able to reproduce SE behavior up to the hardening of the SMA after the transition to martensite (approximately 8% strain). The model also takes into account the strain rate effect. However, no relation between the uniaxial test data and the model was provided and no procedure to determine different parameters was described in the study.

6.2.4. Auricchio's Model

A one-dimensional model was proposed by Auricchio and Sacco (1997) for SE SMA that takes into account the effect of asymmetry in stress-strain behavior (Fig. 6.9). Four critical points of the curve are defined in tension and compression. Even though values for the critical points were provided for only two SE SMA wires, there was no procedure to relate these points to the actual test data. This model has been widely used in finite element software packages such as ANSYIS and SeismoStruct.

Several other complex models are available for SMA in different martensite and austenite phases. However, the simple model developed by Auricchio was adopted in this study and key parameters were identified to suit structural engineering perspectives.

6.3. Standard Tensile Test for NiTi SE SMA

There is only one ASTM standard regarding tensile testing of NiTi SE SMA, ASTM F2516-07 (2007), which was originally developed for medical and surgical materials and devices to determine the upper plateau strength, lower plateau strength, residual elongation, tensile strength, and elongation. These terminologies for NiTi SE SMA are according to ASTM F2005-05 (2010). However, those parameters do not sufficiently

address the interest of structural engineers. The aforementioned ASTM standard test procedure was adopted in this study to either define or extract the key points of interest.

Figure 6.10 shows an example of a SE SMA sample tested using the ASTM procedure. The tensile test procedure includes loading to 6% strain, unloading to 1-*ksi* (7-*MPa*) stress or less then pulling to failure. The key points can be determined using new parameters are listed below. Full stress-strain hysteretic curve can be developed using these parameters.

- Observed yield strength (f_{yo}) is the stress at the initiation of nonlinearity on the first cycle of loading to the upper plateau.
- Austenite modulus (k_1) is the average slope between 15 to 70% of f_{yo}.
- Post yield stiffness (k_2) is the average slope of curve between 2.5% and 3.5% of strain on the upper plateau of the first cycle of loading to 6% strain.
- Austenite yield strength (f_y) is the stress at intersection of line passing through origin with slope of k_1 and line passing through stress at 3% strain with slope of k_2.
- Lower plateau inflection strength (f_i) is the stress at the inflection point of lower plateau during unloading from the first cycle to 6% strain.
- Lower plateau stress factor, $\beta = 1 - (f_i/f_y)$.
- Residual strain (ε_{res}) is the tensile strain after one cycle to 6% and unloading to 1 *ksi* (7 *Mpa*).
- Recoverable superelastic strain (ε_r) is maximum strain with at least 90% strain recovery capacity. Using the ASTM standard for tensile testing, $\varepsilon_r \leq 6\%$.
- Martensite modulus (k_3) is the slope of the curve between 8 to 9% strain, subsequent to one cycle of loading to 6% strain, unloading to 1 *ksi* (7 *MPa*) and reloading to the ultimate stress.
- Secondary post-yield stiffness ratio, $\alpha = k_3/k_1$.
- Ultimate strain (ε_u) is strain at failure.

Note that there is no standard test procedure for NiTi SE SMA under compressive loads. However, the same parameters are defined in compression to establish the complete hysteretic behavior.

6.4. SE SMA Model

As mentioned before, a flag-shape hysteretic behavior according to Auricchio's model is used in this study (Fig. 6.10 and 6.11). The following constitutive stress-strain variation rules are proposed in this study using the aforementioned parameters measured from tensile tests as follows:

1. Upon loading, the path is a line starting from origin (elastic behavior) with a slope of k_1 up to f_y. Upon unloading at any strain between 0 and f_y/k_1, the path is on the same line but toward the origin.
2. After f_y, the slope changes to k_2 and remains constant up to 6% strain. Upon unloading at any strain between f_y/k_1 and 6%, the path is a line with the slope of k_1

until the stress reduces by $\beta.f_y$. Then, unloading path is a line with the slope of k_2 until intersecting with the initial elastic line where the unloading path is the same as of that in step (1).

3. The loading path beyond 6% strain is a line with the slope of k_3 up to ε_u. Upon unloading at any strain between 6% and ε_u, the path is similar to the loading line but toward 6% strain then unloading path is the same as the unloading path of the step (2).

Compressive behavior can be modeled either symmetrically or asymmetrically with similar constitutive rules as mentioned for tension.

6.5. Design Specification

An extensive literature review was conducted to statistically determine a range for the mechanical properties of NiTi SE SMA to be used in structural design of the SMA-reinforced structures. Measured tensile or compressive stress-strain curve presented in each study was used to extract the model parameters (Table 6.1). Most of the test samples were SMA circular bars but a few were wires or rectangular section samples. In the cases that either test was not according to the ASTM standard or it was a cyclic test, the closest loop to 6% strain was used for the data extraction. Figure 6.12 shows all test data used in this study except SAES (2012 and 2013). An example of extracted model is shown in Fig. 6.13.

Noting that the mechanical properties presented in the table are for NiTi SE SMA samples produced by different manufacturers and tested with different methods, the average measured data are proposed as expected mechanical properties for design (Table 6.2). Based on communications with experts from the SMA industry, it is not necessary to specify minimum mechanical properties for all parameters. Considering the relatively small size of the database on NiTi SE SMA properties, the industry uses a large safety factor for SMA products calculated based on the average properties minus three standard deviations. For seismic design of SMA-reinforced members, it is recommended to use the expected mechanical properties.

Since there is no standard test procedure to determine the compressive mechanical properties of NiTi SE SMA, only the expected values are proposed (Table 6.3), which are the average of available test data.

At the time of this study, only plain NiTi SE SMA wires and bars are available. The available bar sizes are from #4 (Ø12.7 *mm*) to #10 (Ø32 *mm*) (Table 6.4). It is recommended that the austenite finish temperature (A_f) of NiTi SE SMA to be 14^oF (-10^oC) or average low temperature of the site of the structure less 9^oF (5^oC), whichever is smaller. SMA remains superelastic at temperatures above A_f. Density and Poisson's ratio of SMA may be considered as 405 lb/ft^3 (6500 kg/m^3) and 0.33, respectively (McCormick, 2006). Coefficient of thermal expansion of SE SMA is 6.1×10^{-6} $/^oF$ (11×10^{-6} $/^oC$) (Otsuka, et al, 1998). Electrical resistivity of SE SMA may be used as 32.3 $\mu\Omega$-*in.* (820 $\mu\Omega$-*mm*) (Faulkner et al., 2000). Research has shown that welding process is difficult for NiTi SMA since SMA may become brittle by reacting to oxygen, nitrogen,

and hydrogen at high temperature (Schlossmacher et al, 1997). Therefore, welding of SMA is not recommended.

6.6. Concluding Remarks

The actual behavior of NiTi superelastic (SE) SMA was presented in this chapter. It was shown that four factors affect the stress-strain hysteresis of NiTI SE SMA: (1) ambient temperature, (2) loading direction, (3) number of loading cycles, and (4) strain rate. A simple constitutive stress-strain model was adopted in this study for SE SMA, and key parameters of the model were identified from structural engineering viewpoints. Then, a procedure was developed to determine these parameters using the ASTM standard tensile test method for NiTi SE SMA. Test data presented in previous studies was used to extract the key parameters of the model and to determine a range for each mechanical property. The average of all available test data was proposed as expected mechanical properties to be used in seismic design of SMA-reinforced concrete members. However, minimum mechanical properties were specified to be used in material production.

Chapter 7: Analytical Modeling

7.1. Introduction

The experimental results for 14 large-scale pullout tests and three half-scale column tests were presented in previous chapters. Analytical modeling methods for those tests are presented in this chapter. A finite element computer program, OpenSees (2013), was used for simulations.

Several types of constitutive material models are available in OpenSees for concrete, reinforcements, and other materials. Different types of elements exist for beams, columns, and other members. Materials and elements that were used in the present study are described in this chapter. The modeling method for the pullout tests and the column tests (CIP, PNC, GCDP, and HCS) are presented. A new analytical model was developed and presented to include the effect of bond-slip in simulation of reinforced concrete (RC) members using a modified stress-strain model for reinforcements. In addition, a new model was developed to account for the effect of bar debonding on seismic responses of RC members. Concluding remarks are presented at the end of the chapter.

7.2. Material Models

Several types of cementitious materials were used in this study (conventional concrete, SCC, ECC, and UHPC), which were unconfined or confined. For analytical investigation presented here or in the following chapter, four uniaxial constitutive concrete material models were used for the cementitious materials: "Concrete01", "Concrete02", "Concrete01WithSITC ", and "Concrete04". The envelope and the key parameters of those models are shown in Fig. 7.1. "Concrete01" has no tensile strength. The tensile behavior of concrete is modeled in "Concrete02" and "Concrete04". The compressive strength after concrete crushing (stress at strains greater than ε_{cu}) is neglected in "Concrete04" but the residual strength (f'_{cu}) is modeled in other material models. The compressive modulus of elasticity (E_c) in all concrete models is calculated automatically. For example, the modulus of elasticity for "Concrete01" and "Concrete02" is $2f'_{cc}/\varepsilon_{cc}$. Figure 7.1d shows the "Concrete01WithSITC" material model, which has similar compressive constitutive rules to "Concrete01" but a trigger tensile strain (ε_t) is used to change the unloading path from tensile field to compressive field. This is to model the effect of crushed concrete trapped in cracks during unloading resulting in an improved seismic analyses in terms of capturing residual displacements (Lee and Billington, 2010). In the following sections of this chapter, the key parameters of the concrete material models used in simulations are presented.

Two types of uniaxial constitutive steel material models were used in this study for reinforcements: "ReinforcingSteel" and "Steel02" (Fig. 7.2). The former steel model,

which was specifically developed for reinforcing steel bars, was extensively used in this study. However, in a few cases the latter steel model was used to improve convergence as well as the overall responses. The mechanical properties used for each model are presented in the following sections.

At the time of this study, no constitutive material model was available in OpenSees for reinforcing SMA. However, "SelfCentering" material, which was originally developed for self-centering steel members, was used for SMA bar modeling. In Chapter 6, a model was proposed for reinforcing SMA (Fig.7.3). Table 7.1 presents relationships between the SMA model parameters and parameters of the "SelfCentering" material model. Residual strain may be simulated using "slip strain" of the "SelfCentering" material model. For example, if 1% residual strain is desired at and above 6% strain cycles, the "slip strain" should be "bearing strain" less 1% strain. These and other parameters used for HCS column simulations are presented later in this chapter.

7.3. Elements

Several types of elements are available in OpenSees to model different members. Two types of nonlinear elements are usually used for RC members (Fig. 7.4): (1) element with distributed plasticity, and (2) element with lumped plasticity at the member ends with a linear-elastic segment in between. Only force-based elements are used in this study. Details regarding the elements used in modeling of each test specimen are presented in subsequent sections.

7.4. Bond-Slip Modeling

Longitudinal bars slippage relative to the surrounding concrete when stressed under tensile forces is known as the bond-slip effect. The slippage usually affects the local and global response of RC members.

7.4.1. Previous Studies

Many bond-slip models are available in the literature and the most cited one is the model proposed by Eligehausen et al. (1982). However, to directly incorporate them in structural analysis of RC members requires additional nonlinear bond-slip springs or additional fiber-section at connections.

Monti and Spacone (2000) presented a fiber-section beam element formulation that includes bond-slip effects in which the steel fiber state is modified (Fig. 7.5a). In other words, the element formulation was derived using a modified stress-strain behavior for reinforcing steel fibers. The modified behavior was obtained by connecting the original steel fibers to a series of bond-slip springs (using Eligehausen' model) at the element ends. Examples of modified stress-strain relationship for steel fiber are shown in Fig. 7.5b. It can be seen that the modified behavior of steel fiber was softer than that in the

original steel fiber. Note that "full bond" represents the original steel fiber behavior with no bond-slip effect and "normal bond" is for the steel fiber including the bond-slip effect. "Weak bond" is for the steel fiber with insufficient anchorage length at which bar pulls out. This element requires an optimization for the number of bond-slip elements and is not available in most finite element computer programs including OpenSees.

Zhao and Sritharan (2007) proposed a constitutive stress-slip model (Fig. 7.6) for reinforcing steel to be used in fiber-section analysis of RC members. To use this bar model, extra elements (such as zero-length element) at the member ends are required. Using the proposed stress-slip model, they obtained good correlation between the calculated local and global responses and those measured in the column and joint tests. This stress-slip bar model was used in finite element models with only displacement-based elements.

Wehbe et al. (1997) developed a method to include bond-slip effects in seismic responses of RC bridge columns using a modified moment-rotation relationship. The modified behavior is included in the model using additional springs or elements at the member ends. Since the modified moment-rotation is based on an initial moment-curvature analysis of the column section, the effect of axial load variation during the column analysis is ignored in the bond-slip spring (or element).

In the present study, an efficient simple method was developed using a modified stress-strain relationship for reinforcing steel fibers to implicitly include the bond-slip effect in response analysis. The method does not require additional elements or pre-nonlinear analysis and can be used in fiber-section analysis of RC members.

7.4.2. Bond-Slip Effect in Conventional Connections

Figure 7.7 shows a schematic view of a single bar anchored in a conventional concrete connection. The effective strain of the bar at the surface of concrete (level A) can be calculated based on the combined deformation of the bar force-deformation spring and the bar bond force-slip spring in series. The modified strain of the bar (ε_s') is:

$$\varepsilon_s' = \varepsilon_s + (\frac{F}{k_b})/L \qquad \text{(Eq. 7.1)}$$

$$k_b = 78.5 d_d . L_{emd} . u \qquad \text{(Eq. 7.2)}$$

$$u = \begin{cases} \dfrac{9.5\sqrt{f'_c}}{d_b} \le 800\ psi, & for\ \#11\ bars\ and\ smaller \\ 6\sqrt{f'_c} & for\ \#14\ and\ \#18\ bars \end{cases} \qquad \text{(Eq. 7.3)}$$

$$L = \frac{F}{\pi . d_b . u} = \frac{f_s . d_b}{4u} \le L_{emb} \qquad \text{(Eq. 7.4)}$$

where ε_s is the strain of the bar (*in./in.*), F is the bar force (*lbs*), k_b is the bond force-slip stiffness (*lbs*/*in.*), d_b is the diameter of the bar (*in.*), L_{emd} is the embedment length of the

bar in the connection (*in*.), u is the bond strength of the bar (*psi*), f'_c is the compressive strength of concrete (*psi*), L is the effective development length (*in*.), and f_s is the bar stress (*psi*). In the present study it is proposed to modify the modulus of elasticity of the bar to account for the softening effect of bond-slip on the overall bar stiffness:

$$E_s' = f_y / \varepsilon_y' \quad \text{(Eq. 7.5)}$$

where f_y is the yield strength of the bar and ε_y' is the modified yield strain.

For a well anchored bar in which bar pullout is avoided, a linear-elastic bond-slip behavior (Eq. 7.2) may be assumed using a secant stiffness as shown in Fig. 7.7. Eligehausen's bond-slip model (Chapter 2) was adopted and modified in this study to calculate k_b in which the bond strength (u) was calculated according to ACI 318-63 (1963) instead of the original model to take into account the effect of the concrete compressive strength and the bar size (Eq. 7.3). The slip at the peak bond stress was 0.04 *in*. (1 *mm*) based on the Eligehausen's bond-slip model. Using $u=F/(\pi.d_b.L_{emd})$, the secant stiffness can be formulated as presented in Eq. 7.2.

The proposed method may be used to account for the bond-slip effect in any reinforcing steel model (such as those shown in Fig. 7.2). However, note that only strain-related parameters are modified. Figure 7.8 shows an example of original and modified reinforcing steel models using the proposed method. It can be seen that the modified steel fiber stress-strain behavior including the bond-slip effect is softer than that of the original model with no bond-slip effect, as expected. A similar behavior was reported by Monti and Spacone (2000) (Fig. 7.5) for a bar embedded $20d_b$ in concrete. To validate the proposed method, the modified stress-strain of a #8 (Ø25 *mm*) bar, which was anchored $20d_b$ in a concrete with 5000-*psi* (34.5-*MPa*) compressive strength, was compared with that calculated by Monti and Spacone (2000) (Fig. 7.9) using finite element analysis. The proposed method resulted in a softer behavior for steel fiber since the proposed method: (1) use secant stiffness instead of Eligehausen's full bond-slip model, and (2) utilizes the ACI bond strength, which is 40% or more lower than that of Eligehausen's model.

The modified stress-strain steel material model may be used only in the fiber sections located at connections, and the original steel fibers may be used elsewhere. No extra fiber section or elements is needed and no preliminary analysis is required. Overall, it is recommended to use the proposed method in analytical modeling of RC members at which the bond-slip effect is significant because of its simplicity, generality, and ease of modeling.

7.4.3. Bond-Slip Effect in UHPC-Filled Duct Connections

Bond behavior of UHPC-filled duct systems and application of those systems in column-to-footing connections were presented in previous chapters. In this section, a similar method to that proposed for conventional connections is presented to include the bond-slip effect in seismic analyses of UHPC-filled duct connections.

Since in a well-designed UHPC-filled duct connection duct or bar pullout is prevented, only initial stiffness of duct or bar bond-slip relationship needs to be considered in model. The initial slope of bar and duct bond-slip curves (section 2.10) are 930 $psi^{0.5}$ (77$MPa^{0.5}$) and 3600 $psi^{0.5}$ (300$MPa^{0.5}$), respectively. To include the bar and duct bond-slip effect in column response analysis, stress-strain of the longitudinal bars immediately above the column-footing interface (Fig. 7.10) is modified using a series of spring. The series include the reinforcing steel force-deformation spring, the bar force-slip spring, and the duct force-slip spring. The modified strain of the bar (ε_s') is:

$$\varepsilon_s' = \varepsilon_s + (\frac{F}{k_d} + \frac{F}{k_b}) / L_{emd} \quad \text{(Eq. 7.6)}$$

$$k_d = 11310 d_d \cdot \sqrt{f'_c} \quad \text{(Eq. 7.7)}$$

$$k_b = 2920 d_b \cdot \sqrt{f'_{UHPC}} \quad \text{(Eq. 7.8)}$$

where ε_s is the strain of the bar (*in./in.*), F is the bar force (*lbs*), k_d is the duct bond force-slip stiffness (*lbs*/*in.*), k_b is the bar bond force-slip stiffness (*lbs*/*in.*), L_{emd} is the embedment length of the bar in the connection (*in.*), f'_c is the compressive strength of concrete (*psi*), f'_{UHPC} is the compressive strength of UHPC (*psi*), d_b is the diameter of the bar (*in.*), and d_d is the inner diameter of the corrugated galvanized duct (*in.*). To account for the softening effect of bond-slip, the modulus of elasticity of the longitudinal bars is modified as:

$$E_s' = f_y / \varepsilon_y' \quad \text{(Eq. 7.9)}$$

where f_y is the yield strength of the bar and ε_y' is the modified yield strain. Note that only the strain-related parameters of reinforcing steel material model are modified. Examples are presented in subsequent sections of this chapter.

7.5. Bar Debonding Modeling

To help spread plasticity, the longitudinal bars were debonded at the connection region in the three column models investigated in this study. Debonding tends to soften the connection and hence should be included in analyses especially for the GCDP column model in which the debonded length was relatively long.

When a bar is debonded from concrete, the strain compatibility assumption between the bar and the surrounding concrete is not valid, thus making analytical modeling of debonded bars very complex. No study regarding modeling of debonded reinforcements in RC members was found in the literature. Therefore, a method was developed in the present study to include the bar debonding effect in response analysis of RC members using a modified stress-strain behavior for reinforcement.

7.5.1. Debonding Effect in Conventional Connections

Experimental studies have shown that the bond strength of plain bars is less than 30% of that of deformed bars (Mo and Chan, 1996; Verderame et al., 2009). A European design code recommends a plain bar bond strength of only 10% of the deformed bar bond strength (CEB-Fib Model Code, 1993). It was therefore decided to ignore the bond strength of plain bars in the present study. The bond behavior of debonded deformed bars was assumed to be the same as the plain bar bond behavior with negligible bond strength. Thus, it can be assumed that behavior of a debonded bar embedded in concrete is similar to behavior of a bar that is not connected on its side surface to concrete. Level B shown in Fig. 7.7 illustrates this condition at which the bar is debonded from level A to B (or is free from level A to B). The modified strain of the debonded bar at level B is calculated based on cumulative displacements at this level, which consists of: (1) the bar deformation at level B assuming full bond (original bar force-deformation relationship), (2) displacement caused by the slippage of the bar at level A due to bond slip, and (3) the bar elongation at level A. The modified strain of the debonded bar (ε_s') at level B is:

$$\varepsilon_s' = \varepsilon_s + (\frac{F}{k_b})/L + \varepsilon_{elong} \quad \text{(Eq. 7.10)}$$

where ε_{elong} can be found using Wehbe's method (Wehbe et al., 1997) as follows:

$$\varepsilon_{elong} = \begin{cases} \frac{\varepsilon_s}{2} & f_s \le f_y \\ \frac{\varepsilon_y}{2} + \frac{\varepsilon_s . L_1}{2L} & f_s > f_y \end{cases} \quad \text{(Eq. 7.11)}$$

$$L_1 = \frac{(f_s - f_y)d_b}{4u} \le L \quad \text{(Eq. 7.12)}$$

All parameters were defined in 7.4.2. The first two terms of Eq. 7.10 are the same as Eq. 7.1 terms. The third term in Eq. 7.10 is the additional strain at level B caused by the bar elongation at level A (Fig. 7.7).

7.5.2. Debonding Effect in UHPC-Filled Duct Connections

A method similar to that presented in the previous section can be used to determine the modified stress-strain for debonded bars in UHPC-filled duct connections (Fig. 7.10). The modified bar strain (ε_s') at level B is:

$$\varepsilon_s' = \varepsilon_s + (\frac{F}{k_d} + \frac{F}{k_b})/L_{emd} + \varepsilon_{elong} \quad \text{(Eq. 7.13)}$$

$$\varepsilon_{elong} = \begin{cases} \frac{\varepsilon_s}{2} & f_s \le f_y \\ \frac{\varepsilon_y}{2} + \frac{\varepsilon_s . L*}{2L_{emb}} & f_s > f_y \end{cases} \quad \text{(Eq. 7.14)}$$

$$L^* = \frac{(f_s - f_y)d_b}{4u_b} \le L_{emb} \quad \text{(Eq. 7.15)}$$

$$u_b = 30\sqrt{f'_{UHPC}} \quad \text{(Eq. 7.16)}$$

All parameters were defined in 7.4.3.

Examples are presented in subsequent sections of the chapter.

7.6. Pullout Test

7.6.1. Modeling Method

A one-dimensional finite element model was developed to simulate the pullout tests responses (Fig. 7.11). Three portions of the bar were modeled. The first portion was the embedded segment of the bar, the second was from the concrete surface to the threads, and the third portion was the threaded segment of the bar. "Stee02" material was used to model the steel bar in all segments. The embedded portion of the bar was divided into 99 elements attached to a series of nonlinear bar and duct bond-slip springs. This was done to determine the stress and strain distribution along the height of the bar. However, if global responses such as duct or bar force-slip are desired, only one bar element working in series with one bar bond-slip spring and one duct bond-slip spring is sufficient. The bar area was reduced in the third segment to account for the reduced size due to threading. "MultiLinear" material model was used in OpenSees to model the bar and duct bond-slip springs. This material utilizes multiple stress-strain points to constitute the hysteretic behavior. Thirteen stress-strain points, ten points to construct the initial nonlinear curve and three points for the linear parts of bond-slip models, were used in the present study to construct the nonlinear bond spring envelopes. The bond-slip models were presented in chapter 2.

7.6.2. Analytical Results

All 14 specimens were analyzed using the modeling method presented in the previous sections. The test day compressive strength of conventional concrete and UHPC (Table 2.4), and the measured yield and ultimate strength of bars (Table 2.5) were used in analyses. Figure 7.12 shows the calculated bar stress, bar bond stress, and duct bond stress profiles for specimen SP1. The bar yielding, the bar fracture, and the duct and the bar bond capacities are also shown. It can be seen that the model can duplicate the bar or duct bond strength as well as the failure mode. For example, the calculated pull force capacity for SP1 was 50.65 *kips* (225.3 *kN*), which underestimated the measured force capacity by 10%. The analytical results for all specimens are summarized in Table 7.2. The calculated mode of failure matched the observed mode of failure in eight of the specimens. Since the bond-slip models were based on the average of the test data, the model failed to reproduce the observed mode of failure in the other specimens and bar or duct pulled out before bar fracture.

The calculated and measured force-strain relationships of the bars are shown in Fig. 7.13 for selected specimens. The responses are at a depth of six bar diameter in UHPC. It can be seen that the model was able to simulate the measured bar strains with a reasonable accuracy.

Duct pullout was observed in SP4 and SP11. Figure 7.14 shows the measured and calculated force-duct slip relationships. It can be seen that the model was able to reproduce the measured duct behavior with good accuracy. Bar pullout was observed in SP6. Figure 7.15 shows the measured and calculated force-bar slip curves. It can be seen that the initial behavior of the analytical model was in a good agreement with the test but the model overestimated the force capacity by 22%. The reason in that the bar bond-slip model was developed based on the average test data of six pullout tests, and the bond strength of SP6 was 80% of the average bond strength (Fig. 2.38). Therefore, the calculated pull force for SP6 was overestimated. More test data is required to evaluate the model behavior at and above peak responses.

Table 7.2 presents a summary of the analytical results for all pullout tests. The error between the measured and calculated pull forces was 7.7% on average with a standard deviation of 6.7%. Figure 7.16 shows the measured and calculated pull forces with a ±10% error band. Only in three specimens (group II specimens in which the bar bond behavior was investigated) the calculated pull force showed more than 10% error.

In summary, the proposed finite element model may be used for analyses of UHPC-filled duct connections for further bond study or seismic analysis of elements incorporating these types of connections.

7.7. Analysis of CIP Column

CIP was a conventional cast-in-place column tested by Haber (2013). In this section, analytical modeling method and results for CIP are presented.

7.7.1. Modeling Method

A three-dimensional finite element fiber-section model was constructed in OpenSees (Fig. 7.17). The footing and the column head were modeled using elastic elements each with a stiffness calculated based on the test day compressive strength of concrete (Table 4.1). The column element was modeled using a force-based element, "forceBeamColumn", with five integration points. Table 7.3 presents material model parameters used in the CIP model. The test day compressive strength of column concrete (Table 4.1) was used for the unconfined concrete fibers, which were modeled using "Concrete01". The Mander's model was used to determine the confined concrete model parameters, which was also "Concrete01". The section discretization is shown in Fig. 7.17. The core concrete was divided into 30 circumferential by 10 radial fibers, and the cover concrete was divided into 10 circumferential by 10 radial fibers. At the first integration point located at the column base, steel fibers were modeled using

"ReinforcingSteel" with a modified stress-strain behavior accounting for bond-slip effects (section 7.4.2). Table 7.4 presents the original and modified mechanical properties for the CIP steel bars and Fig. 7.18 illustrates the original and modified steel stress-strain curves. From the second to the fifth integration points, the steel fibers were modeled using "Steel02". The material model parameters of these steel fibers are presented in Table 7.3. The peak axial load measured during the CIP column test, 221.8 *kips* (986.6 *kN*), was applied to the model, and the P-Δ effect was included.

7.7.2. Analytical Results

The measured and calculated force-drift hysteretic curves for CIP are shown in Fig. 7.19. The calculated responses exhibited good agreement with those measured in the test, especially the strength at each cycle, the loading and unloading paths, the residual drifts upon unloading, and the pinching effect. The measured and calculated force-drift envelopes, averaged for the push and pull loading direction, are shown in Fig. 7.20. The initial stiffness was slightly overestimated, and the calculated base shear capacity was 5% higher than that measured in the test.

The model was also able to simulate the local responses with reasonable accuracy. For example, the measured and calculated base moment-curvature hysteretic relationships for CIP are illustrated in Fig. 7.21, which shows a reasonable match. The CIP base curvature was measured over 1-*in*. (25-*mm*) length of the column immediately above the column-footing interface. In Fig. 7.22, the measured and calculated longitudinal bar strains at the CIP column base section are shown. The model overestimated the bar tensile strains. Note that estimated bar strains in cracked reinforced concrete members at best present a crude approximation. This is because the fundamental assumption of plane section remaining plane in analytical models is violated as soon as the concrete member cracks. Even over a short length of a longitudinal reinforcing bar, the actual strain may be highly variable during the tension stiffening between the cracks. Despite these considerations, the calculated strains were compared with the measured data to determine the trend in the correlation between the two.

It was found that the model with bond-slip effect reproduces better global and local responses compared to a model without the bond-slip effect. For example, Fig.7.23 shows the calculated longitudinal bar B7 strains at the column base with and without the bond-slip effect. It can be seen that the calculated strains including the bond-slip effect were in a better agreement with the measured strains. This also shows the robustness of the proposed bond-slip modeling method (section 7.4) in finite element analyses of concrete members.

Overall, the proposed modeling method for CIP may be used for analytical investigations or design of conventional reinforced concrete bridge columns.

7.8. Analysis of PNC

A UHPC-filled duct connection was used in PNC to connect the precast column to the footing. Conventional materials were used in the plastic hinge of PNC. In this section, analytical modeling method to simulate the PNC column global and local responses is presented.

7.8.1. Modeling Method

A four-node fiber-section model was used for PNC. Figure 7.24 shows the model in detail. Similar to the CIP model, the footing and the column head were modeled using elastic elements, each with a stiffness calculated based on the test day compressive strength of concrete (or SCC for the head) (Table 4.1). The column element was a force-based nonlinear element, "forceBeamColumn", which is a distributed plasticity element. Five integration points were used. The PNC column section discretization is shown in Fig. 7.24. Four types of fibers can be distinguished: cover concrete, core concrete, core SCC, and reinforcements. For cover concrete and core SCC, 10 circumferential by 10 radial fibers were used. However, the confined concrete was discretized into 30 circumferential by 10 radial fibers. The cover concrete fibers were modeled using "Concrete01" material. For confined concrete and confined SCC, "Concrete02"material was used with properties calculated according to the Mander's model. The modulus of rupture was according to ACI318-11 (2011), and the tensile secondary stiffness, E_t, was calculated assuming that the ultimate tensile strain is 3%. Table 7.5 presents the fiber properties used in the PNC column simulation.

In the first integration point located at the column base, a modified stress-strain was used for steel fibers (according to section 7.4.3) to account for bond-slip effects (Fig. 7.25). However, the original steel fiber was used for the rest of the column. "ReinforcingSteel" material model was used for steel fibers in all integration points. The measured peak axial load, 200.5 *kips* (891.8 *kN*), was applied on node 4 of the model, and the P-Δ effect was included.

7.8.2. Analytical Results

The measured and calculated lateral force-drift hysteretic curves for PNC are shown in Fig. 7.26. The model overestimated the initial stiffness in the push direction but the strength at each loop, the loading and unloading paths, and the pinching effect were successfully reproduced. The measured and calculated force-drift envelopes for PNC are shown in Fig. 7.27. The calculated envelope showed good agreement with that measured in the PNC column test. Local responses also show good agreement with those measured in the test. For example, Fig. 7.28 shows the measured and calculated base moment-curvature relationships for PNC. The column base curvature was measured over a 3-*in*. (76-*mm*) length of the column (section 4.3.4) immediately above the footing. It can be seen that the model was able to reproduce the local responses with a good accuracy. The underestimation of curvatures under larger loads is due to concentrated cracking at the

base that is affected by bond slip. This effect is not reflected in the moment-curvature analysis for the section.

7.9. Analysis of GCDP

Grouted mechanical bar splices were used in the plastic hinge of the GCDP. A cast-in-place pedestal was used above the column-footing interface with debonded longitudinal bars.

7.9.1. Modeling Method

Similar to other column analytical models, a three-dimensional four-node fiber-section system was developed for the GCDP simulation. Details regarding the GCDP model are shown in Fig. 7.29. The footing and the column head were modeled as elastic elements. The column element was a nonlinear force-based element, "forceBeamColumn", with 10 integration points. The GCDP column section discretization was similar to that in the PNC model. Table 7.6 presents the fiber material model parameters utilized in the GCDP model. In the first integration point located at the column base, the steel fiber stress-strain was modified according to section 7.4.2 to take into account the bond-slip effect. Figure 7.30 shows the original and modified steel fiber model. The bars were debonded in the pedestal area. Therefore, the steel fibers in the second integration point were further modified according to section 7.5.1 to account for debonding (Fig. 7.31). At other integration points, the original steel fibers were used. The peak measured axial force, 205.2 *kips* (912.8 *kN*), was applied on node 4 of the model, and the P-Δ effect was included.

7.9.2. Analytical Results

The measured and calculated lateral force-drift hysteretic responses of GCDP are shown in Fig. 7.32. It was mentioned in the previous chapters that the lateral load capacity of GCDP in push direction was 18% lower than that in pull direction and the reason could not be identified. The analytical model estimated nearly the same lateral load capacity in the push and pull directions leading to an excellent match in the pull direction but overestimated the push strength. Figure 7.33 shows the measured and calculated force-drift envelopes of the hysteresis curves. The calculated initial stiffness was slightly higher than the measured stiffness, and the calculated lateral force capacity was 8% higher than that measured in the test.

Haber et al. (2013) developed a detailed model to simulate the seismic behavior of grouted coupler columns in which the pedestal was modeled as an individual element, the coupler hysteretic behavior was developed and was used as reinforcements in the fiber sections, and the bond-slip effect at the column-footing interface and the bottom of the coupler level was included. The model successfully reproduced the grouted coupler column tests behavior. Figure 7.34 shows the calculated force-drift hysteretic responses

for GCDP using the proposed model presented in this chapter and the detailed model. Both calculated responses are essentially the same. Therefore, the proposed simple model may be sufficient to conduct analytical investigation of columns with grouted couplers.

Figure 7.35 shows the measured and calculated base moment-curvature relationships for GCDP. The calculated curvatures showed good agreement with those measured in the test. The curvature was measured over a 3-*in*. (76-*mm*) length of the column (section 4.4.4). The curvature was underestimated under larger drifts because of the column-footing interface cracking.

Overall, the proposed modeling method is recommended for general analysis and design of columns with grouted couplers.

7.10. Analysis of HCS

Eight different materials were incorporated in HCS. Advanced materials, ECC and reinforcing SMA bars, were used in the plastic hinge of HCS. The precast column was connected to the footing using a UHPC-filled duct connection.

7.10.1. Modeling Method

Similar to other column analytical models, a three-dimensional four-node fiber-section model was developed for HCS. Figure 7.36 shows the model details. The footing and the column head were modeled with elastic elements. A nonlinear force-based element, "forceBeamColumn", was used for the column element with seven integration points. The HCS column section discretization was similar to that in PNC and GCDP models. Table 7.7 presents the fiber material model parameters in the HCS model. The shell was made with ECC from footing surface to a height of 1.5 column diameter. Confined properties of ECC was calculated according to Motaref et al. (2011) as shown in Fig. 1.19. However, Mander's model was used to calculate confined properties of SCC. ECC fibers were modeled using "Concrete02" material model but the tensile strength and stiffness were ignored. Better overall agreement with test data was observed, especially the initial stiffness and unloading paths, when ECC fibers were modeled with "Concrete02" material model with negligible tensile properties instead of "Concrete01" model, which is a model with no tensile strength. The difference between the two models in this case was the unloading paths in their constitutive stress-strain behavior. Core SCC fibers were modeled with "Concrete01" material model.

At the first integration point located at the column base, the steel fiber stress-strain relationship was modified according to section 7.4.3 to take into account bond-slip effects. Figure 7.37 shows the original and modified steel fiber models. The surface of SMA bars is smooth thus debonding is expected starting at low drift levels. Therefore, the SMA bar fibers at the second integration point were modified according to section 7.5.2 accounting for debonding effects (Fig. 7.38). At the third integration point, original

SMA fiber was used since the headed couplers and deformed mild steel bars restricted the SMA bar slippage at this level. SMA fibers were modeled with "SelfCentering" material. At other integration points, the original steel fibers were used. Since only minor nonlinearity was expected above the ECC level, ECC fibers were used for the column shell at all integration points, and the effect of conventional concrete above the ECC level was ignored. The peak measured axial force, 215.6 *kips* (959.0 *kN*), was applied on node 4 of the model, and the P-Δ effect was included.

7.10.2. Analytical Results

The measured and calculated lateral force-drift hysteretic responses for HCS are shown in Fig. 7.39. It can be seen that the analytical model was able to reproduce the hysteretic behavior with a good accuracy. The initial stiffness, strength at each cycle, flag-shape behavior, and residual displacements were successfully simulated. Figure 7.40 shows the measured and calculated force-drift envelopes for HCS. The model successfully simulated the column test pushover curve.

A single wide crack was developed on both sides of HCS at 10 *in*. (254 *mm*) above the footing surface under 4% drift and resulted in large curvatures and rotations at this level. Figure 7.41 shows the measured and calculated moment-curvature relationships at this level. The column curvature was measured over a 7-*in*. (179-*mm*) length of the column from level 2 to level 3 (Fig. 4.104). The calculated moment-curvature as a local response was in close agreement with that measured data.

Modeling of longitudinal SMA bar strain was also investigated. Figure 7.42 shows the measured and calculated force-strain of SMA bar B2 and B7 at a height of 8.12 *in*. (206 *mm*) above the column-footing interface. The calculated strains were successfully simulated in tension. Since the SMA material model was symmetrical, the calculated compressive strains were not in good agreement with the measured compressive strains but this shortcoming had a negligible effect on overall responses of HCS column model as shown previously. This also confirms that a symmetrical stress-strain material model for reinforcing SMA is a viable alternative to the actual asymmetric SMA behavior because it simplifies the modeling method and yet results in minimal discrepancies with actual global response.

Overall, the proposed modeling method for HCS was found to be sufficiently accurate in simulation of the more important local and global responses and may be used for design or analytical investigations of SMA-reinforced concrete bridge columns.

7.11. Concluding Remarks

In this chapter, analytical modeling methods were proposed to simulate the global and local responses of the pullout test specimens as well as the column models tested in the present study. A one-dimensional finite element model was developed for pullout tests in which the anchored portion of the bar was connected to a series of nonlinear duct and bar

bond-slip springs. The model was able to reproduce the bond behavior of UHPC-filled duct systems with reasonable accuracy.

A new simple method was developed to take into account bond-slip effects in analytical modeling of reinforced concrete (RC) members. A simple method was also developed to include longitudinal bar debonding effects on the response analysis of RC members. In both methods, stress-strain relationship of reinforcement is modified. Finite element models were developed for each column model. The models were able to simulate the seismic responses of the column model tests with good accuracy. Overall, the proposed models may be used for general analysis and design of members detailed similar to those in the present study.

Chapter 8: Parametric Studies

8.1. Introduction

Analytical modeling methods were presented in the previous chapter for all column models using a finite element computer program, OpenSees (2013). Many analytical studies have investigated the seismic behavior of conventional columns but analytical studies of columns with advanced materials, especially reinforcing SMA bars, are scarce. A parametric study was conducted to investigate the effect of each mechanical property of the reinforcing SMA model (presented in Chapter 6) on moment-curvature, pushover, cyclic, and dynamic responses of bridge columns. The objective of the parametric study was to reveal the most important material parameter/s that affects the seismic analysis and design of SMA-reinforced bridge columns. This chapter presents details of the parametric studies and the results.

8.2. Reinforcing SMA Model

The mechanical properties for reinforcing SMA bars were defined and a constitutive material model (Fig. 6.11) was proposed in Chapter 6. A range for each mechanical property was provided (Table 6.1) and a design specification was proposed (Table 6.2 and Table 6.3). The information listed in those tables was used in the present chapter for parametric investigation of SMA-reinforced bridge columns.

"Hysteretic" material model from OpenSees library was used in the moment-curvature and pushover analyses to generate the SMA symmetric and asymmetric stress-strain envelope curves. However, cyclic stress-strain behavior of SMA was modeled with "SelfCentering" material model.

8.3. SMA-Reinforced Bridge Column Analytical Model

A model was proposed for the HCS column test in Chapter 7 (section 7.10) and was found to reproduce the measured data with reasonable accuracy. This model was used in parametric studies for moment-curvature, pushover, and cyclic analyses. However, for dynamic analysis part of the parametric studies, because of a lack of dynamic test data for SMA-reinforced columns, the analytical model of a full-scale steel-reinforced concrete bridge column tested on a shake table was used instead of the analytical model for HCS. The analytical model for the full scale steel-reinforced concrete column had led to good correlation with the dynamic test data (Tazarv and Saiidi, 2013). Therefore there was sufficient confidence in its accuracy to be used for parametric studies.

A symmetric SMA model based on the "expected tensile mechanical properties" (Table 6.2) was used as initial input for all analyses in lieu of using the measured mechanical properties of the SMA bars incorporated in the HCS column. This was done to better understand the applicability of the proposed SMA model and to generalize outcomes of the parametric study.

8.4. Sensitivity of Responses to Reinforcing SMA Mechanical Properties

Sensitivity analyses was performed to investigate the effect of each mechanical property of the reinforcing SMA model on moment-curvature, pushover, cyclic, and dynamic responses of SMA-reinforced bridge columns.

8.4.1. Moment-Curvature Analysis

In Table 6.1, a range was listed for each reinforcing SMA mechanical property. Moment-curvature analysis was performed on the HCS analytical model using the lower bound, average, and upper bound of the mechanical properties. The parameters of the tensile symmetric model were used as initial inputs in all the analyses. However, to generate each moment-curvature relationship (or other curves presented later in pushover, cyclic, or dynamic analysis sections), only the parameters of the interest as indicated on the graphs (such as Fig. 8.1) were changed with respect to the symmetric model.

The effect of the lower bound, average, and upper bound of each individual parameter of the reinforcing SMA model on the moment-curvature relationship of the HCS column model is shown in Fig. 8.1a to 8.1h. The moment-curvature relationship of the column model using the symmetric expected tensile mechanical properties is shown with a solid black line, while the measured HCS column moment-curvature curve is shown with a dashed black line. It is clear that the effect of individual tensile or compressive mechanical property is minor on the overall moment-curvature relationships. However, these responses are slightly more sensitive to the tensile mechanical properties compared to the compressive properties. For example, at a small curvature of 0.00063 *rad*/*in.* (0.025 *rad*/*m*), the moment in the SMA-reinforced column with the upper bound tensile k_1 was 9% higher than that of curve with the upper bound compressive k_1.

Figure 8.1i shows the simultaneous effect of all the tensile mechanical properties on the moment-curvature curves of the SMA-reinforced column. Similarly, the simultaneous effect of all the compressive mechanical properties is shown in Fig. 8.1j. It is observed that the results are somewhat more sensitive to the simultaneous effect of all the tensile properties than that of the compressive properties. For instance, at a large curvature of 0.005 *rad*/*in.* (0.2 *rad*/*m*), the moment of the HCS analytical model using the lower bound, average, and upper bound of all the tensile mechanical properties was 92, 100, and 109% (a range of 17%) of the measured HCS moment at that curvature, respectively. In contrast, at the same curvature, the column moment using the lower bound, average, and upper bound of all the compressive mechanical properties was 109, 113, and 116% (a range of 7%) of the measured HCS moment, respectively. It can be

inferred that the effect of variation in the tensile properties is somewhat more significant than the compressive properties effect.

An extremely rare condition is when all the tensile and compressive mechanical properties of the reinforcing SMA assume either the lower or upper bound at the same time. It can be seen in Fig. 8.2 that the results can vary significantly for this extreme range of variation of parameters. For example, at a curvature of 0.005 *rad*/*in.* (0.2 *rad*/*m*), the moment of the HCS analytical model using the lower bound, average, and upper bound of all the SMA properties was 98, 113, and 127% of the measured HCS moment at the same curvature respectively. The moment of the SMA-reinforced column using the symmetric expected tensile mechanical properties was the same as the HCS column moment at this curvature. It can be also concluded that moment-curvature relationships of the column with a SMA model based on the average tensile and compressive mechanical properties (an asymmetric stress-strain model) is close to that of the column model with a symmetric model based on the expected tensile mechanical properties. In other words, a symmetric stress-strain SMA model is sufficiently accurate to be used instead of the asymmetric model to perform the moment-curvature analysis of SMA-reinforced elements.

Comparing the calculated moment-curvature curves with the measured HCS moment-curvature curve, the calculated moments before the concrete cracking and the moments in the second slope of the SMA model (strains from f_y/k_1 to 6%) are essentially the same as the measured moments. However, the differences are observed after the concrete cracking and before the SMA bar yielding since the moment-curvature analysis is a sectional analysis but the measured moment-curvature curve was obtained over a 7-*in*. (178-*mm*) gauge length of the column over which the concrete cracking and the SMA bars slippage soften the behavior. Another reason is the difference between the actual mechanical properties of the reinforcing SMA bars used in the HCS column test (which were measured and presented in Table 4.3) and the assumed properties used for the reinforcing SMA model in the analysis (Table 6.2).

8.4.2. Pushover Analysis

The effect of each mechanical property of the reinforcing SMA on force-drift relationship of the HCS column analytical model was investigated (Fig. 8.3a to 8.3h). The average envelope of the measured HCS column force-drift hysteretic curve is also shown with a dashed bold line. In addition, pushover response using symmetric expected tensile mechanical properties is shown with a solid black line. It can be seen that the tensile and compressive mechanical properties had individually minor effect on the force-displacement behavior of the HCS column model. However, the tensile austenite modulus (k_1), the tensile post yield stiffness (k_2), and the tensile austenite yield strength (f_y) affected the pushover curves slightly more than the other parameters. The tensile k_1 altered the pushover curves only over the drift ratio of 0.5 to 3.5%. The tensile k_2 affected the pushover curves at drift ratios greater than 3.5%. The tensile f_y effect on the pushover curves can be observed at drift ratios exceeding 2%. Results from the moment-curvature and pushover analyses (Fig. 7.1 to 7.4) show that including the compressive

mechanical properties of the SMA model (asymmetric stress-strain behavior) in the analyses usually results in a higher base shear compared to the symmetric SMA model. .

It is worth mentioning that the effect of debonding of the SMA bars in the second integration point of the HCS column analytical model was ignored (section 7.10) and the original SMA model was used in the second and third integration points to solely investigate the effect of the model parameter variations. That is the analytical force-drift curves after the concrete cracking are stiffer than the force-drift curve measured in the HCS column testing.

The simultaneous effect of all the extreme values of the tensile mechanical properties on the pushover curve is shown in Fig. 8.3i. Likewise, the simultaneous effect of all the extreme values of the compressive mechanical properties is shown in Fig. 8.3j. It is evident that the pushover response of SMA-reinforced columns is more sensitive to variations in the tensile properties. For example, at 5% drift ratio, the lateral force resistance of the HCS analytical model using the lower bound, average, and upper bound of all the tensile SMA properties was 86, 82, and 98% of the measured HCS lateral force at the same drift, respectively, a range of 12%. In contrast, the column force using the lower bound, average, and upper bound of all the compressive mechanical properties was 96, 99, and 100% of the measured HCS force at the same drift, respectively, a range of 4%.

Fig. 8.4 shows simultaneous effect of extreme values for all the mechanical properties. It can be observed that even with the extreme mechanical properties, the model can estimate the pushover behavior with a reasonable accuracy. For example, at 5% drift ratio, the calculated force was in a range of 89 to 108% of the measured force at the same drift level. The best correlation with the test data, a 100% match with the measured forces at and above 4.5% drift ratios, was achieved when an asymmetric SMA model based on the average compressive and tensile mechanical properties (Table 6.1) was utilized in the analysis. However, to facilitate adoption of reinforcing SMA in structural application, a symmetric SMA model based on the "expected tensile mechanical properties" (Table 6.2) is proposed. This model underestimated the measured HCS column forces in high drift levels by 9% on average.

The yield point and the response at 6% SMA bar strain are also marked in Fig. 8.4. The calculated yield displacements of SMA-reinforced columns using different mechanical properties were 30 to 70% higher than the measured yield displacement of the HCS column, which was 1.4 *in*. (35 *mm*). It should be noted that the HCS original analytical model presented in Chapter 7 led to only 10% overestimation of the measured yield displacement and only 4% overestimation of the measured yield force. The calculated drifts using different mechanical properties that caused a 6% tensile strain in the extreme SMA bar was approximately the same as the measured drift associated with 6% tensile strain in the HCS column extreme SMA bar. In other words, the calculated SMA bar strains are in good agreement with the measured strains even using the extreme properties in the reinforcing SMA model. Another conclusion is that a high drift ratio can be achieved for SMA-reinforced bridge columns even if the SMA bars resist only 6% tensile strain without fracture. From Table 6.1, it can be seen that the ultimate strain of SMA bars is more than 20%.

8.4.3. Cyclic Analysis

The effect of several parameters of the reinforcing SMA model on monotonic response was investigated in previous sections. However, some parameters of the model might only affect the hysteretic responses of the columns. Therefore, cyclic analyses were performed to determine the sensitivity of the hysteretic behavior to mechanical property of the reinforcing SMA model.

As mentioned before, no constitutive SMA material model was available in OpenSees at the time of this study. As a result the "SelfCentering" material model was used, which is a symmetric model. It was found from the previous moment-curvature and pushover analyses that a symmetric model based on tensile mechanical properties may be used as an alternative to the asymmetric SMA model. Because of these facts, only tensile properties were incorporated in the "SelfCentering" material model, and the effect of asymmetric material behavior was not investigated in cyclic and dynamic analyses.

Figure 8.5 shows hysteretic force-drift responses of HCS using different mechanical properties. It can be seen that the austenite modulus (k_1) and the lower plateau stress factor (β) have considerable effect on the cyclic behavior. To better show these effects, cumulative dissipated energy of the model using different properties is shown in Fig. 8.6. The dissipated energy was defined as the enclosed area in each force-displacement loop. It is clear that only k_1 and β altered the hysteretic behavior of the SMA-reinforced column. For example, at 10% drift ratio, the cumulative dissipated energy of the column using the lower bound, average, and upper bound of k_1 was 48, 65, and 76% of that of the HCS column test.

Note that the lower dissipated energy of the analytical model compared to the HCS column test is because analysis underestimated residual displacements and resulted in narrower hysteretic loops. This analytical issue can be easily fixed (footnote of Table 7.1) but it is not within the scope of this parametric study.

Even though each mechanical property of the reinforcing SMA model somewhat affected the hysteretic behavior, only two parameters of the model, k_1 and β, were found to have considerable effect on the hysteretic behavior of SMA-reinforced columns and effects of the other parameters were negligible.

8.4.4. Dynamic Analysis

The effect of each mechanical property of the reinforcing SMA model on dynamic responses was investigated. Tazarv and Saiidi (2013) developed a robust analytical modeling method, which closely reproduced a full-scale RC bridge column test responses. The column was tested on a shake table at the University of California, San Diego (UCSD) with the test data being available online (Concrete Column Blind Prediction Contest, 2010). The column height from the footing surface to the center of inertial mass was 27 *ft* (8.23 *m*). The column diameter was 4 *ft* (1.22 *m*). The models

developed by the authors for the steel-reinforced test column and analytical SMA-reinforced column were used in this section. More details regarding the column geometry and the modeling method are presented in the paper.

Near-fault motions are known as the most destructive ground motions with distinct pulse-like waves in ground velocity history (Fig. 8.7). Baker (2007) proposed a quantitative method for classification of near-fault ground motions using wavelet analysis. Using this method, ninety-one records from the next generation attenuation (NGA) project ground motion library (2008) were classified by Baker as the near-fault motions. From those motions, fault-normal records with a peak ground velocity (PGV) of 100 *cm*/*sec* (40 *in*./*sec*) or greater was selected for the parametric study (Table 8.1), resulting in 15 records. It should be noted that one of the criteria of classifying a record as near-fault motion was having a PGV $\geq$ 30 *cm*/*sec* (12 *in*./*sec*). Thus, selected motions are the most severe near-fault ground motions in the NGA database.

The effect of each mechanical property of the reinforcing SMA model on the peak and residual displacements of an assumed SMA-reinforced version of the UCSD column model is shown in Fig. 8.8. The UCSD column analytical model (entitled "RC Column" in the figure) responses are also included for comparison. The column analytical models were allowed for at least 10 seconds of free vibration after each earthquake. Residual displacement was the mean displacement of the last 10 seconds of each analysis. It can be seen that peak displacements were more sensitive to the austenite modulus (k_1) and the austenite yield strength (f_y). However, residual displacements were more affected by variation of k_1, f_y, and the lower plateau stress factor (β).

In general, peak displacement demands of the SMA-reinforced column were higher than those of the conventional column. For example, the average peak displacement of 15 near-fault motions using the lower bound, average, and upper bound of all mechanical properties for the SMA-reinforced column model was 122, 117, 113% of that of the steel-reinforced column model, respectively (Fig. 8.9a). In contrast, residual displacements of the SMA-reinforced column were significantly lower than those of the steel-reinforced column. For instance, the average residual displacement of 15 near-fault motions using the lower bound, average, and upper bound of all mechanical properties for the SMA-reinforced column model was 32, 31, 42% of that of the steel-reinforced column model, respectively (Fig. 8.9b). The Japanese seismic design specifications for highway bridges limit the residual drift ratio to 1% (Kawashima, 2000). It can be seen that the SMA-reinforced column never exceeded this limit even when using the extreme values of the mechanical properties (Fig. 8.9b) but the conventional column failed to meet this limitation under seven out of 15 near-fault motions.

8.5. Concluding Remarks

The effect of mechanical properties of the reinforcing SMA model (presented in Chapter 6) on the seismic responses of SMA-reinforced concrete bridge columns was investigated. The results of moment-curvature, pushover, cyclic, and dynamic analyses were presented in this chapter. It was found that variation of each mechanical property

had individually minor effect on the seismic responses. Among the parameters, the response was generally more sensitive to the tensile properties. The cyclic and dynamic analyses showed that the austenite modulus (k_1), the austenite yield strength (f_y), and the lower plateau stress factor (β) are the more dominant properties of the reinforcing SMA model in controlling the calculated seismic response of SMA-reinforced columns. That is the reason for specifying the minimum mechanical properties for these parameters (Table 6.2) to ensure functionality of SMA-reinforced members under severe ground motions.

Even though including the compressive mechanical properties of the reinforcing SMA bars (asymmetric stress-strain model) resulted in better agreement between the calculated and measured responses, a symmetric stress-strain SMA model based on only the "expected tensile properties" (Table 6.2) is proposed for general analysis and design of SMA-reinforced concrete members because it is sufficiently accurate and it simplifies the analysis. Using a simple model for SMA is proposed to facilitate adoption of SMA in civil engineering applications.

Chapter 9: Design Considerations

9.1. Introduction

New generation of bridge columns for accelerated bridge construction (ABC) were experimentally and analytically investigated and discussed in previous chapters. Ultra-high performance concrete (UHPC) filled duct connections, mechanical bar splice connections, and a low-damage plastic hinge were incorporated in the column models. General design considerations are provided in this chapter and in-depth recommendations are proposed in Appendix D to facilitate design and to ensure functionality of precast columns that are similar to those presented in this document.

9.2. UHPC-Filled Duct Columns

UHPC-filled duct connections are categorized as grouted duct connections (Fig. 9.1) in which column longitudinal bars are anchored in corrugated ducts placed in adjoining members such as footings and cap beams. UHPC may be incorporated as duct filler instead of normal-strength grout to reduce the embedment length in shallow members. Design considerations discussed in this section for UHPC-filled duct columns are based on findings from 14 pullout tests as well as two half-scale bridge column tests.

9.2.1- Bridge columns incorporating UHPC-filed duct connections can be designed similarly to conventional columns based on a design code adopted in the region since these connection types are emulative of conventional columns.

9.2.2- Since UHPC is usually field-cast in actual bridge construction, a lower strength is expected compared to steam-cured laboratory UHPC. Filed-cast 28-day compressive strength for UHPC is usually higher than 18000 *psi* (124 *MPa*).

9.2.3- Previous studies showed that duct material has a significant effect on bond strength in grouted duct connections. Plastic ducts have lower bond strength than galvanized ducts. Therefore, only galvanized ducts are recommended in UHPC-filled duct connections.

9.2.4- The duct diameter should be sufficiently large to provide the necessary bond strength as well as large tolerance for the anchored bar. These were achieved in the previous tests when the duct diameter was at least three times the anchored bar diameter. For bundled bars, a duct diameter equal to 2.8 times the equivalent bar diameter of the group of bars may be used.

9.2.5- Bar embedment length in the UHPC-filled duct connections is according to Chapter 2, section 2.9.2.

9.2.6- It was found that bond strength of bar embedded in UHPC is eight times that in conventional concrete. Therefore, localized failure due to strain concentration especially at the interface of connecting members might occur. To prevent premature failure and to spread yielding, debonding of column longitudinal bars should be considered in the vicinity of the adjoining members interface during construction stage. Wrapping bars with two layers of duct tape was found as a successful debonding technique in the column model tests.

9.2.7- Transverse reinforcements of the columns should be extended into adjoining members. A larger diameter for transverse reinforcements is expected in those members due to presence of ducts.

9.3. Mechanical Grouted Sleeve Bar Splice Columns

Column longitudinal bars and footing dowels are anchored in sleeves then sleeves are filled with a high-strength grout in mechanical grouted bar coupler connections. Location of couplers (Fig. 9.2) usually affects seismic performance of columns due to size of sleeves. Design considerations are provided in this section for mechanical grouted sleeve bar splice columns and design recommendations are presented in Appendix D to ensure that the seismic performance of these types of columns is emulative of conventional columns.

9.3.1- Bridge columns incorporating grouted couplers shifted away from the column ends are emulative of conventional columns provided conditions listed in the following sections are met. Consequently, these column types can be designed similarly to conventional columns according to a design code adopted in the region.
9.3.2- Grouted coupler columns are constructed in two segments: pedestal and precast segment. Pedestal should be cast-in-place in which longitudinal bars are debonded. The precast segment with embedded couplers is installed immediately above pedestal (Fig. 9.2d).
9.3.3- Test results showed that a height of one-half column diameter for pedestal is sufficient for emulative behavior.
9.3.4- Two layers of duct tape are sufficient to debond the column longitudinal bars from concrete.
9.3.5- Minimum cover concrete should be provided for all sections including sections with grouted couplers. This leads to cover concrete on steel reinforcements that is thicker than normal.
9.3.6- Transverse reinforcements of pedestal should be extended over the entire length of column including sections with grouted coupler as well as footings and cap beams. A slight increase in transverse reinforcement diameter is inevitable in sections with coupler.

9.4. SMA-Reinforced ECC Columns

Low-damage materials such as engineered cementitious composite (ECC) and shape memory alloy (SMA) may be incorporated in conventional or accelerated bridge

construction (Fig. 9.3). These materials are usually used in plastic hinge of columns to improve the seismic performance over conventional columns. Design considerations are provided in this section for SMA-reinforced ECC columns for either conventional or accelerated bridge construction. Design recommendations are presented in Appendix D.

9.4.1- Experimental studies have confirmed that the seismic performance of SMA-reinforced ECC columns is better than conventional steel-reinforced concrete columns. SMA-reinforced ECC columns can be designed similarly to conventional columns in accordance to a bridge code adopted in the region even though their performance is better.

9.4.2- Reinforcing SMA model is based on the design specification presented in Chapter 6, section 6.5. A symmetric stress-strain model based on "expected tensile properties" (Table 6.2) was found to be a viable alternative to asymmetric behavior and may be used in general design and analysis of SMA-reinforced members.

9.4.3- SMA and ECC are more expensive than conventional materials. Therefore, these materials may be used only in the plastic hinge area to save cost.

9.4.4- Reinforcing SMA bars are connected to reinforcing steel bars with mechanical bar splices such as headed bar couplers or threaded couplers.

9.4.5- SMA-reinforced ECC columns may be built cast-in-place or precast. UHPC-filled duct connections may be incorporated in precast columns as shown in Fig. 9.3b.

Chapter 10: Summary and Conclusions

10.1. Summary

Accelerated bridge construction (ABC) utilizes advanced planning, new construction techniques, and innovative detailing to facilitate construction. ABC offers many advantages over conventional construction, the most important of which is the reduction of onsite construction time. According to the Feral Highway Administration (FHWA), more than 150,000 bridges in the USA need rehabilitation, repair, or total replacement. ABC is a viable alternative to cast-in-place construction to alleviate the economical, social, and industrial costs or impact associated with long bridge construction duration.

Even though ABC has been widely used in low seismic regions of the country mostly in superstructure, application of ABC in seismic areas has been limited due to the lack of seismic performance data regarding substructure connections, which are critical in moderate and high seismic zones. The main objective of this study was to develop new ABC connections for bridge columns using novel detailing and advanced materials.

Three low-damage materials were incorporated in this study: (1) ultra-high performance concrete (UHPC), (2) Nickel-Titanium shape memory alloy (NiTi SMA), and (3) engineered cementitious composite (ECC). Furthermore, two types of mechanical bar splices were utilized: (1) grouted coupler and (2) headed bar coupler. Grouted duct connections have been used in actual bridges to connect columns to precast cap beams. UHPC was proposed as duct filler instead of conventional grout to reduce bar embedment length in these connections. Fourteen large-scale pullout specimens were tested to determine the bond behavior of UHPC-filled duct systems. After observing satisfactory performance, UHPC-filled duct connections were incorporated in two of three large-scale column models to connect the precast columns to footings. Connection of the third precast column to the footing was provided using grouted coupler connections. All columns were half-scale models. SMA and ECC were incorporated in the plastic hinge of one of the UHPC-filled-duct columns to improve the overall seismic performance of the column and post-earthquake serviceability. Headed bar couplers were utilized to connect SMA bars to steel bars.

Design equations for bar embedment length and bond-slip models were developed for UHPC-filled duct connections. New simple methods were developed to take into account bond-slip effects and bar debonding effects in response analyses of reinforced concrete members. These methods rely on the modification of stress-strain behavior of reinforcements. Material model and design specifications were proposed for NiTi superelastic reinforcing SMA bars. Analytical investigation was then conducted to simulate global and local responses of the pullout and three column model tests. A parametric study was performed to investigate the effect of SMA material model parameters on overall bridge column seismic response. Furthermore, design

considerations and design recommendations were proposed for bridge columns incorporated the abovementioned ABC connections or low-damage plastic hinge to facilitate their implementations in actual bridges.

10.2. Conclusions

Findings from experimental and analytical studies on precast bridge column connections and low-damage materials used in critical areas of precast members led to the following conclusions:

1. Bond strength of deformed bars in UHPC is eight times higher than that in conventional concrete. This results in relatively low bar embedment length in UHPC-filled duct connections compared to conventional or grouted duct connections.
2. Duct bond strength, which was introduced in the present study, was found to control the UHPC-filled duct connection behavior and the required bar embedment length in these systems.
3. UHPC-filled duct connections incorporated in column-to-footing connections of two column model tests exhibited no damage even under 12% drift cycles.
4. Column model tests confirmed that UHPC-filled duct connections are emulative of conventional connections in which precast columns can be designed in accordance to current bridge codes with no limitations.
5. Detailing proposed in the present study for grouted coupler columns by shifting the couplers and debonding longitudinal bars in the plastic hinge ("GCDP" column details), improved the seismic performance compared to detailing investigated previously (Haber et al. 2013). The displacement capacity and displacement ductility capacity were increased by 47 and 56%, respectively. GCDP column displacement ductility was only 4% lower than the reference cast-in-place (CIP) column ductility.
6. Debonding was a successful technique to spread bar yielding and prevent premature failure of reinforcements in UHPC-filled duct connections and grouted coupler column pedestal.
7. The SMA-reinforced ECC column ("HCS") showed improved seismic performance over CIP. The plastic hinge exhibited substantially less damage than steel-reinforced concrete hinges. ECC damage was limited only to cover ECC even under 12% drift cycles. HCS column residual displacements were 79% lower than CIP residual displacements on average due to using superelastic NiTi SMA longitudinal reinforcement.
8. HCS column model test confirmed the feasibility of a new generation of precast columns in which columns can be built in a shorter time with better seismic performance and less post-event repair costs compared to conventional cast-in-place columns.
9. Analytical models presented for pullout tests and column model tests were found to be simple and sufficiently accurate. The models may be used for general design or analysis of these members and systems.

10. The proposed simple methods for taking into account bond-slip and bar debonding effects improved analytical model accuracy in the simulation of both global and local responses of column models.
11. The proposed reinforcing SMA material model used in the HCS column simulation resulted in good agreements between the calculated and the measured global and local responses. Parametric studies showed that a symmetrical stress-strain model based on the expected tensile mechanical properties is a viable alternative to the more realistic but complicated asymmetrical model.
12. It was found from parametric studies that the austenite modulus (k_1), the austenite yield strength (f_y), and the lower plateau stress factor (β) of the reinforcing SMA material model were the more dominant properties in controlling the calculated seismic response of SMA-reinforced columns. The response was more sensitive to the SMA tensile mechanical properties compared to compressive properties.

Overall, precast column connections proposed in the present study utilizing UHPC-filled duct connections and grouted coupler connections, as well as the low-damage plastic hinges were found to be viable alternatives to conventional connections or plastic hinges because they led to equal or improved seismic performance compared to conventional construction. UHPC-filled duct connections fully comply with current bridge codes. Even though using mechanical bar splices is prohibited in plastic hinge of reinforced members according to the most bridge seismic design codes, experimental findings from the present study showed that this limitation should be revisited and reevaluated in light of recent research data.

References

1. AASHTO. (2010). "AASHTO LRFD Bridge Design Specification," Washington, DC: American Association of State Highway and Transportation Officials.
2. Abrishami, H.H. and Mitchell, D. (1992). "Simulation of Uniform Bond Stress," *ACI Material Journal*, Vol. 89, No. 2, pp. 161-168.
3. ACI Committee 239. (2012). "Ultra-High Performance Concrete," ACI Fall Convention, Toronto, Ontario, Canada.
4. ACI318. (1963). "Building Code Requirements for Reinforced Concrete," Detroit, Michigan: American Concrete Institute.
5. ACI318. (2011). "Building Code Requirements for Reinforced Concrete," Detroit, Michigan: American Concrete Institute.
6. ACI408R-03. (2003). "Bond and Development of Straight Reinforcing Bars in Tension," ACI Committee 408, 49 pp.
7. Alam, M.S., Youssef, M.A. and Nehdi, M. (2007). "Utilizing Shape Memory Alloys to Enhance the Performance and Safety of Civil Infrastructures: a Review," *Canadian Journal of Civil Engineering*, Vol. 34, pp. 1075-1086.
8. Alvord Lake Bridge. (2014). Retrieved June 26, 2014, from http://www.asce.org/People-and-Projects/Projects/Landmarks/Alvord-Lake-Bridge/.
9. Ameli, M.J., Parks, J.E., Brown, D.N., and Pantelides, C.P. (2014). "Grouted Splice Sleeve Connection Alternatives for Precast Reinforced Concrete Bridge Piers in Moderate-to-High Seismic Regions," *Proceeding of Tenth U.S. National Conference on Earthquake Engineering*, Anchorage, Alaska, 10 pp.
10. ASTM A536-84 (Reapproved 2009). (2009). "Standard Specification for Ductile Iron Castings," West Conshohocken, PA, 5 pp.
11. ASTM A576-90b (Reapproved 2012). (2012). "Standard Specification for Steel Bars, Carbon, Hot-Wrought, Special Quality," West Conshohocken, PA, 6 pp.
12. ASTM A615/A615M-09b. (2009). "Standard Specification for Deformed and Plain Carbon-Steel Bars for Concrete Reinforcement," West Conshohocken, PA, 6 pp.
13. ASTM A653/A653M-11. (2011). "Standard Specification for Steel Sheet, Zinc-Coated (Galvanized) or Zinc-Iron Alloy-Coated (Galvannealed) by the Hot-Dip Process," West Conshohocken, PA, 14 pp.
14. ASTM A706/A706M-09b. (2009). "Standard Specification for Low-Alloy Steel Deformed and Plain Bars for Concrete Reinforcement," West Conshohocken, PA, 6 pp.
15. ASTM C109/C109M-11b. (2011). "Standard Test Method for Compressive Strength of Hydraulic Cement Mortars (Using 2-in. or [50-mm] Cube Specimens)," West Conshohocken, PA, 10 pp.

16. ASTM C1610/C1610M-10. (2010). "Standard Test Method for Static Segregation of Self-Consolidating Concrete Using Column Technique," West Conshohocken, PA, 4 pp.
17. ASTM C1611/C1611M-09b. (2009). "Standard Test Method for Slump Flow of Self-Consolidating Concrete," West Conshohocken, PA, 6 pp.
18. ASTM C39/C39M-12. (2012). "Standard Test Method for Compressive Strength of Cylindrical Concrete Specimens," West Conshohocken, PA, 7 pp.
19. ASTM E8/E8M-11. (2011). "Standard Test Methods for Tension Testing of Metallic Materials," West Conshohocken, PA, 27 pp.
20. ASTM F2005-05. (2010). "Standard Terminology for Nickel-Titanium Shape Memory Alloys," West Conshohocken, PA, 3 pp.
21. ASTM F2516-07. (2007). "Standard Test Method for Tension Testing of Nickel-Titanium Superelastic Materials," West Conshohocken, PA, 6 pp.
22. Atanackovic, T. and Achenbach, M. (1989). "Moment-Curvature Relations for a Pseudoelastic Beam," *Continuum Mechanics and Thermodynamics*, Vol. 1, pp. 73-80.
23. Auricchio, F. and Sacco, E. (1997). "A Superelastic Shape-Memory-Alloy Beam Model," *Journal of Intelligent Material Systems and Structures*, Vol. 8, pp. 489-501.
24. Ayoub, C., Saiidi, M., and Itani, A. (2003). "A Study of Shape-Memory Alloy-Reinforced Beams and Cubes," *Rep. No. CCEER-03-7*, Center for Civil Engineering Earthquake Research, Dept. of Civil Engineering, Univ. of Nevada, Reno, NV.
25. Baker, J. (2007). "Quantitative Classification of Near-Fault Ground Motions Using Wavelet Analysis," *Bulletin of the Seismological Society of America*, Vol. 97, No. 5, pp. 1486–1501.
26. Billington, S.L. and Yoon, J.K. (2002). "Cyclic Behavior of Precast Post-Tensioned Segmental Concrete Columns with ECC," *Proceedings of the JCI International Workshop on Ductile Fiber Reinforced Cementitious Composites*, Takayama, Japan, pp. 279-288.
27. Brenes, F.J., Wood, S.L. and Kreger, M.E. (2006). "Anchorage Requirements for Grouted Vertical-Duct Connectors in Precast Bent Cap Systems," *FHWA/TX-06/0-4176-1*, Center for Transportation Research, University of Texas at Austin.
28. Buehler, W. and Wiley, R. (1961). "The Properties of TiNi and Associated Phases," *NOLTR 61-75* [AD 266607], US Naval Ordnance Laboratory, White Oak, Maryland, 91 pp.
29. Caltrans. (2006). "Seismic Design Criteria (SDC)," version 1.4. Sacramento, CA.: California Department of Transportation.
30. Caltrans. (2010). "Seismic Design Criteria (SDC)," version 1.6. Sacramento, CA.: California Department of Transportation,.
31. Carroll, W.M., and Kelly, M.J. (2003). "Corrosion Behavior of Nitinol Wires in Body Fluid Environments," *Journal of Biomedical Materials Research*, Vol. 67A, pp. 1123–1130.
32. CEB-FIB. (1993). "CEB-FIP Model Code 1990: Design Code Comite EURO-International Du Buton," London, UK: Thomas Telford.

33. Concrete Column Blind Prediction Contest. (2010). http://nisee2.berkeley.edu/peer/prediction_contest/.
34. Cruz Noguez C.A. and Saiidi, M.S. (2012). "Shake Table Studies of a 4-Span Bridge Model with Advanced Materials," *Journal of Structural Engineering*, *ASCE*, Vol. 138, No. 2, pp. 183-192.
35. Culmo, M. (2009). "Connection Details for Prefabricated Bridge Elements and Systems," Federal Highway Administration *Report No. FHWA-IF-09-010*.
36. Culmo, M. P. (2011). "Accelerated Bridge Construction - Experience in Design, Fabrication and Erection of Prefabricated Bridge Elements and Systems," Federal Highway Administration *Report No. FHWA-HIF-12-013*.
37. DesRoches, R. and Delemont, M. (2002). "Seismic Retrofit of Simply Supported Bridges Using Shape Memory Alloys," *Engineering Structures*, Vol. 24, pp. 325–332.
38. DesRoches, R. and Smith, B. (2003). "Shape Memory Alloys in Seismic Resistant Design and Retrofit: A Critical Review of their Potential and Limitations," *Journal of Earthquake Engineering*, Vol. 7, No. 3, pp. 1-15.
39. Dong, J., Cai, C.S. and Okeil, A.M. (2011). "Overview of Potential and Existing Applications of Shape Memory Alloys in Bridges," *Journal of Bridge Engineering*, Vol. 16, No. 2, pp. 305-315.
40. Eligehausen, R., Popov, E.P. and Bertero, V.V. (1982). "Local Bond Stress-Slip Relationships of Deformed Bars under Generalized Excitations," *Proceedings of the 7th European Conference on Earthquake Engineering*. Vol. 4. Athens: Techn. Chamber of Greece. pp. 69-80.
41. ENV 1992-1-2. (1996). "Eurocode 2: Design of Concrete Structures- Part 1-2: General Rules-Structural Fire Design," CEN, Brussels.
42. Faulkner, M.G., Amalraj, J.J. and Bhattacharyya, A. (2000). "Experimental Determination of Thermal and Electrical Properties of Ni–Ti Shape Memory Wires," *Smart Materials and Structures*, Vol. 9, pp. 632–639.
43. Frick, C.P., Ortega, A.M., Tyber, J., Gall, K. and Maier, H. (2004). "Multiscale Structure and Properties of Cast and Deformation Processed Polycrystalline NiTi Shape-Memory Alloys," *Metallurgical and Materials Transactions A*, Vol. 35A, pp. 2013-2025.
44. Gowripalan, N., and Gilbert, IR. (2000). "Design Guidelines for Ductal Prestressed Concrete Beams," School of Civil and Environmental Engineering, The University of New South Wales, 54 pp.
45. Graesser, E.J. and Cozzarelli, F.A. (1991). "Shape-Memory Alloys as New Materials for Aseismic Isolation," *Journal of Engineering Mechanics*, Vol. 117, No. 11, pp. 2590–608.
46. Graybeal, B. (2006). "Material Property Characterization of Ultra-High Performance Concrete," McLean, VA: FHWA, U.S. Department of Transportation, *Report No. FHWA-HRT-06-103*.
47. Graybeal, B. (2010). "Behavior of Field-Cast Ultra-High Performance Concrete Bridge Deck Connections under Cyclic and Static Structural Loading," Federal Highway Administration *Report No. FHWA-HRT-11-023*.

48. Graybeal, B. and Davis, M. (2008). "Cylinder or Cube: Strength Testing of 80 to 200 MPa (11.6 to 29 ksi) Ultra-High-Performance Fiber-Reinforced Concrete," *ACI Materials Journal*, Vol. 105, No. 6, pp. 603-609.
49. Haber, Z. (2013). "Precast Column-Footing Connections for Accelerated Bridge Construction in Seismic Zones," PhD Dissertation, University of Nevada Reno, 612 pp.
50. Haber, Z.B., Saiidi, M.S. and Sanders, D.H. (2013). "Precast Column-Footing Connections for Accelerated Bridge Construction in Seismic Zones," Center for Civil Engineering Earthquake Research, Department of Civil and Environmental Engineering, University of Nevada, Reno, Nevada, *Report No. CCEER-13-08*, 502 pp.
51. Haraldsson, O.S., Janes, T.M., Eberhard, M.O. and and Stanton, J.F. (2012). "Seismic Resistance of Socket Connection between Footing and Precast Column," *Journal of Bridge Engineering, ASCE*, Vol. 18, No. 9, pp. 910-919.
52. JSCE Concrete Library 127. (2008). "Recommendations for Design and Construction of High Performance Fiber Reinforced Cement Composites with Multiple Fine Cracks (HPFRCC)," Japan Society of Civil Engineers.
53. Kavianipour, F. and Saiidi, M.S. (2013). "Experimental and Analytical Seismic Studies of a Four-span Bridge System with Composite Piers," Center for Civil Engineering Earthquake Research, Department of Civil and Environmental Engineering, University of Nevada, Reno, Nevada, *Report No. CCEER-13-17*. 587 pp.
54. Kawashima, K. (2000). "Seismic Design and Retrofit of Bridges," *Proceeding of 12th World Conference on Earthquake Engineering*, New Zealand Society for Earthquake Engineering, CD-ROM No. 2828. Auckland, New Zealand.
55. Khaleghi, B., Schultz, E., Seguirant, S., Marsh, L., Haraldsson, O., Eberhard, M. and Stanton, J. (2012). "Accelerated Bridge Construction in Washington State: From research to Practice," *PCI Journal*, pp 34-49.
56. Lee, W. K. and Billington S. (2010). "Modeling Residual Displacements of Concrete Bridge Columns under Earthquake Loads Using Fiber Elements," *Journal of Bridge Engineering*, Vol. 15, No. 3, pp. 201-249.
57. Li, V.C. (2008). "Engineered Cementitious Composites (ECC)-Material, Structural, and Durability Performance," in Concrete Construction Engineering Handbook, Chapter 24, Ed. E. Nawy: published by CRC Press.
58. Li, V.C., and Fischer, G. (2003). "Deformation Behavior of Fiber-Reinforced Polymer Reinforced Engineered Cementitious Composite (ECC) Flexural Members under Reversed Cyclic Loading Conditions," *ACI Structural Journal*, Vol. 100, No. 1, pp. 25-35.
59. Machado, L.G., and Savi, M.A. (2003). "Medical Applications of Shape Memory Alloys," *Brazilian Journal of Medical and Biological Research*, Vol. 36, pp. 683-691.
60. Mander, J.B., Priestley, M.J.N., Park, R. (1988). "Theoretical Stress-Strain Model for Confined Concrete," *Journal of Structural Engineering, ASCE*, Vol. 114, No. 8, pp. 1804-1826.
61. Marriott, D., Palermo, A., and Pampanin, S. (2006). "Quasi-static and Pseudo-Dynamic Testing of Damage Resistant Bridge Piers with Hybrid Connections,"

Proceeding of the First European Conference on Earthquake Engineering and Seismology, Geneva, Switzerland, Paper No. 794.

62. Marsh, M.L., Wernli, M., Garrett, B.E., Stanton, J.F., Eberhard, M.O. and Weinert, M.D. (2011). "Application of Accelerated Bridge Construction Connections in Moderate-to-High Seismic Regions," Washington, D.C.: *National Cooperative Highway Research Program (NCHRP) Report No. 698*.
63. Matsumoto, E.E., Waggoner, M.C., Sumen, G. and Kreger, M.E. (2001). "Development of a Precast Bent Cap System," Center for Transportation Research, The University of Texas at Austin: *FHWA Report No. FHWA/TX-0-1748-2*.
64. McCormick, J.P. (2006). "Cyclic Behavior of Shape Memory Alloys Materials Characterization and Optimization," PhD Dissertation, Georgia Institute of Technology, 351 pp.
65. Mehrsoroush, A. and Saiidi, M.S. (2014). "Seismic Performance of Two-Column Bridge Piers with Innovative Precast Members and Pipe Pin Connections," *Proceeding of 7th International Conference on Bridge Maintenance, Safety and Management (IABMAS)*, Shanghai, China.
66. Miyazaki, S., Imai, T., Igo, Y. and Otsuka, K. (1986). "Effect of Cyclic Deformation on the Pseudoelasticity Characteristics of Ti-Ni Alloys," *Metallurgical Transactions A*, Vol. 17A, pp. 115-120.
67. Mo, Y.L., and Chan, J. (1996). "Bond and Slip of Plain Rebars in Concrete," *Journal of Materials in Civil Engineering, ASCE*, Vol. 8, No.4, pp. 208-211.
68. Monti, G., and Spacone, E. (2000). "Reinforced Concrete Fiber Beam Element with Bond-Slip," *Journal of Structural Engineering, ASCE*, Vol. 126, No. 6, pp. 654-661.
69. Motaref, S., Saiidi, M.S., and Sanders, D. (2011). "Seismic Response of Precast Bridge Columns with Energy Dissipating Joints," Center for Civil Engineering Earthquake Research, Department of Civil and Environmental Engineering, University of Nevada, Reno, *Report No. CCEER-11-01*.
70. Nakashoji, B., Saiidi, M.S., Bingle, J. and Khaleghi, B. (2013). "Implementation of NEESR-SG Study on Seismic Performance of Bridges with Novel Materials in a Bridge in Seattle," NEES Annual Meeting, Quake Summit 2013. Reno, Nevada.
71. Next Generation Attenuation. (2008). http://peer.berkeley.edu/peer_ground_motion_database/site.
72. OpenSees. (2013). "Open System for Earthquake Engineering Simulations," Version 2.4.1, Berkeley, CA, Available online: http://opensees.berkeley.edu.
73. Otsuka, K., and Wayman, C. M. (1998). "Mechanism of Shape Memory Effect and Superplasticity," Cambridge University Press, Cambridge, U.K.
74. Pang, J.B.K., Steuck, K.P., Cohagen, L., Stanton, J.F. and Eberhard, M.O. (2008). "Rapidly Constructible Large-Bar Precast Bridge-Bent Seismic Connection," WA-RD 684.2 University of Washington, Seattle, Washington.
75. Plietsch, R. and Ehrich, K. (1997). "Strength Differential Effect in Pseudoelastic NiTi Shape Memory Alloys," *Acta Materialia*, Vol. 45, No.6, pp. 2417-2424.
76. Restrepo, J.I., Tobolski, M.J. and Matsumoto, E.E. (2011). "Development of a Precast Bent Cap System for Seismic Regions," *NCHRP Report 681*, Washington, D.C.

77. Russell, H.G. and Graybeal B.A. (2013). "Ultra-High Performance Concrete: A State-of-the-Art Report for the Bridge Community," Federal Highway Administration, *Report No. FHWA-HRT-13-060*, 171 pp.
78. SAES. (2013). http://www.saesgetters.com/product-groups/shape-memory-alloys.
79. Saiidi, M.S. and Wang H. (2006). "Exploratory Study of Seismic Response of Concrete Columns with Shape Memory Alloys Reinforcement," *ACI Structural Journal*, Vol. 103, No. 3, pp. 436-443.
80. Saiidi, M.S., O'Brien, M. and Sadrossadat-Zadeh, M. (2009). "Cyclic Response of Concrete Bridge Columns Using Superelastic Nitinol and Bendable Concrete," *ACI Structural Journal*, Vol. 106, No. 1, pp. 69-77.
81. Saiidi, M.S., Sadrossadat-Zadeh, M., Ayoub, C., and Itani, A. (2007). "Pilot Study of Behavior of Concrete Beams Reinforced with Shape Memory Alloys," *Journal of Materials in Civil Engineering, ASCE*, Vol. 19, No. 6, pp. 454-461.
82. Schlossmacher, P., Haas, T., and Schüssler, A. (1997). "Laser-Welding of a Ni-Rich TiNi Shape Memory Alloy: Mechanical Behavior," J*ournal De Physique IV France*, Vol. 07, No. C5, pp. 251-256.
83. SETRA-AFGC. (2002). "Ultra High Performance Fibre-Reinforced Concretes," Interim Recommendations, SETRA-AFGC, Groupe de travail BFUP, Paris, France, 98 pp.
84. Song, G., Ma, N. and Li, H.N. (2006). "Applications of Shape Memory Alloys in Civil Structures," *Engineering Structures*, Vol. 28, pp. 1266–1274.
85. Soroushian, P. and Choi, K.B. (1989). "Local Bond of Deformed Bars with Different Diameters in Confined Concrete," *ACI Structural Journal*, Vol. 86, No.2, pp. 217-222.
86. SR99 SMA-ECC Bridge. (2014). Retrieved July 09, 2014, from http://wolfweb.unr.edu/homepage/saiidi/WashDOT/SR99/index.html.
87. Standard Specifications. (2010). State of California. Sacramento, USA: Business, Transportation and Housing Agency, Department of Transportation.
88. Steuck, K.P., Eberhard, M.O. and Stanton, J.F. (2009). "Anchorage of Large-Diameter Reinforcing Bars in Ducts," *ACI Structural Journal*, Vol. 106, No. 4, pp. 506-513.
89. Steuck, K.P., Pang, J.B.K., Eberhard, M.O. and Stanton, J.F. (2008). "Anchorage of Large-diameter Reinforcing Bars Grouted into Ducts," *WA-RD 684.1*, University of Washington, Seattle, Washington.
90. Strnadel, B., Ohashi, S., Ohtsuka, H., Ishihara, T. and Miyazaki, S. (1995). "Cyclic Stress-Strain Characteristics of Ti-Ni and Ti-Ni-Cu Shape Memory Alloys," *Materials Science and Engineering*, Vol. A202, pp. 148-156.
91. Tarnita, D., Tarnita, D.N., Bizdoaca, N., Mindrila, I., and Vasilescu, M. (2009). "Properties and Medical Applications of Ahape Memory Alloys," *Romanian Journal of Morphology and Embryology*, Vol. 50, No. 1, pp. 15–21.
92. Tazarv, M. and Saiidi, M.S. (2013). "Analytical Studies of the Seismic Performance of a Full-Scale SMA-Reinforced Bridge Column," *International Journal of Bridge Engineering*, Vol. 1, No. 1, pp. 37-50.
93. Tazarv, M. and Saiidi, M.S. (201x). "Reinforcing NiTi Superelastic SMA for Concrete Structures," Submitted to *Journal of Structural Engineering, ASCE*, Vol. xx, No. xx, pp. xx-xx.

94. Utah Department of Transportation. (2010). “Precast Substructure Elements,” http://dot.utah.gov, 24 pp.
95. Varela, S. and Saiidi, M.S. (2013). “Innovation in Sustainable Earthquake-Resistant Highway Bridges with Advanced Materials,” NEES Annual Meeting, Quake Summit 2013, Session 13. Reno, Nevada.
96. Verderame, G.M., Carlo, G.D., Ricci, P., Fabbrocino, G. (2009). “Cyclic Bond Behaviour of Plain Bars. Part II: Analytical Investigation,” *Construction and Building Materials*, Vol. 23, pp. 3512–3522.
97. Walnut Lane Memorial Bridge. (2014). Retrieved June 26, 2014, from http://en.wikipedia.org/wiki/Walnut_Lane_Memorial_Bridge.
98. Wang, J.C., Ou, Y.C., Chang, K.C., and Lee, G.C. (2008). “Large-Scale Seismic Tests of Tall Concrete Bridge Columns with Precast Segmental Construction,” *Earthquake Engineering and Structural Dynamics*, Vol. 37, pp. 1449-1465.
99. Wehbe, N., Saiidi, M., and Sanders, D. (1997). “Effect of Confinement and Flares on the Seismic Performance of Reinforced Concrete Bridge Columns,” Civil Engineering Department, *Report No. CCEER-97-2*, University of Nevada, Reno.
100. Wilson, J.C. and Wesolowsky, M.J. (2005). “Shape Memory Alloys for Seismic Response Modification: A State-of-the-Art Review,” *Earthquake Spectra*, Vol. 21, No. 2, pp. 569–601.
101. Wu, M.H., and Schetky, L.M. (2000). “Industrial Applications for Shape Memory Alloys,” *Proceedings of the International Conference on Shape Memory and Superelastic Technolgies*, Pacific Grove, California, pp. 171-182.
102. Youssef, M.A., Alam, M.S. and Nehdi, M. (2008). “Experimental Investigation on the Seismic Behavior of Beam-Column Joints Reinforced with Superelastic Shape Memory Alloys,” *Journal of Earthquake Engineering*, Vol. 12, No. 7, pp. 1205-1222.
103. Zhao, J. and Sritharan, S. (2007). “Modeling of Strain Penetration Effects in Fiber-Based Analysis of Reinforced Concrete Structures,” *ACI Structural Journal*, Vol. 104, No. 2, pp 133-141.

Tables

Table 1.1- UHPC Mechanical Properties (Russell and Graybeal, 2013)

Properties	Range	Equation
Compressive Strength (f'_{UHPC})	20 to 30 *ksi*, (140 to 200 *MPa*)	A time-dependent equation for UHPC strength is available.
Tensile Cracking Strength ($f_{t,UHPC}$)	0.9 to 1.5 *ksi*, (6 to 10 *MPa*)	$f_{t,UHPC} = 6.7\sqrt{f'_{UHPC}} \quad (psi)$
Modulus of Elasticity (E_{UHPC})	6000 to 10000 *ksi*, (40 to 70 *GPa*)	$E_{UHPC} = 49000\sqrt{f'_{UHPC}} \quad (psi)$
Poisson's Ratio	0.2	
Coefficient of Thermal Expansion	(5.5 to 8.5)x10^{-6}/^{o}F, (10 to 15)x10^{-6}/^{o}C	
Creep Coefficient*	0.2 to 0.8	
Specific Creep*	(0.04 to 0.3)x10^{-6}/*psi*, (6 to 45)x10^{-6}/*MPa*	
Total Shrinkage**	up to 900x10^{-6}	

* Depends on curing conditions and age of loading

** Combination of drying shrinkage and autogenous shrinkage and depends on curing method

Table 1.2- ECC Mechanical Properties (Li, 2008)

Properties	Range
Compressive Strength	3 to 14 *ksi* (20 to 95 *MPa*)
First Crack Strength	0.4 to 1.0 *ksi* (3 to 7 *MPa*)
Ultimate Tensile Strength	0.6 to 1.7 *ksi* (4 to 12 *MPa*)
Ultimate Tensile Strain	1 to 8%
Modulus of Elasticity	2600 to 5000 *ksi* (18 to 34 *GPa*)
Flexural Strength	1.5 to 4.5 *ksi* (10 to 30 *MPa*)

Table 2.1- Grouted Vertical Duct Test Matrix and Results (Matsumoto et al., 2001)

Test ID	Bars		Embedment Length, *in* (*mm*)	Grout Brand	f'_c, *ksi* (*MPa*)		P_{max}, *kips* (*kN*)	*u*, *psi* (*MPa*)
	No.	Anchor			Grout	Concrete		
VD01	#11 (Ø36)	straight	12 (305)	MF928*	4.2 (28.9)	5.4 (37.2)	76 (338)	1430 (9.9)
VD02	#11 (Ø36)	Upset Head	12 (305)	MF928	4.2 (28.9)	5.4 (37.2)	92 (409)	1730 (11.9)
VD03	#11 (Ø36)	straight	18 (457)	MF928	5.7 (39.3)	5.6 (38.6)	119 (529)	1492 (10.3)
VD04	#11 (Ø36)	straight	18 (457)	EHF†	3.1 (21.3)	5.6 (38.6)	94 (418)	1179 (8.1)
VD05	#11 (Ø36)	straight	18 (457)	SIKA‡	3.8 (26.2)	5.5 (37.9)	114 (507)	1430 (9.9)
VD06	#11 (Ø36)	Upset Head	18 (457)	MF928	4.8 (33.1)	5.5 (37.9)	120 (534)	1505 (10.4)
VD07	#11 (Ø36)	straight	24 (610)	MF928	5.2 (35.8)	5.5 (37.9)	100 (445)	941 (6.5)
VD08	#11 (Ø36)	straight	24 (610)	EHF	4.5 (31.0)	5.5 (37.9)	118 (525)	1110 (7.6)

* Masterflow 928; † Euclid High Flow; ‡ Sika 212

Table 2.2- Test Matrix for Group I & II of Pullout Tests

SP. No.	Bar Size	Test Group No.	Embed. Length	Bundled	Duct Diam., d_d $in.(mm)$	Multiple Ducts	SP. Size, $D \times H$ $in.\times in.$ $(mm \times mm)$	Test Variable
1	#8 (Ø25)	I	$8d_b$	No	3.12 (79)	No	24×16 (610×406)	Embedment Length
2	#8 (Ø25)	I	$12d_b$	No	3.12 (79)	No	24×20 (610×508)	Embedment Length
3	#8 (Ø25)	II	$3d_b$	No	3.12 (79)	No	24×20 (610×508)	Embedment Length
4*	2#8 (2Ø25)	I	$8d_b$	a pair	4 (102)	No	24×16 (610×406)	Bundled Bars
5*	2#8 (2Ø25)	I	$12d_b$	a pair	4 (102)	No	24×20 (610×508)	Bundled Bars
6*	2#8 (2Ø25)	II	$3d_b$	a pair	4 (102)	No	24×20 (610×508)	Bundled Bars
7	#8 (Ø25)	I	$8d_b$	No	4 (102)	No	24×16 (610×406)	Duct Diam.
8	#8 (Ø25)	II	$5d_b$	No	3.12 (79)	No	24×20 (610×508)	Embedment Length
9**	2#8 (2Ø25)	I	$8d_b$	No	3.12 (79)	a pair	24×16 (610×406)	Multi Ducts
10**	2#8 (2Ø25)	I	$12d_b$	No	3.12 (79)	a pair	30×20 (762×508)	Multi Ducts
11	#11 (Ø36)	I	$8d_b$	No	4 (102)	No	30×16 (762×406)	Embedment Length
12	#11 (Ø36)	I	$12d_b$	No	4 (102)	No	30×20 (762×508)	Embedment Length
13	#11 (Ø36)	II	$3d_b$	No	4 (102)	No	30×28 (762×711)	Embedment Length
14	#11 (Ø36)	I	$8d_b$	No	5.26 (134)	No	30×16 (762×406)	Duct Diam.

d_b is nominal diameter of bar; d_d is inner diameter of duct; D is diameter of specimen, H is height of specimen

* : Investigating effect of a pair of bars (bundled bars) in a single duct

**: Investigating effect of multiple ducts in a specimen

Table 2.3- Diameters of Corrugated Galvanized Ducts

Nominal Diameter $in.$ (mm)	Actual	
	Inner Diameter $in.$ (mm)	Outer Diameter $in.$ (mm)
3 (75)	3.12 (79)	3.31 (84)
4 (100)	4 (102)	4.19 (106)
5 (125)	5.26 (134)	5.45 (138)

Table 2.4- Measured Test-Day Compressive Strength of Materials in Pullout Tests

Specimen No.	Test Group No.	Concrete*, *psi* (*MPa*)	UHPC*, *psi* (*MPa*)
1	I	6720 (46.3)	24296 (167.5)
2	I	6778 (46.7)	25928 (178.8)
3	II	7471 (51.5)	21307 (146.9)
4	I	6755 (46.6)	24863 (171.4)
5	I	6770 (46.7)	25573 (176.3)
6	II	7506 (51.8)	21356 (147.2)
7	I	6778 (46.7)	25928 (178.8)
8	II	7506 (51.8)	21356 (147.2)
9	I	6786 (46.8)	26284 (181.2)
10	I	6881 (47.4)	26776 (184.6)
11	I	6881 (47.4)	26776 (184.6)
12	I	7039 (48.5)	24457 (168.6)
13	II	7387 (50.9)	19444 (134.1)
14	I	7039 (48.5)	24457 (168.6)

* At least three samples were used for testing. Only the average of test data is reposted

Table 2.5- Measured Mechanical Properties of Bars in Pullout Tests

Bar Size	No. of Samples	Yield Strength, f_y *ksi* (*MPa*)	Ultimate Strength, f_u *ksi* (*MPa*)	Strain at onset of Strain Hardening, ε_{sh} (%)	Strain Hardening Slop, E_{sh} *ksi* (*MPa*)	Strain at Ultimate Stress, ε_{su} (%)
#3 (Ø10)	4	69.7 (480.9)	94.2 (649.7)	N/A	N/A	11.09
#8 (Ø25)	2	75.0 (517.1)	111.2 (766.8)	0.23	2896 (19967)	9.66
#11 (Ø36)	1*	72.4 (499.4)	> 90.5 (> 623.9)	0.68	N/A	N/A

* Tensile test could not be completed due to slippage of #11 bar in grips

Table 2.6- Mode of Failure and Observed Damage in Pullout Tests

SP. No.	Bar Size	Test Group No.	Embed. Length	Mode of Failure	Observed Damage
1	#8 (Ø25)	I	$8d_b$	Bar Fracture	Failure of bar at thread, few minor cracks toward duct on surface of concrete, no damage of UHPC
2	#8 (Ø25)	I	$12d_b$	Bar Fracture	Failure of bar at thread, two minor cracks on surface of concrete, no damage of UHPC
3	#8 (Ø25)	II	$3d_b$	Bar Fracture	Failure of bar at thread, no damage of concrete, no damage of UHPC
4	2#8 (2Ø25)	I	$8d_b$	Duct Pullout	Severe damage of concrete surrounding the duct with cone-shape, no damage of UHPC, no bar yielding
5	2#8 (2Ø25)	I	$12d_b$	Bars Fracture	Failure of bars at thread, few minor cracks toward duct, no damage of UHPC
6	2#8 (2Ø25)	II	$3d_b$	Bar Pullout	No concrete damage, no UHPC damage
7	#8 (Ø25)	I	$8d_b$	Bar Fracture	Failure of bar at thread, few minor cracks toward duct, no damage of UHPC
8	#8 (Ø25)	II	$5d_b$	Bar Fracture	Failure of bar at thread, no damage of concrete and UHPC
9	2#8 (2Ø25)	I	$8d_b$	Bars Fracture	Failure of bars at thread, few minor cracks toward ducts, no damage of UHPC
10	2#8 (2Ø25)	I	$12d_b$	Bars Fracture	Failure of bars at thread, few minor cracks toward ducts, no damage of UHPC
11	#11 (Ø36)	I	$8d_b$	Duct Pullout	Severe damage of concrete surrounding the duct with cone-shape, no damage of UHPC
12	#11 (Ø36)	I	$12d_b$	Bars Fracture	Failure of bar at thread, few minor cracks toward duct, no damage of UHPC
13	#11 (Ø36)	II	$3d_b$	Bar Fracture	Failure of bar at thread, no damage of concrete and UHPC
14	#11 (Ø36)	I	$8d_b$	Bars Fracture	Failure of bar at thread, few minor cracks toward duct, no damage of UHPC

d_b is diameter of bar

Table 2.7- Duct and Bar Bond Strength for Group I & II of Pullout Tests

SP. No.	Bar Size	Test Group No.	Embed. Length, *in*. (*mm*)	n (n_b or n_d)	Duct Diam., d_d *in*. (*mm*)	Force, *kips* (*kN*)	Duct Bond Strength, u_d, *psi* (*MPa*)	Bar Bond Strength, u_b, *psi* (*MPa*)
1	#8 (Ø25)	I	8 (203)	1	3.12 (79)	56.4 (388.9)	720* (4.96)	N/A
2	#8 (Ø25)	I	12 (305)	1	3.12 (79)	55.0 (379.2)	467* (3.22)	N/A
3	#8 (Ø25)	II	3 (76)	1	3.12 (79)	56.2 (387.5)	N/A	5967* (41.14)
4	2#8 (2Ø25)	I	8 (203)	2	4 (102)	67.5 (465.4)	671 (4.63)	N/A
5	2#8 (2Ø25)	I	12 (305)	2	4 (102)	107.7 (742.6)	712* (4.90)	N/A
6	2#8 (2Ø25)	II	3 (76)	2	4 (102)	78.4 (540.6)	N/A	4162 (28.70)
7	#8 (Ø25)	I	8 (203)	1	4 (102)	54.7 (377.1)	544* (3.75)	N/A
8	#8 (Ø25)	II	5 (127)	1	3.12 (79)	56.0 (386.1)	N/A	3568* (24.60)
9	2#8 (2Ø25)	I	8 (203)	2	3.12 (79)	109.8 (757.0)	700* (4.83)	N/A
10	2#8 (2Ø25)	I	12 (305)	2	3.12 (79)	102.4 (706.0)	435* (3.00)	N/A
11	#11 (Ø36)	I	11.28 (286)	1	4 (102)	93.9 (647.4)	662 (4.29)	N/A
12	#11 (Ø36)	I	16.92 (430)	1	4 (102)	106.4 (733.6)	500* (3.45)	N/A
13	#11 (Ø36)	II	4.23 (107)	1	4 (102)	110.8 (763.9)	N/A	5920* (40.82)
14	#11 (Ø36)	I	11.28 (286)	1	5.26 (134)	110.9 (764.6)	595* (4.10)	N/A

d_b is nominal diameter of bar; d_d is inner diameter of duct

* Lower bound bond strength

Table 2.8– Bond Strength of Bars in FHWA Pullout Tests (Graybeal, 2010)

Sample ID	Bar Size	Embed. Length** *in*. (*mm*)	Force, *kips* (*kN*)	Strength of UHPC, *psi* (*MPa*)	Duct Bond Strength, u_d, *psi* (*MPa*)	Bar Bond Strength, u_b, *psi* (*MPa*)	Mode of Failure
T-13-B	#4 (Ø13)	2.95 (75)	20223 (89.9)	15000 (103.4)	N/A	4291.5* (29.6)	Bar Fracture
T-16-B	#5 (Ø16)	3.93 (100)	32474 (144.5)	15000 (103.4)	N/A	4134.7* (28.5)	Bar Fracture
T-19-B	#6 (Ø19)	4.92 (125)	46207 (205.5)	15000 (103.4)	N/A	3922.2* (27.0)	Bar Fracture

* Lower bound bond strength

** Bars were anchored in 15.74-*in*. × 7.87-*in* (400-*mm* × 200-*mm*) UHPC Cylinders

Table 3.1- Test Matrix for ABC Column Models

Test	Specimen	Connection	Load	Investigating
Previous Research at UNR	CIP	Conventional connection	Slow Cyclic	Reference column with a thicker clear cover than standard column
	GCNP	Grouted couplers w/o pedestal	Slow Cyclic	Column performance with grouted couplers installed above column-footing interface
	GCPP	Grouted couplers w/ partial pedestal	Slow Cyclic	Column performance with grouted couplers installed 12" (305) above column-footing interface
	HCNP	Headed couplers w/o pedestal	Slow Cyclic	Column performance with headed bar couplers installed above column-footing interface
	HCPP	Headed couplers w/ partial pedestal	Slow Cyclic	Column performance with headed bar couplers installed 12" (305) above column-footing interface
Present Study	PNC	No Coupler; UHPC-filled duct connection	Slow Cyclic	The column-footing connection using UHPC-filled ducts
	GCDP	Grouted couplers w/ debonded bars in pedestal	Slow Cyclic	Column performance with grouted couplers and debonded longitudinal bars in pedestal
	HCS	UHPC-filled ducts and headed couplers	Slow Cyclic	Column performance incorporating damage-free materials: SMA bars and ECC in plastic hinge

Table 3.2- Summary of Column Models Design

Item/Specimen	CIP	PNC	GCDP	HCS*
Longitudinal Reinforcement	11-#8 (Ø25) mild bars, ρ_l=1.92%	11-#8 (Ø25) mild bars, ρ_l=1.92%	11-#8 (Ø25) mild bars, ρ_l=1.92%	10-#10 (Ø32) SMA bars, ρ_l=2.8%
Transverse Reinforcement	#3(Ø10) spiral at 2-*in*. (51-*mm*) pitch, ρ_s=1.05%	#3(Ø10) spiral at 2-*in*. (51-*mm*) pitch, ρ_s=1.03%	#3(Ø10) spiral at 2-*in*. (51-*mm*) pitch, ρ_s=1.05%	#3(Ø10) spiral at 2-*in*. (51-*mm*) pitch, ρ_s=1.04%
Clear Cover	1.75 *in*. (44 *mm*)	1.5 *in*. (38 *mm*)	1.0 *in*. (25 *mm*)† 1.75 *in*. (44 *mm*) ‡	1.31 *in*. (33 *mm*) † 1.62 *in*. (41 *mm*) ‡
Aspect Ratio	4.5	4.5	4.5	4.5
Column Diameter	24 *in*. (610 *mm*)	24 *in*. (610 *mm*)	24 *in*. (610 *mm*)	24 *in*. (610 *mm*)
Hollow Section	N/A	6-*in*. (152-*mm*) wall thickness	6-*in*. (152-*mm*) wall thickness	6-*in*. (152-*mm*) wall thickness
Axial Load Index	10%	10%	10%	10%

* SMA-reinforced column
† Section with couplers
‡ Section without couplers

Table 3.3- SCC Mix Design Requirements (Standard Specification for CA, 2010)

Property	Test	Requirement
Slump flow	ASTM C 1611	At least 20 inches
Flow rate, T_{50}	ASTM C 1611	2–7 seconds
Visual stability index	ASTM C 1611	1 or less
J-Ring flow	ASTM C 1621	The difference between J-Ring flow and slump flow must not exceed 2 inches
Column segregation	ASTM C 1610	Static segregation must not exceed 15 percent
Bleeding	ASTM C 232	Bleeding capacity must not exceed 2.5 percent
Compressive strength	California Test 521	The average of 5 test cylinders must be at least 600 psi greater than the strength described*
Minimum compressive strength	California Test 521	The minimum for an individual test cylinder must not be less than the strength described*

* At the maximum age specified or allowed

Table 3.4- SCC Mix Design

Material	Weight
Cement- Nevada Type II	564 *lbs*
Pozzolan- Nevada Type N	141 *lbs*
Water	282 *lbs*
No. 7 Stone- Palute Pit	1150 *lbs*
No. 8 Stone- Palute Pit	320 *lbs*
Sand- Palute Pit	1406 *lbs*
Grace ADVA 190	42 *oz*
Grace ADVA 405	99 *oz*
Grace VMAR 3	11 *oz*
Grace Recover	49 *oz*
Air Content	3.0%

For 4000-*psi* mix design

Table 3.5- Typical Field-Cast UHPC Mix Design

Material	Weight (*lbs/yd*)	Percent by Weight
Portland Cement	1200	28.5
Fine Sand	1720	40.8
Silica Fume	390	9.3
Ground Quartz	355	8.4
Superplasticizer	51	1.2
Steel Fibers	263	6.2
Water	218	5.2

Table 3.6- ECC Mix Design

Material	Weight (*lbs*)	Percent by Weight
Cement- Nevada Cement Type I/II	20.5	37.0
Fly Ash- Ft. Bridger, Type F	17.5	31.5
Sand- Average 60#	13.75	24.7
Silica Powder 90#	3.0	5.4
PVA Fiber-Kuraray Kuralon REC 8x15	0.8	1.4
Superplasticizer- BASF polycarboxylate ether or FritzPak No. 7	17g	---

Water to Cement & Fly Ash ratio= 0.315; Fly Ash to Cement ratio= 0.85

Table 4.1- Measured Compressive Strength of Cementitious Materials Used in Column Models

			Column Models, *psi* (*MPa*)			
Material	Element	Measured at	CIP	PNC	GCDP	HCS
Conventional Concrete*	Footing	7-Day	3350 (23.1)	3425 (23.6)	3425 (23.6)	3425 (23.6)
		28-Day	4695 (32.3)	4595 (31.7)	4595 (31.7)	5420 (37.4)
		Col. test Day	5415 (37.3)	5485 (37.8)	5660 (39.0)	6880 (47.4)
	Shell & Pedestal	7-Day	2760 (19.0)	2635 (18.2)	2635 (18.2)	3910 (26.9)
		28-Day	4115 (28.3)	3325 (22.9)	3325 (22.9)	5190 (35.8)
		Col. test Day	4445 (30.6)	3290 (22.7)	3210 (22.1)	6775 (46.7)
SCC*	Core & Head	7-Day	N/A	4740 (32.7)	4740 (32.7)	2970 (20.5)
		28-Day	N/A	6410 (44.2)	6410 (44.2)	4110 (28.3)
		Col. test Day	N/A	9510 (65.6)	8750 (60.3)	5065 (34.9)
UHPC†	UHPC-Filled Duct	7-Day	N/A	16940 (116.8)	N/A	11490 (79.2)
		28-Day	N/A	20535 (141.6)	N/A	20090 (138.5)
		Col. test Day	N/A	22970 (158.4)	N/A	21030 (145.0)
ECC**	Plastic Hinge	7-Day	N/A	N/A	N/A	1980 (13.6)
		28-Day	N/A	N/A	N/A	4990 (34.4)
		Col. test Day	N/A	N/A	N/A	6390 (44.0)
SS Mortar‡	NMB Couplers	7-Day	N/A	N/A	13355 (92.1)	N/A
		28-Day	N/A	N/A	16365 (112.8)	N/A
		Col. test Day	N/A	N/A	16970 (117.0)	N/A
Grout‡	Closure Region	7-Day	N/A	N/A	9670 (66.7)	N/A
		28-Day	N/A	N/A	--	N/A
		Col. test Day	N/A	N/A	16890 (116.5)	N/A

*: 6-*in*. (152-*mm*) by 12-*in*. (305-*mm*) cylinder mold
**: 4-*in*. (102-*mm*) by 8-*in*. (203-*mm*) cylinder mold
†: 3-*in*. (76-*mm*) by 6-*in*. (152-*mm*) cylinder mold
‡: 2-*in*. (51-*mm*) cubic mold

Table 4.2- Measured Strength of Reinforcing Steel

Bar	Column Model	Bar Size	ASTM Type	Yield Strength, f_y *ksi* (*MPa*)	Ultimate Strength, f_u *ksi* (*MPa*)	Post-Yield Stiffness, E_{sh} *ksi* (*MPa*)	Ultimate Strain, ε_{su} (%)
Longitudinal	CIP*	#8 (Ø25)	A615 Grade 60	68.8 (460.6)	111.3 (767.4)	1250 (8618.4)	9.0
	PNC†	#8 (Ø25)	A706 Grade 60	65.8 (453.4)	91.7 (632.0)	1727.8 (11912.8)	11.9
	GCDP†	#8 (Ø25)	A706 Grade 60	65.8 (453.4)	91.7 (632.0)	1727.8 (11912.8)	11.9
	HCS*	#11 (Ø36)	A706 Grade 60	71.8 (495.1)	99.3 (684.8)	623.1 (4296.1)	19.5
Spiral	CIP†	#3 (Ø10)	A615 Grade 60	81.8 (564.0)	111.5 (768.8)	N/A	9.6
	PNC*	#3 (Ø10)	A615 Grade 60	70.5 (486.1)	110.7 (763.2)	1305.2 (8999.0)	10.6
	GCDP*	#3 (Ø10)	A615 Grade 60	70.5 (486.1)	110.7 (763.2)	1305.2 (8999.0)	10.6
	HCS†	#3 (Ø10)	A615 Grade 60	66.2 (456.4)	92.4 (637.6)	N/A	12.9

*: Average of three tensile tests
†: Average of four tensile tests

Table 4.3- Measured Mechanical Properties for NiTi SE SMA Used in HCS Column

Parameter	#10 Bar, Sample 1	#10 Bar, Sample 2*
Austenite modulus, k_1	7288 *ksi* (50251 *MPa*)	6039 *ksi* (41639 *MPa*)
Post yield stiffness, k_2	146.1 *ksi* (1007 *MPa*)	N/A
Austenite yield strength, f_y	69.1 *ksi* (746.4 *MPa*)	≥ 65
Lower plateau stress factor, β	0.55	N/A
Recoverable superelastic strain, ε_r	≥ 5%	N/A
Secondary post-yield stiffness ratio, α	N/A	N/A
Ultimate strain, ε_u	≥ 5%	N/A

* SMA bar Sample 2 fractured during first cycle of 2% strain at the head

Table 4.4- Material Properties for Couplers and Ducts

Coupler/Duct	Base Material Requirements	Minimum Yield Strength of Base Material, *psi* (*MPa*)
Headed Reinforcement Coupler	ASTM A576-06 Grade 1141	75000 (517)
NMB Grouted Coupler	ASTM A536-85	40000 (275)
Corrugated Galvanized Metal Duct	ASTM A653	33000 (227)

Table 4.5- PNC Column Observed Damage

PuSH/LL No.	Drift (%)	PNC Observed Damage	Highlights
1	0.25 Push toward S	No damage, maximum compressive strain was 840 micro-strain ($\mu\varepsilon$) at SG66 (Bar B7 24" above Column-Footing Interface (**CFI**)), maximum tensile strain was 410 $\mu\varepsilon$ at SG12 (Bar B1 5" below CFI)	Flexural Cracks, Axial Load was 198.3 *kips*
3	-0.25 Pull toward N	Few flexural cracks above 15" of CFI on S-face, maximum compressive strain was 745 $\mu\varepsilon$ at SG46 (Bar B1 12" above CFI), maximum tensile strain was 480 $\mu\varepsilon$ at SG57 (Bar B7 18" above CFI)	
5	0.25 Push toward S	Few flexural cracks above 10" of CFI on N-face, maximum compressive strain was 840 $\mu\varepsilon$ at SG29 (Bar B7 1" below CFI), maximum tensile strain was 415 $\mu\varepsilon$ at SG12 (Bar B1 5" below CFI)	
7	-0.25 Pull toward N	Few flexural cracks above 5" of CFI on S-face, maximum compressive strain was 785 $\mu\varepsilon$ at SG46 (Bar B1 12" above CFI), maximum tensile strain was 785 $\mu\varepsilon$ at SG57 (Bar B7 18" above CFI)	
9	0.5 Push toward S	Few flexural cracks above 15" of CFI on N-face, few shear cracks on W-face, maximum compressive strain was 1265 $\mu\varepsilon$ at SG39 (Bar B7 6" above CFI), maximum tensile strain was 1105 $\mu\varepsilon$ at SG12 (Bar B1 5" below CFI)	Shear Cracks
11	-0.5 Pull toward N	Few flexural cracks above 5" of CFI on S-face, few shear cracks on E-face, maximum compressive strain was 1110 $\mu\varepsilon$ at SG46 (Bar B1 12" above CFI), maximum tensile strain was 1200 $\mu\varepsilon$ at SG39 (Bar B7 6" above CFI)	
13	0.5 Push toward S	Few cracks above 7" of CFI on N-face, cracking at CFI on N-face, maximum compressive strain was 1265 $\mu\varepsilon$ at SG39 (Bar B7 6" above CFI), maximum tensile strain was 1055 $\mu\varepsilon$ at SG12 (Bar B1 5" below CFI)	CFI Cracking on N-face
15	-0.5 Pull toward N	Few flexural cracks above 21" of CFI on S-face, maximum compressive strain was 1100 $\mu\varepsilon$ at SG46 (Bar B1 12" above CFI), maximum tensile strain was 1190 $\mu\varepsilon$ at SG57 (Bar B7 18" above CFI)	
17	0.75 Push toward S	Few flexural cracks above 4" of CFI on N-face, maximum compressive strain was 1670 $\mu\varepsilon$ at SG39 (Bar B7 6" above CFI), maximum tensile strain was 1800 $\mu\varepsilon$ at SG18 (Bar B1 4" below CFI)	
19	-0.75 Pull toward N	Few flexural cracks above 10" of CFI on S-face, few shear cracks on E & W faces, maximum compressive strain was 1440 $\mu\varepsilon$ at SG46 (Bar B1 12" above CFI), maximum tensile strain was 1905 $\mu\varepsilon$ at SG39 (Bar B7 6" above CFI)	
21	0.75 Push toward S	Few flexural cracks above 25" of CFI on N-face, maximum compressive strain was 1655 $\mu\varepsilon$ at SG39 (Bar B7 6" above CFI), maximum tensile strain was 1775 $\mu\varepsilon$ at SG18 (Bar B1 4" below CFI)	
23	-0.75 Pull toward N	Few flexural cracks above 7" of CFI on S-face, few shear cracks on S, E & W faces, maximum compressive strain was 1435 $\mu\varepsilon$ at SG46 (Bar B1 12" above CFI), maximum tensile strain was 1870 $\mu\varepsilon$ at SG39 (Bar B7 6" above CFI)	
25	1 Push toward S	Few flexural and shear cracks above 15" of CFI on N-face, maximum compressive strain was 1960 $\mu\varepsilon$ at SG39 (Bar B7 6" above CFI), maximum tensile strain was 2340 $\mu\varepsilon$ at SG18 (Bar B1 4" below CFI). Yield displacement was 1.06 *in*. at 39.43 *kips* force. Bar B2 was also yielded 5" below the interface (SG11) shortly after first yielding	Tensile Bar B1 Yielded 4" below CFI, 1.06 *in*.
27	-1 Pull toward N	Extending flexural and shear cracks above 7" of CFI on S-face, maximum compressive strain was 1765 $\mu\varepsilon$ at SG46 (Bar B1 12" above CFI), maximum tensile strain was 2575 $\mu\varepsilon$ at SG39 (Bar B7 6" above CFI). Yield displacement was -0.858 *in*. at -41.21 *kips* force. Bars also yielded at SG57, SG40, SG30, SG14, SG66, SG29, SG35 and SG58	First Column Bar Yielding at Bar B7, Δ_y= -0.858 *in*.
29	1 Push toward S	Extending flexural and shear cracks above 15" of CFI on N-face, maximum compressive strain was 1940 $\mu\varepsilon$ at SG39 (Bar B7 6" above CFI), maximum tensile strain was 2265 $\mu\varepsilon$ at SG18 (Bar B1 4" below CFI)	
31	-1 Pull toward N	Extending flexural and shear cracks above 7" of CFI on E & S faces, maximum compressive strain was 1760 $\mu\varepsilon$ at SG46 (Bar B1 12" above CFI), maximum tensile strain was 2530 $\mu\varepsilon$ at SG39 (Bar B7 6" above CFI)	
33	2 Push toward S	Extending flexural and shear cracks above 7" of CFI on N, E and W faces, maximum compressive strain was 10660 $\mu\varepsilon$ at SG39 (Bar B7 6" above CFI), maximum tensile strain was 17410 $\mu\varepsilon$ at SG46 (Bar B1 12" above CFI)	Axial load increased from 193.5 to 195.5 *kips*
35	-2 Pull toward N	Extending flexural and shear cracks above 5" of CFI on E, S and W faces, spalling of concrete on NE-side, maximum compressive strain was 5875 $\mu\varepsilon$ at SG27 (Bar B1 1" below CFI), maximum tensile strain was 22390 $\mu\varepsilon$ at SG30 (Bar B6 1" below CFI)	Concrete Spalling in NE-Side
37	2 Push toward S	Extending flexural and shear cracks above 20" of CFI on N, E and W faces, maximum compressive strain was 5818 $\mu\varepsilon$ at SG39 (Bar B7 6" above CFI), maximum tensile strain was 15960 $\mu\varepsilon$ at SG11 (Bar B2 5" below CFI).	

PuSH/LL No.	Drift (%)	PNC Observed Damage	Highlights
39	-2 Pull toward N	Extending flexural and shear cracks above 25" of CFI on S-face, spalling of concrete in NE-side, maximum compressive strain was 6210 $\mu\varepsilon$ at SG27 (Bar B1 1" below CFI), maximum tensile strain was 18590 $\mu\varepsilon$ at SG30 (Bar B6 1" below CFI)	
41	3 Push toward S	Extending flexural and shear cracks above 5" of CFI on E and S faces, spalling of concrete on SE-side, crack width increasing at 10" above CFI, maximum compressive strain was 17130 $\mu\varepsilon$ at SG40 (Bar B6 6" above CFI), maximum tensile strain was 17590 $\mu\varepsilon$ at SG31 (Bar B2 0.5" above CFI)	Concrete Spalling on SE-Side
43	-3 Pull toward N	Extending flexural and shear cracks above 5" of CFI on S and W faces, spalling of concrete on NW-side, 0.25-*in.* gap at CFI at S-face, 0.08-*in.* crack width, maximum compressive strain was 9840 $\mu\varepsilon$ at SG27 (Bar B1 1" below CFI), maximum tensile strain was 25570 $\mu\varepsilon$ at SG30 (Bar B6 1" below CFI)	Concrete Spalling on NW-Side
45	3 Push toward S	Extending flexural and shear cracks above 1" of CFI on E and N faces, spalling of concrete on SW-side, crack width increasing at 10" above CFI, 0.25-*in.* gap at CFI on N-face, maximum compressive strain was 13010 $\mu\varepsilon$ at SG40 (Bar B6 6" above CFI), maximum tensile strain was 17800 $\mu\varepsilon$ at SG11 (Bar B2 5" below CFI)	Concrete Spalling on SE-Side
47	-3 Pull toward N	Extending flexural and shear cracks above 10" of CFI on S-face, 0.27-*in.* gap at CFI on S-face, 0.11-*in.* crack width on S-face, more concrete spalling on N-side, maximum compressive strain was 10210 $\mu\varepsilon$ at SG27 (Bar B1 1" below CFI), maximum tensile strain was 25230 $\mu\varepsilon$ at SG30 (Bar B6 1" below CFI)	
49	4 Push toward S	Crushing of cover concrete on S-side, two spirals exposed on S-side, 0.35-*in.* gap at CFI on N-face, 0.12-*in.* crack width on N-face at 7" height, maximum compressive strain was 16780 $\mu\varepsilon$ at SG40 (Bar B6 6" above CFI), maximum tensile strain was 23170 $\mu\varepsilon$ at SG11 (Bar B2 5" below CFI)	Axial load increased from 192.7 to 196.5 *kips*, Spiral Exposed
51	-4 Pull toward N	Crushing of cover concrete on N-side, two spirals exposed on N-side, 0.39-*in.* gap at CFI on S-face, maximum compressive strain was 13860 $\mu\varepsilon$ at SG27 (Bar B1 1" below CFI), maximum tensile strain was 34780 $\mu\varepsilon$ at SG30 (Bar B6 1" below CFI)	
53	4 Push toward S	More crushing of cover concrete on S-side, four spirals exposed on S-side, 0.35-*in.* gap at CFI on N-face and 0.20-*in.* gap on NE-face, maximum compressive strain was 20110 $\mu\varepsilon$ at SG30 (Bar B6 1" below CFI), maximum tensile strain was 23790 $\mu\varepsilon$ at SG11 (Bar B2 5" below CFI)	
55	-4 Pull toward N	More crushing of cover concrete on N-side, maximum compressive strain was 15310 $\mu\varepsilon$ at SG27 (Bar B1 1" below CFI), maximum tensile strain was 33920 $\mu\varepsilon$ at SG30 (Bar B6 1" below CFI)	
57	5 Push toward S	More crushing of cover concrete on S-side, 0.47-*in.* gap at CFI on N-face, maximum compressive strain was 27660 $\mu\varepsilon$ at SG30 (Bar B6 1" below CFI), maximum tensile strain was 28970 $\mu\varepsilon$ at SG11 (Bar B2 5" below CFI), losing SG7 and SG14	
59	-5 Pull toward N	More crushing of cover concrete on N-side, 0.47-*in.* gap at CFI on S-face, maximum compressive strain was 17530 $\mu\varepsilon$ at SG37 (Bar B1 6" above CFI), maximum tensile strain was 33770 $\mu\varepsilon$ at SG15 (Bar B6 5" below CFI)	
61	5 Push toward S	More crushing of cover concrete in S-side, 0.59-*in.* gap at CFI at N-face, maximum compressive strain was 26150 $\mu\varepsilon$ at SG29 (Bar B7 1" below CFI), maximum tensile strain was 27460 $\mu\varepsilon$ at SG11 (Bar B2 5" below CFI)	
63	-5 Pull toward N	Long. bar B7 exposed on S-side at CFI, more crushing of cover concrete on N-side, 0.47-*in.* gap at CFI on S-face, 0.16-*in*. and 0.24-*in*. gap on W and E faces respectively, maximum compressive strain was 19830 $\mu\varepsilon$ at SG37 (Bar B1 6" above CFI), maximum tensile strain was 34790 $\mu\varepsilon$ at SG15 (Bar B6 5" below CFI)	Exposing of Bar B7 on S-Side
65	6 Push toward S	More crushing of cover concrete on S-side, 0.51-*in.* gap at CFI on N-face, 0.31-*in*. and 0.16-*in*. gap on E and W faces respectively, maximum compressive strain was 29440 $\mu\varepsilon$ at SG39 (Bar B7 6" above CFI), maximum tensile strain was 32050 $\mu\varepsilon$ at SG12 (Bar B1 5" below CFI)	
67	-6 Pull toward N	More crushing of cover concrete on N-side, 0.63-*in.* gap at CFI on S-face, 0.20-*in*. and 0.31-*in*. gap on W and E faces respectively, maximum compressive strain was 30590 $\mu\varepsilon$ at SG37 (Bar B1 6" above CFI), maximum tensile strain was 43110 $\mu\varepsilon$ at SG15 (Bar B6 5" below CFI)	
69	6 Push toward S	Long. bar B6 exposed on S-side, long. bar B2 exposed on N-side at CFI, more crushing of cover concrete on S-side, 0.71-*in.* gap at CFI on N-face, 0.31-*in*. and 0.16-*in*. gap on E and W faces respectively, maximum compressive strain was 44670 $\mu\varepsilon$ at SG40 (Bar B6 6" above CFI), maximum tensile strain was 31910 $\mu\varepsilon$ at SG28 (Bar B11 1" below CFI)	Exposing of Bars B6 and B2
71	-6 Pull toward N	Long. bar B1 exposed on N-side, more crushing of cover concrete on N-side, 0.63-*in.* gap at CFI on S-face, 0.23-*in*. and 0.20-*in*. gap on W and E faces respectively, maximum compressive strain was 54600 $\mu\varepsilon$ at SG37 (Bar B1 6" above CFI), maximum tensile strain was 41190 $\mu\varepsilon$ at SG15 (Bar B6 5" below CFI)	Exposing of Bar B1 on N-Side

PuSH/LL No.	Drift (%)	PNC Observed Damage	Highlights
73	8 Push toward S	Kinking of spirals on S-side, bar B7 buckled, more crushing of cover concrete on S-side, 0.79-*in.* gap at CFI on N-face, 0.24-*in*. and 0.20-*in*. gap on E and W faces respectively, maximum compressive strain was 75460 $\mu\varepsilon$ at SG40 (Bar B6 6" above CFI), maximum tensile strain was 43510 $\mu\varepsilon$ at SG20 (Bar B11 4" below CFI), 21 SGs were lost	Buckling of Bar B7 on S-Side
75	-8 Pull toward N	Kinking of spirals on N-side, bar B1 buckled, more crushing of cover concrete on N-side, 0.91-*in.* gap at CFI on S-face, 0.31-*in*. and 0.39-*in*. gap on W and E faces respectively	Buckling of Bar B1 on N-Side
77	8 Push toward S	Kinking of spirals on S-side, bar B6 buckled, more crushing of cover concrete on S-side, 0.98-*in.* gap at CFI on N-face, 0.20-*in*. and 0.26-*in*. gap on E and W faces respectively	Buckling of Bar B6 on S-Side
79	-8 Pull toward N	Kinking of spirals on N-side, bar B1 buckled, more crushing of cover concrete on N-side, 0.91-*in.* gap at CFI on S-face, 0.31-*in*. and 0.39-*in*. gap on W and E faces respectively	
81	10 Push toward S	Three bars B1, B2 and B? fractured on N-side, penetration of crushing to core concrete on N-side	Fracturing of Three Bars on N-Side
83	-10 Pull toward N	One bar B7 fractured on S-side, penetration of crushing to core concrete on S-side	Fracturing of One Bar on S-Side

1 *in*.= 25.4 *mm*; 1 *kip*=4.45 *kN*; N: North; S: South; E: East; W:West

Table 4.6- GCDP Column Observed Damage

PuSH/LL No.	Drift %)	GCDP Observed Damage	Highlights
1	0.25 Push toward S	Few flexural cracks, maximum compressive strain was 1007 micro-strain ($\mu\varepsilon$) at SG19 (Bar B7 0.5" above Column-Footing Interface (**CFI**)), maximum tensile strain was 655 $\mu\varepsilon$ at SG12 (Bar B1 1" below CFI)	Flexural Cracks, Axial Load was 201.6 kips
3	-0.25 Pull toward N	Few flexural cracks above pedestal, maximum compressive strain was 897 $\mu\varepsilon$ at SG18 (Bar B11 0.5" above CFI), maximum tensile strain was 442 $\mu\varepsilon$ at SG19 (Bar B7 0.5" above CFI)	
5	0.25 Push toward S	Few flexural cracks above pedestal, maximum compressive strain was 1001 $\mu\varepsilon$ at SG19 (Bar B7 0.5" above CFI), maximum tensile strain was 670 $\mu\varepsilon$ at SG12 (Bar B1 1" below CFI)	
7	-0.25 Pull toward N	Few flexural cracks above pedestal on S-side, maximum compressive strain was 876 $\mu\varepsilon$ at SG18 (Bar B11 0.5" above CFI), maximum tensile strain was 400 $\mu\varepsilon$ at SG19 (Bar B7 0.5" above CFI)	
9	0.5 Push toward S	Few flexural cracks above pedestal on N-side, maximum compressive strain was 1421 $\mu\varepsilon$ at SG19 (Bar B7 0.5" above CFI), maximum tensile strain was 1505 $\mu\varepsilon$ at SG12 (Bar B1 1" below CFI)	
11	-0.5 Pull toward N	Few flexural cracks above pedestal on S-side, maximum compressive strain was 1284 $\mu\varepsilon$ at SG22 (Bar B1 6" above CFI), maximum tensile strain was 1263 $\mu\varepsilon$ at SG19 (Bar B7 0.5" above CFI)	
13	0.5 Push toward S	Few cracks above pedestal on N-side, maximum compressive strain was 1346 $\mu\varepsilon$ at SG19 (Bar B7 0.5" above CFI), maximum tensile strain was 1470 $\mu\varepsilon$ at SG12 (Bar B1 1" below CFI)	
15	-0.5 Pull toward N	Few flexural cracks above pedestal on S-side, column-footing interface cracking, maximum compressive strain was 1305 $\mu\varepsilon$ at SG22 (Bar B1 6" above CFI), maximum tensile strain was 1235 $\mu\varepsilon$ at SG19 (Bar B7 0.5" above CFI)	Crack at CFI
17	0.75 Push toward S	Few flexural cracks above pedestal at N-side, maximum compressive strain was 1746 $\mu\varepsilon$ at SG19 (Bar B7 0.5" above CFI), maximum tensile strain was 2222 $\mu\varepsilon$ at SG12 (Bar B1 1" below CFI)	
19	-0.75 Pull toward N	Few flexural cracks above pedestal on S-side, maximum compressive strain was 1705 $\mu\varepsilon$ at SG22 (Bar B1 6" above CFI), maximum tensile strain was 2008 $\mu\varepsilon$ at SG19 (Bar B7 0.5" above CFI)	
21	0.75 Push toward S	Few flexural cracks above pedestal on N-face, 0.04 *in.* gap at CFI on N-side, maximum compressive strain was 1688 $\mu\varepsilon$ at SG19 (Bar B7 0.5" above CFI), maximum tensile strain was 2167 $\mu\varepsilon$ at SG12 (Bar B1 1" below CFI)	
23	-0.75 Pull toward N	Few flexural cracks above pedestal on S-side, maximum compressive strain was 1705 $\mu\varepsilon$ at SG22 (Bar B1 6" above CFI), maximum tensile strain was 1974 $\mu\varepsilon$ at SG19 (Bar B7 0.5" above CFI)	
25	1 Push toward S	Few cracks in and above pedestal on N-side, maximum compressive strain was 2091 $\mu\varepsilon$ at SG19 (Bar B7 0.5" above CFI), maximum tensile strain was 3057 $\mu\varepsilon$ at SG12 (Bar B1 1" below CFI). First yield happened below the CFI at displacement of 0.867 *in.* with 34.49 *kips* force. First yielding in the column happened at SG22 (Bar B1 6" above CFI) at the displacement of 0.889 *in*. and 35.52 kips force. Bars also yielded at SG17, SG18, SG30, SG47, SG16, SG32 and SG21	Cracks in Pedestal, First Yielding at Bar B7 at Δ_y= 0.889 *in*.
27	-1 Pull toward N	Few flexural cracks above pedestal on S-side, 0.08 *in.* cracking at CFI on S-side, maximum compressive strain was 2133 $\mu\varepsilon$ at SG22 (Bar B1 6" above CFI), maximum tensile strain was 2705 $\mu\varepsilon$ at SG19 (Bar B7 0.5" above CFI)	
29	1 Push toward S	Few flexural cracks above pedestal on N-side, maximum compressive strain was 2043 $\mu\varepsilon$ at SG19 (Bar B7 0.5" above CFI), maximum tensile strain was 2982 $\mu\varepsilon$ at SG12 (Bar B1 1" below CFI)	
31	-1 Pull toward N	Few flexural cracks above pedestal on S-side, maximum compressive strain was 2120 $\mu\varepsilon$ SG22 (Bar B1 6" above CFI), maximum tensile strain was 2670 $\mu\varepsilon$ at SG12 (Bar B1 1" below CFI)	
33	2 Push toward S	Cracks in and above pedestal on N, E and S sides, 0.14 *in.* cracking at CFI on N-side, 0.06 *in*. gap below coupler and 0.02 *in*. cracking above coupler on N-side, Spalling of concrete on S-side, maximum compressive strain was 12270 $\mu\varepsilon$ at SG19 (Bar B7 0.5" above CFI), maximum tensile strain was 19270 $\mu\varepsilon$ at SG22 (Bar B1 6" above CFI)	Concrete Cover Spalling on S-Side, Shear Cracks
35	-2 Pull toward N	Cracks in and above pedestal on S, E and W sides, 0.16 *in.* cracking at CFI on S-side, 0.04 *in*. gap below coupler and 0.02 *in*. cracking above coupler on S-side, Spalling of concrete on N-side 1" above CFI, maximum compressive strain was 6090 $\mu\varepsilon$ at SG22 (Bar B1 6" above CFI), maximum tensile strain was 15320 $\mu\varepsilon$ at SG25 (Bar B6 6" above CFI)	Concrete Spalling on N Side
37	2	No new crack, 0.2 *in.* crack width at CFI on N-side, 0.04 *in*. gap below coupler and 0.02 *in*. cracking above coupler on N-side, maximum compressive strain was 6341	

PuSH/LL No.	Drift %)	GCDP Observed Damage	Highlights
	Push toward S	$\mu\varepsilon$ at SG19 (Bar B7 0.5" above CFI), maximum tensile strain was 14420 $\mu\varepsilon$ at SG22 (Bar B1 6" above CFI)	
39	-2 Pull toward N	Extending flexural and shear cracks in and above pedestal on all sides, spalling of concrete on N-side, maximum compressive strain was 5116 $\mu\varepsilon$ at SG22 (Bar B1 6" above CFI), maximum tensile strain was 11880 $\mu\varepsilon$ at SG25 (Bar B6 6" above CFI)	
41	3 Push toward S	Extending flexural and shear cracks in and above pedestal on N, E and W sides, 0.24 *in.* cracking at CFI on N-side, 0.1 *in*. gap below coupler and 0.02 *in*. cracking above coupler on N-side, extending of spalling in pedestal on S-side, maximum compressive strain was 11460 $\mu\varepsilon$ at SG33 (Bar B7 11" above CFI), maximum tensile strain was 24220 $\mu\varepsilon$ at SG30 (Bar B2 11" above CFI)	Partial conical failure in Footing on N-side
43	-3 Pull toward N	Cracks in and above pedestal on all sides, 0.32 *in.* cracking at CFI on S-side, 0.14 *in*. gap below coupler and 0.04 *in*. cracking above coupler on S-side, Spalling of concrete on N-side, maximum compressive strain was 9632 $\mu\varepsilon$ at SG17 (Bar B1 0.5" above CFI), maximum tensile strain was 19620 $\mu\varepsilon$ at SG33 (Bar B7 11" above CFI)	
45	3 Push toward S	Extending flexural and shear cracks in pedestal, 0.28 *in.* cracking at CFI on N-side, 0.12 *in*. gap below coupler and 0.04 *in*. cracking above coupler on N-side, Spalling of concrete on N-side, partial conical failure of footing concrete on N-side, maximum compressive strain was 10890 $\mu\varepsilon$ at SG20 (Bar B6 0.5" above CFI), maximum tensile strain was 24730 $\mu\varepsilon$ at SG12 (Bar B1 1" below CFI)	
47	-3 Pull toward N	Extending flexural and shear cracks in pedestal, 0.35 *in.* cracking at CFI on S-side, 0.18 *in*. gap below coupler and 0.04 *in*. cracking above coupler on S-side, maximum compressive strain was 13270 $\mu\varepsilon$ at SG17 (Bar B1 0.5" above CFI), maximum tensile strain was 19200 $\mu\varepsilon$ at SG33 (Bar B7 11" above CFI)	New Loading Rate after 3% Drift
49	4 Push toward S	Crushing of cover concrete on S-side, two spirals exposed on S-side, 0.47 *in.* cracking at CFI on N-side, 0.16 *in*. gap below coupler and 0.04 *in*. cracking above coupler on N-side, , maximum compressive strain was 14980 $\mu\varepsilon$ at SG20 (Bar B6 0.5" above CFI), maximum tensile strain was 32440 $\mu\varepsilon$ at SG12 (Bar B1 1" below CFI)	Spiral Exposing on S-side
51	-4 Pull toward N	Extending flexural and shear cracks in pedestal, 0.47 *in.* cracking at CFI on S-side, 0.24 *in*. gap below coupler and 0.04 *in*. cracking above coupler on S-side, maximum compressive strain was 19170 $\mu\varepsilon$ at SG17 (Bar B1 0.5" above CFI), maximum tensile strain was 29260 $\mu\varepsilon$ at SG33 (Bar B7 11" above CFI)	
53	4 Push toward S	More crushing of cover concrete on S-side, 0.47 *in.* cracking at CFI on N-side, 0.16 *in*. gap below coupler and 0.04 *in*. cracking above coupler on N-side, partial conical failure of footing concrete with radius of 10.5 *in*. from column N-side, maximum compressive strain was 19620 $\mu\varepsilon$ at SG20 (Bar B6 0.5" above CFI), maximum tensile strain was 34070 $\mu\varepsilon$ at SG12 (Bar B1 1" below CFI)	
55	-4 Pull toward N	More crushing of cover concrete a on t N-side, 0.55 *in.* cracking at CFI on S-side, 0.24 *in*. gap below coupler and 0.04 *in*. cracking above coupler on S-side, maximum compressive strain was 21480 $\mu\varepsilon$ at SG17 (Bar B1 0.5" above CFI), maximum tensile strain was 28770 $\mu\varepsilon$ at SG33 (Bar B7 11" above CFI)	
57	5 Push toward S	More crushing of pedestal cover concrete on S-side, partial conical failure of footing concrete with 0.24 *in*. uplift at the edges, 0.43 *in.* cracking at CFI on N-side, 0.16 *in*. gap below coupler and 0.04 *in*. cracking above coupler on N-side, maximum compressive strain was 28700 $\mu\varepsilon$ at SG25 (Bar B6 6" above CFI), maximum tensile strain was 36980 $\mu\varepsilon$ at SG30 (Bar B2 11" above CFI)	
59	-5 Pull toward N	More crushing of cover concrete on N-side, 0.47 *in.* cracking at CFI on S-side, 0.26 *in*. gap below coupler and 0.06 *in*. cracking above coupler on S-side, maximum compressive strain was 36230 $\mu\varepsilon$ at SG17 (Bar B1 0.5" above CFI), maximum tensile strain was 37530 $\mu\varepsilon$ at SG33 (Bar B7 11" above CFI), 1.6 *in*. damage penetration to core with angle of 30 degree at the CFI level	
61	5 Push toward S	More crushing of cover concrete on S-side, partial conical failure of footing concrete with 0.28 *in*. uplift at the edges, 0.35 *in.* cracking on CFI at N-side, 0.16 *in*. gap below coupler and 0.04 *in*. cracking above coupler on N-side, maximum compressive strain was 33430 $\mu\varepsilon$ at SG20 (Bar B6 0.5" above CFI), maximum tensile strain was 36280 $\mu\varepsilon$ at SG7 (Bar B1 4" below CFI)	
63	-5 Pull toward N	More crushing of cover concrete on N-side, 0.2 *in.* core cracking at CFI on S-side, 0.18 *in*. gap below coupler and 0.06 *in*. cracking above coupler on S-side, maximum compressive strain was 47760 $\mu\varepsilon$ at SG17 (Bar B1 0.5" above CFI), maximum tensile strain was 35160 $\mu\varepsilon$ at SG33 (Bar B7 11" above CFI)	
65	6 Push toward S	Long. bar B11 exposed on N-side, Long. bar B6 exposed on S-side, Kinking in spirals on S-side, more crushing of cover concrete on S-side, partial conical failure of footing concrete with 0.43 *in*. uplift at the edges, 0.37 *in.* cracking at CFI on N-side, 0.1 *in*. gap below coupler and 0.04 *in*. cracking above coupler on N-side, maximum compressive strain of good SGs was 50180 $\mu\varepsilon$ at SG20 (Bar B6 0.5" above CFI), maximum tensile strain was 45330 $\mu\varepsilon$ at SG22 (Bar B1 6" above CFI)	Exposing of Bars B11 and B6, Spiral Kinking on S-Side

PuSH/LL No.	Drift %)	GCDP Observed Damage	Highlights
67	-6 Pull toward N	Long. bar B1 exposed on N-side, Kinking in spirals on N-side, Long. bar B7 exposed on S-side, more crushing of cover concrete on N-side, 0.24 *in.* core cracking at CFI on S-side, 0.18 *in*. gap below coupler and 0.06 *in*. cracking above coupler on S-side, maximum compressive strain of survived SGs was 83430 $\mu\varepsilon$ at SG17 (Bar B1 0.5" above CFI), maximum tensile strain was 44290 $\mu\varepsilon$ at SG33 (Bar B7 11" above CFI)	Exposing of Bars B1 and B7
69	6 Push toward S	Kinking in spirals on S-side, bars B6 & B7 buckled, more crushing of cover concrete on S-side, partial conical failure of footing concrete with 0.53 *in*. uplift at the edges, 0.39 *in.* core cracking at CFI on N-side, 0.8 *in*. gap below coupler and 0.04 *in*. cracking above coupler on N-side, maximum compressive strain of good SGs was 70470 $\mu\varepsilon$ at SG20 (Bar B6 0.5" above CFI), maximum tensile strain was 45930 $\mu\varepsilon$ at SG7 (Bar B1 4" below CFI)	Buckling of Bars B6 and B7 on S-Side
71	-6 Pull toward N	Bar B1 buckled on N-side, more crushing of cover concrete on N-side, 0.2 *in.* core cracking at CFI on S-side	Buckling of Bar B1 on N-Side
73	8 Push toward S	Bars B6 and B7 buckled for the second time, 0.59 *in.* core cracking at CFI on S-side, 0.11 *in*. cracking above coupler on S-side, partial conical failure of footing concrete with 0.59 *in*. uplift at the edges	
75	-8 Pull toward N	Bars B1 and B11 buckled again on N-side, more crushing of cover concrete on N-side, 0.39 *in.* core cracking at CFI on S-side, 0.18 *in*. gap below coupler and 0.08 *in*. cracking above coupler on S-side	Buckling of Bars B1 & B11 on N-Side
77	8 Push toward S	Spiral rupture 4" above CIP on S-side tangent to Bar B7, Bars B6 and B7 buckled for the third time, bar B2 exposed, partial conical failure of footing concrete with 0.91 *in*. uplift at the edges, 0.59 *in.* core cracking at CFI on N-side, 0.27 *in*. cracking above coupler on N-side	Fracturing of Spiral on S-side
79	-8 Pull toward N	Bars B1 and B11 buckled again on N-side, Bar B2 buckled for the first time, Bar B6 ruptured on S-side at 4" above CFI,	Fracturing of Bar B6
81	-10 Pull toward N	Continue the test to -10% drift, two more bars B? and B? ruptured	Continue the test to -10% Drift
83	10 Push toward S	Two bars B1 and B? ruptured on N-side, severe concrete damage, penetration of damage to the core	Fracturing of two Bars on N-face

1 *in*.= 25.4 *mm*; 1 *kip*=4.45 *kN*; N: North; S: South; E: East; W:West

Table 4.7- HCS Column Observed Damage

PuSH/LL No.	Drift (%)	HCS Observed Damage	Highlights
1	0.25 Push toward S	No damage, maximum compressive strain was 798 micro-strain ($\mu\varepsilon$) at SG23 (SMA Bar B6, 8.125" above Column-Footing Interface (**CFI**)), maximum tensile strain was 576 $\mu\varepsilon$ at SG20 (SMA Bar B1, 8.125" above CFI)	No cracks, axial load was 200.2 *kips*
3	-0.25 Pull toward N	Few flexural cracks above 10" of CFI on S-face, maximum compressive strain was 917 $\mu\varepsilon$ at SG21 (SMA Bar B10, 8.125" above CFI), maximum tensile strain was 805 $\mu\varepsilon$ at SG24 (SMA Bar B5, 8.125" above CFI)	
5	0.25 Push toward S	Few flexural cracks above 15" of CFI on N-face, maximum compressive strain was 870 $\mu\varepsilon$ at SG23 (SMA Bar B6, 8.125" above CFI), maximum tensile strain was 615 $\mu\varepsilon$ at SG20 (SMA Bar B1, 8.125" above CFI)	
7	-0.25 Pull toward N	Few flexural cracks above 18" of CFI on S-face, maximum compressive strain was 969 $\mu\varepsilon$ at SG21 (SMA Bar B10, 8.125" above CFI), maximum tensile strain was 785 $\mu\varepsilon$ at SG24 (SMA Bar B5, 8.125" above CFI)	
9	0.5 Push toward S	Few flexural cracks on N-face, maximum compressive strain was 1498 $\mu\varepsilon$ at SG23 (SMA Bar B6, 8.125" above CFI), maximum tensile strain was 2763 $\mu\varepsilon$ at SG21 (SMA Bar B10, 8.125" above CFI)	
11	-0.5 Pull toward N	Few flexural cracks above 15" of CFI on S-face, maximum compressive strain was 1617 $\mu\varepsilon$ at SG21 (SMA Bar B10, 8.125" above CFI), maximum tensile strain was 3467 $\mu\varepsilon$ at SG23 (SMA Bar B6, 8.125" above CFI).	
13	0.5 Push toward S	Few cracks above 20" of CFI on N-face, maximum compressive strain was 1571 $\mu\varepsilon$ at SG22 (SMA Bar B7, 8.125" above CFI), maximum tensile strain was 2894 $\mu\varepsilon$ at SG21 (SMA Bar B10, 8.125" above CFI)	
15	-0.5 Pull toward N	No new crack, maximum compressive strain was 1611 $\mu\varepsilon$ at SG21 (SMA Bar B10, 8.125" above CFI), maximum tensile strain was 3565 $\mu\varepsilon$ at SG23 (SMA Bar B6, 8.125" above CFI)	
17	0.75 Push toward S	No new crack, maximum compressive strain was 1754 $\mu\varepsilon$ at SG22 (SMA Bar B7, 8.125" above CFI), maximum tensile strain was 4661 $\mu\varepsilon$ at SG21 (SMA Bar B10, 8.125" above CFI)	CFI cracking on N-face
19	-0.75 Pull toward N	Extension of a crack above 10" of CFI on S-face, maximum compressive strain was 1715 $\mu\varepsilon$ at SG20 (SMA Bar B1, 8.125" above CFI), maximum tensile strain was 5861 $\mu\varepsilon$ at SG13 (Steel Bar B2, 1" below CFI)	
21	0.75 Push toward S	No new cracks, maximum compressive strain was 1682 $\mu\varepsilon$ at SG22 (SMA Bar B7, 8.125" above CFI), maximum tensile strain was 4877 $\mu\varepsilon$ at SG21 (SMA Bar B10, 8.125" above CFI)	
23	-0.75 Pull toward N	Few flexural cracks above 25" of CFI on S-face, maximum compressive strain was 1748 $\mu\varepsilon$ at SG21 (SMA Bar B10, 8.125" above CFI), maximum tensile strain was 5894 $\mu\varepsilon$ at SG13 (Steel Bar B2, 1" below CFI)	
25	1 Push toward S	No flexural cracks, maximum compressive strain was 1995 $\mu\varepsilon$ at SG23 (SMA Bar B6, 8.125" above CFI), maximum tensile strain was 6390 $\mu\varepsilon$ at SG21 (SMA Bar B10, 8.125" above CFI)	
27	-1 Pull toward N	Few flexural above 20" of CFI on S-face, maximum compressive strain was 2000 $\mu\varepsilon$ at SG21 (SMA Bar B10, 8.125" above CFI), maximum tensile strain was 7778 $\mu\varepsilon$ at SG23 (SMA Bar B6, 8.125" above CFI)	
29	1 Push toward S	No new cracks, maximum compressive strain was 1962 $\mu\varepsilon$ at SG23 (SMA Bar B6, 8.125" above CFI), maximum tensile strain was 6225 $\mu\varepsilon$ at SG21 (SMA Bar B10, 8.125" above CFI)	
31	-1 Pull toward N	No new cracks, maximum compressive strain was 2048 $\mu\varepsilon$ at SG20 (SMA Bar B1, 8.125" above CFI), maximum tensile strain was 7837 $\mu\varepsilon$ at SG23 (SMA Bar B6, 8.125" above CFI)	
33	2 Push toward S	Few flexural cracks above 20" of CFI on N-face, extending of a crack on N-side 10" above CFI w/ a width of 3/16", maximum compressive strain was 3585 $\mu\varepsilon$ at SG23 (SMA Bar B6, 8.125" above CFI), maximum tensile strain was 12400 $\mu\varepsilon$ at SG21 (SMA Bar B10, 8.125" above CFI). First SMA bar yielding was observed at a displacement 1.556 *in*. with a 44.58-*kip* force. SMA bar B1 was also yielded measured by SG20	SMA bar B10 was yielded 8.125" above CFI, at 1.556 *in*. and 44.58 *kips*
35	-2 Pull toward N	Few flexural cracks above 20" of CFI on S-face, extension of a crack on S-side 10" above CFI w/ a width of 5/16", maximum compressive strain was 3724 $\mu\varepsilon$ at SG20 (SMA Bar B1, 8.125" above CFI), maximum tensile strain was 13910 $\mu\varepsilon$ at SG23 (SMA Bar B6, 8.125" above CFI)	
36	Zero-Force	Minor damage of plastic hinge, the residual drift ratio was 0.144%	
37	2 Push toward S	Few flexural cracks above 20" of CFI on N-face, extension of a crack on N-side 10" above CFI w/ a width of 3/16", maximum compressive strain was 3428 $\mu\varepsilon$ at	

PuSH/LL No.	Drift (%)	HCS Observed Damage	Highlights
		SG23 (SMA Bar B6, 8.125" above CFI), maximum tensile strain was 12070 $\mu\varepsilon$ at SG21 (SMA Bar B10, 8.125" above CFI)	
39	-2 Pull toward N	Few flexural cracks above 20" of CFI on S-face, extension of a crack on S-side 10" above CFI w/ a width of 5/16", maximum compressive strain was 3665 $\mu\varepsilon$ at SG20 (SMA Bar B1, 8.125" above CFI), maximum tensile strain was 13890 $\mu\varepsilon$ at SG23 (SMA Bar B6, 8.125" above CFI)	
41	3 Push toward S	Few flexural cracks above 20" of CFI on N-face, extension of a crack on N-side 10" above CFI w/ a width of 5/16", spalling of concrete on S-side, maximum compressive strain was 6424 $\mu\varepsilon$ at SG23 (SMA Bar B6, 8.125" above CFI), maximum tensile strain was 19780 $\mu\varepsilon$ at SG21 (SMA Bar B10, 8.125" above CFI). First steel bar yielding was observed at a displacement of 2.426 *in*. with a 57.59-*kip* force	Concrete spalling in S-Side, first steel yielding at 2.426 *in*. displacement
43	-3 Pull toward N	Few flexural cracks above 20" of CFI on S-face, extension of a crack on S-side 10" above CFI w/ a width of 7/16", spalling of concrete on N-side, maximum compressive strain was 6649 $\mu\varepsilon$ at SG20 (SMA Bar B1, 8.125" above CFI), maximum tensile strain was 17080 $\mu\varepsilon$ at SG23 (SMA Bar B6, 8.125" above CFI)	Concrete spalling in N-Side
44	Zero-Force	Minor damage of plastic hinge, visible cracks on both side of column, the residual drift ratio was 0.147%	
45	3 Push toward S	Few flexural cracks above 20" of CFI on N-face, extension of a crack on N-side 10" above CFI w/ a width of 5/16", maximum compressive strain was 6201 $\mu\varepsilon$ at SG23 (SMA Bar B6, 8.125" above CFI), maximum tensile strain was 18800 $\mu\varepsilon$ at SG21 (SMA Bar B10, 8.125" above CFI)	
47	-3 Pull toward N	No new cracks, extension of a crack on S-side 10" above CFI w/ a width of 0.5", maximum compressive strain was 4853 $\mu\varepsilon$ at SG21 (SMA Bar B10, 8.125" above CFI), maximum tensile strain was 17330 $\mu\varepsilon$ at SG23 (SMA Bar B6, 8.125" above CFI)	
49	4 Push toward S	No new cracks, extension of a crack in N-side 10" above CFI w/ a width of 0.5", maximum compressive strain was 8452 $\mu\varepsilon$ at SG23 (SMA Bar B6, 8.125" above CFI), maximum tensile strain was 32210 $\mu\varepsilon$ at SG21 (SMA Bar B10, 8.125" above CFI)	
51	-4 Pull toward N	No new cracks, extension of a crack on S-side 10" above CFI w/ a width of 5/8", maximum compressive strain was 5827 $\mu\varepsilon$ at SG30 (SMA Bar B1, 14.625" above CFI), maximum tensile strain was 22950 $\mu\varepsilon$ at SG23 (SMA Bar B6, 8.125" above CFI)	
52	Zero-Force	Minor damage of plastic hinge, visible cracks on both sides of column, the residual drift ratio was 0.199%	
53	4 Push toward S	No new cracks, extension of a crack on N-side 10" above CFI w/ a width of 9/16", maximum compressive strain was 7824 $\mu\varepsilon$ at SG23 (SMA Bar B6, 8.125" above CFI), maximum tensile strain was 32680 $\mu\varepsilon$ at SG30 (SMA Bar B1, 14.625" above CFI)	
55	-4 Pull toward N	No new cracks, extension of a crack in S-side 10" above CFI w/ a width of 5/8", maximum compressive strain was 5682 $\mu\varepsilon$ at SG19 (SMA Bar B2, 8.125" above CFI), maximum tensile strain was 22990 $\mu\varepsilon$ at SG23 (SMA Bar B6, 8.125" above CFI)	
56	Zero-Force	Minor damage of plastic hinge, crack width 10" above CFI was extending	
57	5 Push toward S	Few shear cracks on W-side, extension of a crack on N-side 10" above CFI w/ a width of 3/4", maximum compressive strain was 9688 $\mu\varepsilon$ at SG23 (SMA Bar B6, 8.125" above CFI), maximum tensile strain was 39200 $\mu\varepsilon$ at SG30 (SMA Bar B1, 14.625" above CFI)	Shear Cracks
59	-5 Pull toward N	No new cracks, extension of a crack on S-side 10" above CFI w/ a width of 15/16", maximum compressive strain was 7781 $\mu\varepsilon$ at SG20 (SMA Bar B1, 8.125" above CFI), maximum tensile strain was 45010 $\mu\varepsilon$ at SG23 (SMA Bar B6, 8.125" above CFI)	
60	Zero-Force	Cover concrete began to crush on S-sides, the residual drift ratio was 0.247%	
61	5 Push toward S	No new cracks, extension of a crack on N-side 10" above CFI w/ a width of 3/4", maximum compressive strain was 8452 $\mu\varepsilon$ at SG23 (SMA Bar B6, 8.125" above CFI), maximum tensile strain was 41400 $\mu\varepsilon$ at SG30 (SMA Bar B1, 14.625" above CFI)	
63	-5 Pull toward N	No new cracks, extension of a crack on S-side 10" above CFI w/ a width of 15/16", maximum compressive strain was 6728 $\mu\varepsilon$ at SG19 (SMA Bar B2, 8.125" above CFI), maximum tensile strain was 48280 $\mu\varepsilon$ at SG23 (SMA Bar B6, 8.125" above CFI)	
65	6 Push toward S	Few flexural cracks on N-side, extension of a crack on N-side 10" above CFI w/ a width of 7/8", maximum compressive strain of functional SG was 11180 $\mu\varepsilon$ at SG17 (steel Bar B6, 1" below CFI), maximum tensile strain of functional SG was 48250 $\mu\varepsilon$ at SG19 (SMA Bar B2, 8.125" above CFI)	

PuSH/LL No.	Drift (%)	HCS Observed Damage	Highlights
67	-6 Pull toward N	Crushing of cover concrete on N-side, no new cracks, extension of a crack on S-side 10" above CFI w/ a width of 1.187", maximum compressive strain of functional SG was 11410 $\mu\varepsilon$ at SG20 (SMA Bar B1, 8.125" above CFI), maximum tensile strain of functional SG was 58770 $\mu\varepsilon$ at SG23 (SMA Bar B6, 8.125" above CFI)	
68	Zero-Force	Damage of cover concrete on S-side was more than N-side, , two major cracks on S-side and one major crack in N-side remained open, the residual drift ratio was 0.317%	
69	6 Push toward S	No new cracks, extension of a crack on N-side 10" above CFI, maximum compressive strain of functional SG was 11600 $\mu\varepsilon$ at SG17 (steel Bar B6, 1" below CFI), maximum tensile strain of functional SG was 49300 $\mu\varepsilon$ at SG19 (SMA Bar B2, 8.125" above CFI)	
71	-6 Pull toward N	No new cracks, extension of a crack on S-side 10" above CFI w/ a width of 1.187", maximum compressive strain of functional SG was 7264 $\mu\varepsilon$ at SG19 (SMA Bar B2, 8.125" above CFI), maximum tensile strain of functional SG was 58990 $\mu\varepsilon$ at SG23 (SMA Bar B6, 8.125" above CFI)	
73	8 Push toward S	Width of a crack on N-side 10" above CFI was 1.187" in which the SMA bars were visible, more crushing of cover concrete on S-side	
75	-8 Pull toward N	Width of a crack on S-side 10" above CFI was 1.437" in which the SMA bars were visible, more crushing of cover concrete on N-side	
76	Zero-Force	Damage of cover concrete on S-side was more than N-side, two major cracks on S-side and one major crack on N-side remained open, the residual drift ratio was 0.468%	
77	8 Push toward S	Width of a crack on N-side 10" above CFI was 1.187" in which the SMA bars were visible, more crushing of cover concrete on S-side	
79	-8 Pull toward N	Width of a crack on S-side 10" above CFI was 1.437" in which the SMA bars were visible, more crushing of cover concrete on N-side	
81	10 Push toward S	Width of a crack on N-side 10" above CFI was 1.187" in which the SMA bars were visible, more crushing of cover concrete on S-side, column-footing cracking was 1/8"	
83	-10 Pull toward N	One bar fractured on S-side, cover concrete damage was slightly more than the previous loading	Fracturing of one bar on S-side
84	Zero-Force	Damage of cover concrete on S-side was more than N-side, cover concrete crushed on S-side, the residual drift ratio was 1.281%, no visible spiral	No visible spiral
85	10 Push toward S	A major crack on N-side, no extra bar rupture	
87	-10 Pull toward N	Cover concrete damage was slightly more than the previous loading, no extra bar rupture	
89	12 Push toward S	Two bars ruptured on N-side	Fracturing of two bars on N-side
91	-12 Pull toward N	One bar fractured on S-side	Fracturing of one bars on S-side

1 *in*.= 25.4 *mm*; 1 *kip*=4.45 *kN*; N: North; S: South; E: East; W:West

Table 5.1- Mode of Failure for All ABC Column Models

Test	Specimen	Drift Capacity*	Mode of Failure	No. of Ruptured Bars	Location of Ruptured Bars
Previous Research at UNR	CIP	10%	Longitudinal Bar Fracture	Three	3 *in*. (76 *mm*) to 12 *in*. (305 *mm*) above column-footing interface (**CIF**)
	GCNP	6%	Longitudinal Bar Fracture	Two	Both at 4.25 *in* (108 *mm*) below CIF
	GCPP	6%	Longitudinal Bar Fracture	Two	Both at 4.94 *in*. (125 *mm*) below CIF
	HCNP	10%	Longitudinal Bar Fracture	Two	One just below CIF, another 2 *in*. (51 *mm*) above CIF
	HCPP	10%	Longitudinal Bar Fracture	Four	All at 5.13 *in*. (130 *mm*) below CIF
Present Study	PNC	8%	Longitudinal Bar Fracture	Four	Three at 4 *in*. (102 *mm*) above CIF, 4th bar rupture could not be observed
	GCDP	8%	Longitudinal Bar Fracture	Five	Two at 4 *in*. (102 *mm*) above CIF, other fractures could not be observed
	HCS	10%	Longitudinal Bar Fracture	Four	Bar fracture location could not be observed

*: Largest drift level where column withstood at least one full cycle without any longitudinal bar fracture

Table 5.2- Lateral Load Strength Reduction Ratio at Each Drift Level for All ABC Columns (%)

Column Model	5% Drift		6% Drift		8% Drift		10% Drift	
	Push	Pull	Push	Pull	Push	Pull	Push	Pull
CIP	3.9	3.0	3.0	3.3	3.7	3.4	5.4*	17.9
GCNP	4.7	3.5	4.9	43.5*	N.A.	N.A.	N.A.	N.A.
GCPP	4.0	3.1	30.3*	26.5	N.A.	N.A.	N.A.	N.A.
HCNP	4.6	2.9	3.6	2.7	6.5	1.9	5.5	20.1*
HCPP	4.3	2.9	3.8	2.5	4.7	2.9	42.6*	12.2
PNC	4.0	2.5	4.4	3.1	8.7	6.7	N.A.*	N.A.
GCDP	4.1	3.2	5.2	3.3	16.0*	33.7	N.A.	N.A.
HCS	3.4	1.8	1.4	1.6	2.9	1.9	1.2	19.8*

* First longitudinal bar fracture

Table 5.3- Displacement Capacity for All ABC Column Models

Column Model	First Yield Point			Effective Yield Point			Ultimate Point		Disp. Ductility Capacity
	Disp., *in*.	Drift, (%)	Force, *kips*	Disp., *in*.	Drift, (%)	Force, *kips*	Disp., *in*.	Drift, (%)	
CIP	0.86	0.79	38.8	1.46	1.35	66.0	10.7	9.93	7.36
GCNP	0.81	0.75	38.1	1.42	1.31	66.9	6.43	5.95	4.52
GCPP	0.96	0.89	43.1	1.41	1.31	63.8	6.41	5.93	4.53
HCNP	1.26	1.17	51.8	1.64	1.52	67.5	10.6	9.85	6.49
HCPP	0.95	0.88	40.2	1.57	1.45	66.4	11.1	10.28	7.07
PNC	0.96	0.89	40.3	1.54	1.42	63.7	9.67	8.96	6.30
GCDP	0.86	0.8	38.9	1.33	1.23	59.9	9.43	8.73	7.07
HCS	1.56	1.44	44.6	2.33	2.16	68.3	11.19	10.37	4.80

1 *in*.=25.4 *mm*; 1 *kip*=4.448 *kN*; Column Height=108 *in*.; Design Displacement Ductility Capacity=7

Table 6.1- Mechanical Properties for NiTi Superelastic SMA

Reference	Specimens	Field	Austenite modulus, k_1, *ksi*	Post-yield Stiffness, k_2, *ksi*	Austenite yield strength, f_y, *ksi*	Lower plateau stress factor, β	Ultimate Strain, ε_u (%)	Post-yield Stiffness Ratio, $\alpha=k_3/k_1$
Saiidi and Wang, 2006	#4 Bar (Ø12.7mm)	Tension	5760	76	54.9	0.59	≥ 5.5	--
		Comp.	--	--	--	--	--	--
Youssef et al., 2008	Bar Ø20.6 mm	Tension	9065	269	58.2	0.35	≥ 6	0.14
		Comp.	--	--	--	--	--	--
SAES Ref. Bar, 2012	#10 Bar (Ø32.26*mm*)	Tension	5402	356	55.6	0.61	≥ 6	0.21
		Comp.	--	--	--	--	--	--
SAES, 2013	#10 Bar (Ø32.26*mm*)	Tension	5701	222	53.8	0.77	23.1	0.18
		Comp.	--	--	--	--	--	--
SAES, 2013	#10 Bar (Ø32.26*mm*)	Tension	6162	225	54.1	0.64	22.3	0.15
		Comp.	--	--	--	--	--	--
SAES, 2013	#10 Bar (Ø32.26*mm*)	Tension	5733	182	54.2	0.75	22.3	0.18
		Comp.	--	--	--	--	--	--
SAES, 2013	#10 Bar (Ø32.26*mm*)	Tension	5480	218	53.9	0.76	20.8	0.20
		Comp.	--	--	--	--	--	--
SAES, 2013	#10 Bar (Ø32.26*mm*)	Tension	6889	217	58.7	0.63	21.6	0.13
		Comp.	--	--	--	--	--	--
SAES, 2013	#10 Bar (Ø32.26*mm*)	Tension	6058	275	48.0	0.86	23.1	0.21
		Comp.	--	--	--	--	--	--
SAES Ref. Bar, 2012	#4 Bar (Ø12.7*mm*)	Tension	3978	391	55.6	0.52	≥ 6	0.58
		Comp.	--	--	--	--	--	--
UNR One End Headed	#10 Bar (Ø32.26*mm*)	Tension	6392	--	60.0	--	--	--
		Comp.	--	--	--	--	--	--
UNR Both Ends Headed	#4 Bar* (Ø12.7*mm*)	Tension	9820	235	59.6	0.69	6.11**	--
		Comp.	--	--	--	--	--	--
UNR Both Ends Headed	#10 Bar* (Ø32.26*mm*)	Tension	4951	29	60.0	0.38	5.5**	--
		Comp.	--	--	--	--	--	--
Nakashoji, 2014	#4 Bar (Ø12.7*mm*)	Tension	4450	260	51.0	0.65	6.5**	0.38
		Comp.	--	--	--	--	--	--
Nakashoji, 2014	#4 Bar (Ø12.7*mm*)	Tension	4880	265	57.0	0.57	6.0**	0.3
		Comp.	--	--	--	--	--	--
McCormick, 2006	#8 Bar (Ø25.4*mm*)	Tension	4061	440	55.6	0.52	≥ 6	--
		Comp.	--	--	--	--	--	--
McCormick, 2006	#4 Bar (Ø12.7*mm*)	Tension	4000	563	60.0	0.39	≥ 6	--
		Comp.	--	--	--	--	--	--
Frick et al., 2004	Hot-Rolled†	Tension	6265	10	55.9	0.89	≥ 7.5	0.3
		Comp.	12545	1098	73.0	0.64	≥ 3.5	0.21
Frick et al., 2004	Cold-Drawn†	Tension	3785	544	48.7	0.77	≥ 7.5	0.61
		Comp.	7513	1752	68.0	0.78	≥ 3.5	0.85
Plietsch, Ehrich,	Ø3.0*mm*	Tension	3476	95	45.8	0.72	≥ 8	0.24
		Comp.	6647	1329	69.8	0.61	≥ 4	0.33
Statistic analysis for NiTi SE SMA properties to be used in design and analysis. Range: average (Ave.) ± one standard deviation (STD)		Ave. Tension	5615	256	55.0	0.63	--	0.27
		Ave. Comp.	8902	1393	70.3	0.68	--	0.46
		STD Tension	1635	153	4.1	0.15	--	0.15
		STD Comp.	3185	332	2.5	0.09	--	0.34
		Upper Range for Tension	7251	409	59.1	0.79	--	0.43
		Lower Range for Tension	3980	103	50.9	0.48	--	0.12
		Upper Range for Comp.	12086	1725	72.8	0.77	--	0.80
		Lower Range for Comp.	5717	1061	67.7	0.59	--	0.12

1 *ksi*=6.894 *MPa*

* SMA bar annealed in oven with 525 oC for 15 minutes.

** Connection failure

† Tensile specimen was a flat dog-bone specimen with a 25 mm length and a 3mm ×1mm gage cross section and compressive specimen was a rectangular section with dimensions of 4mm × 4mm × 8mm.

Table 6.2- Minimum and Expected Tensile NiTi SE SMA Mechanical Properties

Parameter	Minimum*	Expected**
Austenite modulus, k_1	4500 *ksi* (31025 *MPa*)	5500 *ksi* (37900 *MPa*)
Post yield stiffness, k_2	--	250 *ksi* (1725 *MPa*)
Austenite yield strength, f_y	45 *ksi* (310 *MPa*)	55 *ksi* (380 *MPa*)
Lower plateau stress factor, β	0.45	0.65
Recoverable superelastic strain, ε_r	6%	6%
Secondary post-yield stiffness ratio, α	--	0.3
Ultimate strain, ε_u	10%	10%

* To be used in material production

** To be used in seismic design of SMA-reinforced concrete members

Table 6.3- Expected Compressive NiTi SE SMA Mechanical Properties

Parameter	Expected
Austenite modulus, k_1	8900 *ksi* (61365 *MPa*)
Post yield stiffness, k_2	1400 *ksi* (9650 *MPa*)
Austenite yield strength, f_y	70 *ksi* (480 *MPa*)
Lower plateau stress factor, β	0.65
Recoverable superelastic strain, ε_r	3%
Secondary post-yield stiffness ratio, α	0.45
Ultimate strain, ε_u	10%

Table 6.4- Plain SMA Bar Dimensions

Bar Size No. (*mm*)	Nominal Diameter *in.* (*mm*)	Cross Sectional Area $in.^2$ (mm^2)	Availability
#3 (Ø10)	0.375 (9.5)	0.11 (71)	No
#4 (Ø13)	0.500 (12.7)	0.20 (129)	Yes
#5 (Ø16)	0.625 (15.9)	0.31 (199)	
#6 (Ø19)	0.750 (19.1)	0.44 (284)	
#7 (Ø22)	0.875 (22.2)	0.60 (387)	
#8 (Ø25)	1.000 (25.4)	0.79 (510)	
#9 (Ø29)	1.128 (28.7)	1.00 (645)	
#10 (Ø32)	1.270 (32.3)	1.27 (819)	
#11 (Ø36)	1.410 (35.8)	1.56 (1006)	No
#14 (Ø43)	1.693 (43.0)	2.25 (1452)	
#18 (Ø57)	2.257 (57.3)	4.00 (2581)	

Table 7.1- Modeling of Reinforcing SMA

Proposed Model (Chapter 6)	OpenSees "SelfCentering" Model
Austenite modulus, k_1	Initial stiffness, k_1
Post yield stiffness, k_2	Post-activation stiffness, k_2
Austenite yield strength, f_y	Forward activation stress, *sigAct*
Lower plateau stress factor, β	Ratio of forward to reverse activation stress, *beta*
Recoverable superelastic strain, ε_r	Bearing strain, *epsBear*
Secondary post-yield stiffness ratio, α	Ratio of bearing stiffness to initial stiffness, *rBear*
Ultimate strain, ε_u	N/A
N/A	Slip strain*, *epsSlip*

* Slip strain, "*epsSlip*", may be used to obtain residual strains. It is recommended that this strain be the "bearing strain" less 0.01 *in./in.* to develop 1% residual strain at and above "bearing strain".

Table 7.2- Measured and Calculated Responses for Pullout Tests

Specimen	Bar Size	Bar Diam., *in.* (*mm*)	Duct Diam., *in* (*mm*)	L_{emd} *in.* (*mm*)	Test Mode of Failure	Measured Force, (*kips*)	Calculated Force, (*kips*)	Error	Predicted Mode of Failure
SP1	#8	1 (25)	3.12 (79)	8 (203)	Bar Fracture	56.47	50.65	10.3	Duct Pullout
SP2	#8	1 (25)	3.12 (79)	12 (305)	Bar Fracture	55.03	55.15	0.2	Bar Fracture
SP3	#8	1 (25)	3.12 (79)	3 (72)	Bar Fracture	56.24	48.01	14.6	Bar Pullout
SP4	2#8	1.418* (36)	4 (102)	8 (203)	Duct Pullout	67.51	65.1	3.6	Duct Pullout
SP5	2#8	1.418* (36)	4 (102)	12 (305)	Bars Fracture	107.46	97.77	9.0	Duct Pullout
SP6	2#8	1.418* (36)	4 (102)	3 (72)	Bar Pullout	78.45	96.1	22.5	Bar Pullout
SP7	#8	1 (25)	4 (102)	8 (203)	Bar Fracture	54.7	55.15	0.8	Bar Fracture
SP8	#8	1 (25)	3.12 (79)	5 (127)	Bar Fracture	56.05	55.15	1.6	Bar Fracture
SP9	2#8	1 (25)	6.24* (158)	8 (203)	Bars Fracture	109.84	101.8	7.3	Duct Pullout
SP10	2#8	1 (25)	6.24* (158)	12 (305)	Bars Fracture	102.45	110.4	7.8	Bar Fracture
SP11	#11	1.41 (36)	4 (102)	11.3 (286)	Duct Pullout	93.93	92.65	1.4	Duct Pullout
SP12	#11	1.41 (36)	4 (102)	16.9 (430)	Bar Fracture	106.49	114.7	7.7	Bar Fracture
SP13	#11	1.41 (36)	4 (102)	4.2 (107)	Bar Fracture	110.76	91.18	17.7	Bar Pullout
SP14b	#11	1.41 (36)	5.26 (134)	11.3 (286)	Bar Fracture	110.93	114.7	3.4	Bar Fracture
							Average Error=	**7.7**	

* Equivalent Diameter

1 *kip* =4.448 *kN*

Table 7.3- Fiber Material Models Used in CIP Column Simulation

Concrete Fibers	
Application: unconfined concrete Type: Concrete01 f'_{cc}= -4446 *psi* (-30.6 *MPa*) ε_{cc}= -0.002 *in./in.* f'_{cu}= 0.0 *psi* (0.0 *MPa*) ε_{cu}= -0.005 *in./in.*	Application: confined concrete (based on Mander's model) Type: Concrete01 f'_{cc}= -6996 *psi* (-48.2 *MPa*) ε_{cc}= -0.0077 *in./in.* f'_{cu}= -6114 *psi* (-42.1 *MPa*) ε_{cu}= -0.0219 *in./in.*
Steel Fibers	
Application: first integration point at column base accounting for bond-slip effect Type: ReinforcingSteel f_y= 66.8 *ksi* (460.6 *MPa*) f_{su}= 111.0 *ksi* (765.3 *MPa*) E_s= 17854 *ksi* (123099 *MPa*) E_{sh}= 0.0693 E_s ε_{sh}= 0.0064 *in./in.* ε_{su}= 0.102 *in./in.*	Application: second to fifth integration points Type: Steel02 f_y= 66.8 *ksi* (460.6 *MPa*) E_s= 29000 *ksi* (200000 *MPa*) E_p= 0.015 E_s R_0=18, c_{R1}=0.925, c_{R2}=0.15

Table 7.4- Reinforcing Steel Material Model Properties Used in CIP

Parameters		Original Steel Model	Modified Steel Model*
Yield stress,	f_y=	66.8 *ksi* (460.6 *MPa*)	66.8 *ksi* (460.6 *MPa*)
Ultimate stress,	f_{su}=	111 *ksi* (765.3 *MPa*)	111 *ksi* (765.3 *MPa*)
Modulus of elasticity,	E_s=	29000 *ksi* (200000 *MPa*)	17858 *ksi* (123126 *MPa*)
Strain hardening stiffness,	E_{sh}=	1247 *ksi* (8783.9 *MPa*)	1239 *ksi* (8542.6 *MPa*)
Strain at strain hardening,	ε_{sh}=	0.005 *in./in.*	0.0064 *in./in.*
Ultimate strain,	ε_{su}=	0.1 *in./in.*	0.102 *in./in.*
Yield strain,	ε_y=	0.0023 *in./in.*	0.0037 *in./in.*

* accounting for the bond-slip effect

Table 7.5- Fiber Material Models Used in PNC Column Simulation

Concrete Fibers	
Application: unconfined concrete Type: Concrete01 f'_{cc}= -3290 *psi* (-22.7 *MPa*) ε_{cc}= -0.002 *in./in.* f'_{cu}= 0.0 *psi* (0.0 *MPa*) ε_{cu}= -0.005 *in./in.*	Application: confined concrete (based on Mander's model) Type: Concrete02 f'_{cc}= -5385 *psi* (-37.1 *MPa*) ε_{cc}= -0.0084 *in./in.* f'_{cu}= -4833 *psi* (-33.3 *MPa*) ε_{cu}= -0.024 *in./in.* f_{ct}= 430 *psi* (2.96 *MPa*), based on ACI318-11 E_t= 14400 *psi* (99.3 *MPa*) Application: confined SCC (based on Mander's model) Type: Concrete02 f'_{cc}= -11940 *psi* (-82.3 *MPa*) ε_{cc}= -0.0045 *in./in.* f'_{cu}= -7757 *psi* (-53.5 *MPa*) ε_{cu}= -0.013 *in./in.* f_{ct}= 730 *psi* (5.0 *MPa*), based on ACI318-11 E_t= 24395 *psi* (168.2 *MPa*)
Steel Fibers	
Application: first integration point at column base accounting for bond-slip effect Type: ReinforcingSteel f_y= 65.7 *ksi* (453.4 *MPa*) f_{su}= 91.66 *ksi* (631.9 *MPa*) E_s= 9174 *ksi* (63252 *MPa*) E_{sh}= 0.185E_s ε_{sh}= 0.0159 *in./in.* (use smaller value to converge*) ε_{su}= 0.126 *in./in.*	Application: second to fifth integration points Type: ReinforcingSteel f_y= 65.7 *ksi* (453.4 *MPa*) f_{su}= 91.66 *ksi* (631.9 *MPa*) E_s= 29000 *ksi* (200000 *MPa*) E_{sh}= 0.0596E_s ε_{sh}= 0.011 *in./in.* (use smaller value to converge*) ε_{su}= 0.119 *in./in.*

* It was found that the yield plateau of this steel model is source of convergence issue in many cases. Smaller yield plateau (smaller ε_{sh}) may be used.

Table 7.6- Fiber Material Models Used in GCDP Column Simulation

Concrete Fibers	
Application: unconfined concrete Type: Concrete01 f'_{cc}= -3210 *psi* (-22.1 *MPa*) ε_{cc}= -0.002 *in./in.* f'_{cu}= 0.0 *psi* (0.0 *MPa*) ε_{cu}= -0.005 *in./in.*	Application: confined concrete (based on Mander's model) Type: Concrete02 f'_{cc}= -5327 *psi* (-36.7 *MPa*) ε_{cc}= -0.0086 *in./in.* f'_{cu}= -4799 *psi* (-33.1 *MPa*) ε_{cu}= -0.025 *in./in.* f_{ct}= 425 *psi* (2.93 *MPa*), based on ACI318-11 E_t= 14227 *psi* (98.1 *MPa*) Application: confined SCC (based on Mander's model) Type: Concrete02 f'_{cc}= -11241 *psi* (-77.5 *MPa*) ε_{cc}= -0.0048 *in./in.* f'_{cu}= -7750 *psi* (-53.4 *MPa*) ε_{cu}= -0.014 *in./in.* f_{ct}= 700 *psi* (4.83 *MPa*), based on ACI318-11 E_t= 23395 *psi* (161.3 *MPa*)
Steel Fibers	
Application: first integration point at column base accounting for bond-slip effect Type: ReinforcingSteel f_y= 65.7 *ksi* (453.4 *MPa*) f_{su}= 91.66 *ksi* (631.9 *MPa*) E_s= 17750 *ksi* (122382 *MPa*) E_{sh}= 0.097E_s ε_{sh}= 0.0125 *in./in.* (use smaller value to converge*) ε_{su}= 0.121 *in./in.*	Application: second integration point accounting for bar debonding effect Type: ReinforcingSteel f_y= 65.7 *ksi* (453.4 *MPa*) f_{su}= 91.66 *ksi* (631.9 *MPa*) E_s= 13591 *ksi* (93707 *MPa*) E_{sh}= 0.109E_s ε_{sh}= 0.013 *in./in.* (use smaller value to converge*) ε_{su}= 0.139 *in./in.* Application: third to tenth integration points Type: ReinforcingSteel f_y= 65.7 *ksi* (453.4 *MPa*) f_{su}= 91.66 *ksi* (631.9 *MPa*) E_s= 29000 *ksi* (200000 *MPa*) E_{sh}= 0.0596E_s ε_{sh}= 0.011 *in./in.* (use smaller value to converge*) ε_{su}= 0.119 *in./in.*

* It was found that the yield plateau of this steel model is source of convergence issue in many cases. Smaller yield plateau (smaller ε_{sh}) may be used.

Table 7.7- Fiber Material Models Used in HCS Column Simulation

Concrete Fibers	
Application: unconfined ECC Type: Concrete02 f'_{cc}= -6390 *psi* (-44.0 *MPa*) ε_{cc}= -0.002 *in./in.* f'_{cu}= 0.0 *psi* (0.0 *MPa*) ε_{cu}= -0.005 *in./in.* f_{ct}= 0.0 E_t= 0.0 Note: 1- No tensile strength for ECC resulted in a better match in terms of initial stiffness and unloading path. 2- The conventional concrete above the ECC level (1.5 column diameter) was not included in the model but ECC was used in all integration points of the column element.	Application: confined ECC (based on Motaref's model) Type: Concrete02 f'_{cc}= -7436 *psi* (-51.3 *MPa*) ε_{cc}= -0.0036 *in./in.* f'_{cu}= 0.4 f'_{cc} ε_{cu}= -0.011 *in./in.* f_{ct}= 0.0 E_t= 0.0 Application: confined SCC (based on Mander's model) Type: Concrete01 f'_{cc}= -7863 *psi* (-54.2 *MPa*) ε_{cc}= -0.0059 *in./in.* f'_{cu}= -6047 *psi* (-41.7 *MPa*) ε_{cu}= -0.0207 *in./in.*
Steel Fibers	
Application: first integration point at column base accounting for bond-slip effect Type: ReinforcingSteel f_y= 71.8 *ksi* (495.1 *MPa*) f_{su}= 99.3 *ksi* (684.8 *MPa*) E_s= 7013 *ksi* (48353 *MPa*) E_{sh}= 0.087E_s ε_{sh}= 0.021 *in./in.* ε_{su}= 0.206 *in./in.*	Application: forth to seventh integration points Type: ReinforcingSteel f_y= 71.8 *ksi* (495.1 *MPa*) f_{su}= 99.3 *ksi* (684.8 *MPa*) E_s= 29000 *ksi* (200000 *MPa*) E_{sh}= 0.0215E_s ε_{sh}= 0.013 *in./in.* ε_{su}= 0.195 *in./in.*
SMA Fibers	
Application: second integration point accounting for debonding effect Type: SelfCentering k_1= 4110.6 *ksi* (28341 *MPa*) k_2= 147.0 *ksi* (1013 *MPa*) f_y= 69.1 *ksi* (476 *MPa*) β = 0.55 ε_r = 0.067 *in./in.* α = 0.458 ε_u=0.113 *in./in.*	Application: third integration point Type: SelfCentering k_1= 7288.4 *ksi* (50251 *MPa*) k_2= 146.1 *ksi* (1007 *MPa*) f_y= 69.1 *ksi* (476 *MPa*) β = 0.55 ε_r = 0.06 *in./in.* α = 0.3 ε_u=0.1 *in./in.*

Table 8.1- Near-Fault Motions (From Baker, 2007)

EQ. No.	Earthquake	PGA (*g*)	PGV *cm*/*s* (*in*./*s*)	Station	Year	M_w	Distance *km* (*mile*)
1	San Fernando	1.43	116.5 (45.8)	Pacoima Dam	1971	6.6	1.8 (1.1)
2	Imperial Valley-06	0.38	115.0 (45.3)	EC Meloland Overpass FF	1979	6.5	0.1 (0.06)
3	Imperial Valley-06	0.44	111.9 (44.0)	El Centro Array #6	1979	6.5	1.4 (0.87)
4	Imperial Valley-06	0.46	108.8 (42.8)	El Centro Array #7	1979	6.5	0.6 (0.37)
5	Superstition Hills-02	.42	106.8 (42.0)	Parachute Test Site	1987	6.5	1.0 (0.62)
6	Landers	0.71	140.3 (55.2)	Lucerne	1992	7.3	2.2 (1.36)
7	Northridge-01	1.37	107.1 (42.2)	Pacoima Dam	1994	6.7	7.0 (4.35)
8	Northridge-01	0.87	167.2 (65.8)	Rinaldi Receiving Station	1994	6.7	6.5 (4.04)
9	Northridge-01	0.59	130.3 (51.3)	Sylmar, Converter Station	1994	6.7	5.4 (3.35)
10	Northridge-01	0.84	116.6 (45.9)	Sylmar, Converter Station East	1994	6.7	5.2 (3.23)
11	Northridge-01	0.73	122.7 (48.3)	Sylmar, Olive View Med FF	1994	6.7	5.3 (3.29)
12	Kobe, Japan	0.68	169.6 (66.8)	Takatori	1995	6.9	1.5 (0.93)
13	Chi-Chi, Taiwan	0.82	127.7 (50.3)	TCU065	1999	7.6	0.6 (0.37)
14	Chi-Chi, Taiwan	0.56	191.1 (75.2)	TCU068	1999	7.6	0.3 (0.18)
15	Chi-Chi, Taiwan	0.29	106.6 (41.9)	TCU102	1999	7.6	1.5 (0.93)

Figures

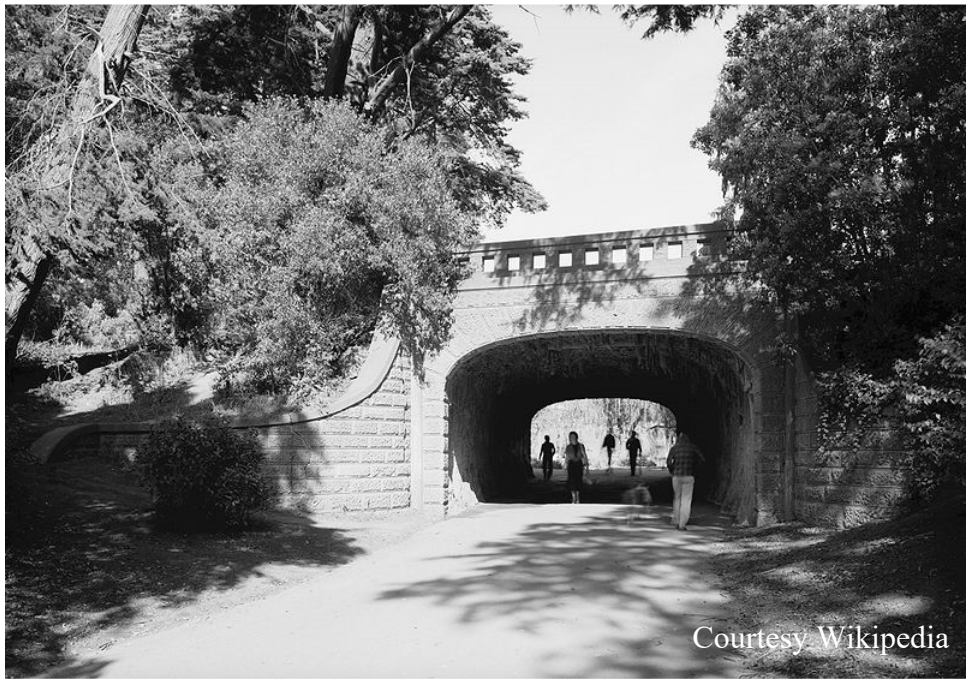

Figure 1.1- First Reinforced Concrete Bridge in USA

Figure 1.2- First Prestressed Concrete Bridge in USA

Figure 1.3- High-Five Interchange Bridges, Dallas

(a) Head Bar Coupler [hrc-usa.com]

(b) Threaded Bar Coupler [erico.com]

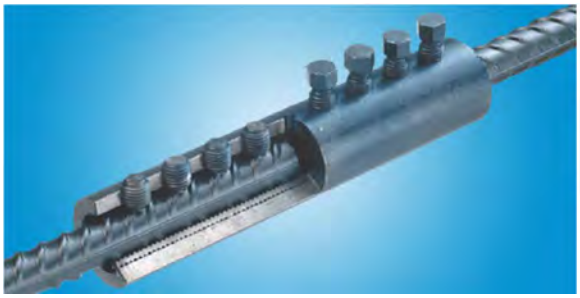

(c) Clamping Screw Coupler [daytonsuperior.com]

(d) Bar Grip Coupler [barsplice.com]

[splicesleeve.com]

[bsitaliagroup.com]

(e) Grouted Sleeve Couplers

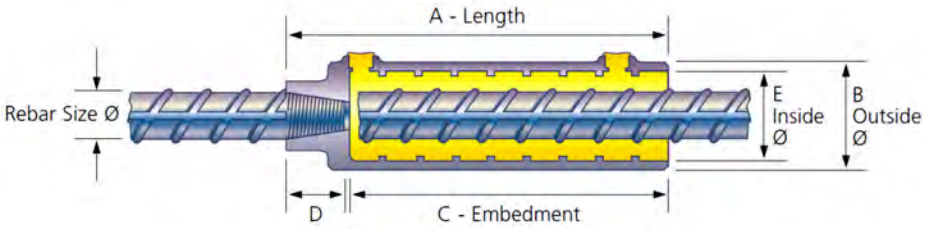

(f) Grouted-Threaded Coupler [erico.com]

Figure 1.4- Mechanical Bar Splices

(a) Column Section

(b) Final Bridge

Figure 1.5- Bridge Built with Grouted Bar Couplers (Culmo, 2009)

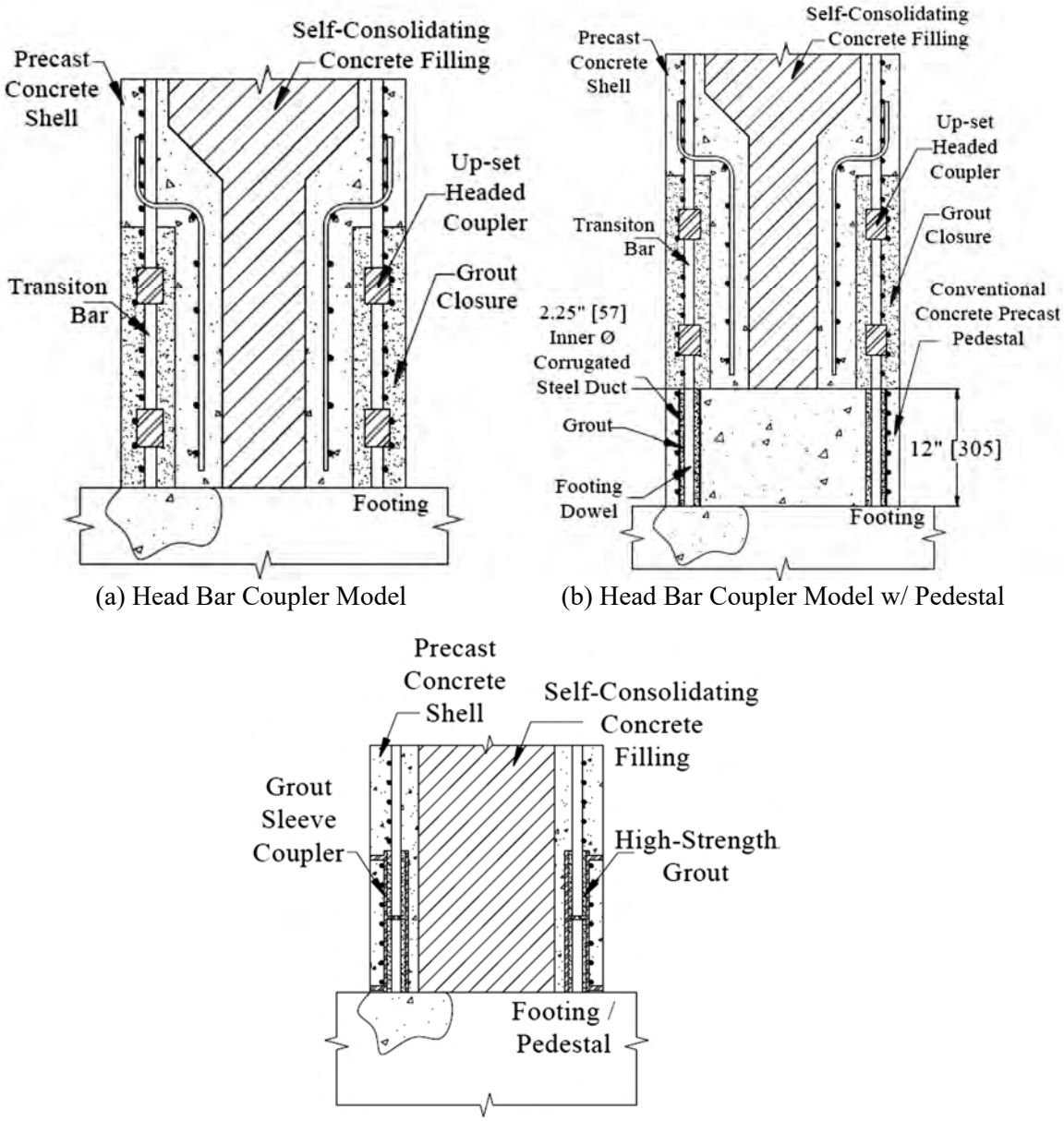

(a) Head Bar Coupler Model

(b) Head Bar Coupler Model w/ Pedestal

(c) Grouted Sleeve Coupler Models w/ or w/o Pedestal

Figure 1.6- Bar Couplers in Column-to-Footing Connections (Haber et al., 2013)

(a) Lake Ray Hubbard Bridge
(Brenes et al., 2006)

(b) Lake Belton Bridge
(Brenes et al., 2006)

(c) A bridge in the State of Washington (Khaleghi et al., 2012)

Figure 1.7- Bridges Built with Grouted Duct Connections

(a) Corrugated Duct Placed in Cap Beam (Elevation)

(b) Plan View of Pocket

Figure 1.8- Pocket Connection (Restrepo et al., 2011)

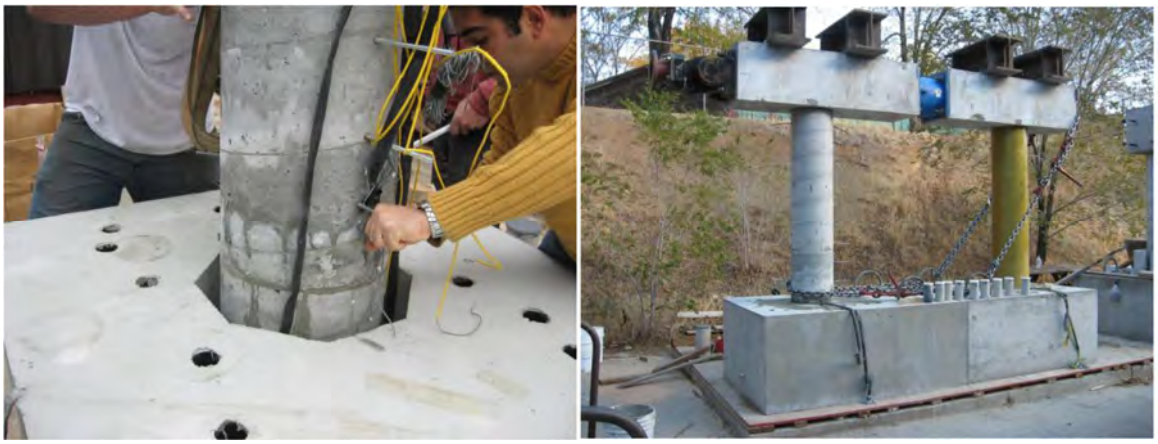

(a) Column Embedded in Footing Socket (b) Final Bent

Figure 1.9- Pocket Connection (Motaref et al., 2011)

(a) Column Embedded in Footing (b) Final Bridge

Figure 1.10- Member Socket Connection with Cast-in-Place Footing (Khaleghi et al., 2012)

Figure 1.11- Integral Connection (Marsh et al., 2011)

(a) Rubber Pad Placed in Steel Cage (b) Final Column

Figure 1.12- Segmental Column with Elastomeric Rubber Plastic Hinge (Motaref et al., 2011)

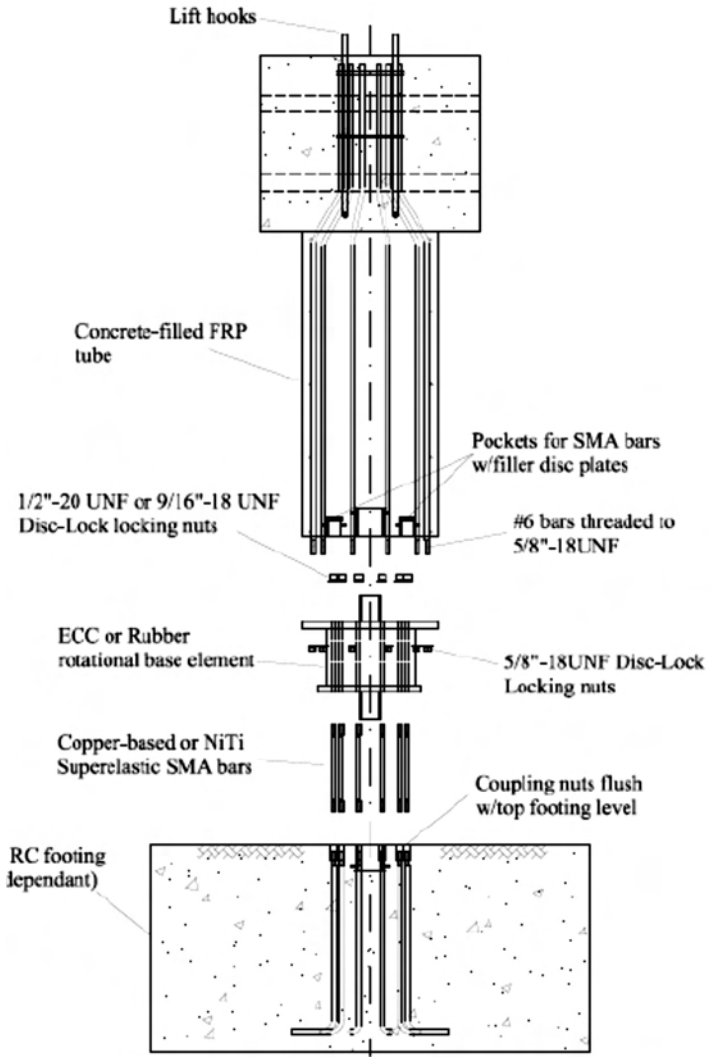

Figure 1.13- Deconstructible Bridge Column (Varela and Saiidi, 2013)

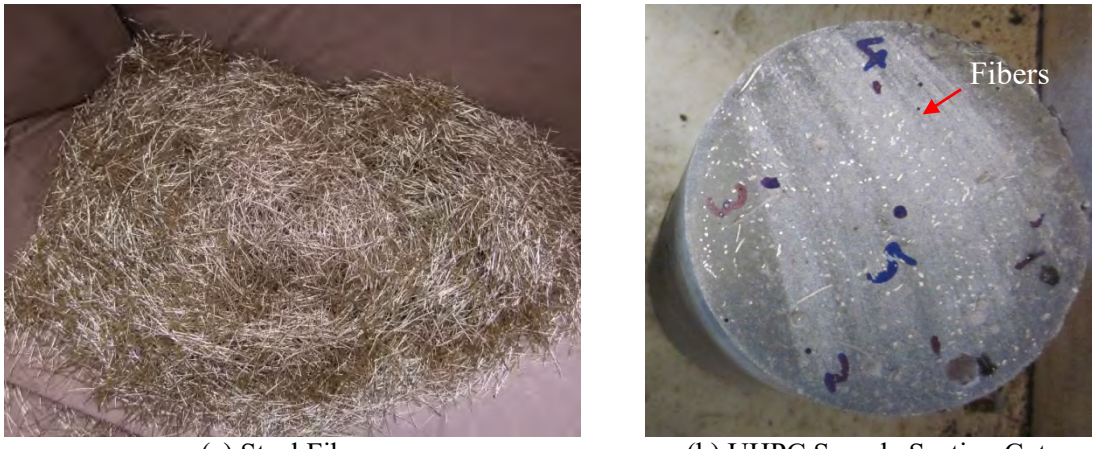

(a) Steel Fibers (b) UHPC Sample Section Cut

Figure 1.14- Steel Fibers for UHPC

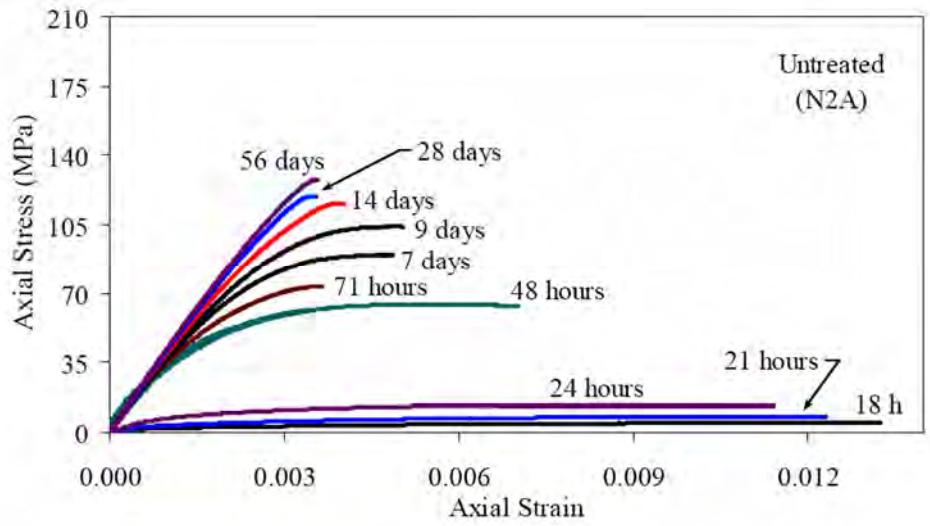

(a) Compressive Behavior in Different Ages (Graybeal, 2006)

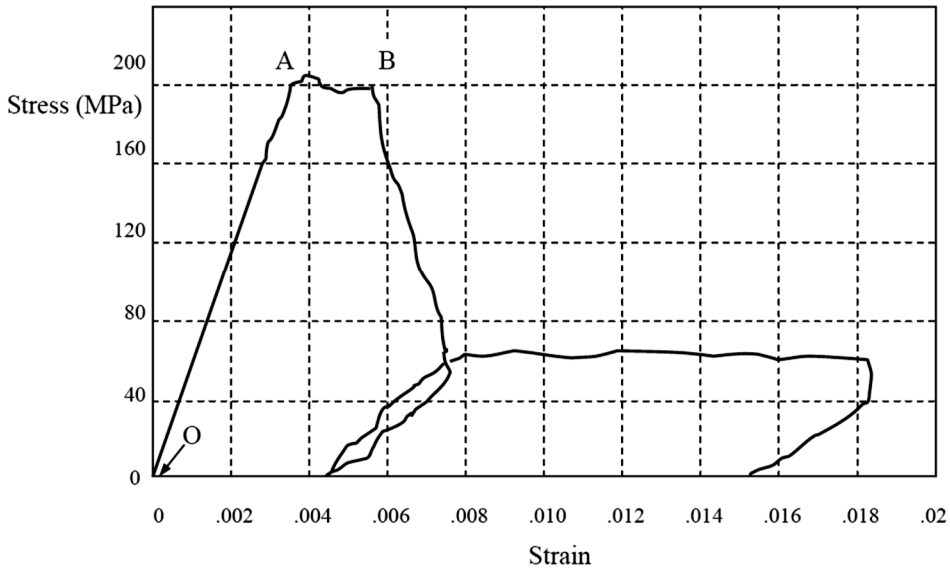

(b) Complete Compressive Stress-Strain Relationship (Gowripalan and Gilbert, 2000)

Figure 1.15- Measured UHPC Compressive Behavior

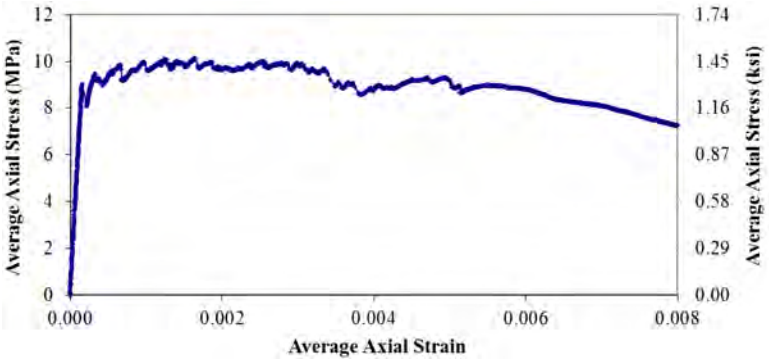

(a) Measured Tensile Stress-Strain

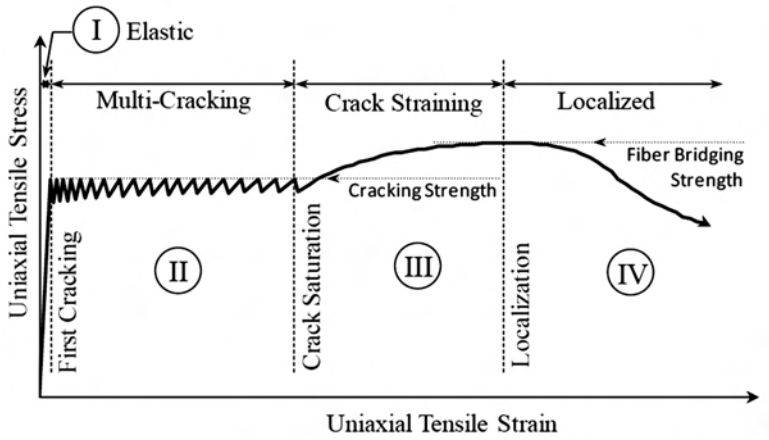

(b) Idealized Tensile Stress-Strain

Figure 1.16- UHPC Tensile Behavior (Graybeal, 2006)

(a) Sakata-Mirai bridge, Sakata, Japan (b) Footbridge of Peace, Seoul, South Korea

Figure 1.17- UHPC Worldwide Applications (Russell and Graybeal, 2013)

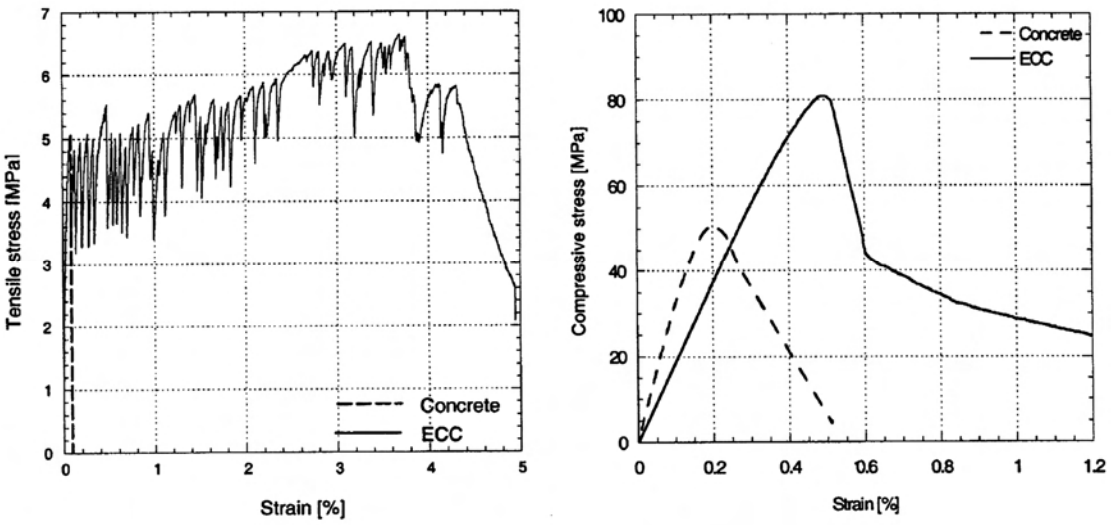

(a) Tensile (b) Compressive

Figure 1.18- ECC Stress-Strain (Li and Fischer, 2003)

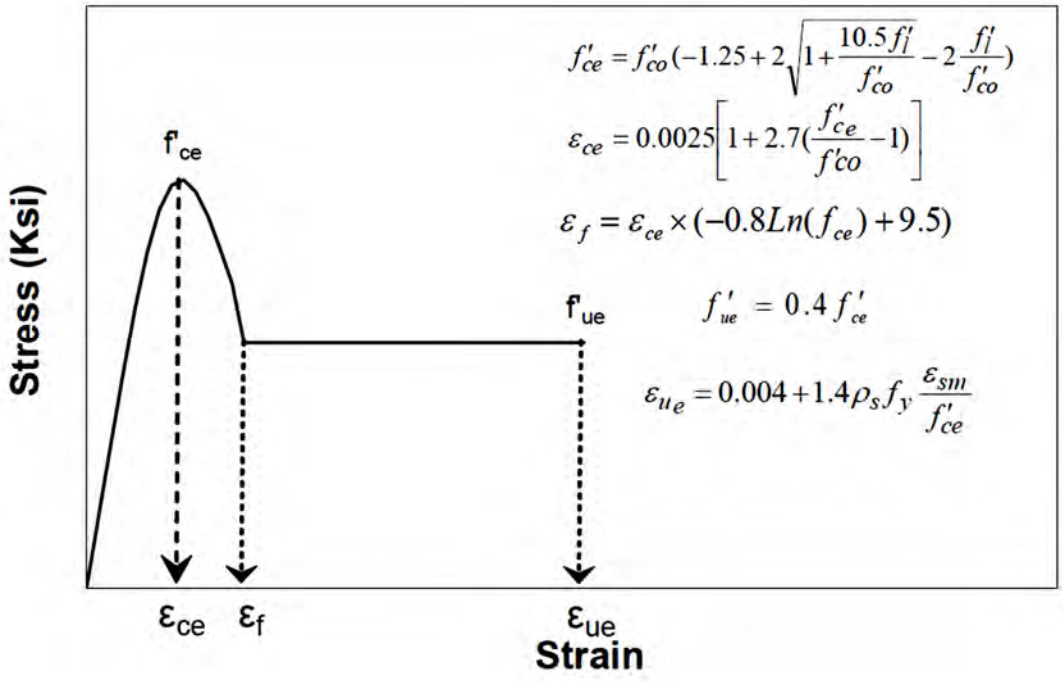

Figure 1.19- Confined ECC Stress-Strain Model (Motaref et al., 2011)

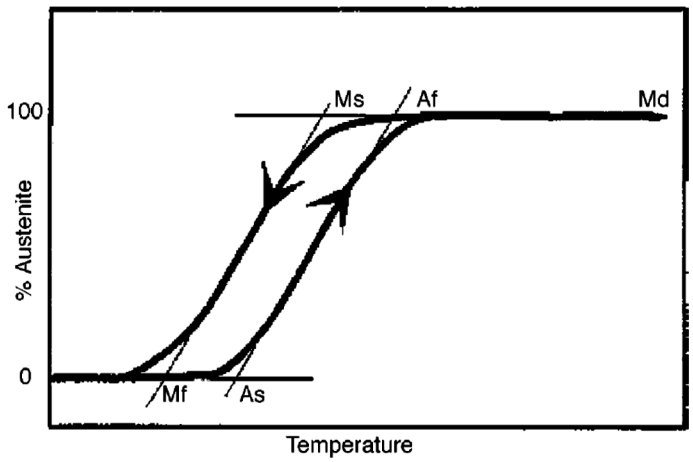

Figure 1.20- Phase Transformation for SMA (Wilson and Wesolowsky, 2005)

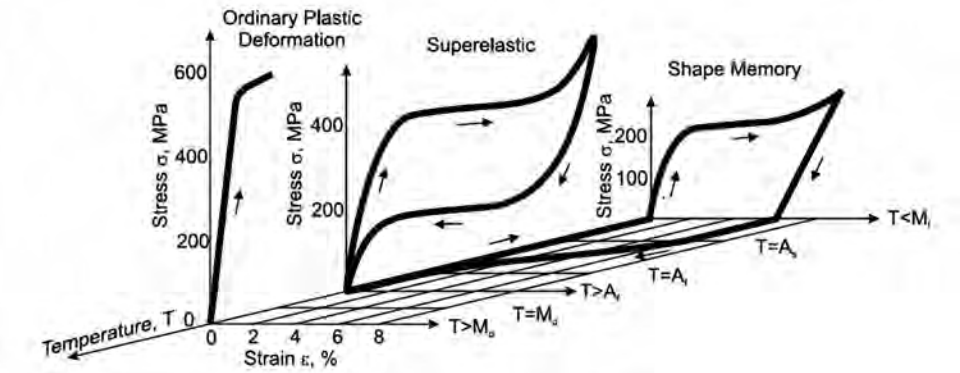

Figure 1.21- 3D Stress-Strain-Temperature Relationship for SMA (McCormick, 2006)

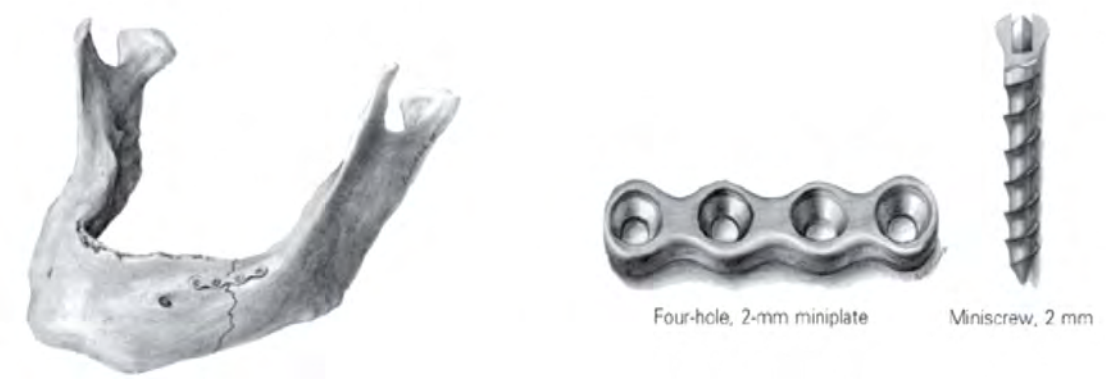

(a) SMA bone plates

(b) Spinal Vertebrae and SMA Spacers

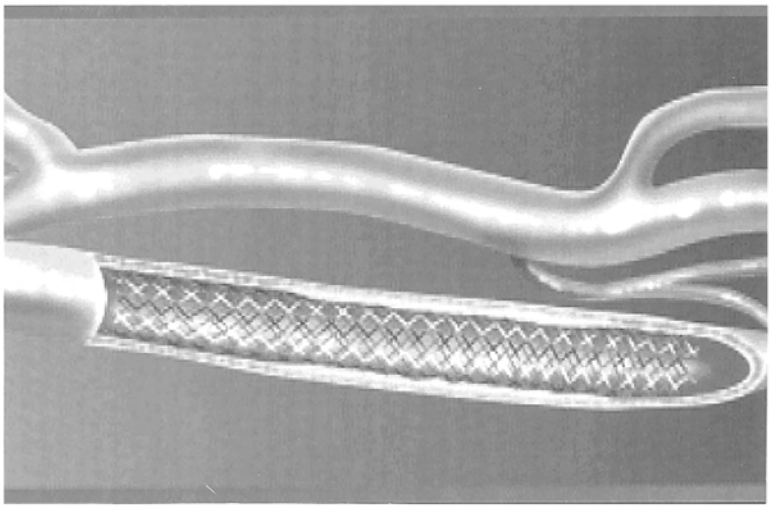

(c) Stent Introduced in Internal Carotid Artery

Figure 1.22- SMA Medical Applications (Tarnita et al., 2009)

(a) NiTi Eyeglass Frames (b) Cellular Phone Antenna

Figure 1.23- SMA Industrial Applications (Wu and Schetky, 2000)

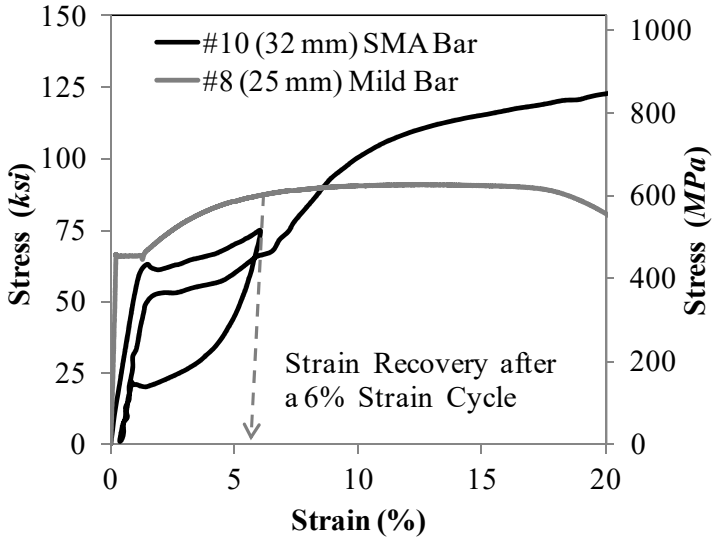

Figure 1.24- Measured Stress-Strain for NiTi SMA and Steel Bars (Tazarv and Saiidi, 2014)

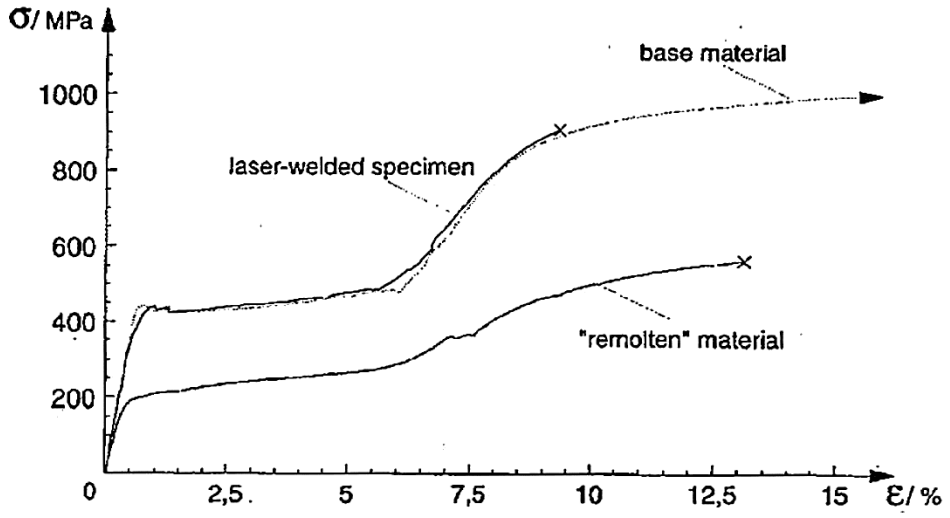

Figure 1.25- Welding Effects on Stress-Strain Behavior of NiTi SMA (Schlossmacher et al., 1997)

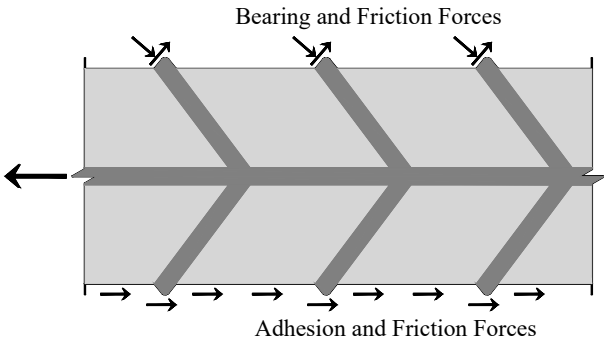

Figure 2.1- Bond Force Transfer Mechanism

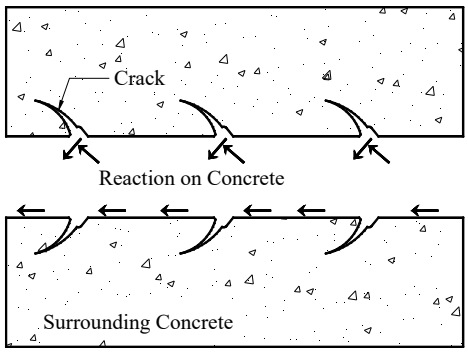

Figure 2.2- Bar Force Reaction on Concrete

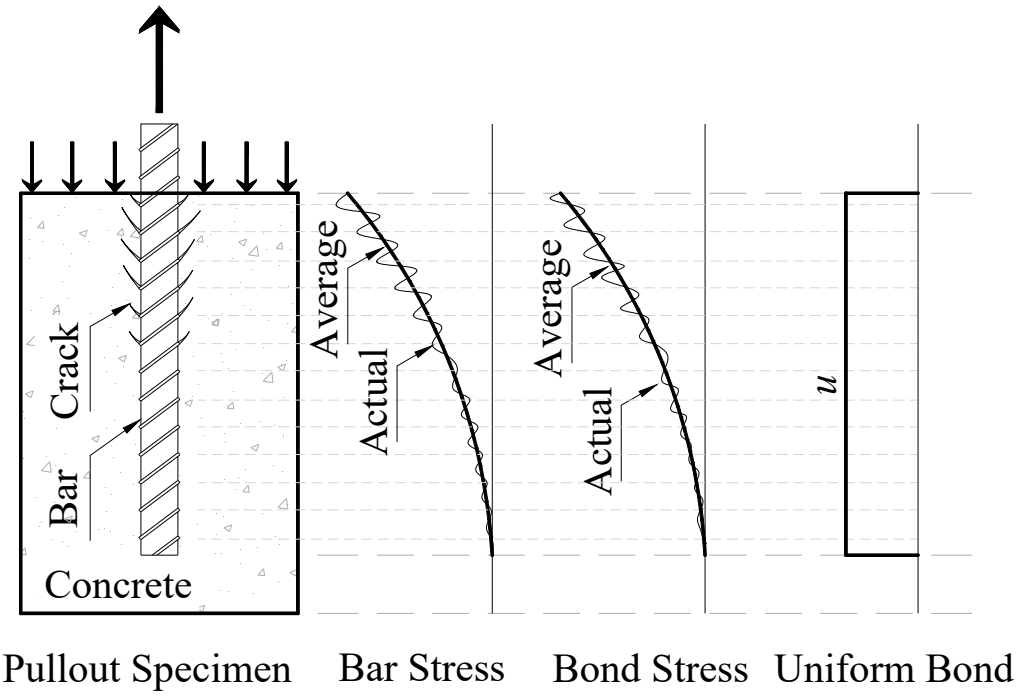

Figure 2.3- Distribution of Steel Stress and Bond Stress along Development Length of Pullout Unit

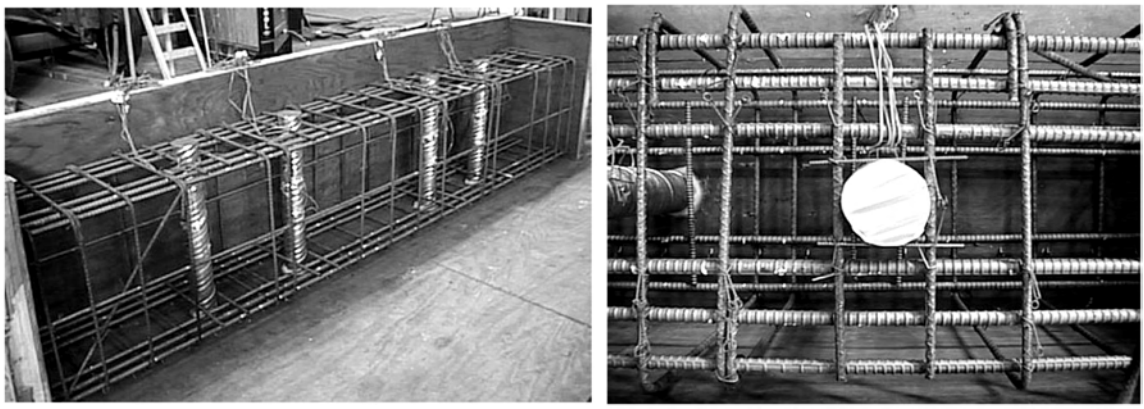

(a) Side View (b) Top View

Figure 2.4- Grout-Filled Ducts in Cap Beam before Casting (Matsumoto et al., 2001)

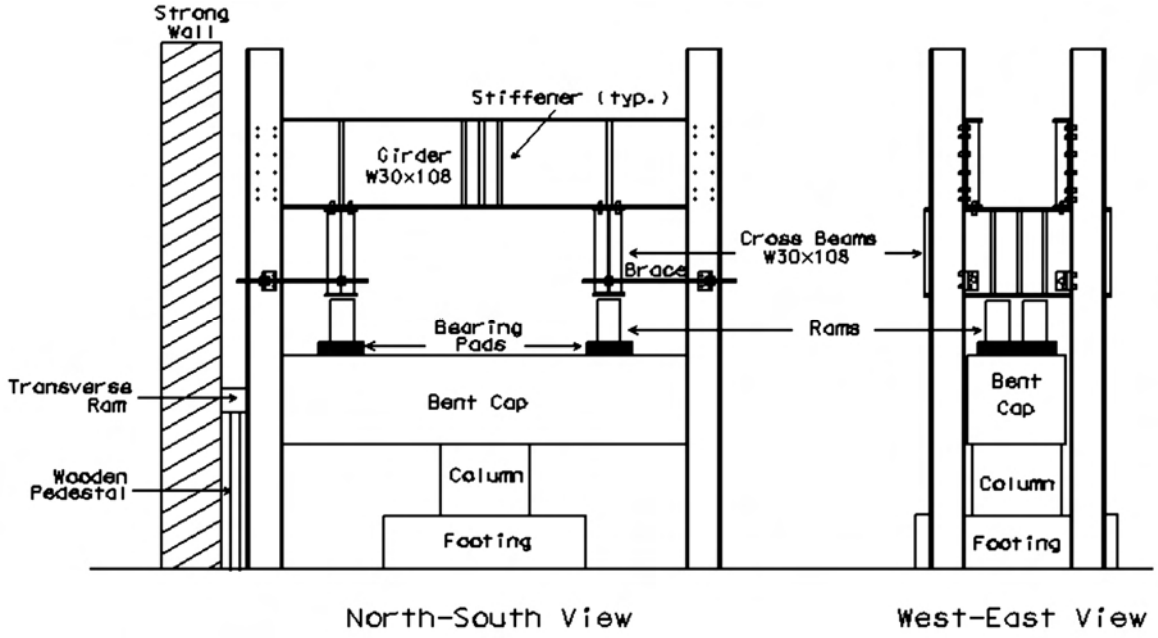

Figure 2.5- Column to Cap Beam Connection Test Setup (Matsumoto et al., 2001)

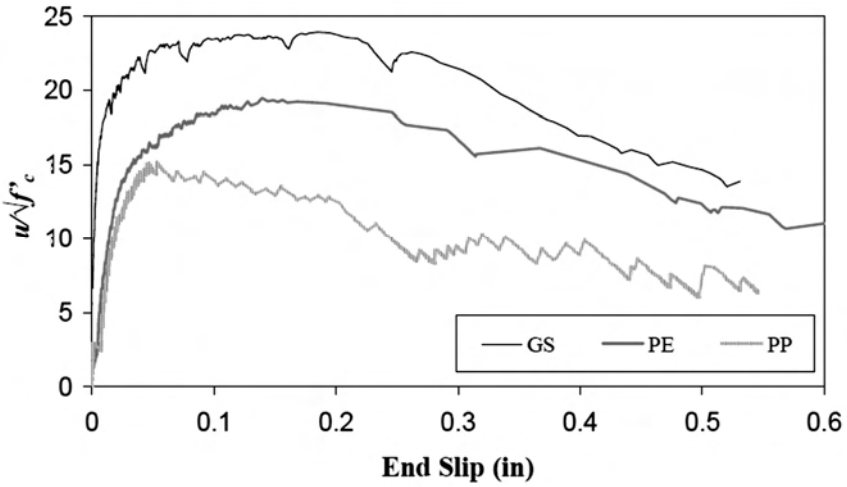

Figure 2.6- Effect of Duct Materials in Single-Duct Specimens Embedded 8d_b (Brenes et al., 2006)

(a) Top View (b) Side View

Figure 2.7- Test 4 Observed Damage, Specimen with Single Galvanized Steel Duct (Brenes et al., 2006)

(a) Ducts in Bent Cap Before Casting Concrete (b) Test Setup

Figure 2.8- Bent Cap Rebar Cage in Form During Fabrication and Test Setup (Restrepo et al., 2011)

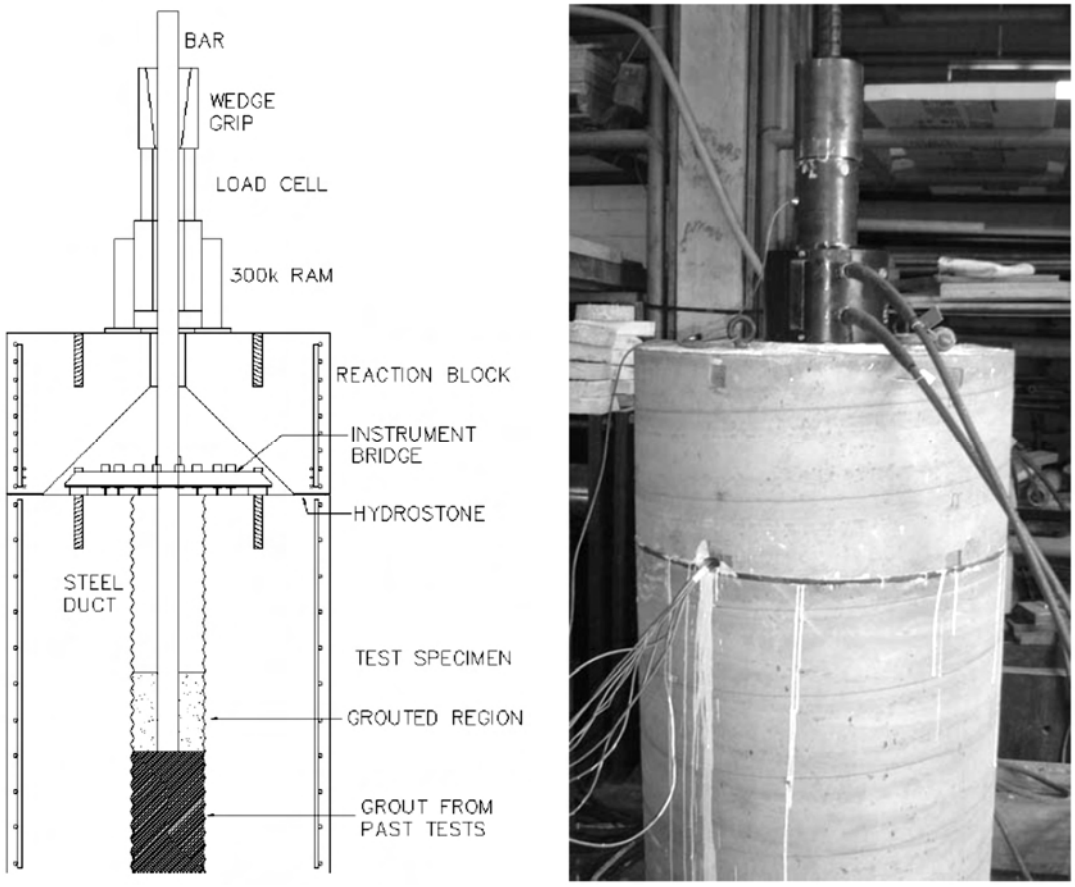

(a) Drawing (b) Photograph

Figure 2.9- Pullout Test Setup (Steuck et al., 2009)

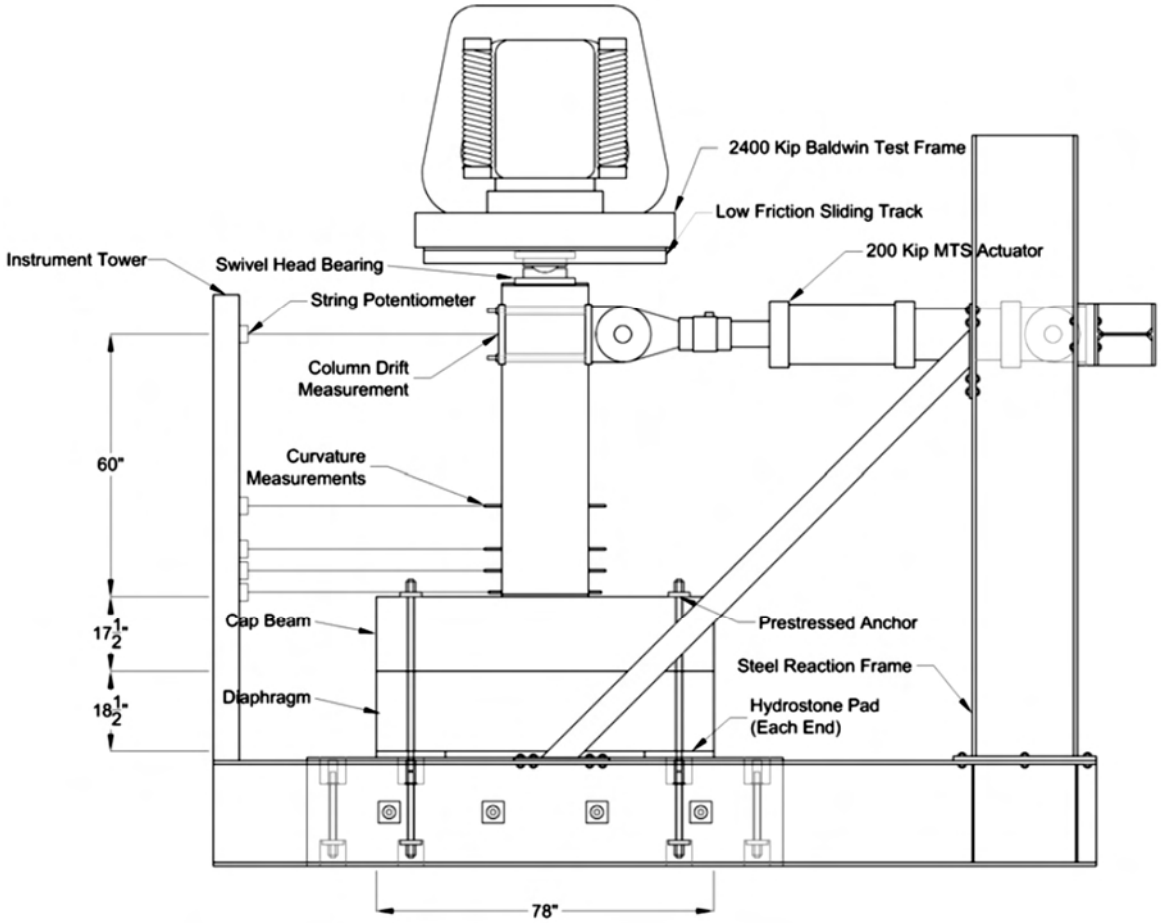

Figure 2.10- Grout-Filled Duct Column-Cap Beam Connection Test Setup (Pang et al., 2008)

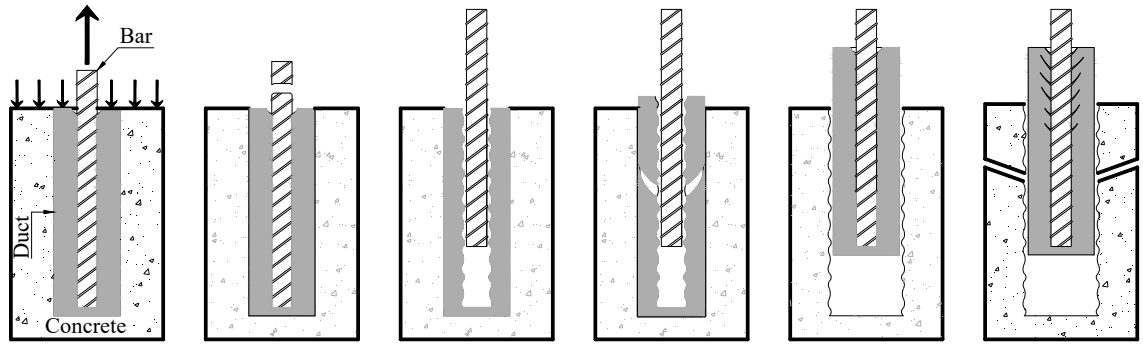

Figure 2.11- Modes of Failure in Grout-Filled Duct Connections

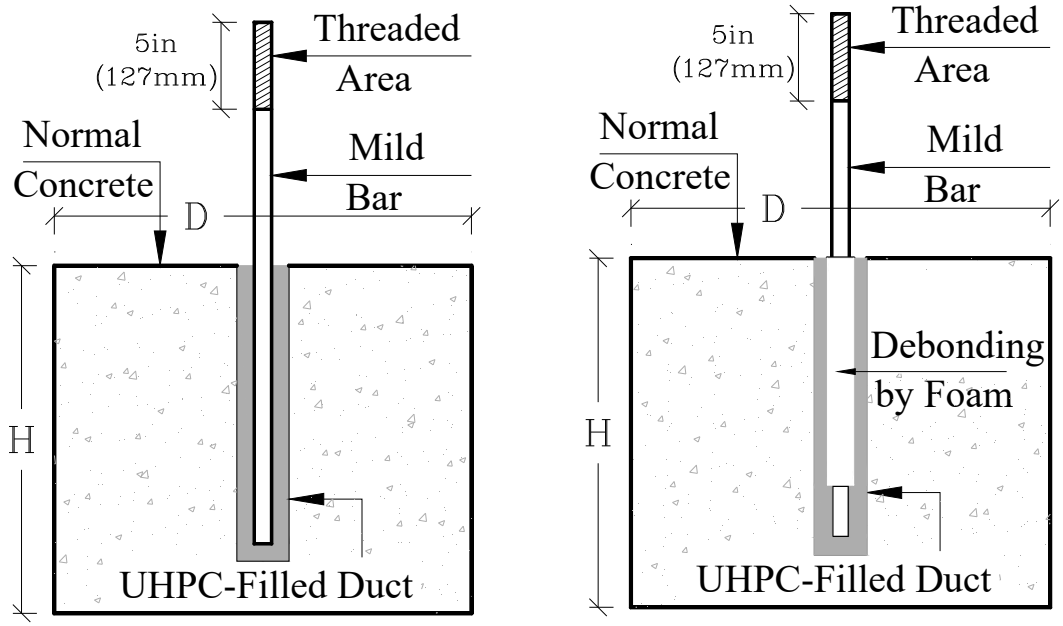

Figure 2.12- Schematic View of Pullout Tests Specimens

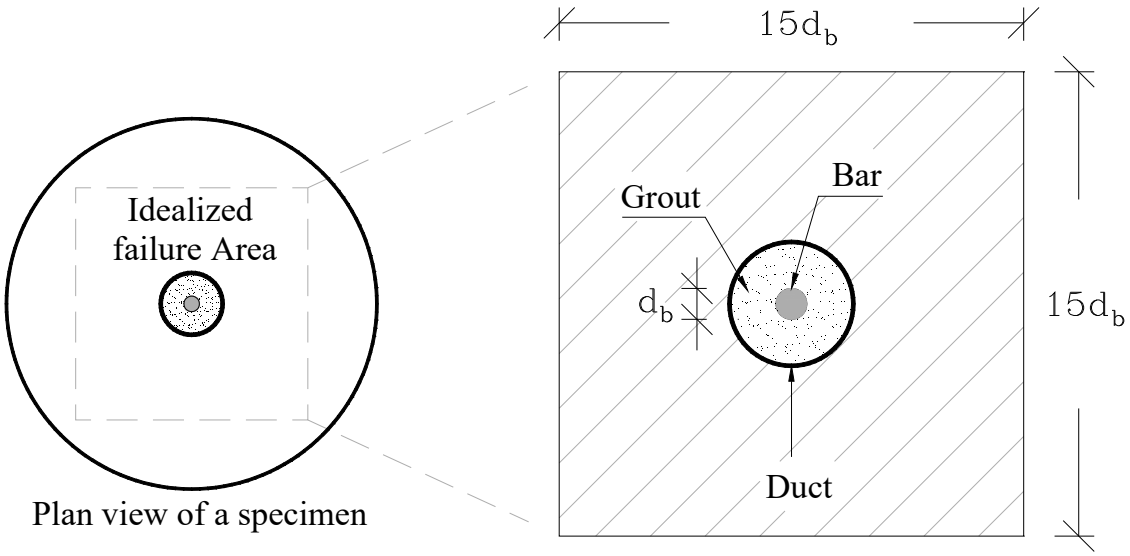

Figure 2.13- Idealized Projected Failure Surface of Bar in Tension in Grout-Filled Duct Systems

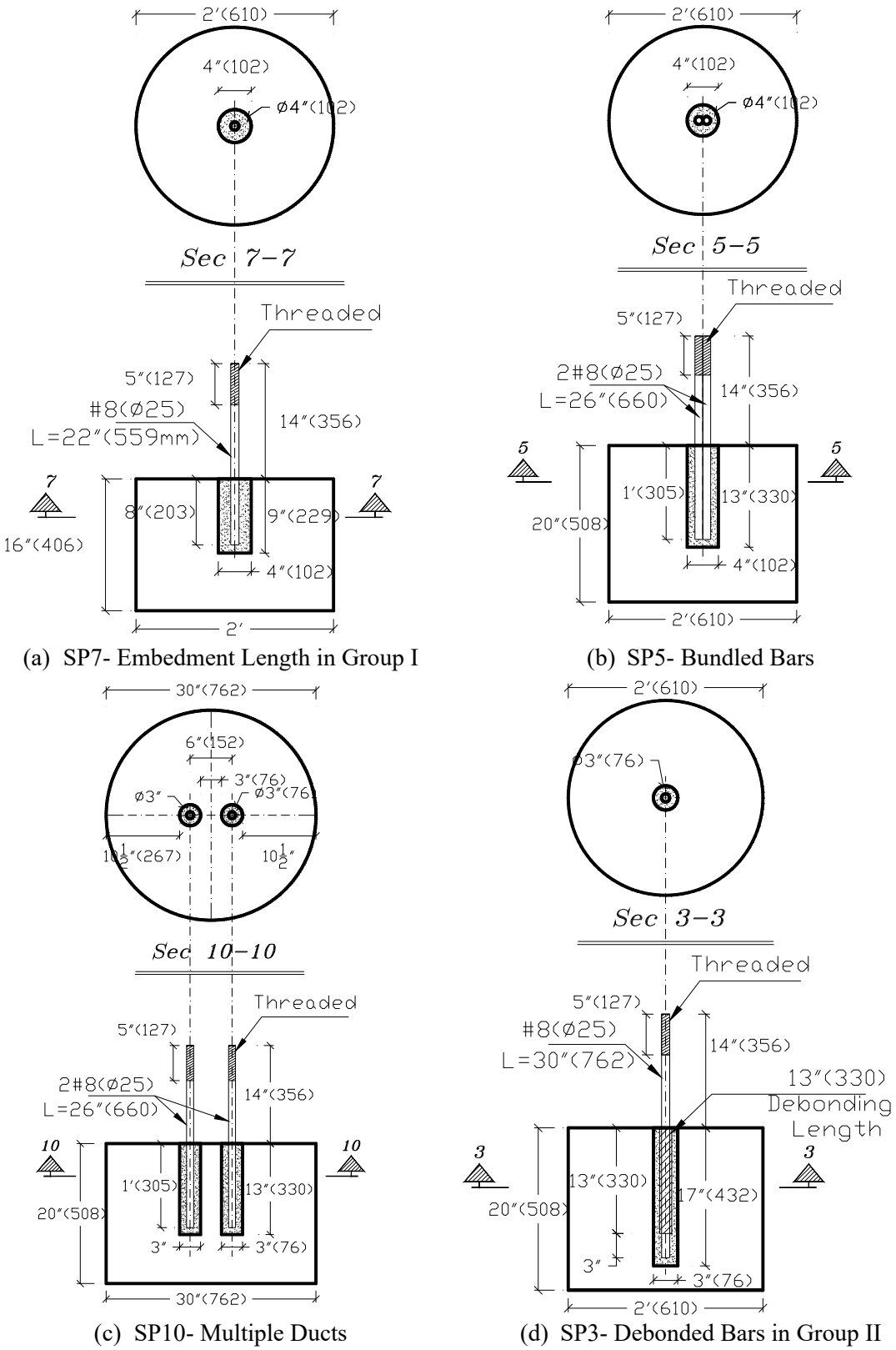

(a) SP7- Embedment Length in Group I

(b) SP5- Bundled Bars

(c) SP10- Multiple Ducts

(d) SP3- Debonded Bars in Group II

Figure 2.14- Detailing of Some of Pullout Test Specimens (*mm*)

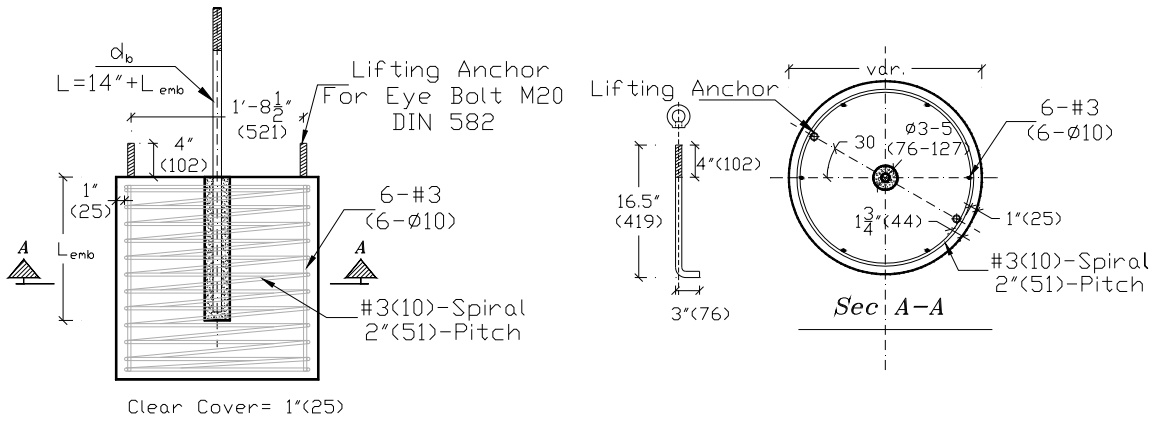

Figure 2.15- Pullout Test Specimens Reinforcements and Lifting Anchors

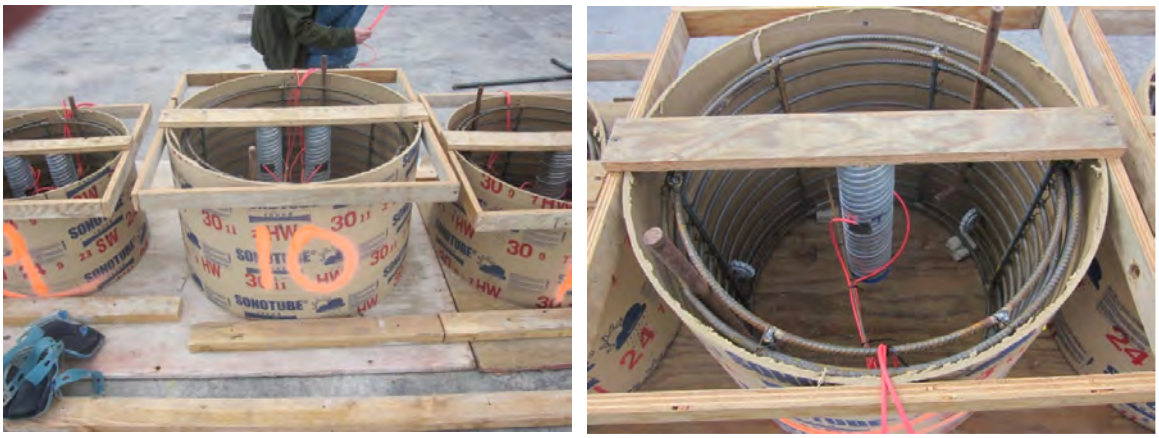

(a) Double-Duct Specimens (b) Single Duct Specimen

Figure 2.16- Formwork for Pullout Test Specimens

(a) Casting UHPC (b) Inside View of Duct During Casting UHPC

Figure 2.17- Tremie-Tube Method Used in Pullout Tests

(a) Bar Frame for Single Duct (b) Bar Frame for Double-Duct

Figure 2.18- Bars Frames for Pullout Test Specimens

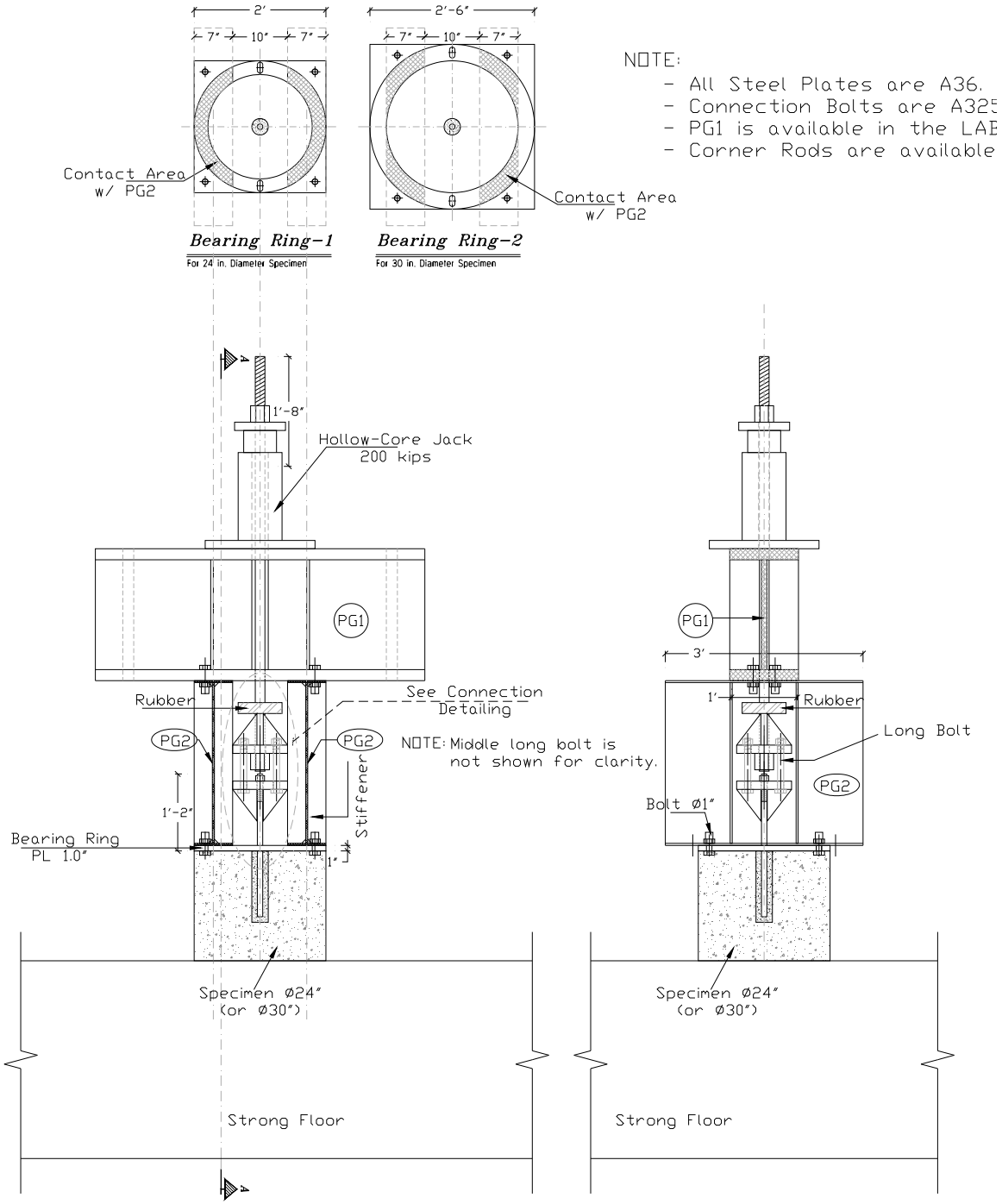

Figure 2.19- Detail of Pullout Test Setup (1 *in.*=25.4 *mm*)

Figure 2.20- Photographs of Pullout Test Setup

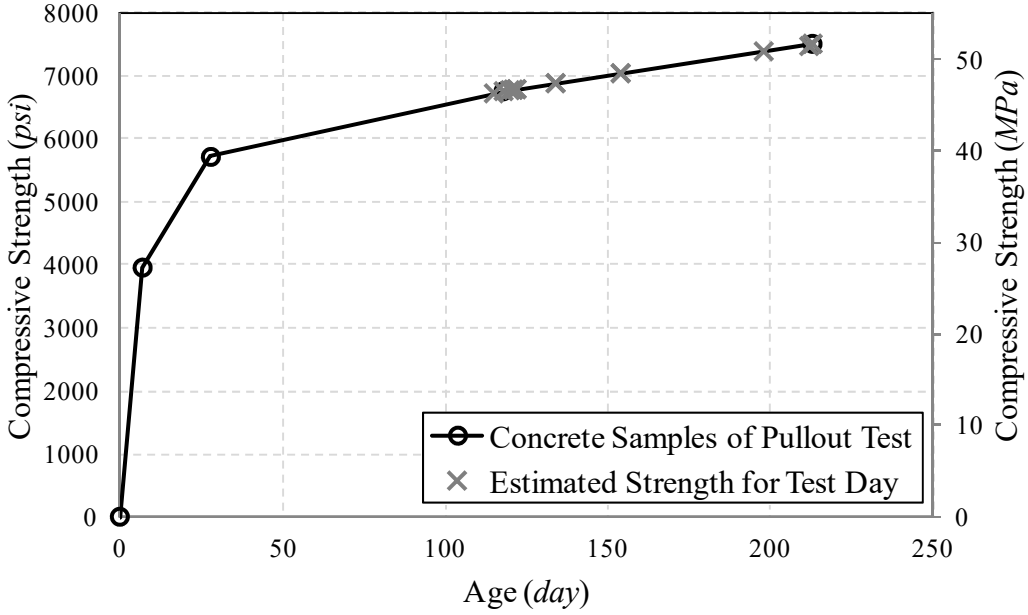

Figure 2.21- Measured Strength History of Concrete in Pullout Tests

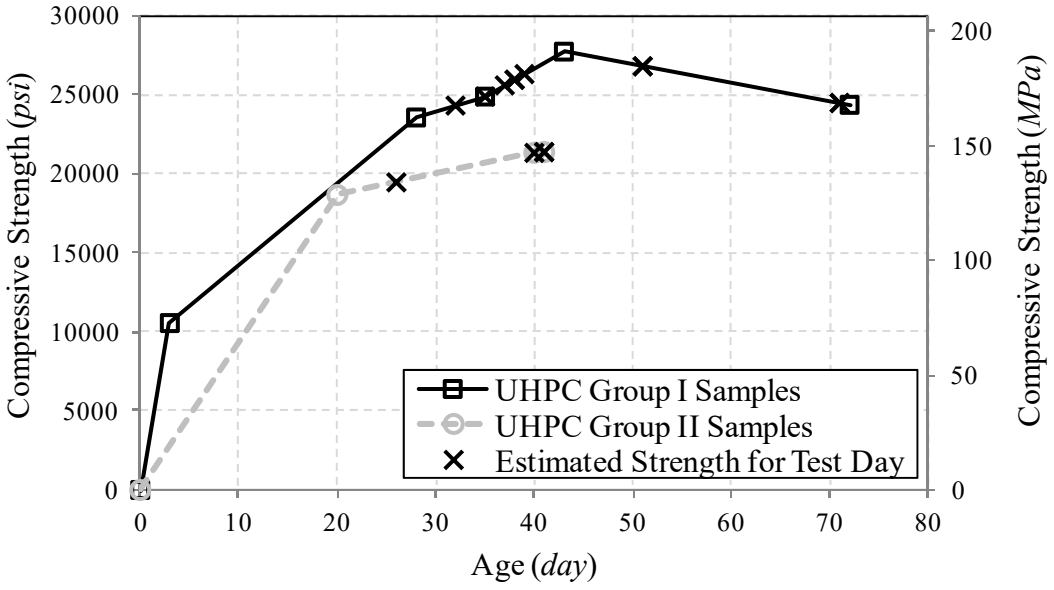

Figure 2.22- Measured Strength History of UHPC in Pullout Tests

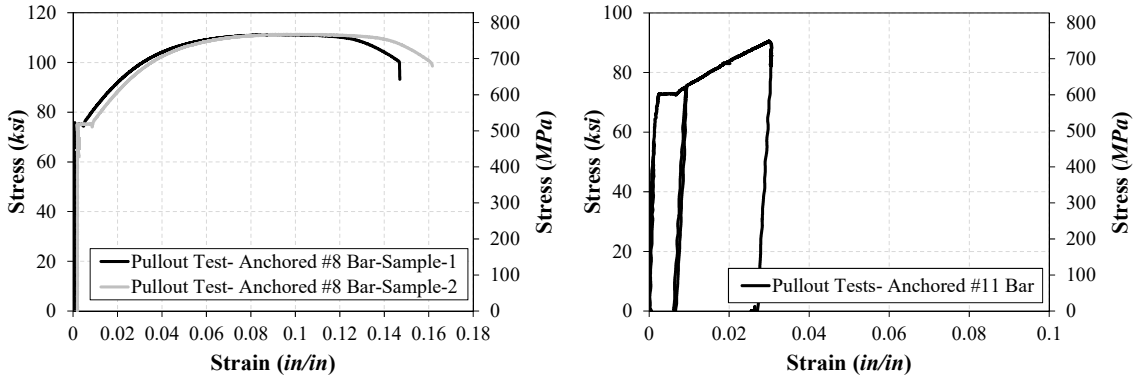

(a) #8 (Ø25 *mm*) Bars (b) #11 (Ø36 *mm*) Bar

Figure 2.23- Measures Stress-Strain for Anchored bars in Pullout Tests

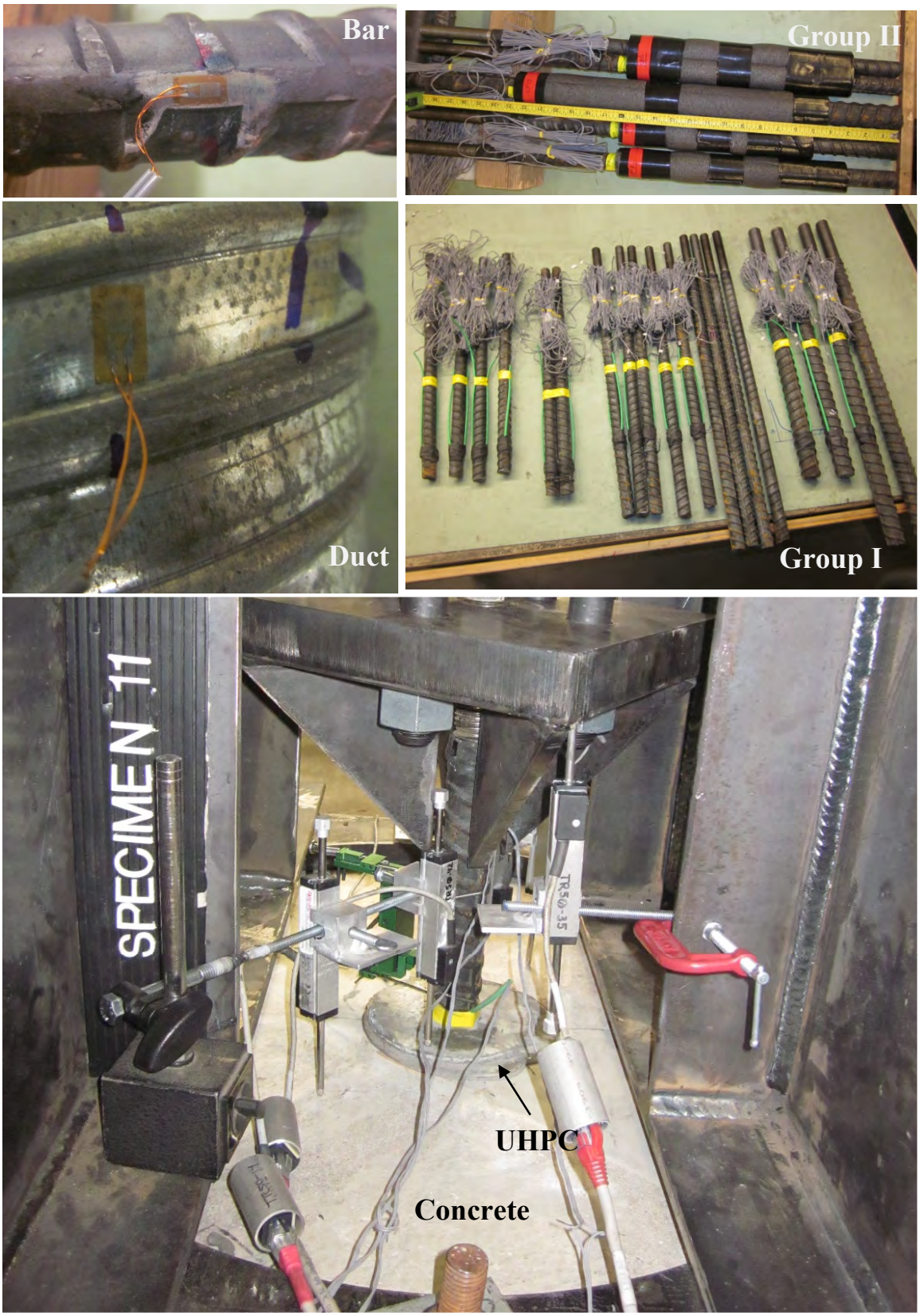

Figure 2.24- Pullout Test Instrumentation

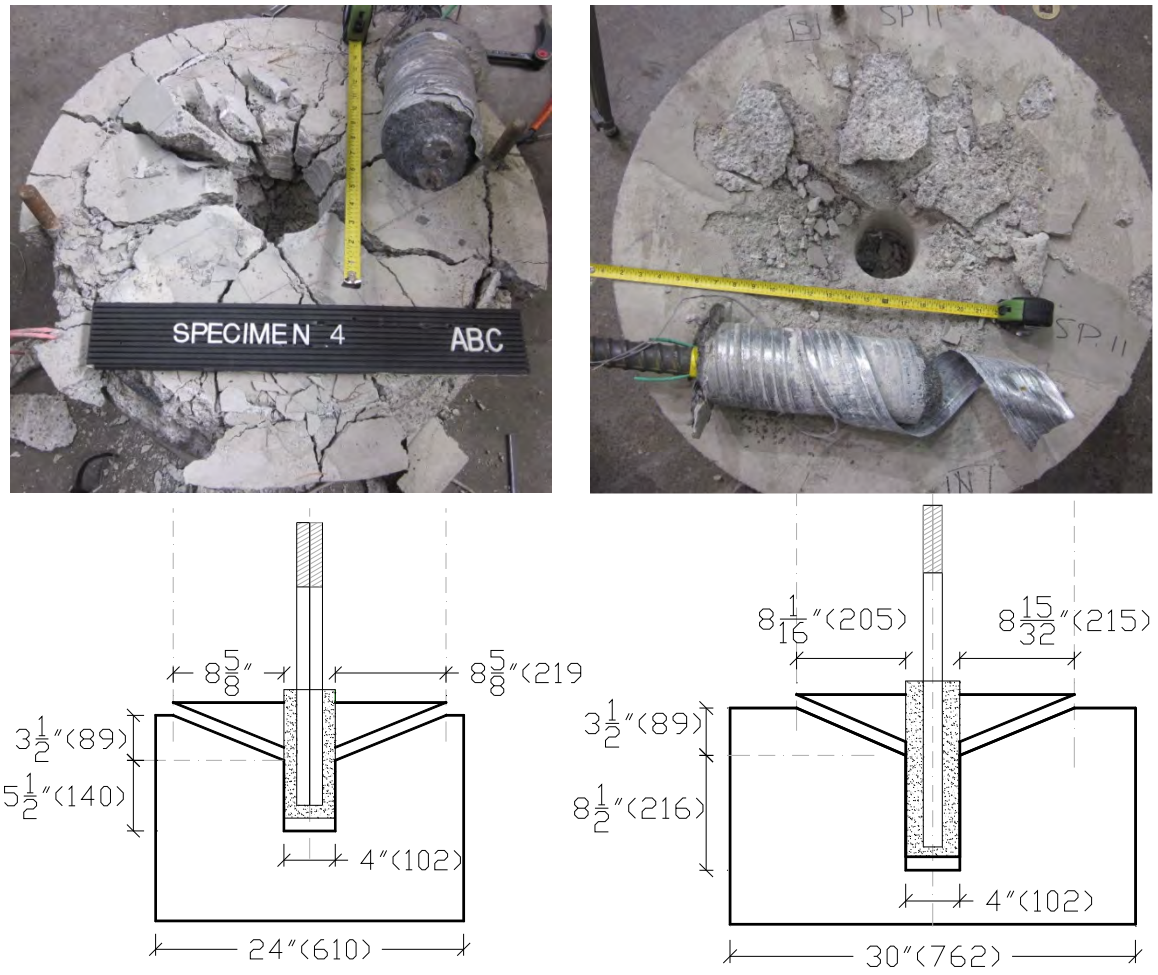

(a) Specimen SP4 (b) Specimen SP11

Figure 2.25- Damage of Group I Specimens in Pullout Tests [unit: *in*. (*mm*)]

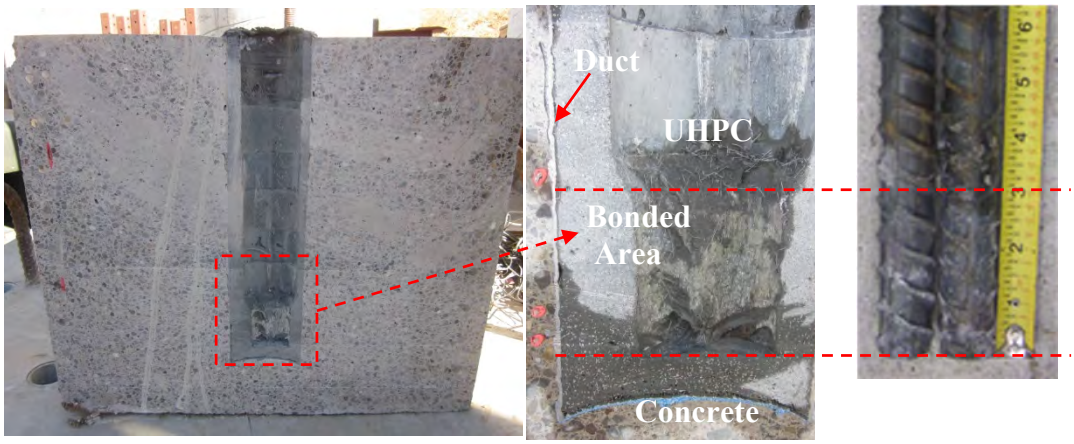

Figure 2.26- Damage of Specimen SP6 in Vertical Cut-in-Half View

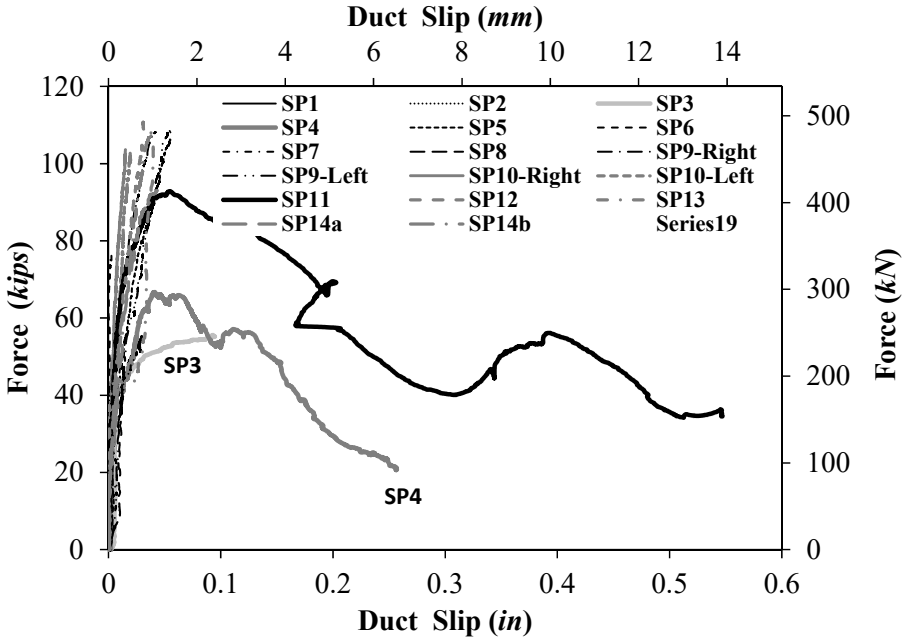

Figure 2.27- Force versus Duct Slip for All Pullout Tests

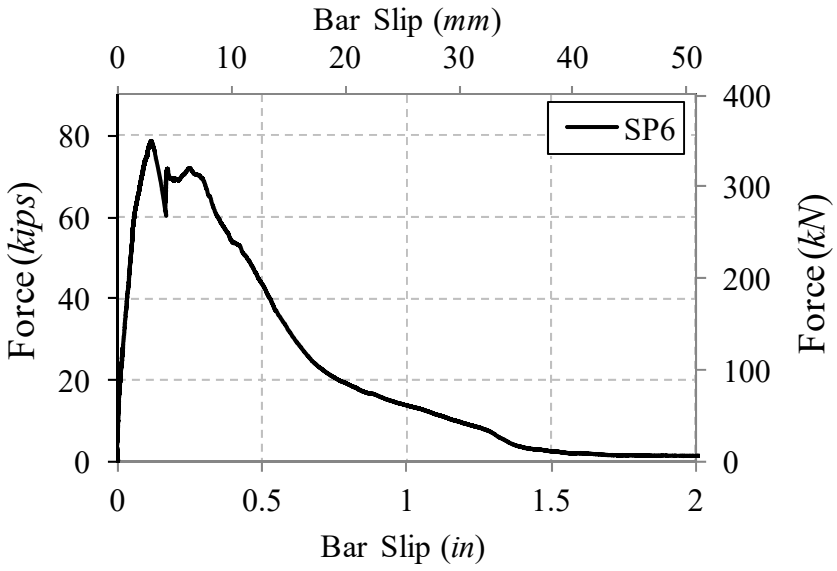

Figure 2.28- Force versus Bar Slip for SP6 of Pullout Tests

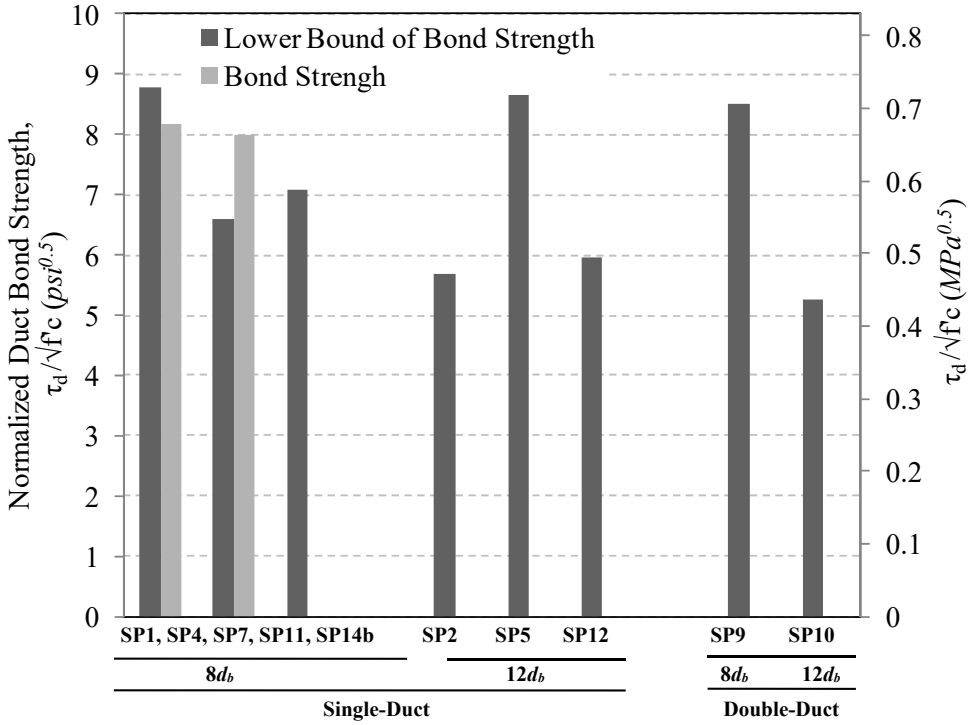

Figure 2.29- Normalized Duct Bond Strength for All Specimens

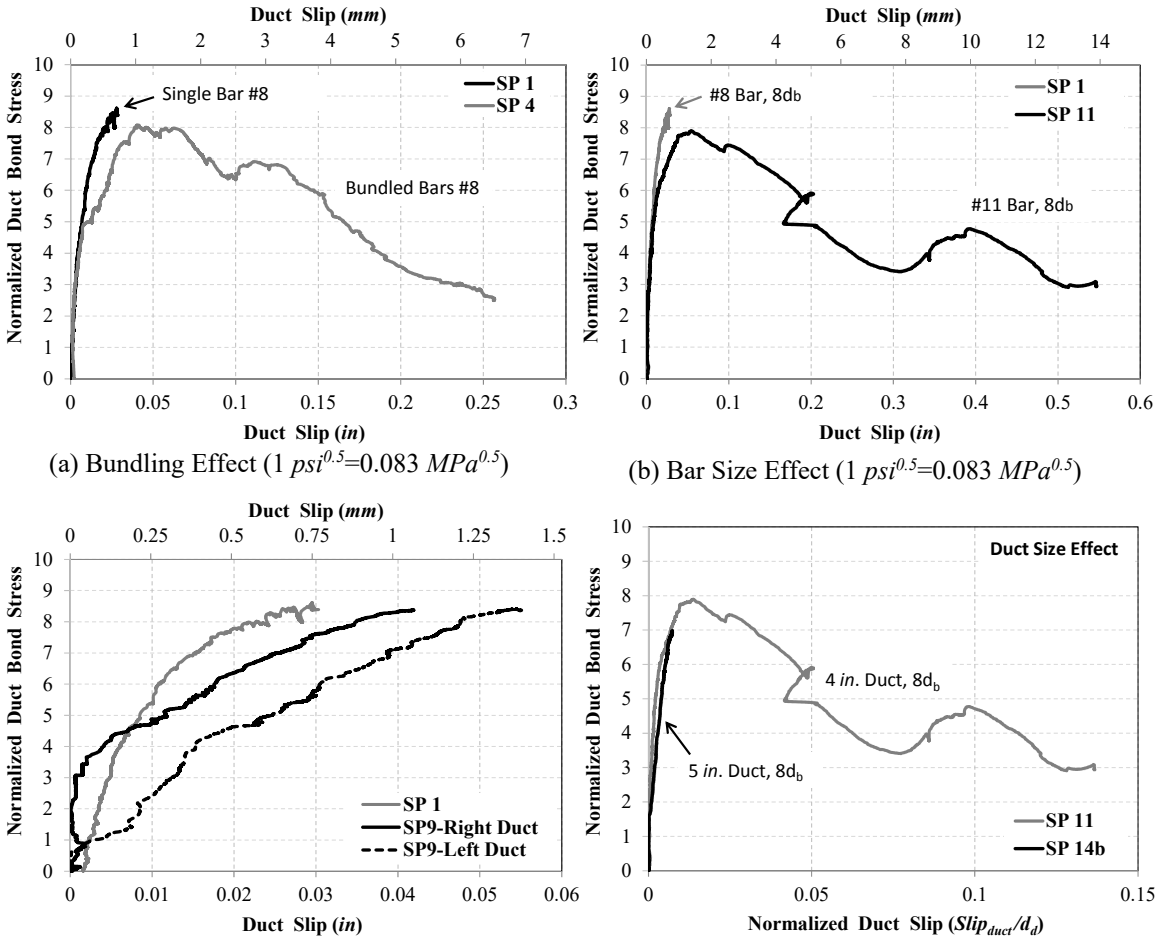

(a) Bundling Effect (1 $psi^{0.5}$=0.083 $MPa^{0.5}$)

(b) Bar Size Effect (1 $psi^{0.5}$=0.083 $MPa^{0.5}$)

(c) Multiple Duct Effect (1 $psi^{0.5}$=0.083 $MPa^{0.5}$)

(d) Duct Diameter Effect (1 $psi^{0.5}$=0.083 $MPa^{0.5}$)

Figure 2.30- Bond-Slip Relationships in Pullout Tests

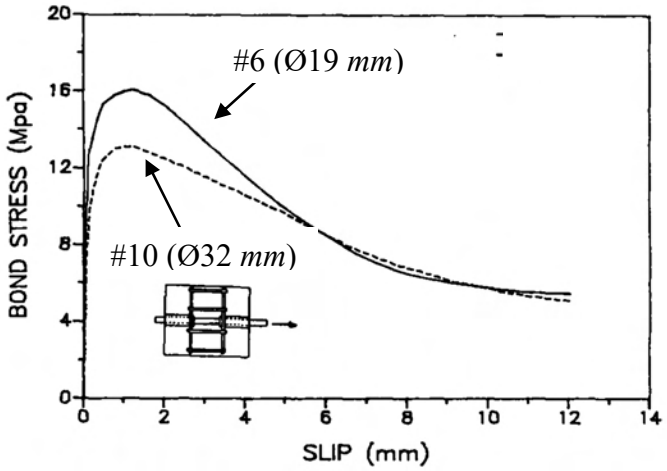

Figure 2.31- Bar Bond Stress versus Bar Slippage (Soroushian and Choi, 1989)

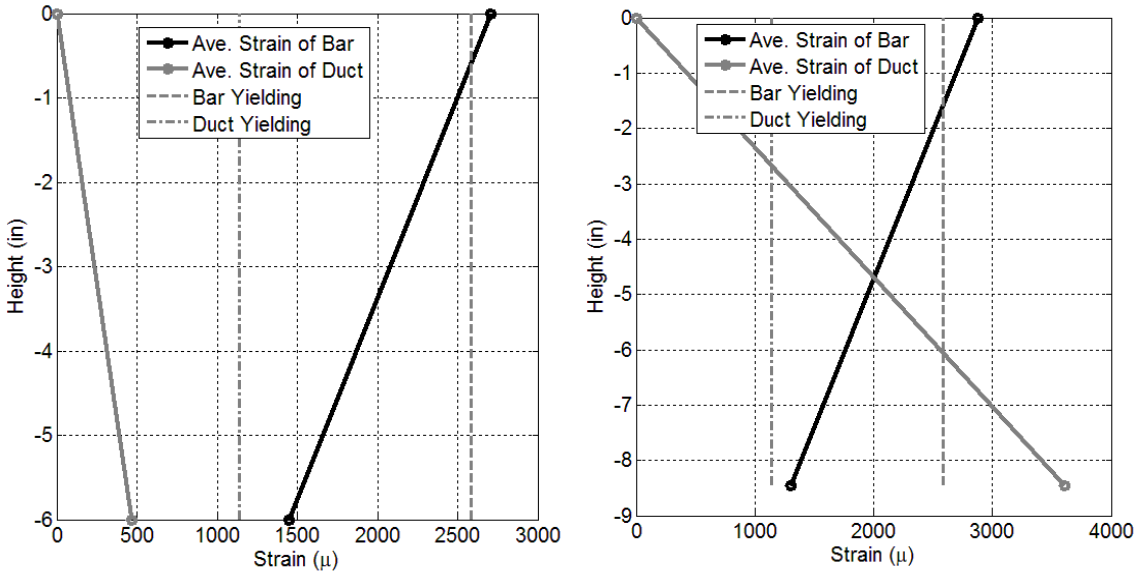

(a) SP1- #8 (Ø25 *mm*) Bar (b) SP11- #11 (Ø36 *mm*) Bar

Figure 2.32- Strain Profile for (a) Specimen with Bar Fracture, and (b) Specimens with Duct Pullout

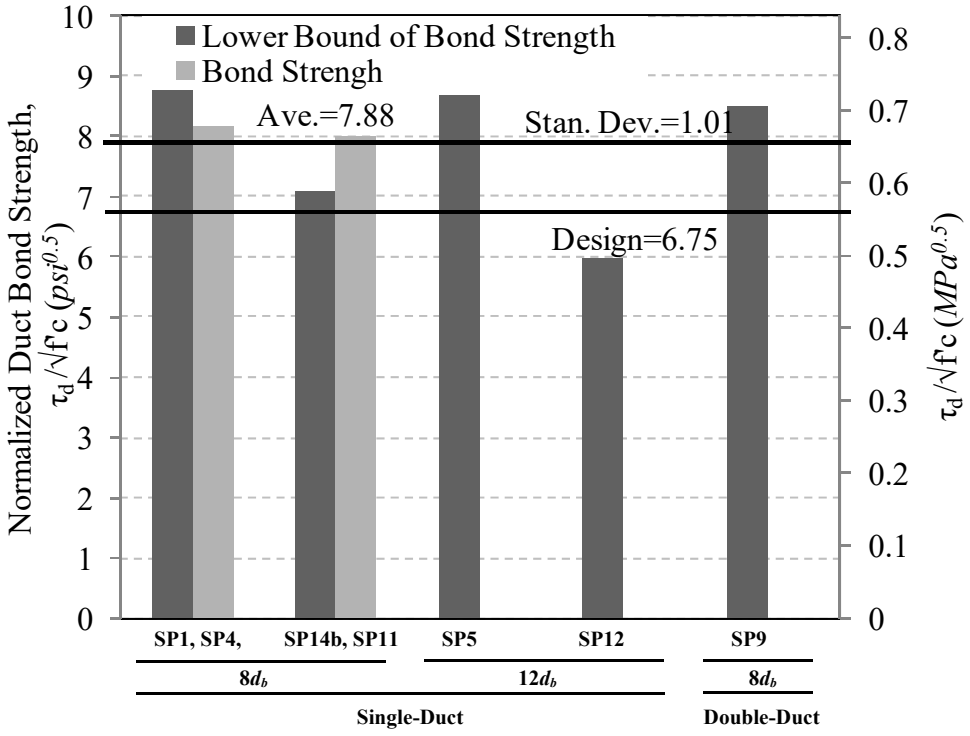

Figure 2.33- Normalized Duct Bond Strength for All Specimens Except SP2, SP7 & SP10

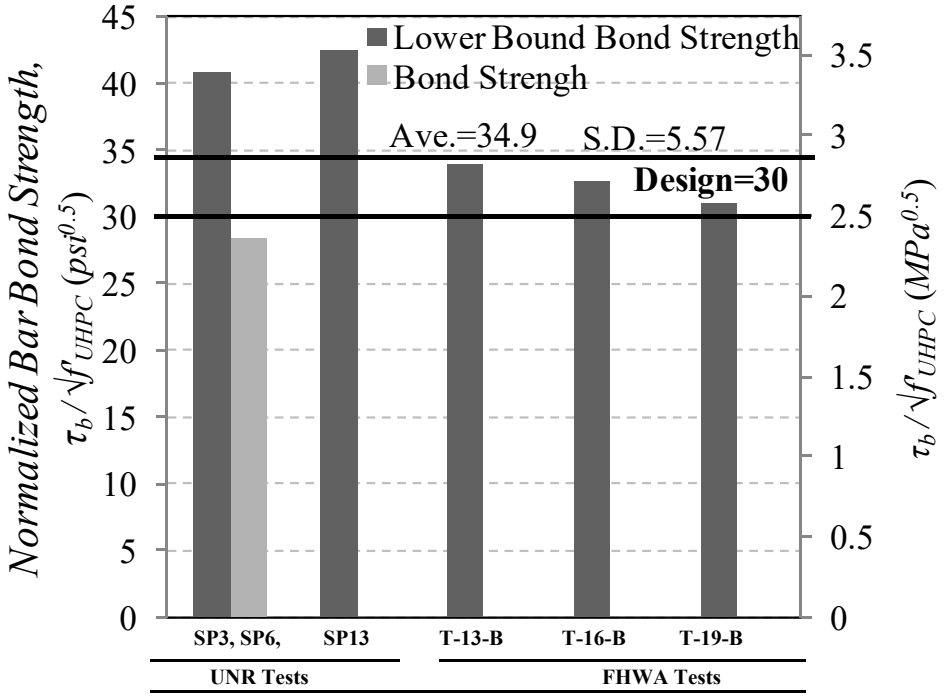

Figure 2.34- Normalized Bar Bond Strength for All Specimens Except SP8 and Including FHWA Tests

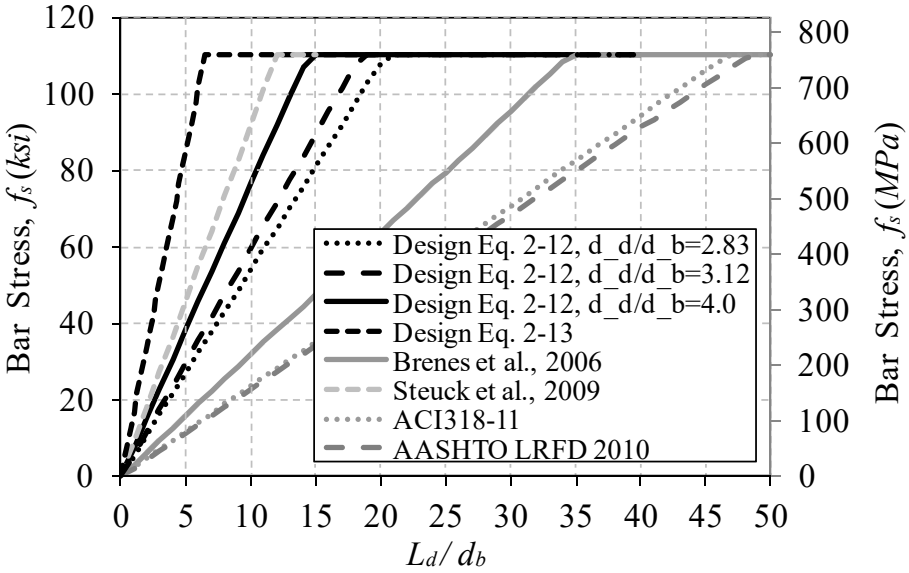

Figure 2.35- Bar Stress versus Normalized Development Length

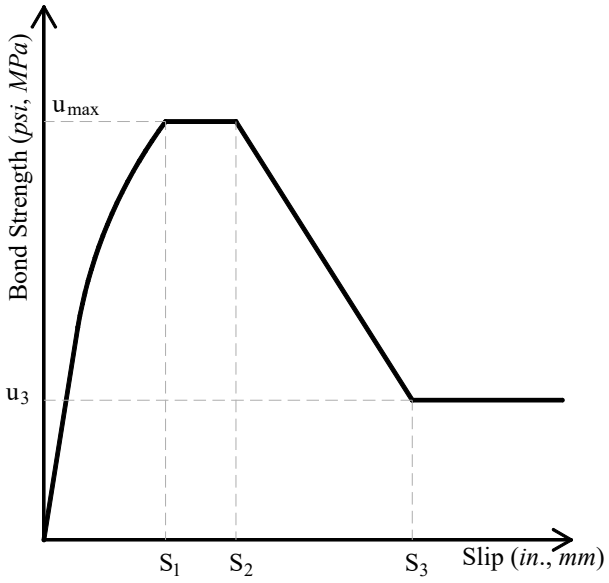

Figure 2.36- Bar Bond-Slip Model by Eligehausen et al. (1982)

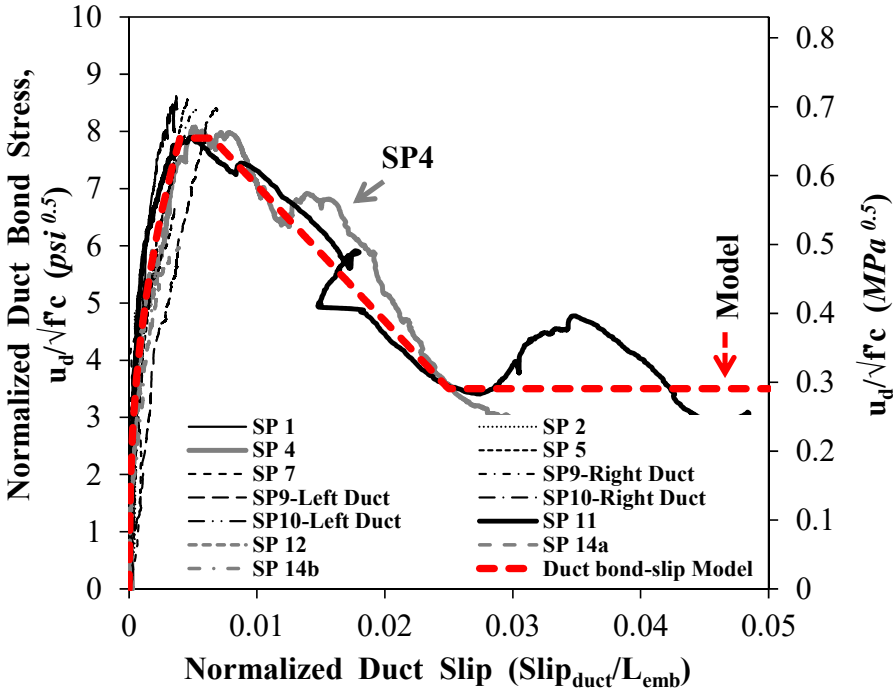

Figure 2.37- Normalized Duct Bond Stress versus Normalized Duct Slip

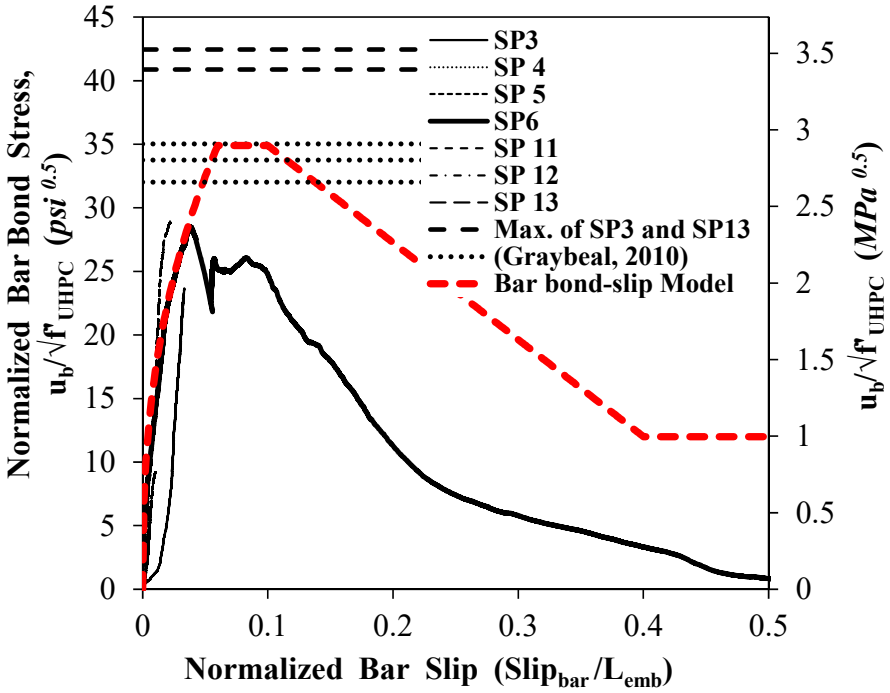

Figure 2.38- Normalized Bar Bond Stress versus Normalized Bar Slip

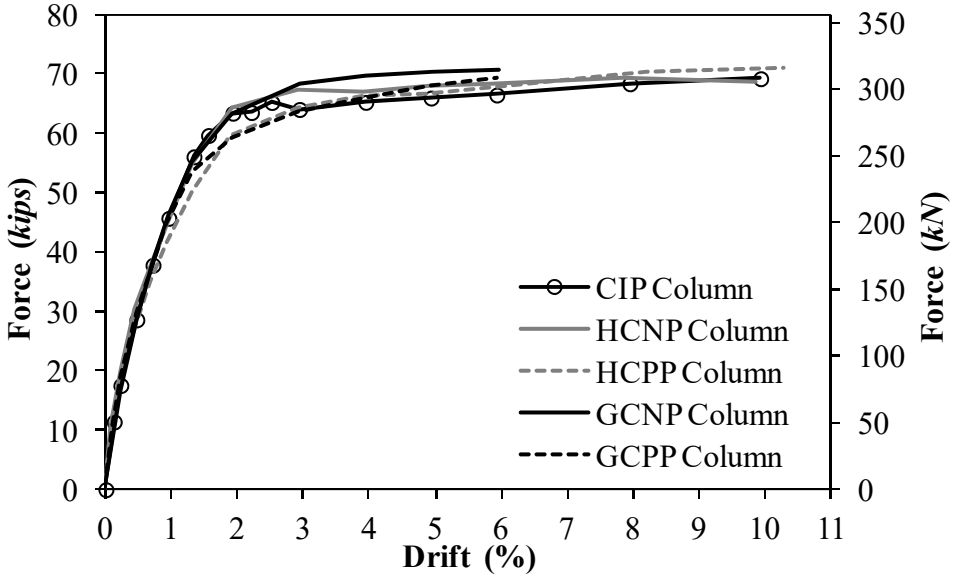

Figure 3.1- Force-Displacement Backbones for Previous Column Model Tests (Haber, 2013)

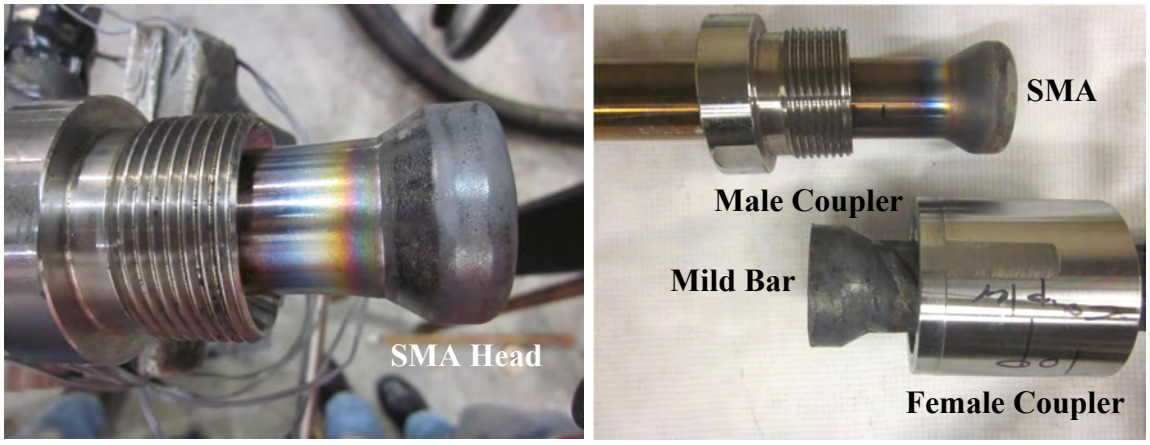

Figure 3.2- Headed SMA-Mild Bar Connection for #10 (Ø32 *mm*) Bars

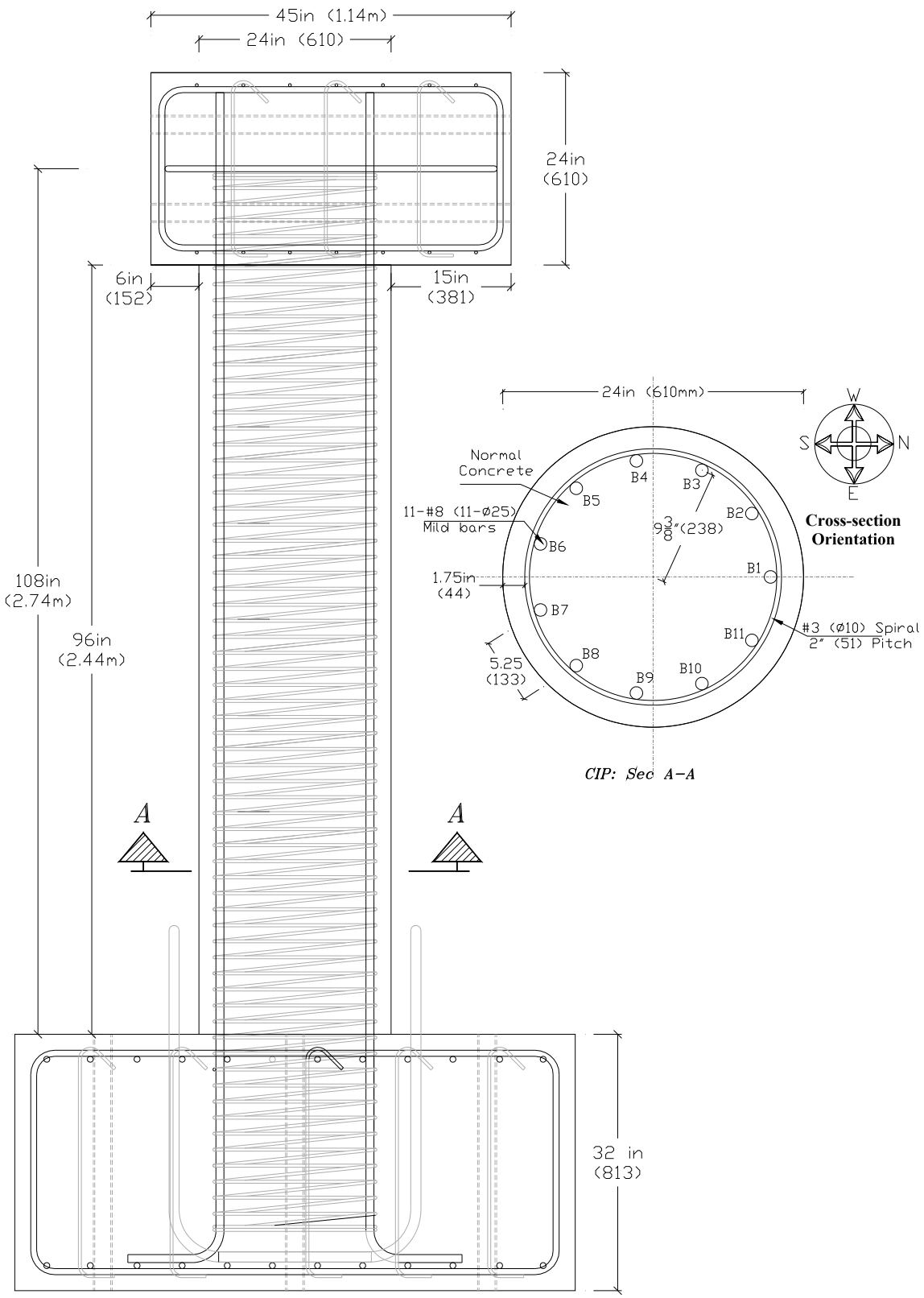

Figure 3.3- CIP Column Model

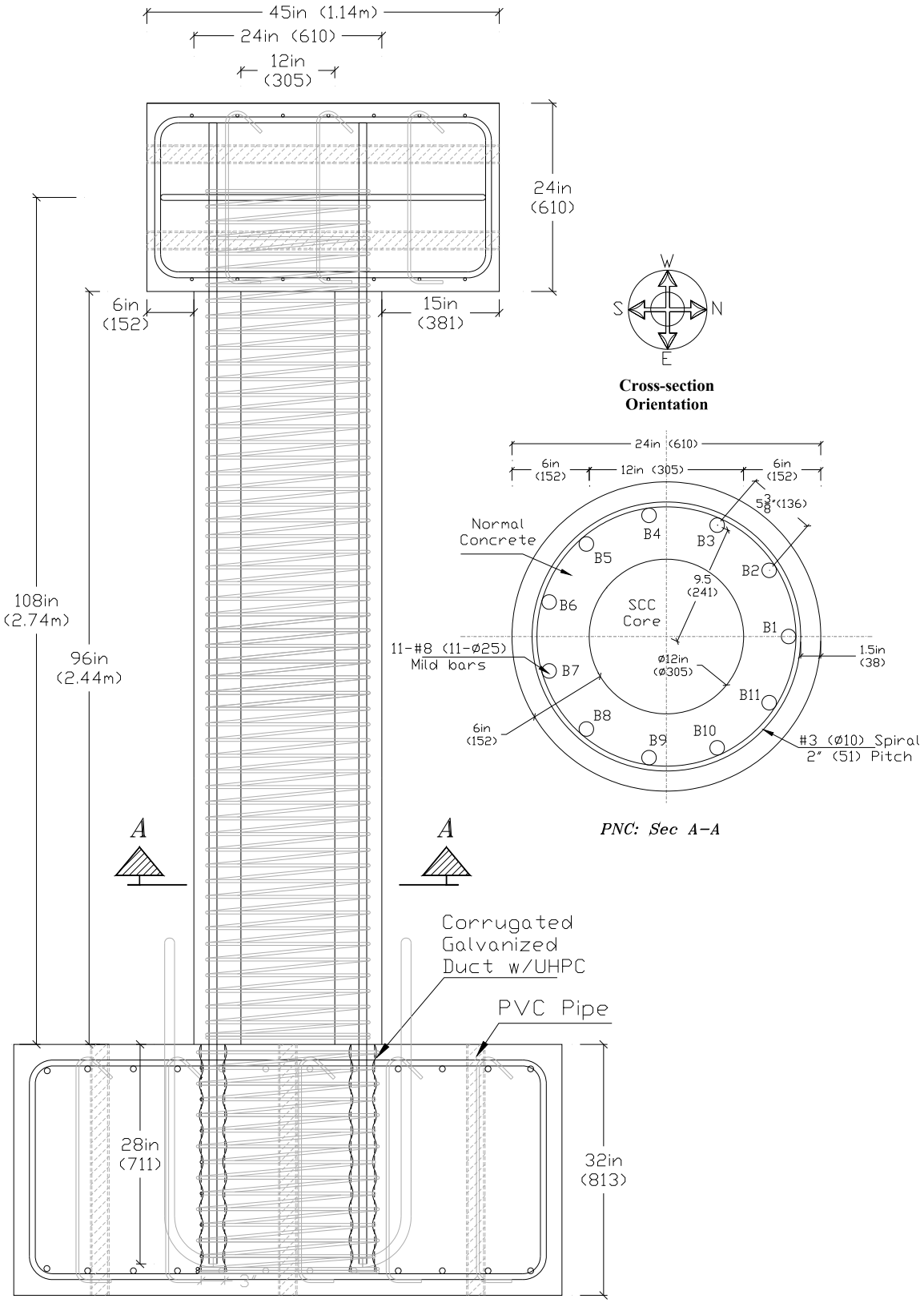

Figure 3.4- PNC Column Model (Unit: *mm*)

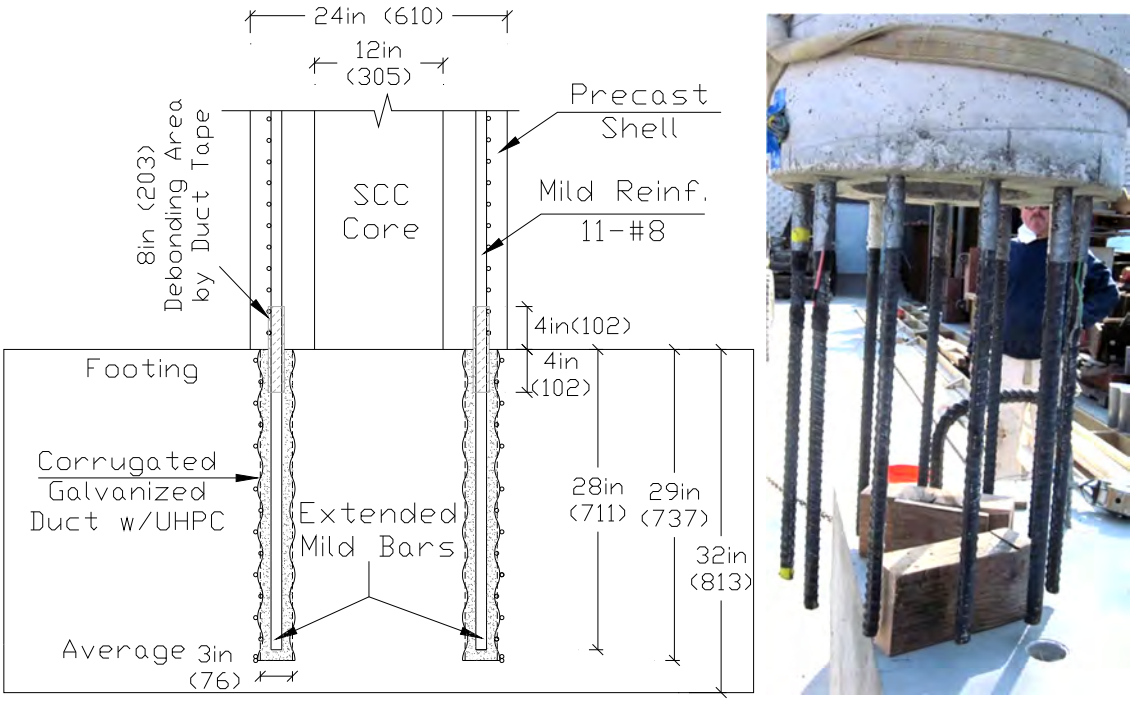

(a) Drawing (b) Photograph

Figure 3.5- PNC Column Base Connection Detail (Unit: *mm*)

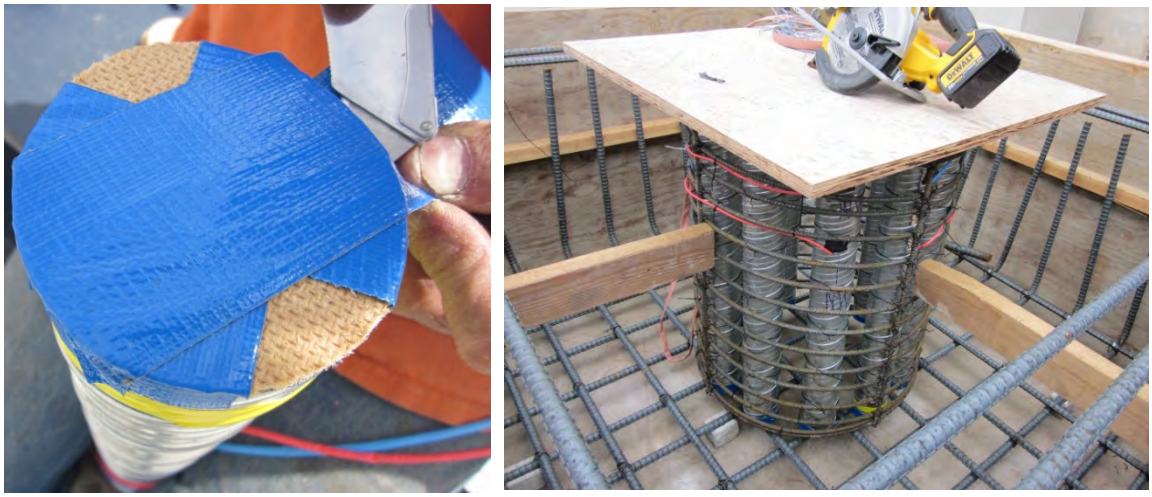

(a) Plugging Duct End (b) Duct Cage Prior to Installing Footing Top Rebars

Figure 3.6- Duct Cage in Footing of PNC Column

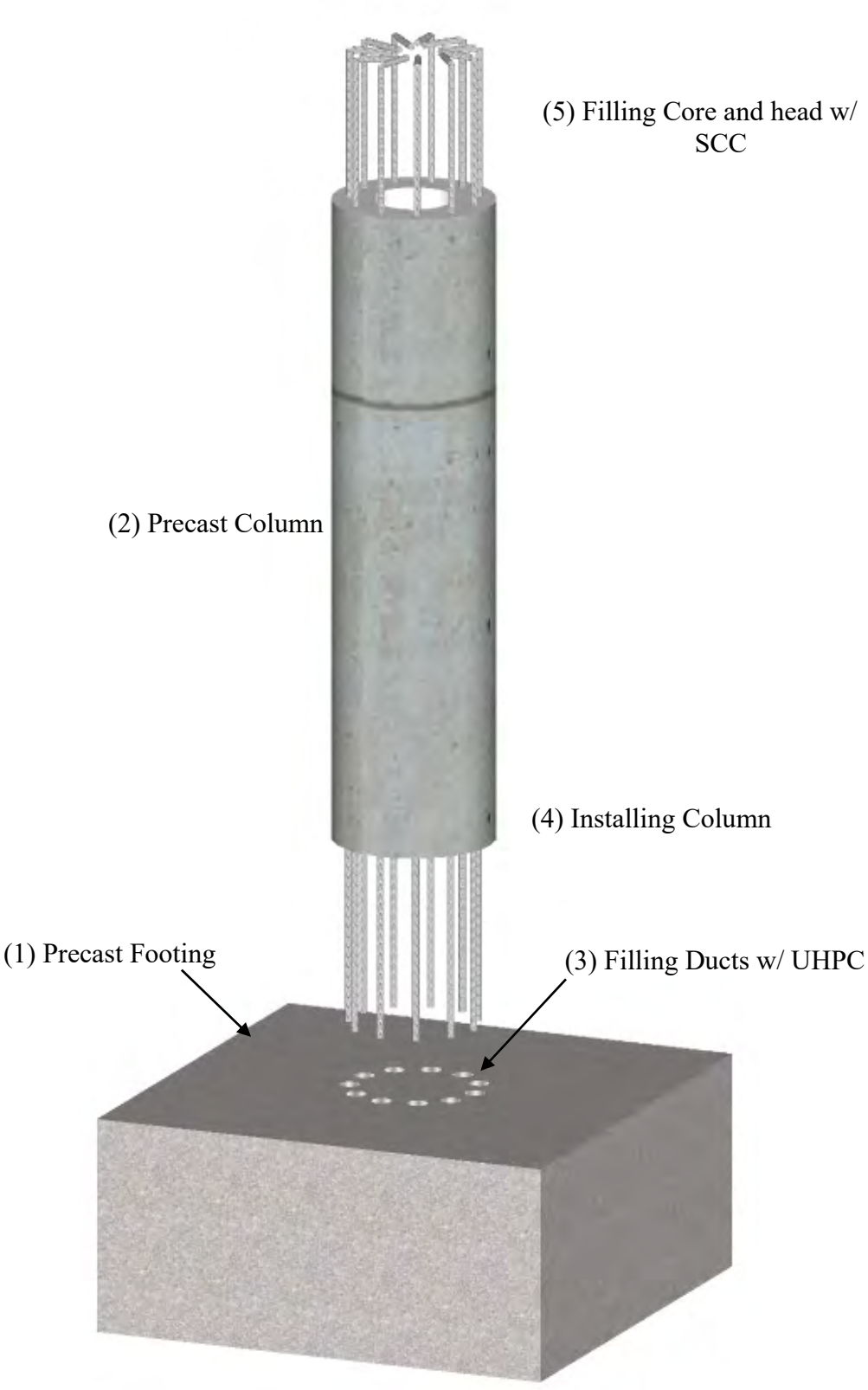

Figure 3.7- Construction Stages for PNC Column w/ UHPC-Filled Duct Connection at Base

Figure 3.8- Precast Footing with Embedded Ducts in PNC Model

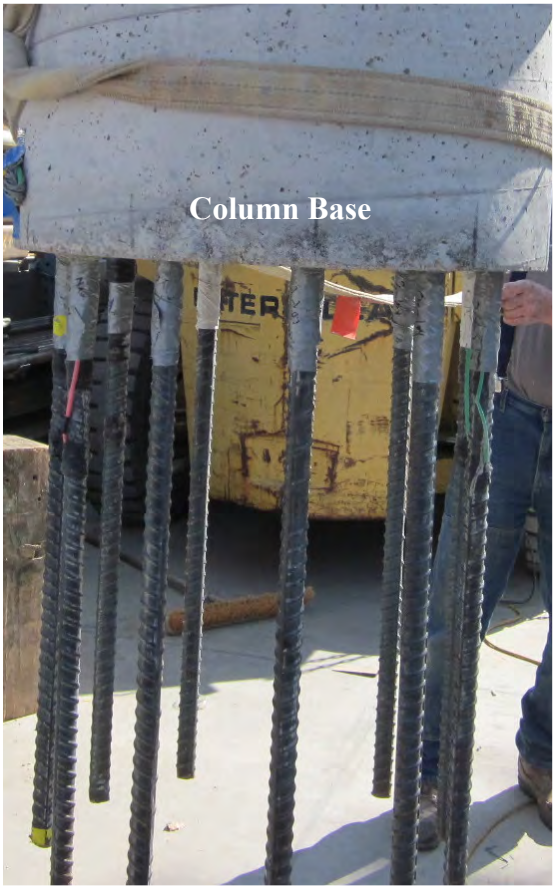

(a) Elevation

Column Base

(b) Bottom View of Column

Figure 3.9- PNC Precast Hollow Column

(a) Casting UHPC (b) Duct Filled w/ UHPC

Figure 3.10- Casting UHPC Using Tremie Tube Method in PNC Model

(a) Inserting Reinforcements into Ducts (b) After Installation

Figure 3.11- Erecting and Installing PNC Column

Figure 3.12- Visual Stability Index (VSI) Evaluation for SCC Mix Used in PNC/GCDP Columns

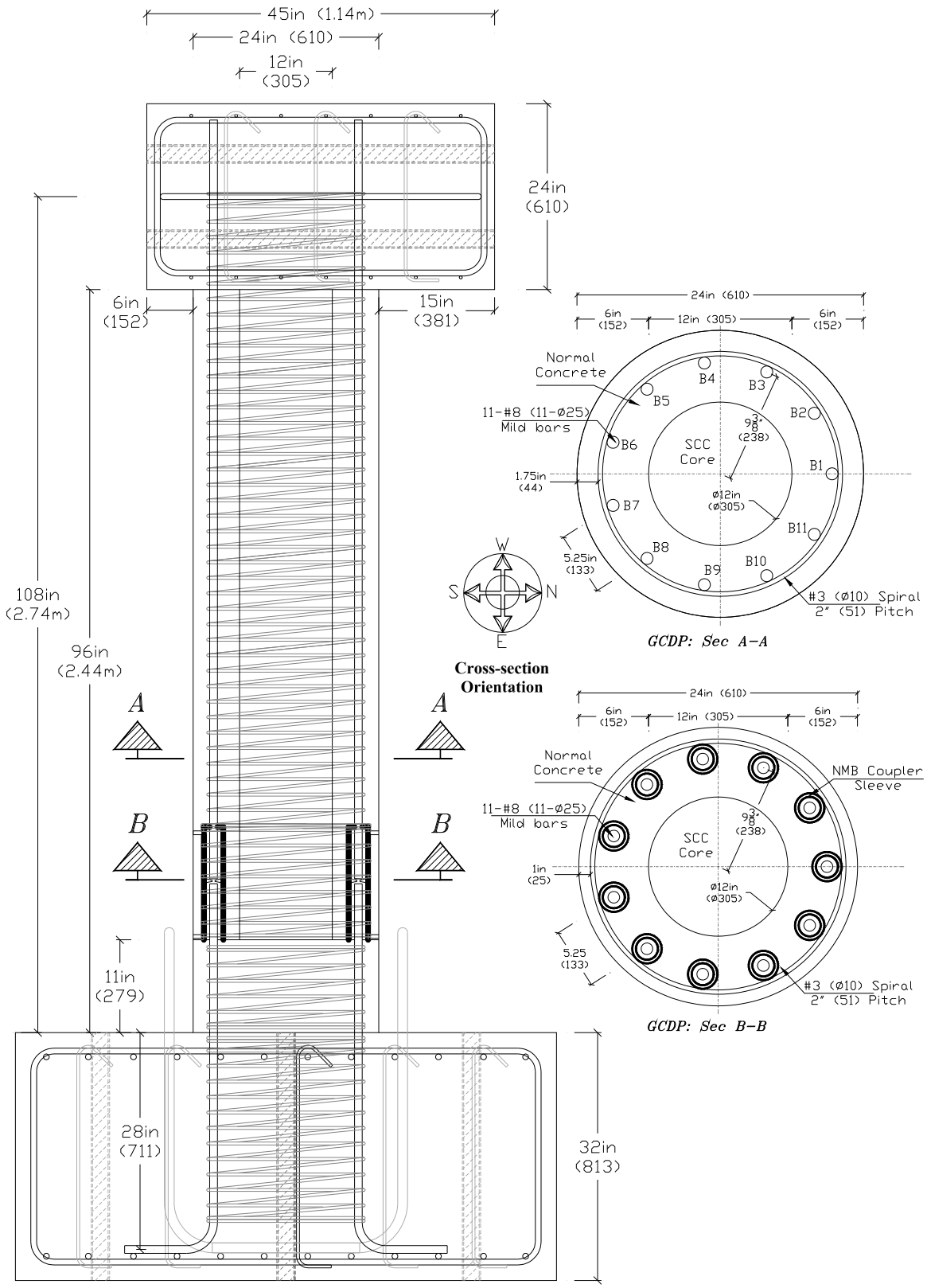

Figure 3.13- GCDP Column Model (Unit: *mm*)

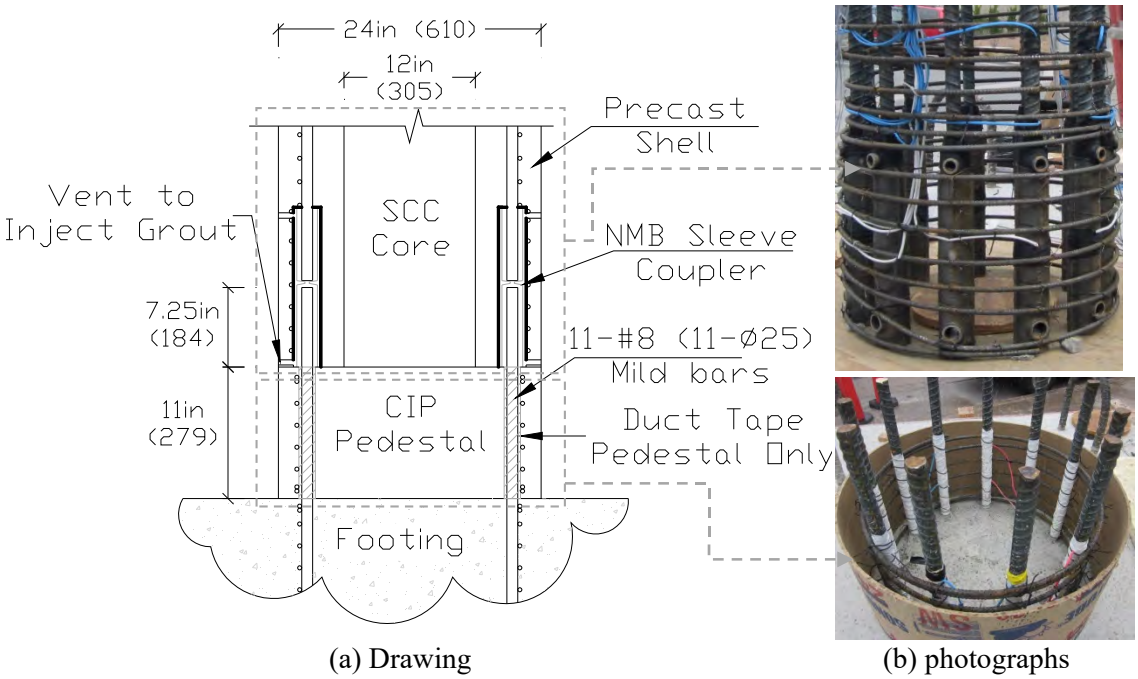

Figure 3.14- GCDP Column Model Base Connection Details (Unit: *mm*)

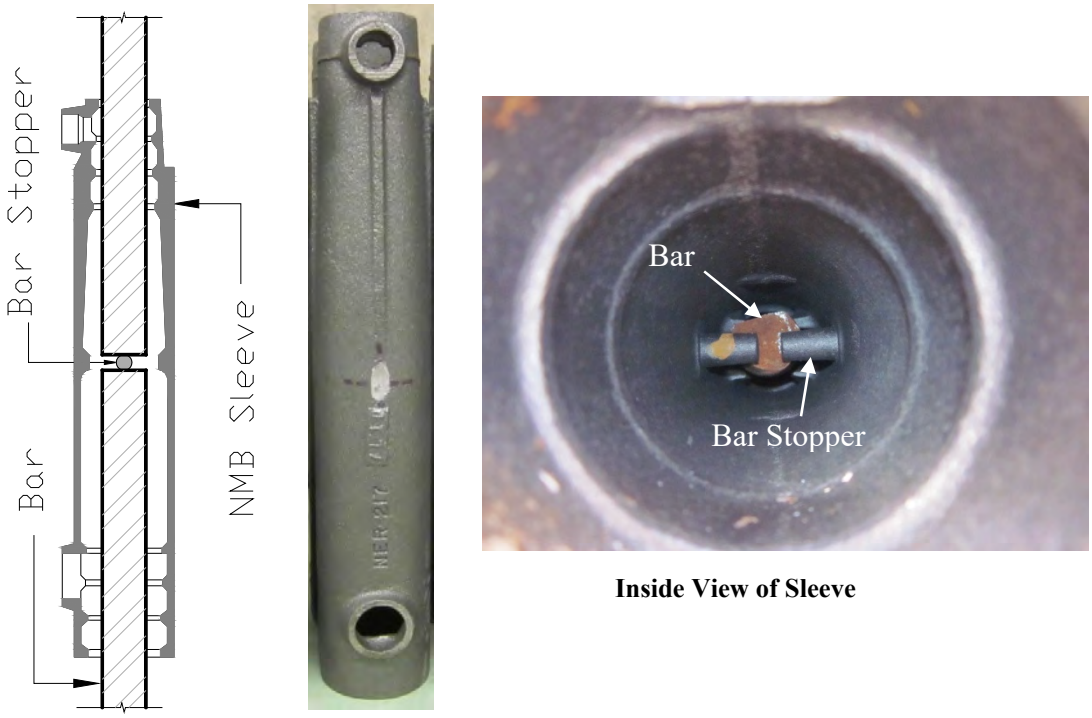

Figure 3.15- Grout-Filled NMB Sleeve Incorporated in GCDP

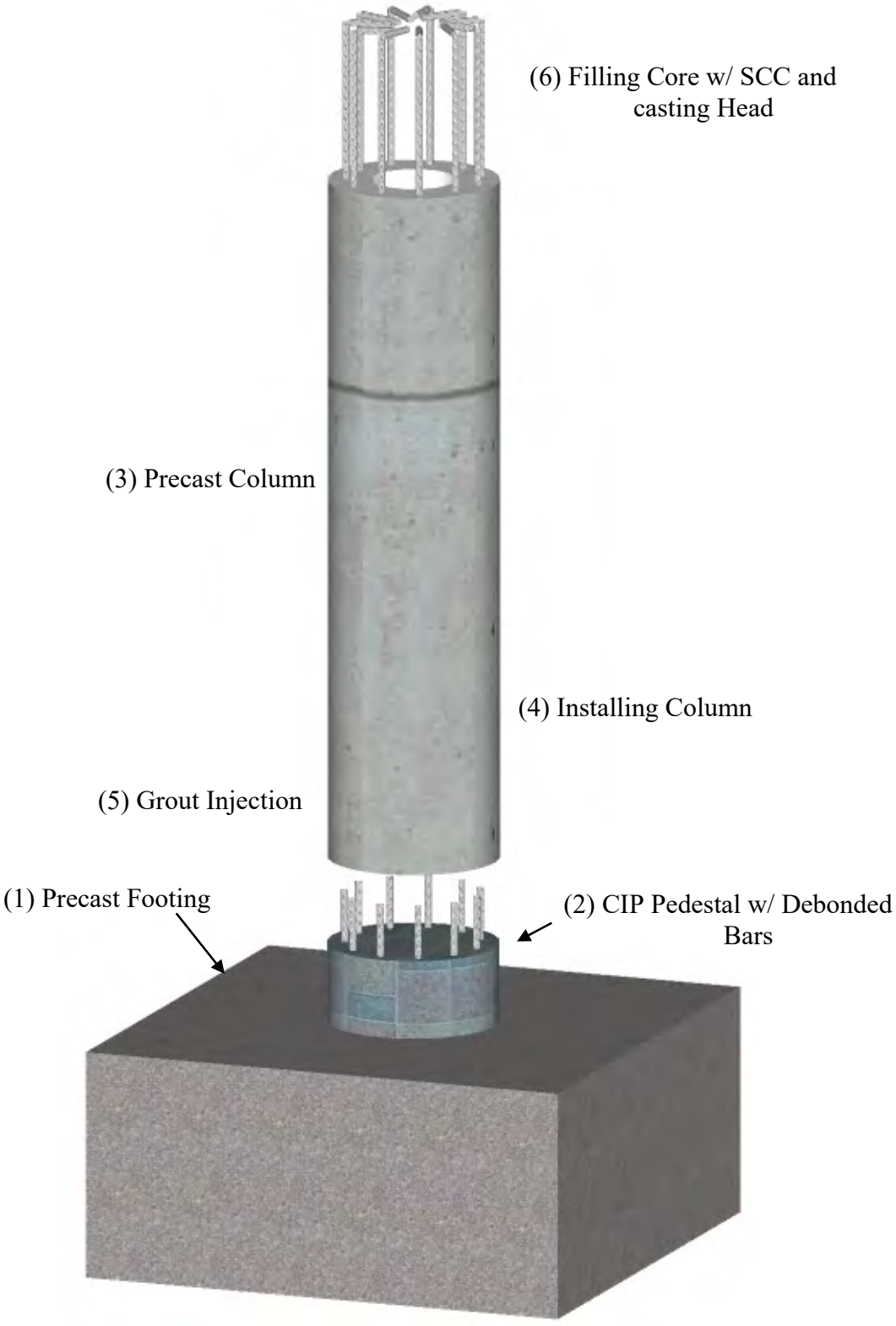

Figure 3.16- Construction Stages for GCDP Column w/ Grouted Coupler Connection at Base

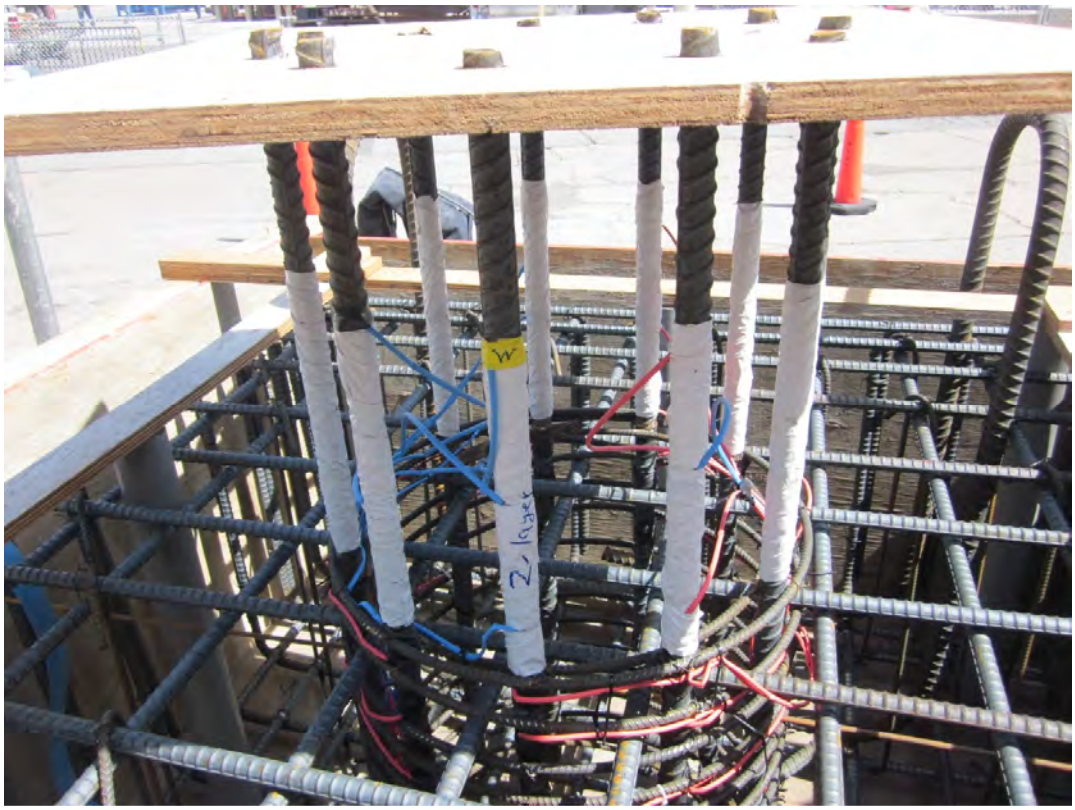

Figure 3.17- Footing Reinforcements and GCDP Column Debonded Bars

Figure 3.18- GCDP Precast Hollow Column w/ Embedded Sleeves

Figure 3.19- Erecting and Installing GCDP Column

Figure 3.20- Injecting SS-Mortar into Sleeves in GCDP Column

Figure 3.21- Filling Construction Gap w/ Dry Packing

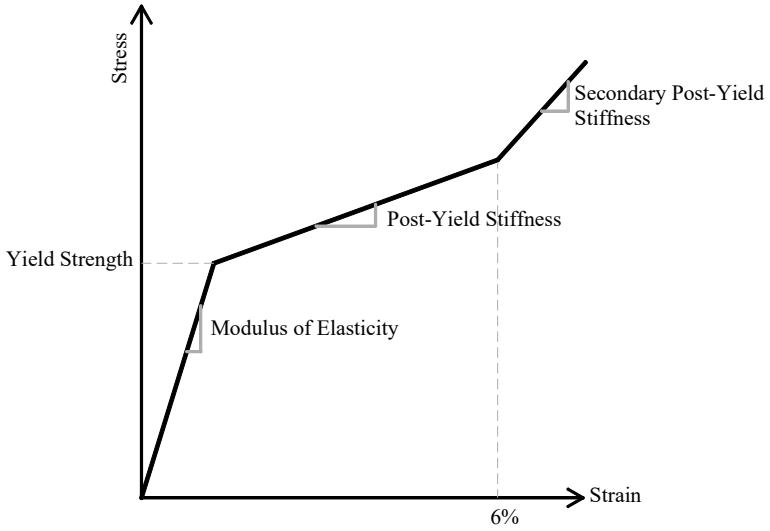

Figure 3.22- Reinforcing SMA Model Used in Moment-Curvature Analysis

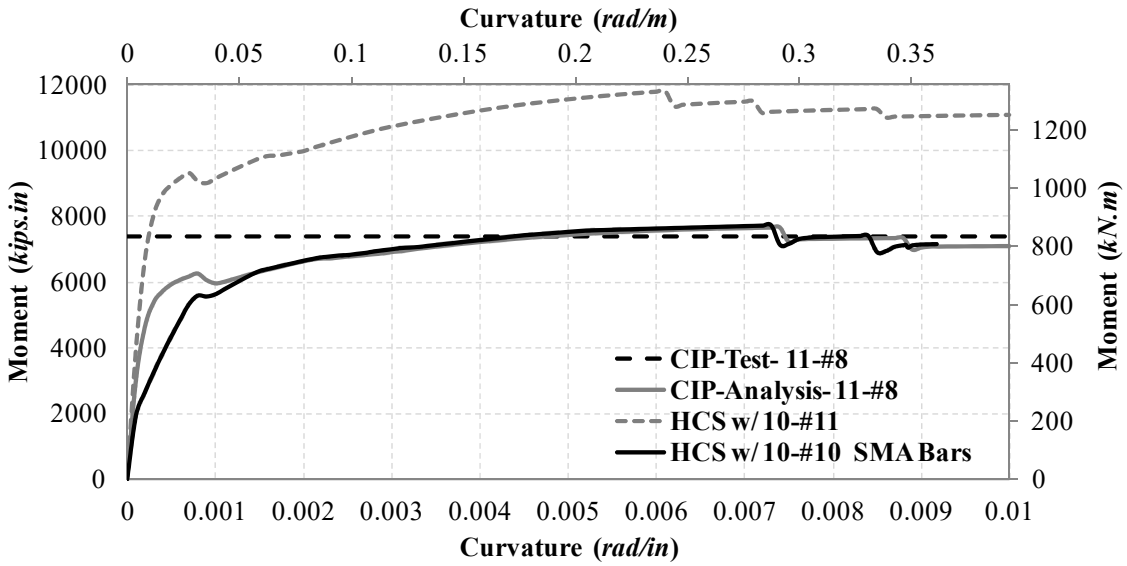

Figure 3.23- Moment-Curvature Analysis for HCS Model

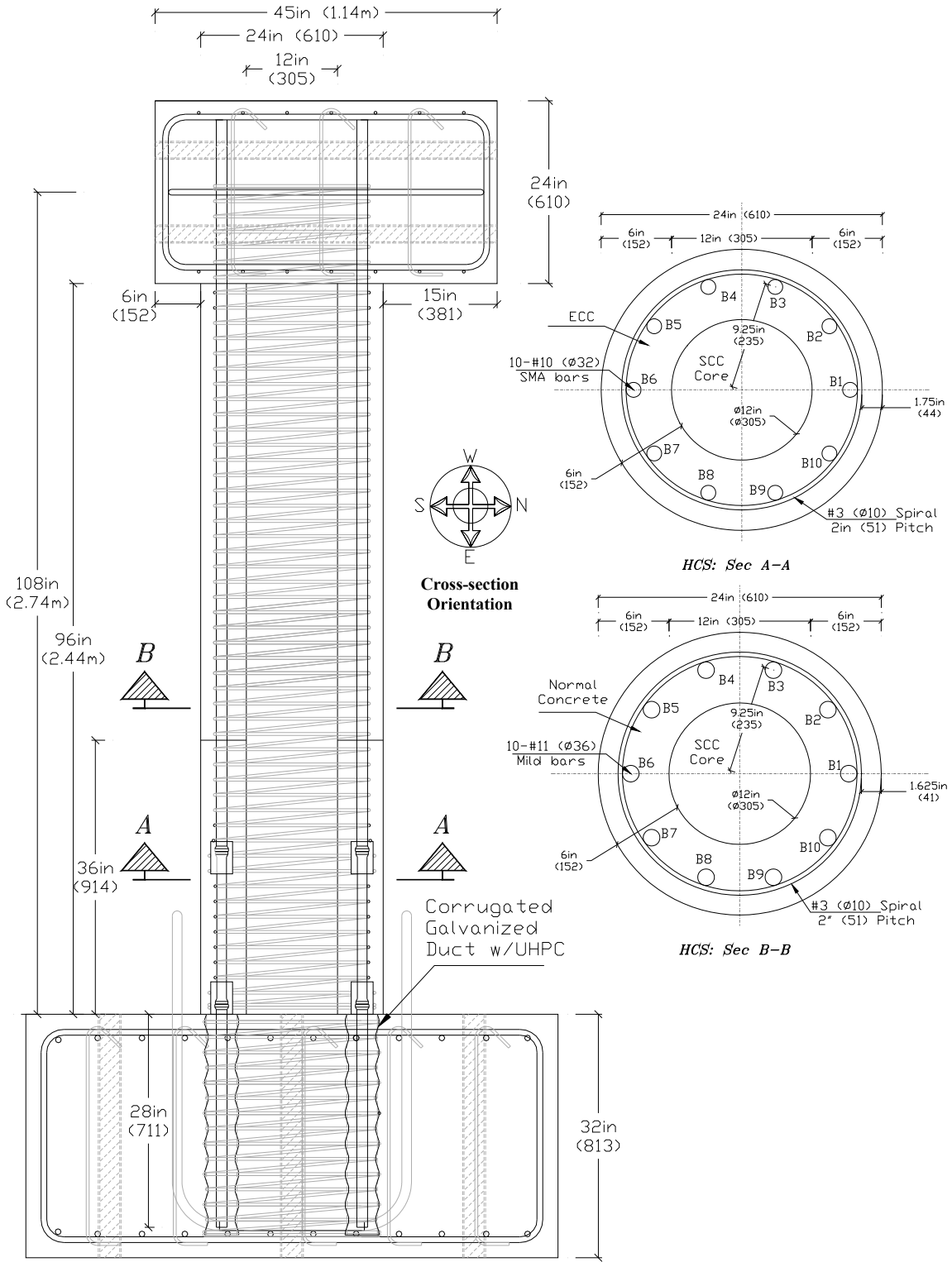

Figure 3.24- HCS Column Model (Unit: *mm*)

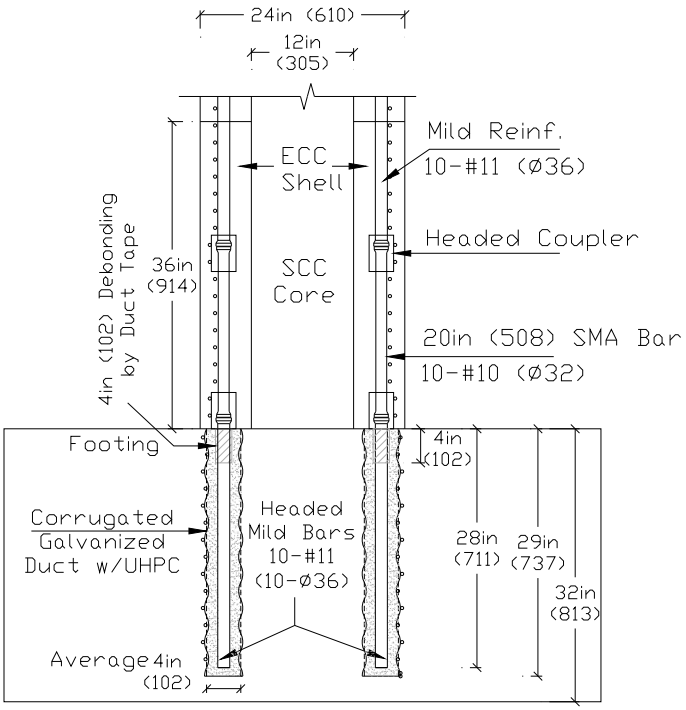

Figure 3.25- HCS Column Model Base Details (Unit: *mm*)

(a) Duct Cage before Casting Concrete (b) Footing after Casting Concrete

Figure 3.26- Precast Footing with Embedded Ducts for HCS Model

Figure 3.27- Bar Cage in HCS Model

(a) ECC Mix

(a) Plastic Gutter Placed at Column Top

Figure 3.28- Casting ECC in Plastic Hinge of HCS Model

Figure 3.29- Erecting and Securing HCS Column

Figure 3.30- Filling Ducts w/ UHPC in HCS Column

Figure 3.31- HCS Column Shell Installation

Figure 3.32- Duct Cap for Plugging Duct End

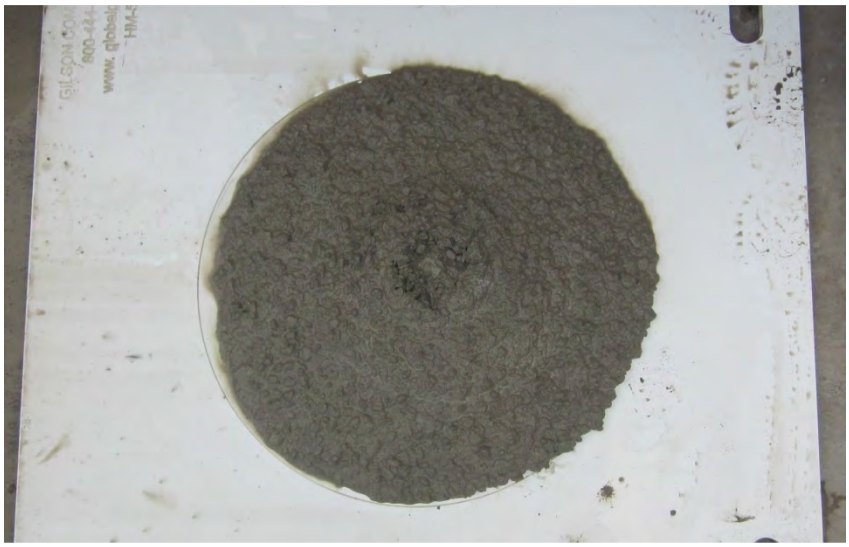

Figure 3.33- Visual Stability Index (VSI) Evaluation for SCC Mix in HCS Column

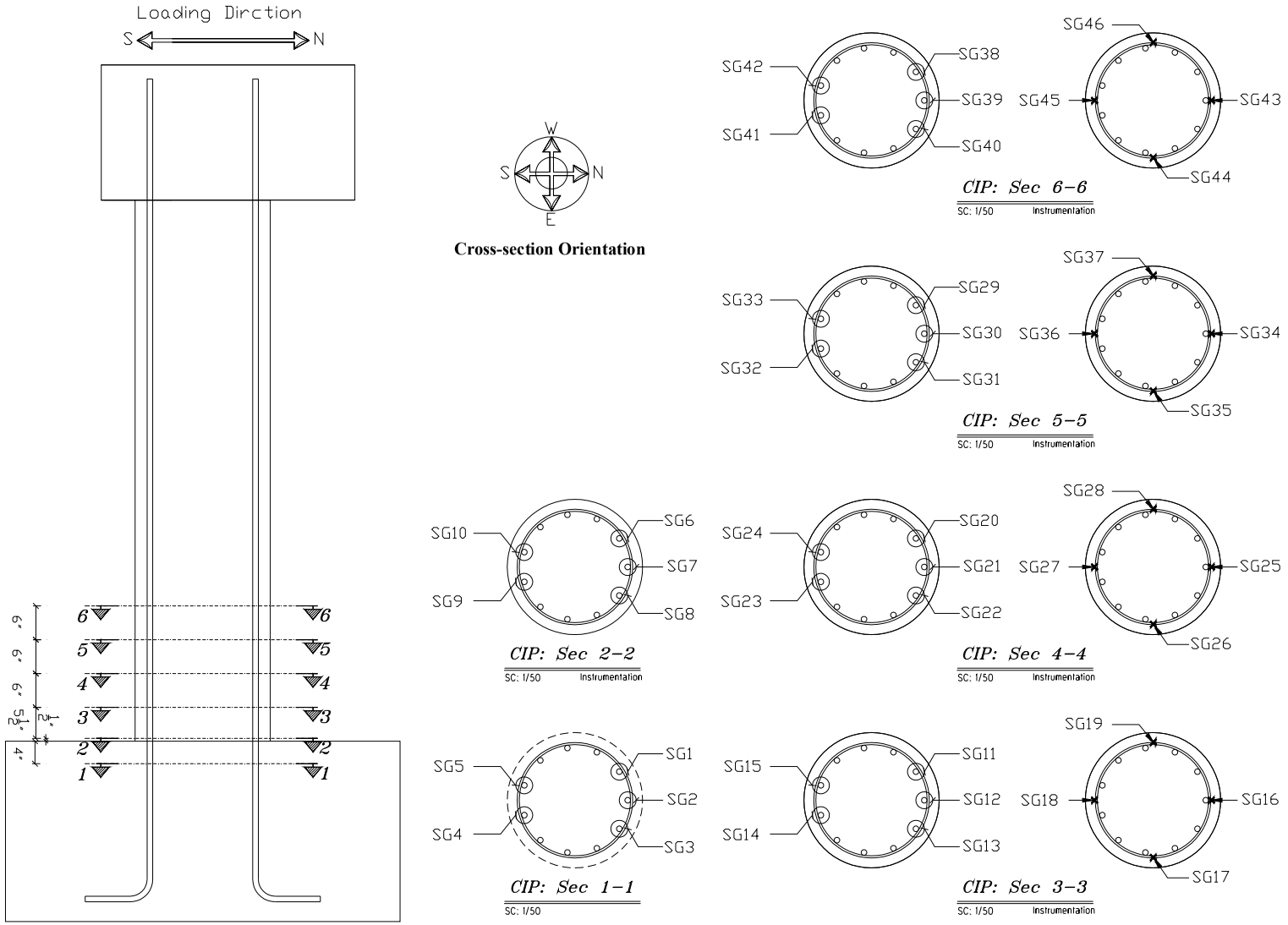

Figure 3.34- Location of Strain Gauges in CIP Column (1 *in.*=25.4 *mm*)

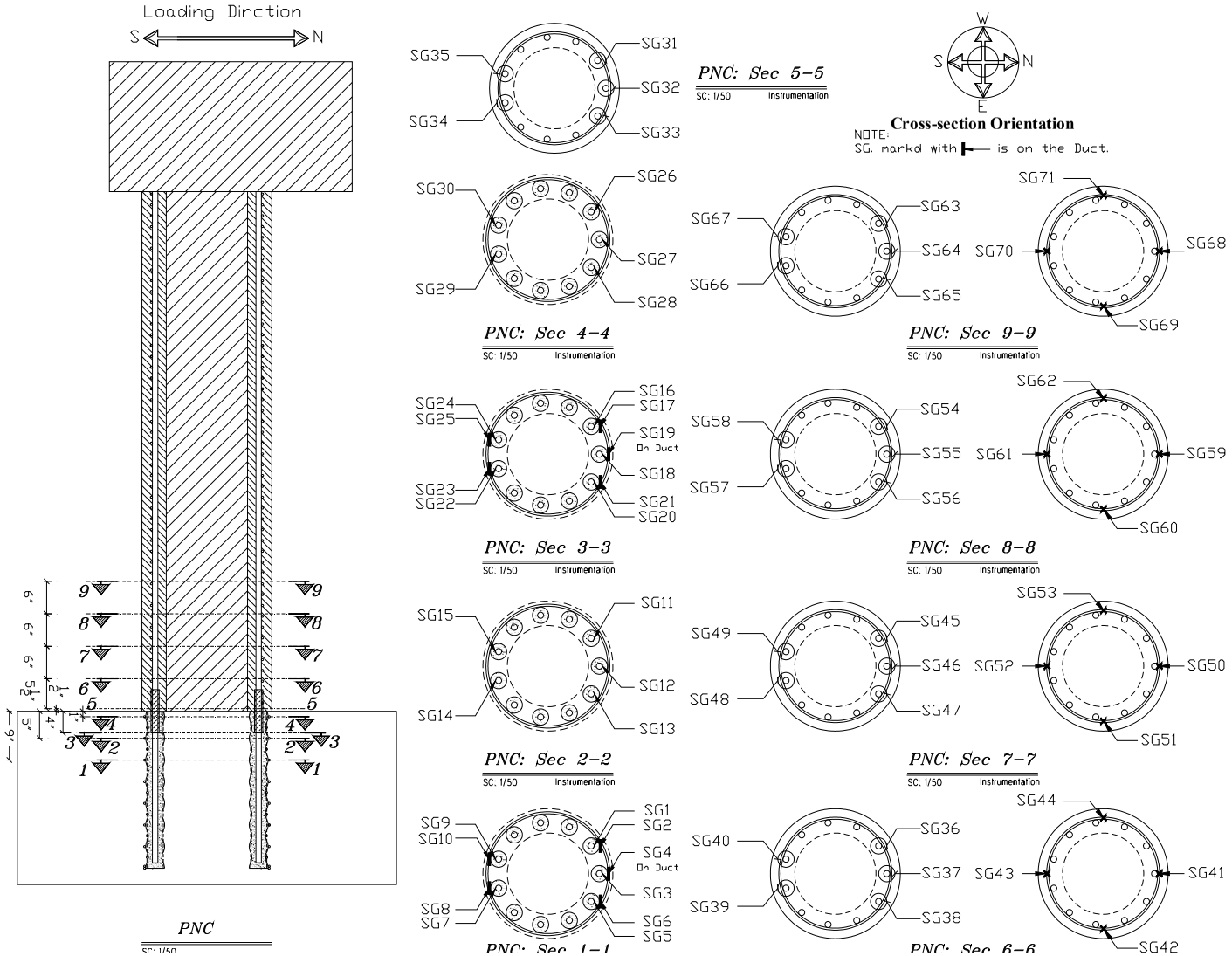

Figure 3.35- Location of Strain Gauges in PNC Column (1 *in.*=25.4 *mm*)

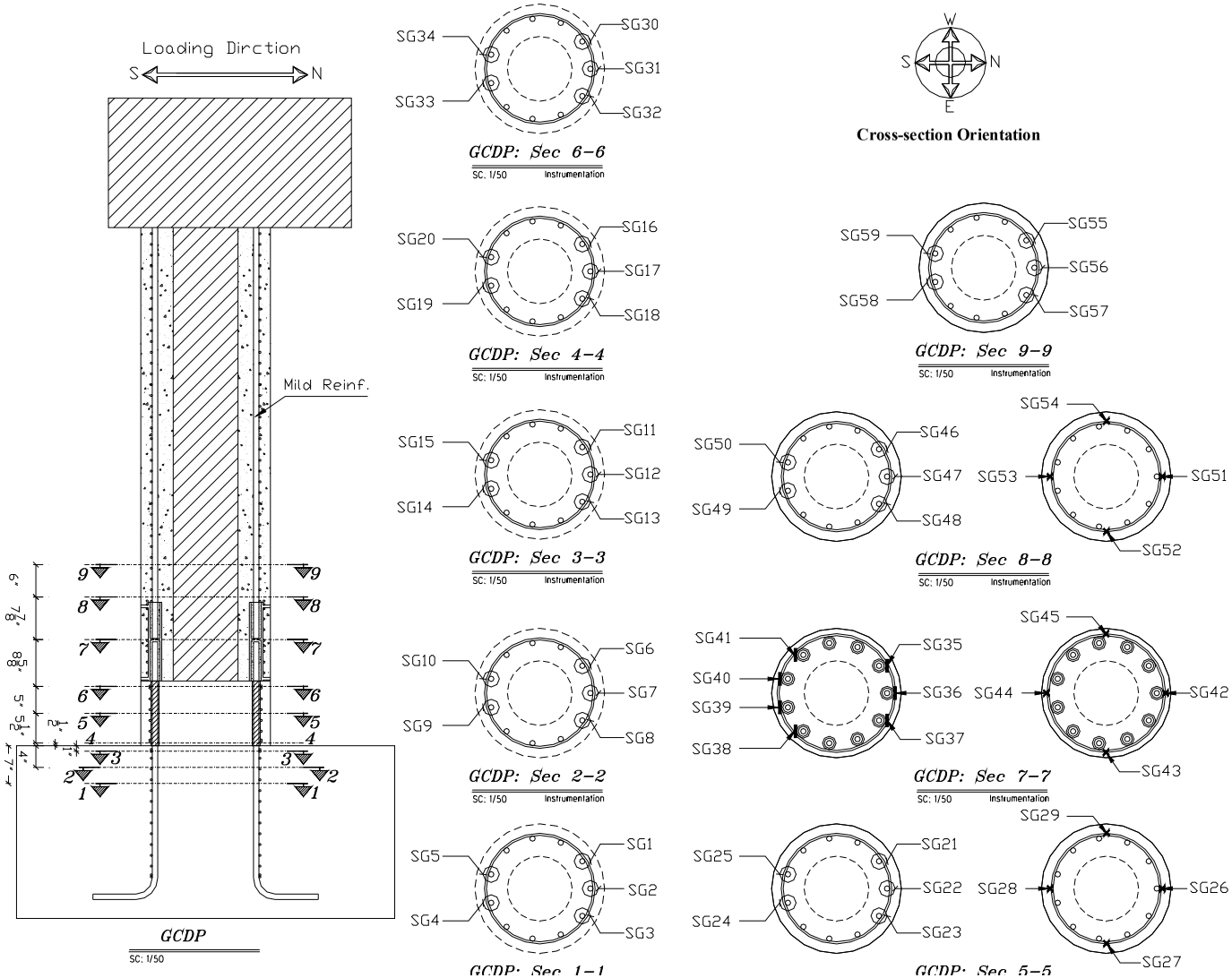

Figure 3.36- Location of Strain Gauges in GCDP Column (1 *in.*=25.4 *mm*)

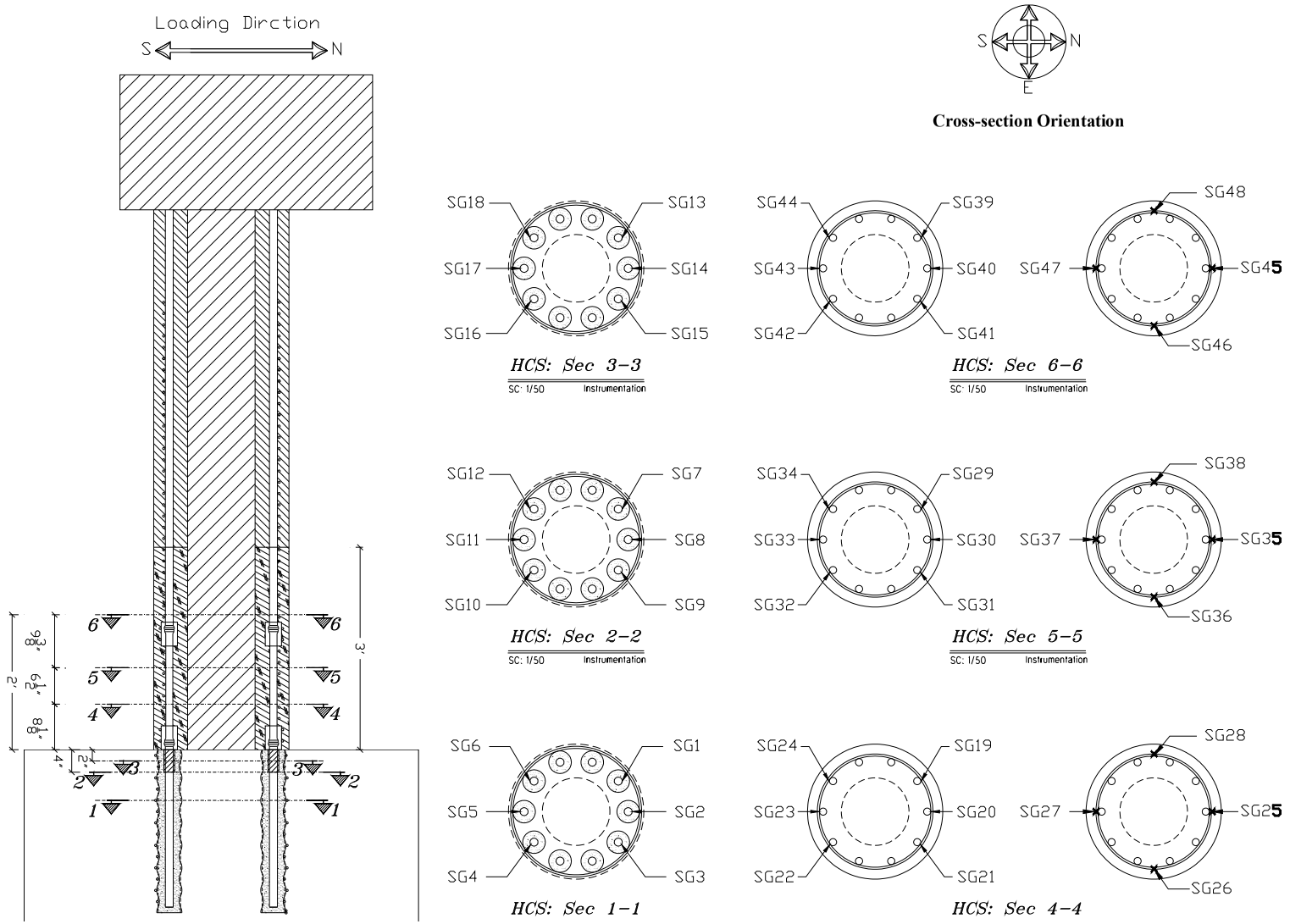

Figure 3.37- Location of Strain Gauges in HCS Column (1 *in.*=25.4 *mm*)

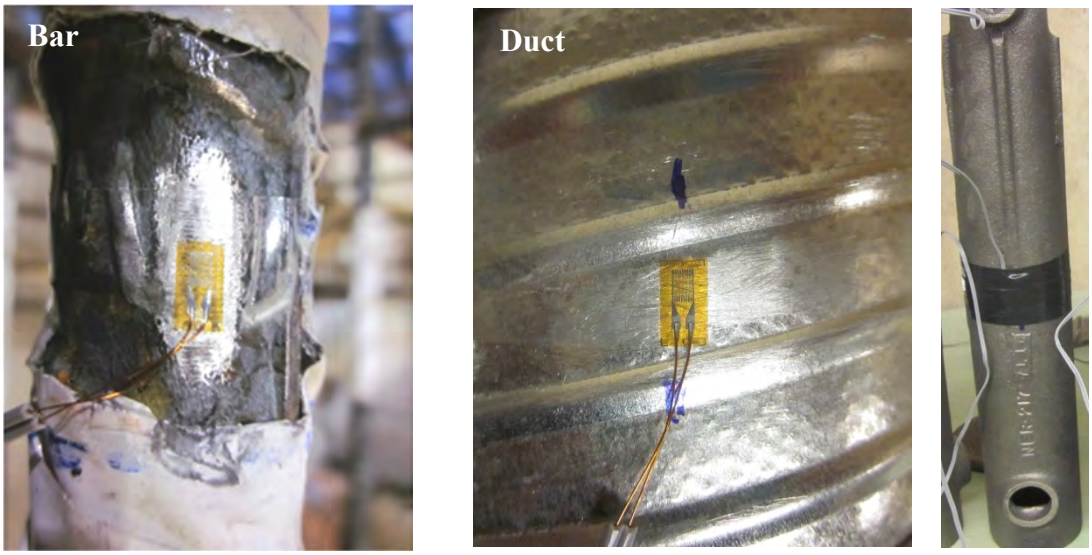

Figure 3.38- Installing Strain Gauges on Bar, Duct, and Grouted Coupler

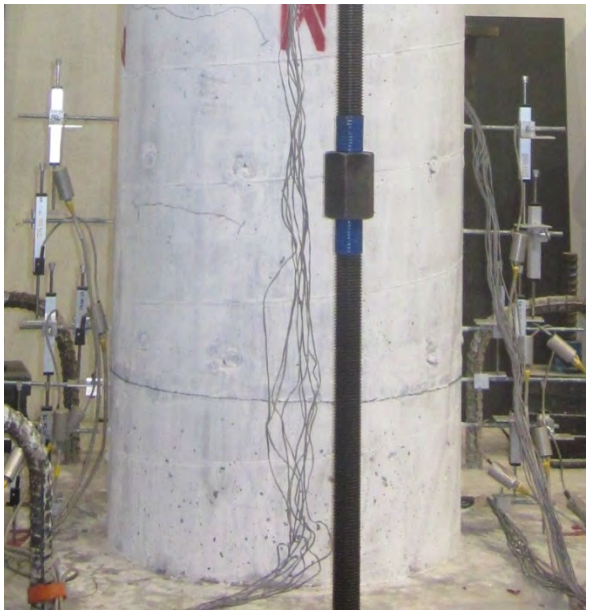

Figure 3.39- Displacement Measurement at Opposite Faces of Columns in Plastic Hinge

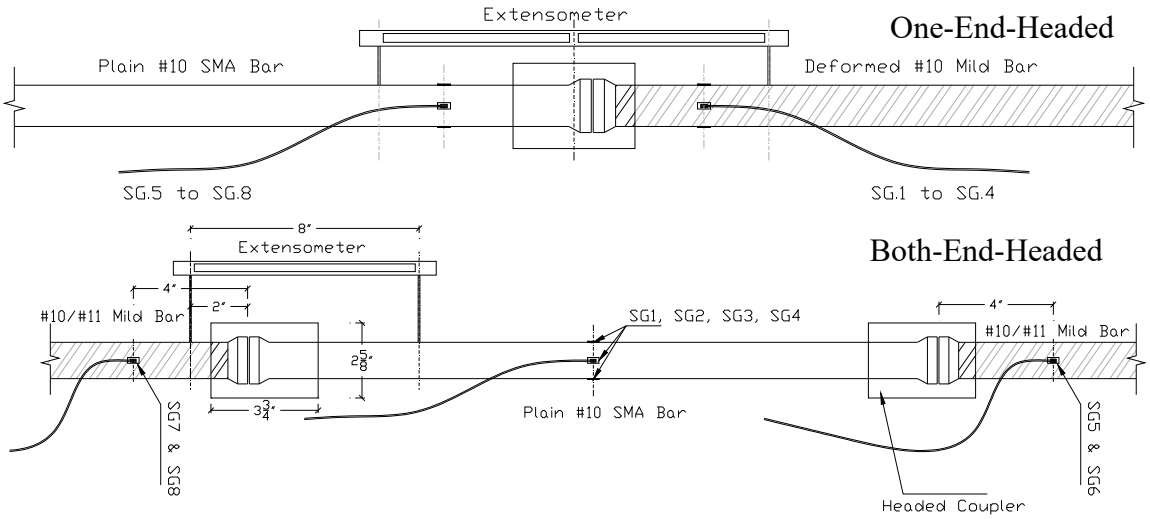

Figure 3.40- Instrumentation Plan for SMA-Steel Bar Connection Tests (1 *in*.=25.4 *mm*)

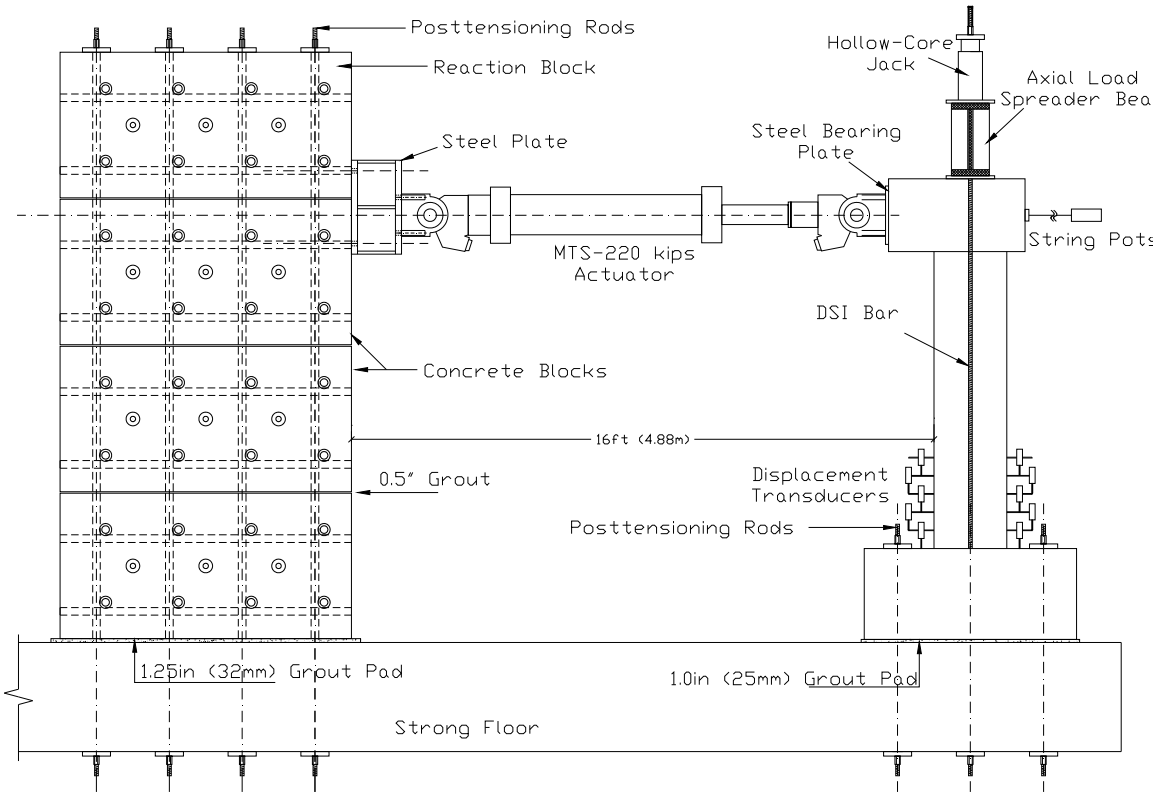

(a) Elevation View

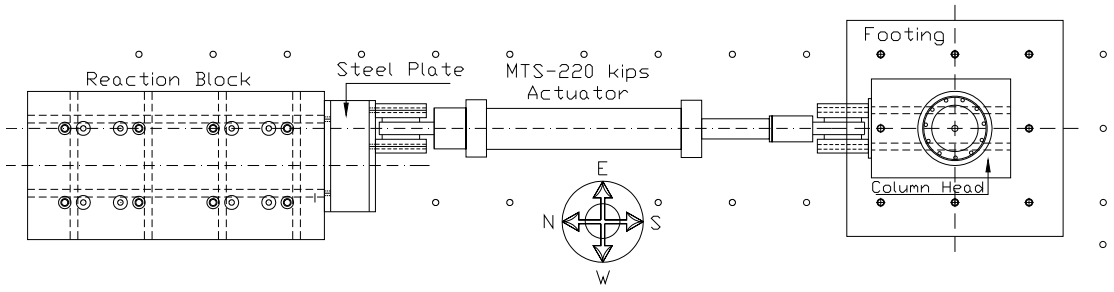

(b) Plan View

Figure 3.41- Column Test Setup

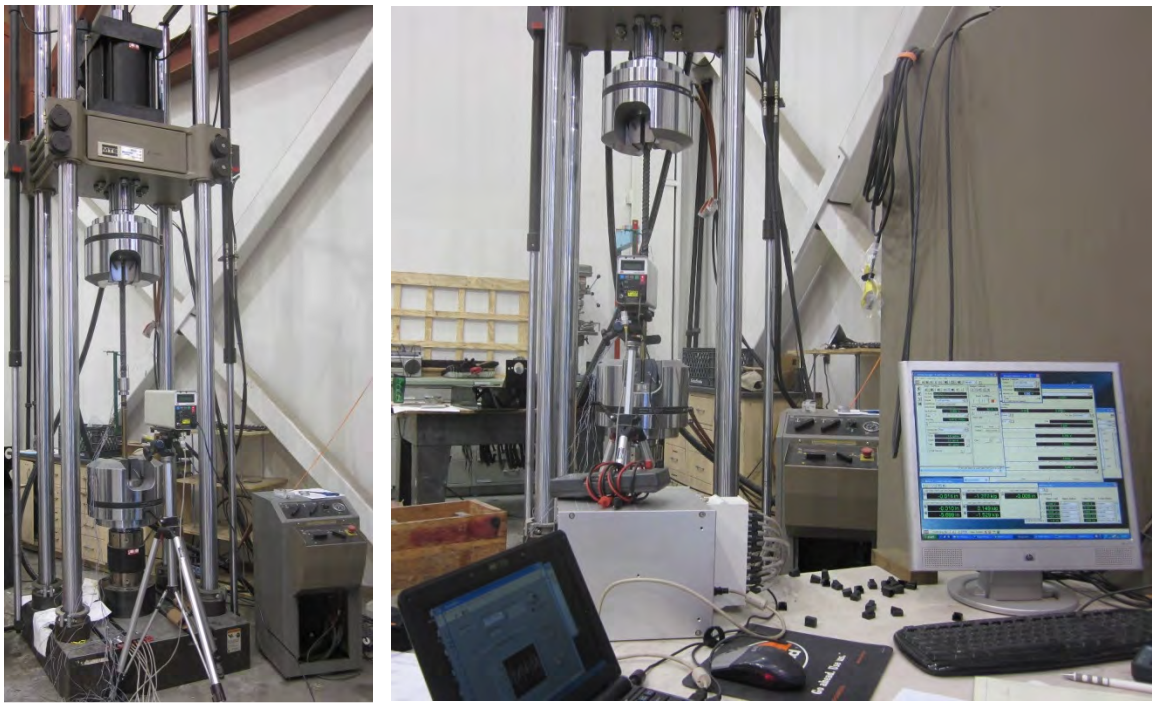

Figure 3.42- SMA-Steel Bar Connection Test Setup

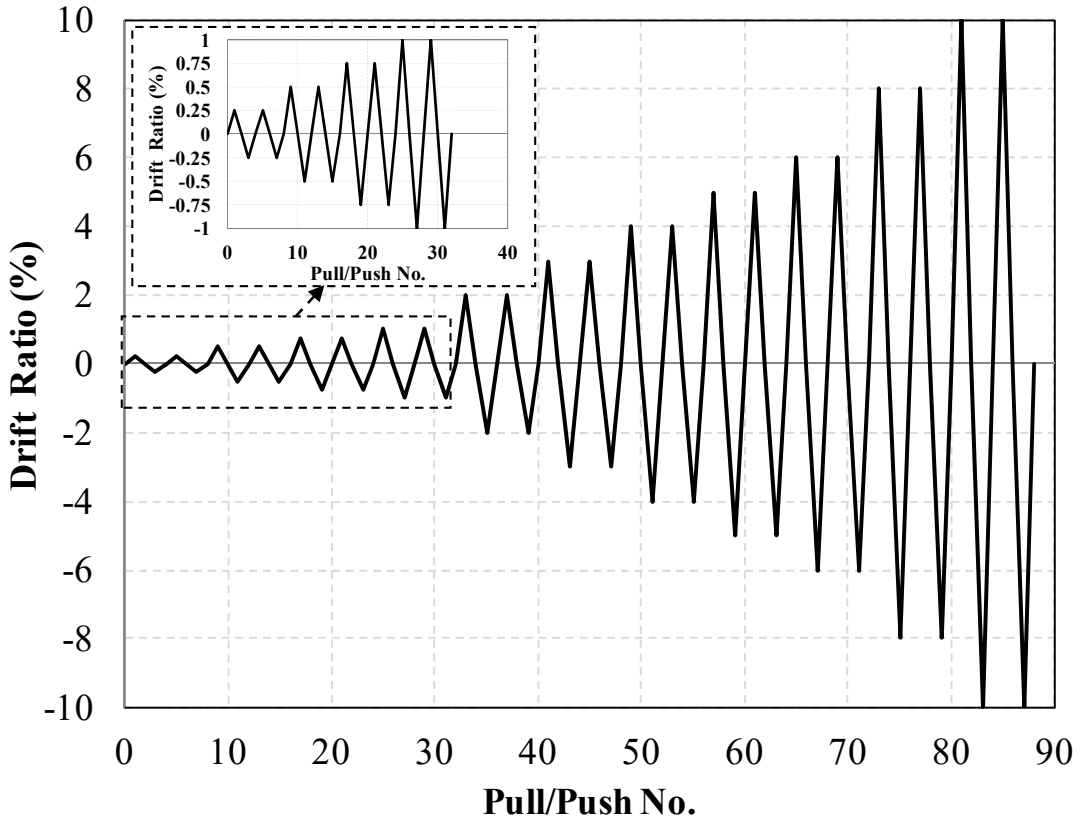

Figure 3.43- Column Test Loading Protocol

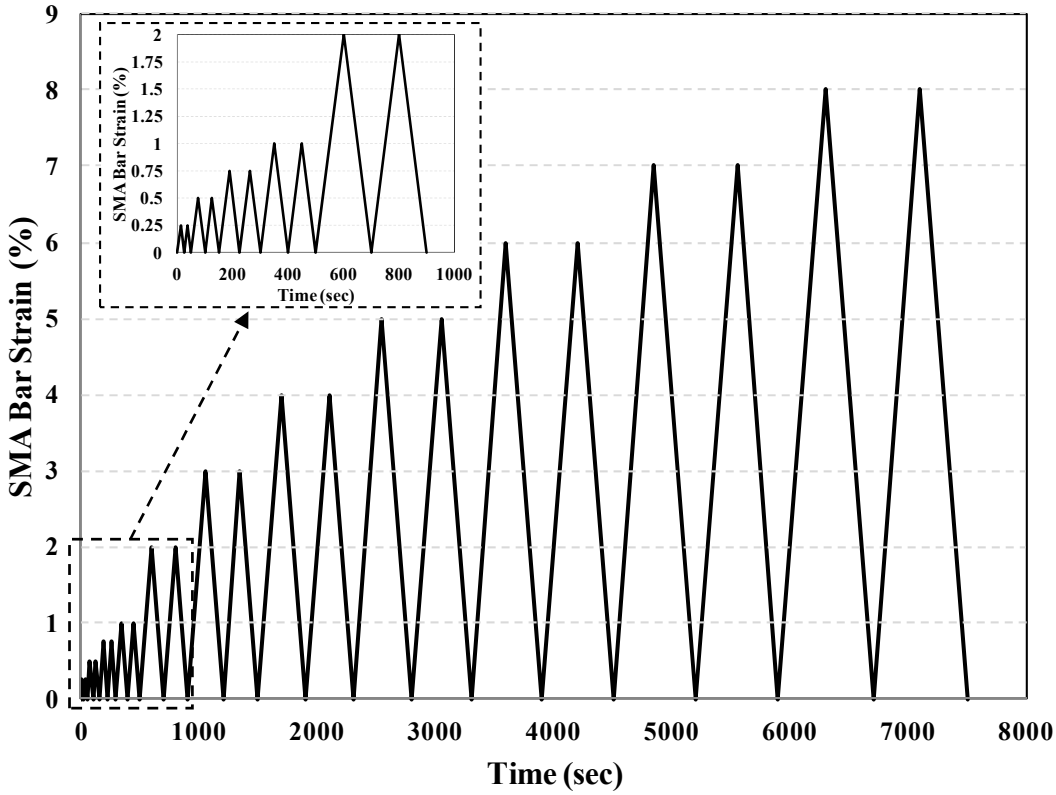

Figure 3.44- SMA-Steel Bar Connection Test Loading Protocol

(a) Saw Cutting

(b) End Grinding

Figure 4.1- UHPC Sample End Preparation

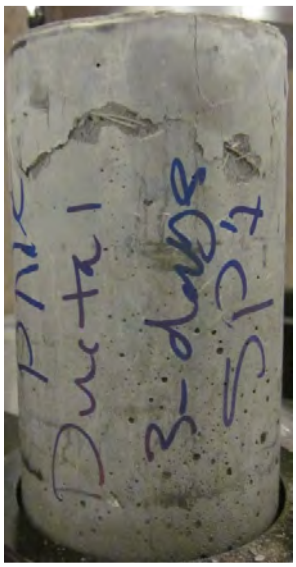

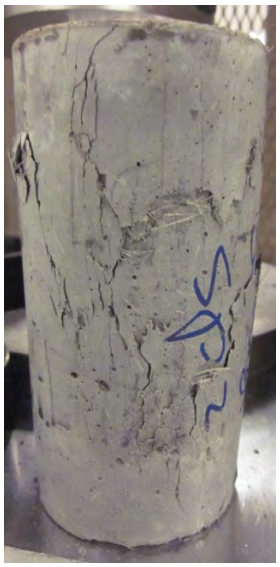

Figure 4.2- UHPC Compressive Mode of Failure

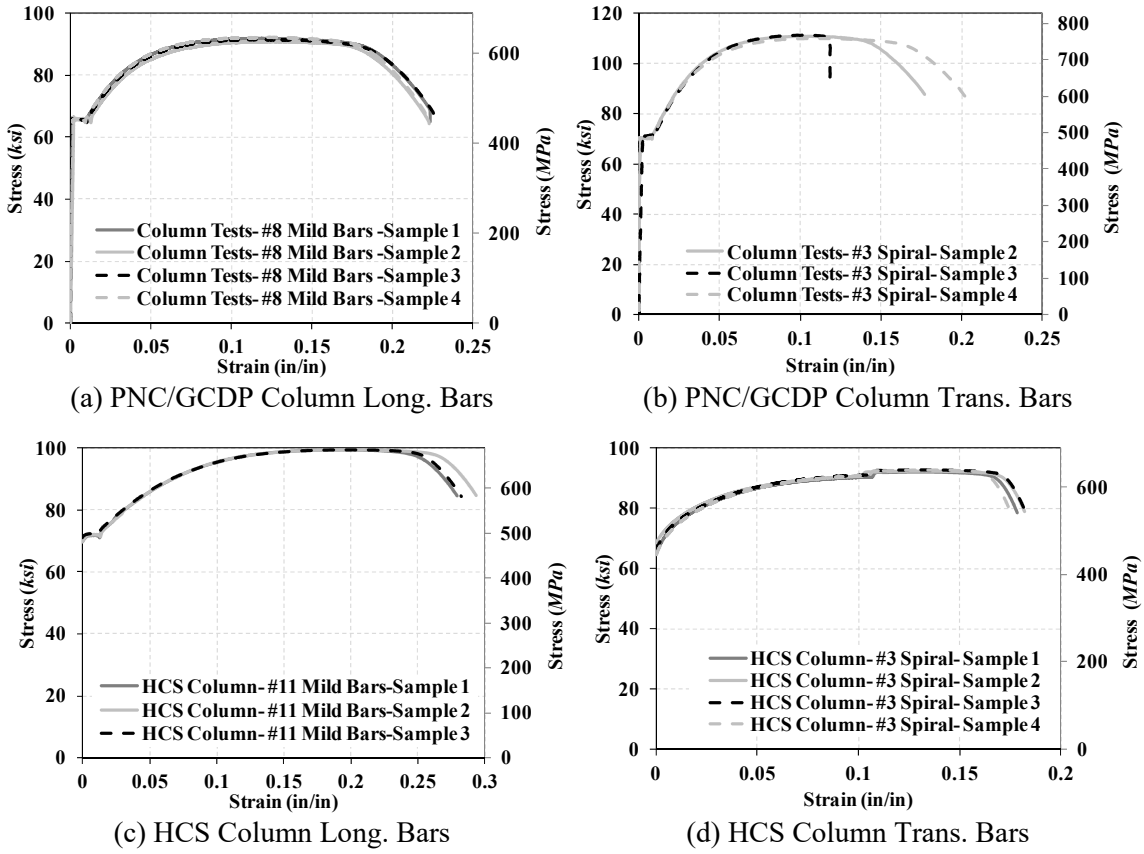

(a) PNC/GCDP Column Long. Bars (b) PNC/GCDP Column Trans. Bars

(c) HCS Column Long. Bars (d) HCS Column Trans. Bars

Figure 4.3- Measured Stress-Strain Curves of Reinforcing Steel Used in Columns

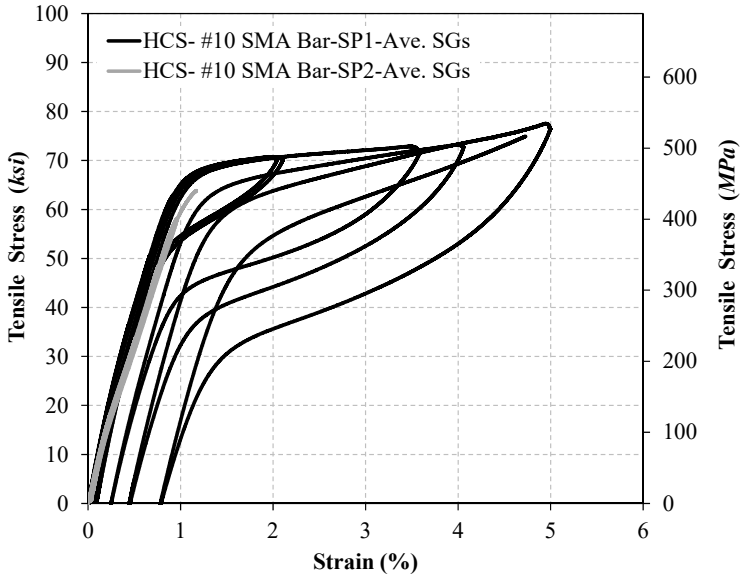

Figure 4.4- Measured Stress-Strain Curves for Reinforcing SMA #10 Bars Used in HCS

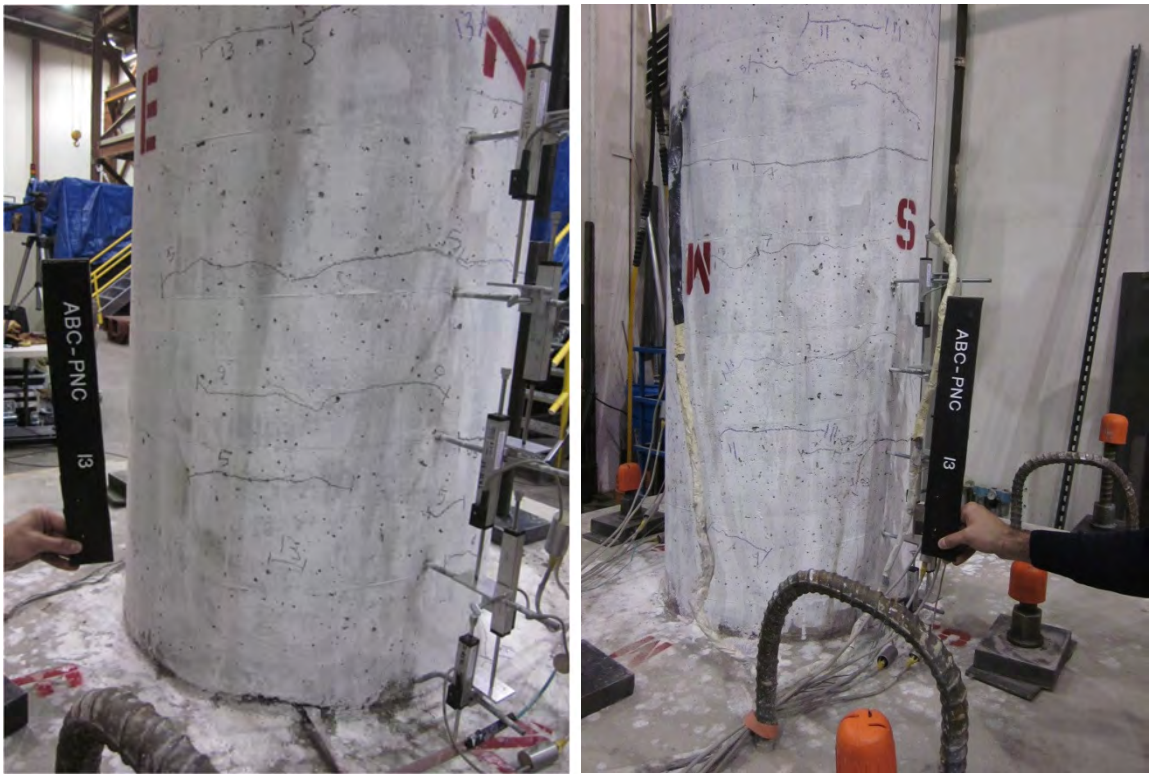

(a) North-East Side (b) South-West Side

Figure 4.5- PNC Column Plastic Hinge Damage, Second Push of 0.5% Drift Cycle

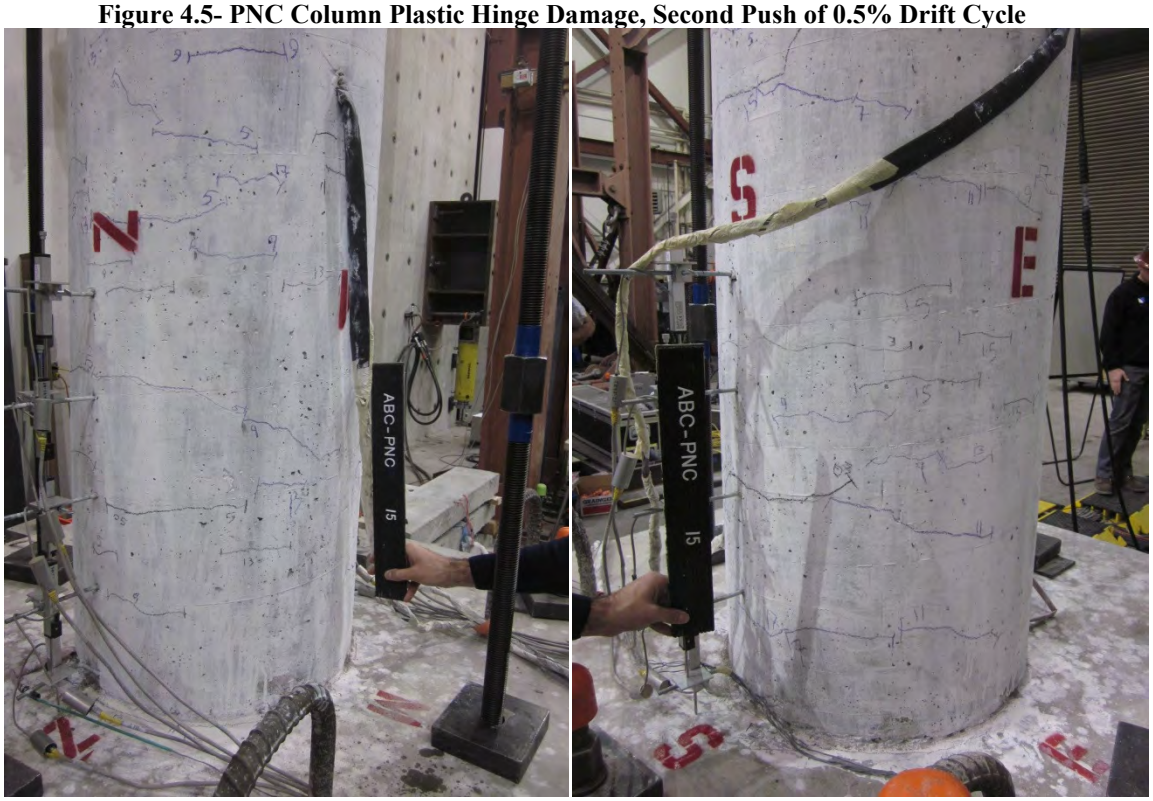

(a) North-West Side (b) South-East Side

Figure 4.6- PNC Column Plastic Hinge Damage, Second Pull of 0.5% Drift Cycle

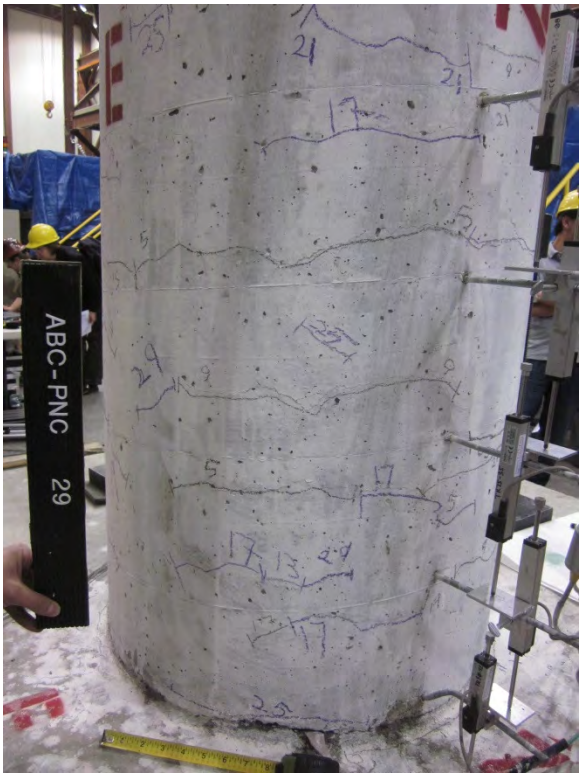

(a) North-East Side

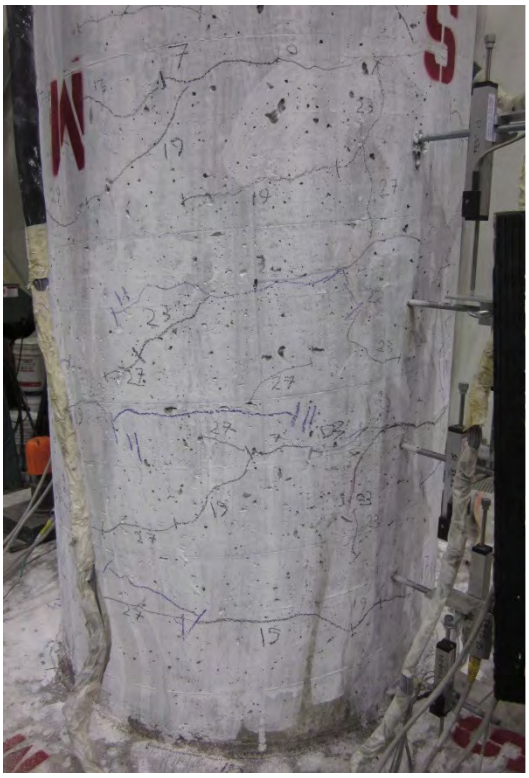

(b) South-West Side

Figure 4.7- PNC Column Plastic Hinge Damage, Second Push of 1.0% Drift Cycle

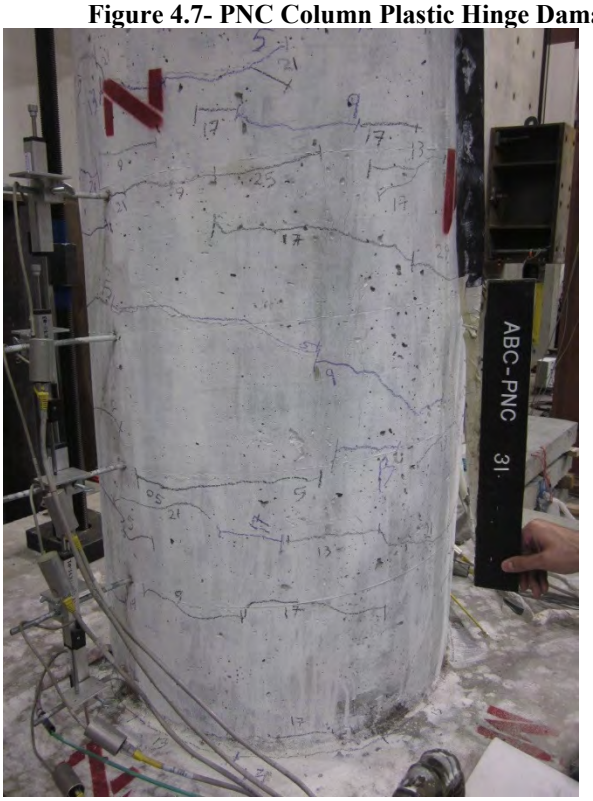

(a) North-West Side

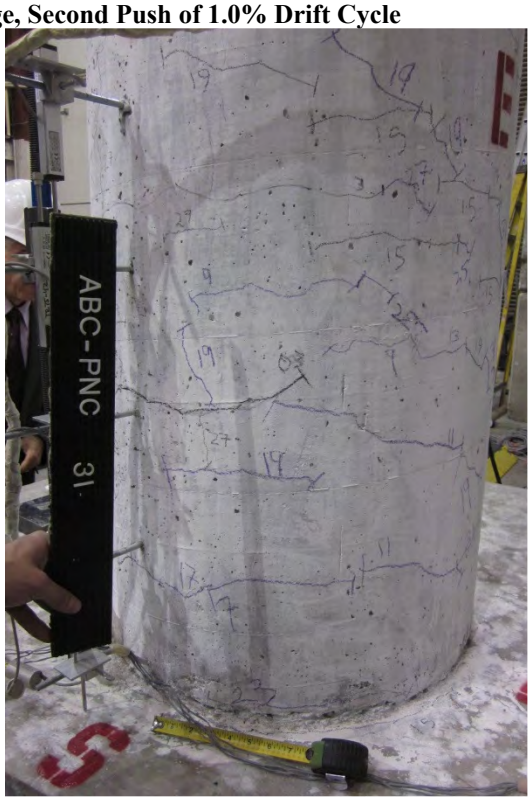

(b) South-East Side

Figure 4.8- PNC Column Plastic Hinge Damage, Second Pull of 1.0% Drift Cycle

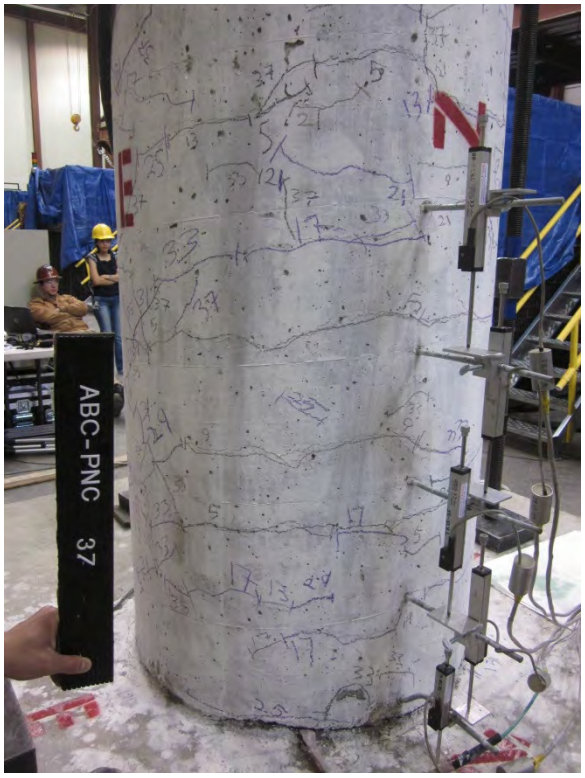

(a) North-East Side

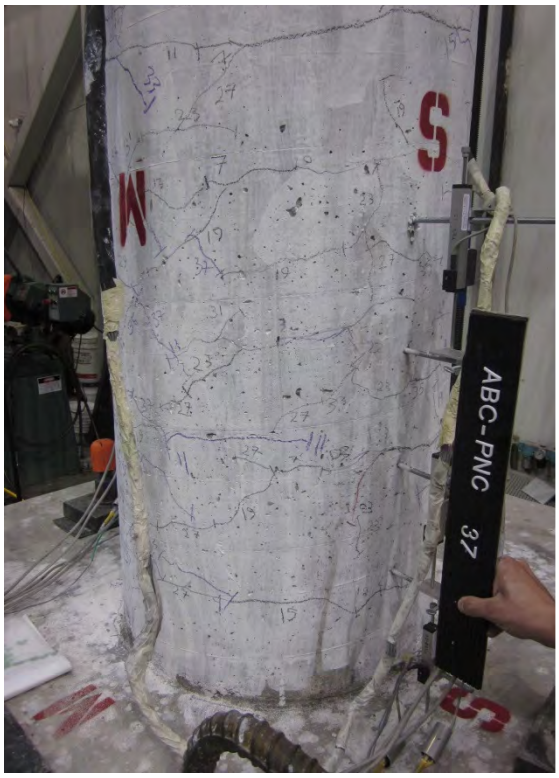

(b) South-West Side

Figure 4.9- PNC Column Plastic Hinge Damage, Second Push of 2.0% Drift Cycle

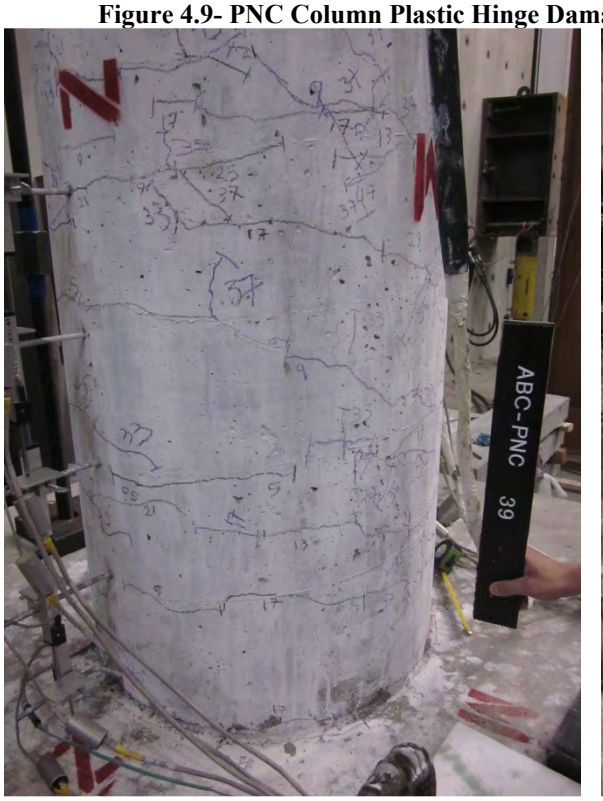

(a) North-West Side

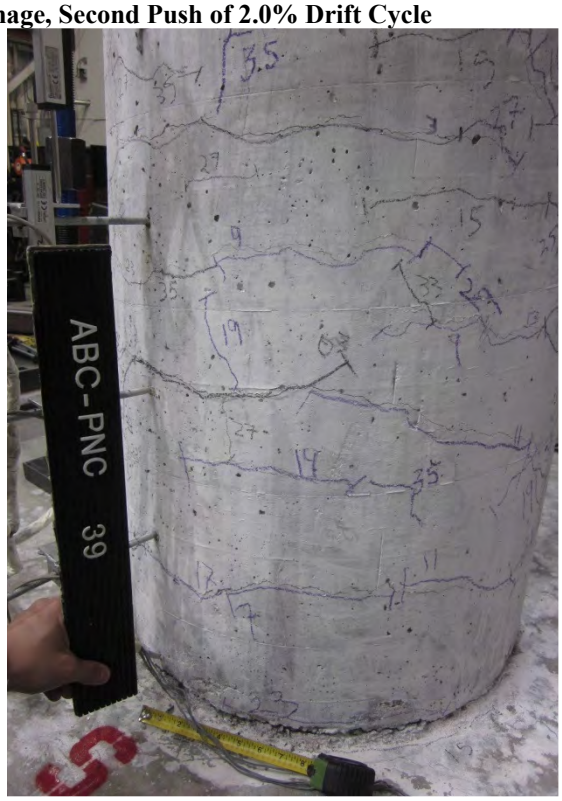

(b) South-East Side

Figure 4.10- PNC Column Plastic Hinge Damage, Second Pull of 2.0% Drift Cycle

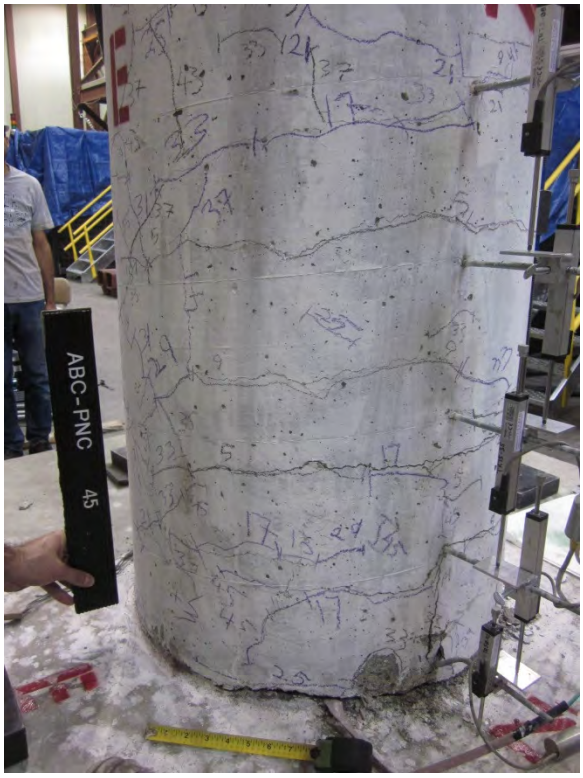

(a) North-East Side

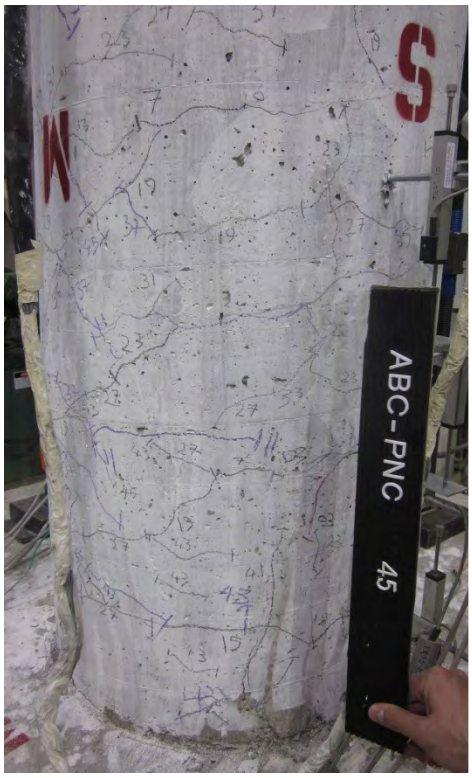

(b) South-West Side

Figure 4.11- PNC Column Plastic Hinge Damage, Second Push of 3.0% Drift Cycle

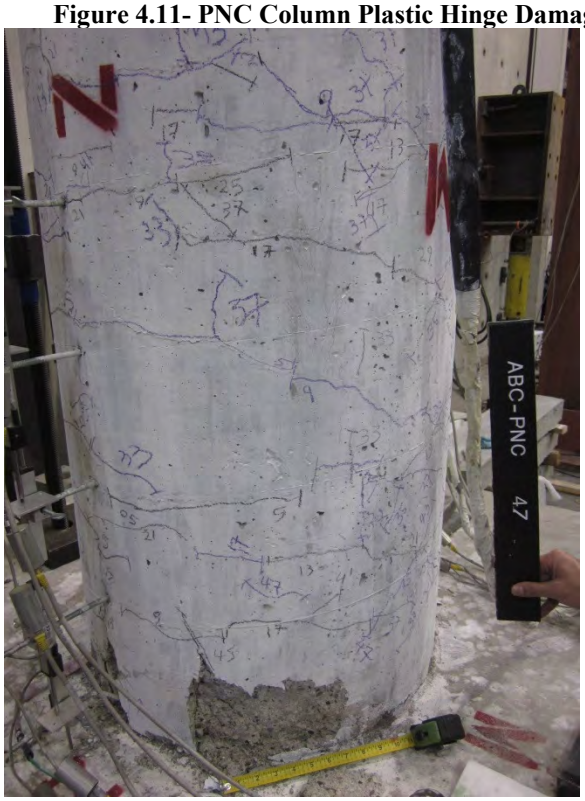

(a) North-West Side

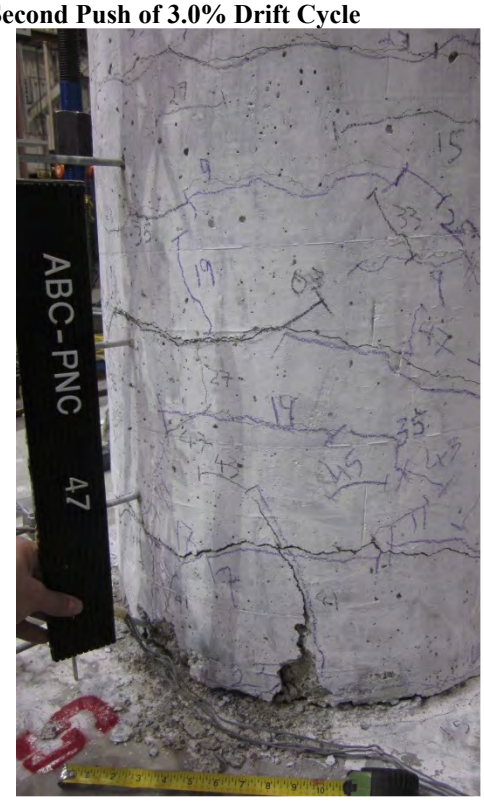

(b) South-East Side

Figure 4.12- PNC Column Plastic Hinge Damage, Second Pull of 3.0% Drift Cycle

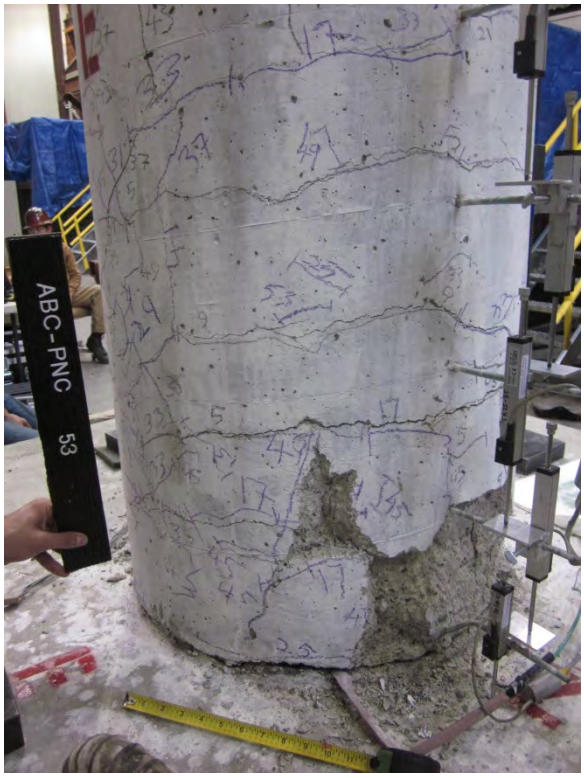

(a) North-East Side

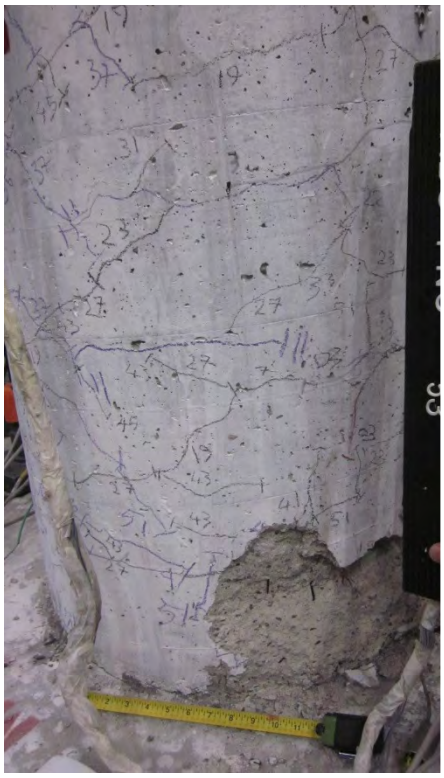

(b) South-West Side

Figure 4.13- PNC Column Plastic Hinge Damage, Second Push of 4.0% Drift Cycle

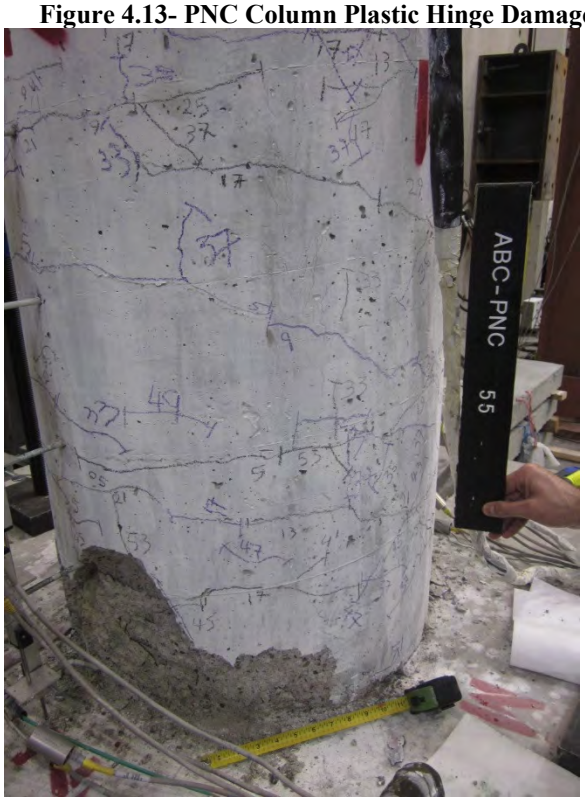

(a) North-West Side

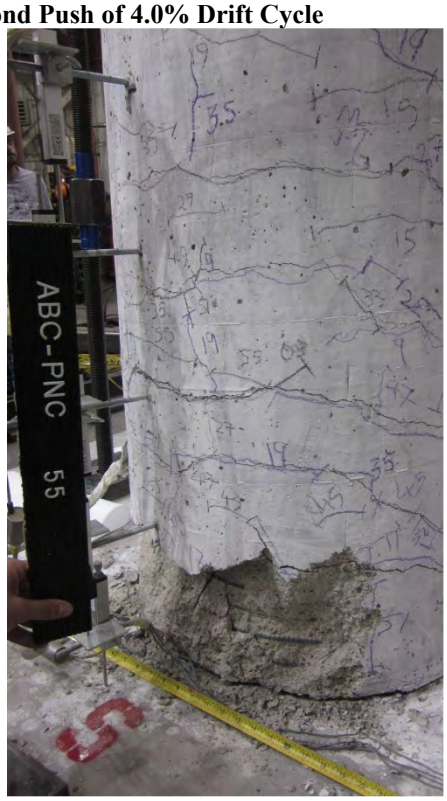

(b) South-East Side

Figure 4.14- PNC Column Plastic Hinge Damage, Second Pull of 4.0% Drift Cycle

(a) North-East Side (b) South-West Side

Figure 4.15- PNC Column Plastic Hinge Damage, Second Push of 5.0% Drift Cycle

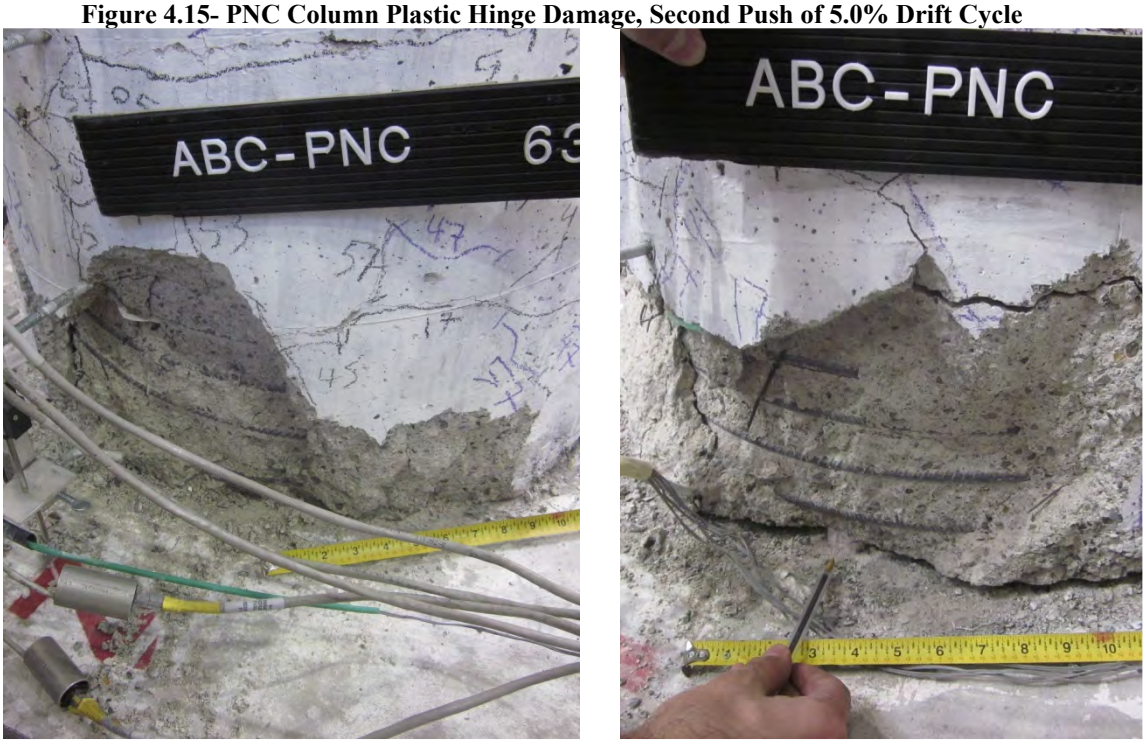

(a) North-West Side (b) South-East Side

Figure 4.16- PNC Column Plastic Hinge Damage, Second Pull of 5.0% Drift Cycle

(a) North-East Side

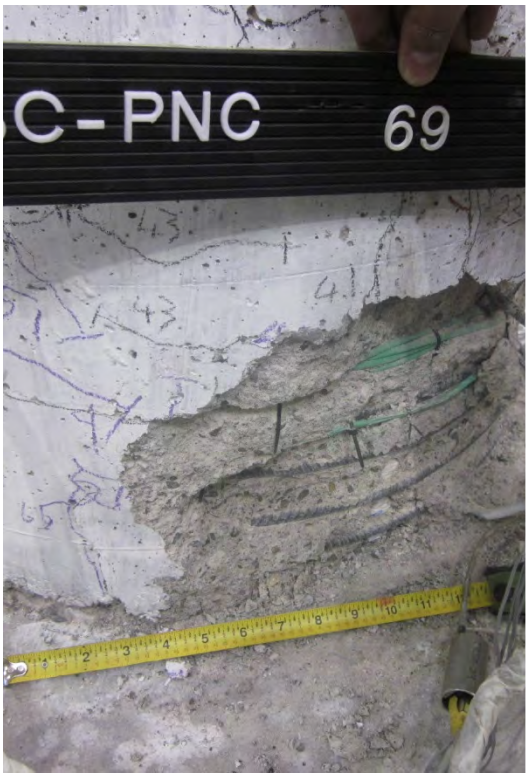

(b) South-West Side

Figure 4.17- PNC Column Plastic Hinge Damage, Second Push of 6.0% Drift Cycle

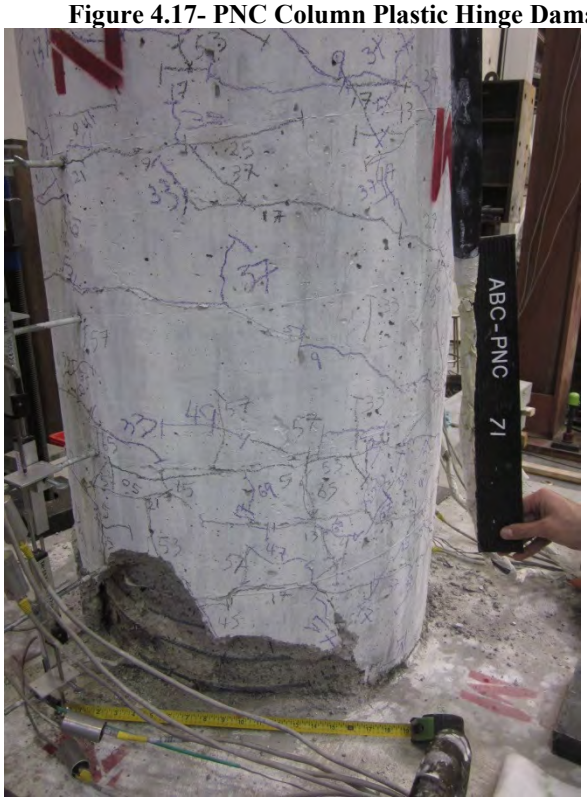

(a) North-West Side

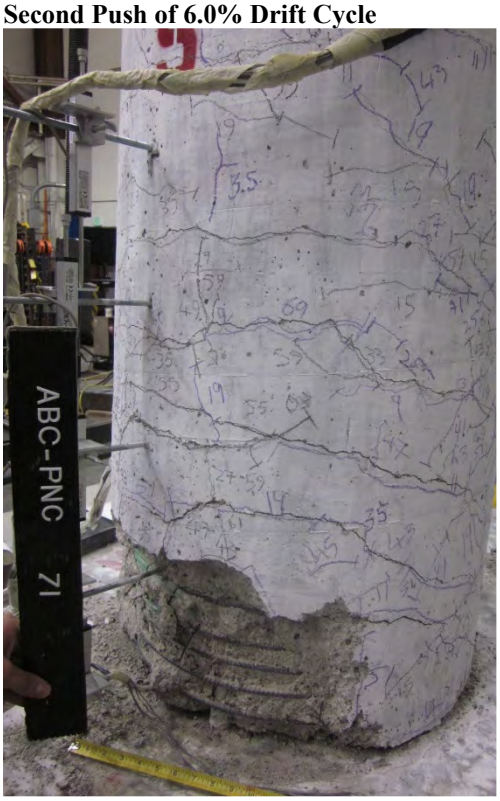

(b) South-East Side

Figure 4.18- PNC Column Plastic Hinge Damage, Second Pull of 6.0% Drift Cycle

(a) North-East Side (b) South-West Side

Figure 4.19- PNC Column Plastic Hinge Damage, Second Push of 8.0% Drift Cycle

(a) North-West Side (b) South-East Side

Figure 4.20- PNC Column Plastic Hinge Damage at Second Pull of 8.0% Drift Cycle

(a) North-East Side (b) South-West Side

Figure 4.21- PNC Column Plastic Hinge Damage, Push of 10.0% Drift Cycle

(a) North-West Side (b) South-East Side

Figure 4.22- PNC Column Plastic Hinge Damage, Pull of 10.0% Drift Cycle

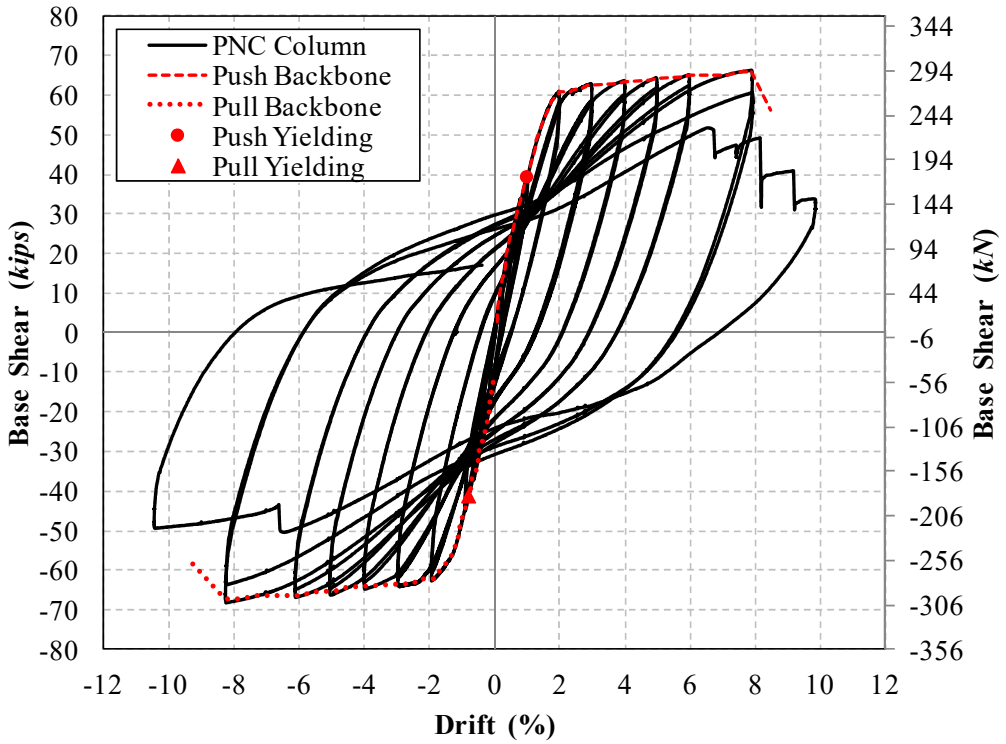

Figure 4.23- PNC Column Force-Drift Hysteretic and Envelope Responses

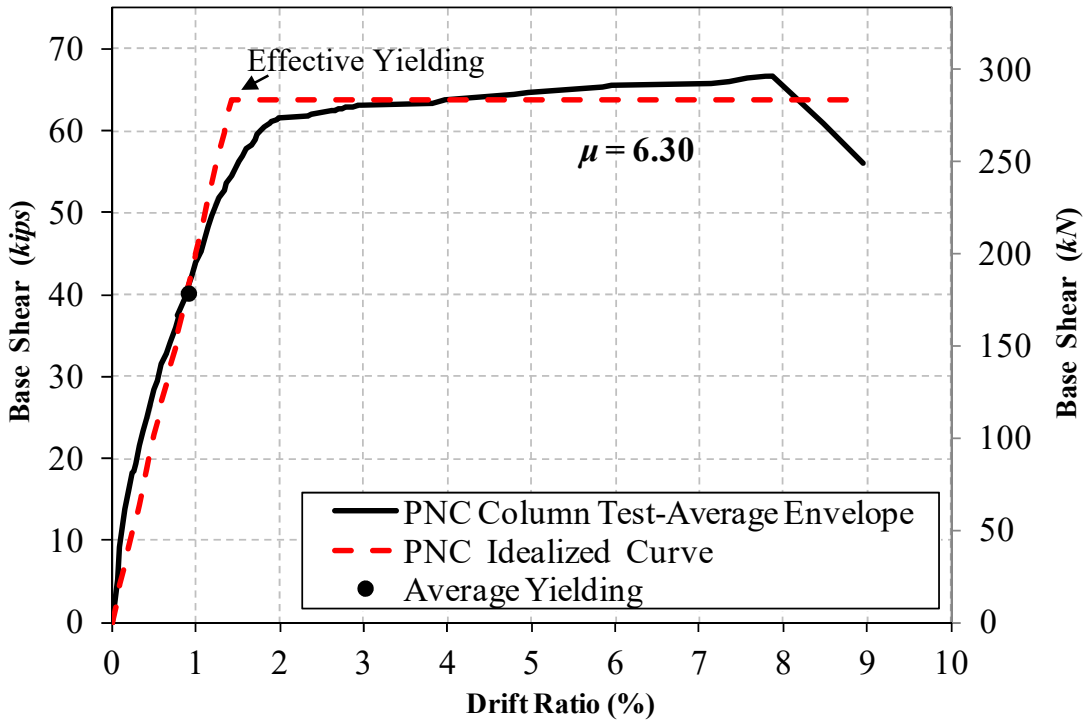

Figure 4.24- PNC Column Average Push/Pull Force-Displacement Envelope and Idealized Curve

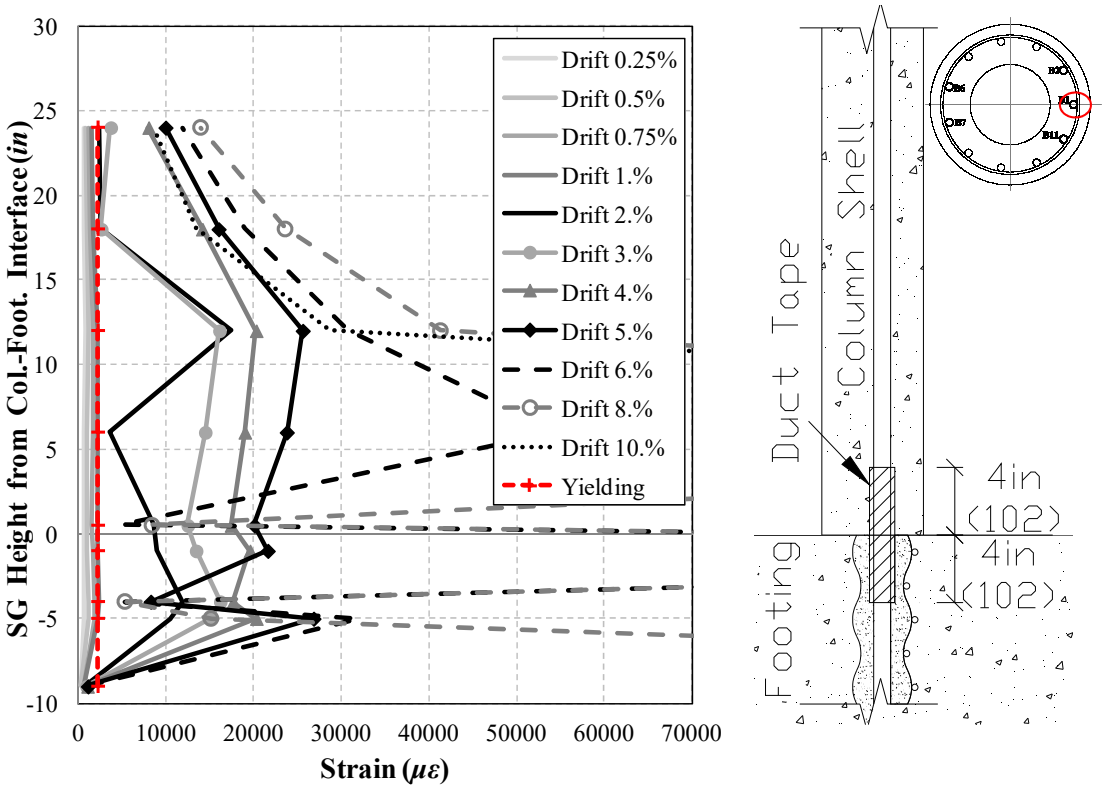

Figure 4.25- Strain Profile for PNC Column Bar B1 (1 *in*.= 25.4 *mm*)

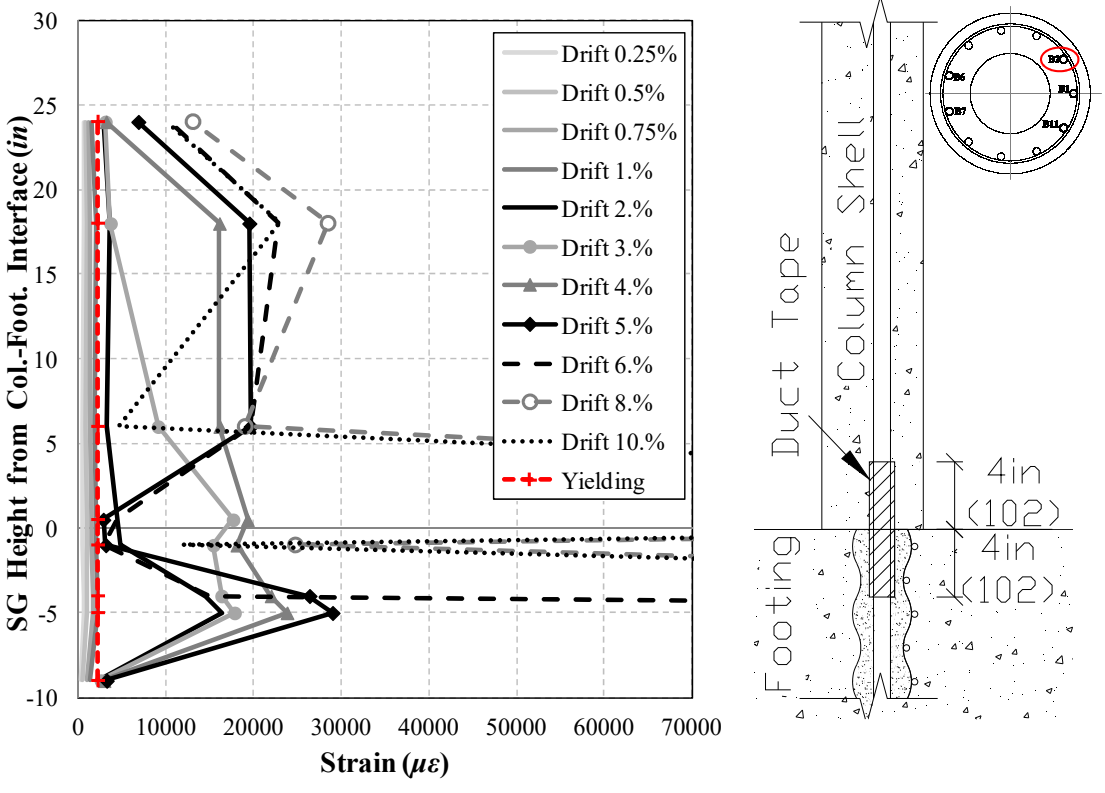

Figure 4.26- Strain Profile for PNC Column Bar B2 (1 *in*.= 25.4 *mm*)

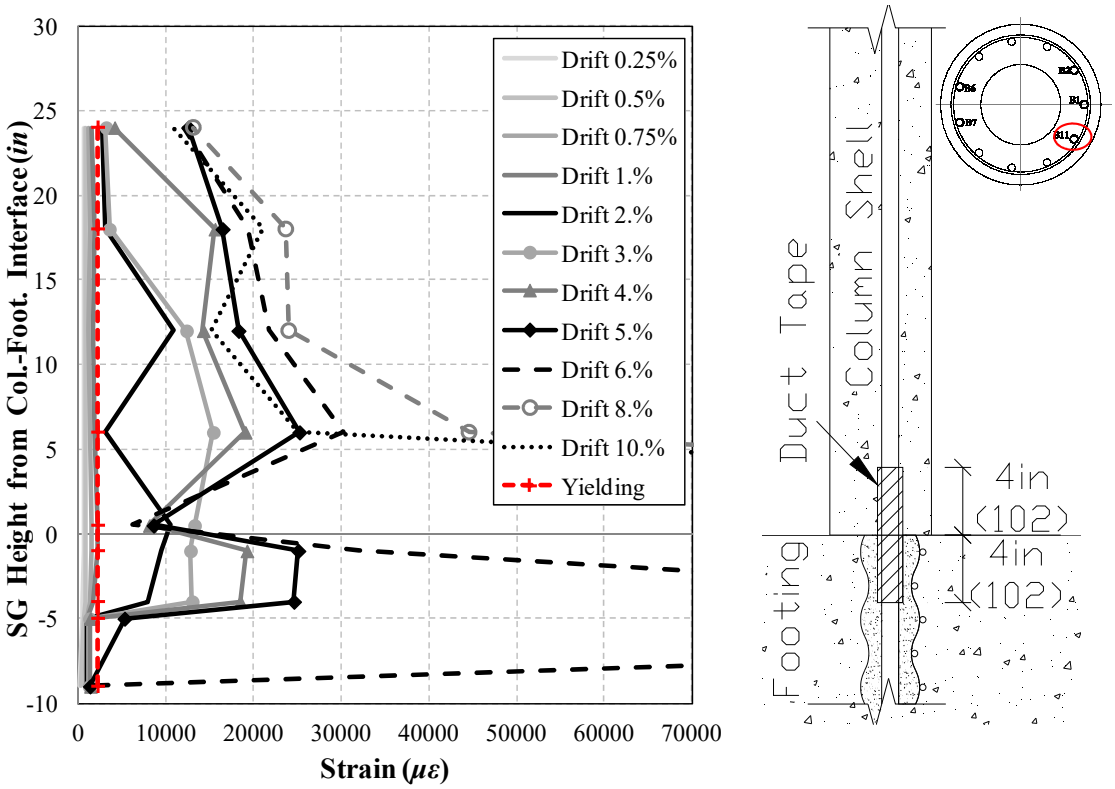

Figure 4.27- Strain Profile for PNC Column Bar B11 (1 *in.*= 25.4 *mm*)

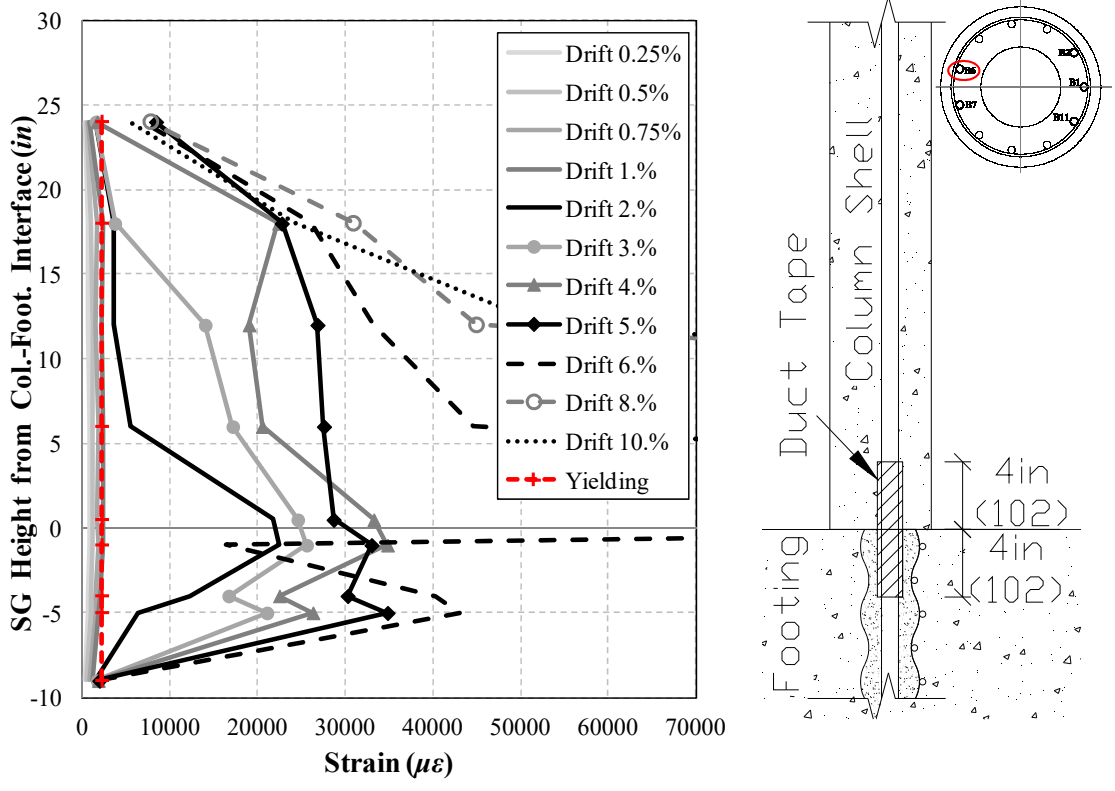

Figure 4.28- Strain Profile for PNC Column Bar B6 (1 *in.*= 25.4 *mm*)

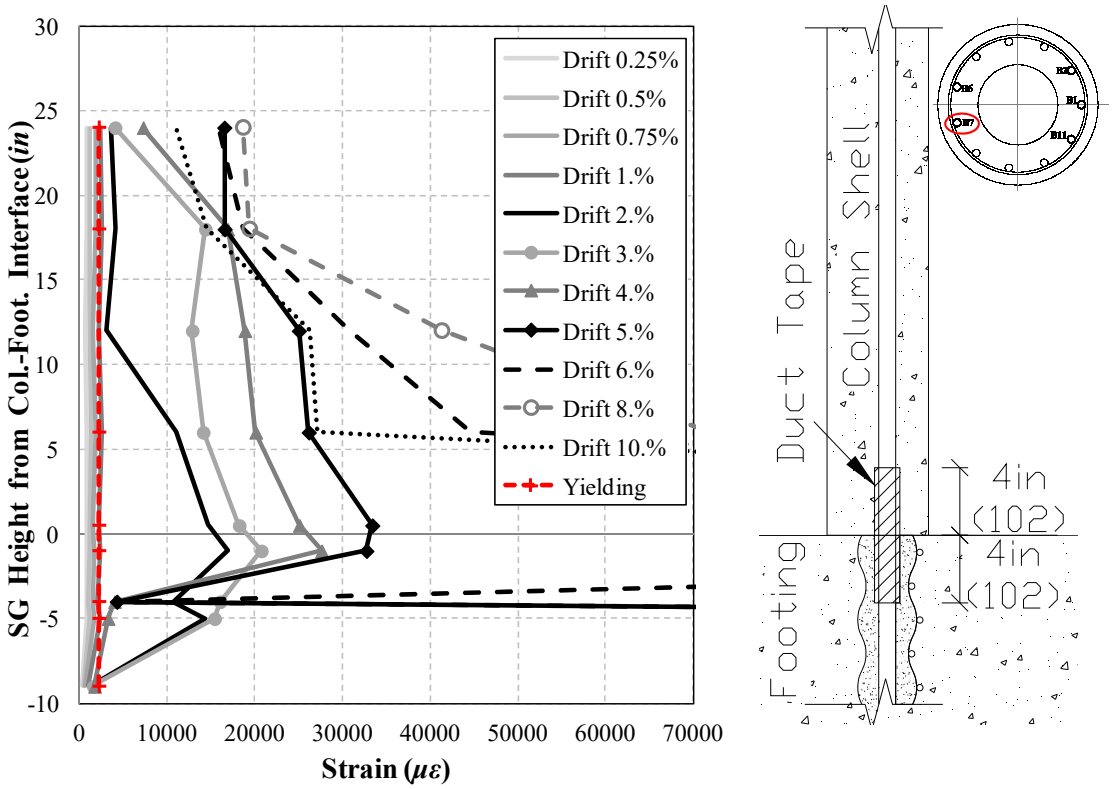

Figure 4.29- Strain Profile for PNC Column Bar B7 (1 *in*.= 25.4 *mm*)

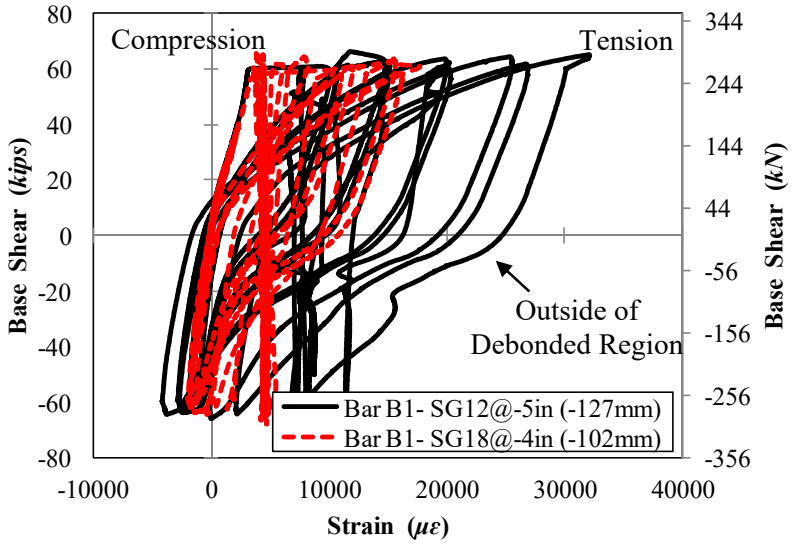

Figure 4.30- Force-Strain Hysteresis for PNC Column Bar B1

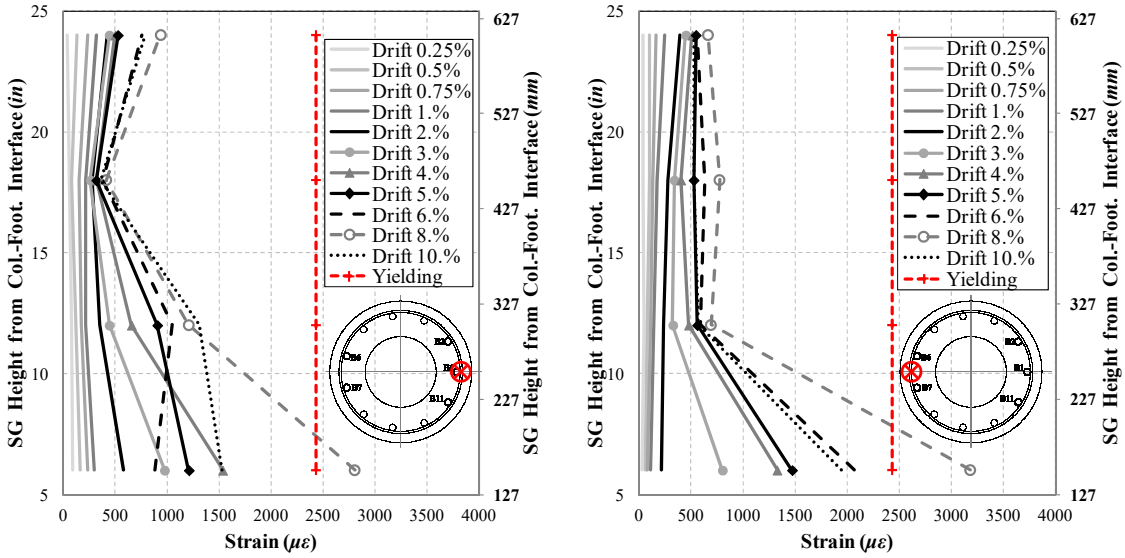

(a) North-Side of Column (b) South-Side of Column

Figure 4.31- Strain Profile for PNC Column Spiral in Compressive Zone

Instrumentation Plan	
Test Lable	Instrument
BS01	TR75-01
BS02	TR75-05
C01	TR50-42
C02	TR75-35
C03	TR75-03
C04	TR75-08
C05	TR50-34
C06	TR75-15
C07	TR75-42
C08	TR75-25
D01	SP40
D02	SP39
D03	NONE
D04	SP38

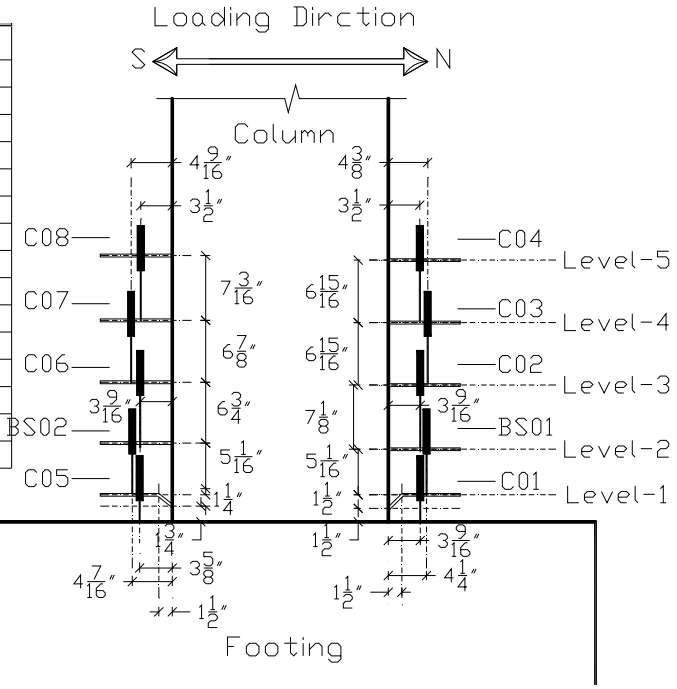

Figure 4.32- As-built Displacement Instrumentation Plan at Base of PNC Column (1 *in*.=25 *mm*)

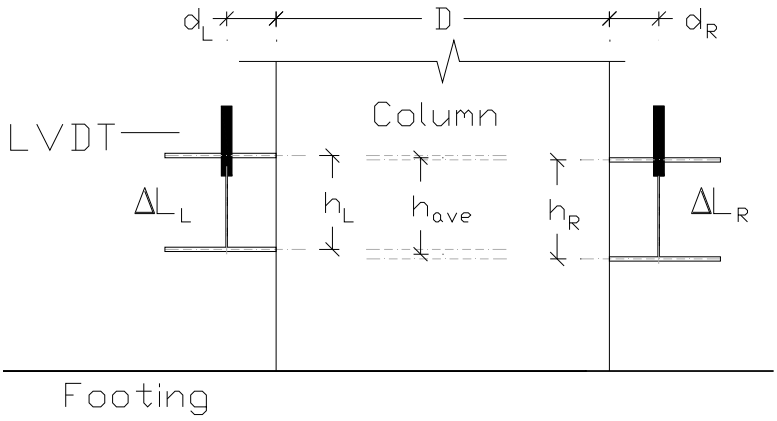

Figure 4.33- Parameter Definition for Curvature and Rotation Measurements

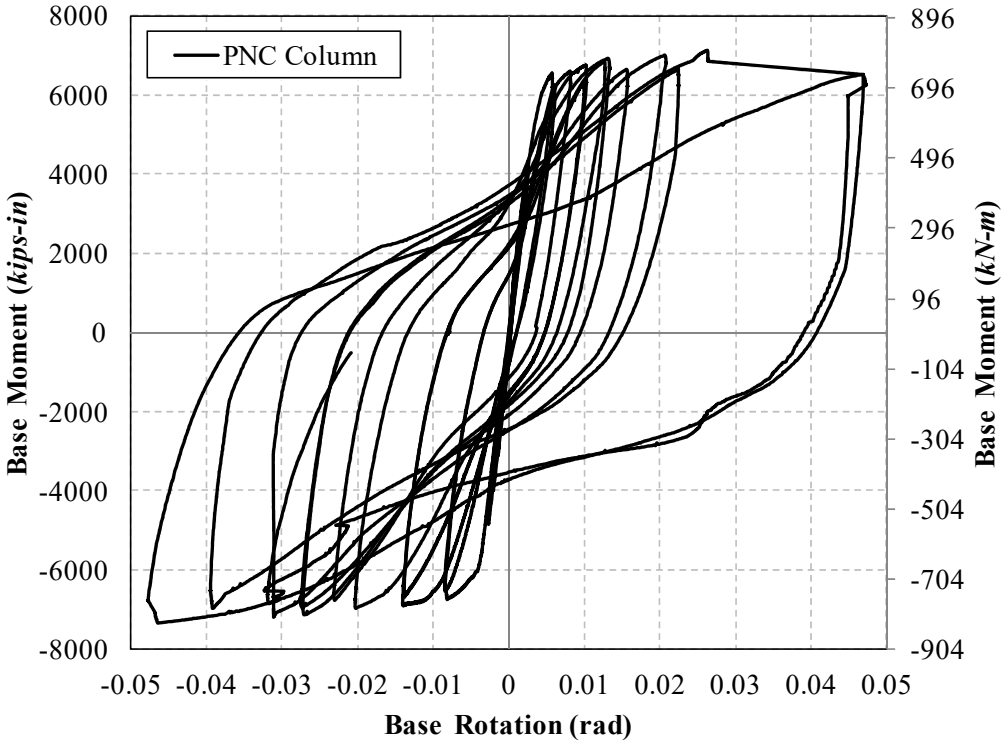

Figure 4.34- Base Moment-Rotation Relationship for PNC Column

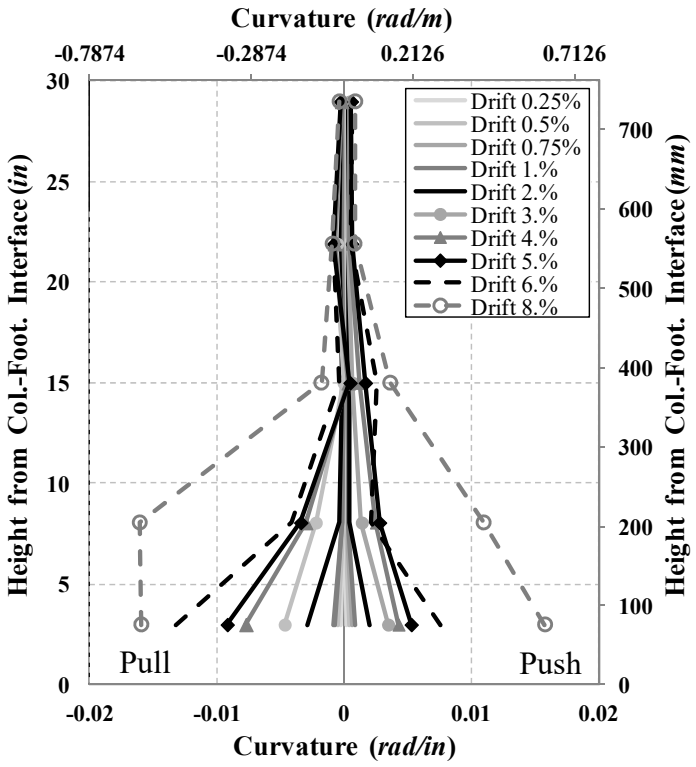

Figure 4.35- Curvature Profile for PNC Column

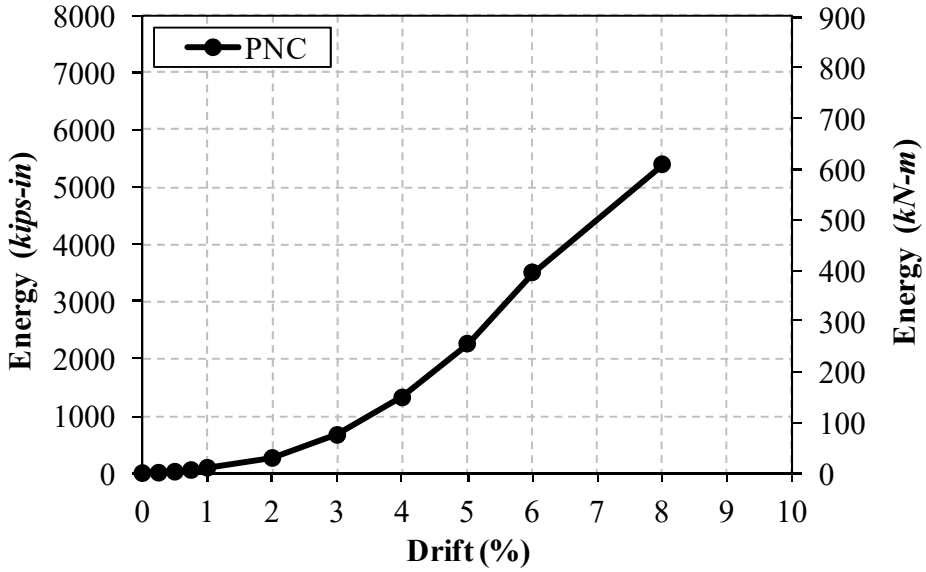

Figure 4.36- Energy Dissipation for PNC Column

(a) North-East Side (b) South-West Side

Figure 4.37- GCDP Column Plastic Hinge Damage, Second Push of 0.5% Drift Cycle

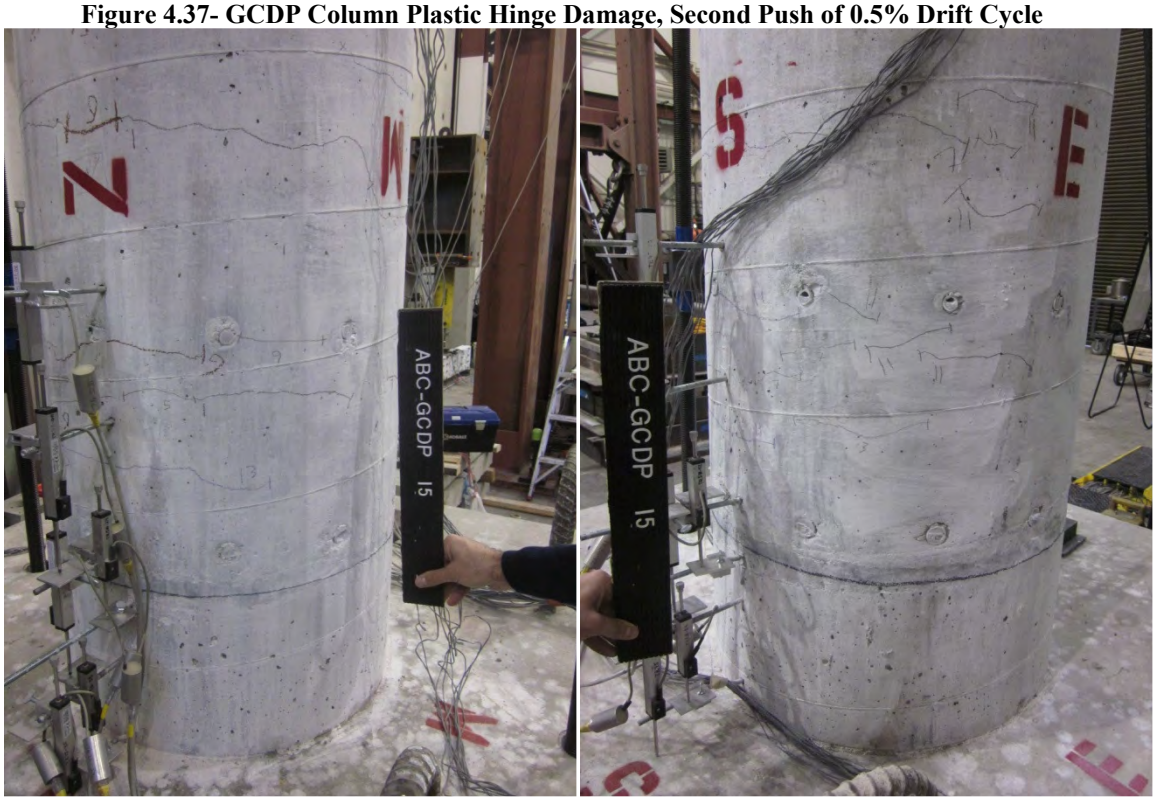

(a) North-West Side (b) South-East Side

Figure 4.38- GCDP Column Plastic Hinge Damage, Second Pull of 0.5% Drift Cycle

(a) North-East Side (b) South-West Side

Figure 4.39- GCDP Column Plastic Hinge Damage, Second Push of 1.0% Drift Cycle

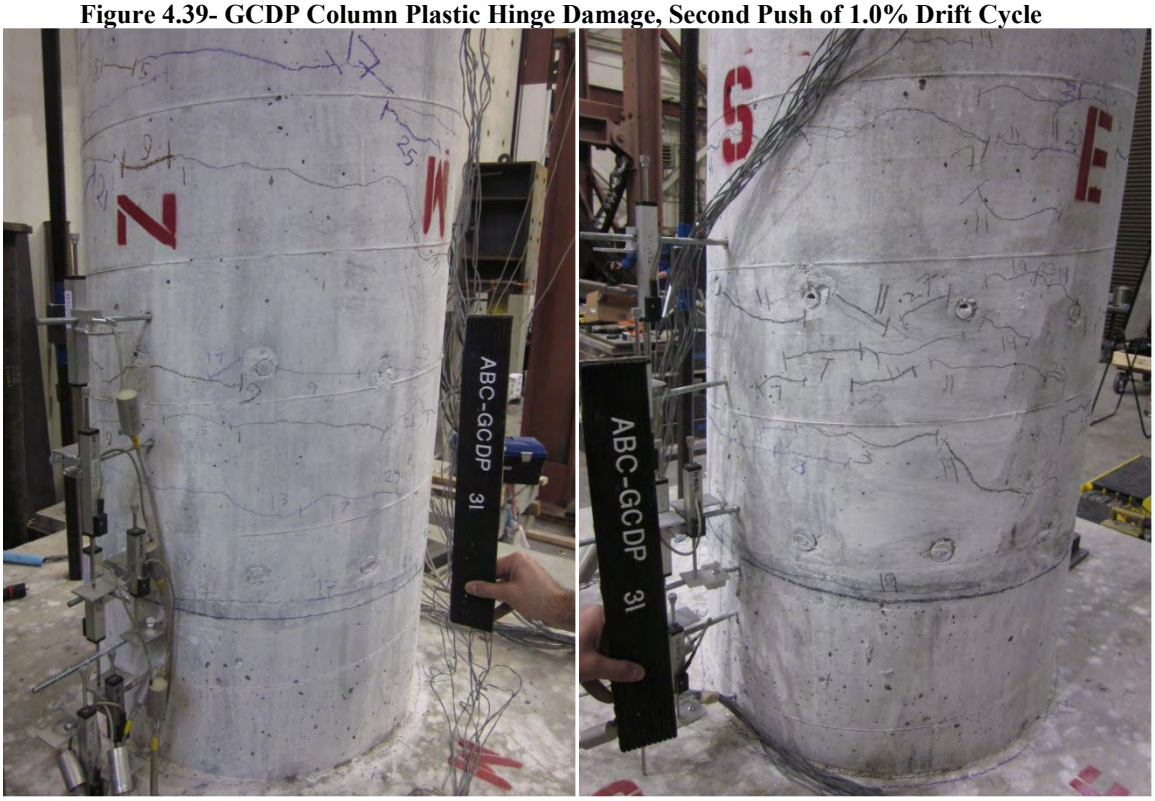

(a) North-West Side (b) South-East Side

Figure 4.40- GCDP Column Plastic Hinge Damage, Second Pull of 1.0% Drift Cycle

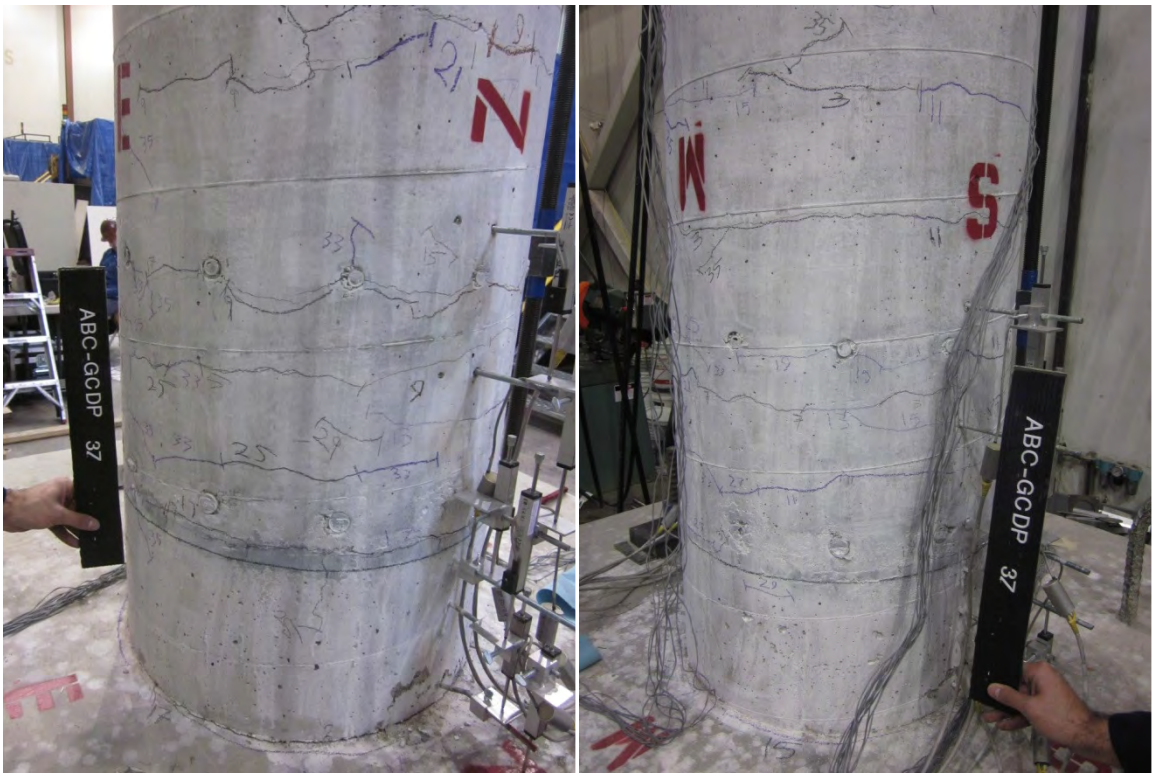

(a) North-East Side (b) South-West Side

Figure 4.41- GCDP Column Plastic Hinge Damage, Second Push of 2.0% Drift Cycle

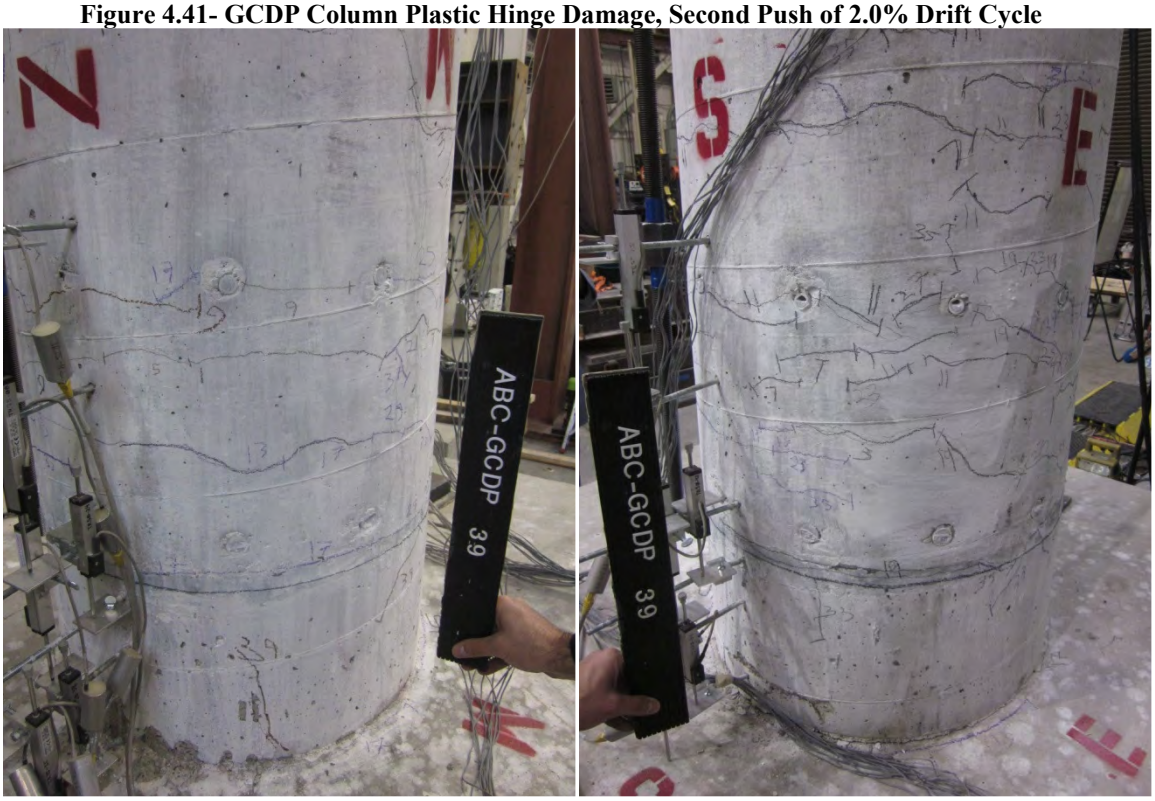

(a) North-West Side (b) South-East Side

Figure 4.42- GCDP Column Plastic Hinge Damage, Second Pull of 2.0% Drift Cycle

(a) North-East Side (b) South-West Side

Figure 4.43- GCDP Column Plastic Hinge Damage, Second Push of 3.0% Drift Cycle

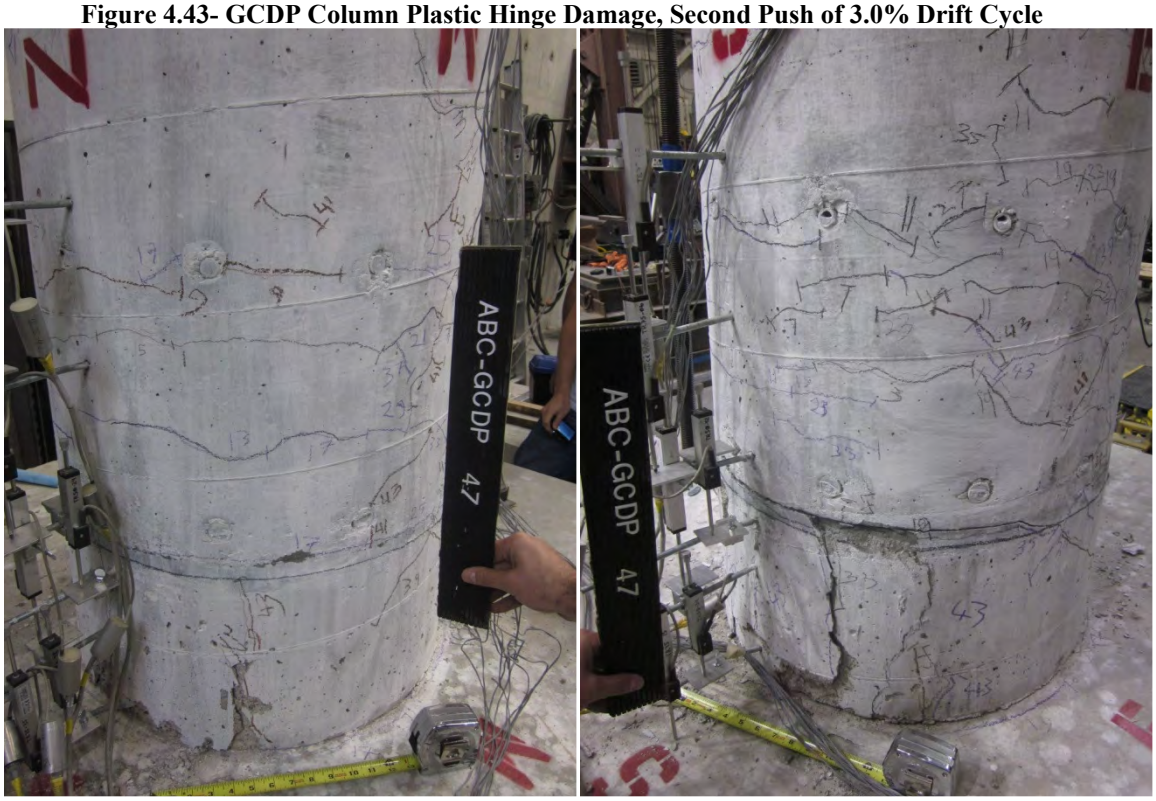

(a) North-West Side (b) South-East Side

Figure 4.44- GCDP Column Plastic Hinge Damage, Second Pull of 3.0% Drift Cycle

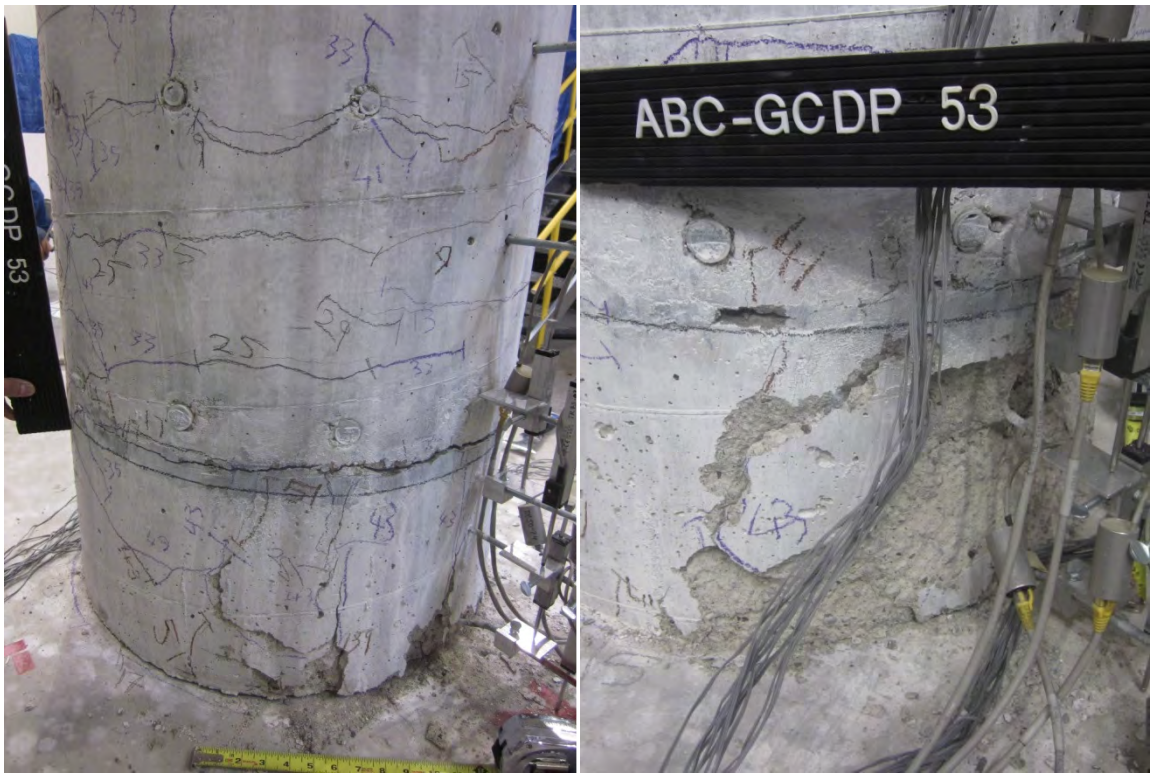

(a) North-East Side (b) South-West Side

Figure 4.45- GCDP Column Plastic Hinge Damage, Second Push of 4.0% Drift Cycle

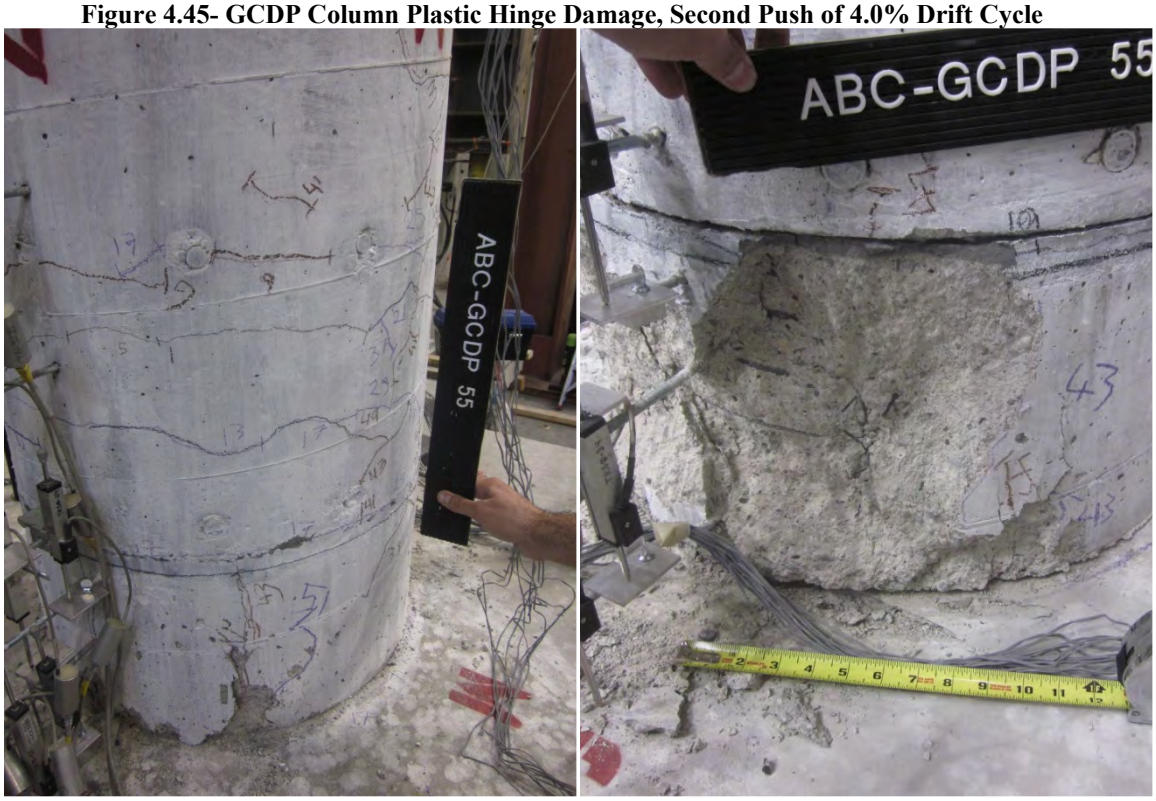

(a) North-West Side (b) South-East Side

Figure 4.46- GCDP Column Plastic Hinge Damage, Second Pull of 4.0% Drift Cycle

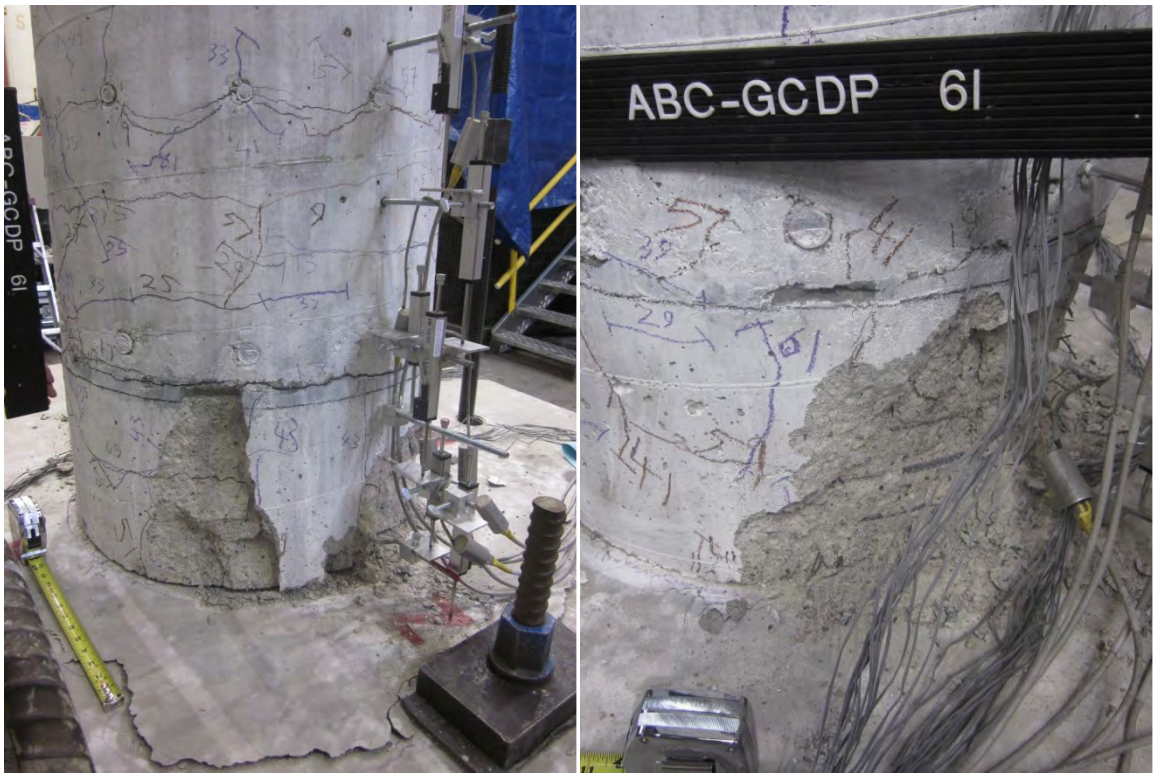

(a) North-East Side (b) South-West Side

Figure 4.47- GCDP Column Plastic Hinge Damage, Second Push of 5.0% Drift Cycle

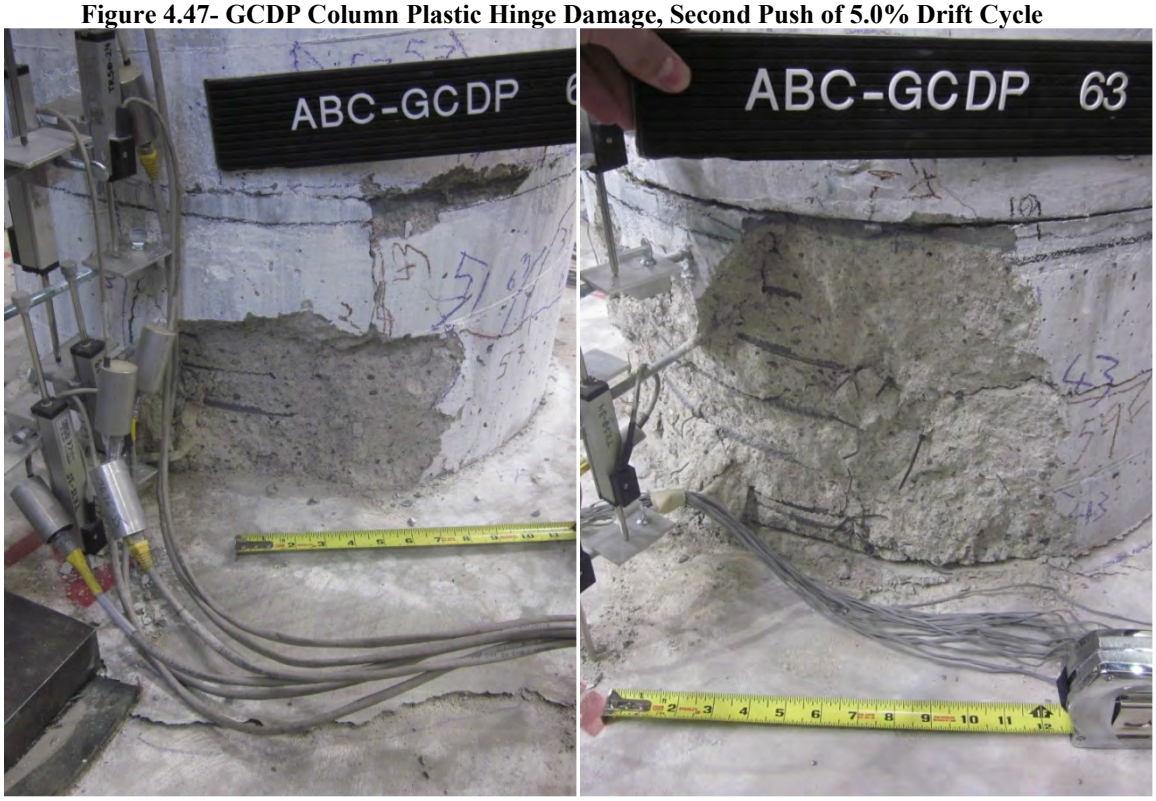

(a) North-West Side (b) South-East Side

Figure 4.48- GCDP Column Plastic Hinge Damage, Second Pull of 5.0% Drift Cycle

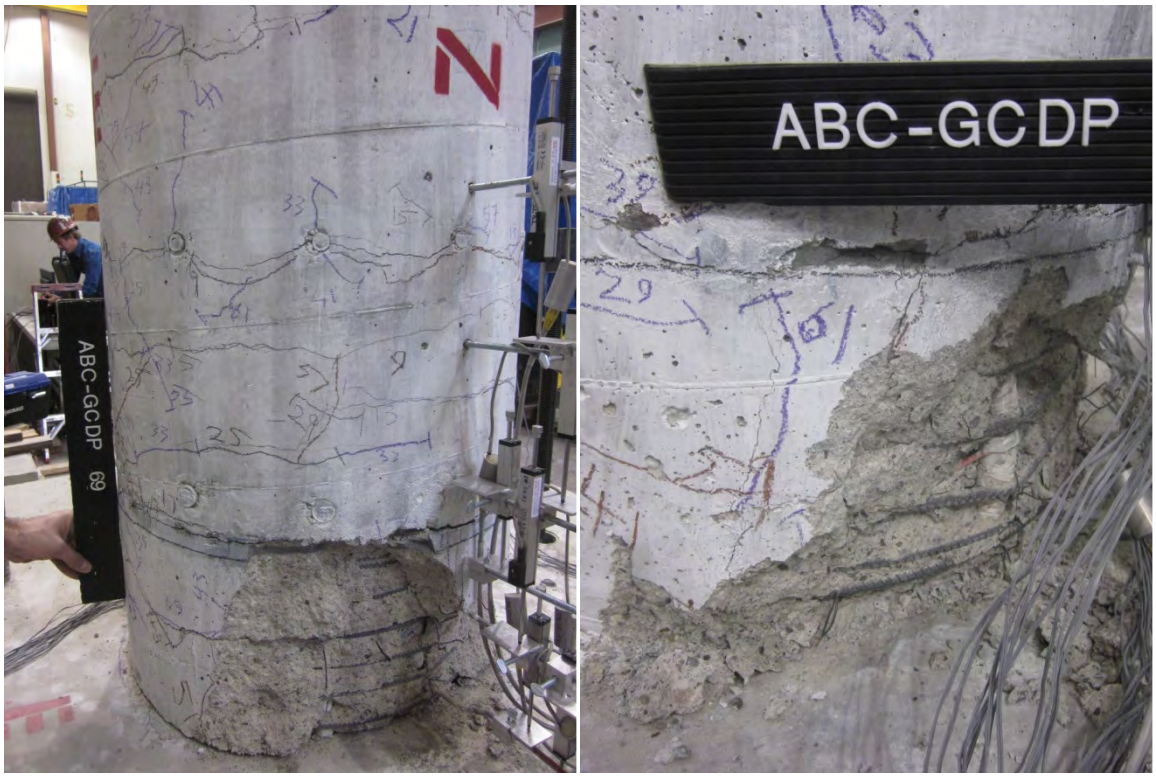

(a) North-East Side (b) South-West Side

Figure 4.49- GCDP Column Plastic Hinge Damage, Second Push of 6.0% Drift Cycle

(a) North-West Side (b) South-East Side

Figure 4.50- GCDP Column Plastic Hinge Damage, Second Pull of 6.0% Drift Cycle

(a) North-East Side (b) South-West Side

Figure 4.51- GCDP Column Plastic Hinge Damage, Second Push of 8.0% Drift Cycle

(a) North-West Side (b) South-East Side

Figure 4.52- GCDP Column Plastic Hinge Damage, Second Pull of 8.0% Drift Cycle

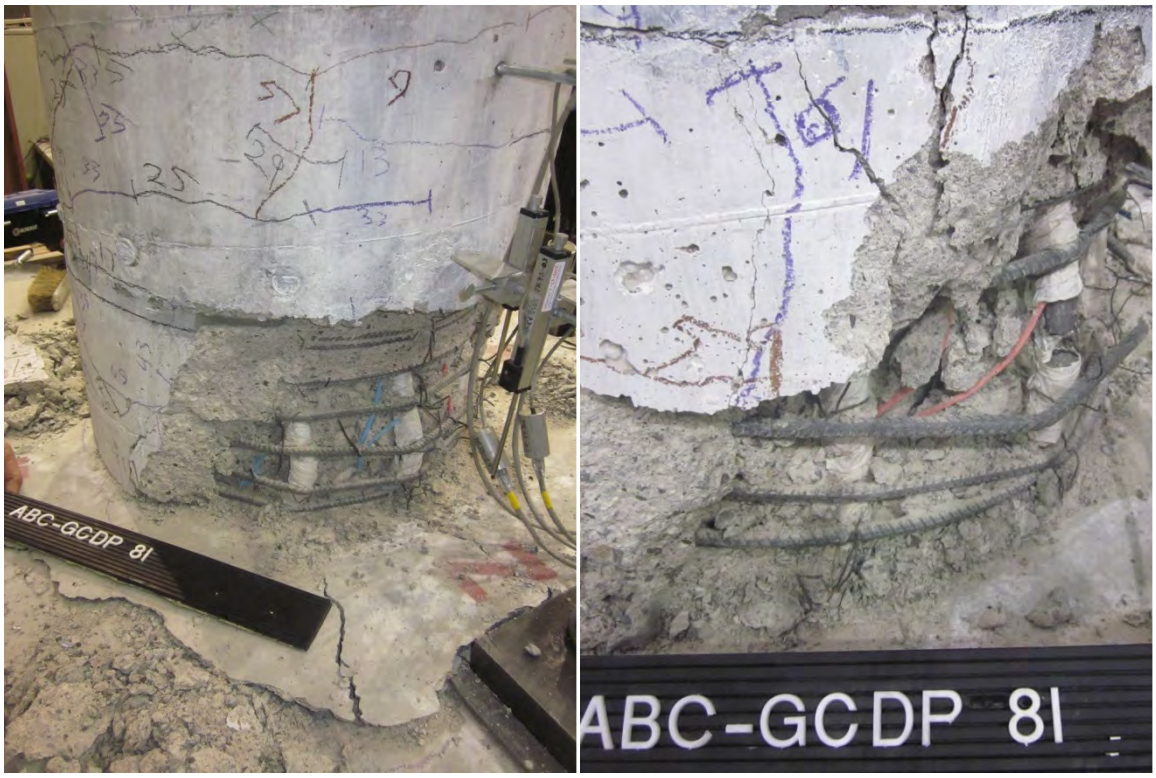

(a) North-East Side (b) South-West Side

Figure 4.53- GCDP Column Plastic Hinge Damage, Pull of 10.0% Drift Cycle

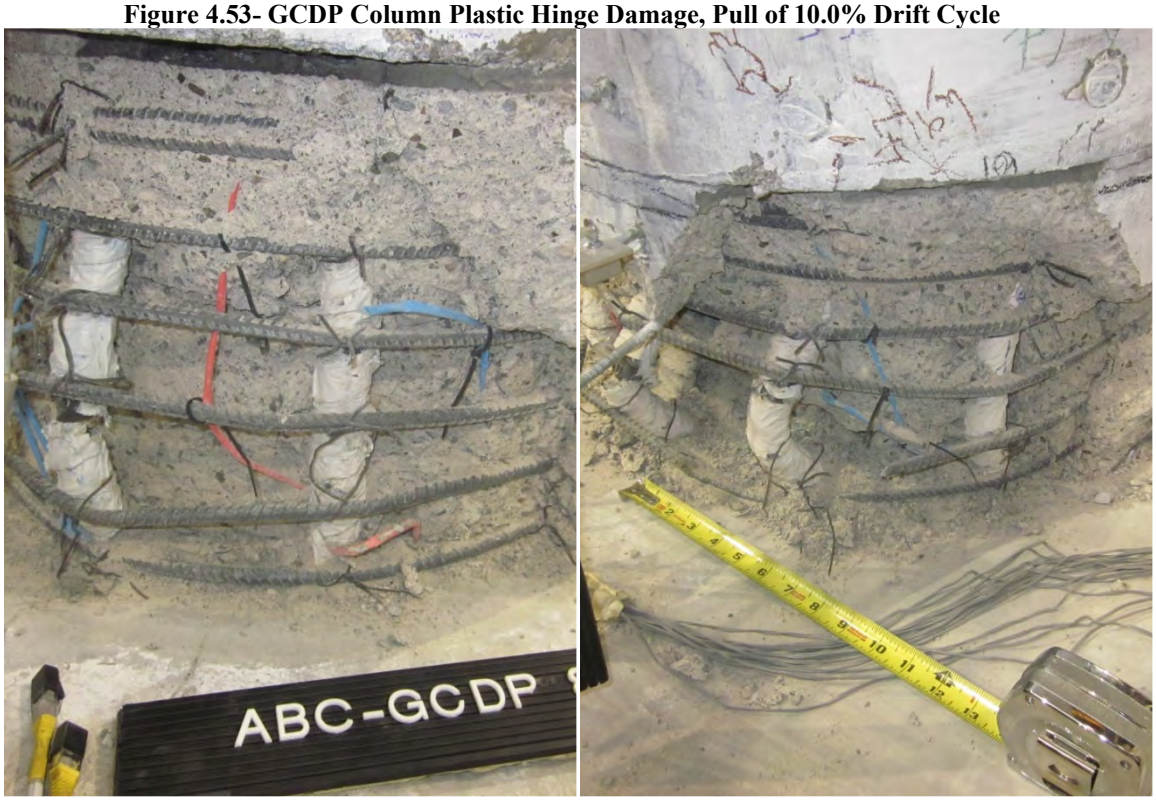

(a) North-West Side (b) South-East Side

Figure 4.54- GCDP Column Plastic Hinge Damage, Second Push of 10.0% Drift Cycle

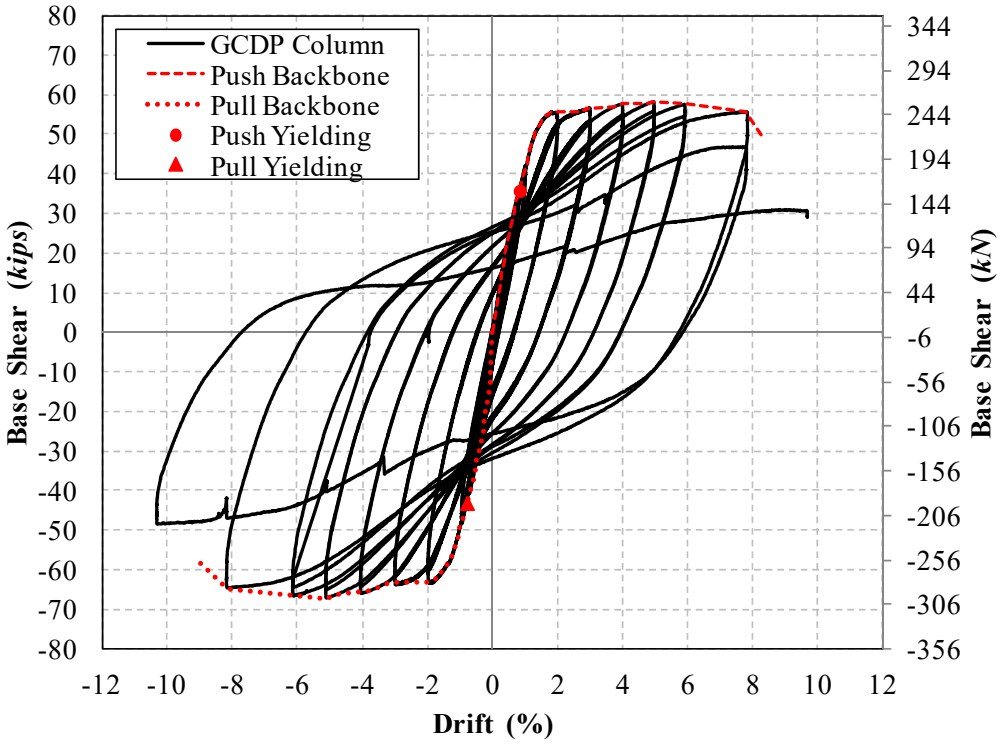

Figure 4.55- GCDP Column Force-Drift Hysteretic and Envelope Responses

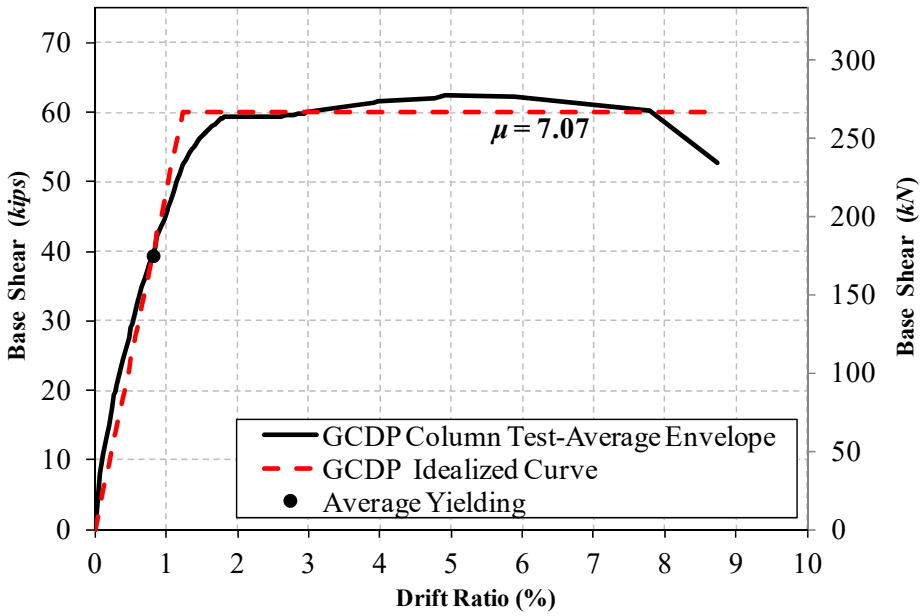

Figure 4.56- GCDP Column Average Push/Pull Force-Displacement Envelope and Idealized Curve

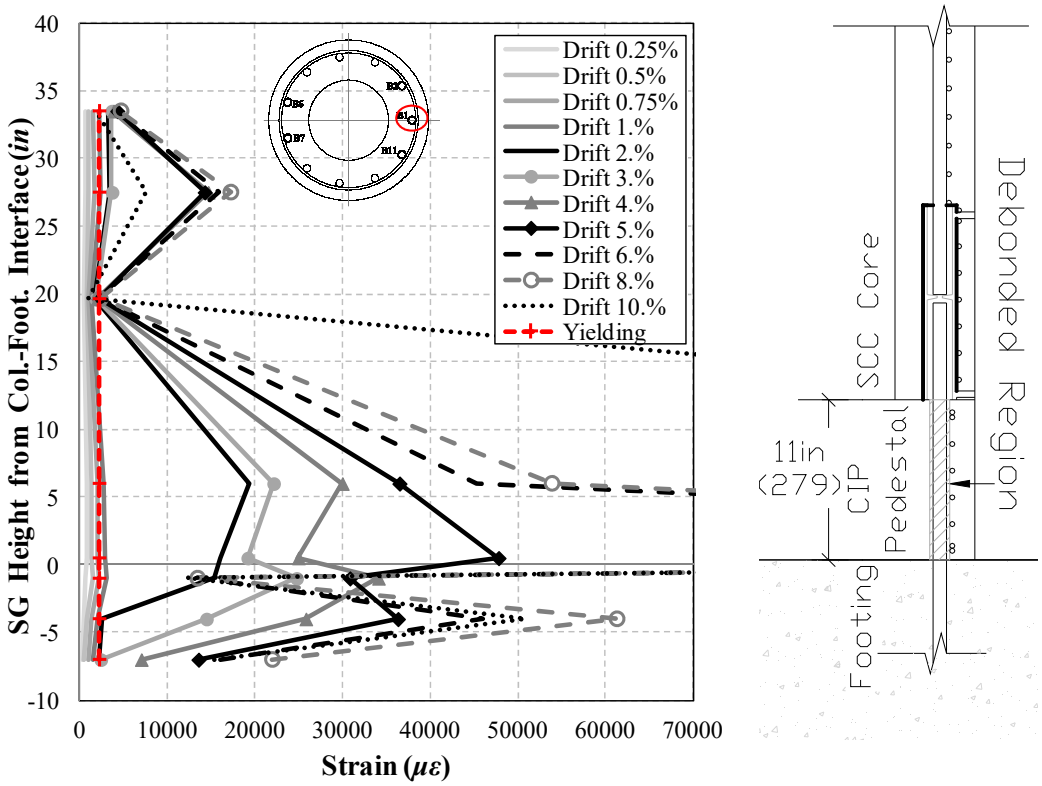

Figure 4.57- Strain Profile for GCDP Column Bar B1 (1 *in*.= 25.4 *mm*)

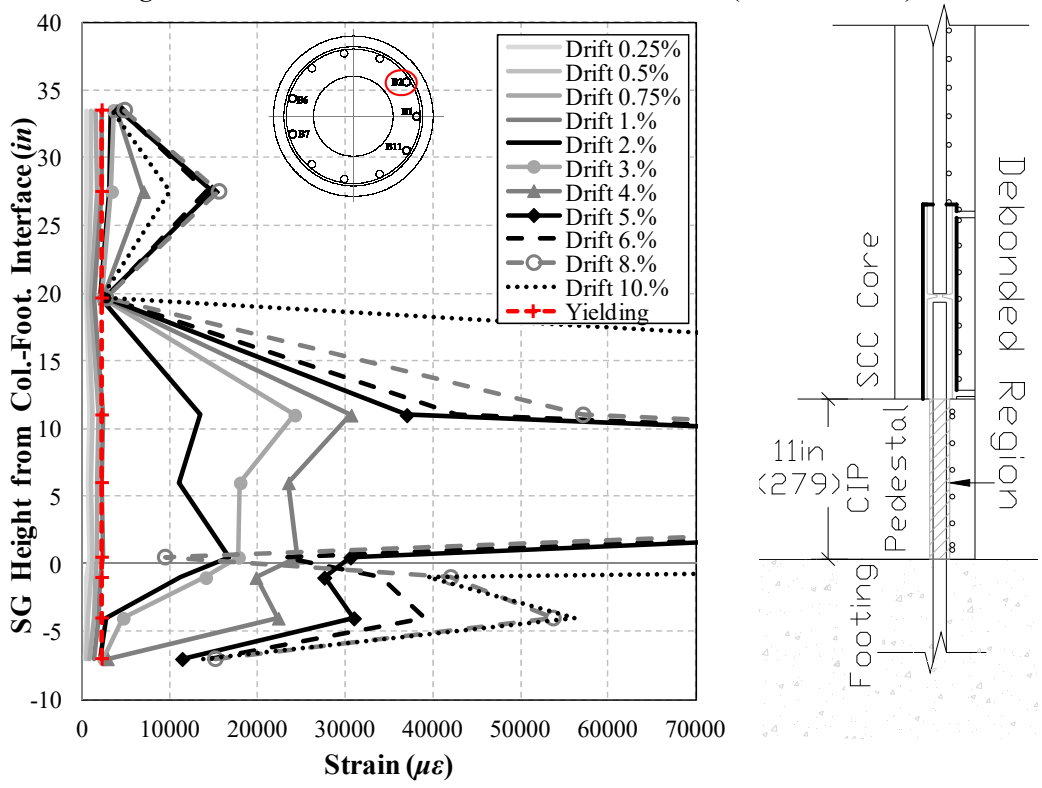

Figure 4.58- Strain Profile for GCDP Column Bar B2 (1 *in*.= 25.4 *mm*)

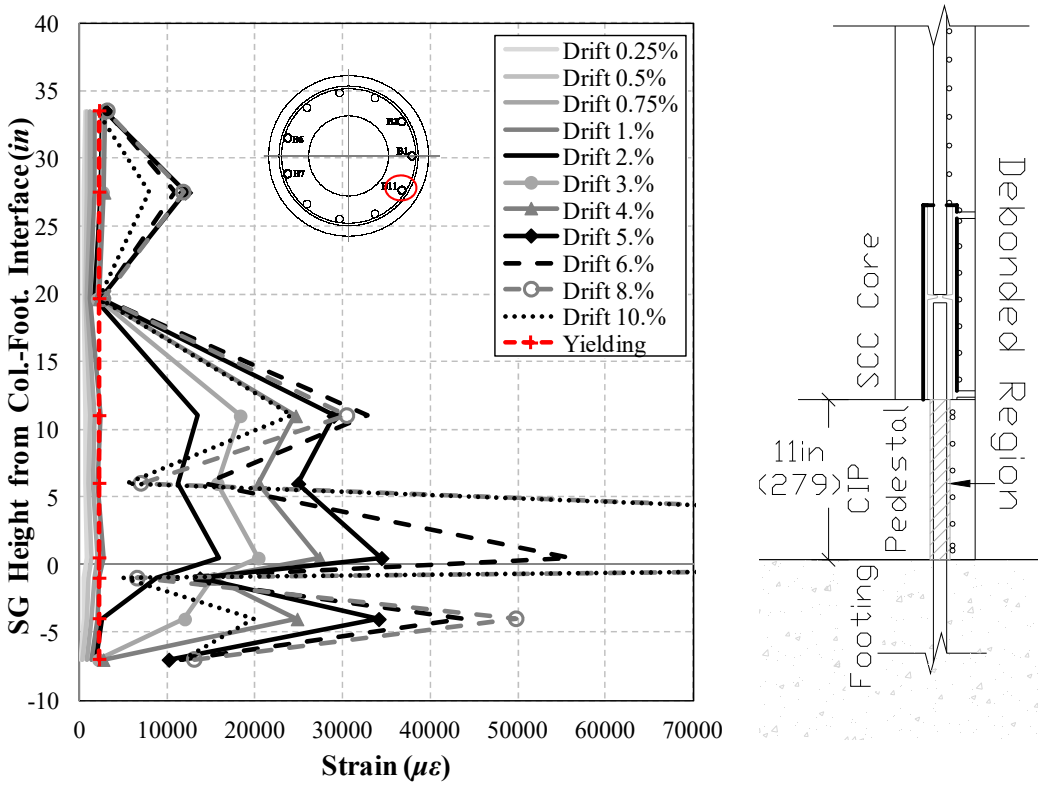

Figure 4.59- Strain Profile for GCDP Column Bar B11 (1 *in.*= 25.4 *mm*)

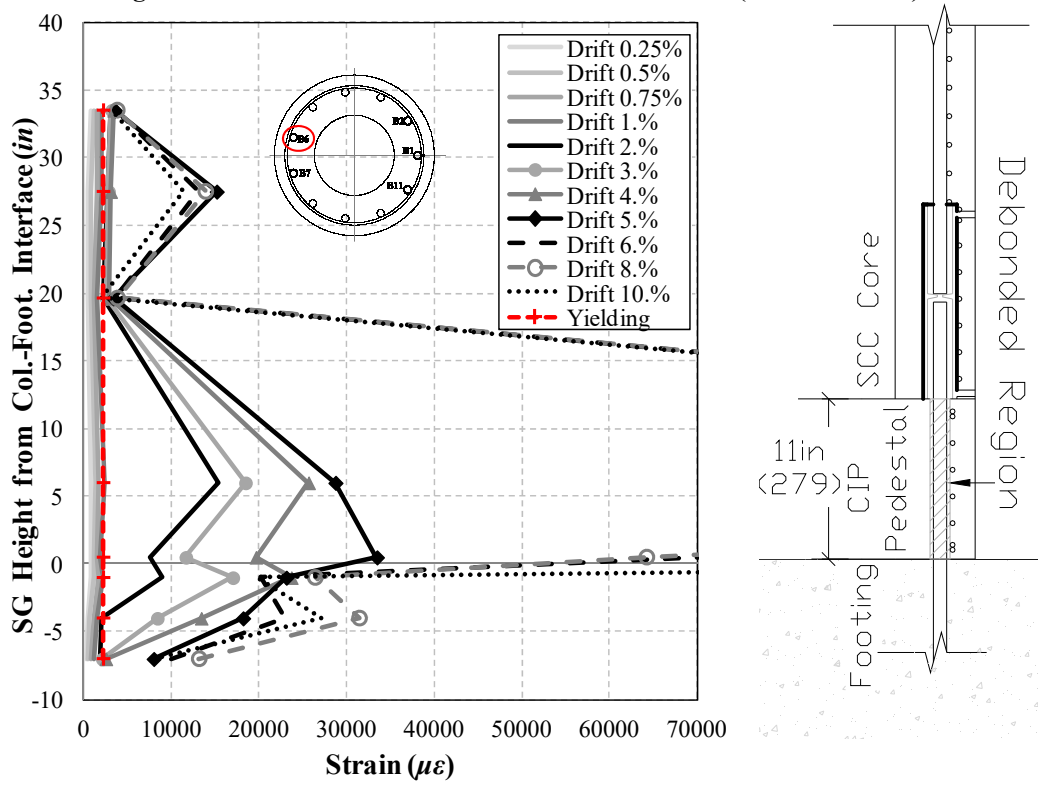

Figure 4.60- Strain Profile for GCDP Column Bar B6 (1 *in.*= 25.4 *mm*)

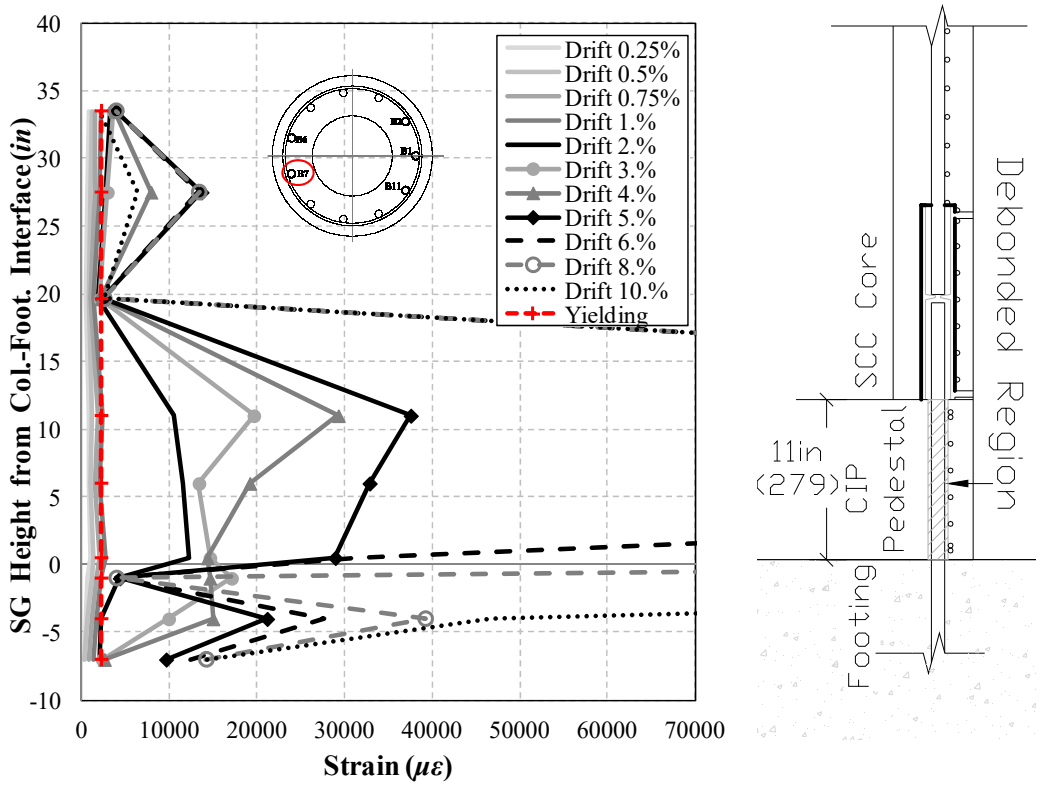

Figure 4.61- Strain Profile for GCDP Column Bar B7 (1 *in*.= 25.4 *mm*)

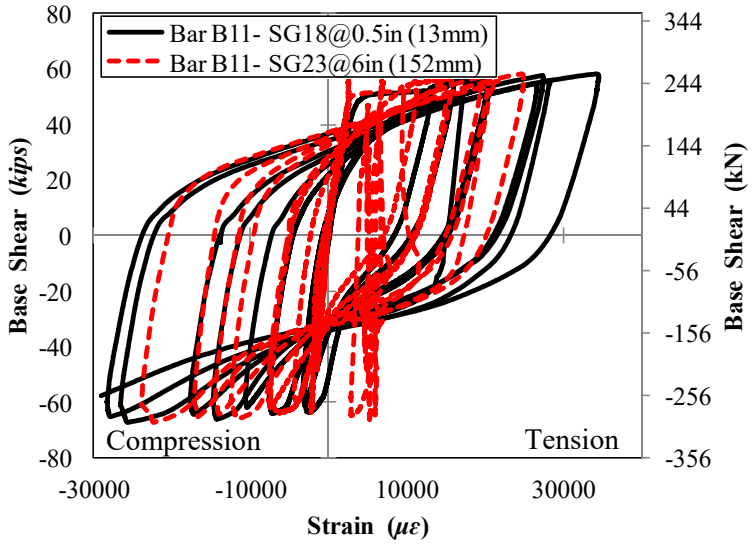

Figure 4.62- Force-Strain Hysteresis for GCDP Column Bar B11 in Debonded Region

Instrumentation Plan	
Test Lable	Instrument
BS01	TR50-38
BS02	TR50-34
J01	TR50-24
J02	TR50-42
C01	TR75-35
C02	TR75-03
C03	TR75-08
C04	TR75-42
C05	TR75-15
C06	TR75-01
C07	TR75-06
C08	TR75-25
D01	SP40
D02	SP39
D03	SP38
D04	NONE

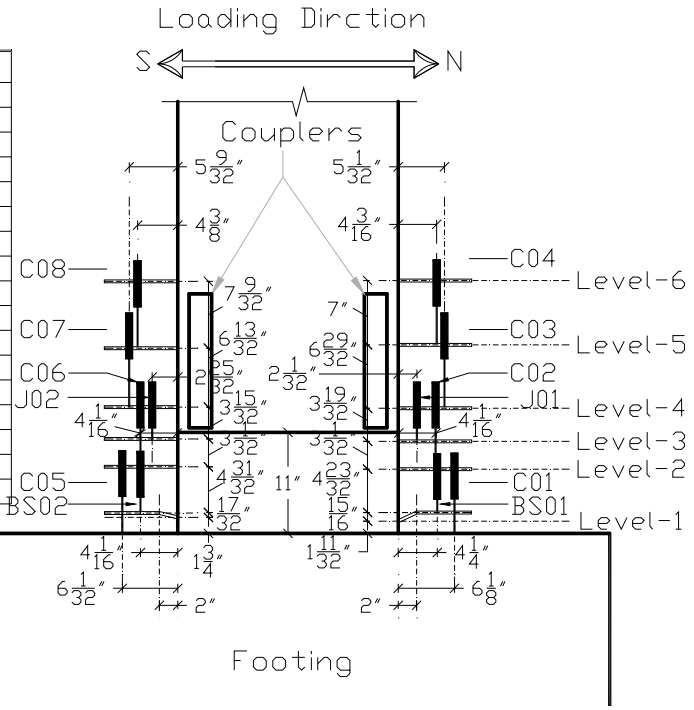

Figure 4.63- Test Displacement Instrumentation Plan at Base of GCDP Column (1 *in*.=25 *mm*)

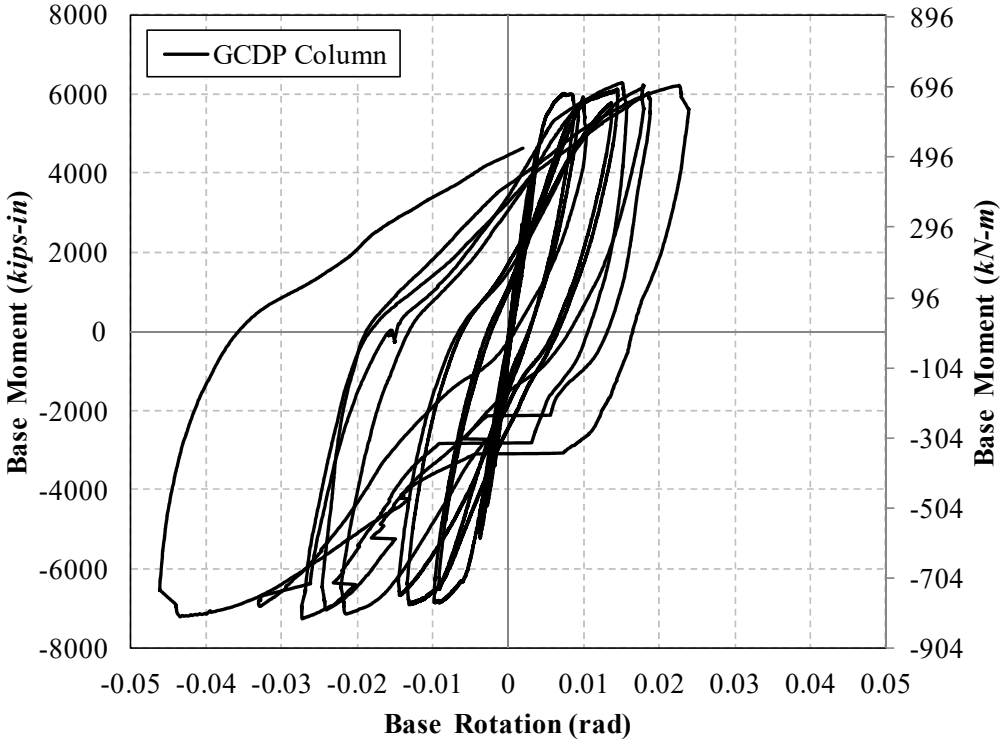

Figure 4.64- Base Moment-Rotation Relationship for GCDP Column

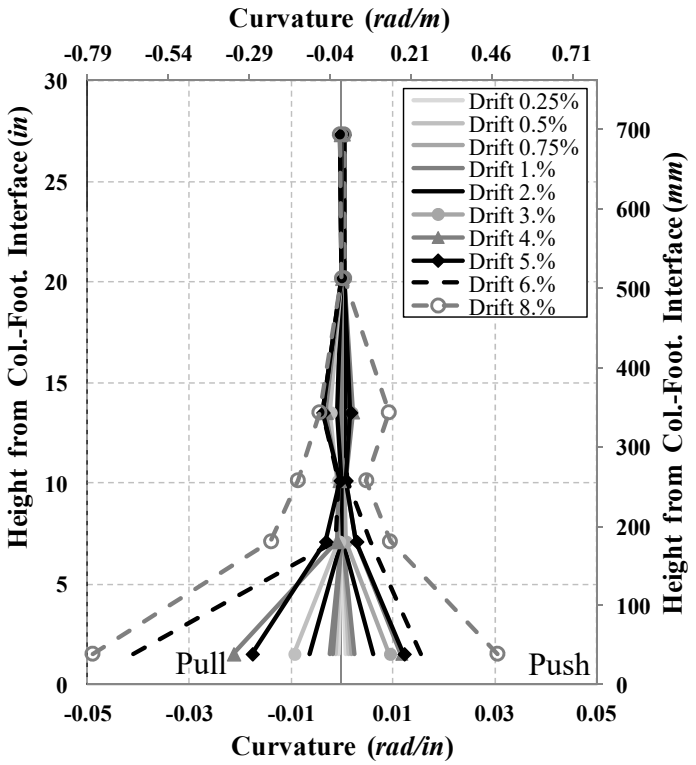

Figure 4.65- Curvature Profile for GCDP Column

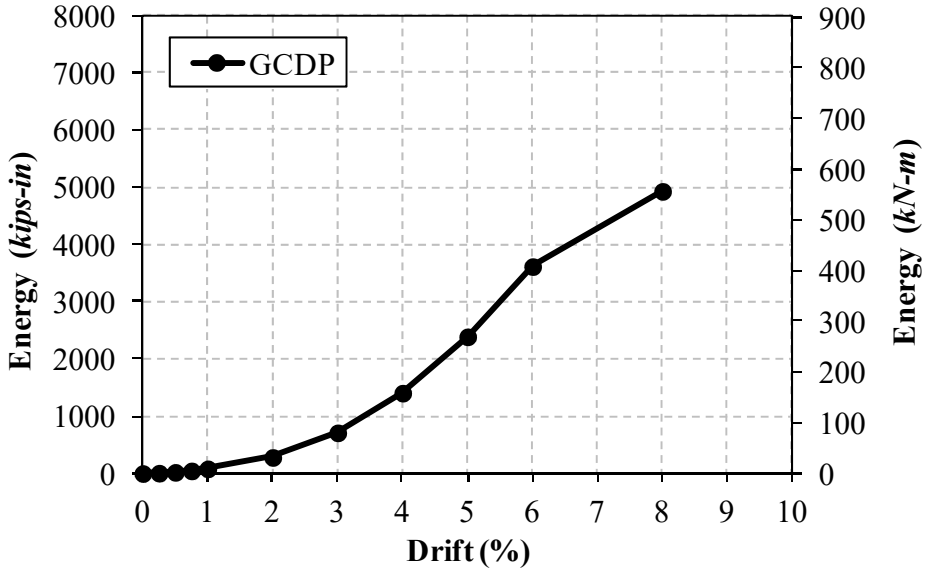

Figure 4.66- Energy Dissipation for GCDP Column

(a) North Side (b) South Side

Figure 4.67- HCS Column Plastic Hinge Damage, Second Push of 0.5% Drift Cycle

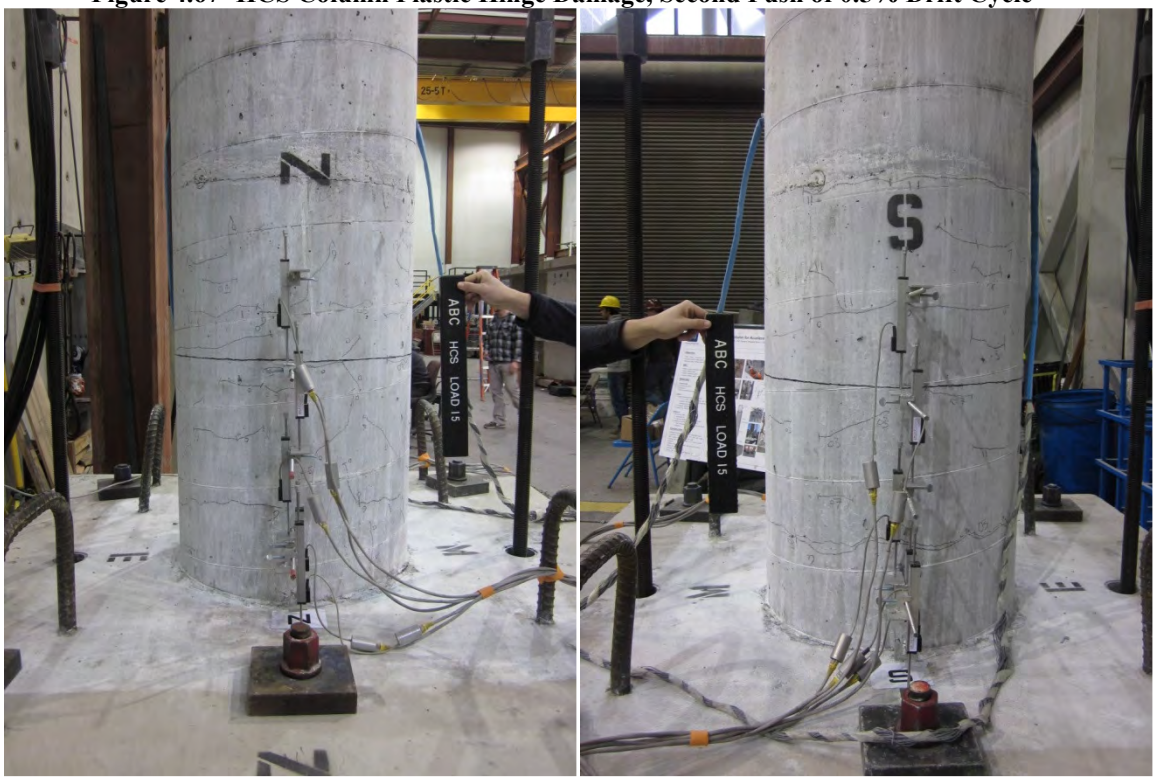

(a) North Side (b) South Side

Figure 4.68- HCS Column Plastic Hinge Damage, Second Pull of 0.5% Drift Cycle

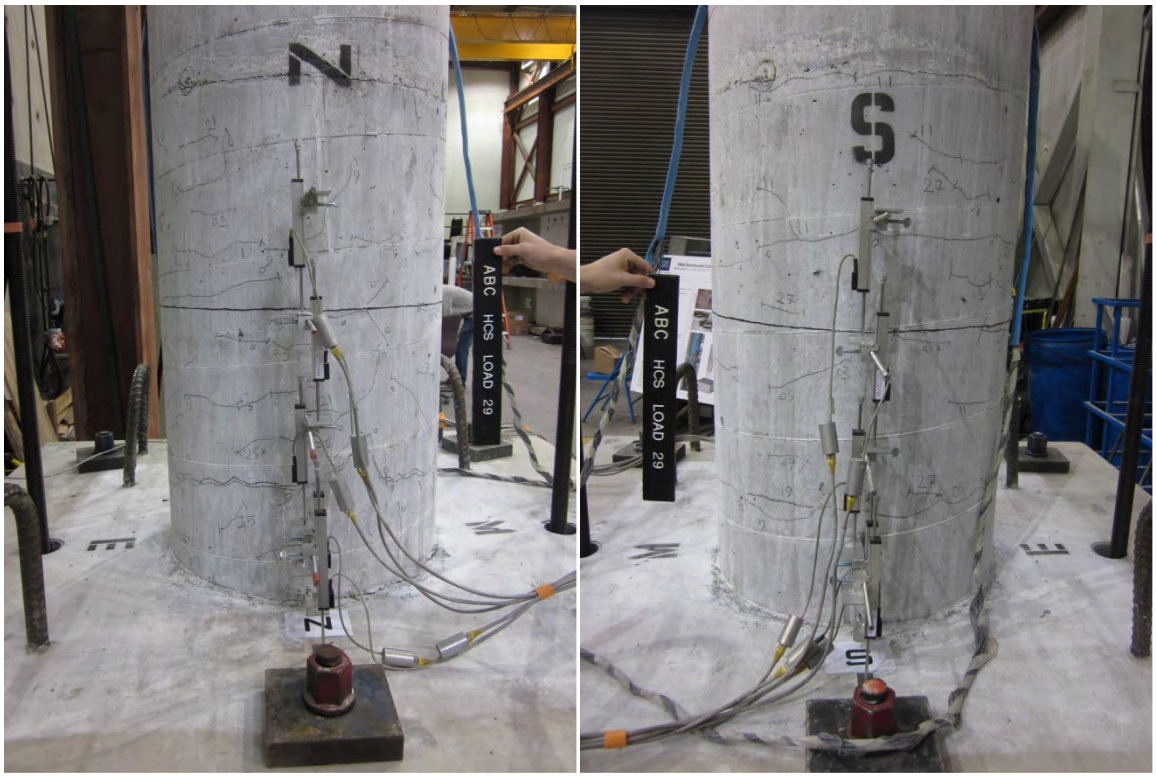

(a) North Side (b) South Side

Figure 4.69- HCS Column Plastic Hinge Damage, Second Push of 1.0% Drift Cycle

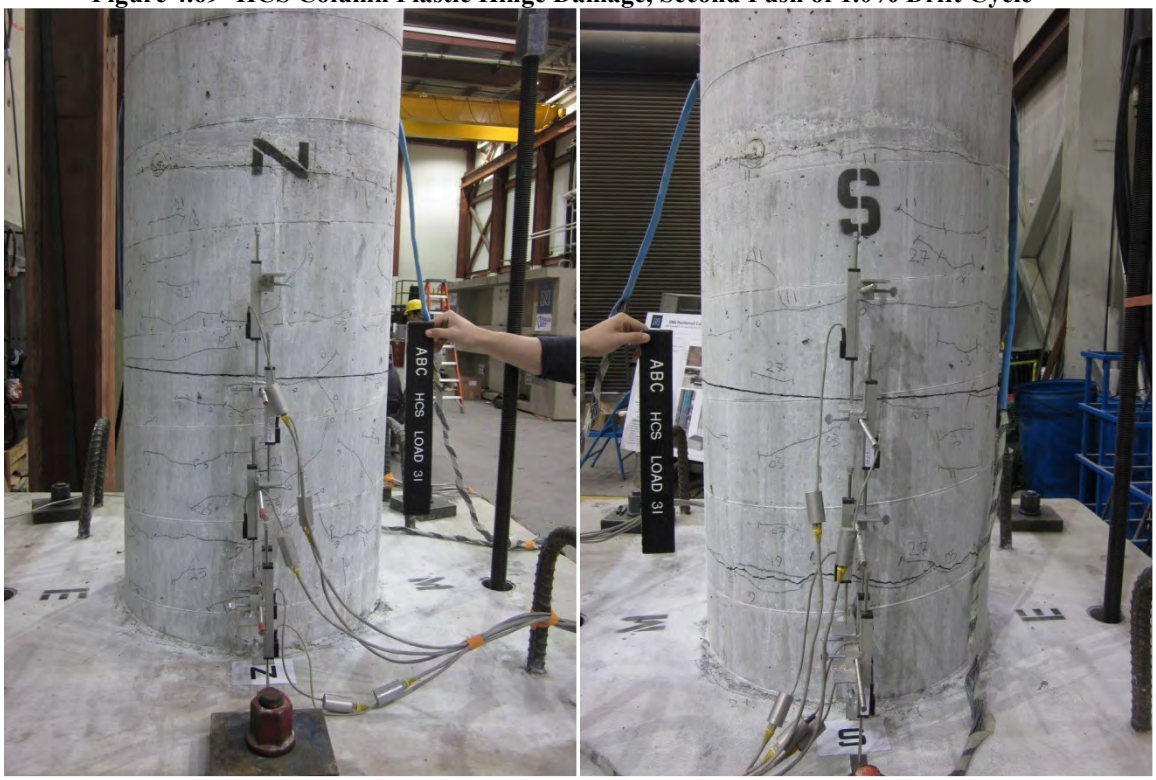

(a) North Side (b) South Side

Figure 4.70- HCS Column Plastic Hinge Damage, Second Pull of 1.0% Drift Cycle

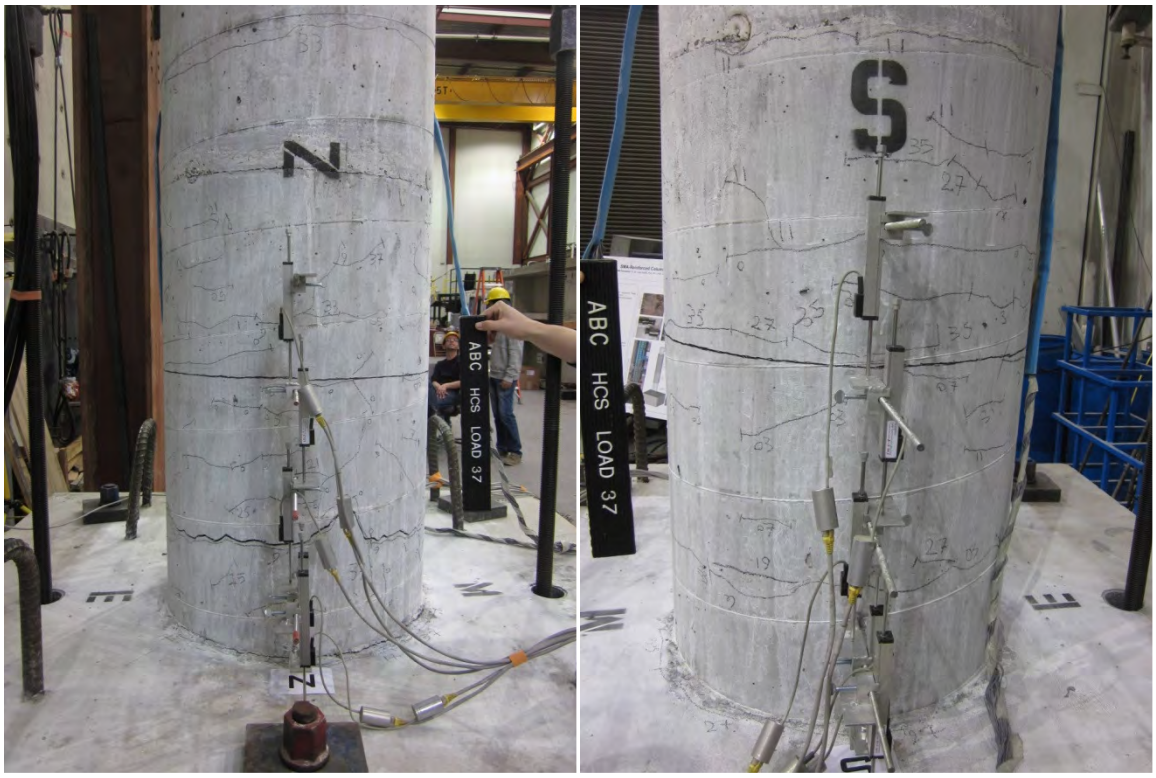

(a) North Side (b) South Side

Figure 4.71- HCS Column Plastic Hinge Damage, Second Push of 2.0% Drift Cycle

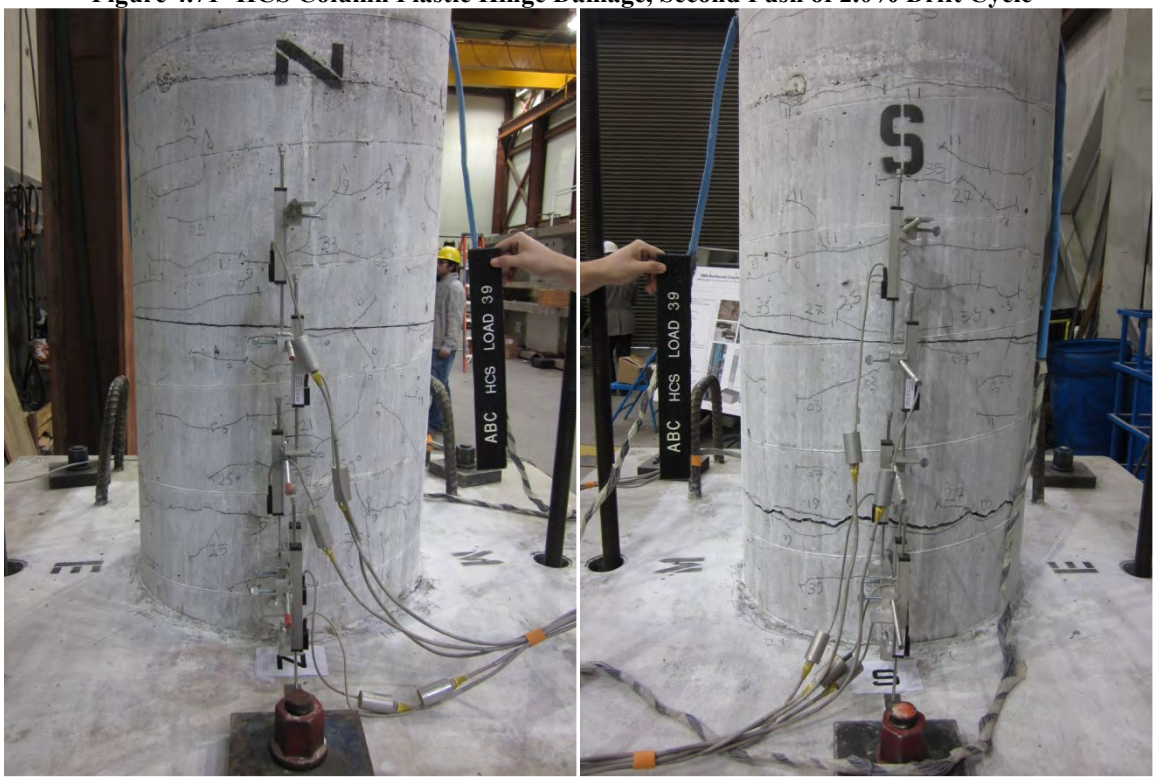

(a) North Side (b) South Side

Figure 4.72- HCS Column Plastic Hinge Damage, Second Pull of 2.0% Drift Cycle

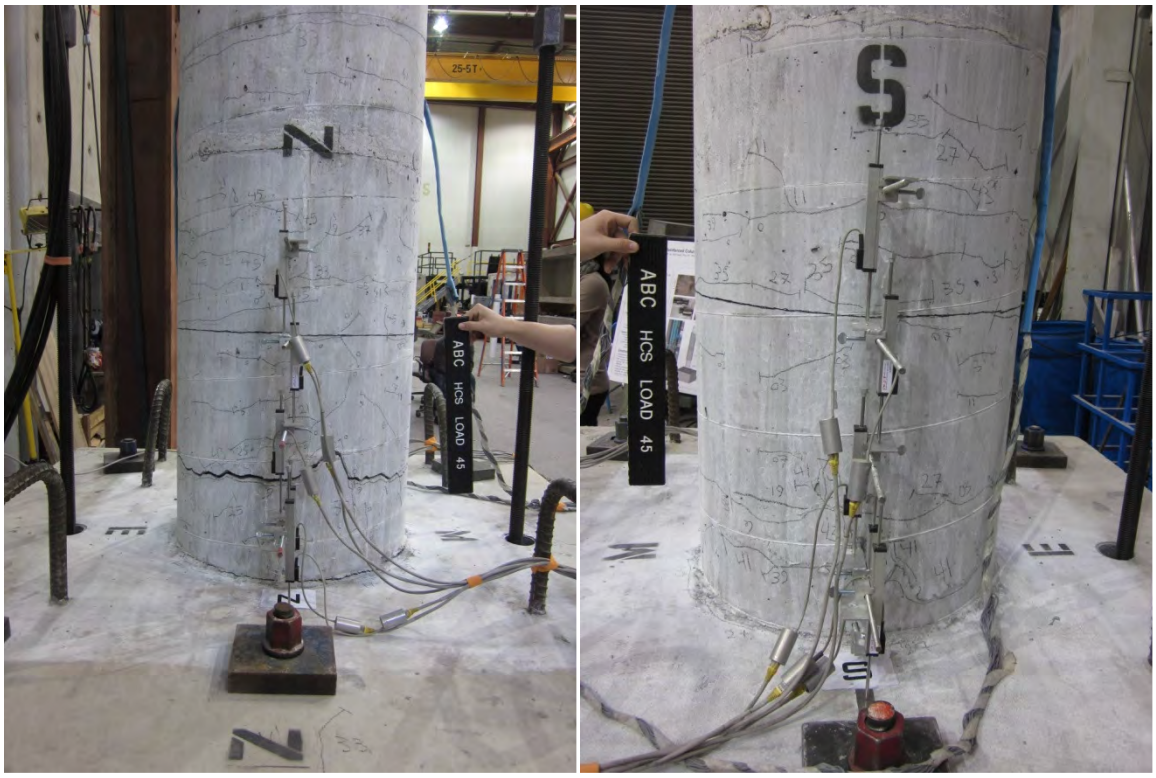

(a) North Side (b) South Side

Figure 4.73- HCS Column Plastic Hinge Damage, Second Push of 3.0% Drift Cycle

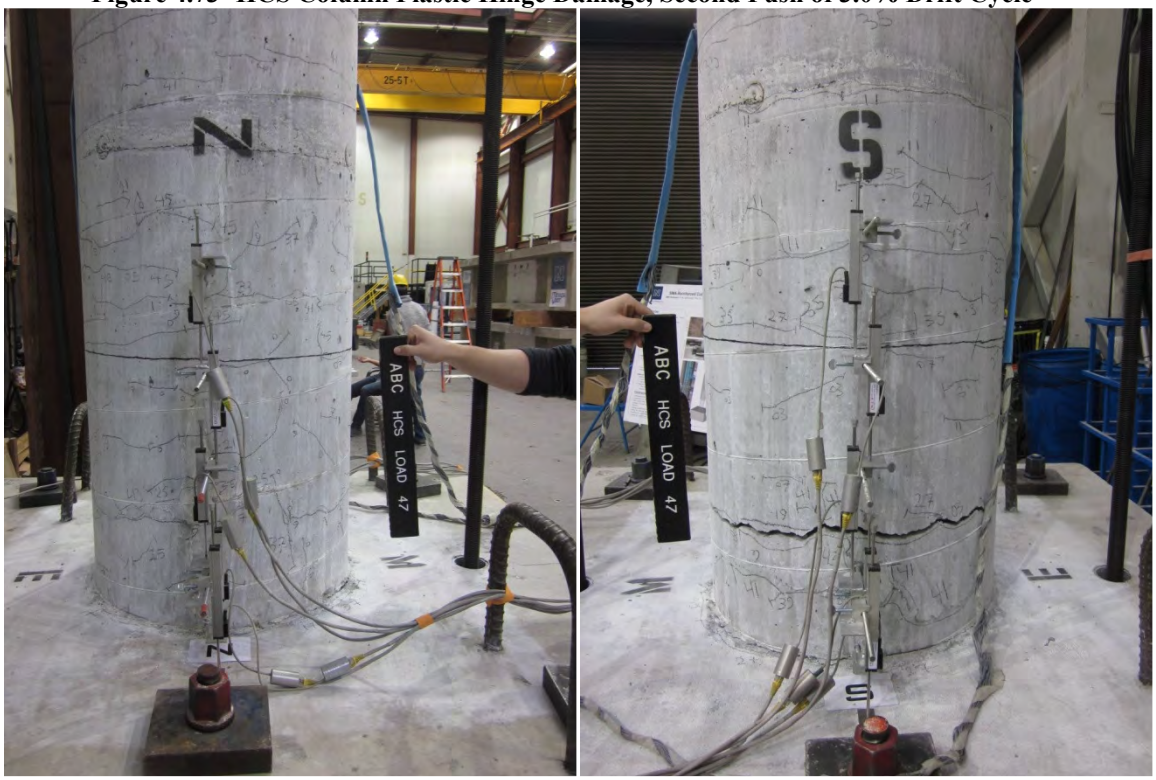

(a) North Side (b) South Side

Figure 4.74- HCS Column Plastic Hinge Damage, Second Pull of 3.0% Drift Cycle

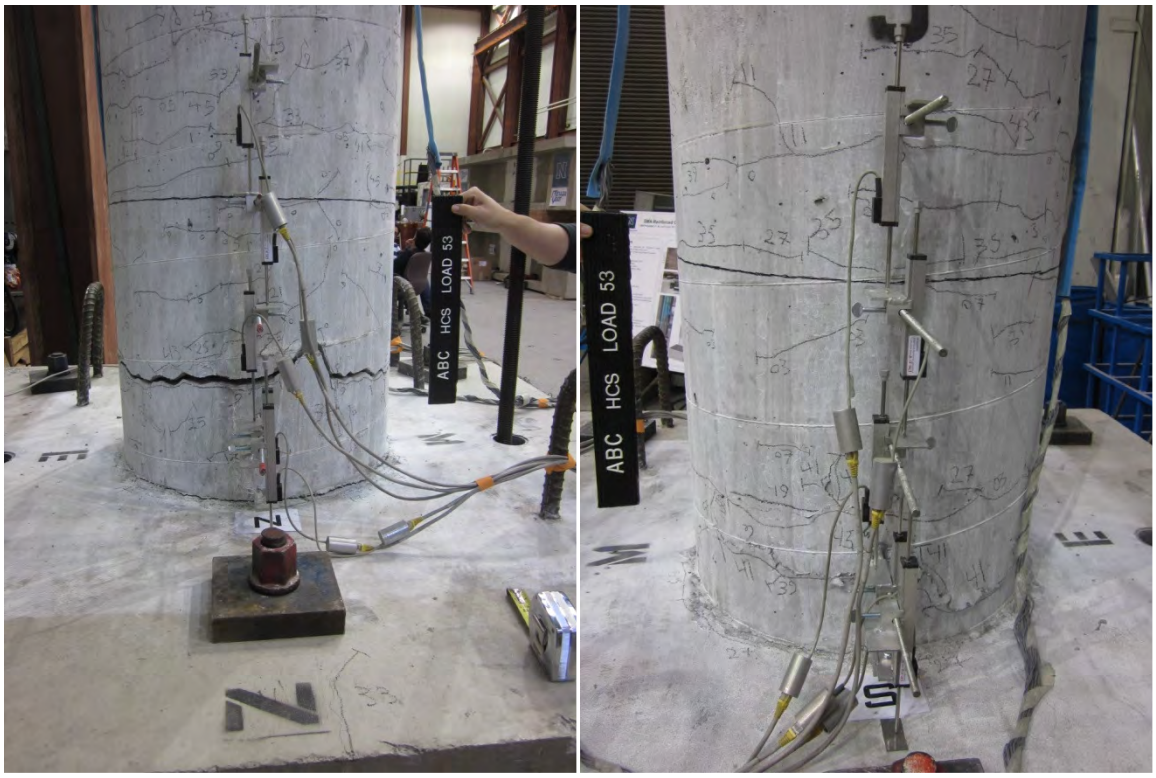

(a) North Side (b) South Side

Figure 4.75- HCS Column Plastic Hinge Damage, Second Push of 4.0% Drift Cycle

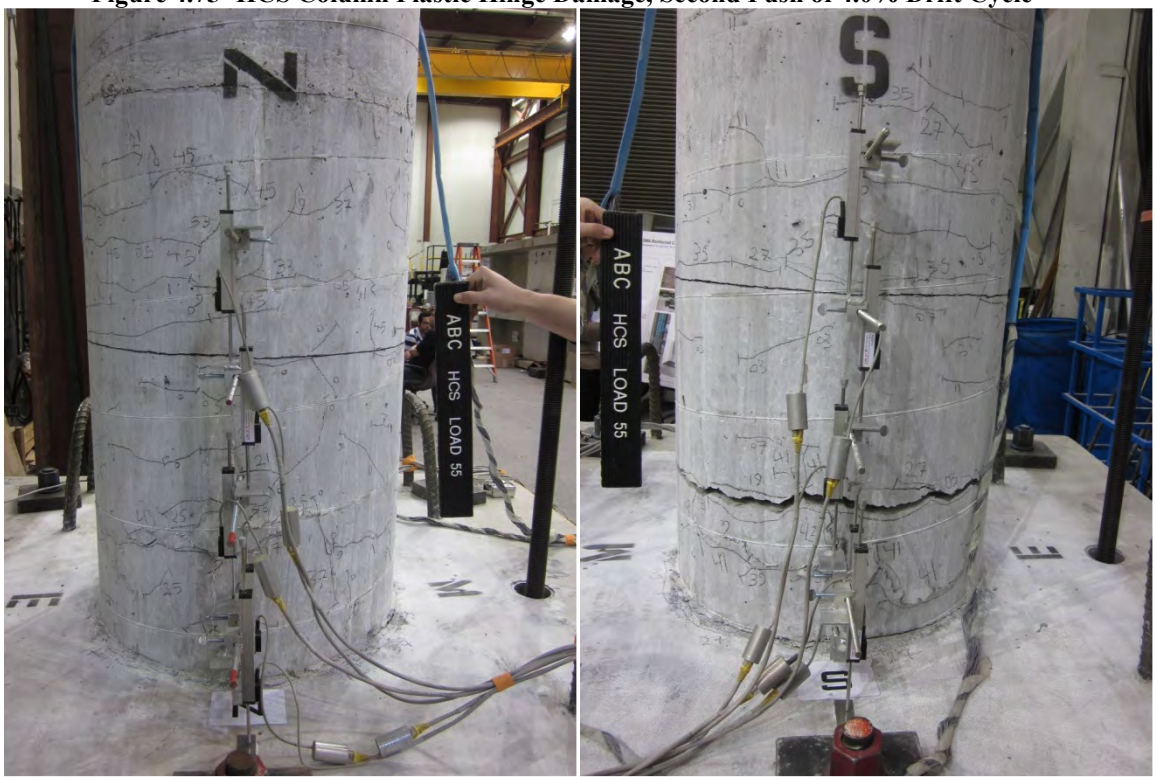

(a) North Side (b) South Side

Figure 4.76- HCS Column Plastic Hinge Damage, Second Pull of 4.0% Drift Cycle

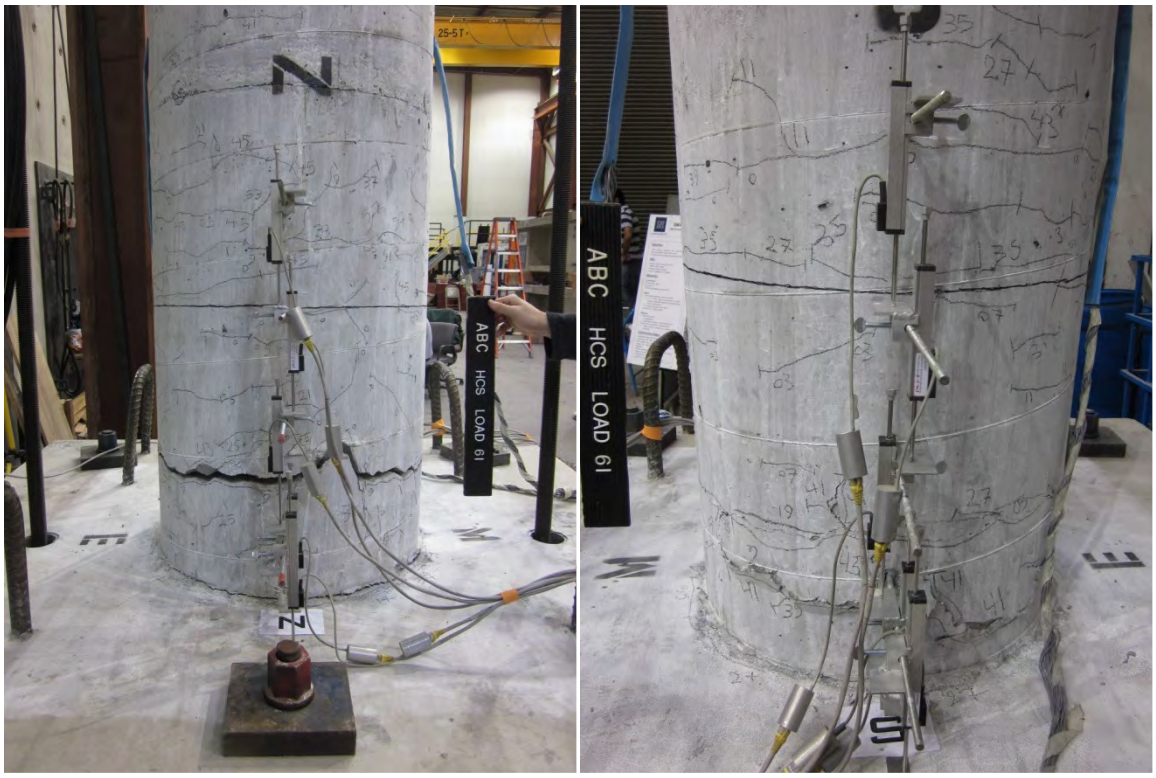

(a) North Side (b) South Side

Figure 4.77- HCS Column Plastic Hinge Damage, Second Push of 5.0% Drift Cycle

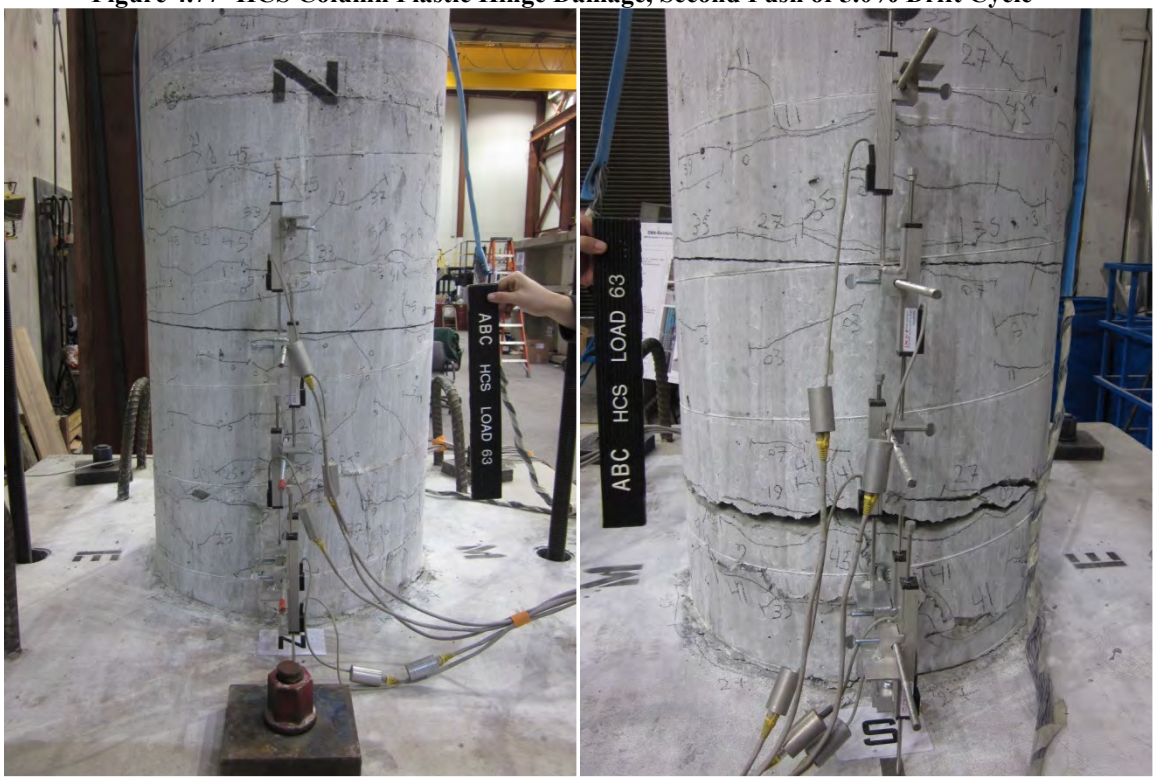

(a) North Side (b) South Side

Figure 4.78- HCS Column Plastic Hinge Damage, Second Pull of 5.0% Drift Cycle

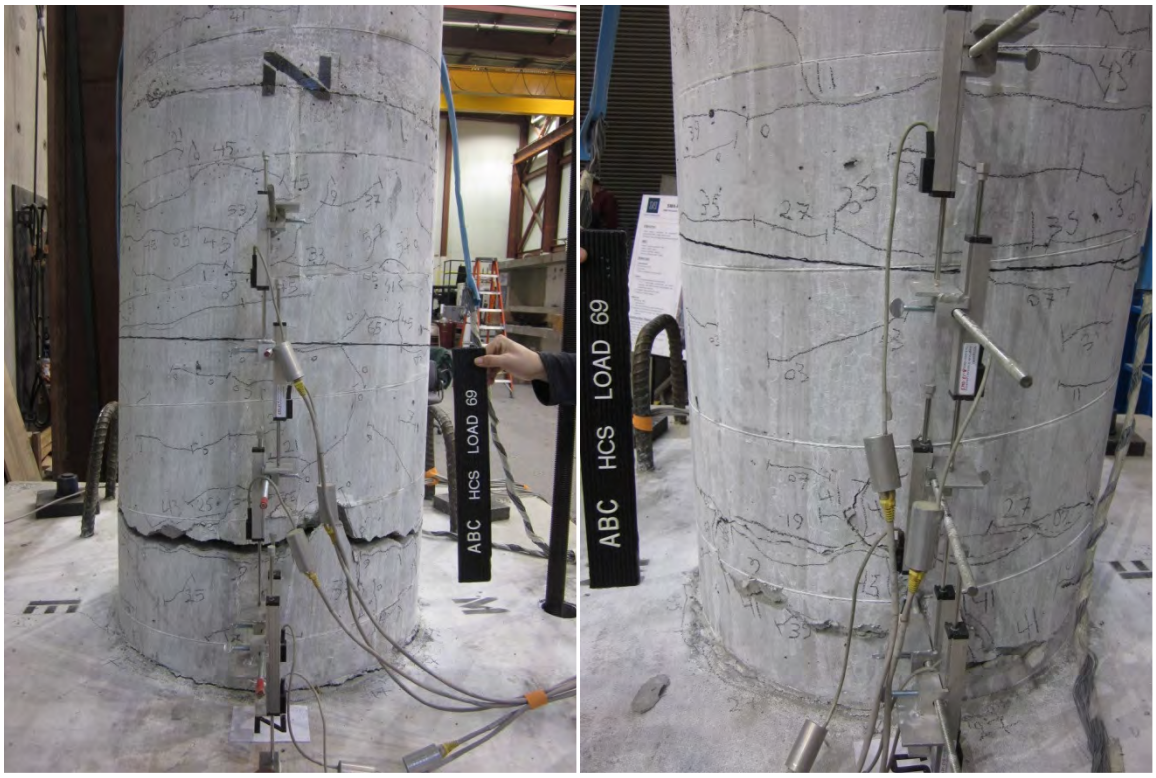

(a) North Side (b) South Side

Figure 4.79- HCS Column Plastic Hinge Damage, Second Push of 6.0% Drift Cycle

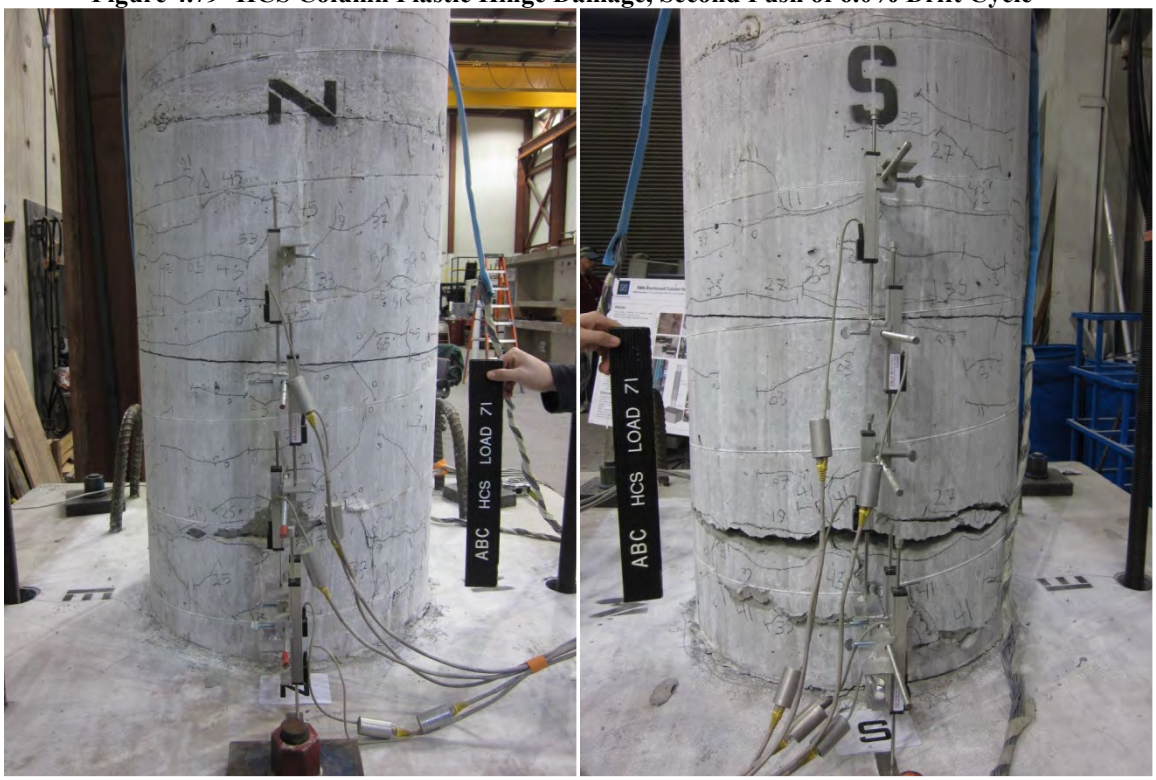

(a) North Side (b) South Side

Figure 4.80- HCS Column Plastic Hinge Damage, Second Pull of 6.0% Drift Cycle

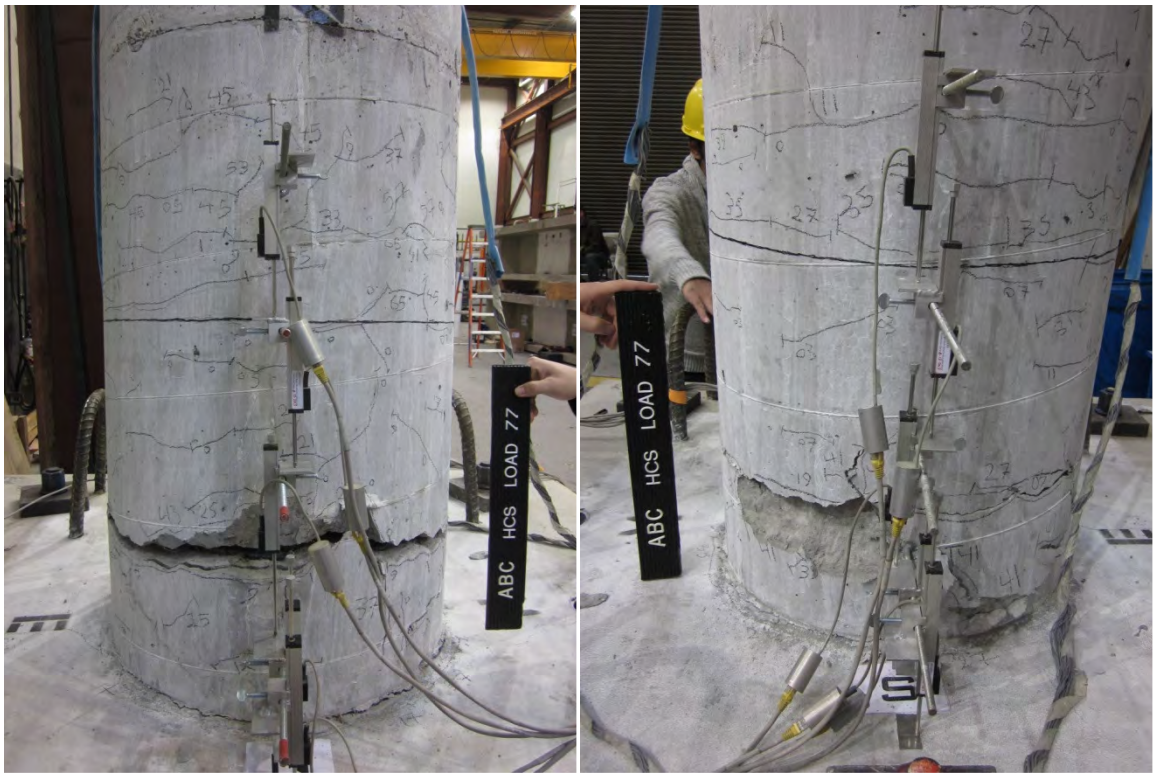

(a) North Side (b) South Side

Figure 4.81- HCS Column Plastic Hinge Damage, Second Push of 8.0% Drift Cycle

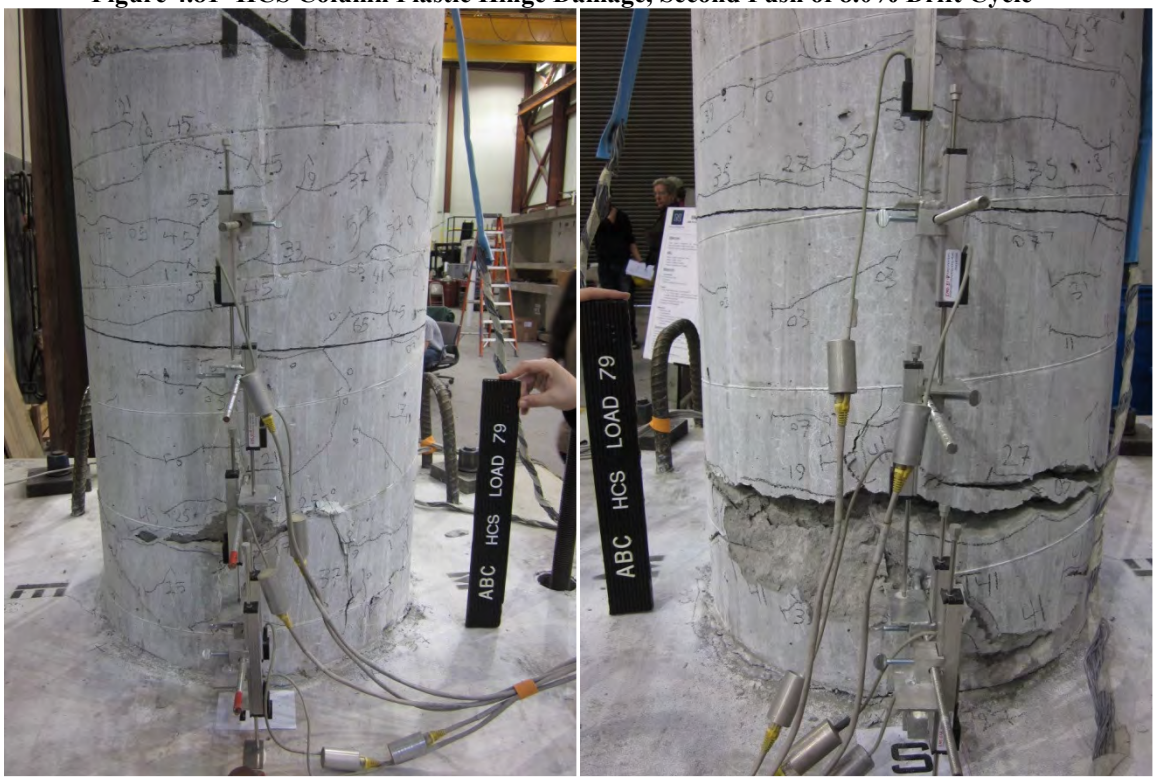

(a) North Side (b) South Side

Figure 4.82- HCS Column Plastic Hinge Damage, Second Pull of 8.0% Drift Cycle

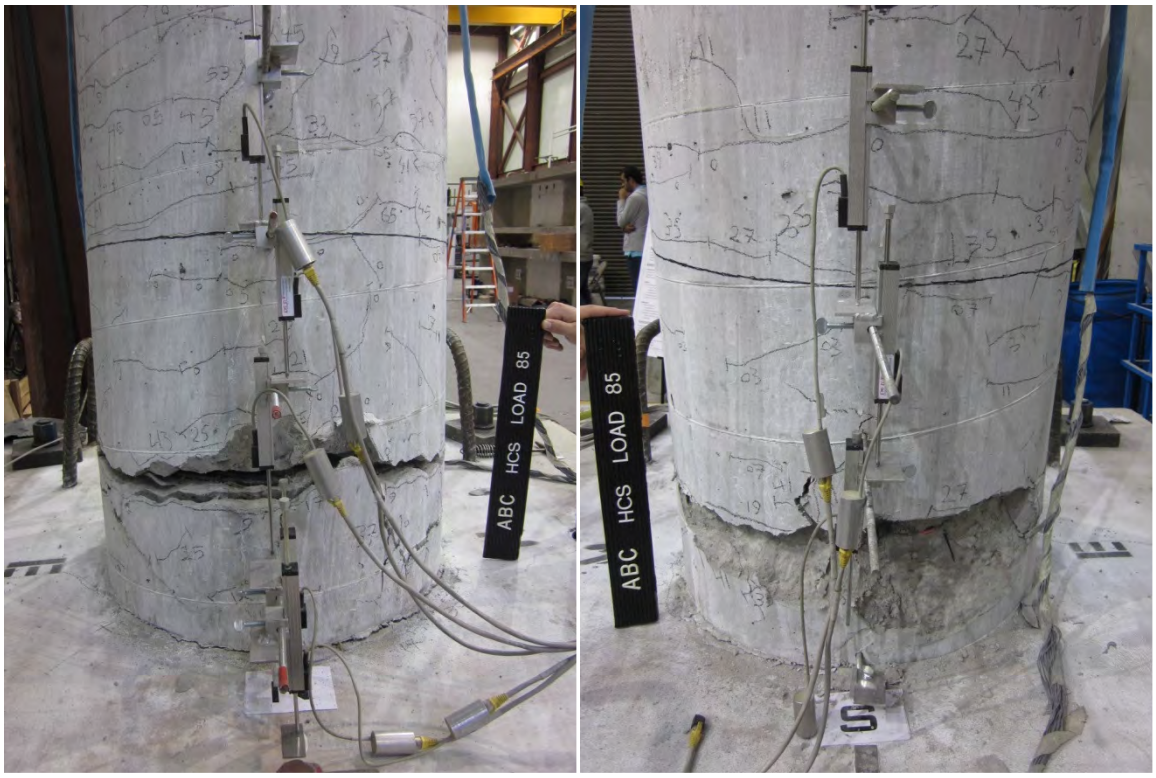

(a) North Side (b) South Side

Figure 4.83- HCS Column Plastic Hinge Damage, Second Push of 10.0% Drift Cycle

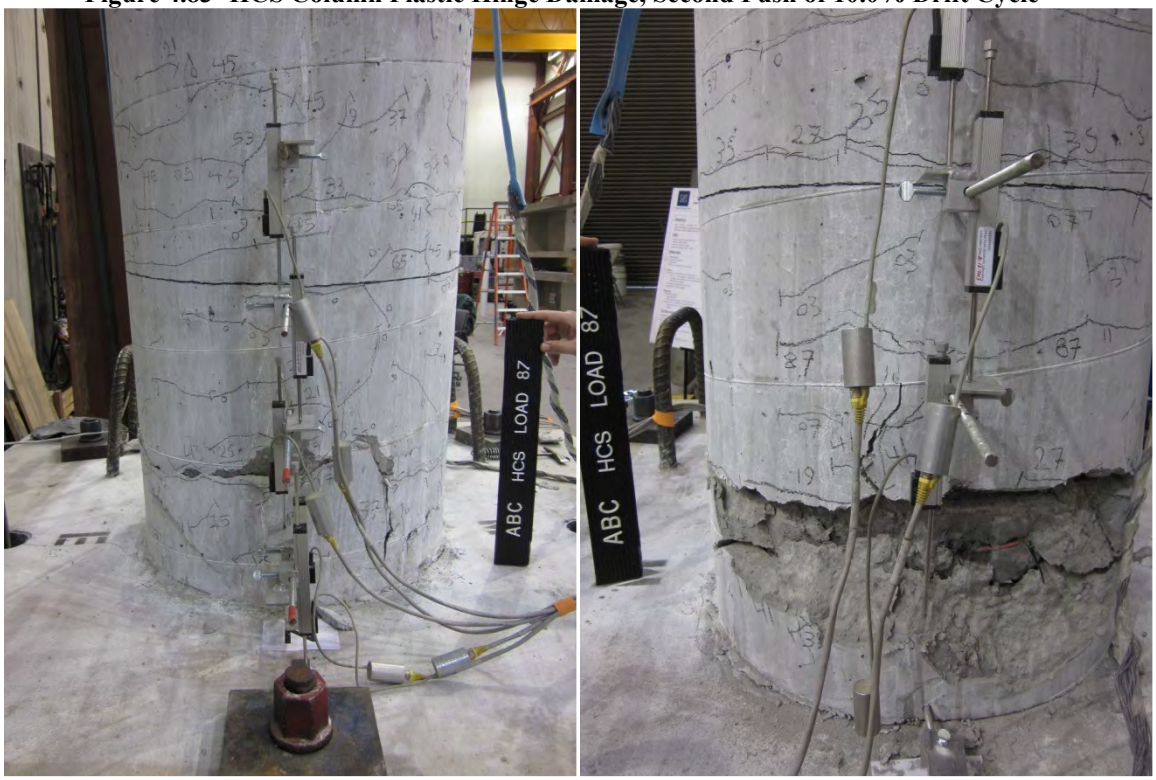

(a) North Side (b) South Side

Figure 4.84- HCS Column Plastic Hinge Damage, Second Pull of 10.0% Drift Cycle

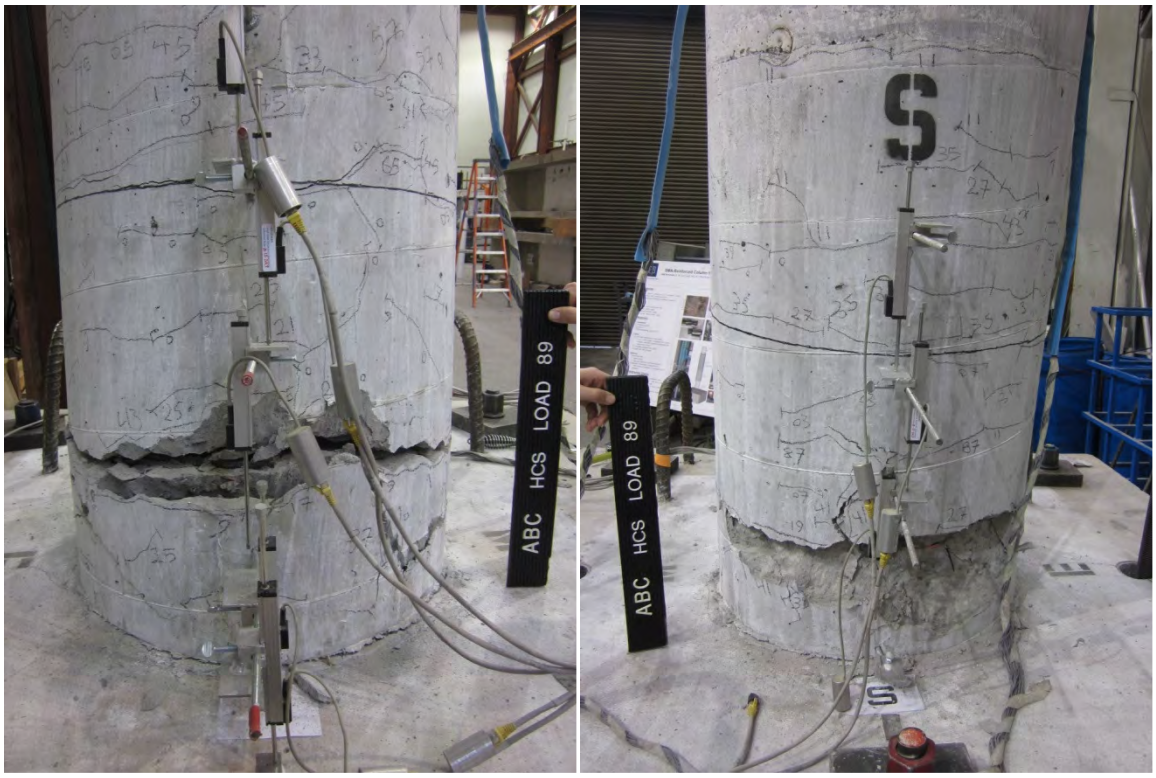

(a) North Side (b) South Side

Figure 4.85- HCS Column Plastic Hinge Damage, Push of 12.0% Drift Cycle

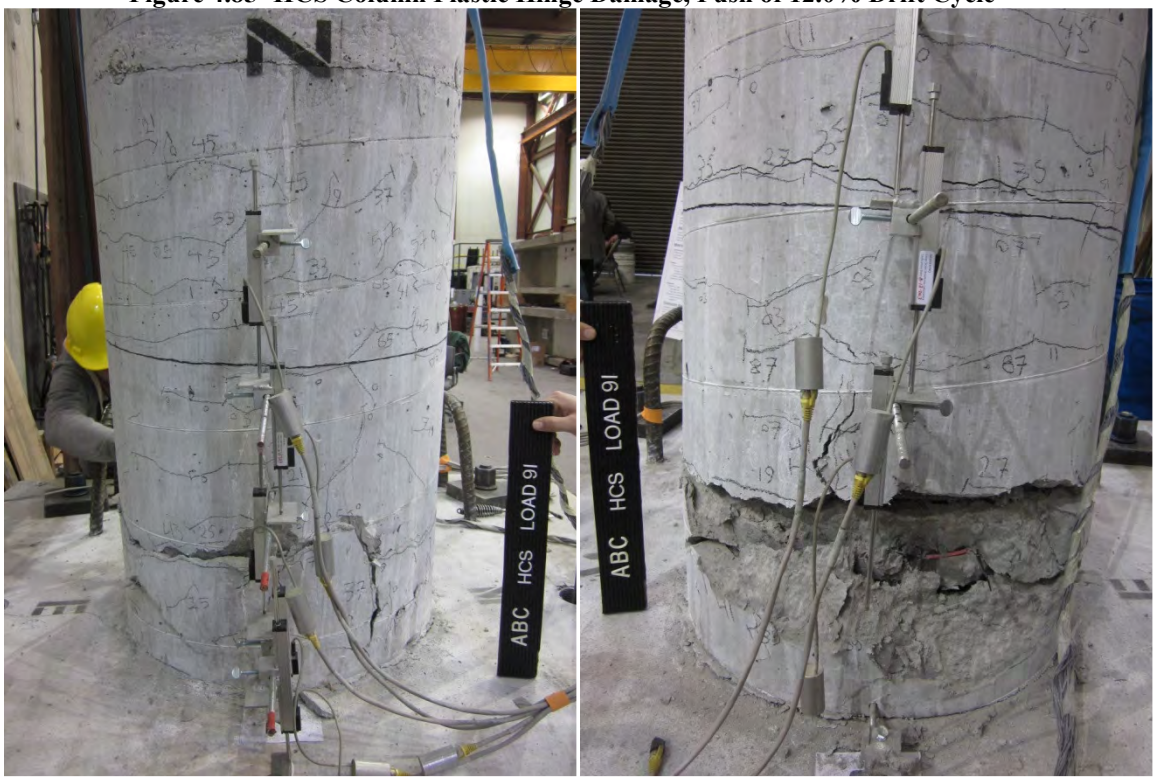

(a) North Side (b) South Side

Figure 4.86- HCS Column Plastic Hinge Damage, Pull of 12.0% Drift Cycle

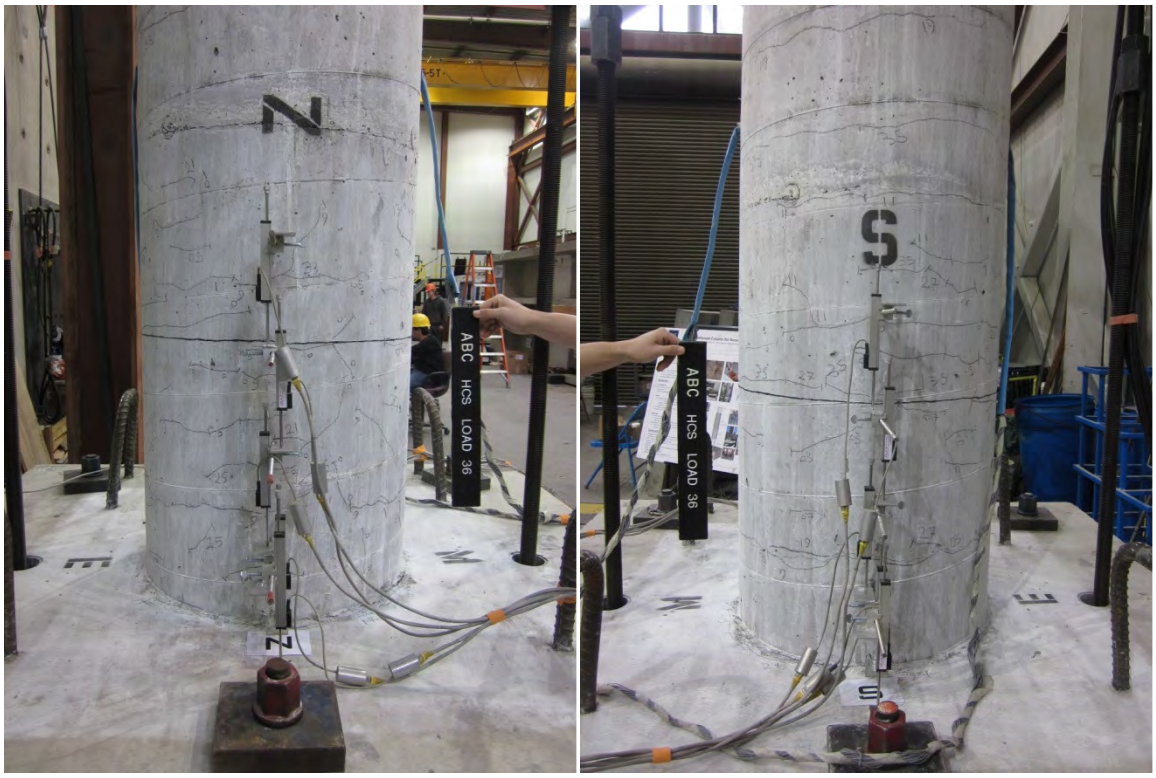

(a) North Side (b) South Side

Figure 4.87- HCS Columns Plastic Hinge Damage after One Complete cycle at ± 2% Drift

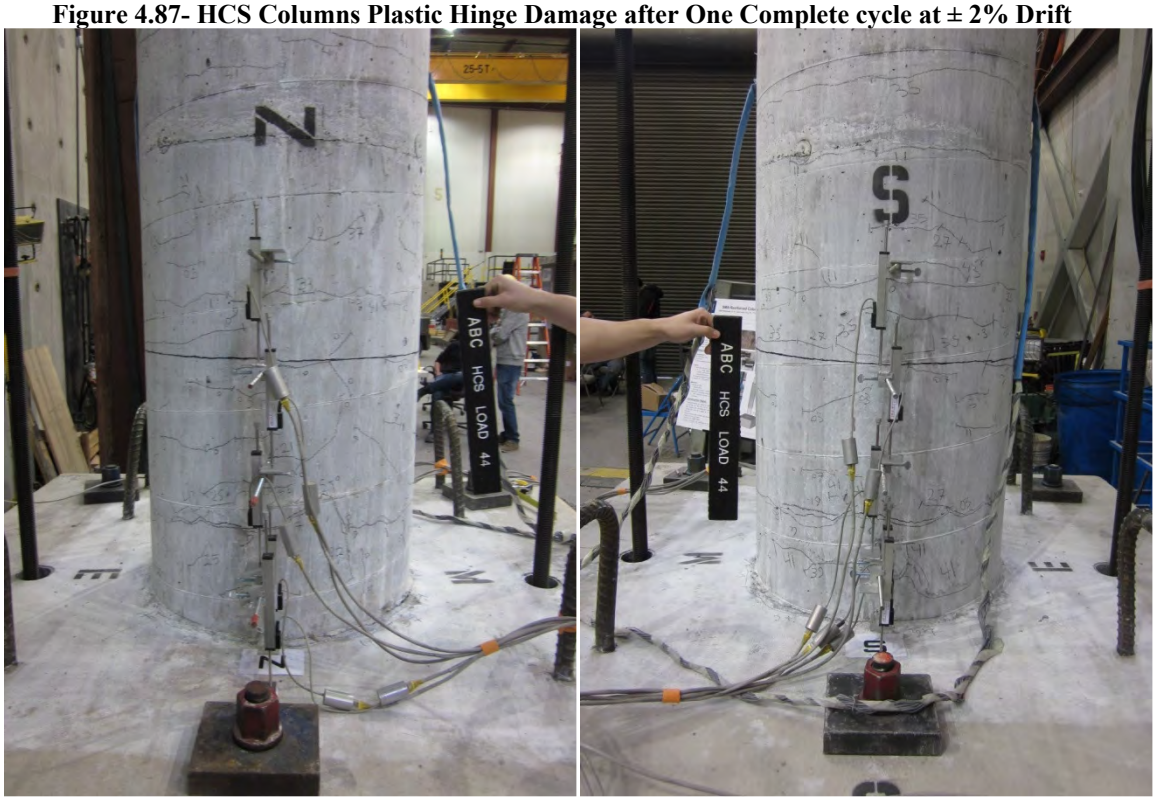

(a) North Side (b) South Side

Figure 4.88- HCS Columns Plastic Hinge Damage after One Complete cycle at ± 3% Drift

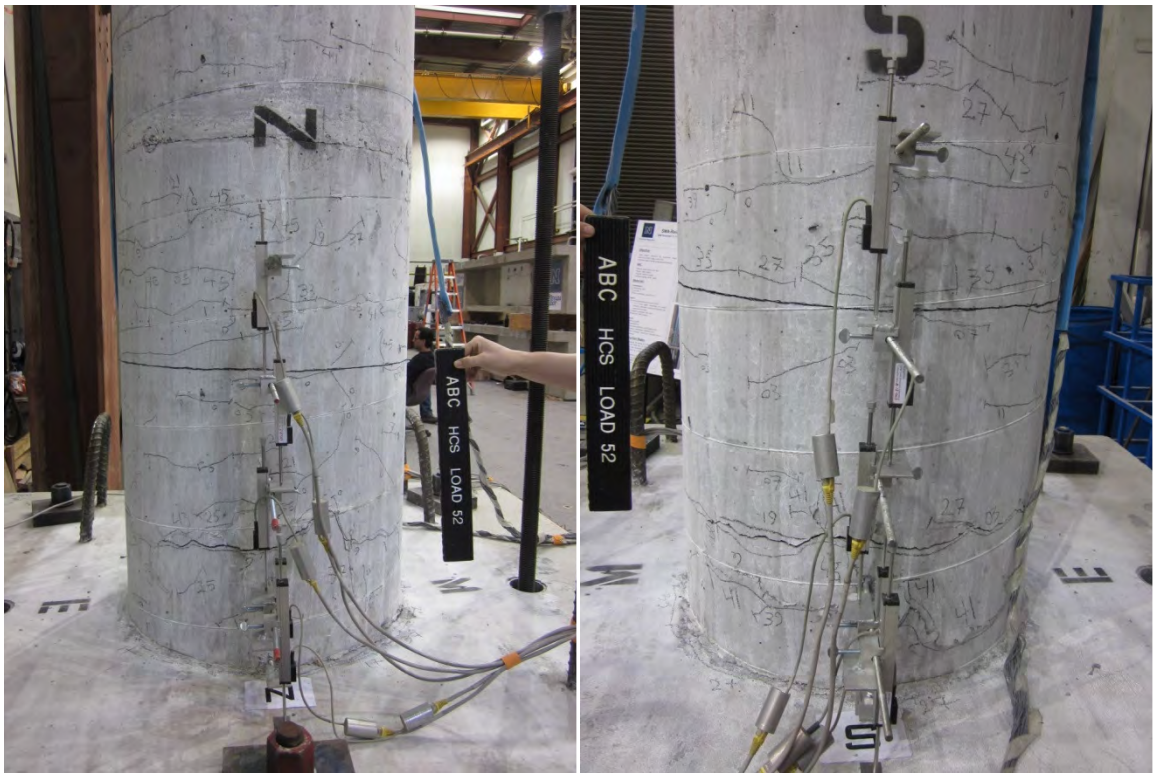

(a) North Side (b) South Side

Figure 4.89- HCS Columns Plastic Hinge Damage after One Complete cycle at ± 4% Drift

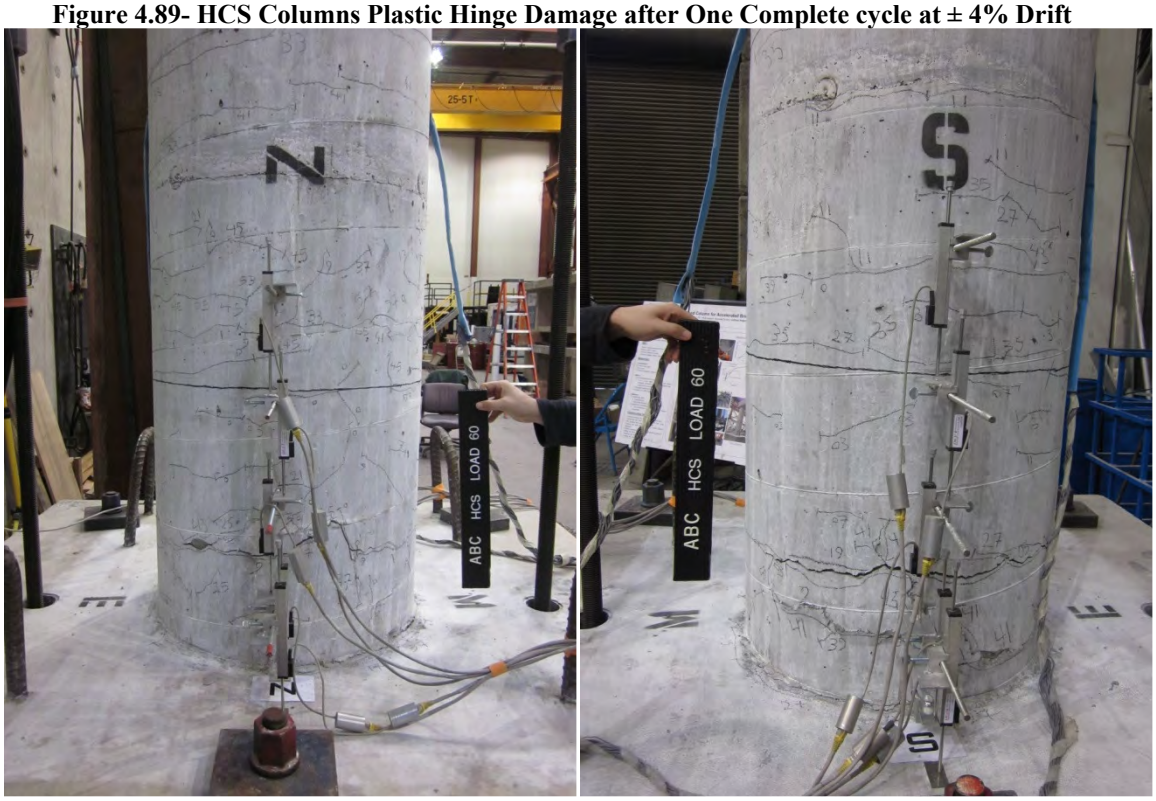

(a) North Side (b) South Side

Figure 4.90- HCS Columns Plastic Hinge Damage after One Complete cycle at ± 5% Drift

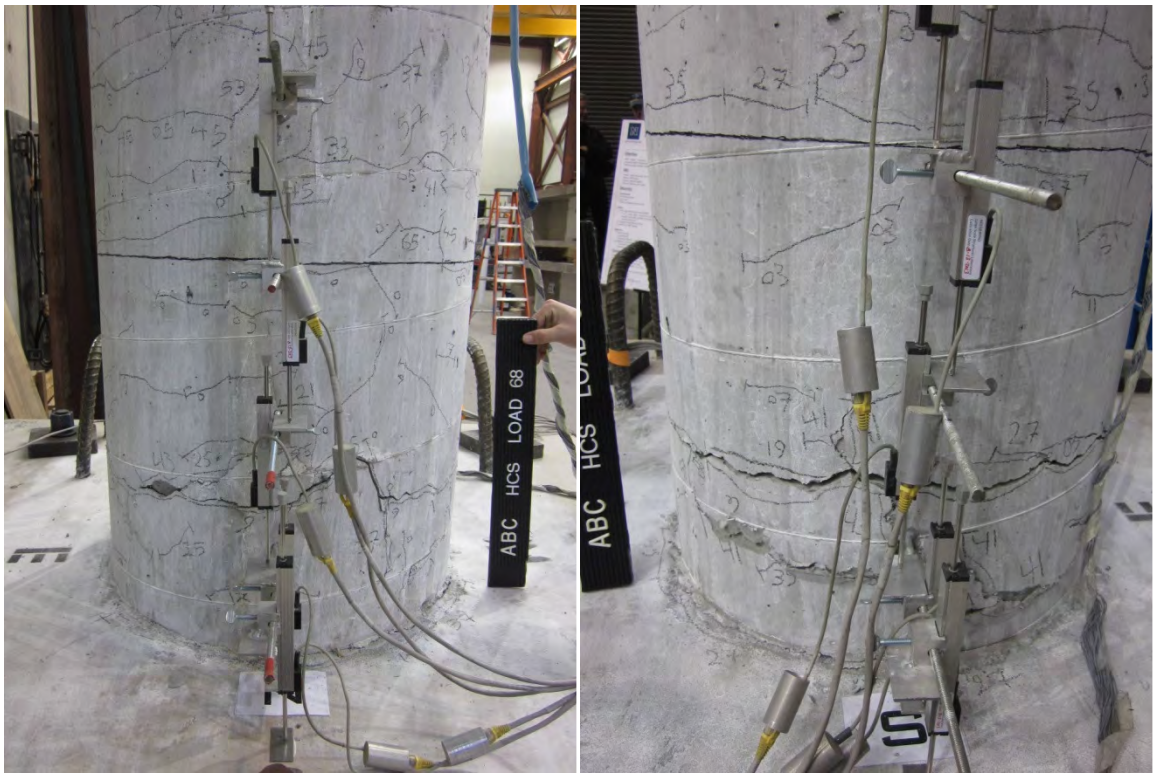

(a) North Side (b) South Side

Figure 4.91- HCS Columns Plastic Hinge Damage after One Complete cycle at ± 6% Drift

(a) North Side (b) South Side

Figure 4.92- HCS Columns Plastic Hinge Damage after One Complete cycle at ± 8% Drift

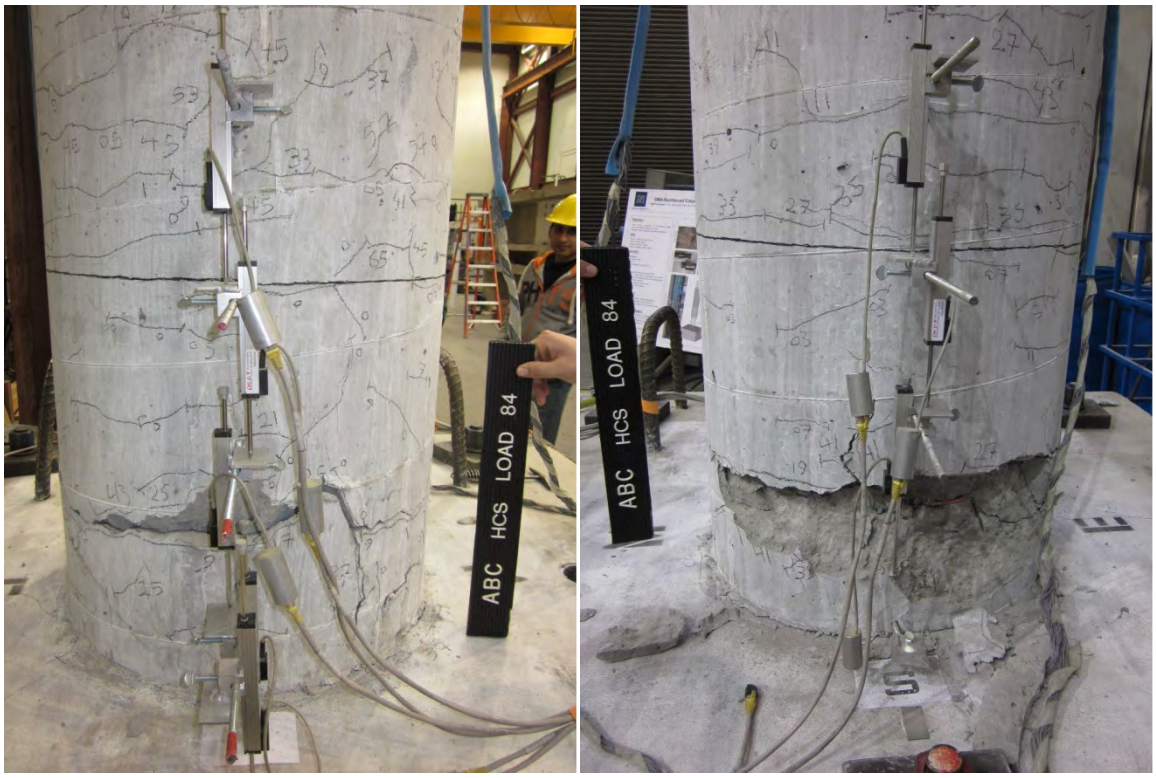

(a) North Side (b) South Side

Figure 4.93- HCS Columns Plastic Hinge Damage after One Complete cycle at ± 10% Drift

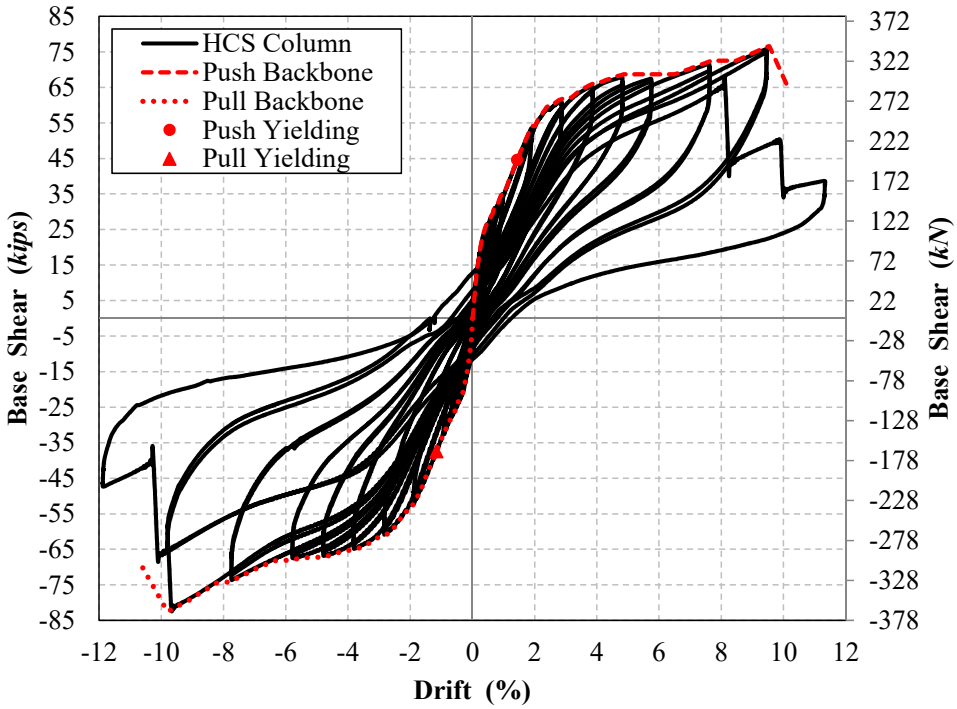

Figure 4.94- HCS Column Force-Drift Hysteretic and Envelope Responses

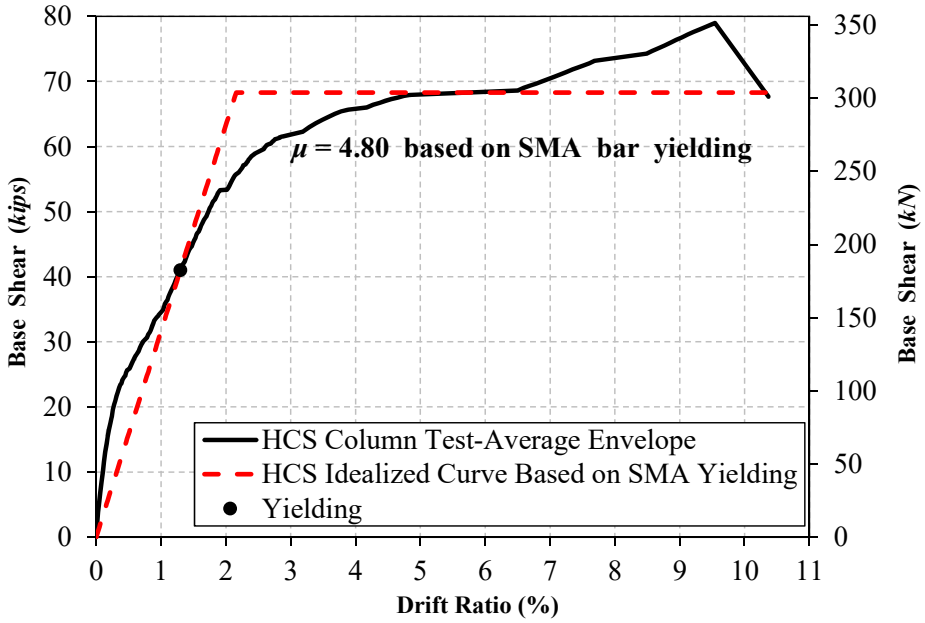

Figure 4.95- HCS Column Average Push/Pull Force-Displacement Envelope and Idealized Curve

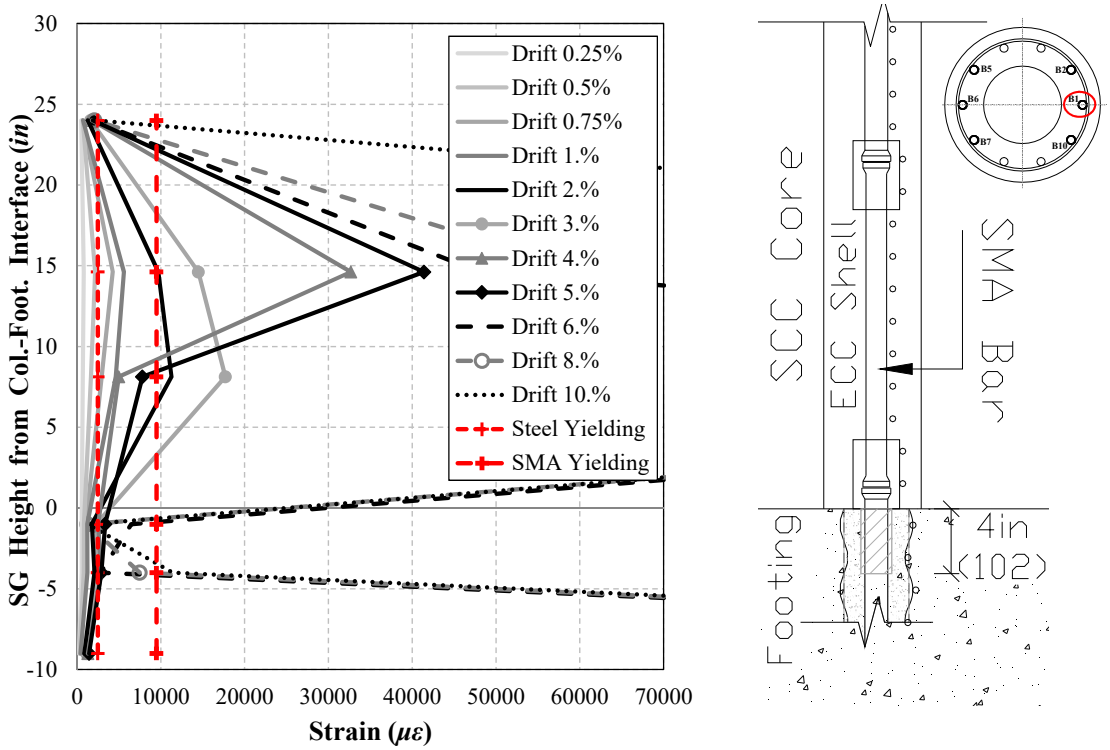

Figure 4.96- Strain Profile for HCS Column Bar B1 (1 *in.*= 25.4 *mm*)

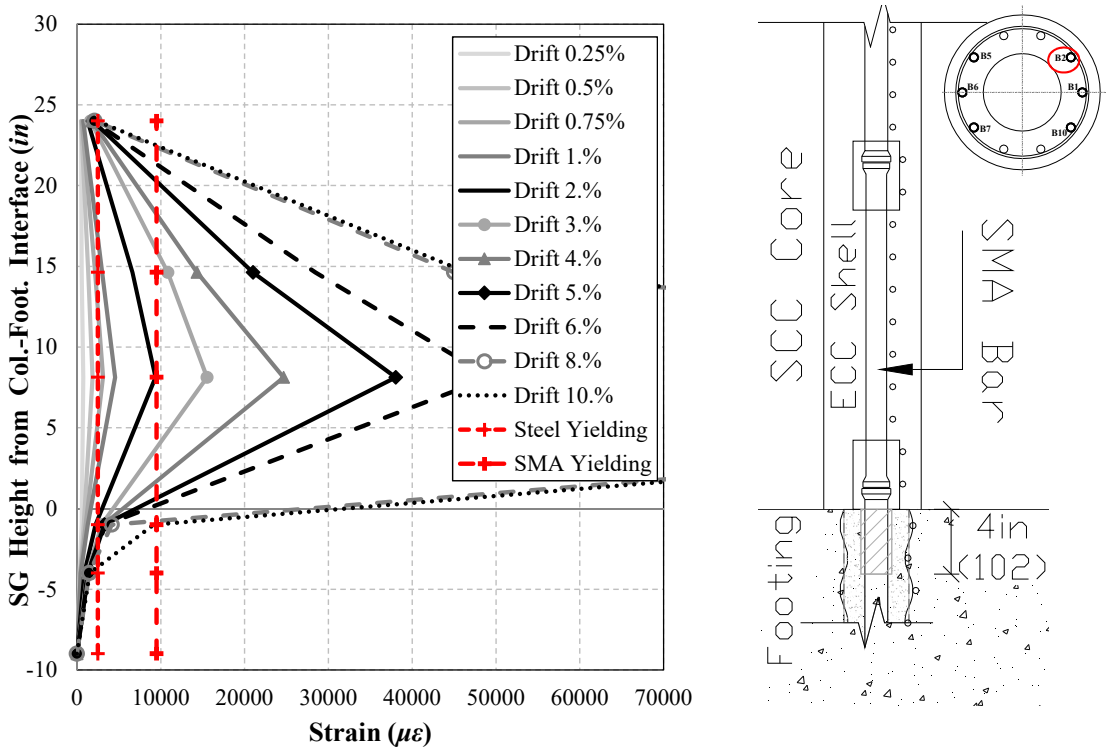

Figure 4.97- Strain Profile for HCS Column Bar B2 (1 *in*.= 25.4 *mm*)

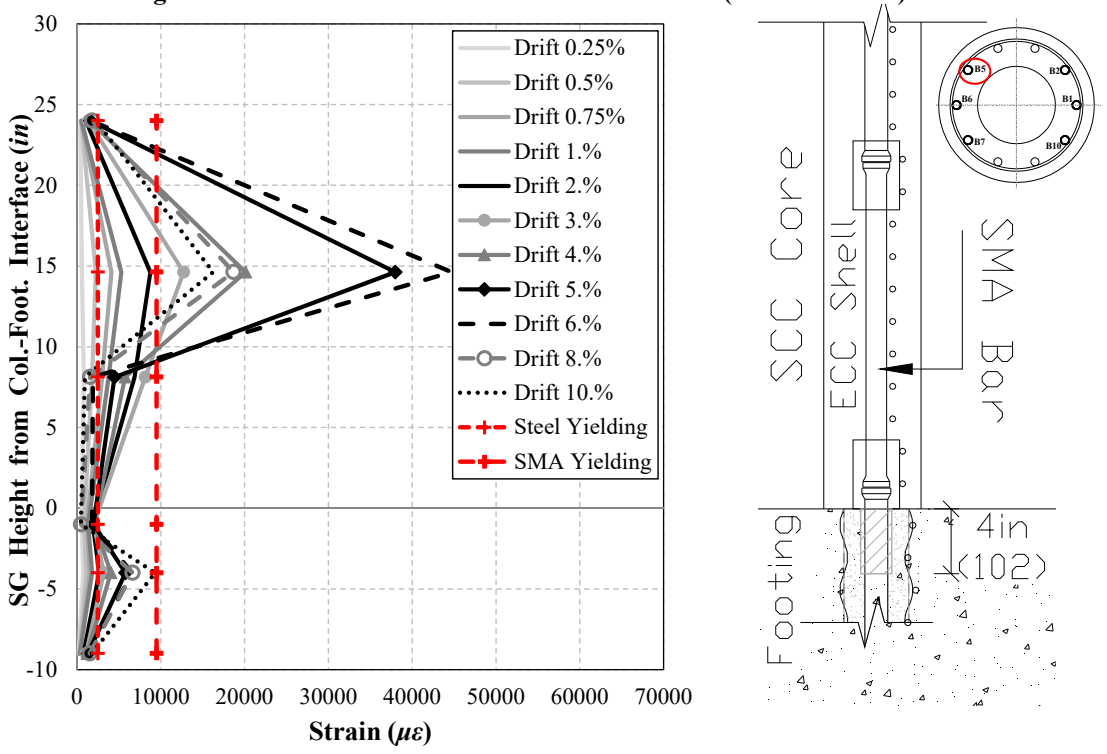

Figure 4.98- Strain Profile for HCS Column Bar B5 (1 *in*.= 25.4 *mm*)

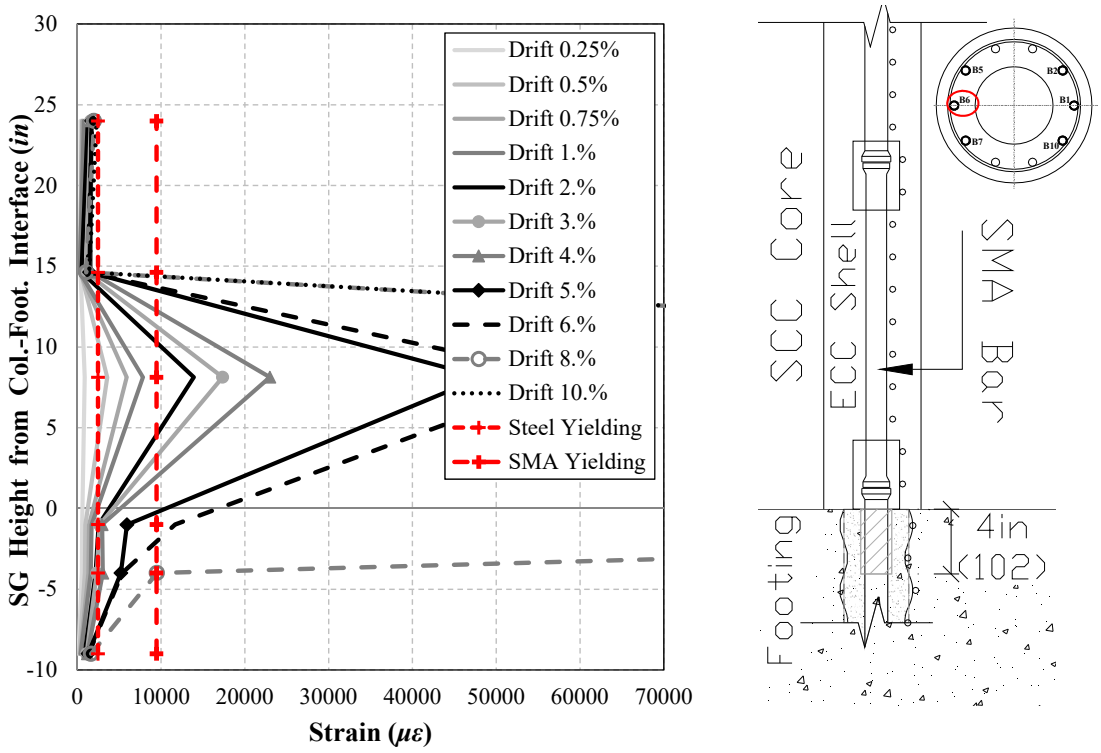

Figure 4.99- Strain Profile for HCS Column Bar B6 (1 *in*.= 25.4 *mm*)

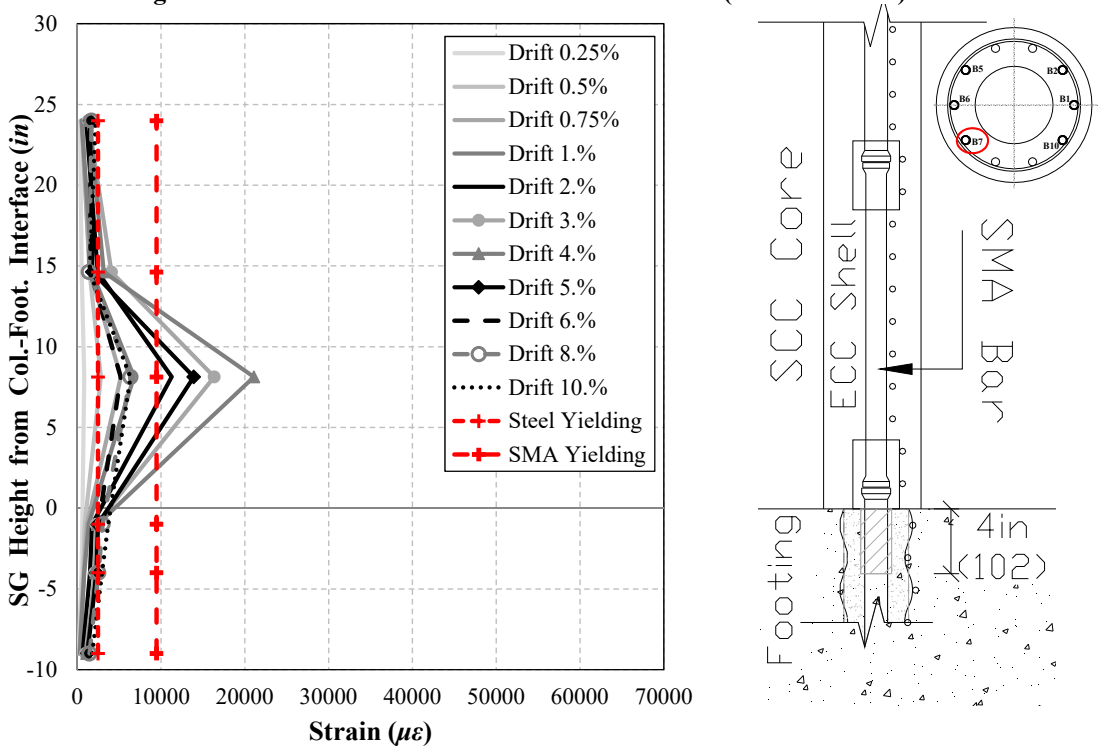

Figure 4.100- Strain Profile for HCS Column Bar B7 (1 *in*.= 25.4 *mm*)

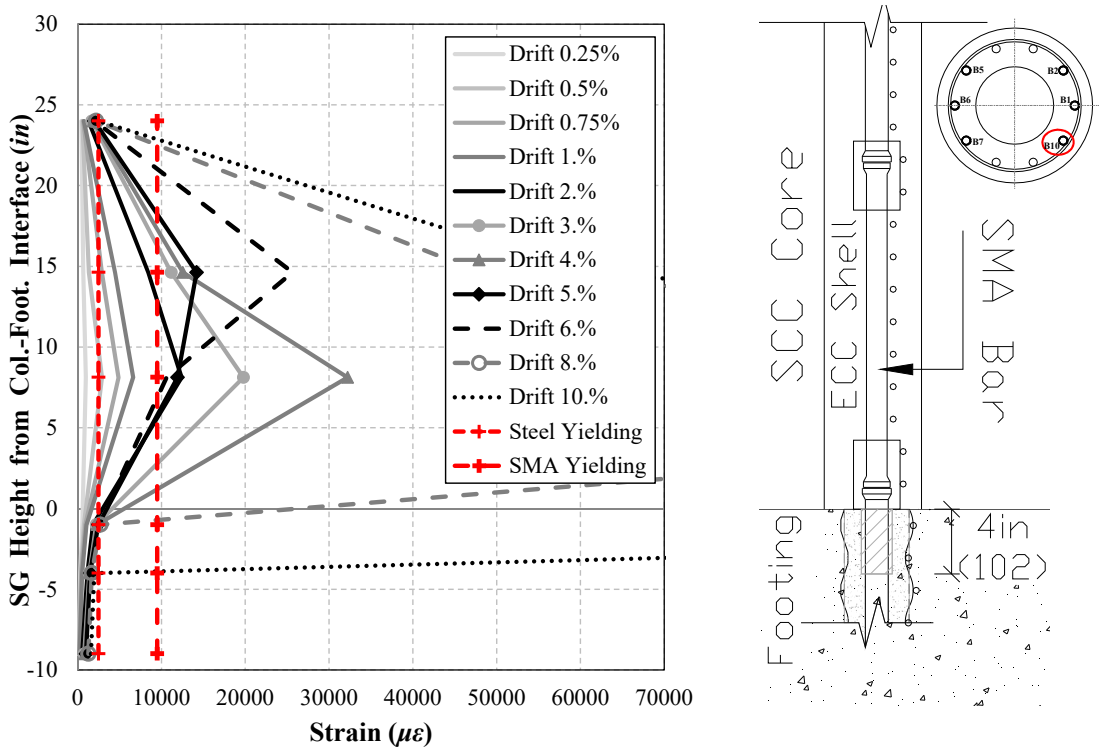

Figure 4.101- Strain Profile for HCS Column Bar B10 (1 *in*.= 25.4 *mm*)

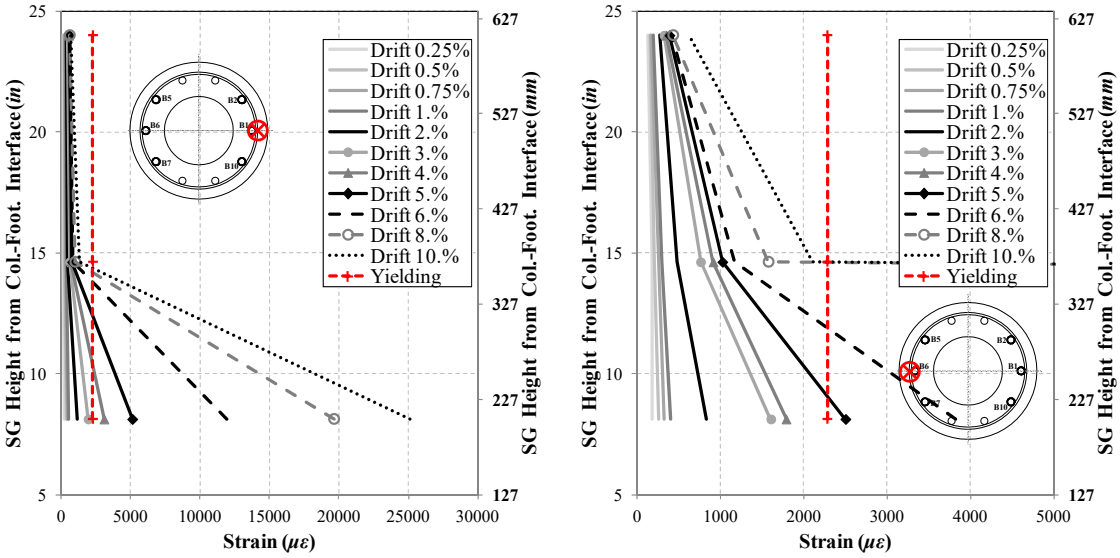

(a) North-Side of Column (b) South-Side of Column

Figure 4.102- Strain Profile for HCS Column Spiral in Compressive Zone

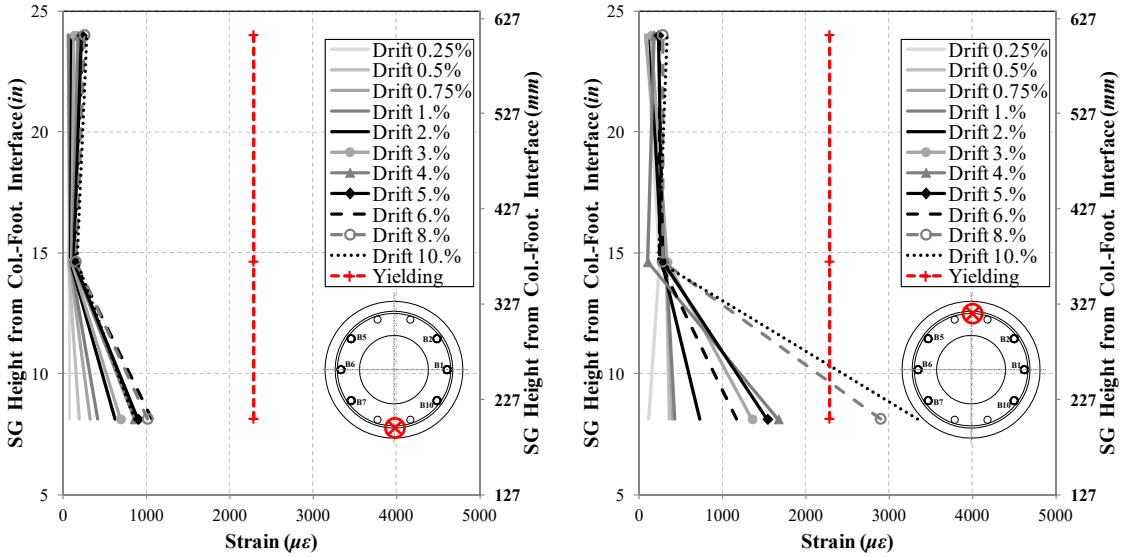

(a) East-Side of Column (b) West-Side of Column

Figure 4.103- Strain Profile for HCS Column Spiral in Shear Cracking Zone

Instrumentation Plan	
Test Lable	Instrument
BS01	TR75-11
BS02	TR75-40
C01	TR100-34
C02	TR75-41
C03	TR75-37
C04	TR75-33
C05	TR100-18
C06	TR75-01
C07	TR75-36
C08	TR75-27
D01	SP63
D02	SP38
D03	SP49
D04	NONE

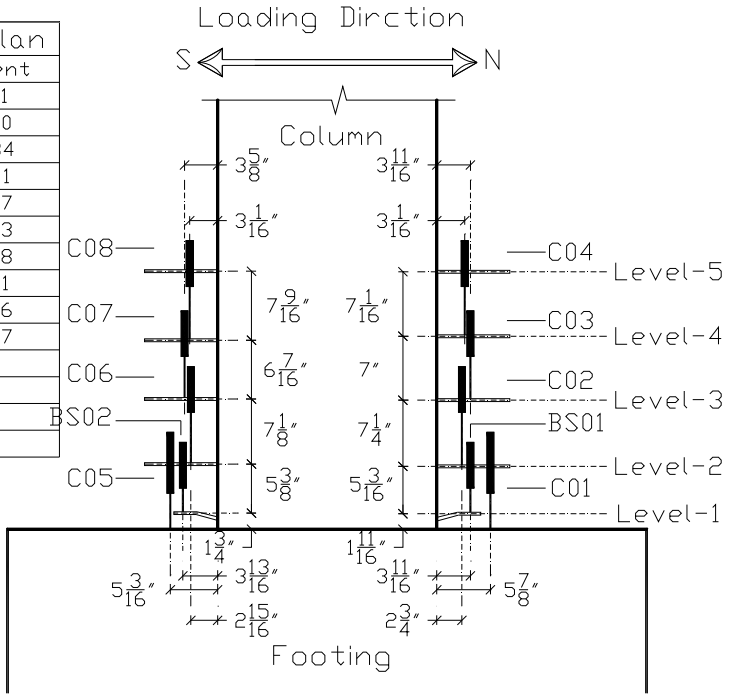

Figure 4.104- As-built Displacement Instrumentation Plan at Base of HCS Column (1 *in.*=25 *mm*)

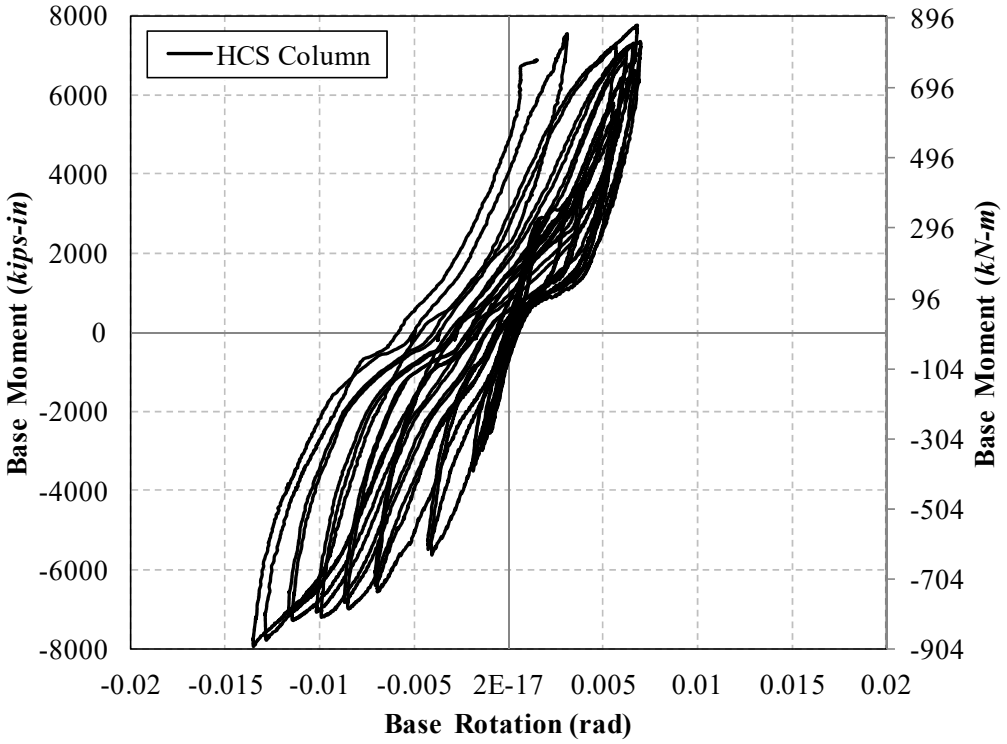

Figure 4.105- Base Moment-Rotation Relationship for HCS Column

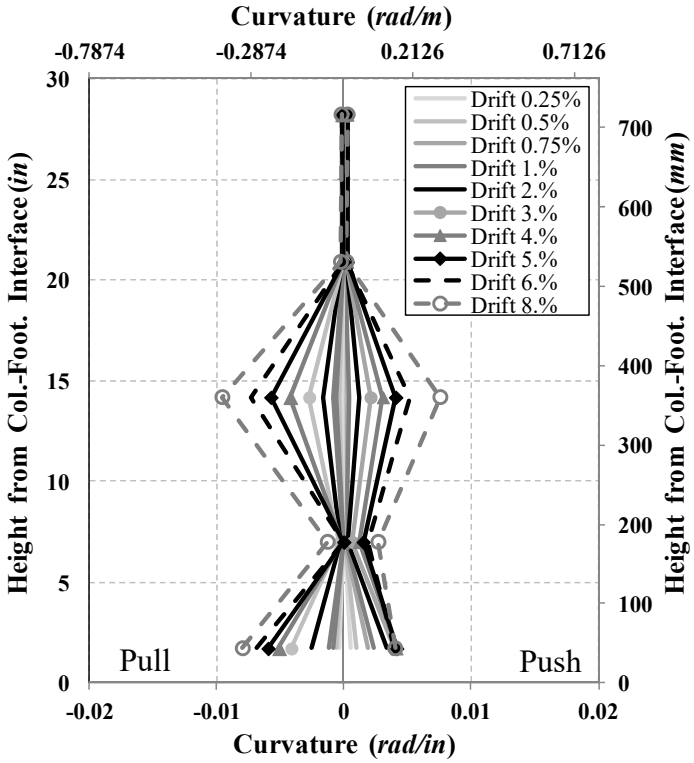

Figure 4.106- Curvature Profile for HCS Column

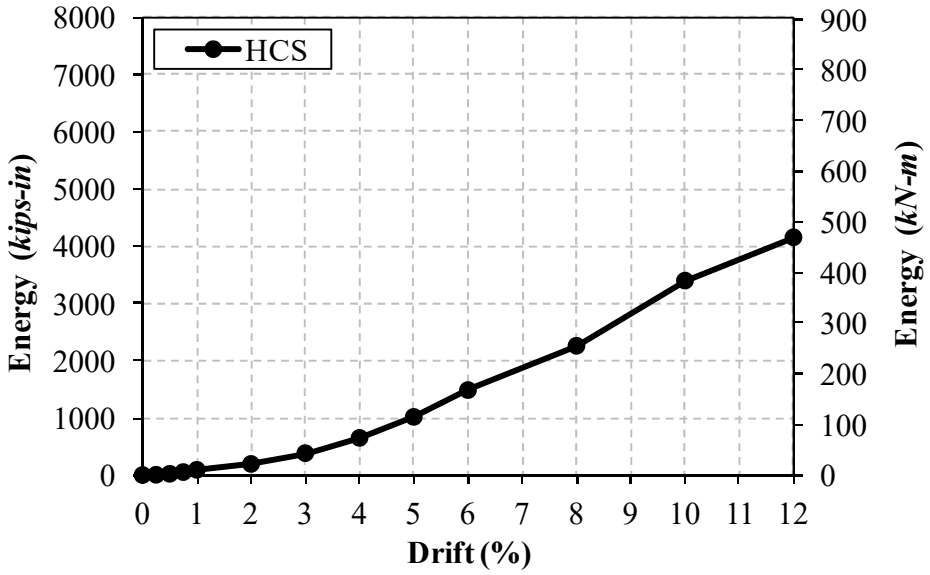

Figure 4.107- Energy Dissipation for HCS Column

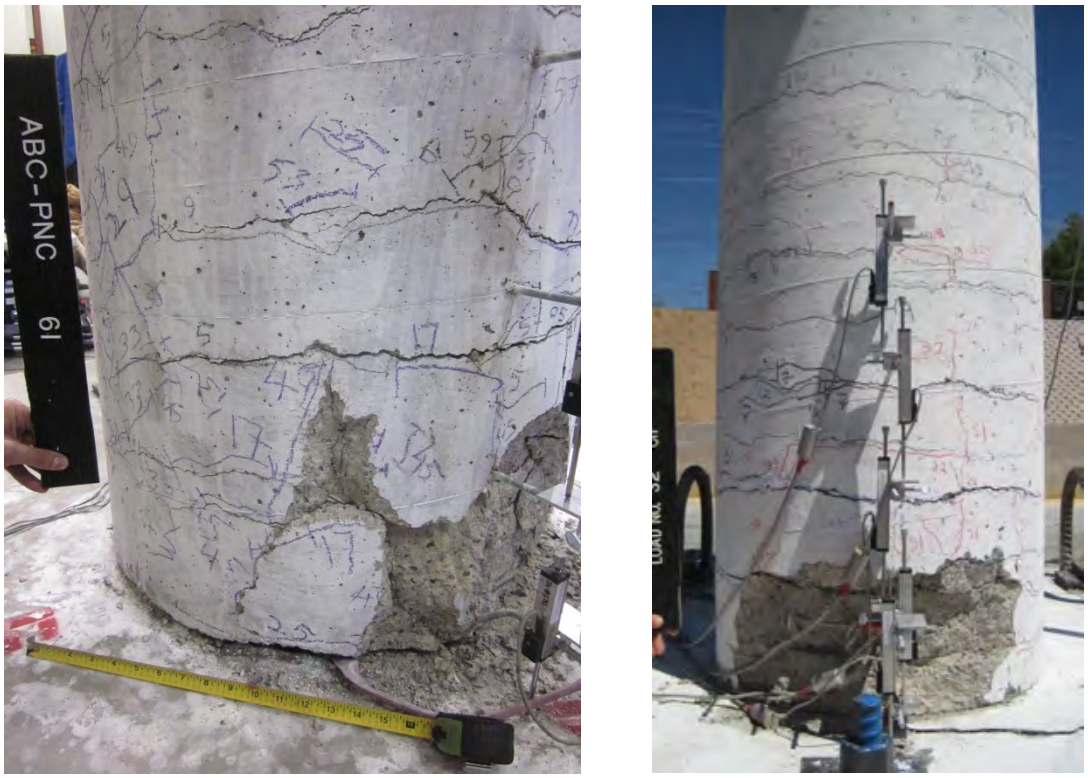

Figure 5.1- PNC (Left) and CIP (Right) Columns Plastic Hinge Damage at Second Push of 5% Drift

Figure 5.2- PNC (Left) and CIP (Right) Columns Plastic Hinge Damage at Second Pull of 5% Drift

Figure 5.3- PNC (Left) and CIP (Right) Columns Plastic Hinge Damage at Second Push of 8% Drift

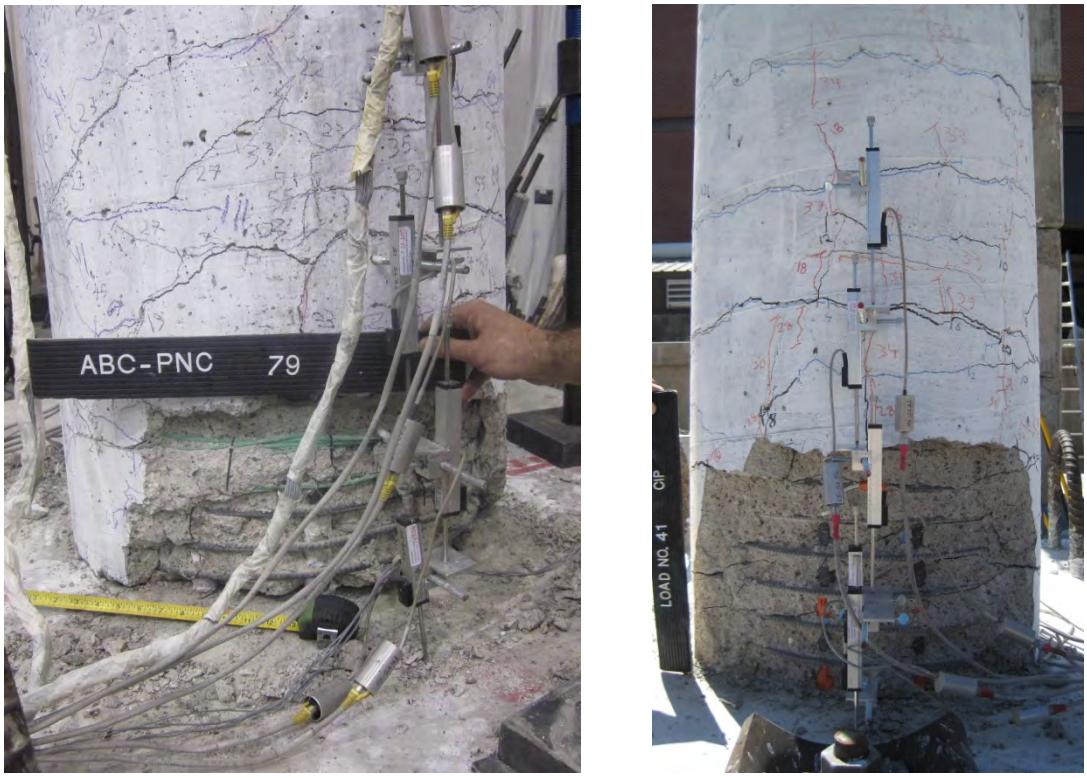

Figure 5.4- PNC (Left) and CIP (Right) Columns Plastic Hinge Damage at Second Pull of 8% Drift

Figure 5.5- PNC (Left) and CIP (Right) Columns Plastic Hinge Damage at Last Push of 10% Drift

Figure 5.6- PNC (Left) and CIP (Right) Columns Plastic Hinge Damage at Last Pull of 10% Drift

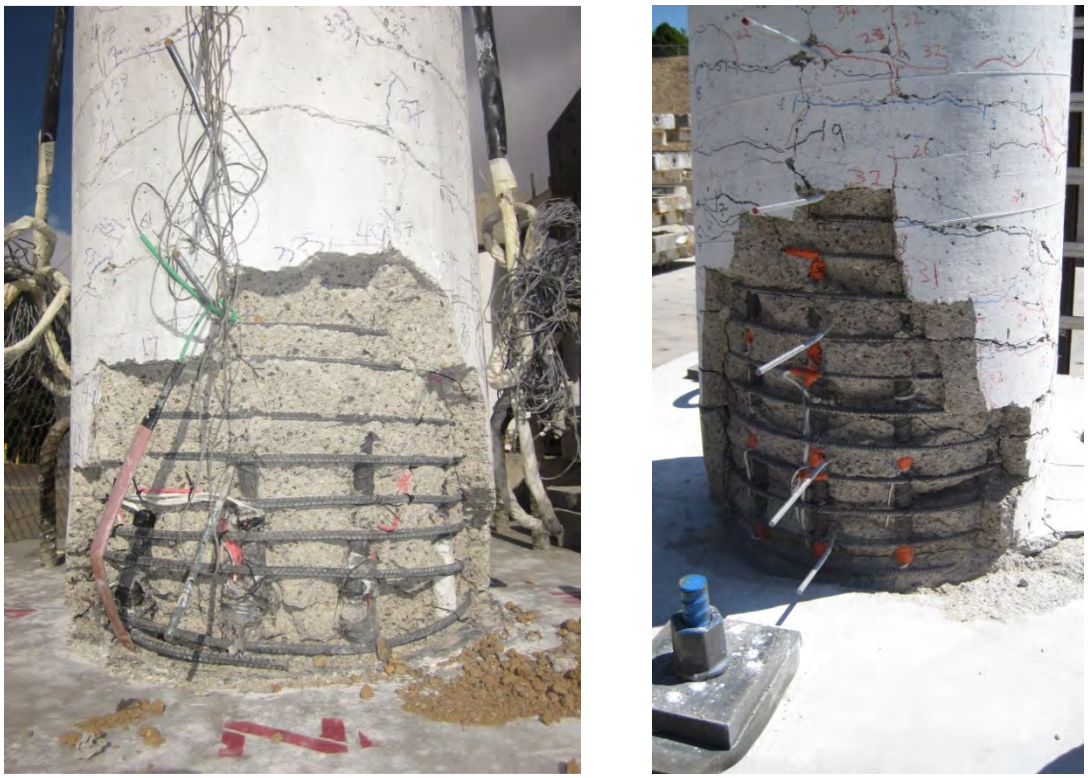

Figure 5.7- PNC (Left) and CIP (Right) Columns Plastic Hinge Damage after Testing

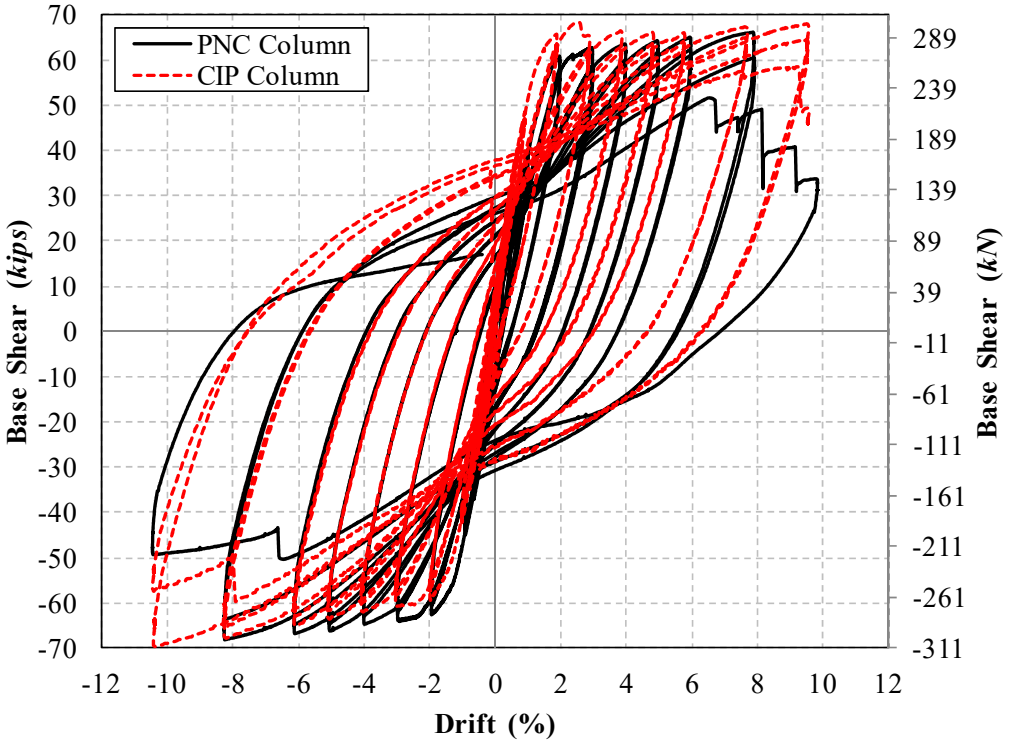

Figure 5.8- PNC and CIP Column Force-Drift Hysteretic Responses

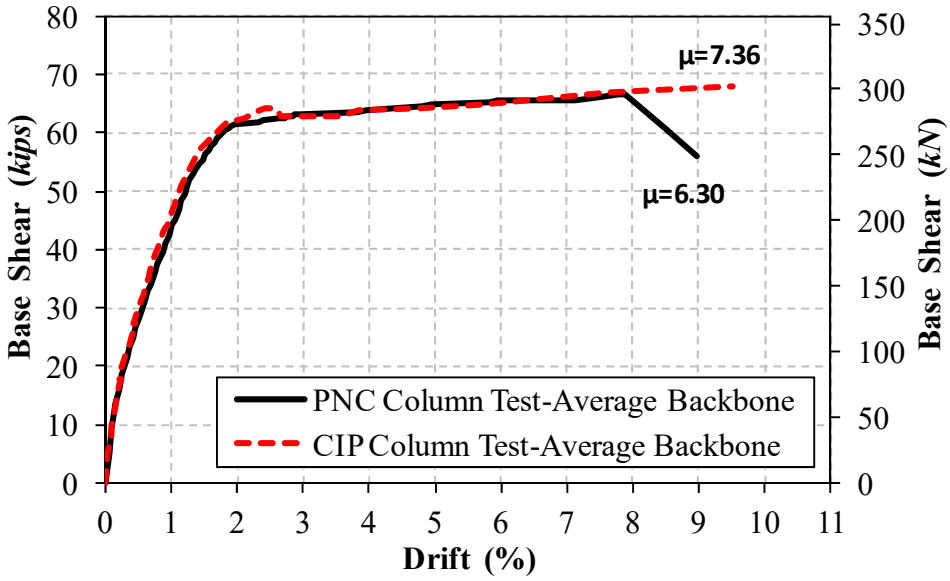

Figure 5.9- PNC and CIP Column Average Push/Pull Force-Drift Envelopes

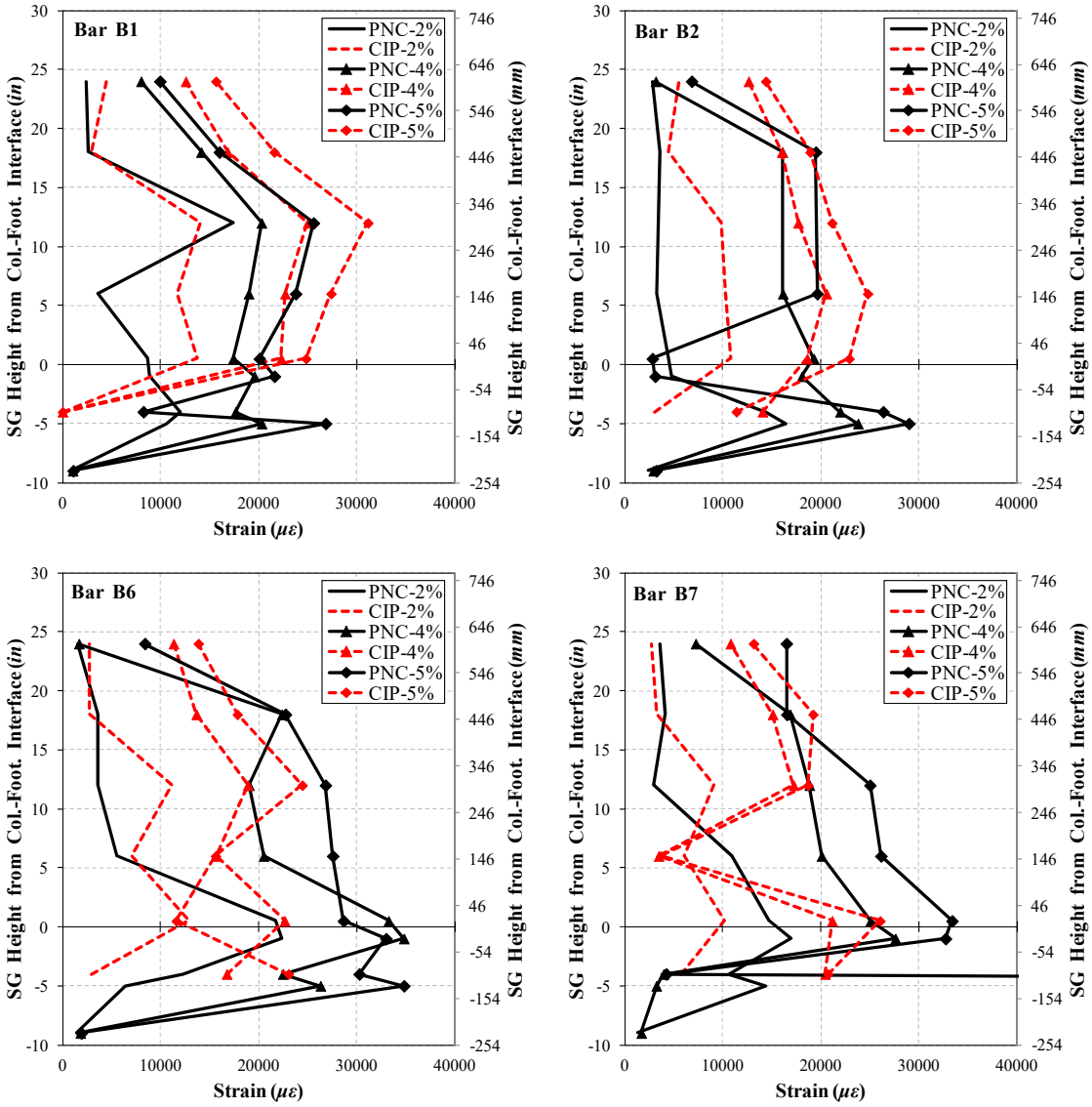

Figure 5.10- Strain Profile for PNC and CIP Columns for Longitudinal Bar B1, B2, B6, and B7

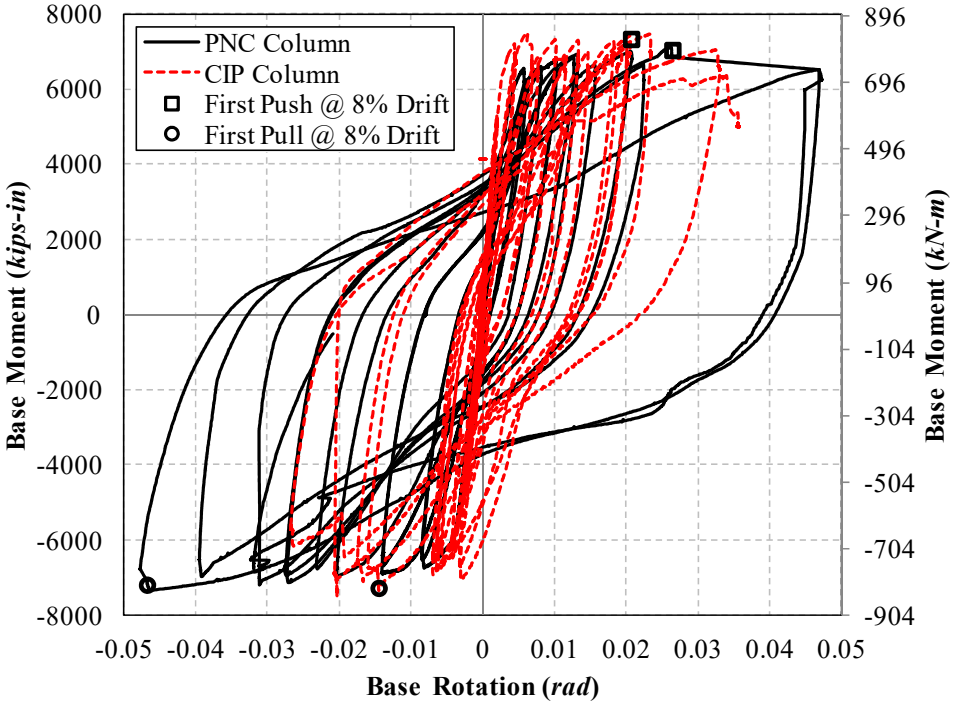

Figure 5.11- Base Moment-Rotation Relationship for PNC and CIP Columns

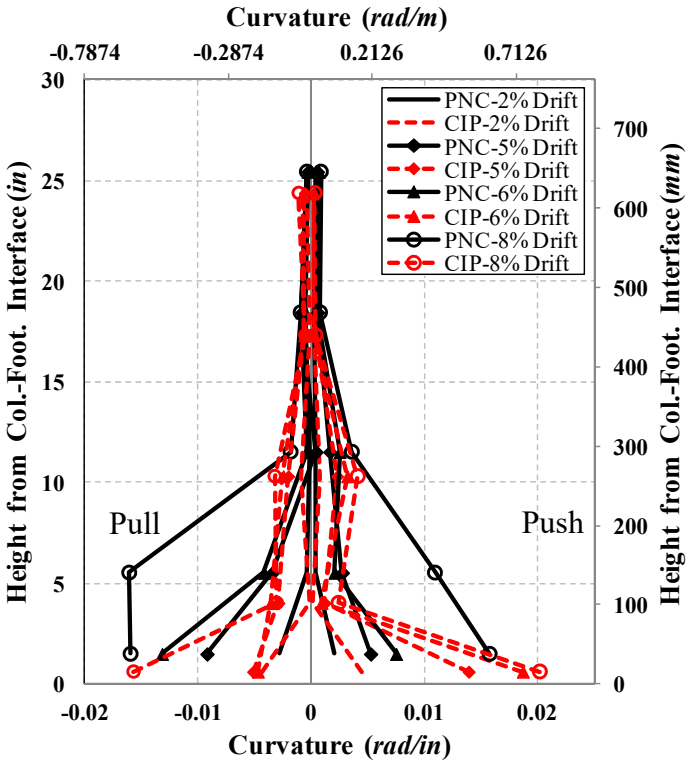

Figure 5.12- Curvature Profile for PNC and CIP Columns

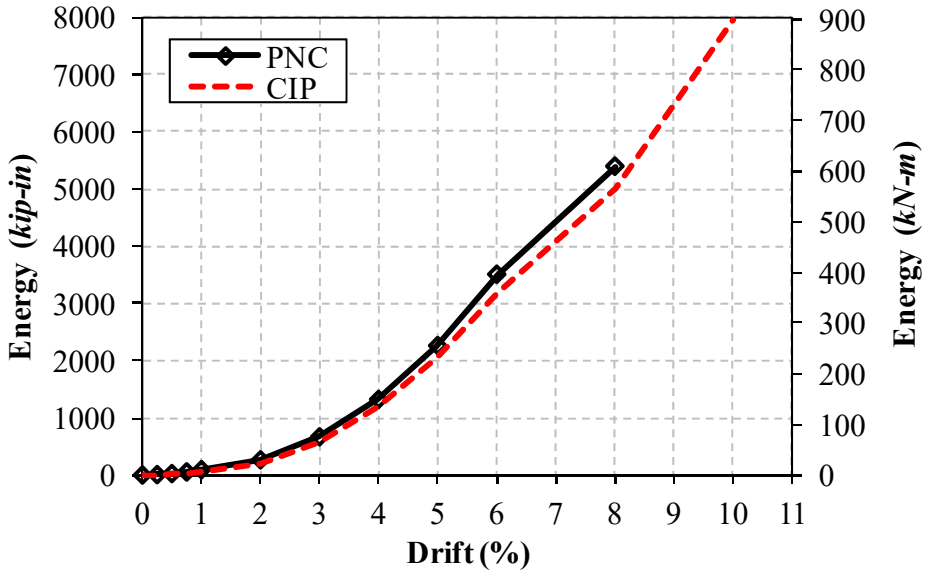

Figure 5.13- Energy Dissipation for PNC and CIP Columns

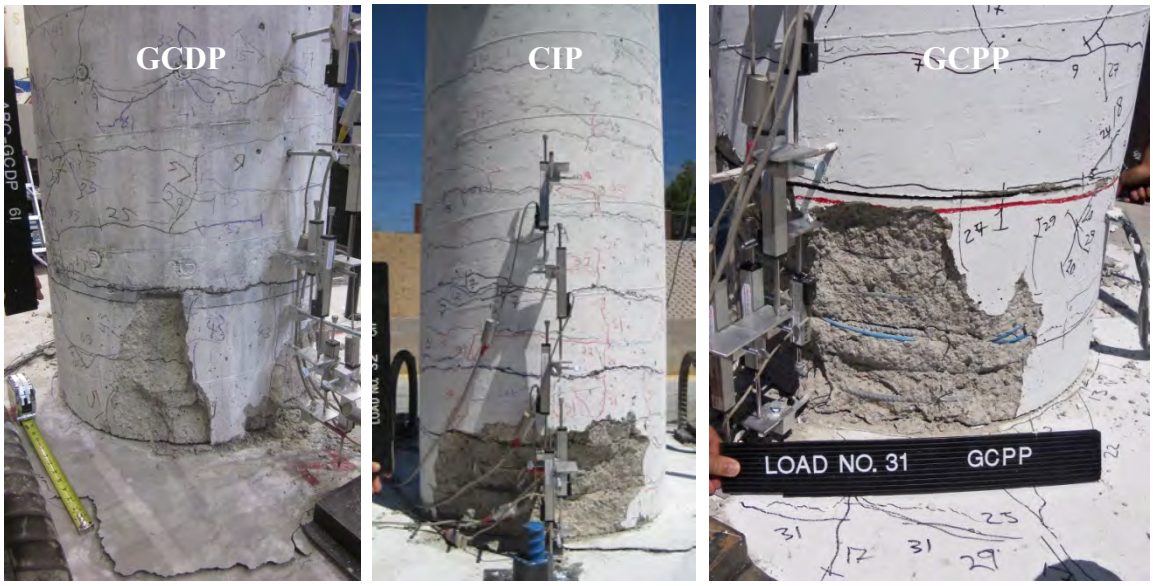

Figure 5.14- GCDP, CIP, and GCPP Columns Plastic Hinge Damage at Second Push of 5% Drift

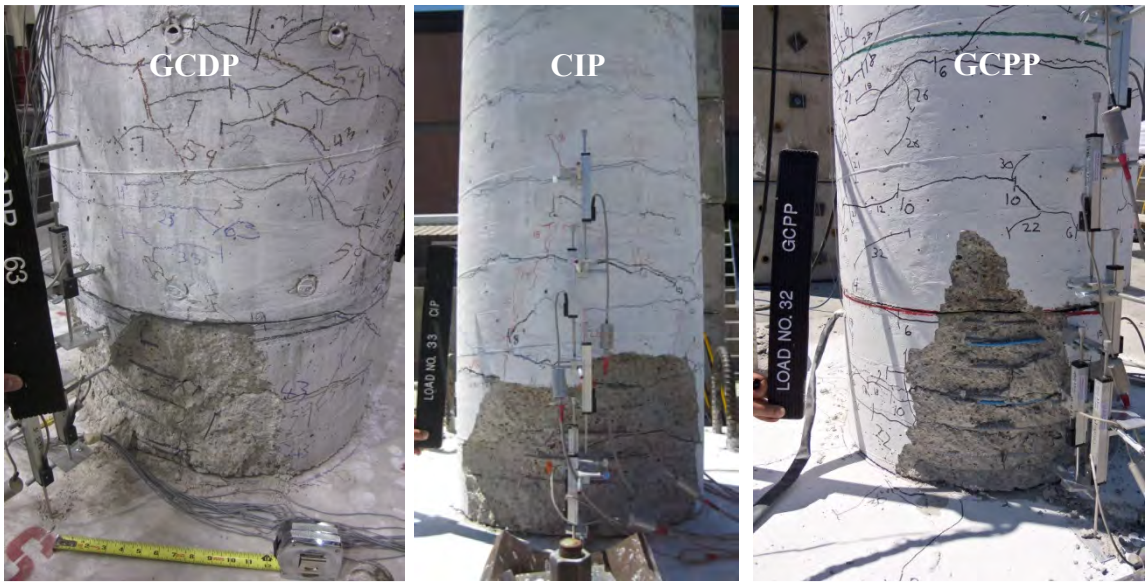

Figure 5.15- GCDP, CIP, and GCPP Columns Plastic Hinge Damage at Second Pull of 5% Drift

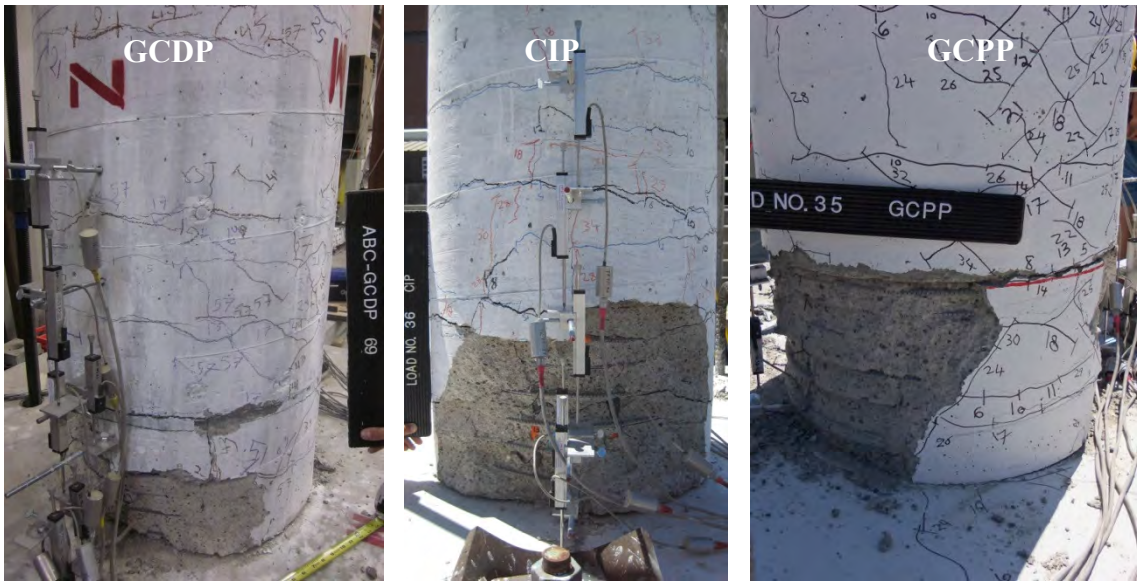

Figure 5.16- GCDP, CIP, and GCPP Columns Plastic Hinge Damage at Second Push of 6% Drift

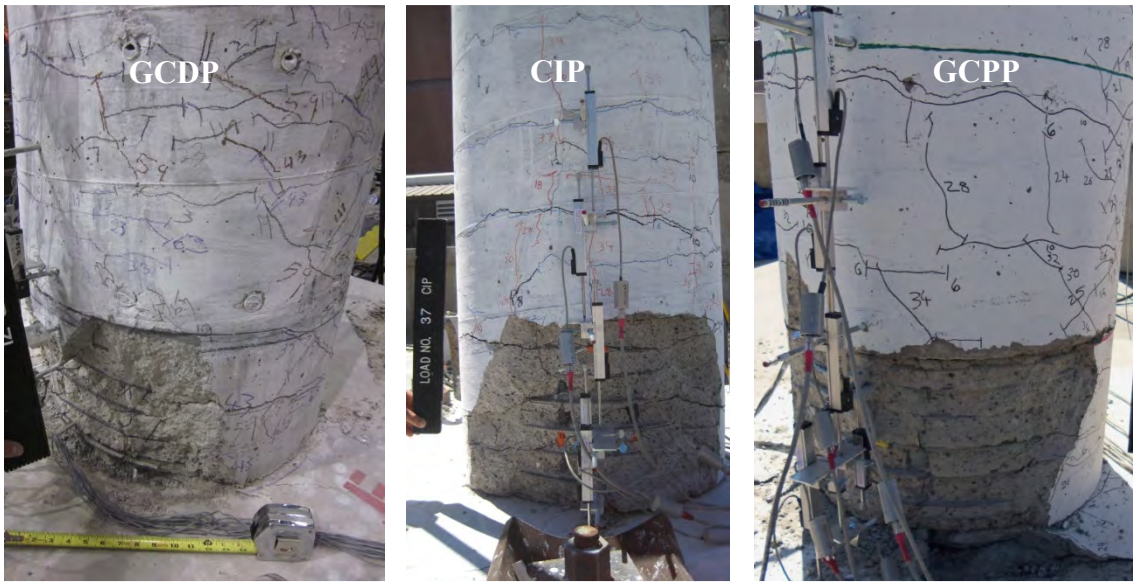

Figure 5.17- GCDP, CIP, and GCPP Columns Plastic Hinge Damage at Second Pull of 6% Drift

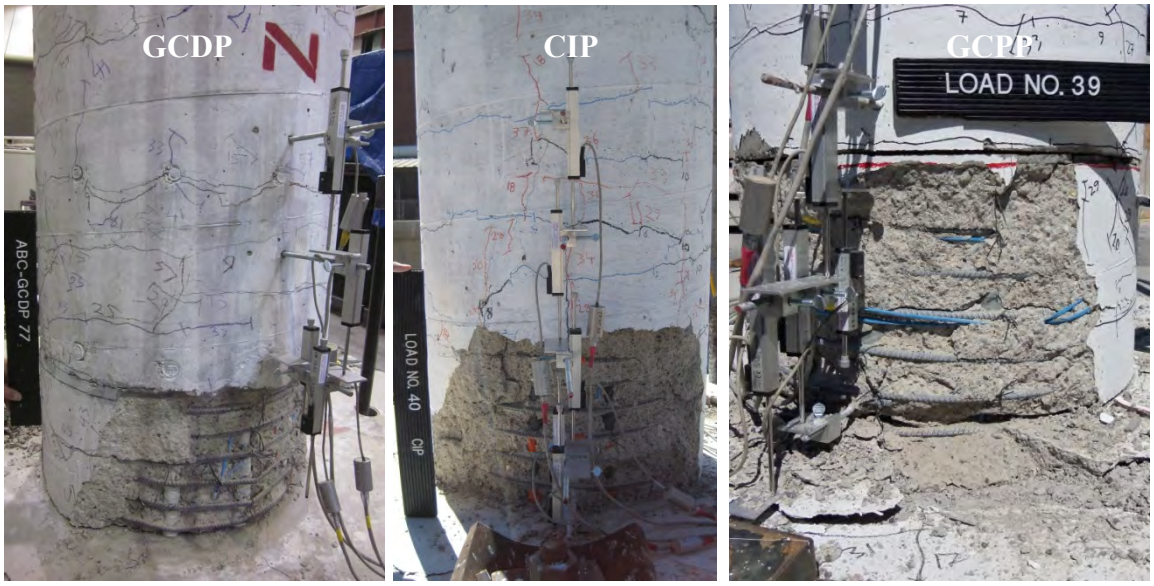

Figure 5.18- GCDP, CIP, and GCPP Columns Plastic Hinge Damage at Second Push of 8% Drift

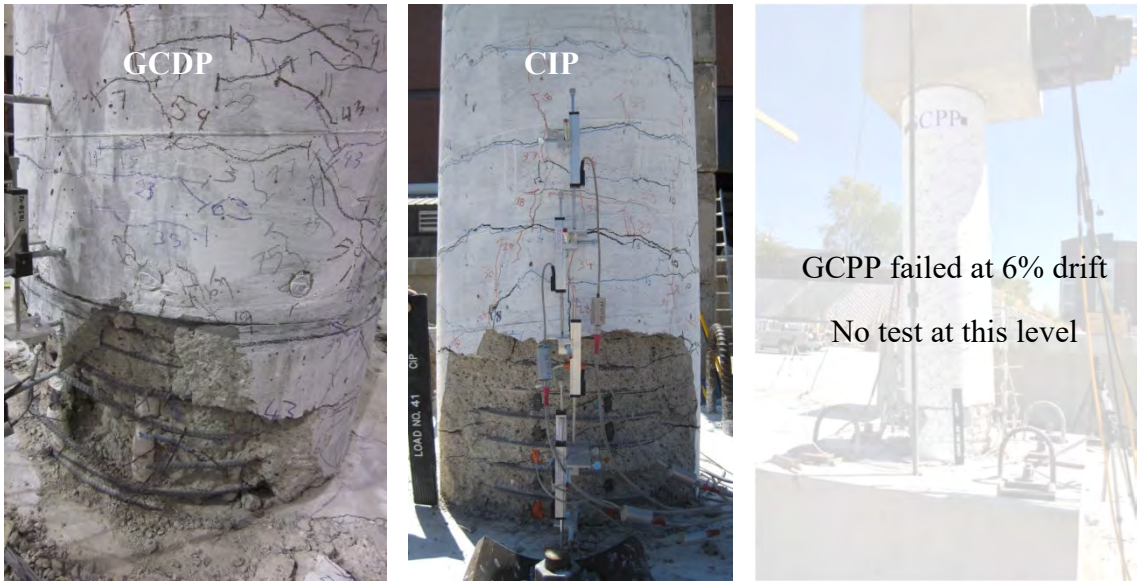

Figure 5.19- GCDP, CIP, and GCPP Columns Plastic Hinge Damage at Second Pull of 8% Drift

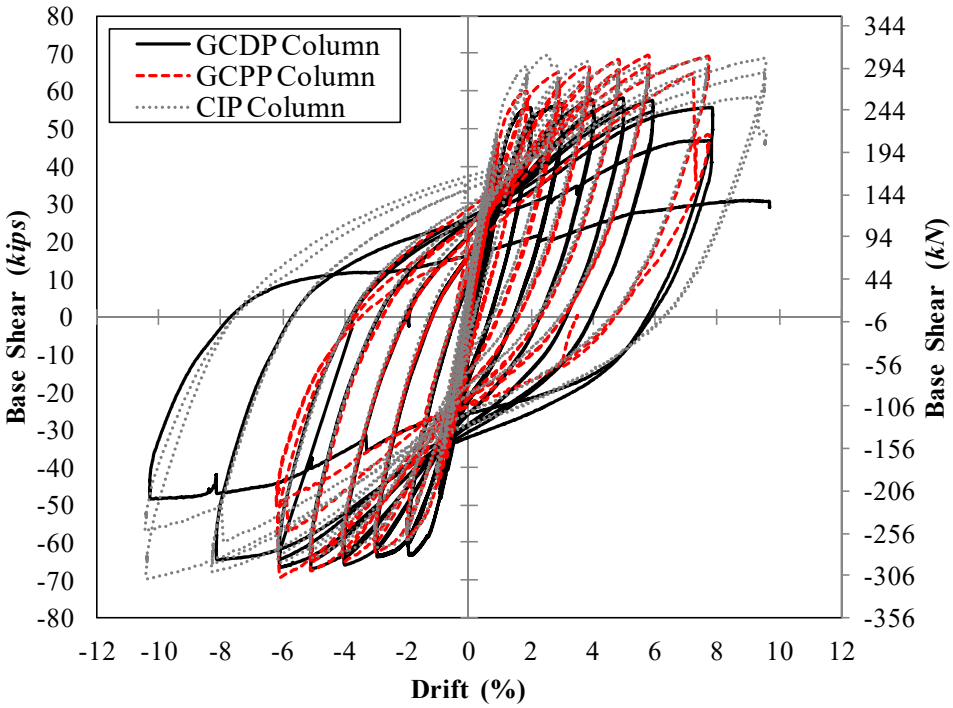

Figure 5.20- GCDP, GCPP, and CIP Force-Drift Hysteretic Responses

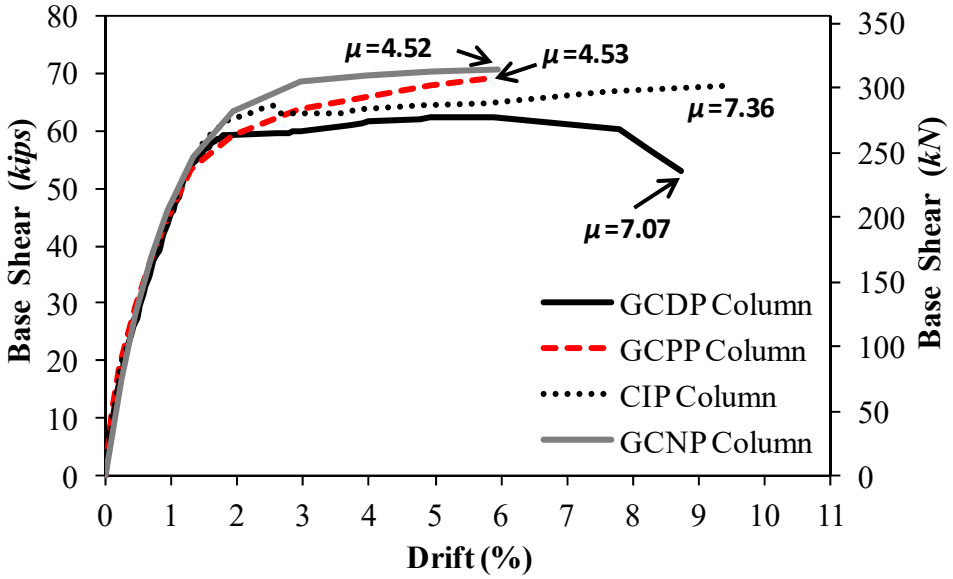

Figure 5.21- Grouted Coupler and CIP Column Average Push/Pull Force-Drift Envelopes

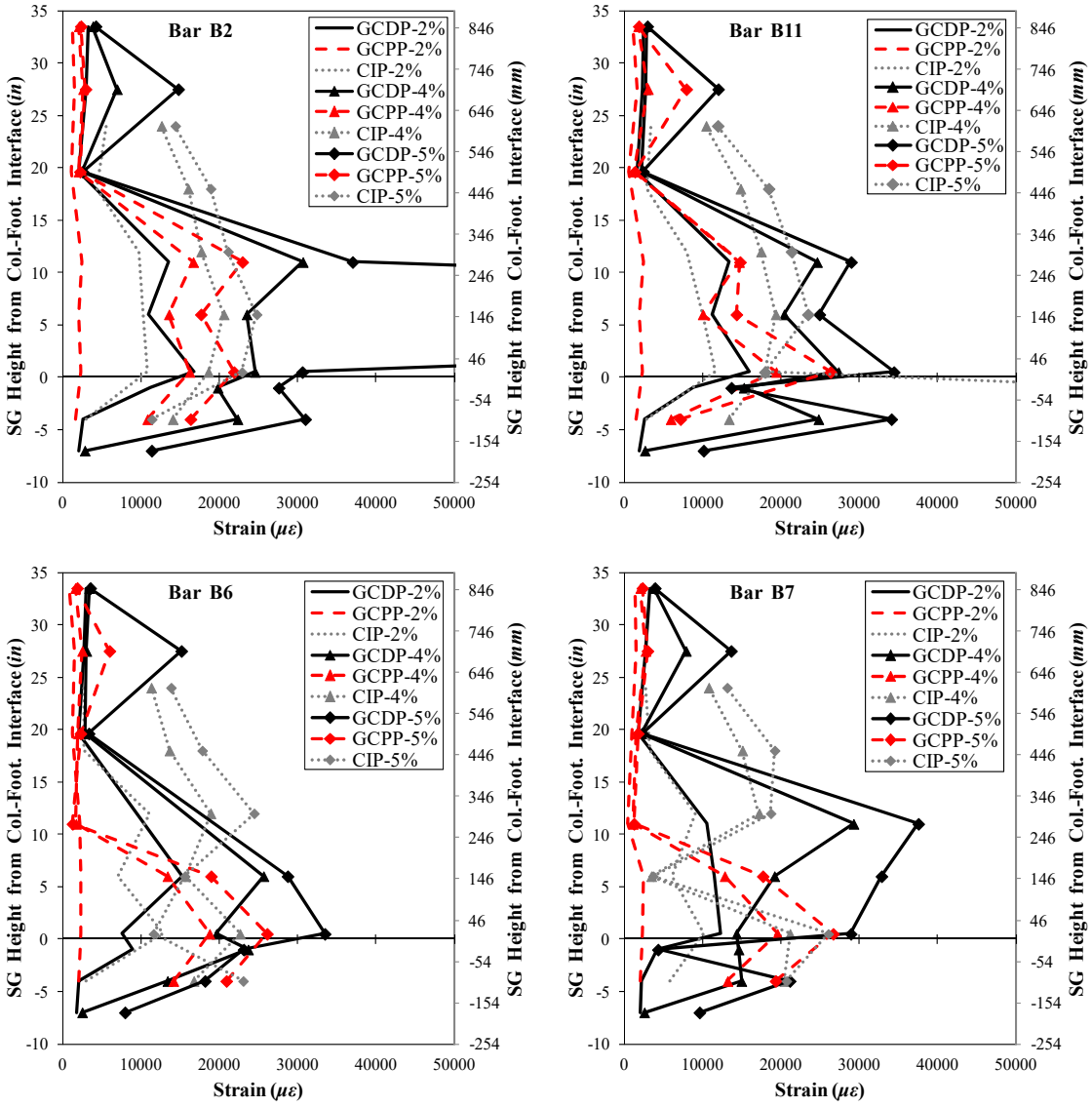

Figure 5.22- Strain Profile for GCDP, GCPP, and CIP Columns for Bar B2, B3, B6, and B7

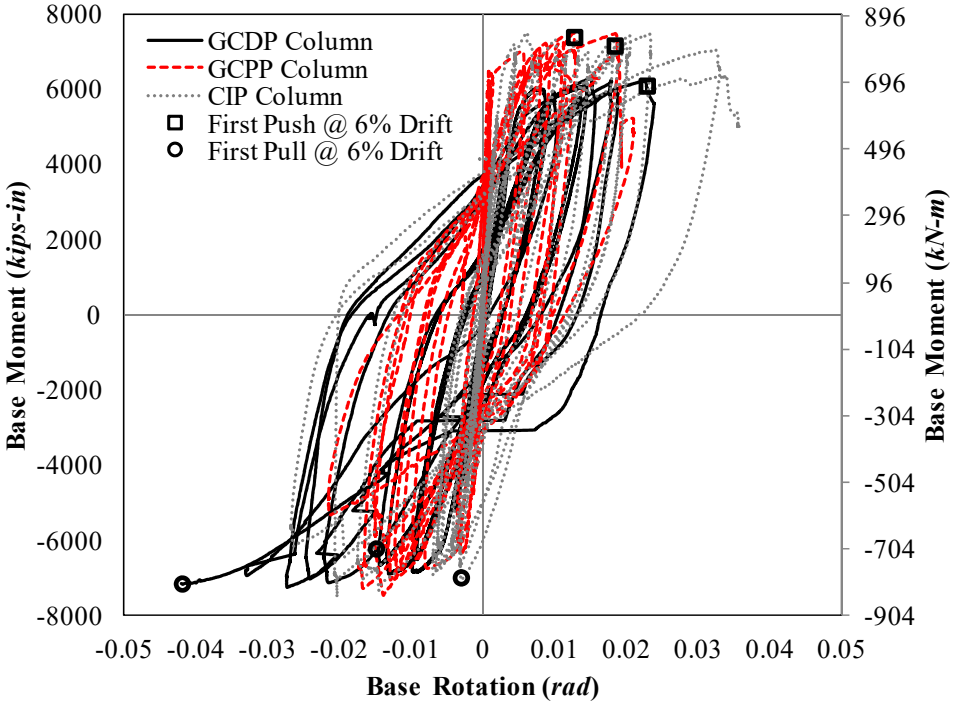

Figure 5.23- Base Moment-Rotation Relationship for GCDP, GCPP, and CIP Columns

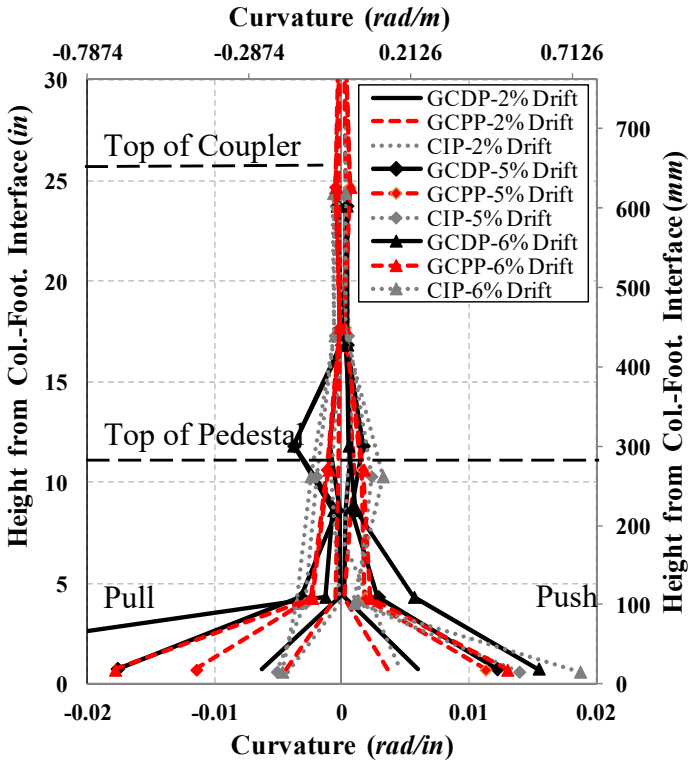

Figure 5.24- Curvature Profile for GCDP, GCPP, and CIP Columns

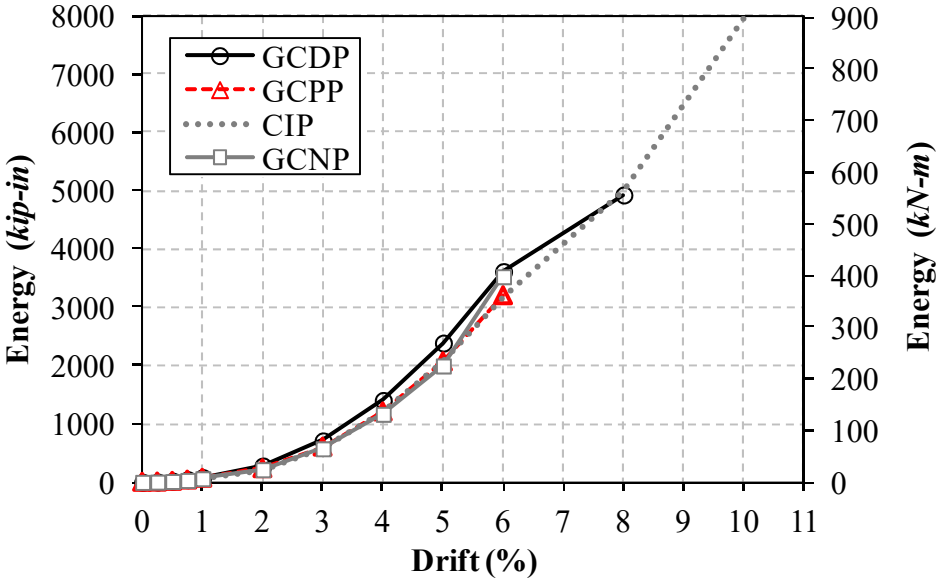

Figure 5.25- Energy Dissipation for Grouted Coupler and CIP Columns

Figure 5.26- HCS, CIP, and HCNP Columns Plastic Hinge Damage at Second Push of 5% Drift

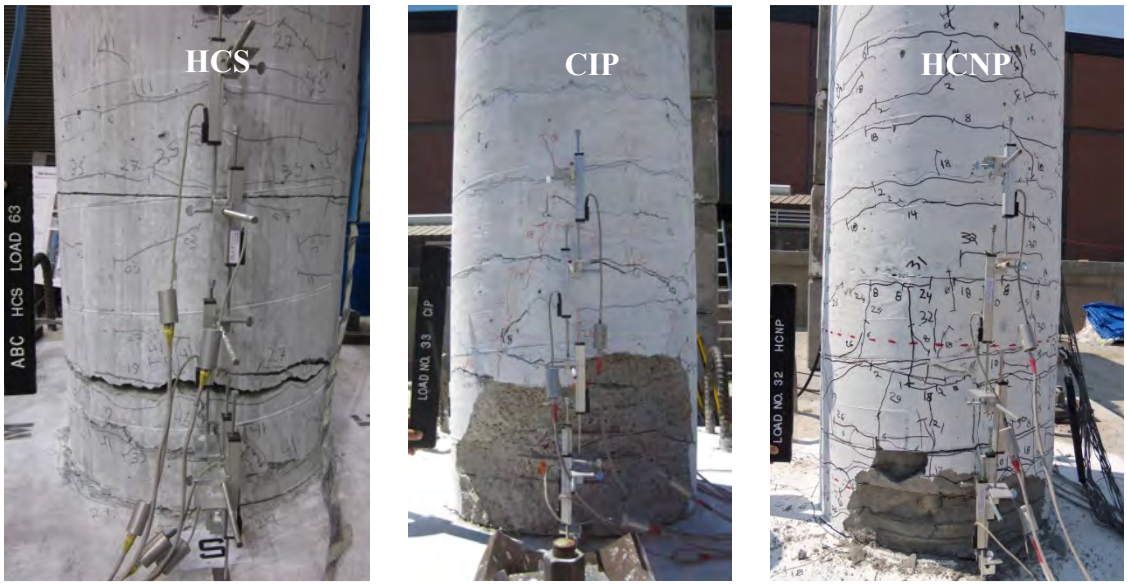

Figure 5.27- HCS, CIP, and HCNP Columns Plastic Hinge Damage at Second Pull of 5% Drift

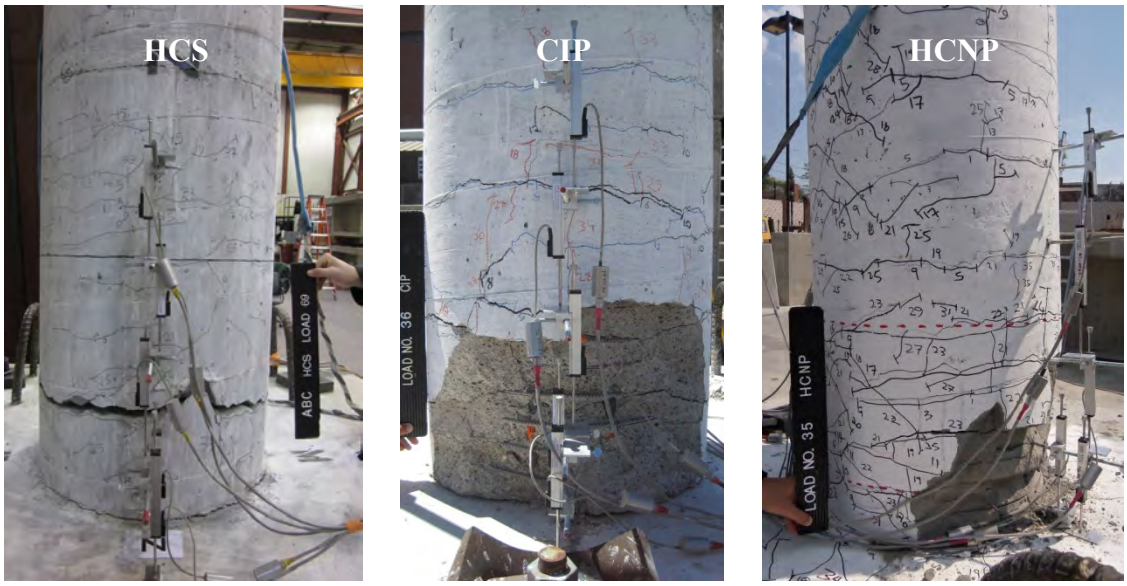

Figure 5.28- HCS, CIP, and HCNP Columns Plastic Hinge Damage at Second Push of 6% Drift

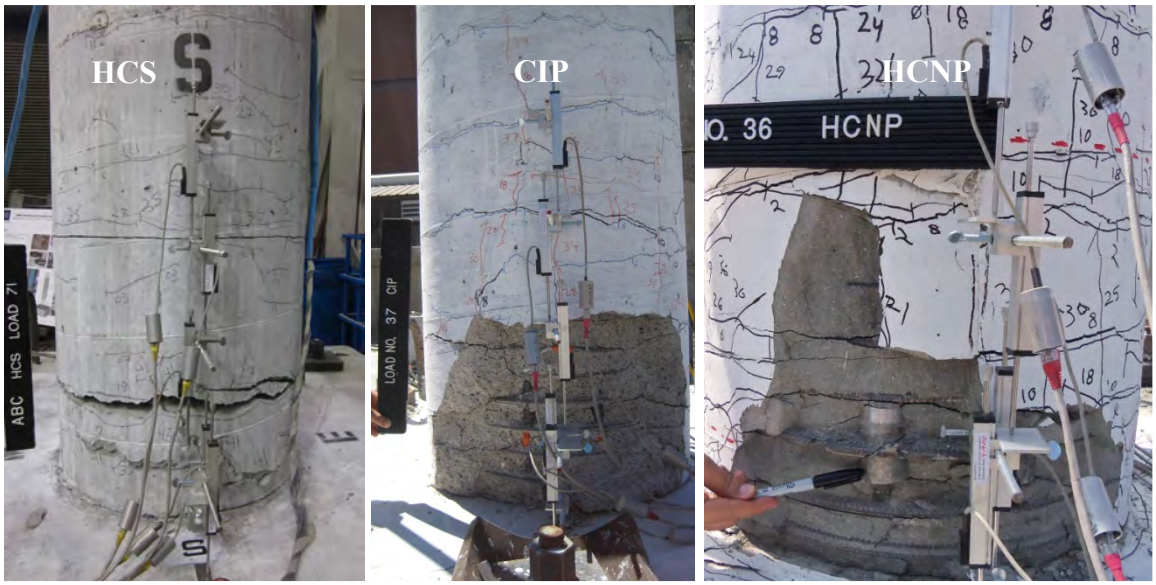

Figure 5.29- HCS, CIP, and HCNP Columns Plastic Hinge Damage at Second Pull of 6% Drift

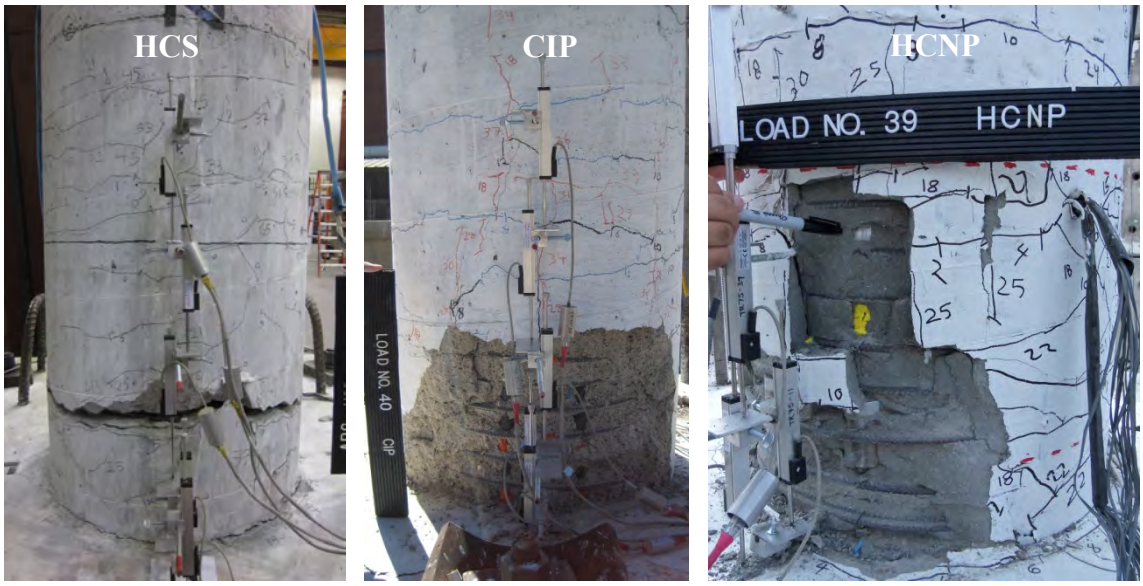

Figure 5.30- HCS, CIP, and HCNP Columns Plastic Hinge Damage at Second Push of 8% Drift

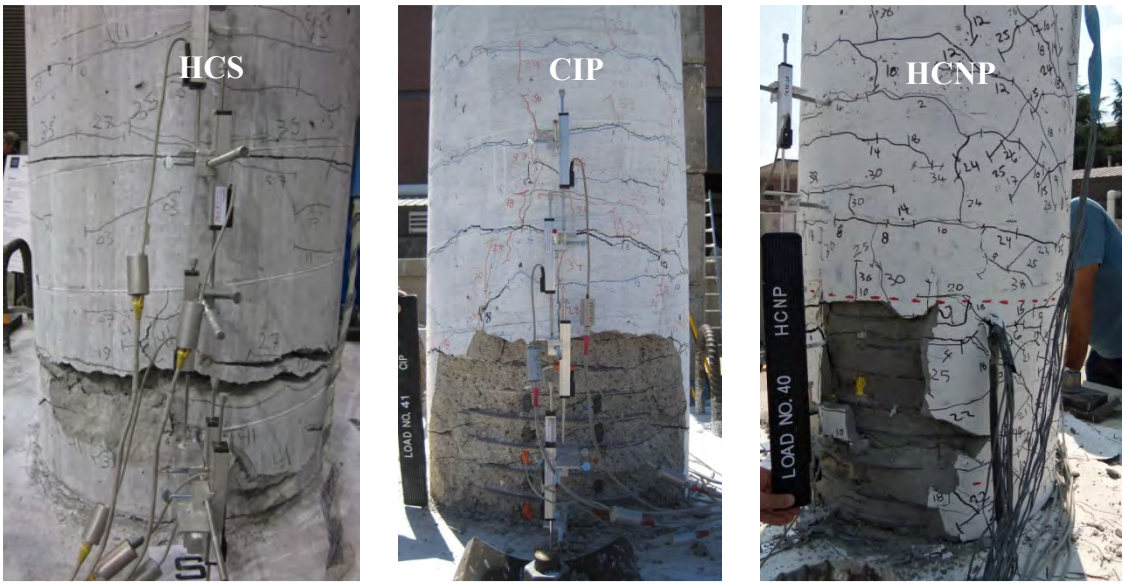

Figure 5.31- HCS, CIP, and HCNP Columns Plastic Hinge Damage at Second Pull of 8% Drift

Figure 5.32- HCS, CIP, and HCNP Columns Plastic Hinge Damage at Second Push of 10% Drift

Figure 5.33- HCS, CIP, and HCNP Columns Plastic Hinge Damage at Second Pull of 10% Drift

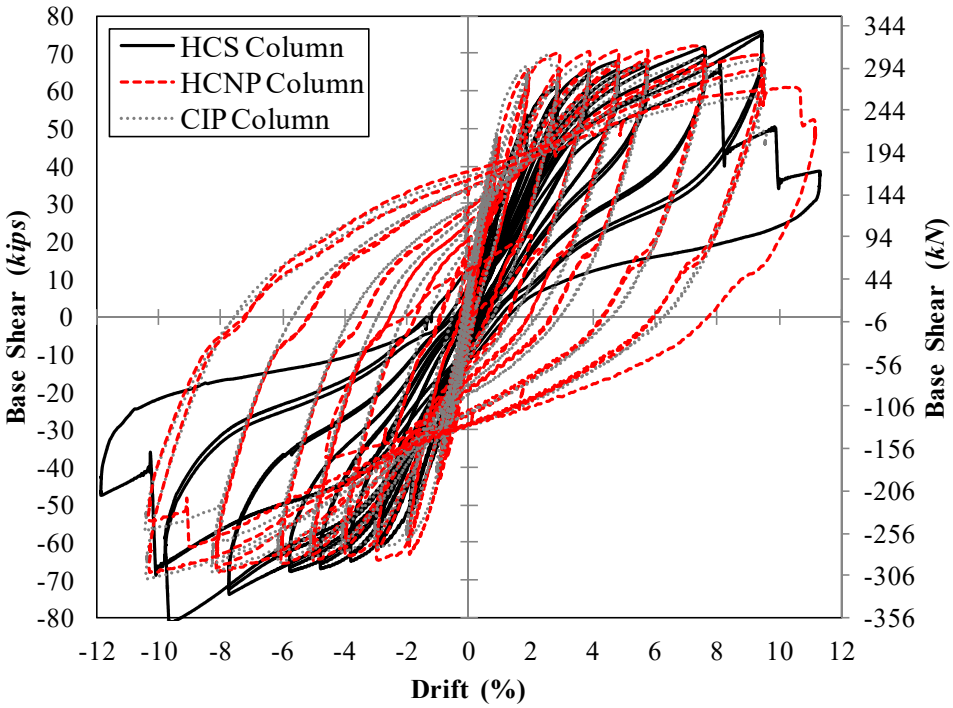

Figure 5.34- HCS, HCNP, and CIP Force-Drift Hysteretic Responses

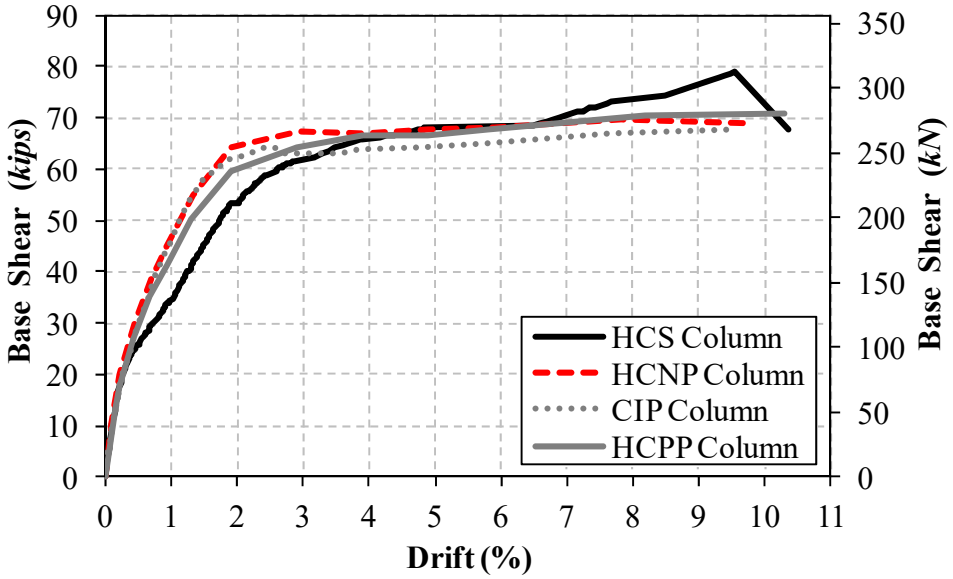

Figure 5.35- Headed Bar Coupler and CIP Column Average Push/Pull Force-Drift Envelopes

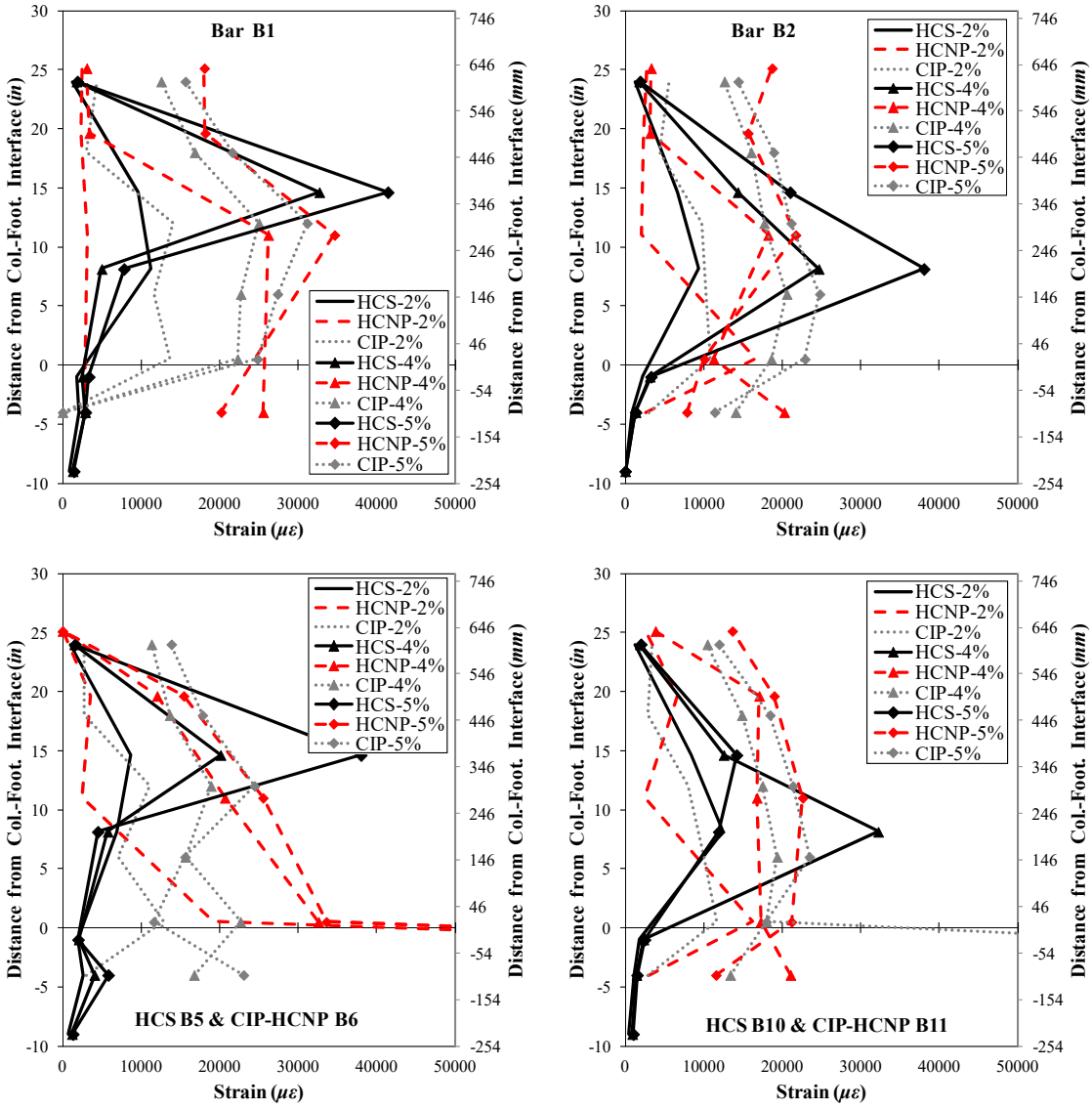

Figure 5.36- Strain Profile for HCS, HCNP, and CIP Columns

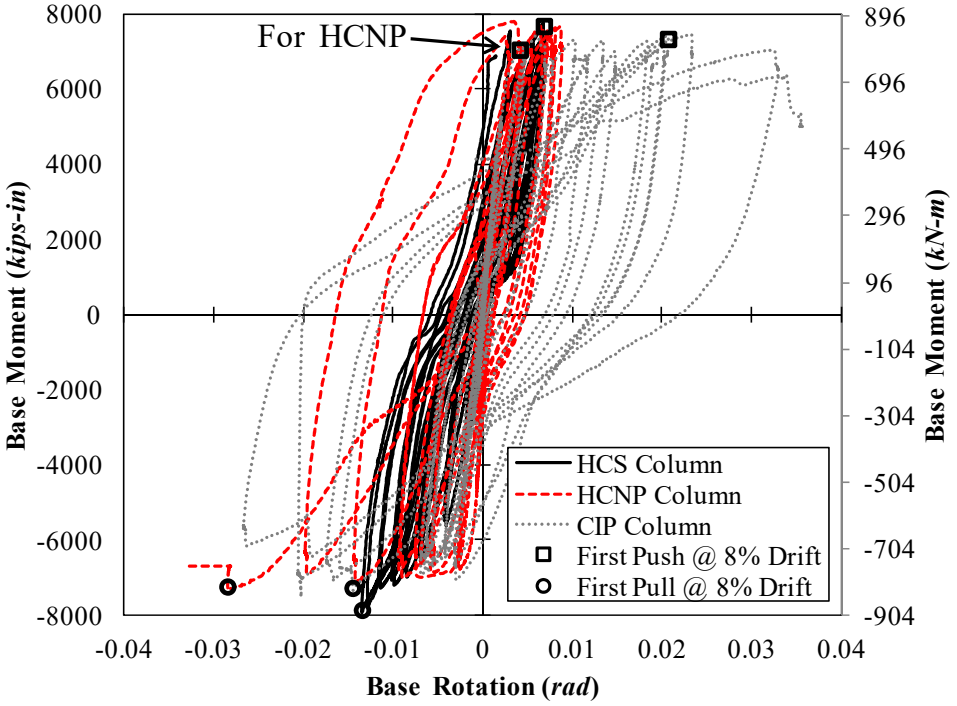

Figure 5.37- Base Moment-Rotation Relationship for HCS, HCNP, and CIP Columns

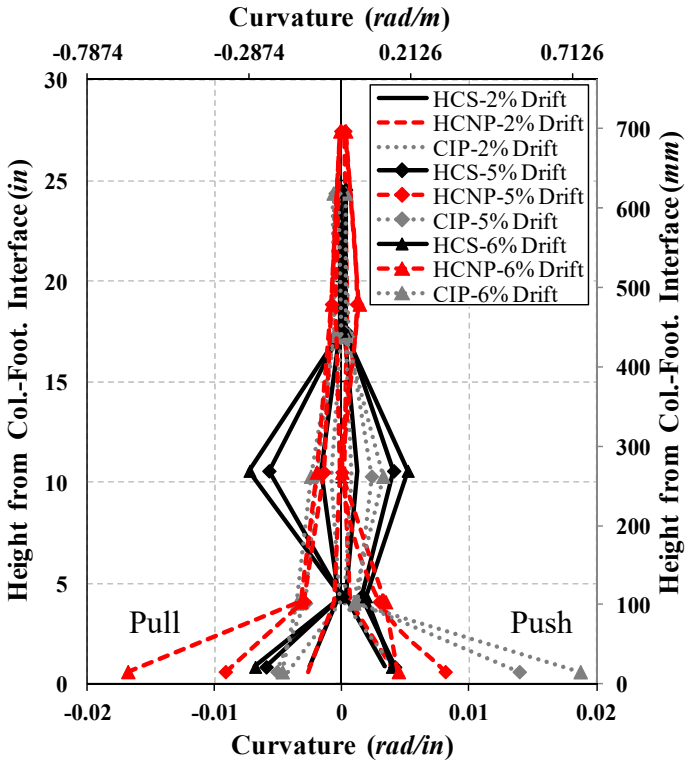

Figure 5.38- Curvature Profile for HCS, HCNP, and CIP Columns

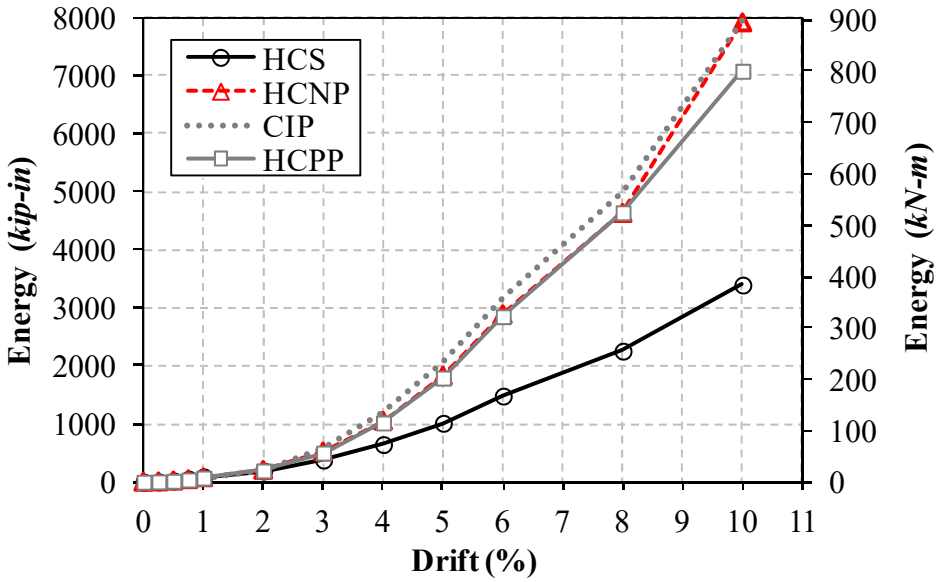

Figure 5.39- Energy Dissipation for Headed Bar Coupler and CIP Columns

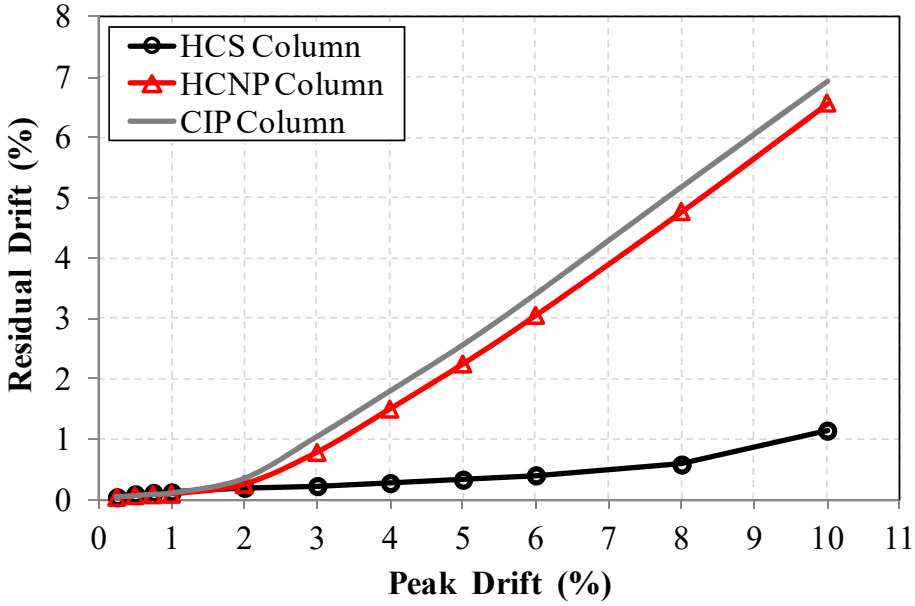

Figure 5.40- HCS, HCNP, and CIP Columns Residual Displacements

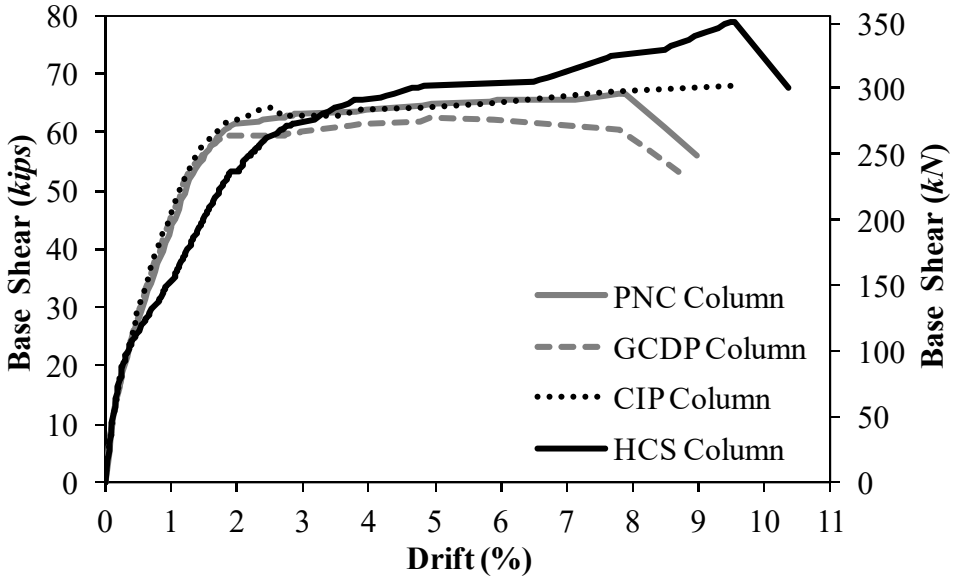

Figure 5.41- PNC, GCDP, HCS, and CIP Column Average Push/Pull Force-Drift Envelopes

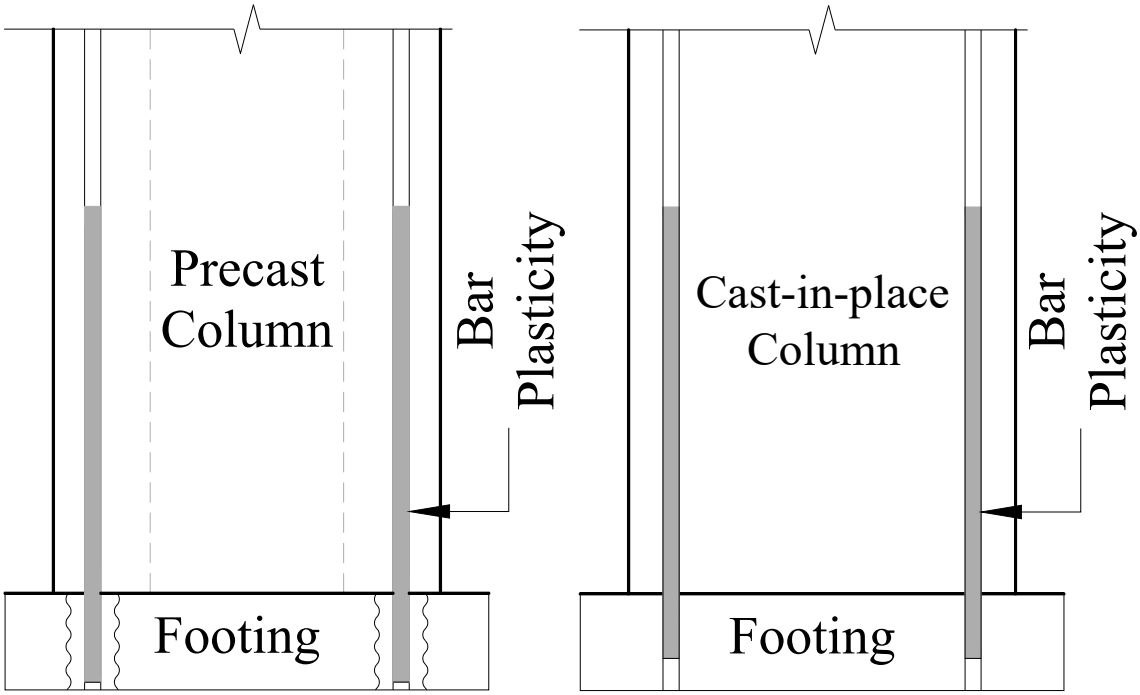

(a) PNC (b) CIP

Figure 5.42- PNC and CIP Columns Bar Large Plasticity

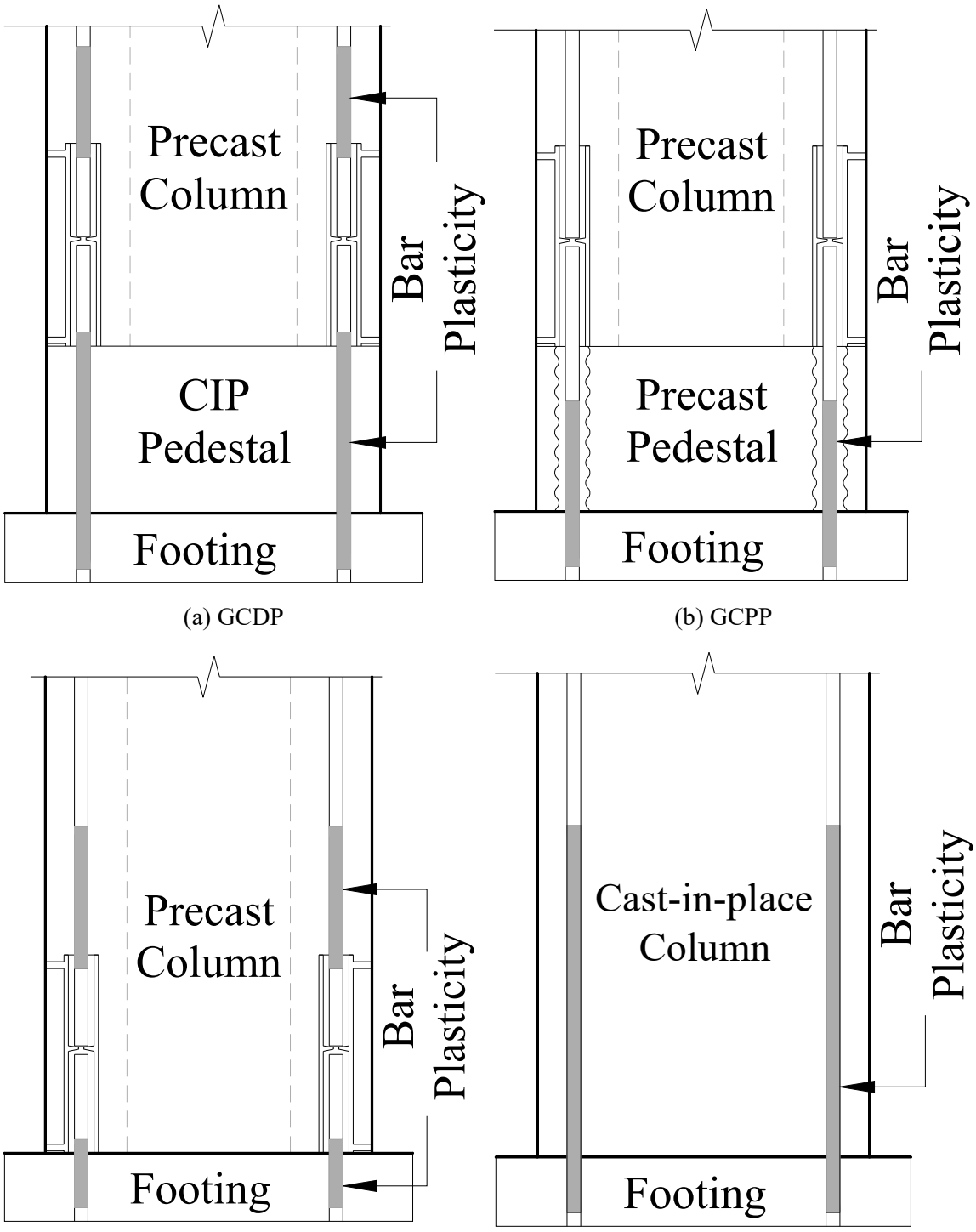

(a) GCDP

(b) GCPP

(c) GCNP

(d) CIP

Figure 5.43- Grouted Coupler and CIP Columns Bar Large Plasticity

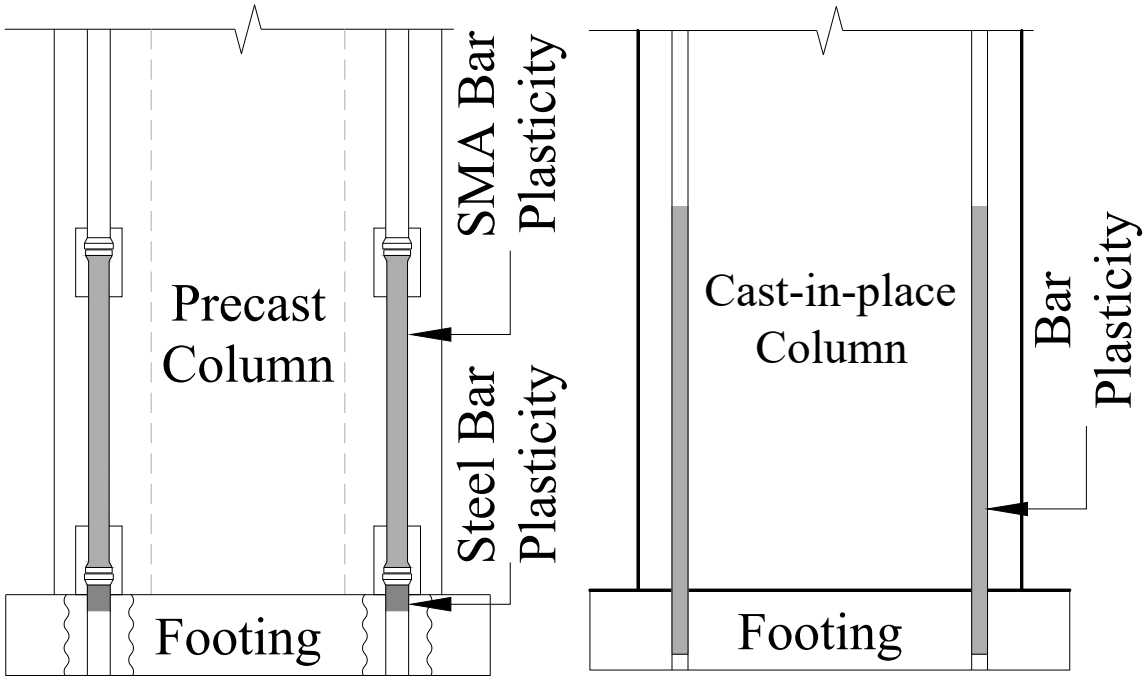

(a) HCS (b) CIP

Figure 5.44- HCS and CIP Columns Bar Large Plasticity

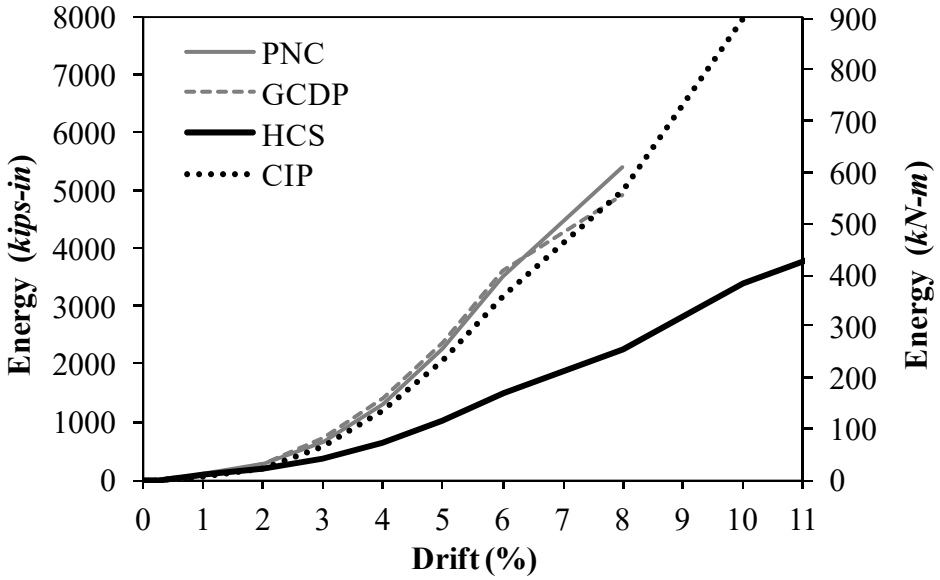

Figure 5.45- Energy Dissipation for PNC, GCDP, HCS, and CIP Columns

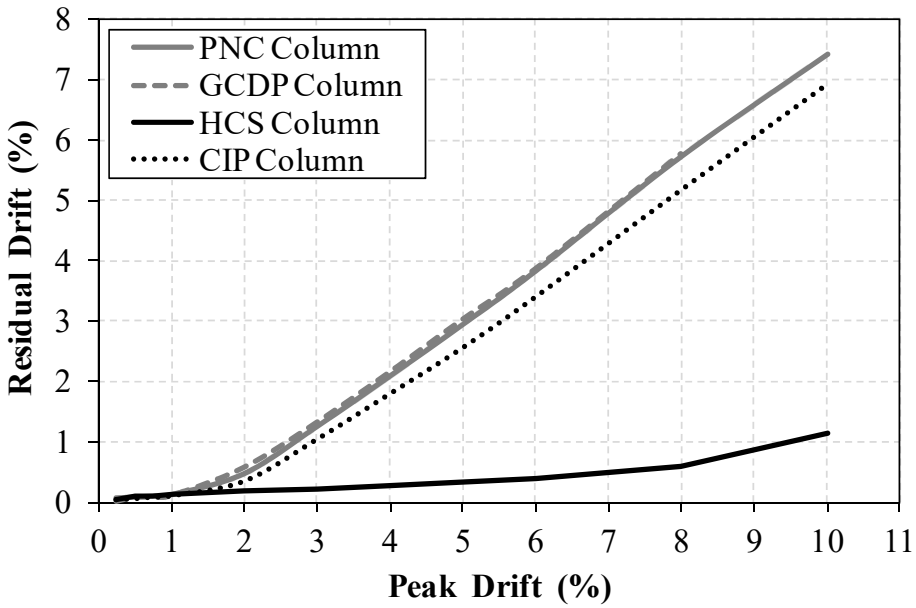

Figure 5.46- Residual Displacements for PNC, GCDP, HCS, and CIP Columns

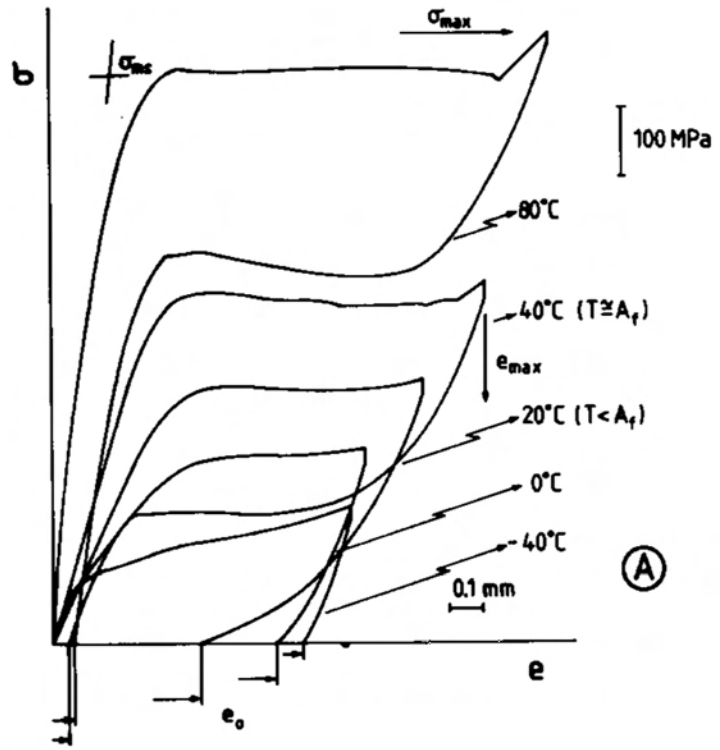

Figure 6.1- NiTi SMA Tensile Stress-elongation at Different Temperatures (Strnadel et al., 1995)

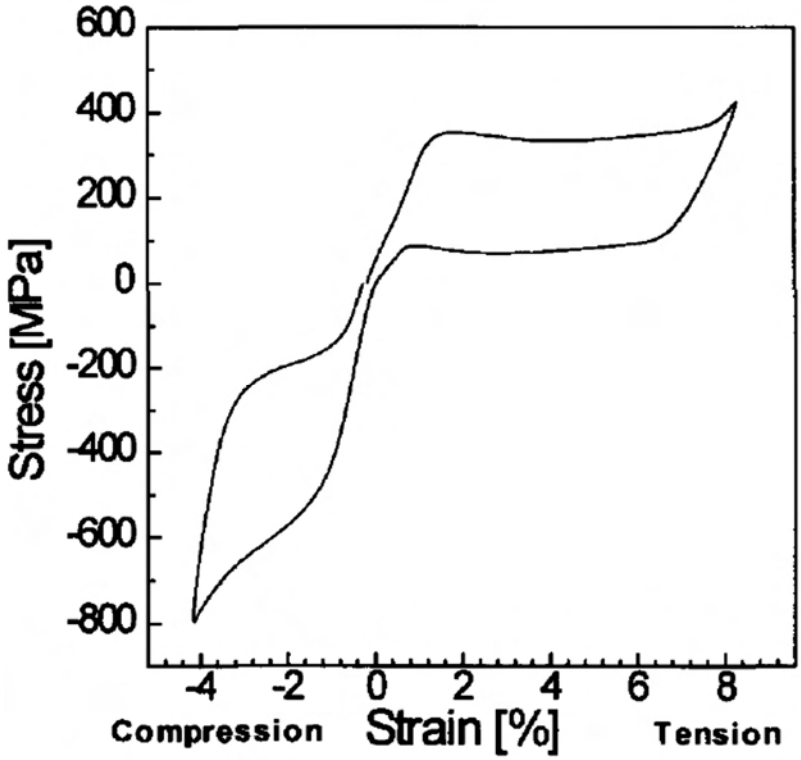

Figure 6.2- Full-cycle Stress-Strain Relationship of NiTi SE SMA (Plietsch and Ehrich, 1997)

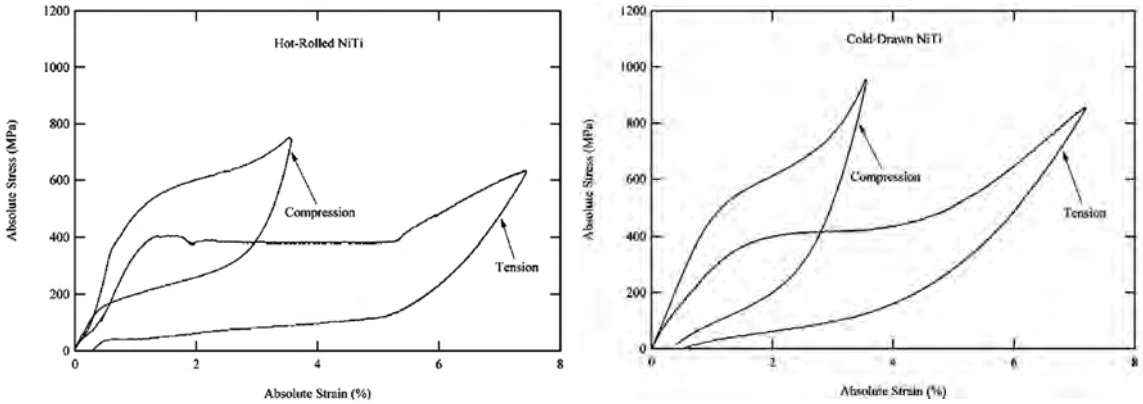

(a) Hot-Rolled NiTi (b) Cold-Drawn NiTi

Figure 6.3- Tensile-Compressive Stress-Strain Relationship of NiTi SE SMA (Frick et al., 2004)

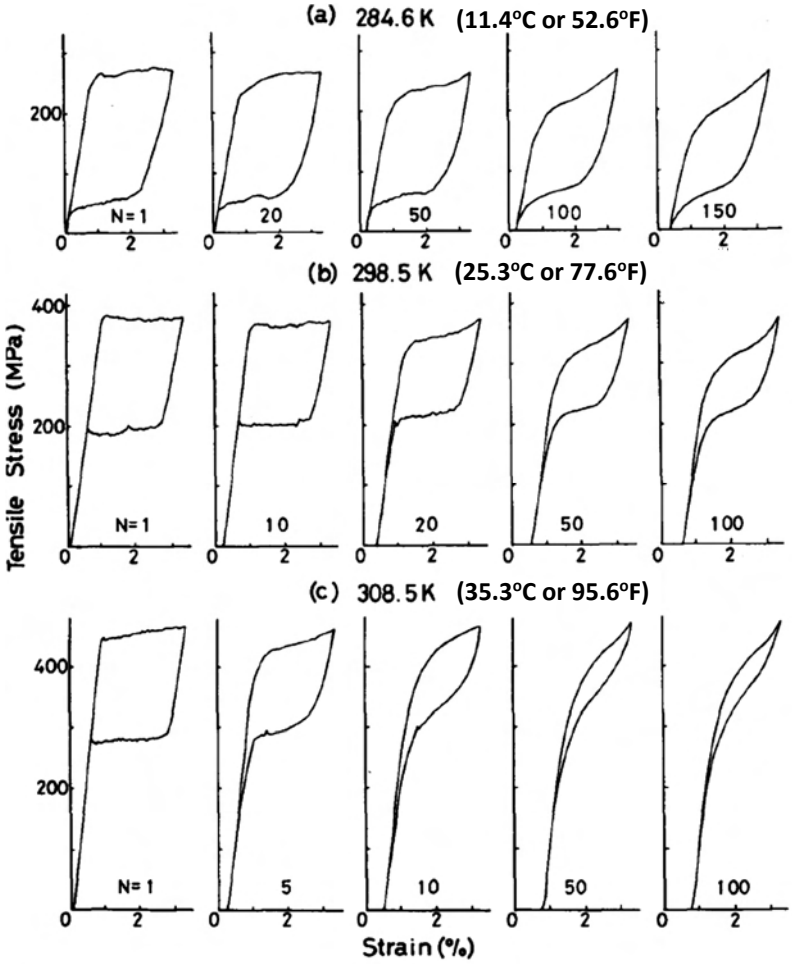

Figure 6.4- Cyclic Stress-Strain Relationship of NiTi SE SMA (Miyazaki et al, 1986)

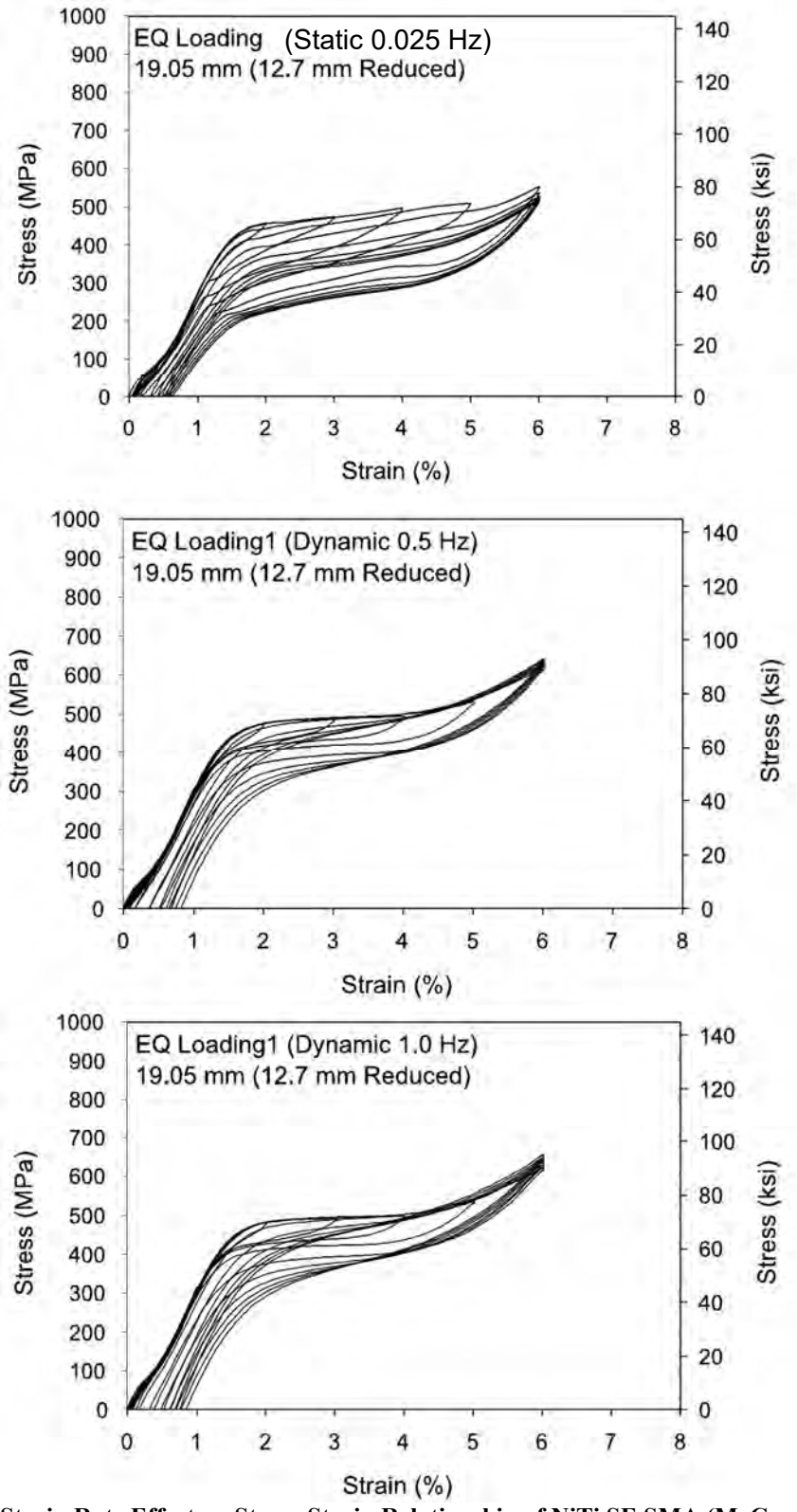

Figure 6.5- Strain Rate Effect on Stress-Strain Relationship of NiTi SE SMA (McCormick, 2006)

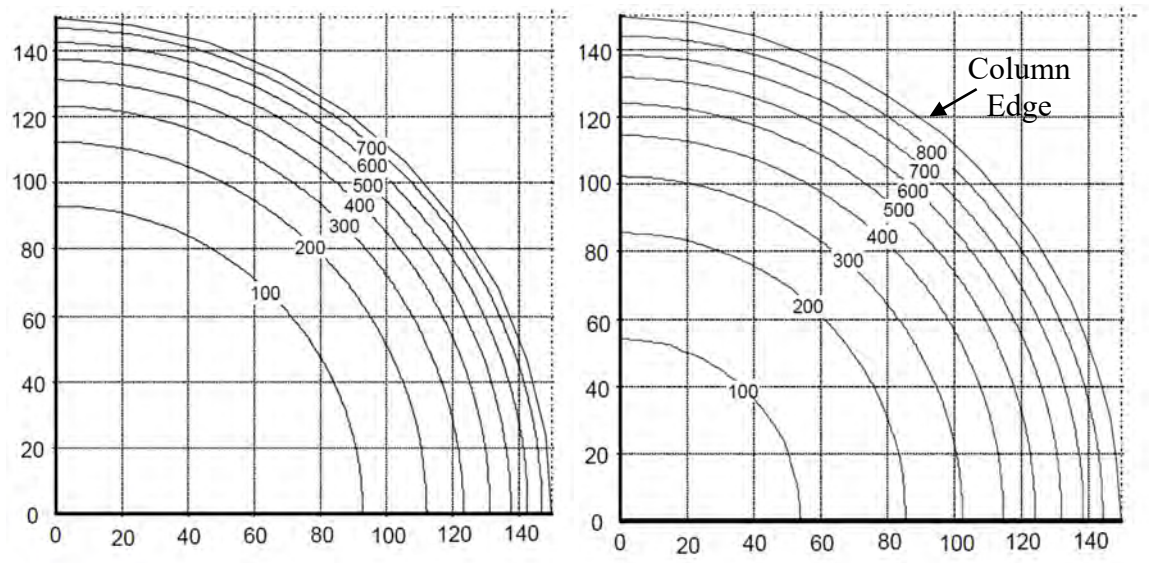

(a) Thirty Minunes Load (R30) (b) Sixty Minunes Load (R60)

(c) Ninty Minunes Load (R90) (d) Hundred-twenty Minunes Load (R120)

Figure 6.6- Temperature profiles (°C) for a quarter 300-*mm* Diameter circular column (EVN 1992-1-2, 1996)

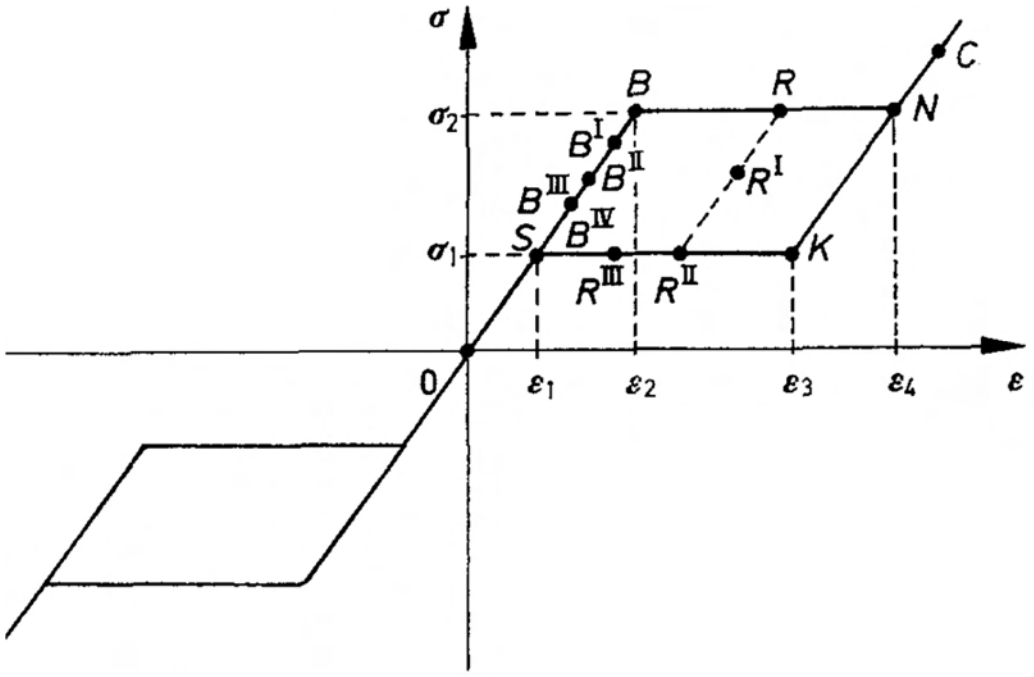

Figure 6.7- Atanackovic's Stress-Strain Model for SE SMA (Atanackovic and Achenbach, 1989)

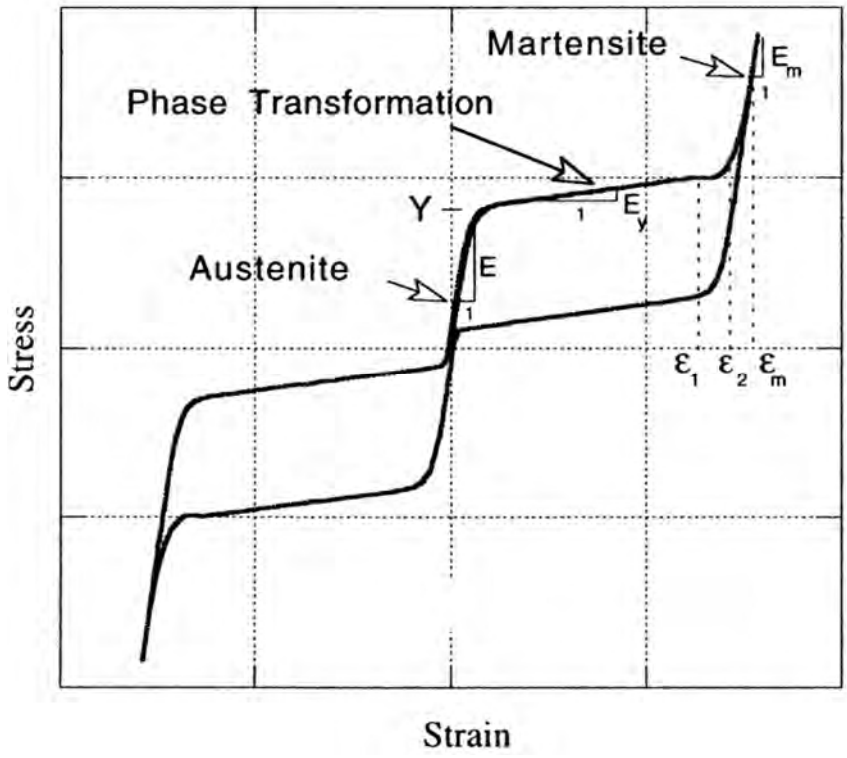

Figure 6.8- Graesser's Stress-Strain Model for SE SMA (Graesser and Cozzarelli, 1991)

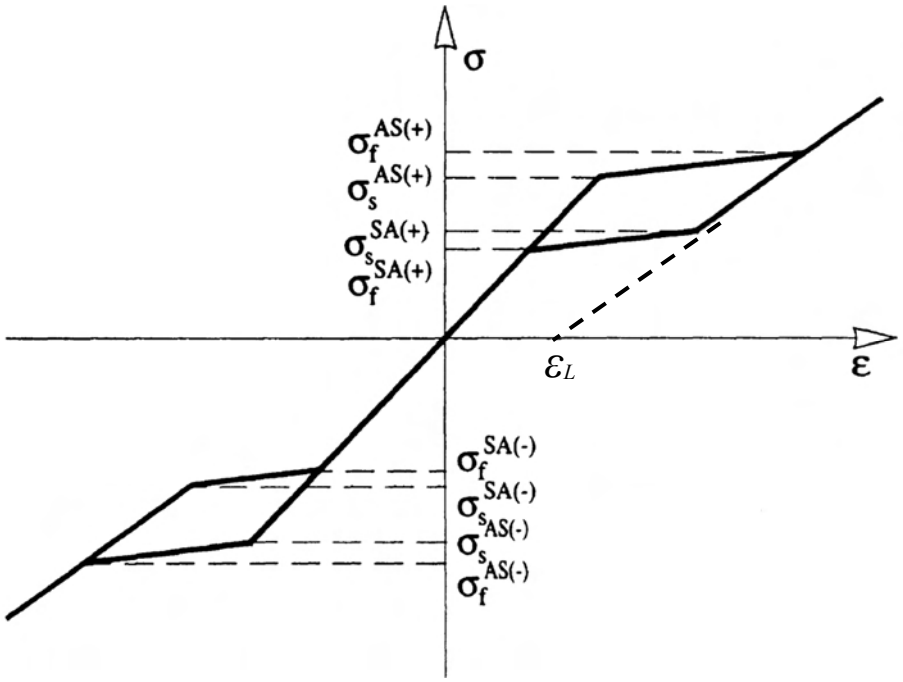

Figure 6.9- Auricchio's Stress-Strain Model for SE SMA (Auricchio and Sacco, 1997)

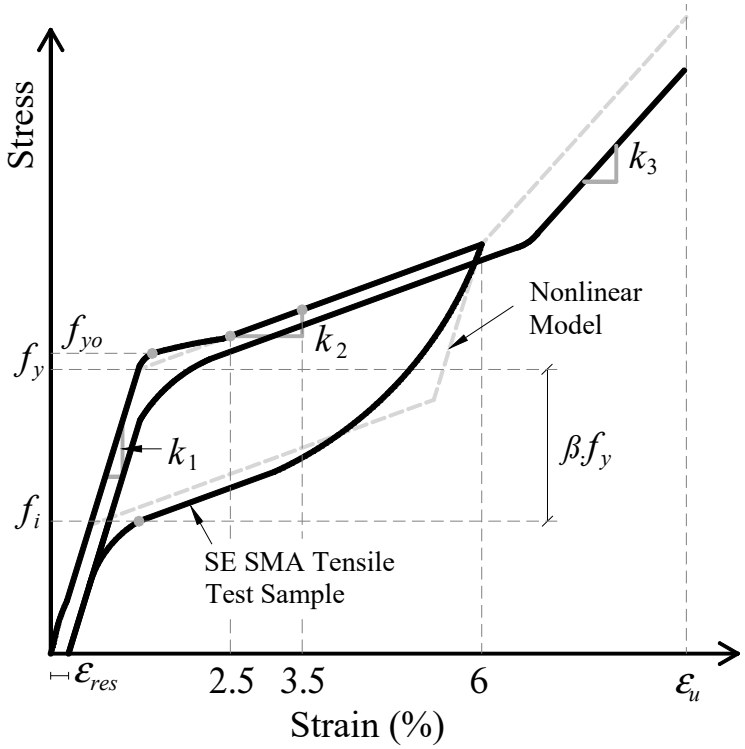

Figure 6.10- ASTM NiTi SE SMA Tensile Test Sample and Nonlinear Model

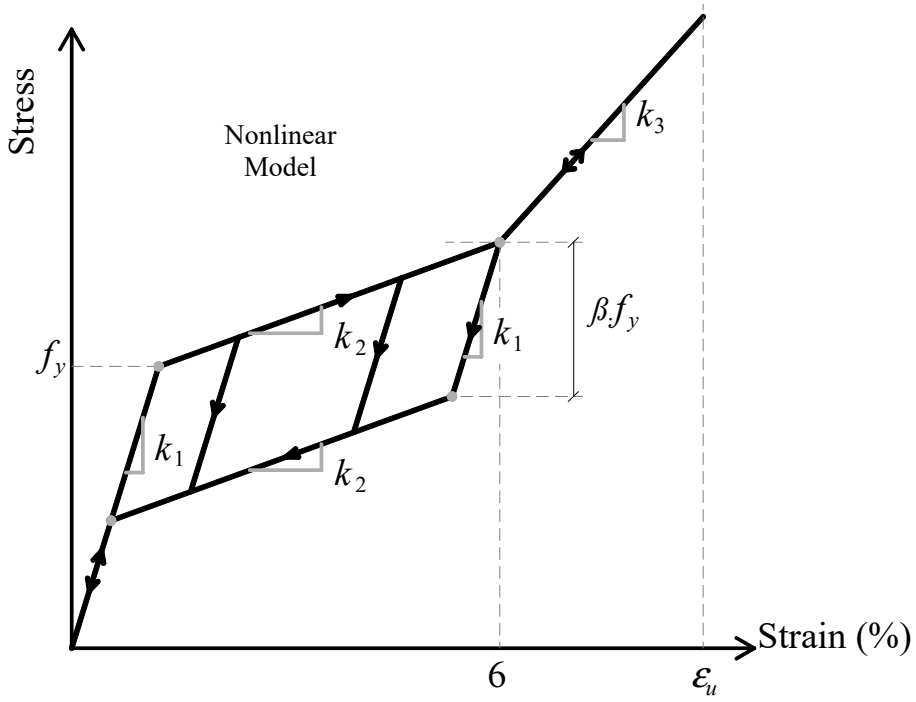

Figure 6.11- Nonlinear Model for SE SMA

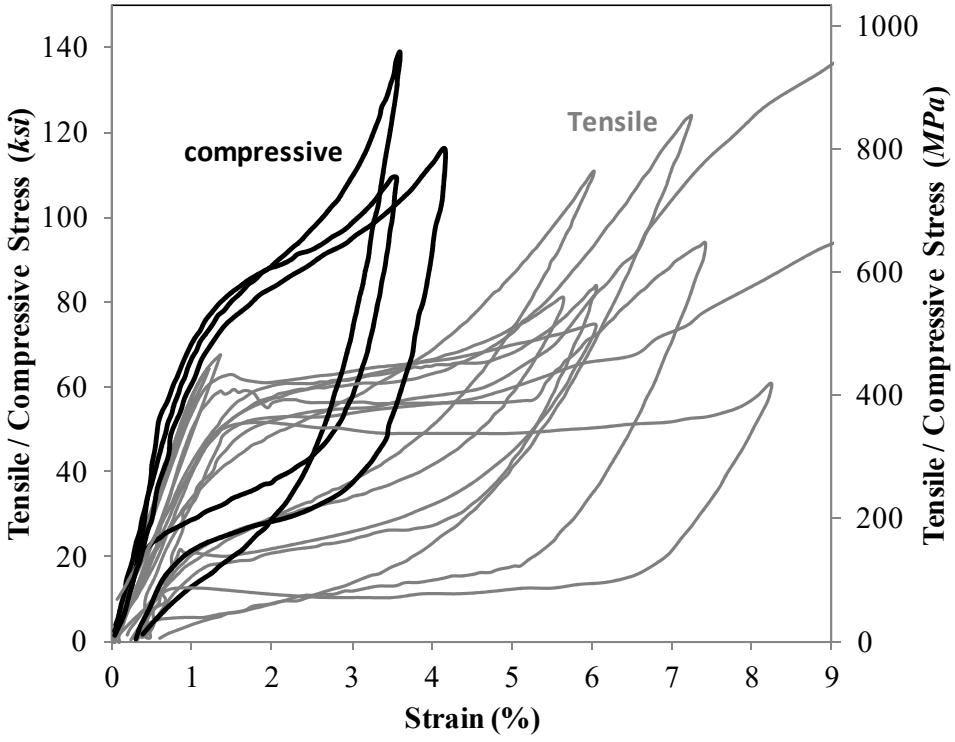

(a) One-Cycle Tests from Different Studies

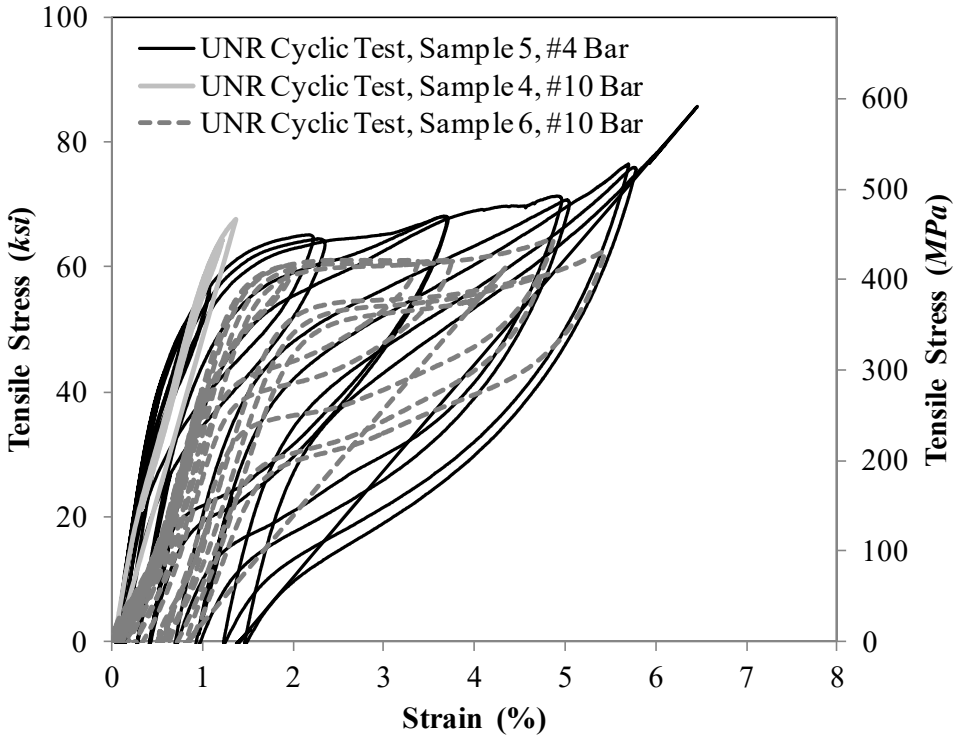

(b) Multi-Cycle Tests

Figure 6.12- Some of Tensile/Compressive Test Data Used for SE SMA Model

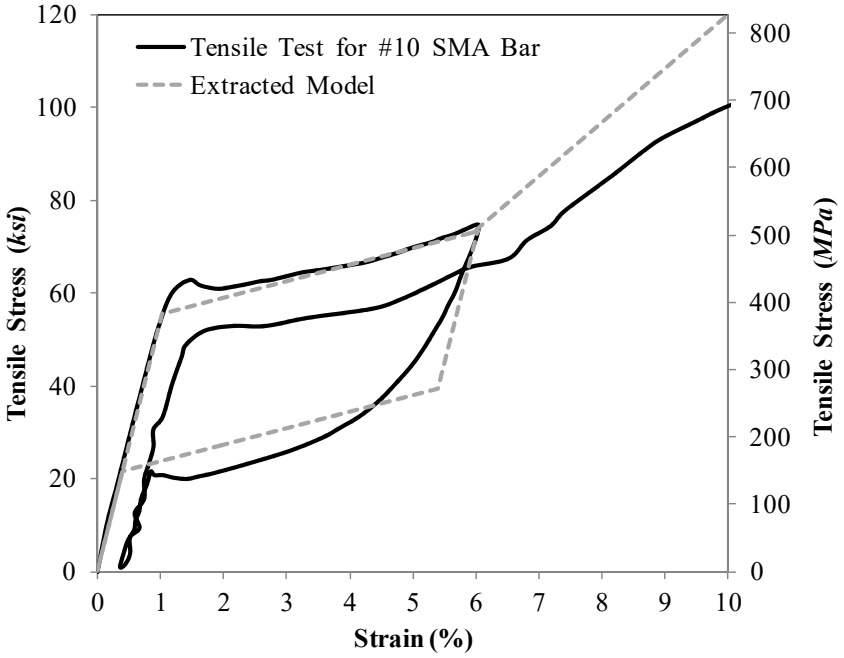

Figure 6.13- Tensile Test and Extracted Model for a #10 SE SMA Bar

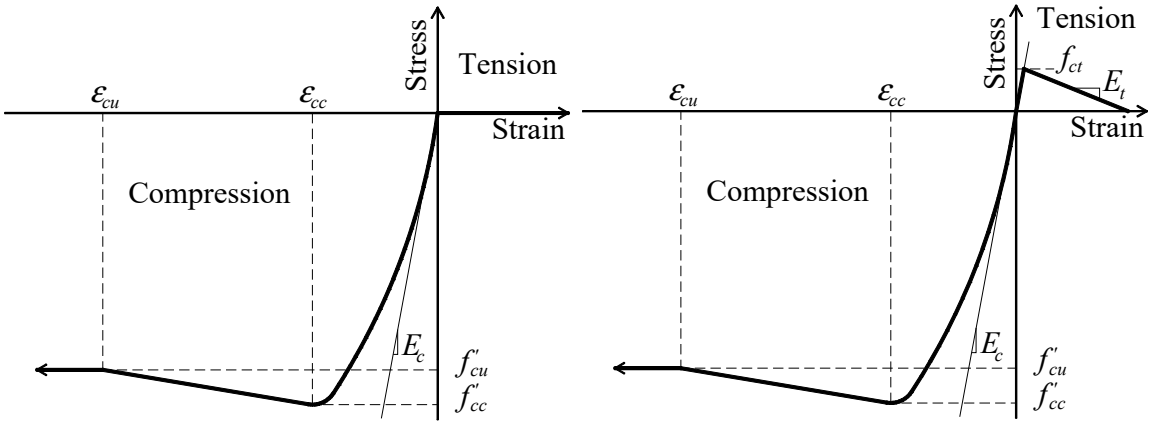

(a) Concrete01

(b) Concrete02

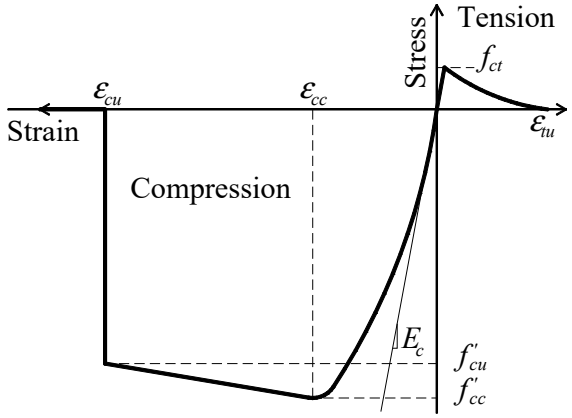

(c) Concrete04

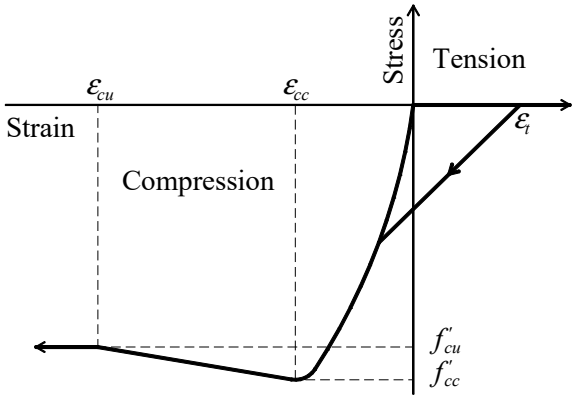

(d) Concrete01WithSITC

Figure 7.1- Constitutive Concrete Material Models

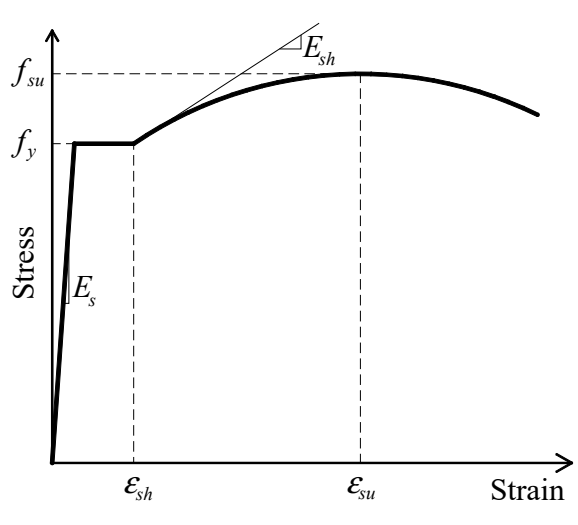

(a) ReinforcingSteel

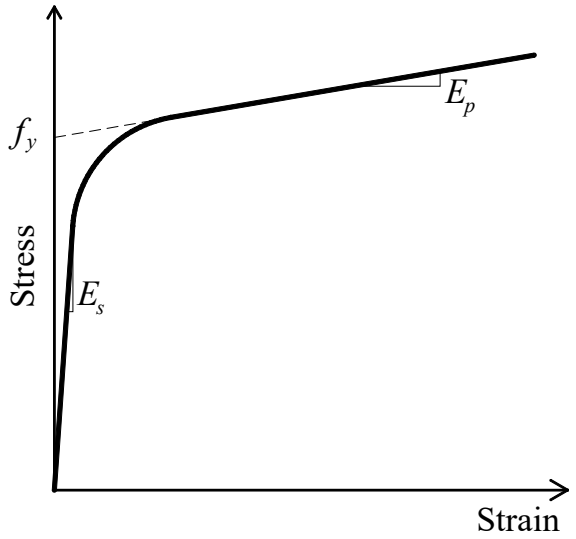

(b) Steel02

Figure 7.2- Constitutive Steel Material Models

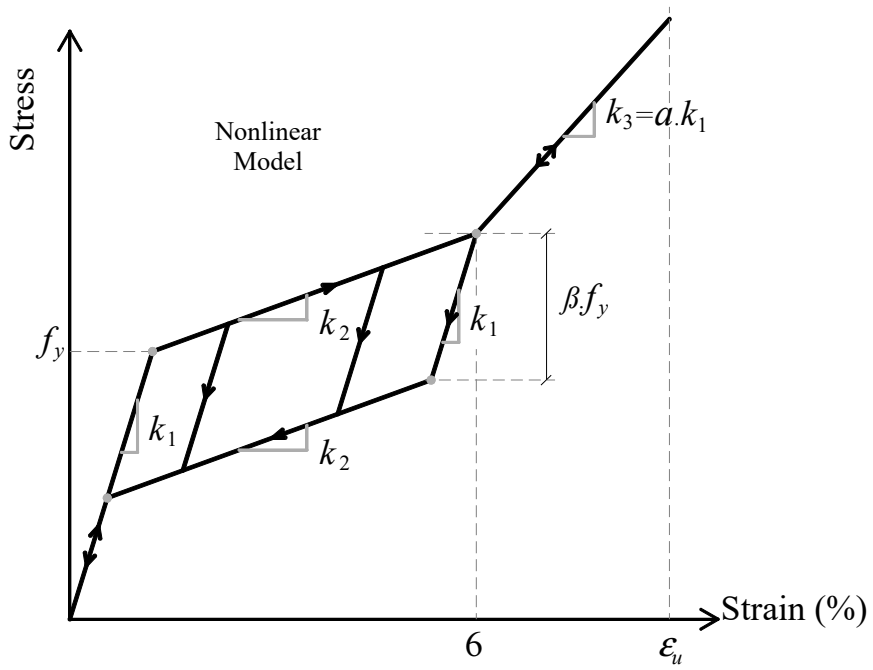

Figure 7.3- Constitutive Reinforcing SMA Material Model

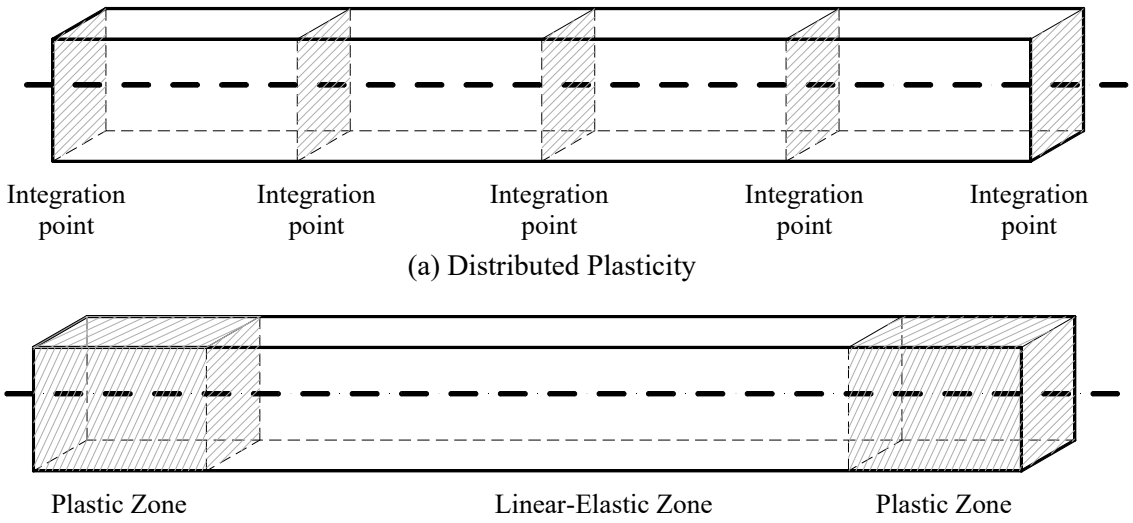

Figure 7.4- Distributed and Lumped Plasticity Elements

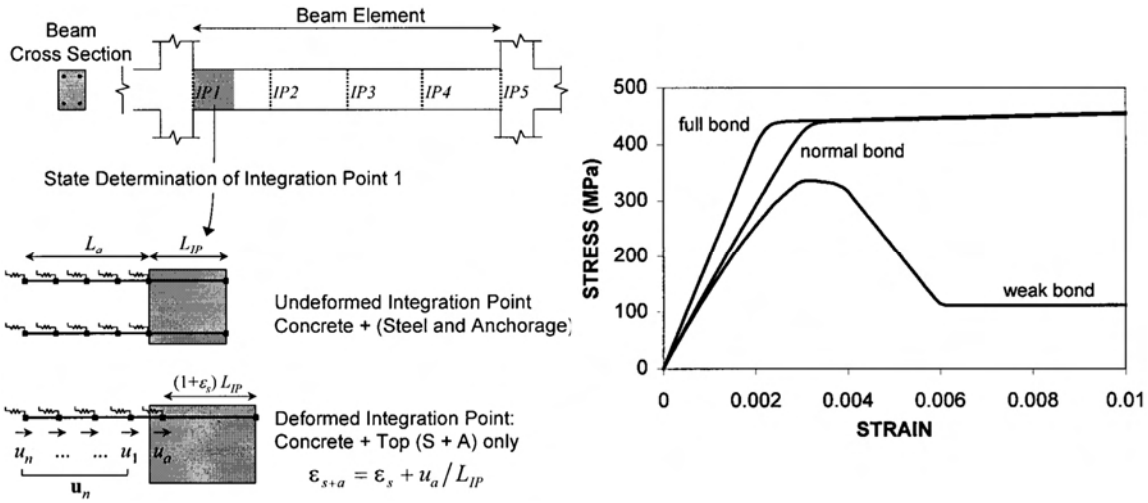

(a) Steel Bar State Determination (b) Modified Steel Fiber

Figure 7.5- Fiber-Section Beam Element with Bond-Slip Effect (Monti and Spacone, 2000)

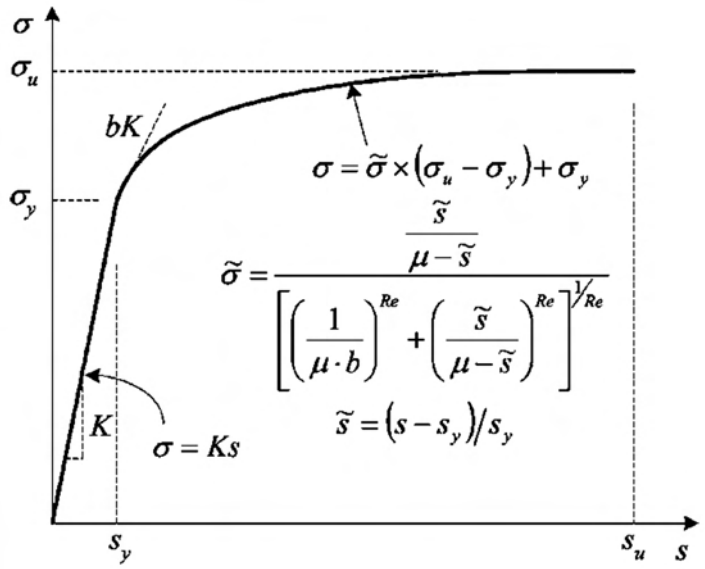

Figure 7.6- Bar Stress-Slip Relationship (Zhao and Sritharan, 2007)

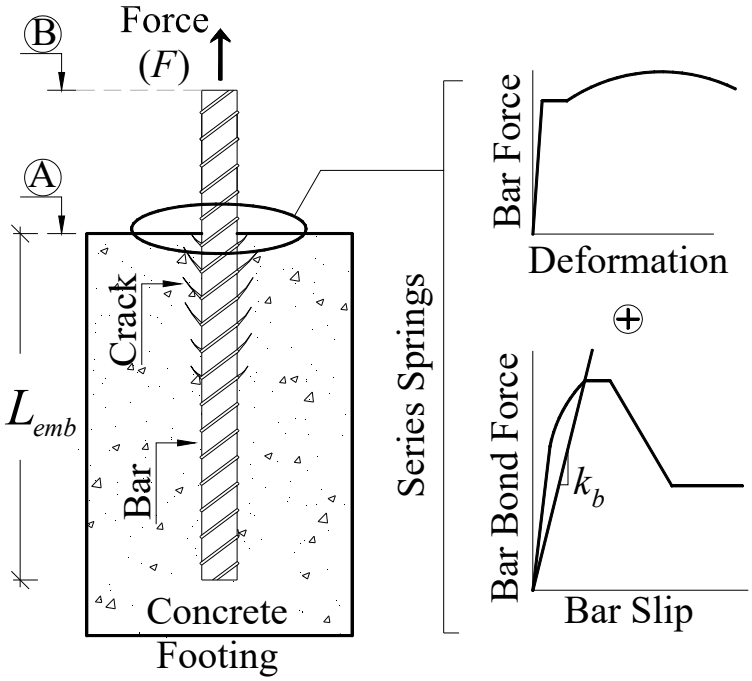

Figure 7.7- Bond-Slip Effect on Bar Stress-Strain in Conventional Connections

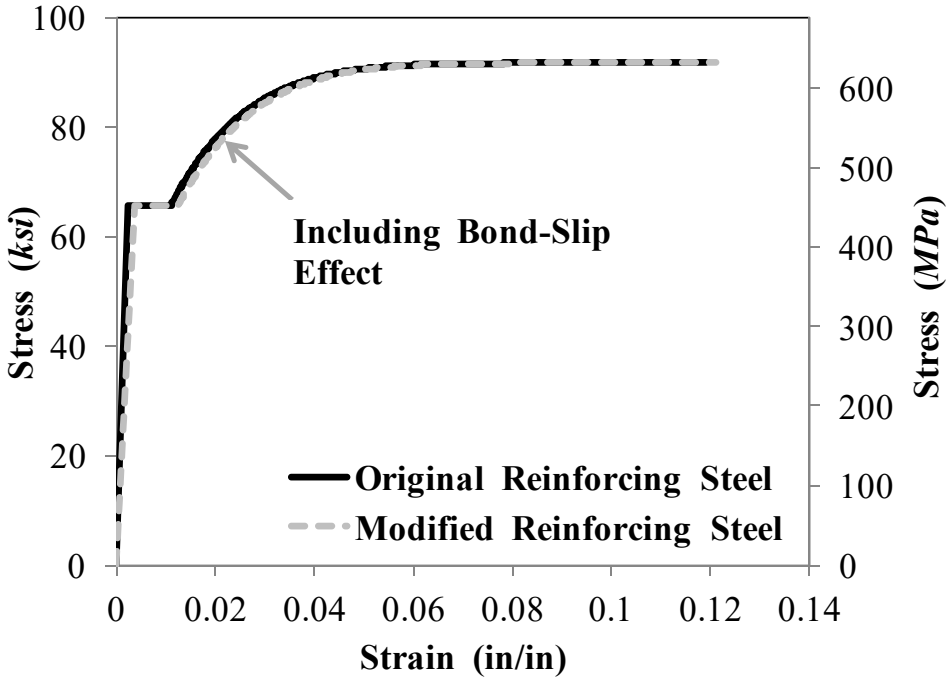

Figure 7.8- Original and Modified Reinforcing Steel Models

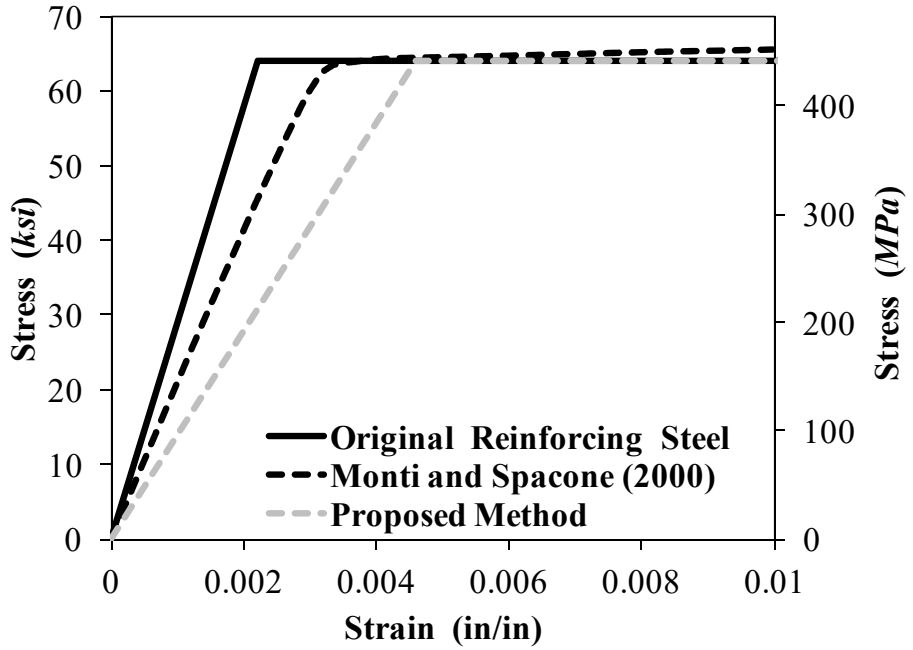

Figure 7.9- Original and Modified Steel Fiber Stress-Strain Curves Accounting for Bond-Slip Effect

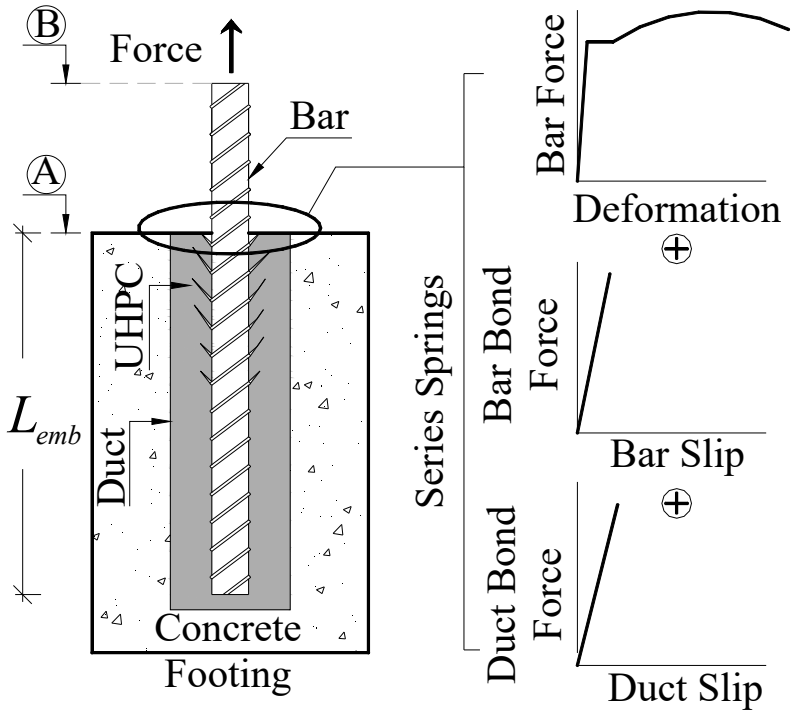

Figure 7.10- Bond-Slip Effect on Bar Stress-Strain in UHPC-Filled Duct Connections

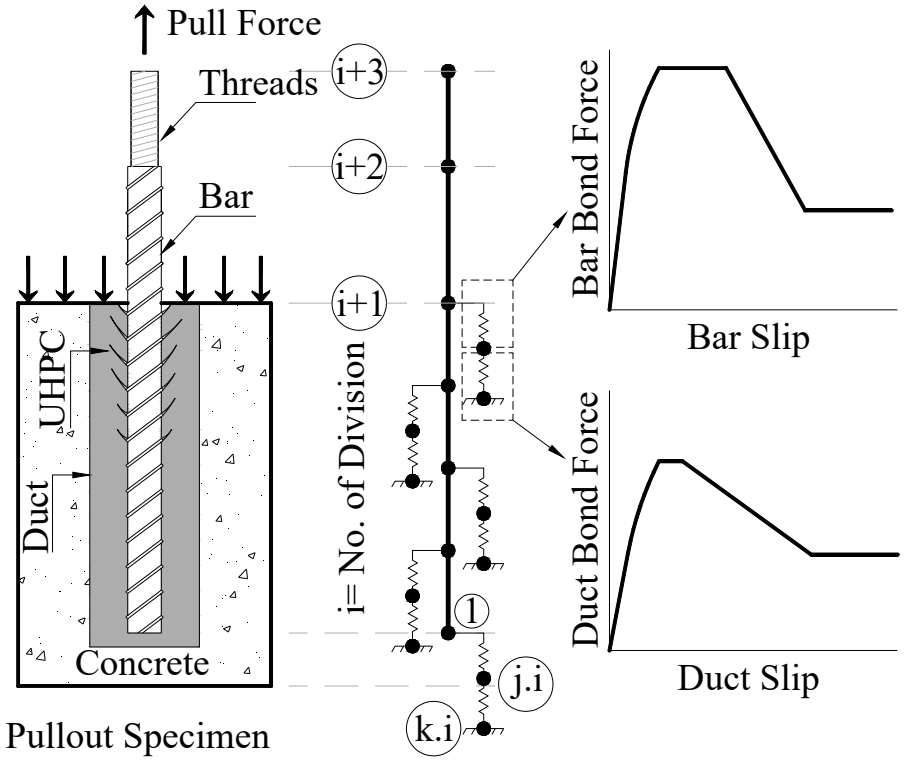

Figure 7.11- Finite Element Model for Pullout Tests

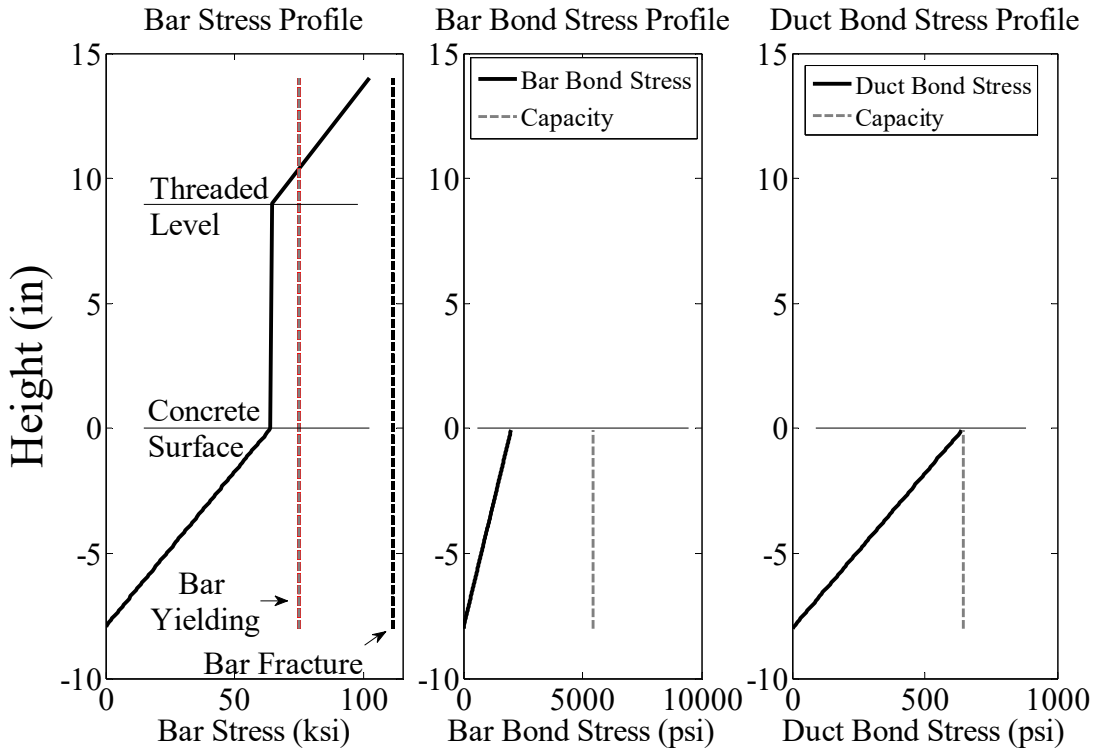

Figure 7.12- Calculated Profiles for SP1 in Pullout Tests

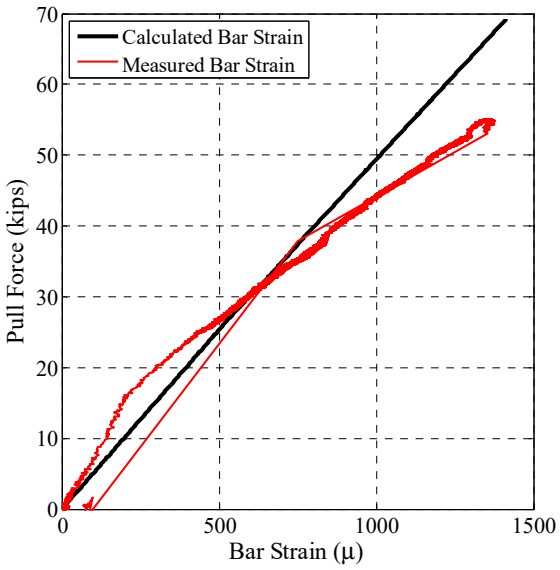

(a) SP2 (1 *kip*=4.45 *kN*)

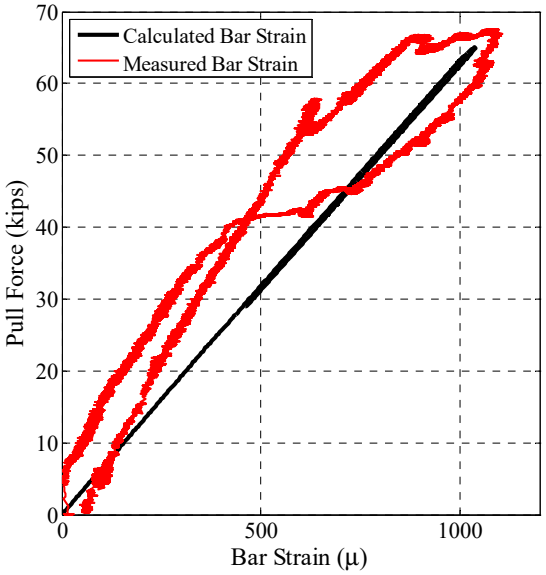

(a) SP4 (1 *kip*=4.45 *kN*)

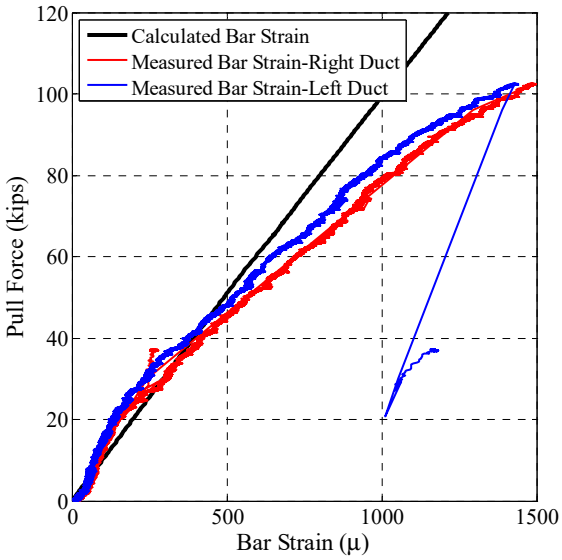

(c) SP10 (1 *kip*=4.45 *kN*)

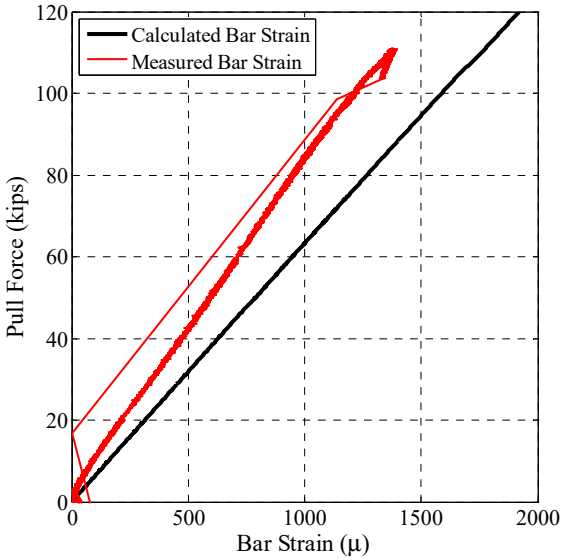

(d) SP14 (1 *kip*=4.45 *kN*)

Figure 7.13- Measured and Calculated Force-Strain for Bars Embedded in UHPC

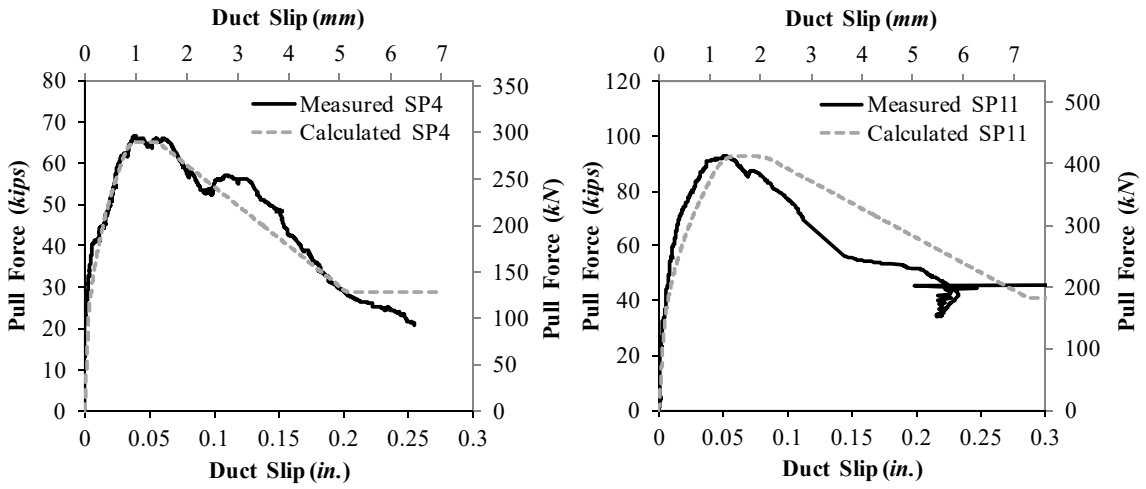

Figure 7.14- Measured and Calculated Pull Force-Duct Slip Curves

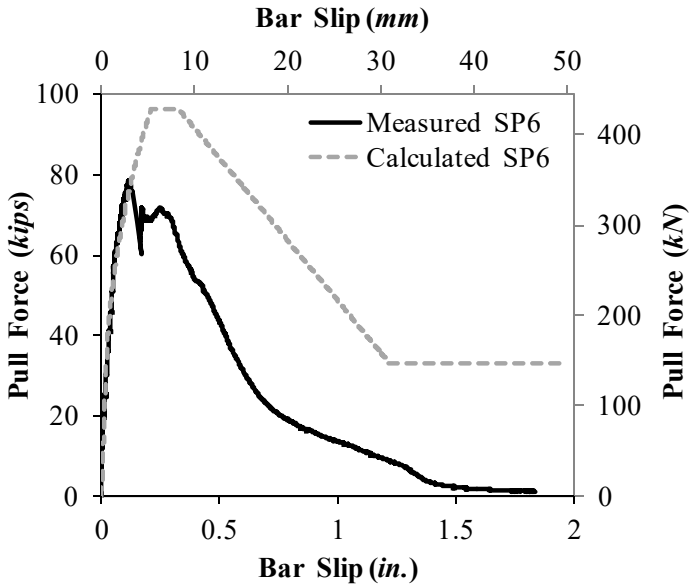

Figure 7.15- Measured and Calculated Pull Force-Bar Slip Curves

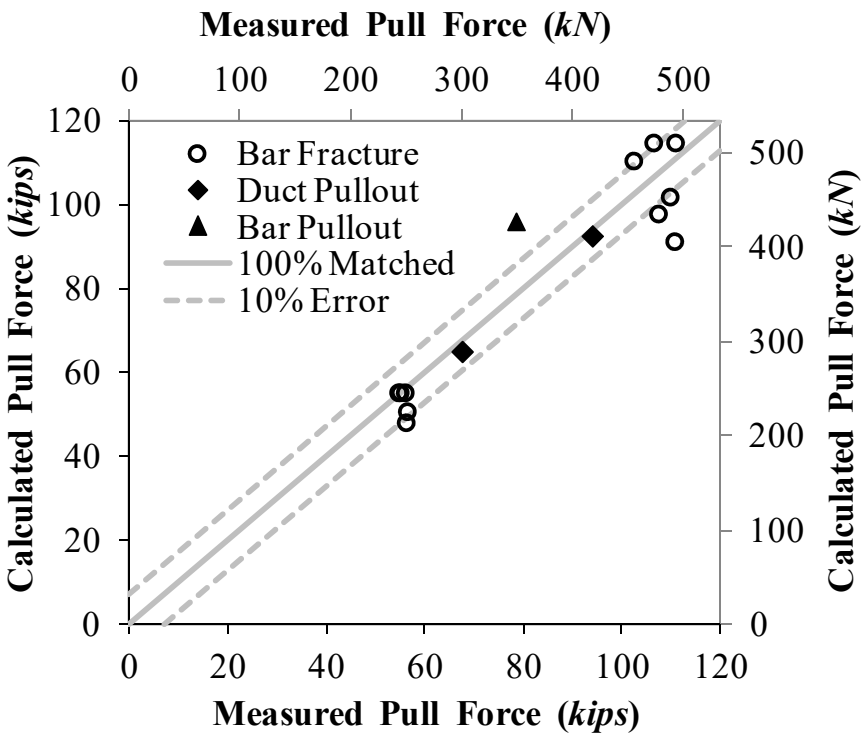

Figure 7.16- Measured and Calculated Pull Forces for Pullout Tests

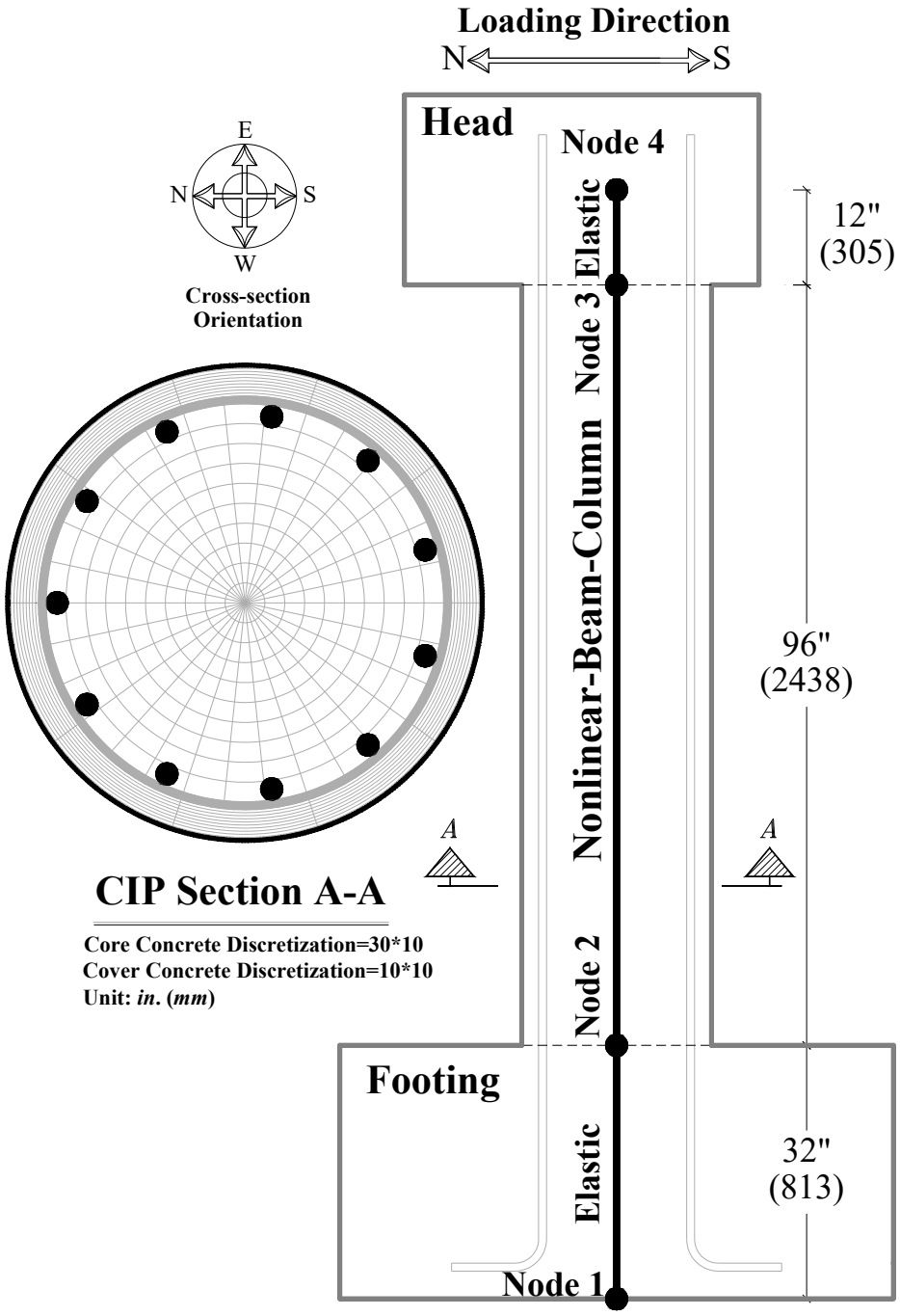

Figure 7.17- CIP Column Analytical Model

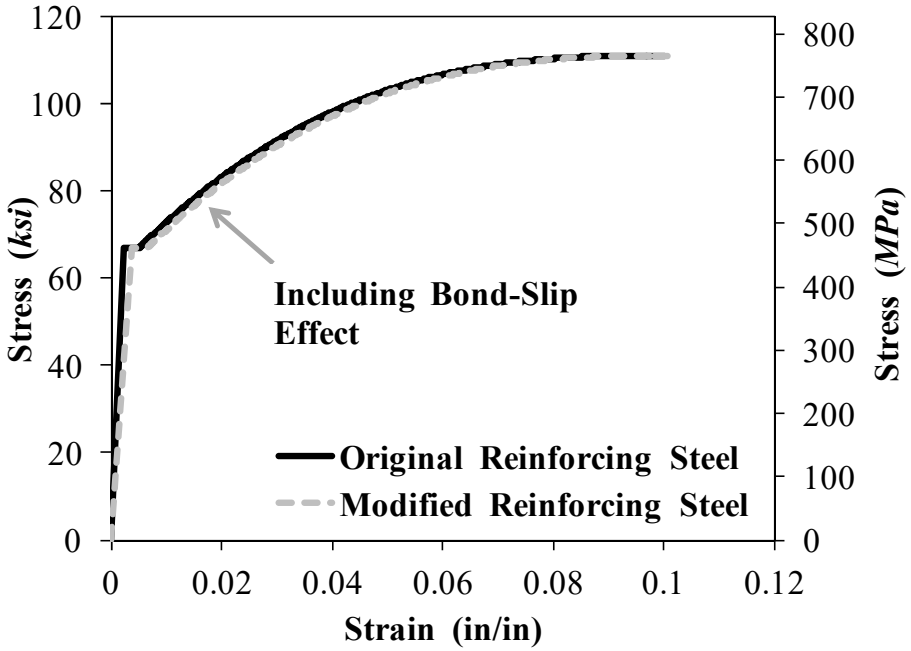

Figure 7.18- Original and Modified Reinforcing Steel Relationships Used in CIP Model

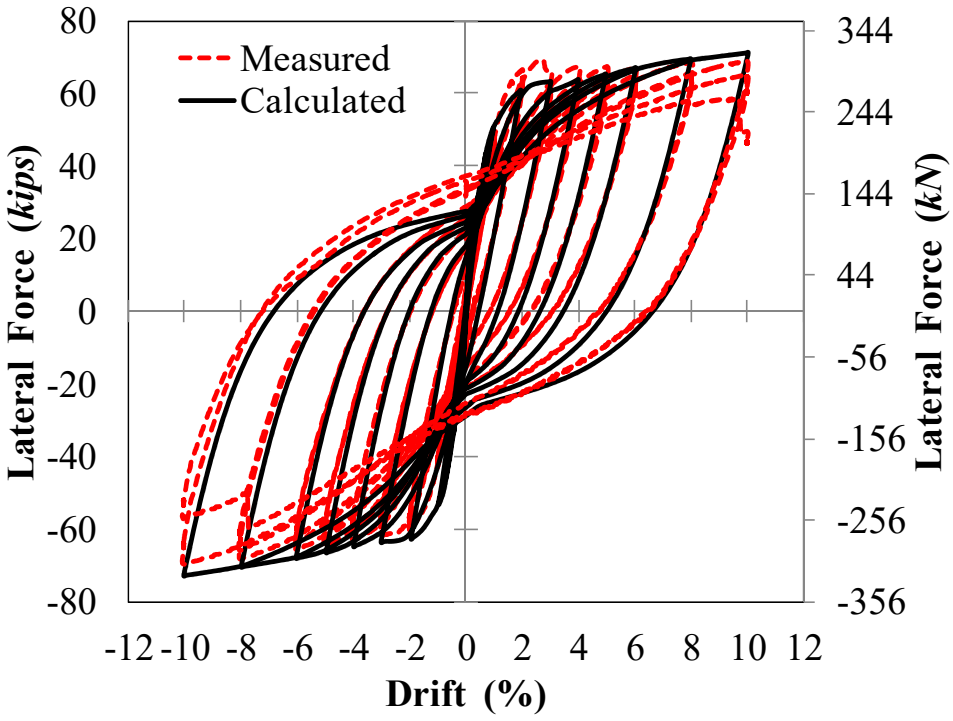

Figure 7.19- Measured and Calculated Force-Drift Hysteretic Curves for CIP

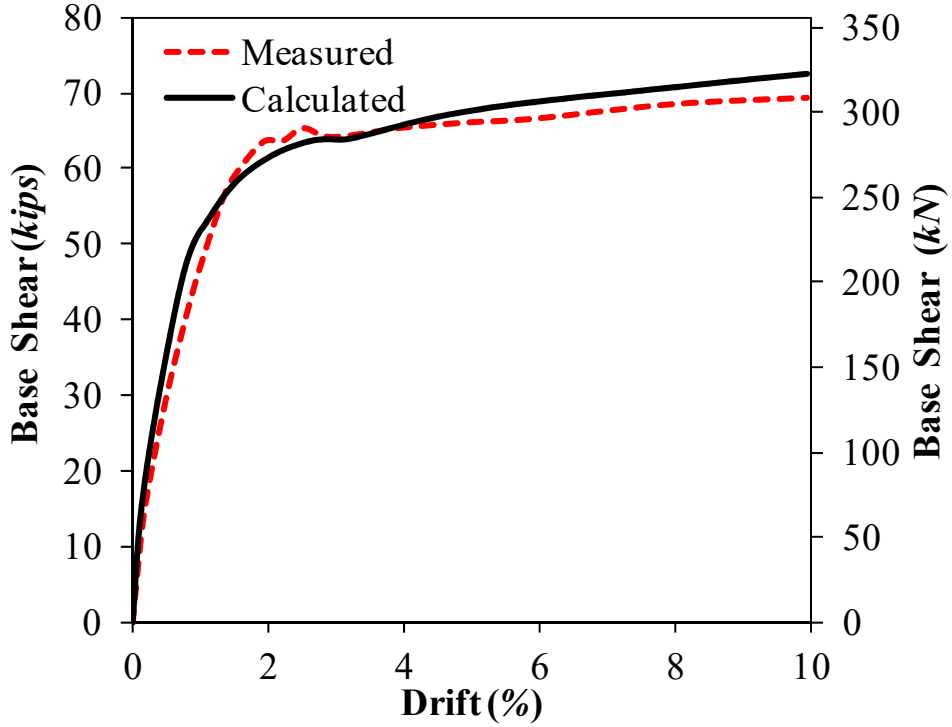

Figure 7.20- Measured and Calculated Force-Drift Envelopes for CIP

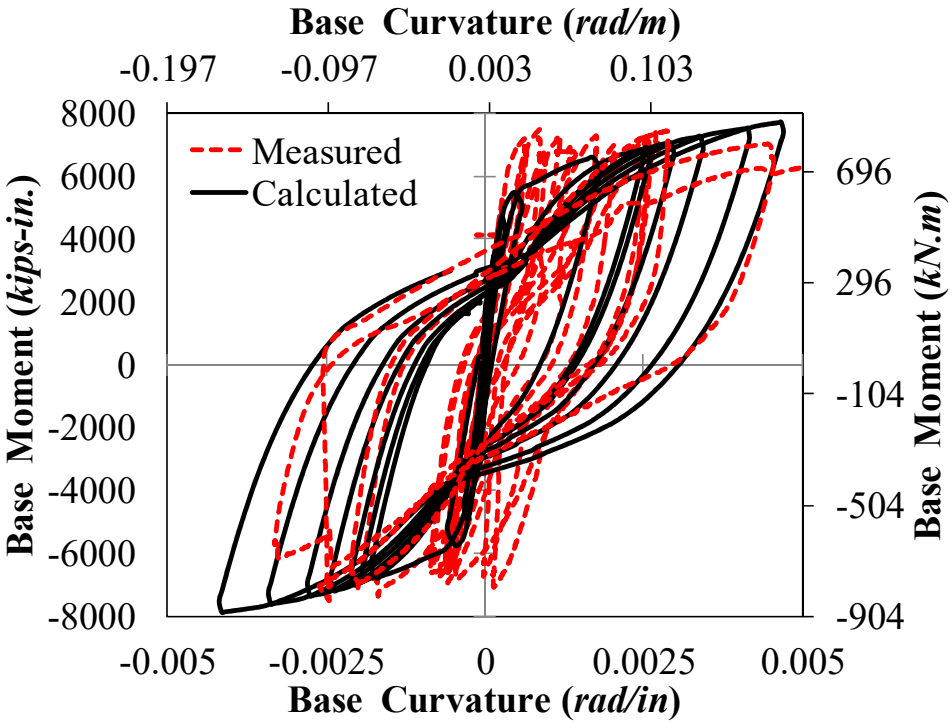

Figure 7.21- Measured and Calculated Base Moment-Curvature Curves for CIP

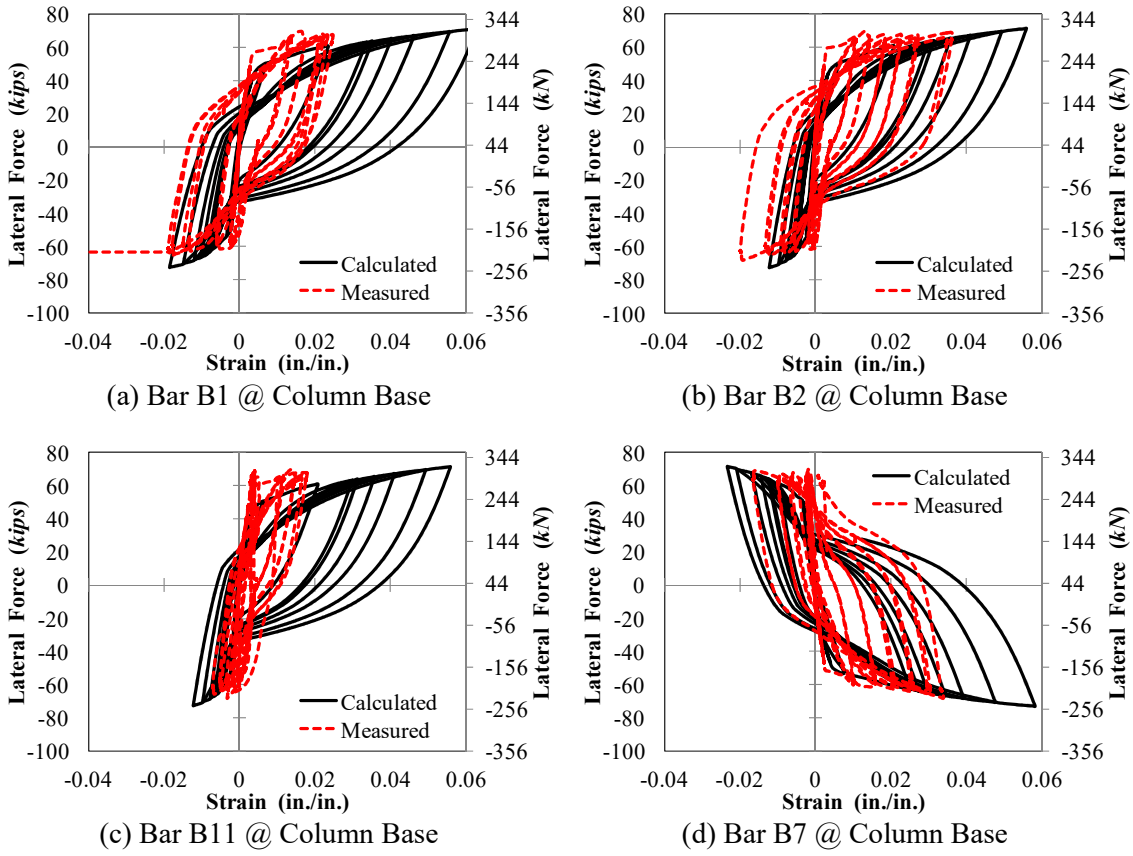

(a) Bar B1 @ Column Base

(b) Bar B2 @ Column Base

(c) Bar B11 @ Column Base

(d) Bar B7 @ Column Base

Figure 7.22- Measured and Calculated Lateral Force-Bar Strain Curves for CIP

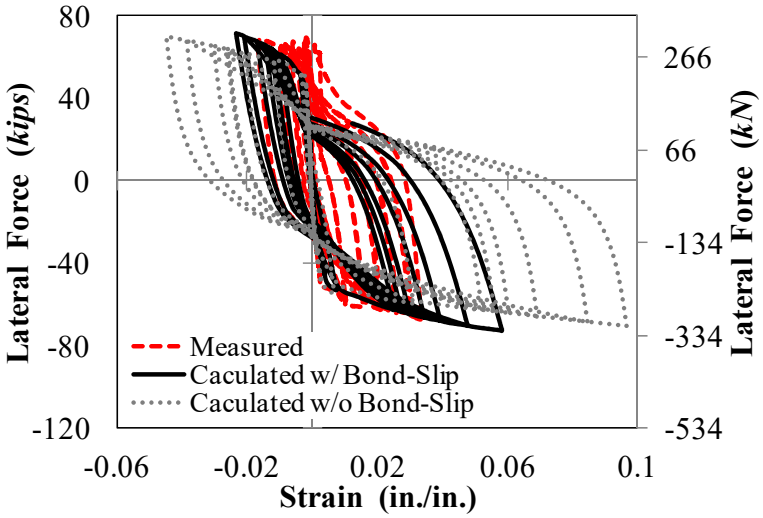

Figure 7.23- Bond-Slip Effect on Local Responses of CIP Column

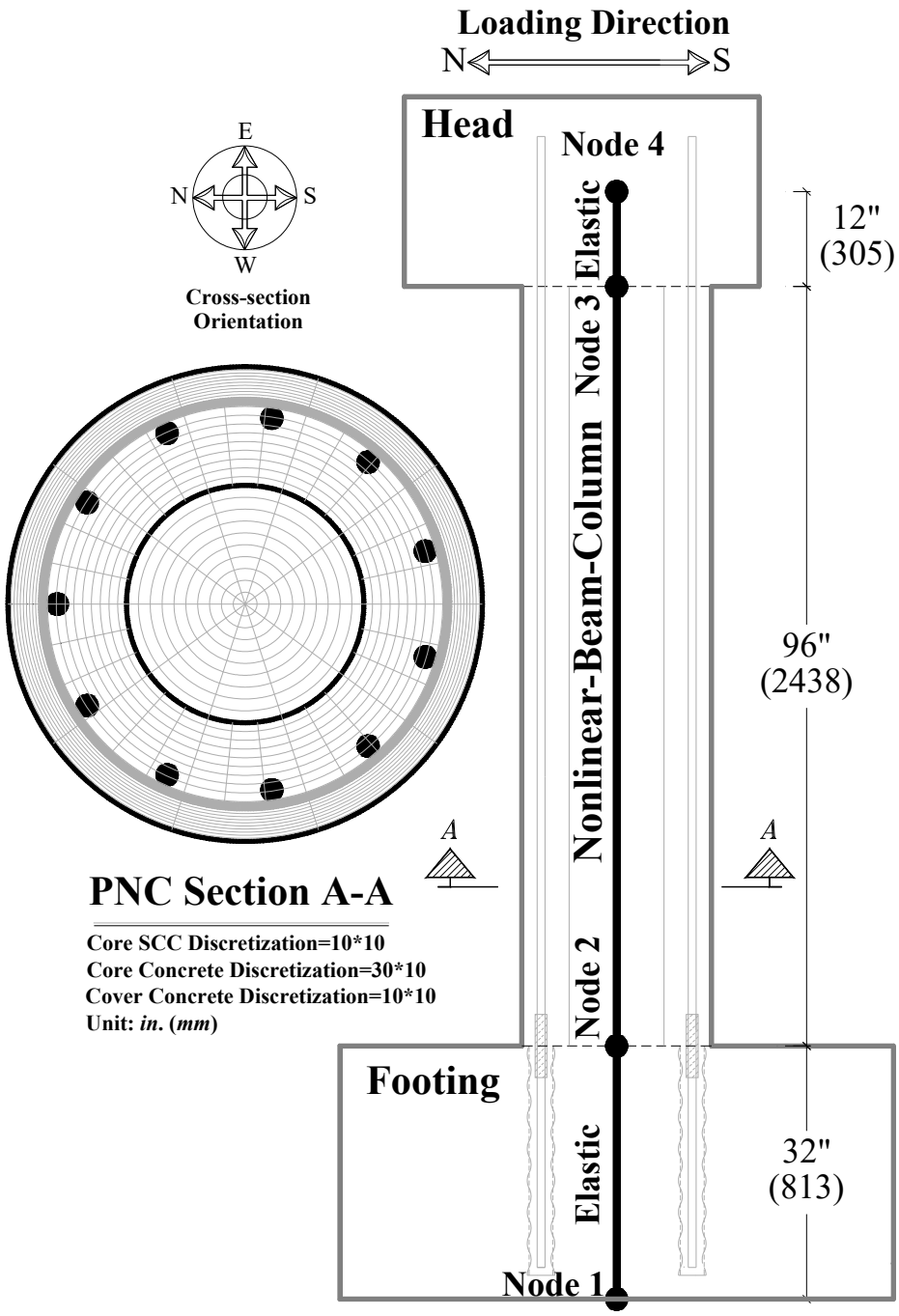

Figure 7.24- PNC Column Analytical Model

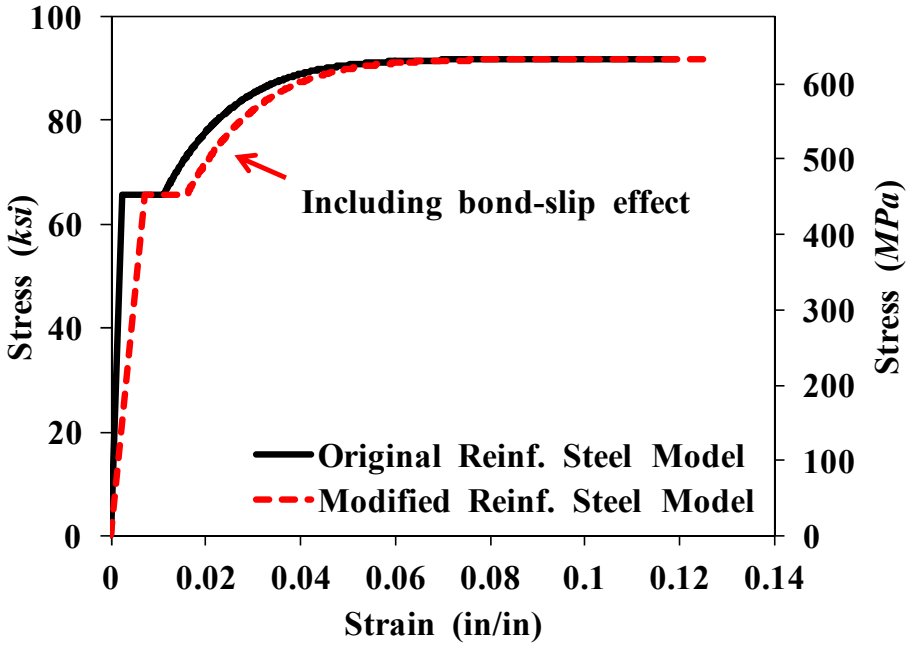

Figure 7.25- Original and Modified Reinforcing Steel Relationships Used in PNC Model

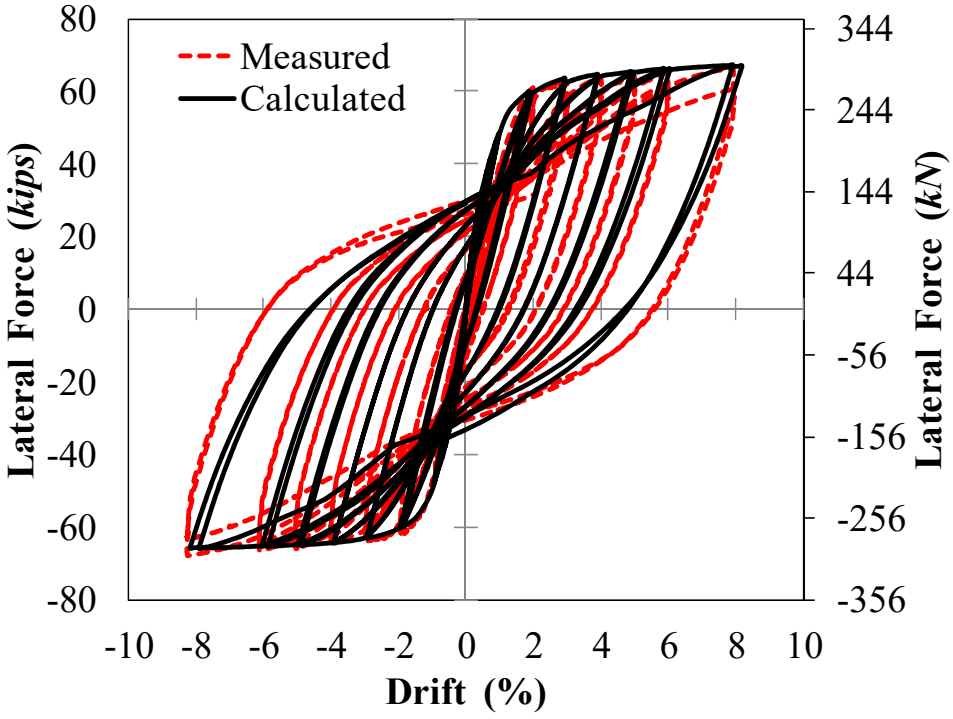

Figure 7.26- Measured and Calculated Force-Drift Hysteretic Curves for PNC

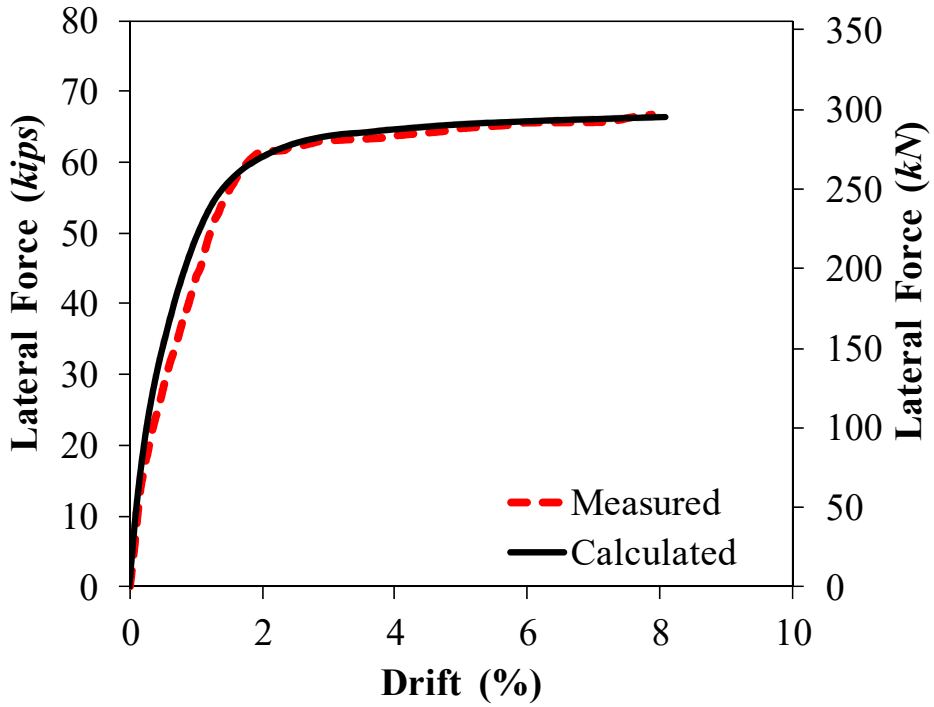

Figure 7.27- Measured and Calculated Force-Drift Envelopes for PNC

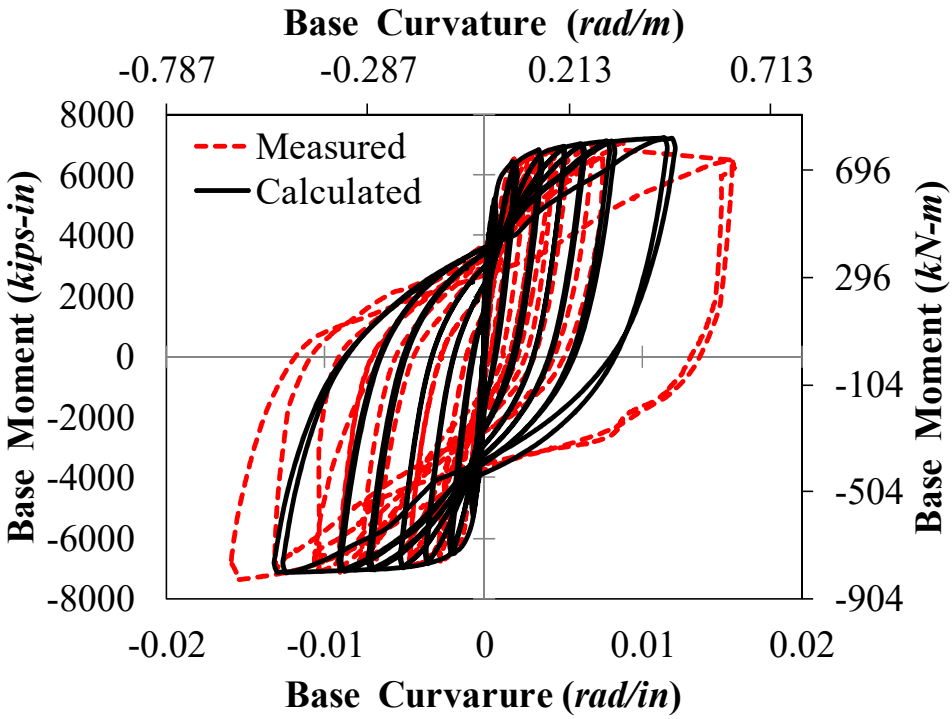

Figure 7.28- Measured and Calculated Base Moment-Curvature Curves for PNC

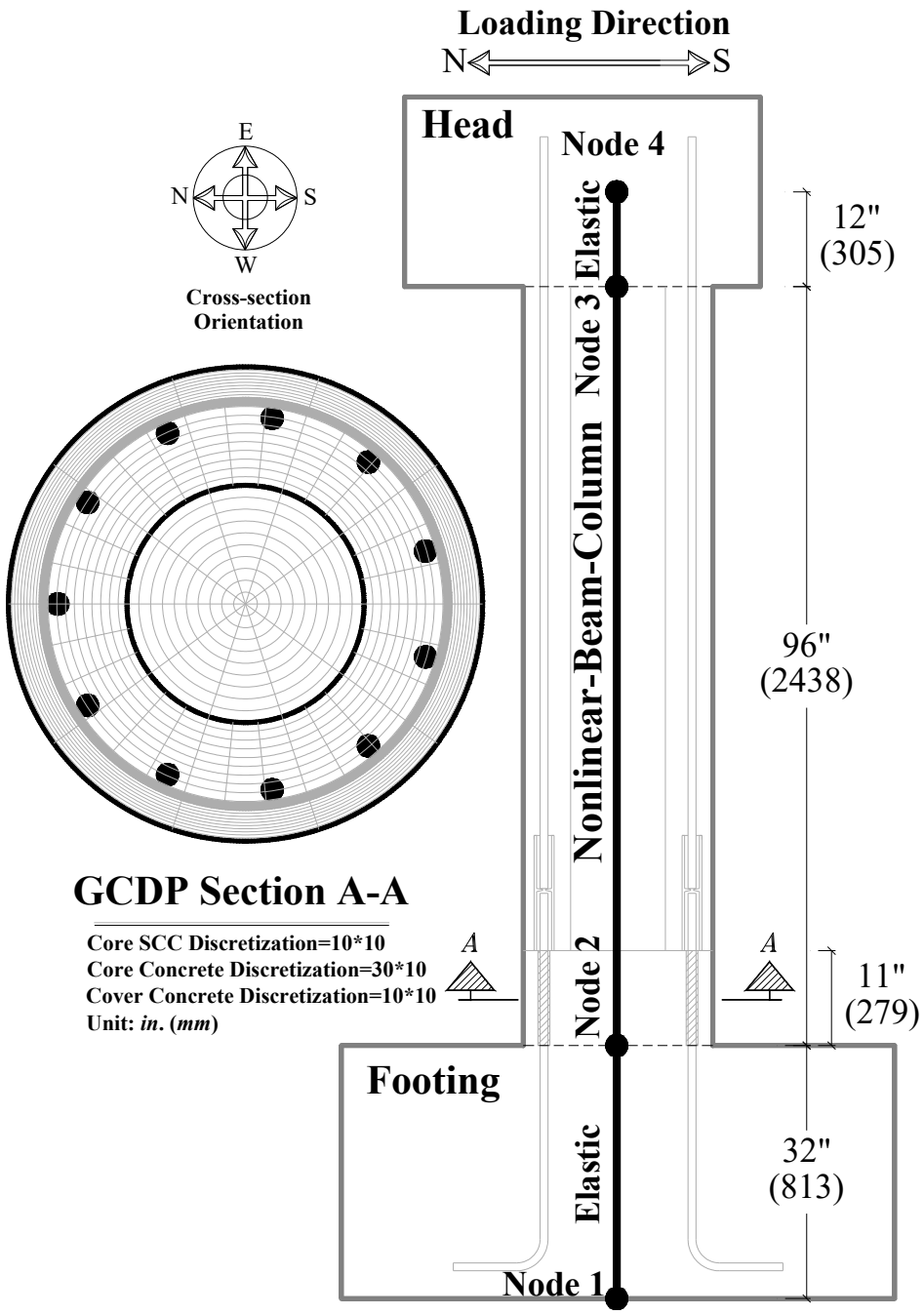

Figure 7.29- GCDP Column Analytical Model

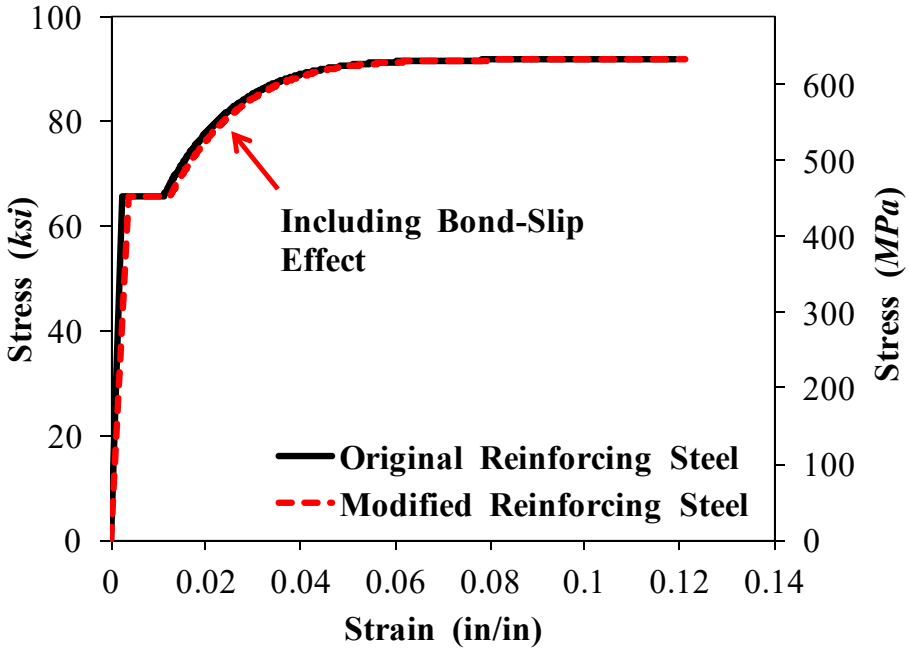

Figure 7.30- Bond-Slip Effect on Steel Fibers Used in GCDP Model

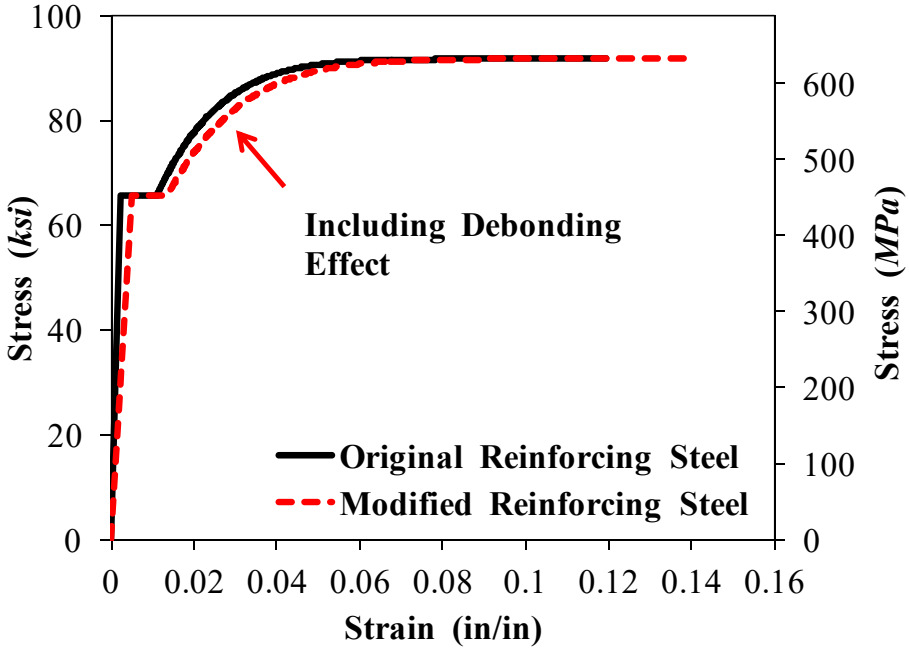

Figure 7.31- Bar Debonding Effect on Steel Fibers Used in GCDP Model

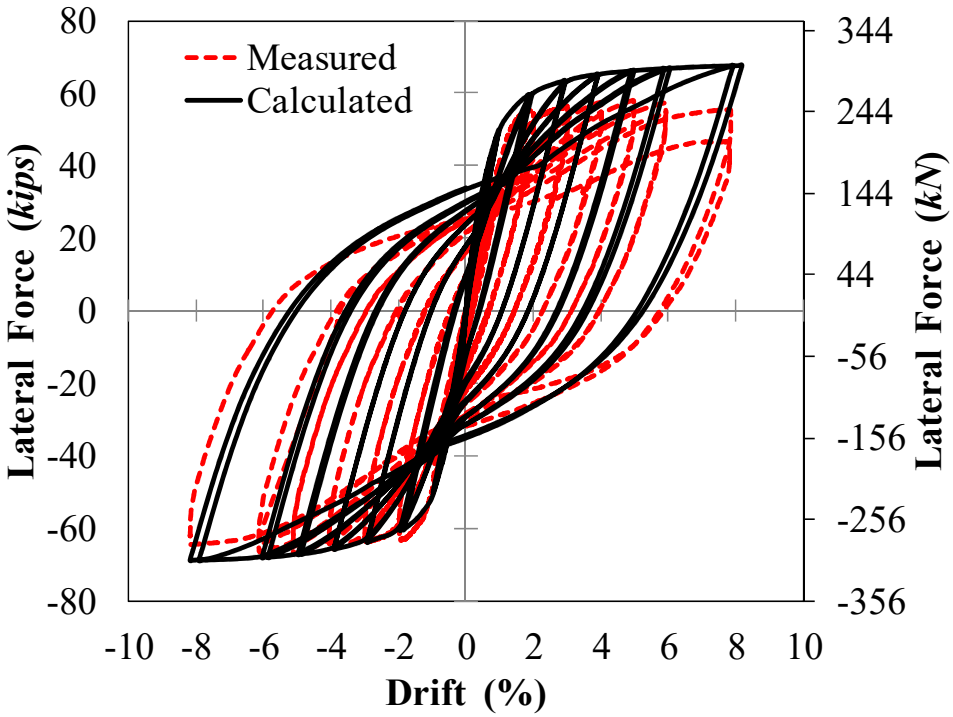

Figure 7.32- Measured and Calculated Force-Drift Hysteretic Curves for GCDP

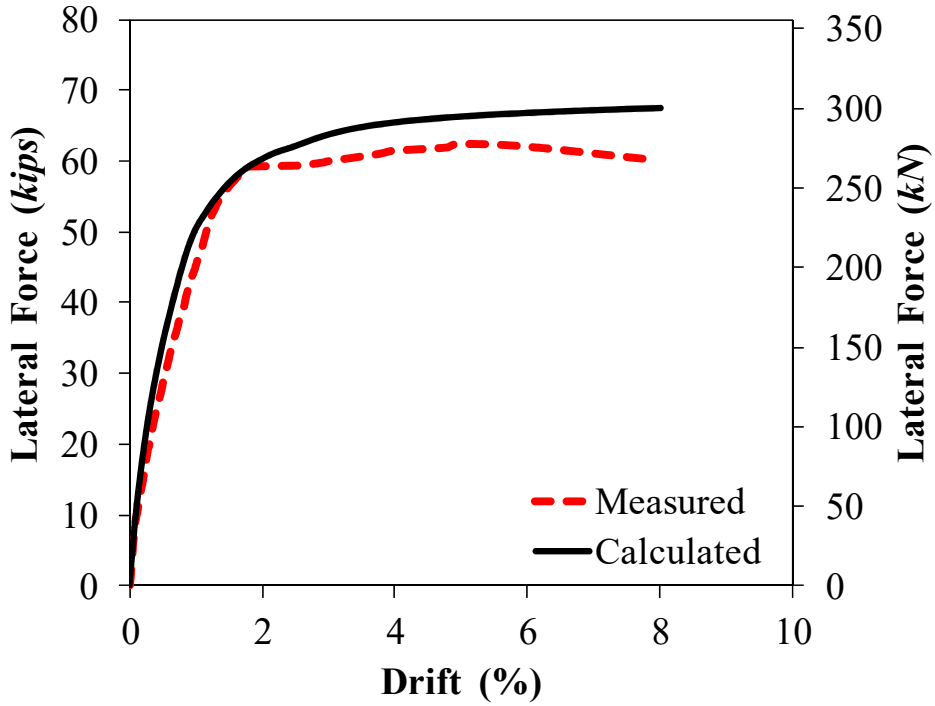

Figure 7.33- Measured and Calculated Force-Drift Envelopes for GCDP

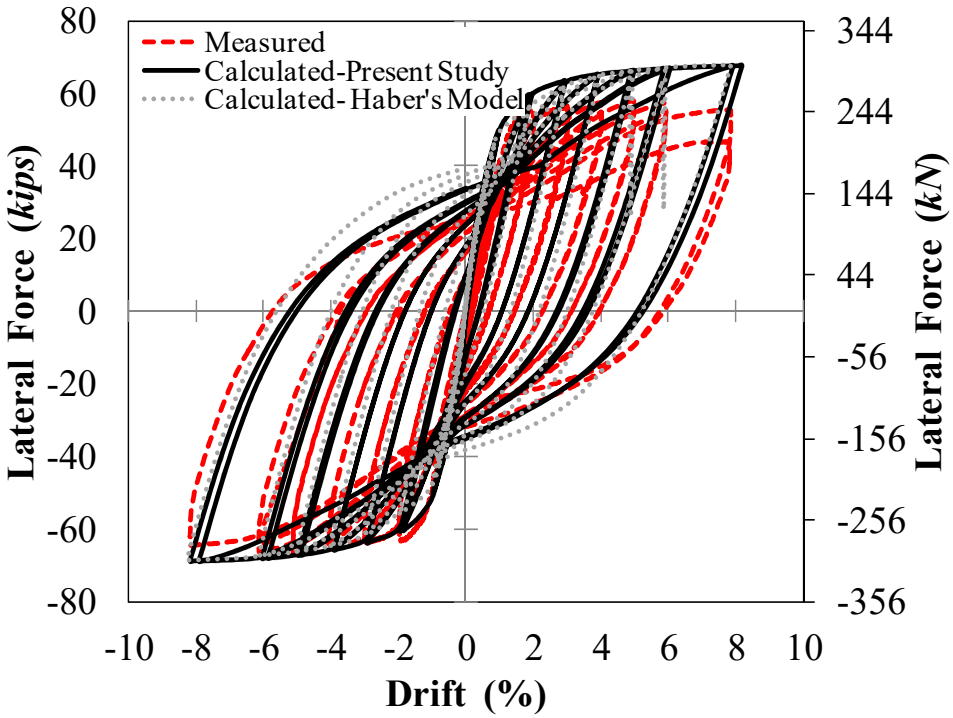

Figure 7.34- Proposed versus Advanced Modeling Method for GCDP Column

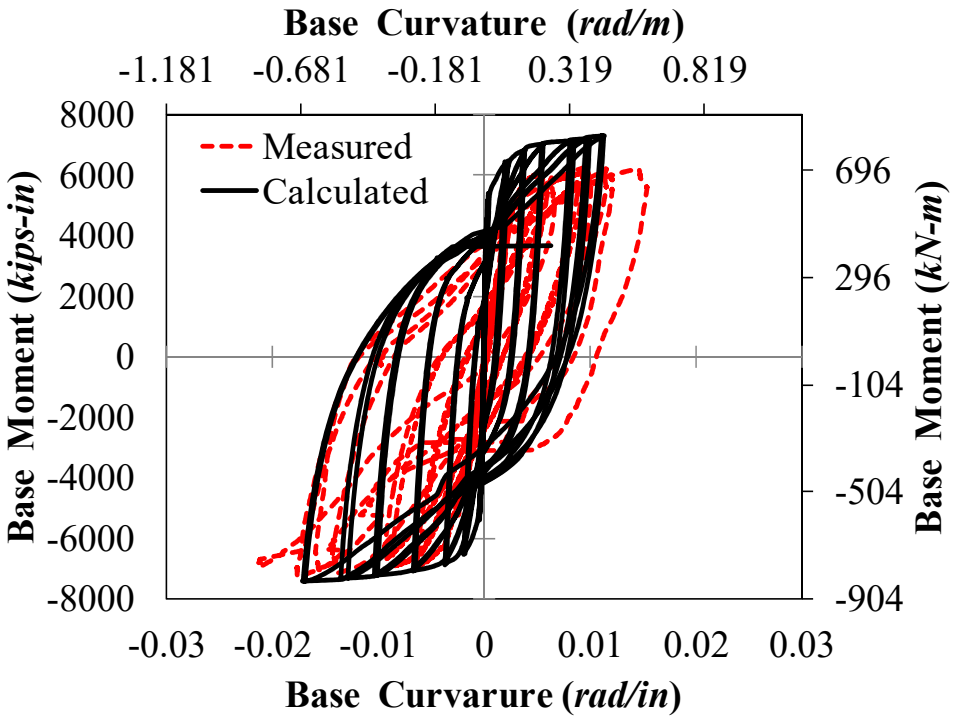

Figure 7.35- Measured and Calculated Base Moment-Curvature Curves for GCDP

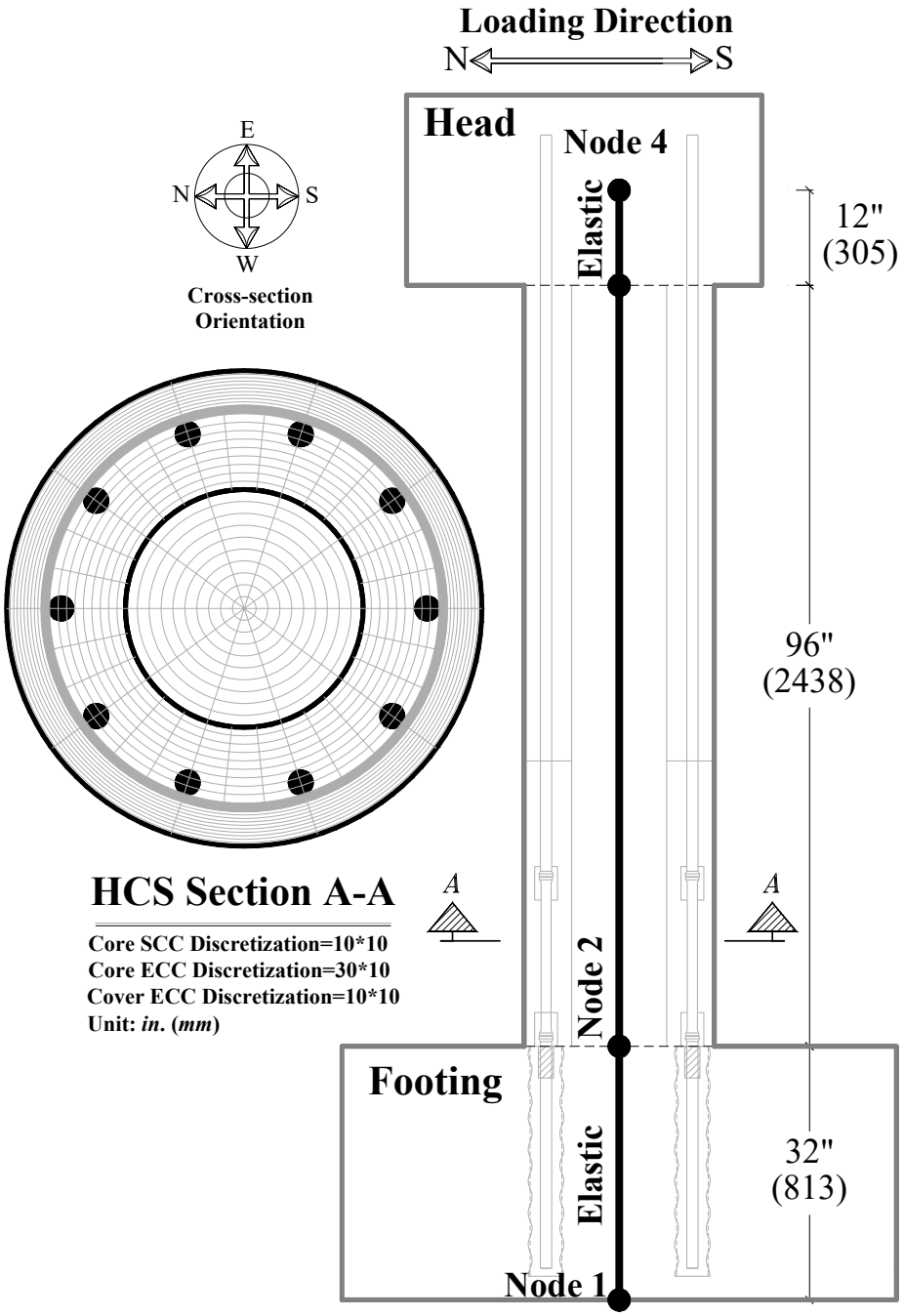

Figure 7.36- HCS Column Analytical Model

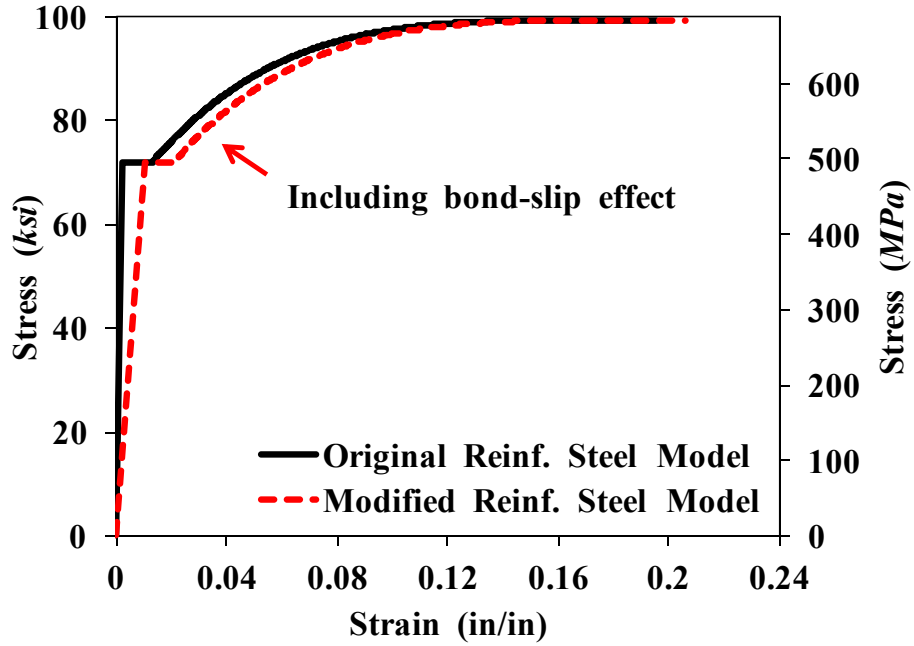

Figure 7.37- Bond-Slip Effect on Steel Fibers Used in HCS Model

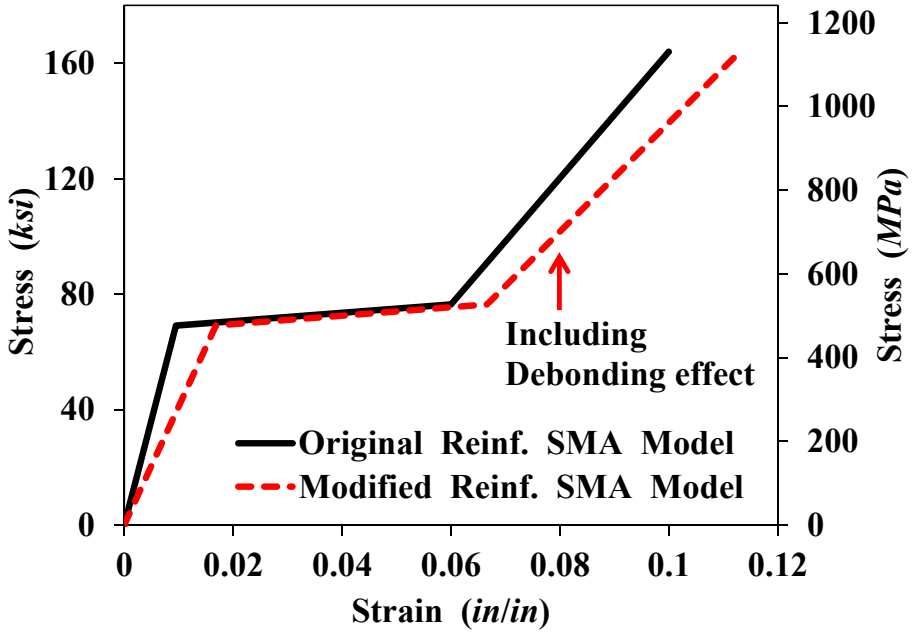

Figure 7.38- Debonding Effect on SMA Fibers Used in HCS Model

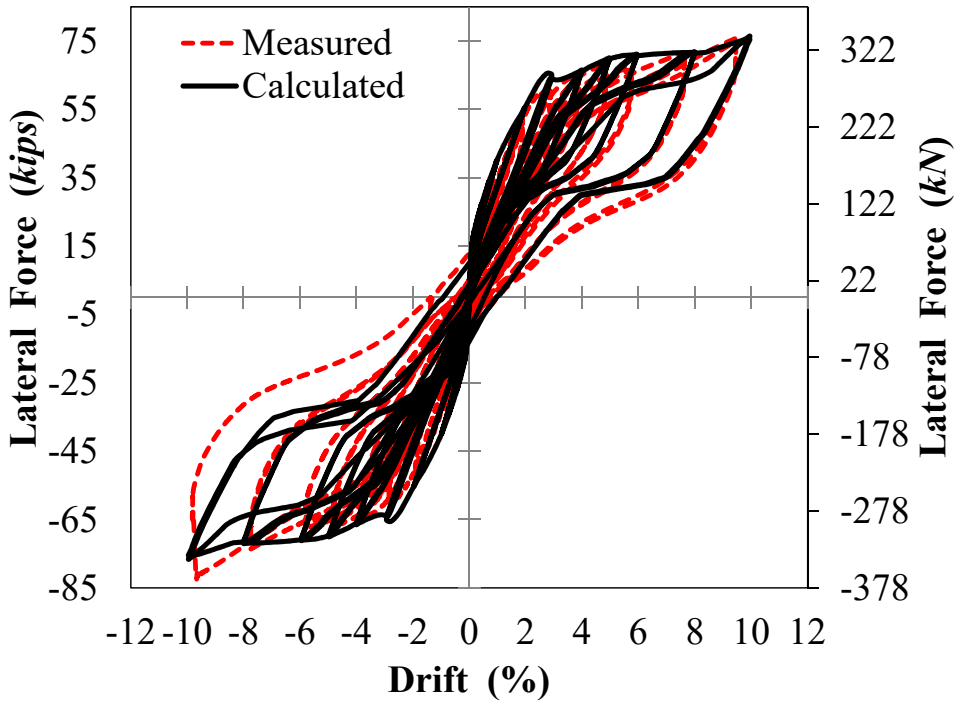

Figure 7.39- Measured and Calculated Force-Drift Hysteretic Curves for HCS

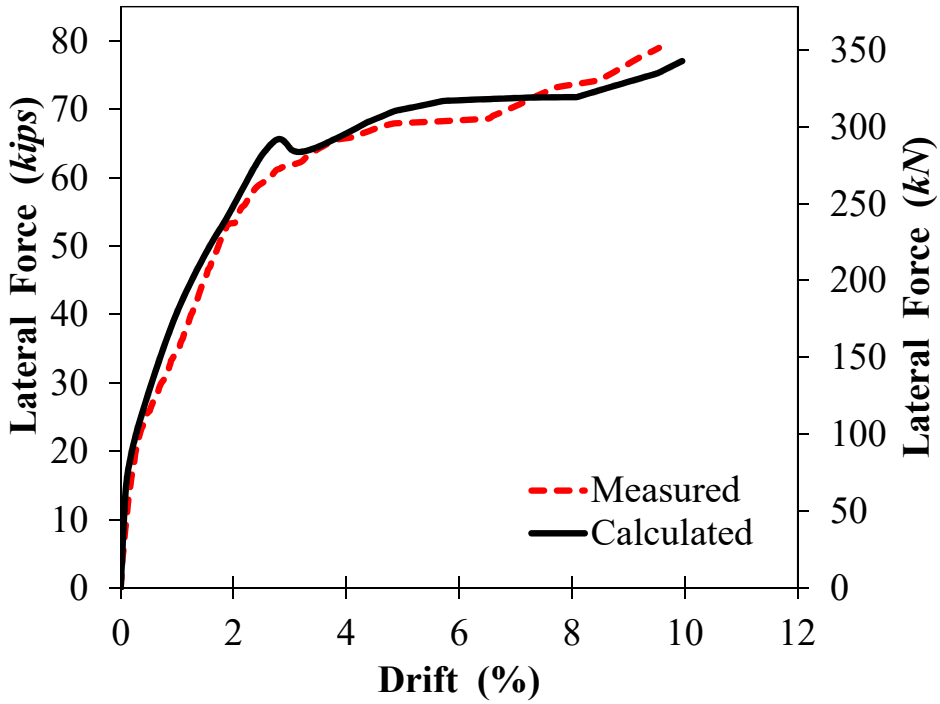

Figure 7.40- Measured and Calculated Force-Drift Envelopes for HCS

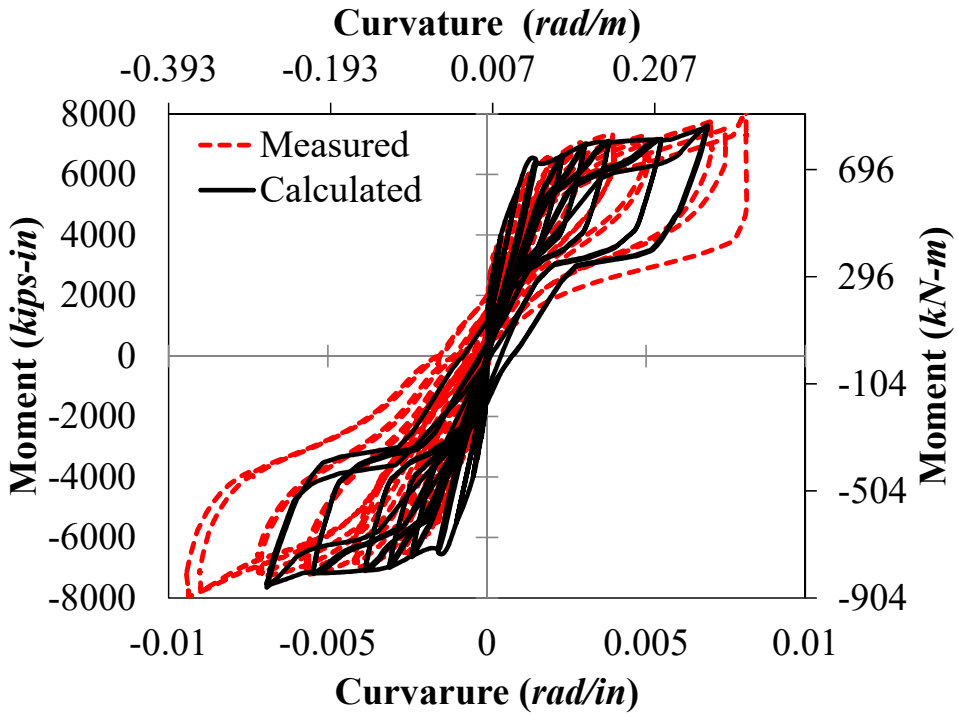

Figure 7.41- Measured and Calculated Moment-Curvature Curves for HCS at Level 3

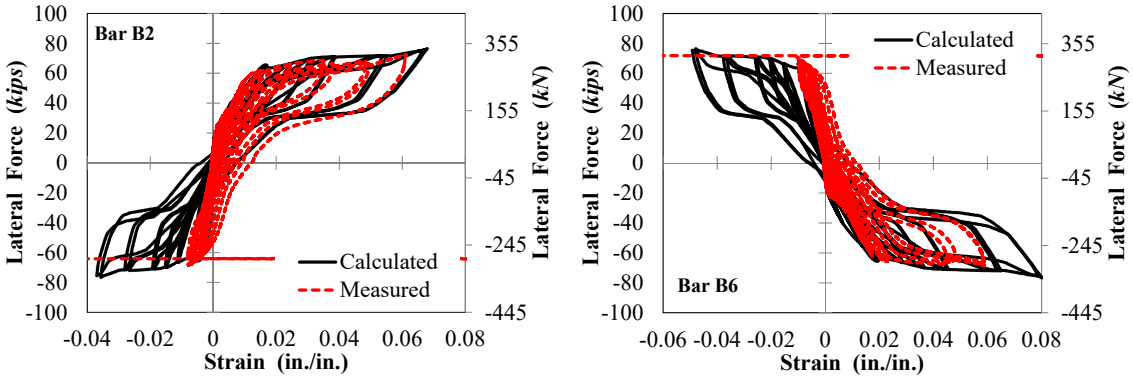

(a) Bar B2 at 8.1 *in*. above Footing (b) Bar B6 at 8.1 *in*. above Footing

Figure 7.42- Measured and Calculated Lateral Force-SMA Bar Strain Curves for HCS

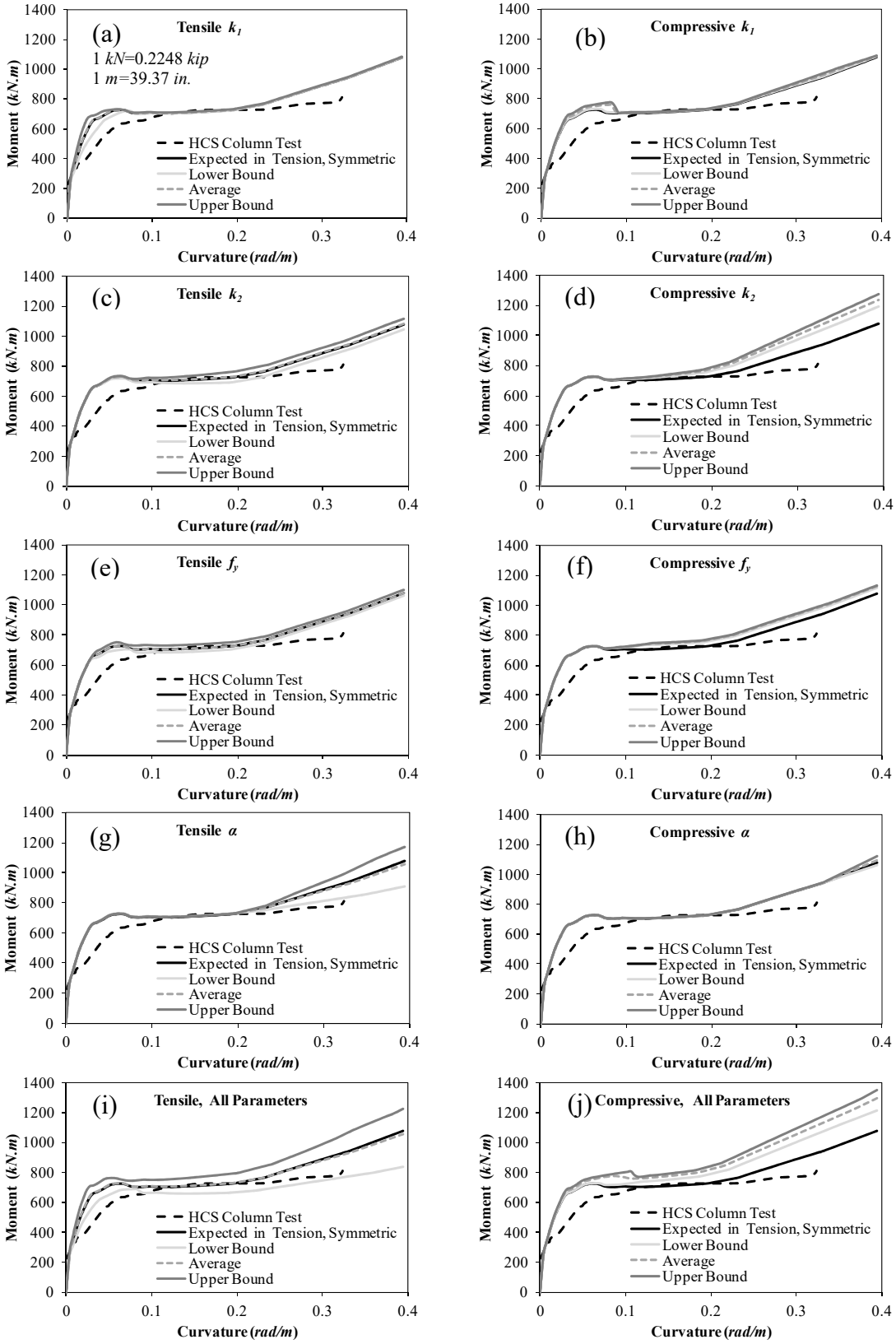

Figure 8.1- Effect of Reinforcing SMA Mechanical Properties on Moment-Curvature Curves

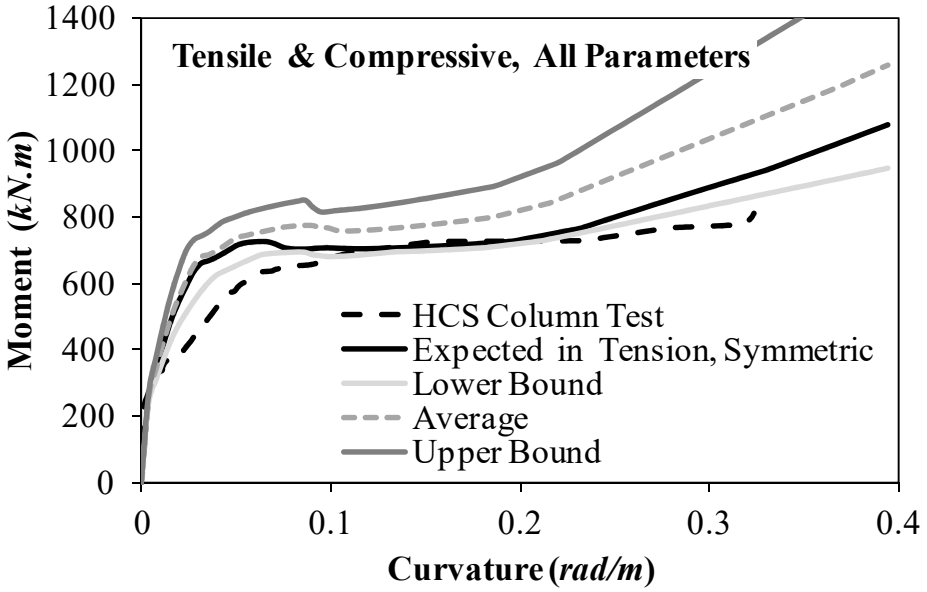

Figure 8.2- Effect of All Reinforcing SMA Mechanical Properties on Moment-Curvature Curves

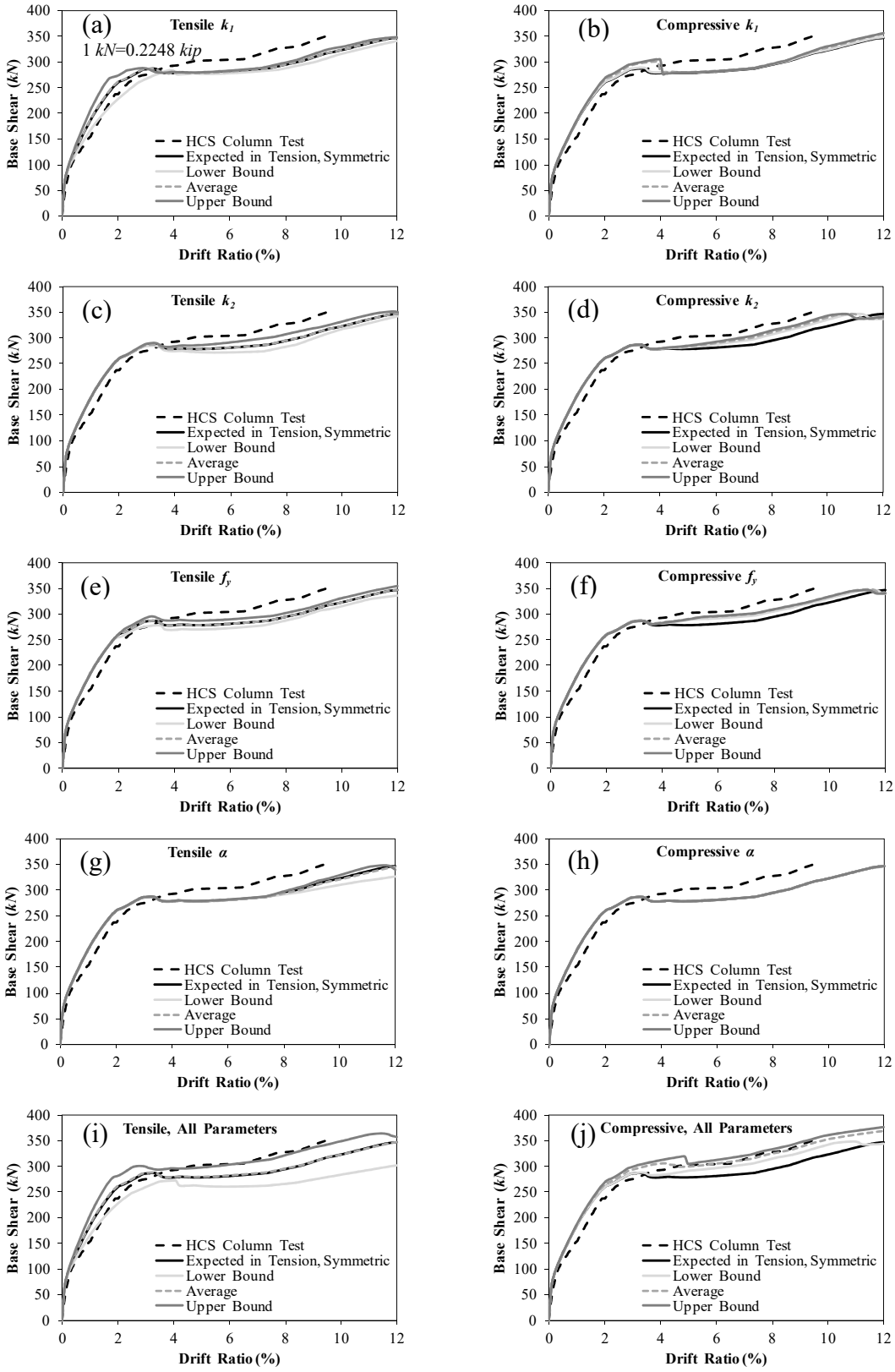

Figure 8.3- Effect of Reinforcing SMA Mechanical Properties on Pushover Curves

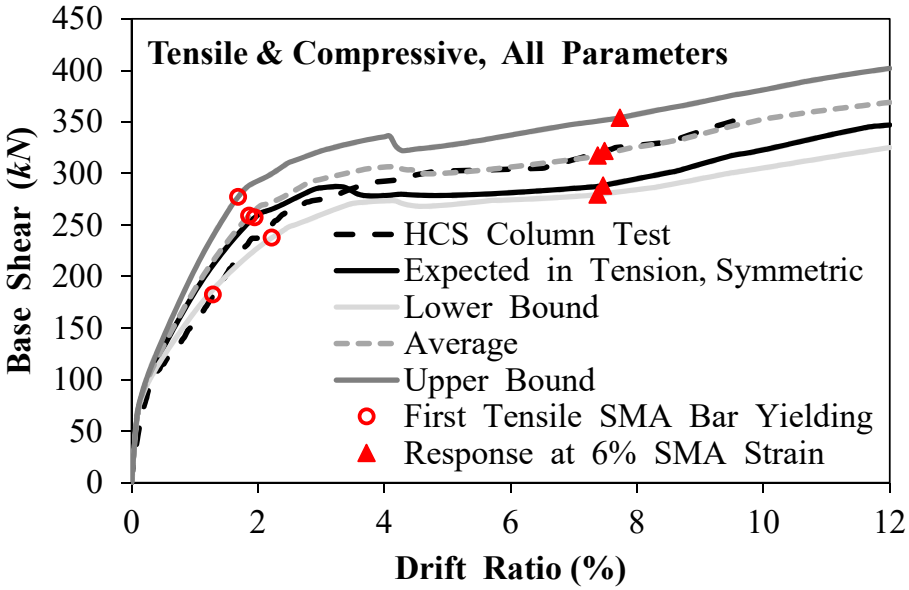

Figure 8.4- Effect of All Reinforcing SMA Mechanical Properties on Pushover Curves

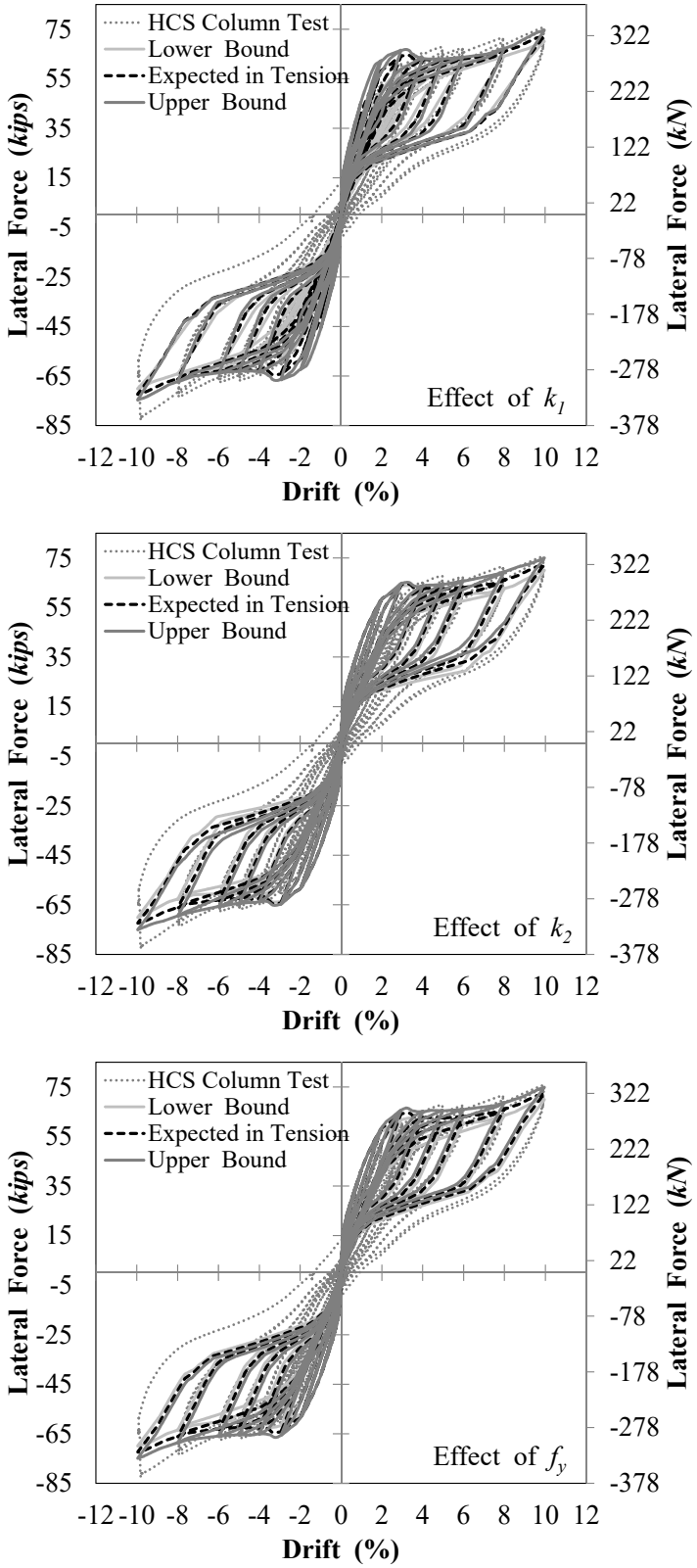

Figure 8.5- Effect of Reinforcing SMA Mechanical Properties Effect on Cyclic Responses

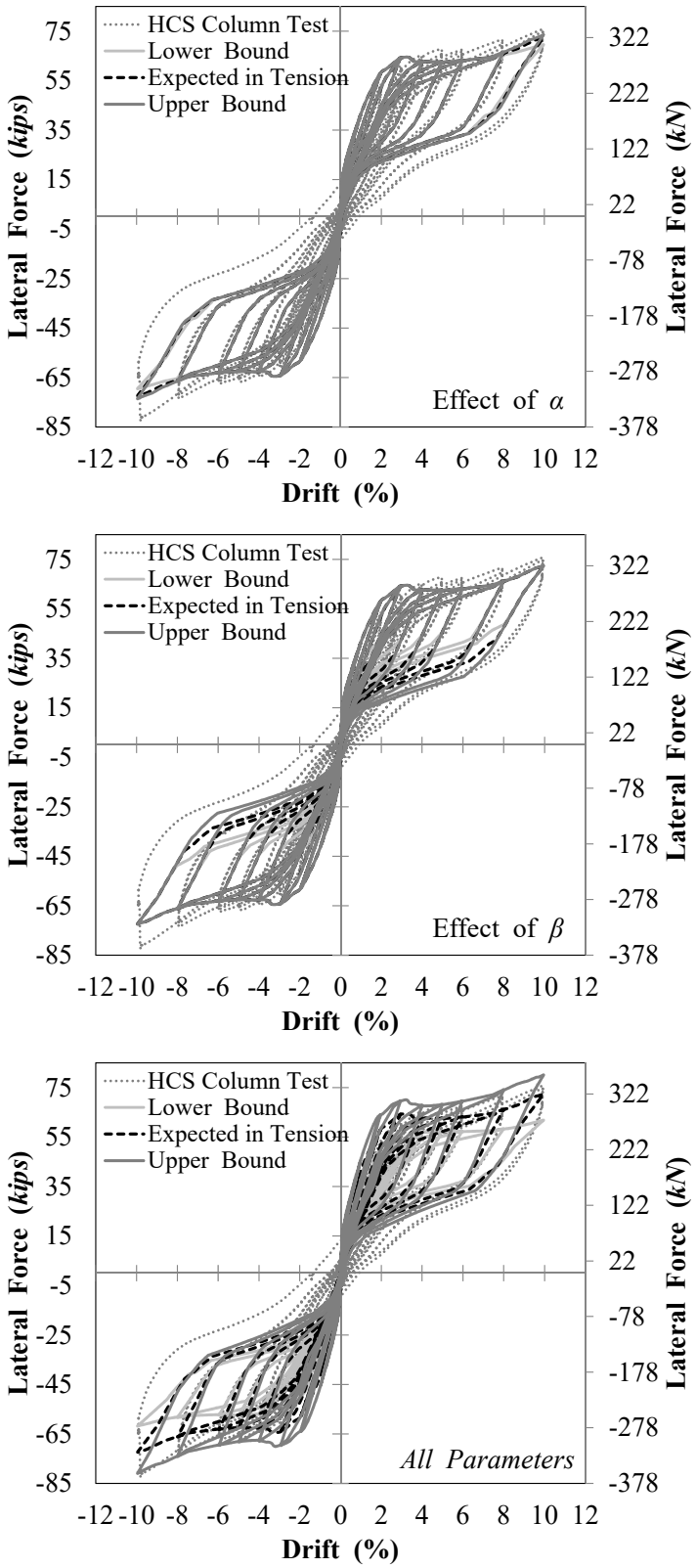

Figure 8.5- Effect of Reinforcing SMA Mechanical Properties on Cyclic Responses (Continued)

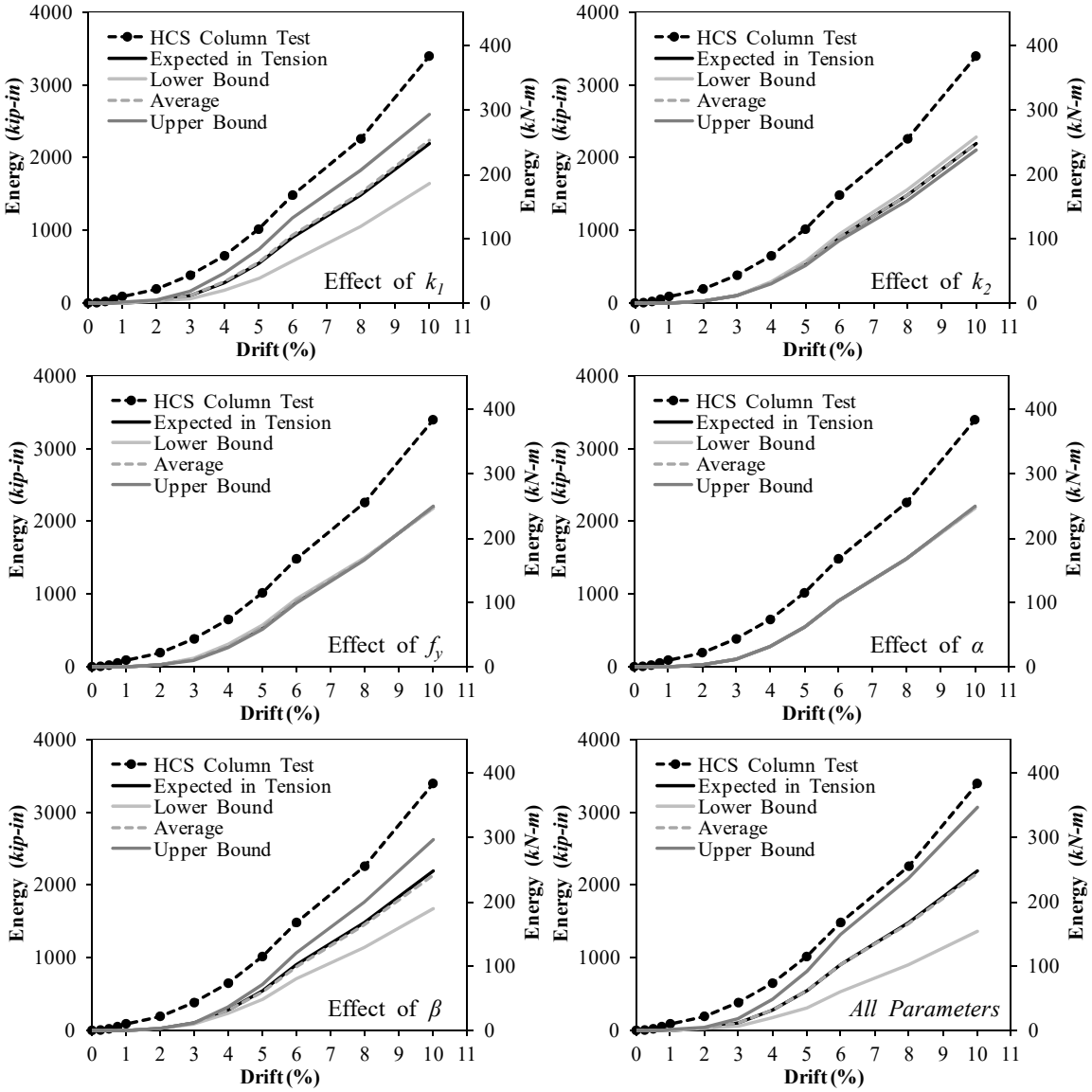

Figure 8.6- Effect of Reinforcing SMA Mechanical Properties on Energy Dissipation

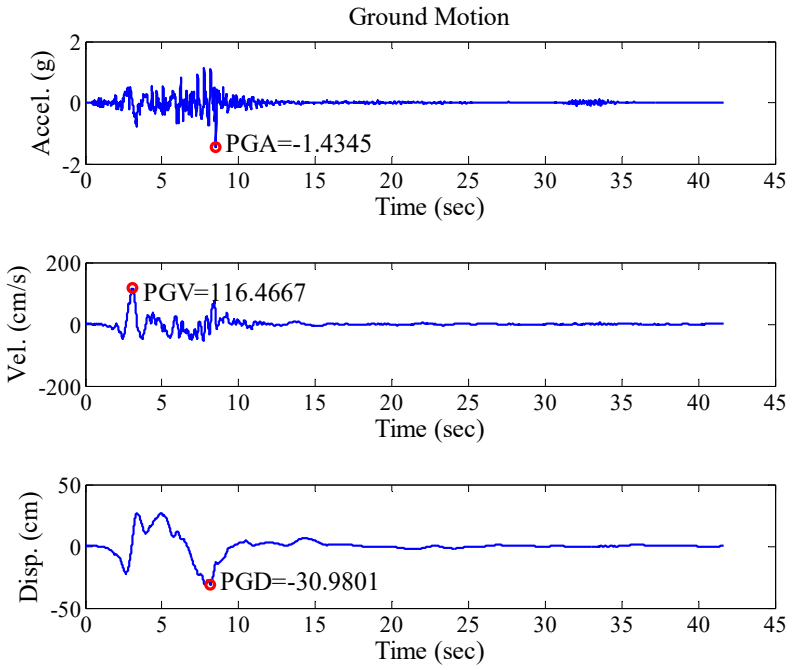

(a) EQ1 [San Fernando]

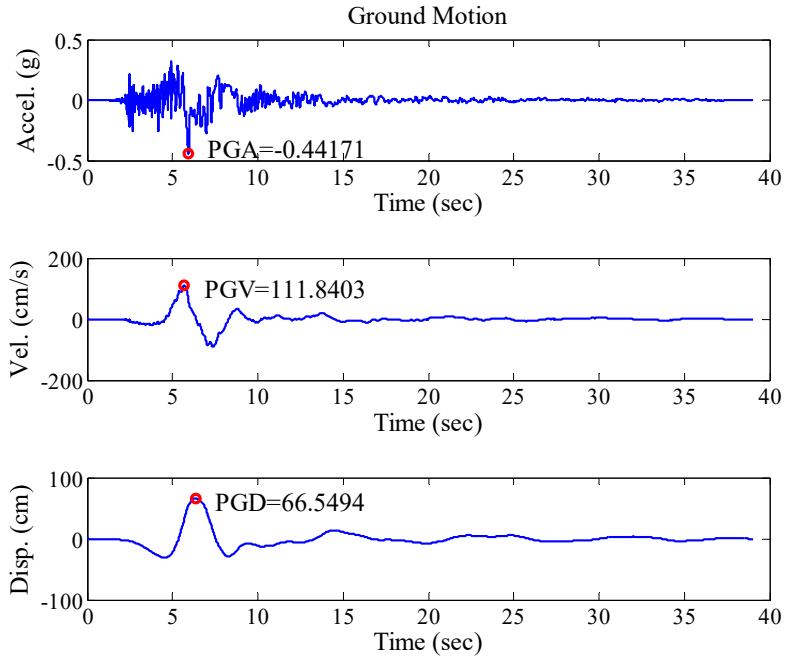

(b) EQ3 [Imperial Valley]

Figure 8.7- Near-Fault Motions

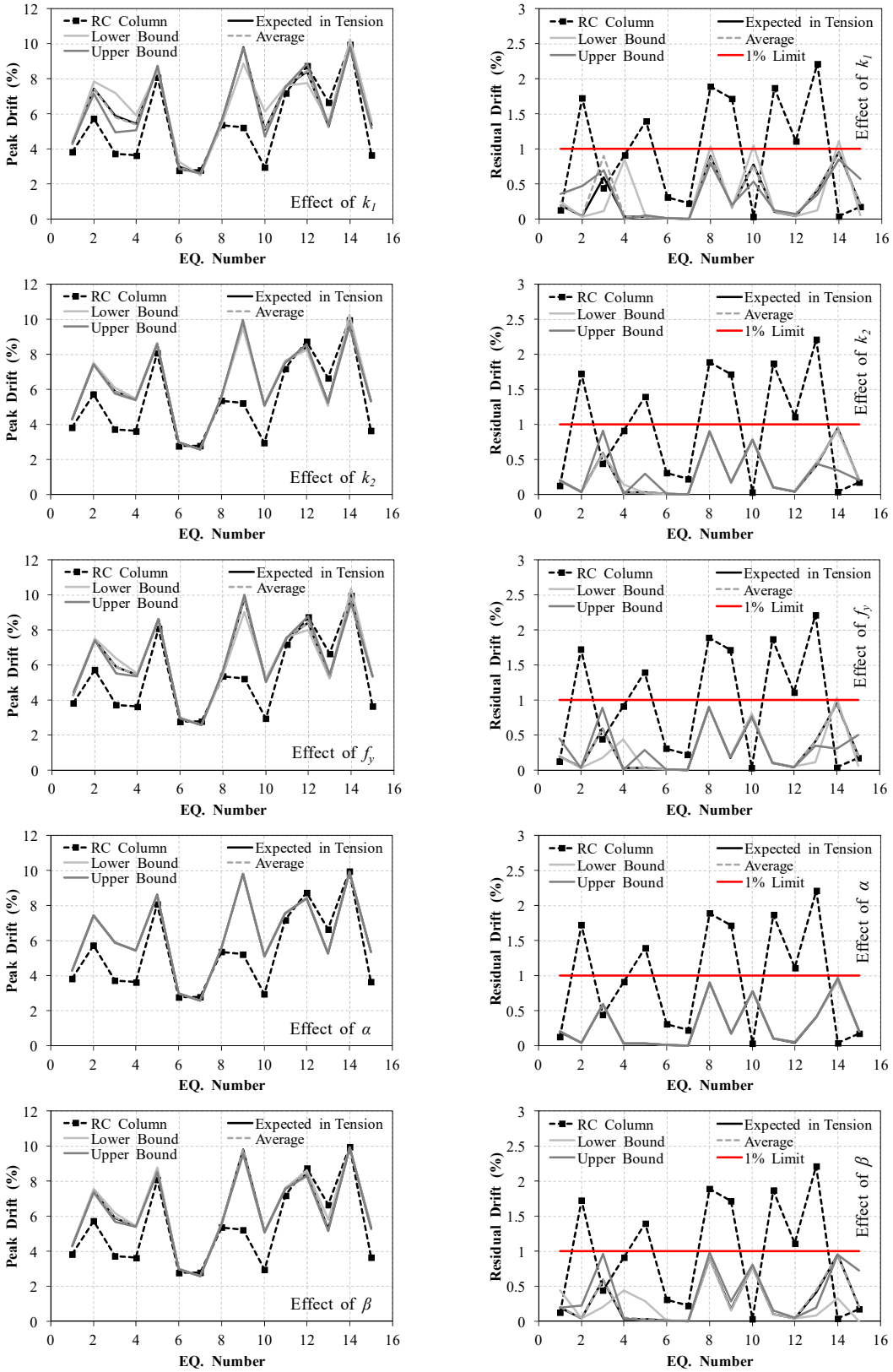

Figure 8.8- Effect of Each SMA Mechanical Property on Peak and Residual Displacements

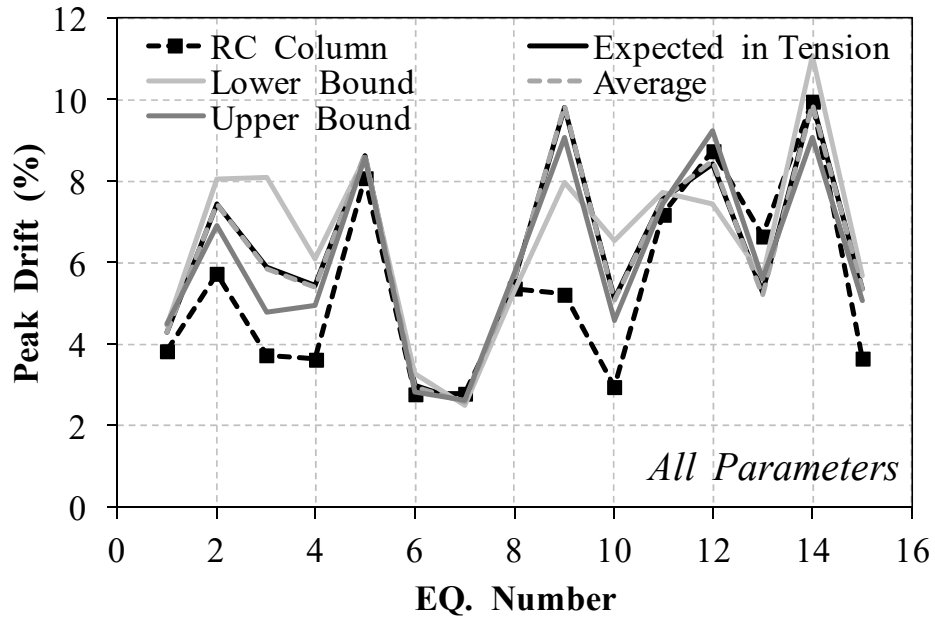

(a) Peak Displacements

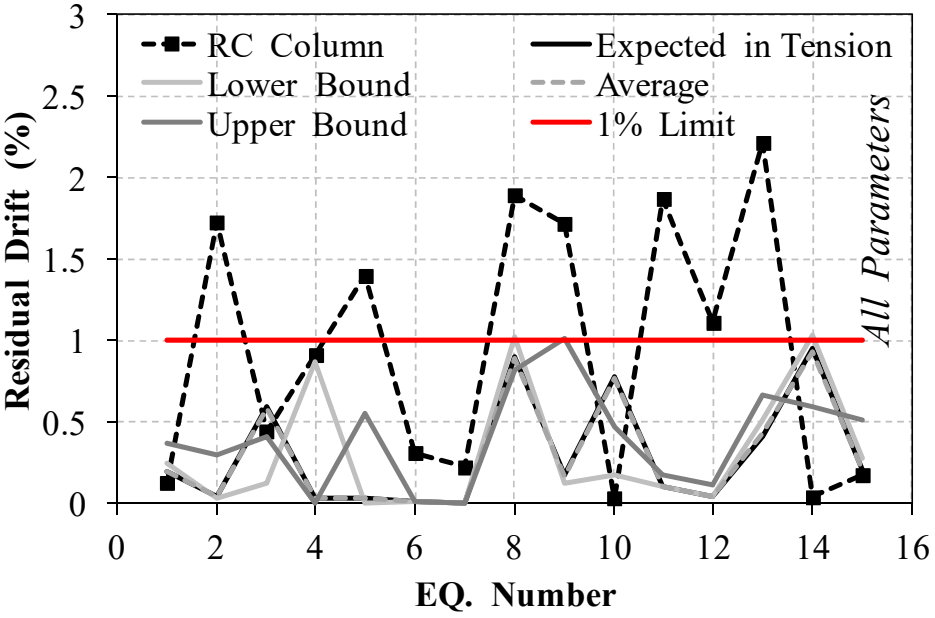

(b) Residual Displacements

Figure 8.9- Effect of All SMA Mechanical Properties on Peak and Residual Displacements

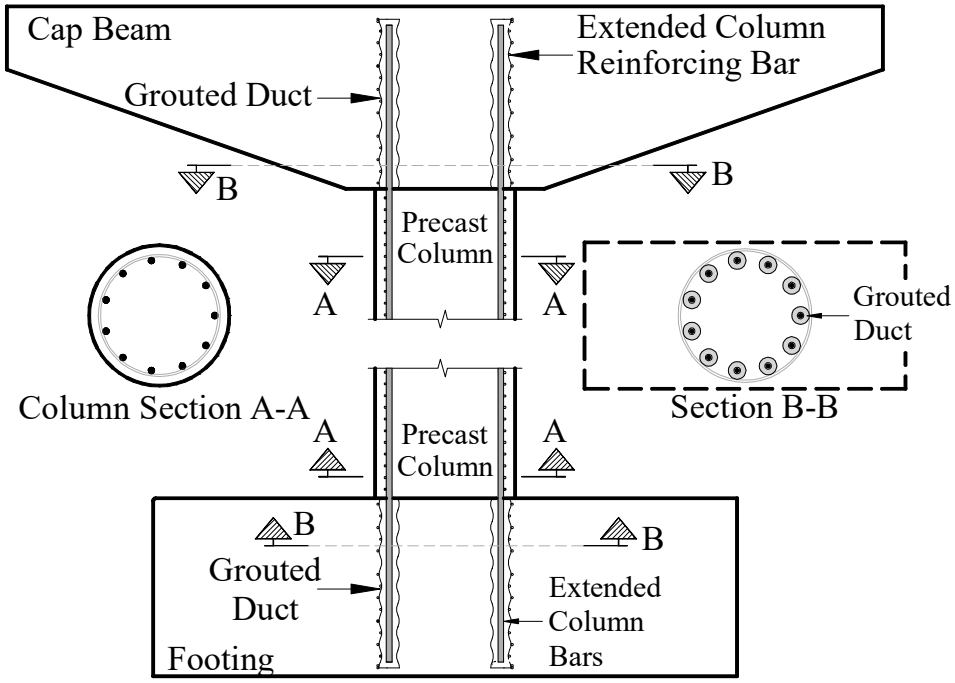

Figure 9.1- Grouted Duct Connections

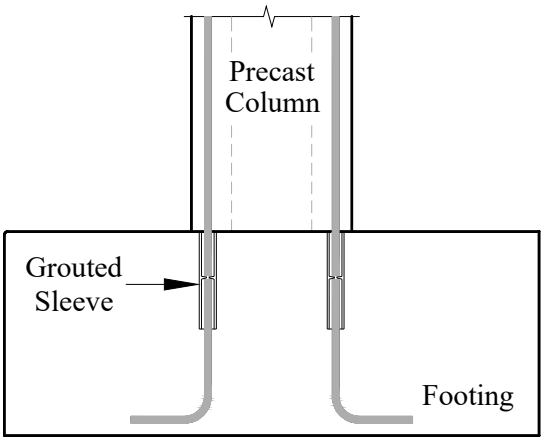

(a) Sleeves in Footing

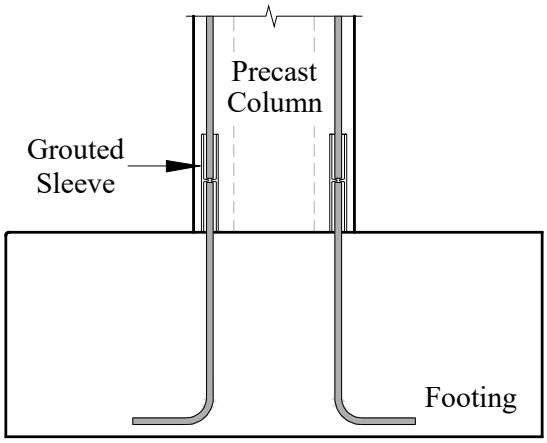

(b) Sleeves Immediately above Footing

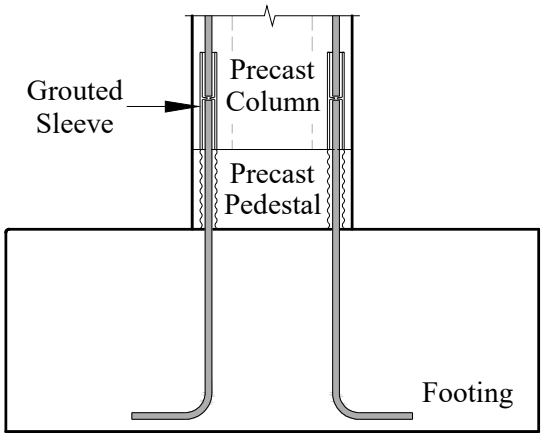

(c) Sleeves above Precast Pedestal

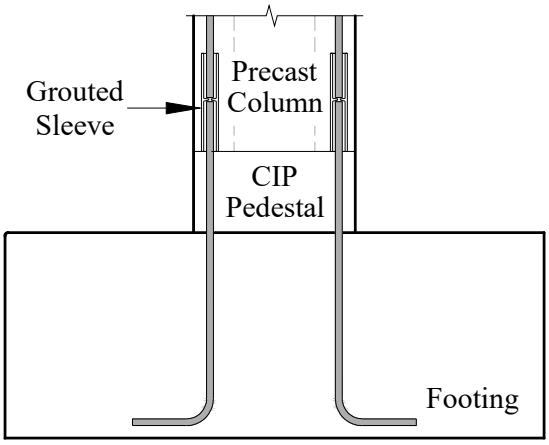

(d) Sleeves above Cast-in-Place Pedestal

Figure 9.2- Grouted Couple Connections

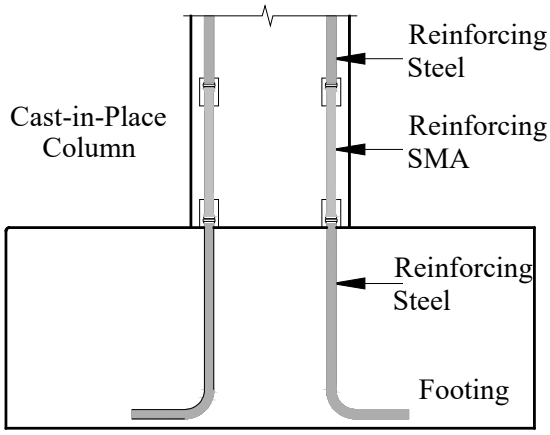

(a) Cast-in-Place SMA Column

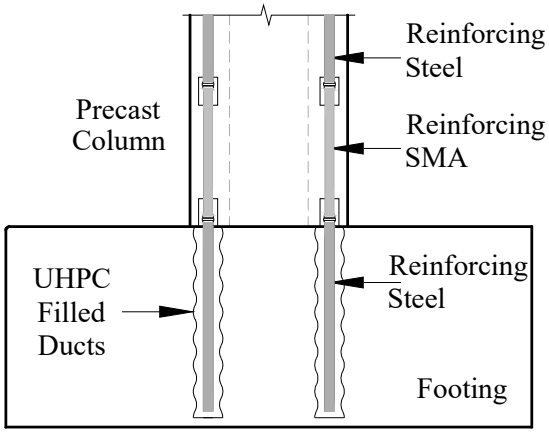

(b) Precast SMA Column

Figure 9.3- SMA-Reinforced Columns

Appendix A: PNC and CIP column Models Plastic Hinge Damage

(a) PNC

(b) CIP

Figure A.1- PNC and CIP Columns Plastic Hinge Damage after Full Cycles of 0.25% Drift

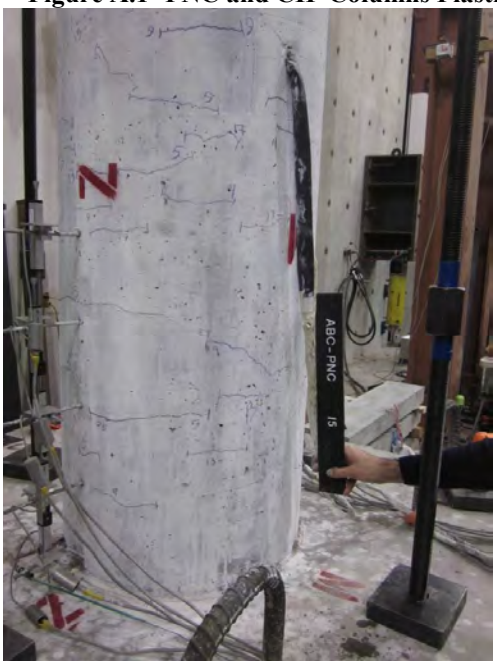

(a) PNC

(b) CIP

Figure A.2- PNC and CIP Columns Plastic Hinge Damage after Full Cycles of 0.5% Drift

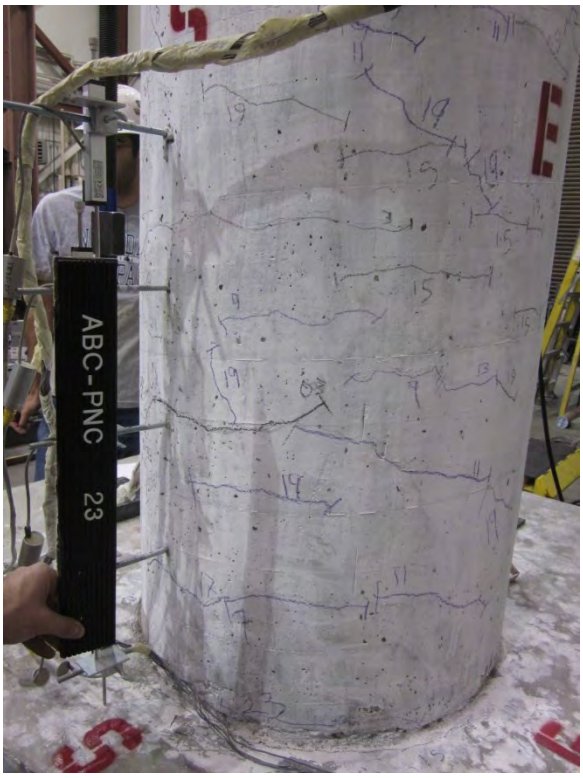

(a) PNC

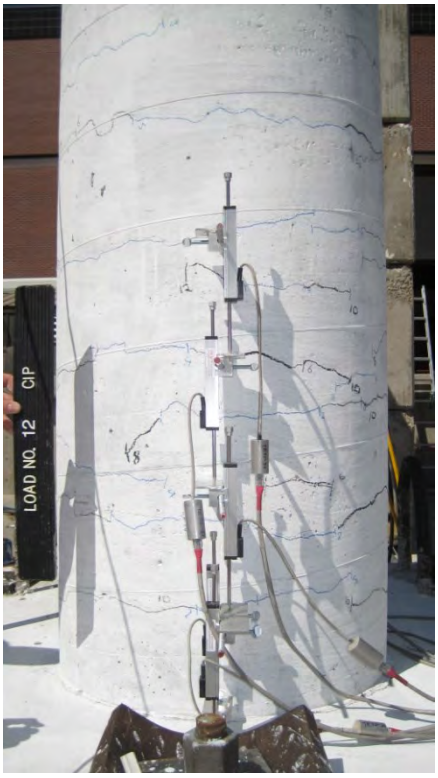

(b) CIP

Figure A.3- PNC and CIP Columns Plastic Hinge Damage after Full Cycles of 0.75% Drift

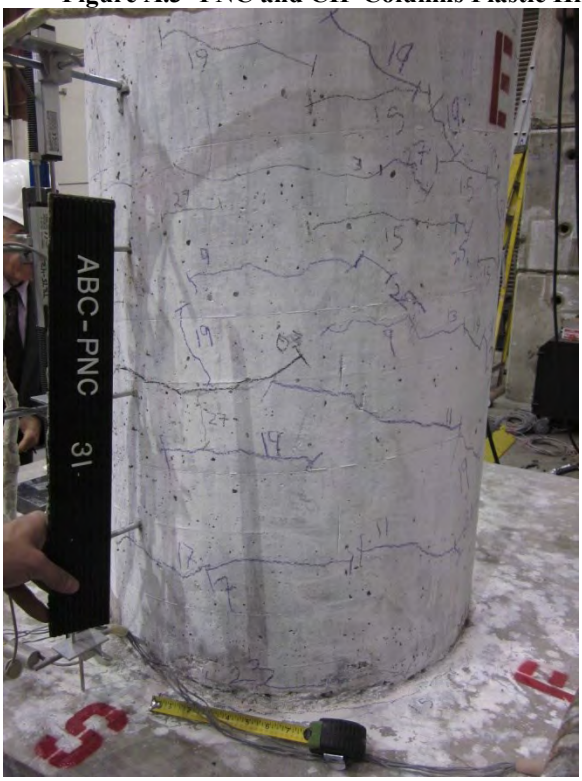

(a) PNC

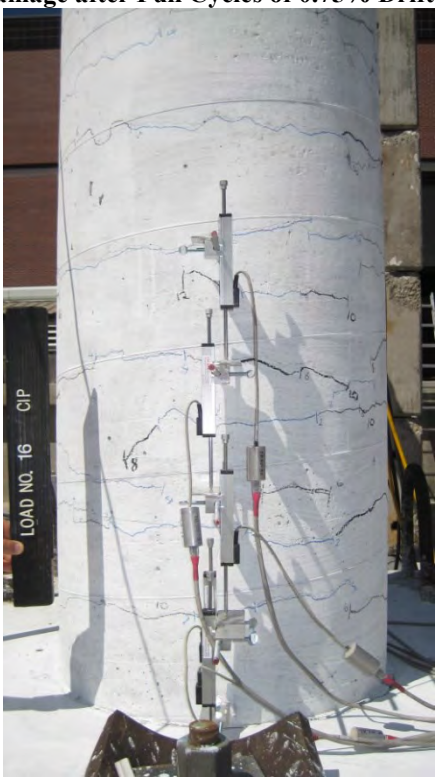

(b) CIP

Figure A.4- PNC and CIP Columns Plastic Hinge Damage after Full Cycles of 1.0% Drift

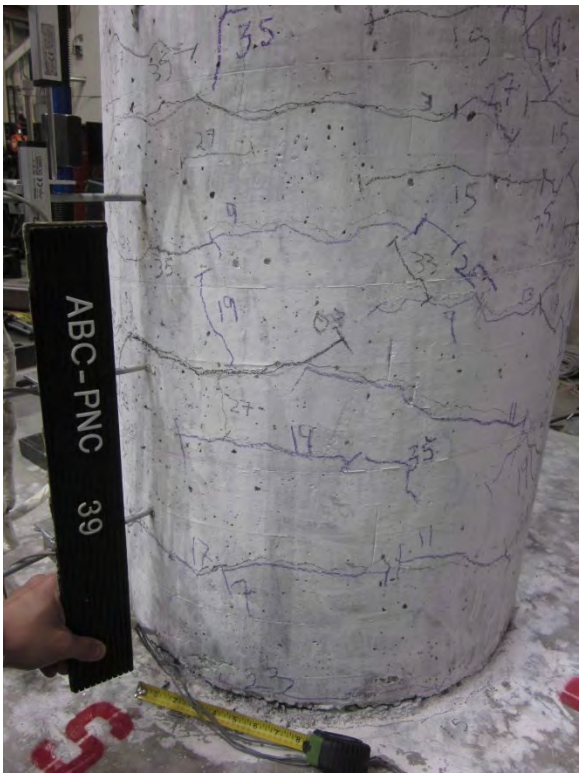

(a) PNC

(b) CIP

Figure A.5- PNC and CIP Columns Plastic Hinge Damage after Full Cycles of 2.0% Drift

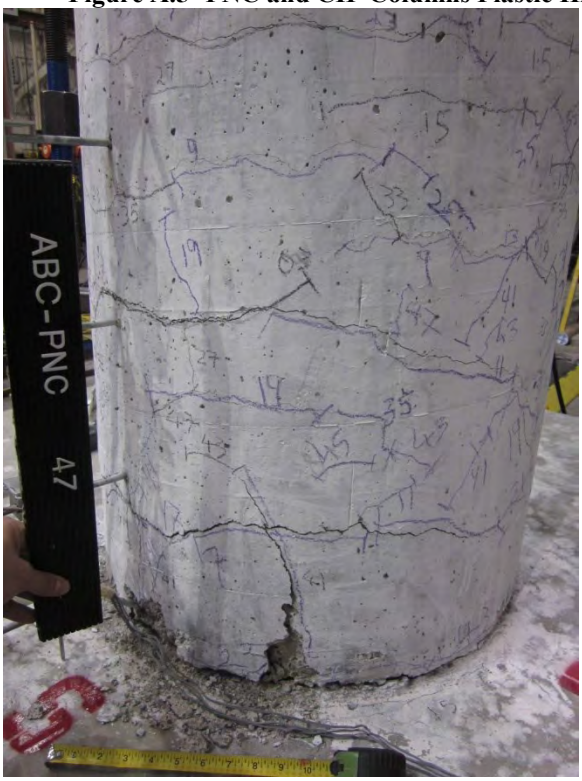

(a) PNC

(b) CIP

Figure A.6- PNC and CIP Columns Plastic Hinge Damage after Full Cycles of 3.0% Drift

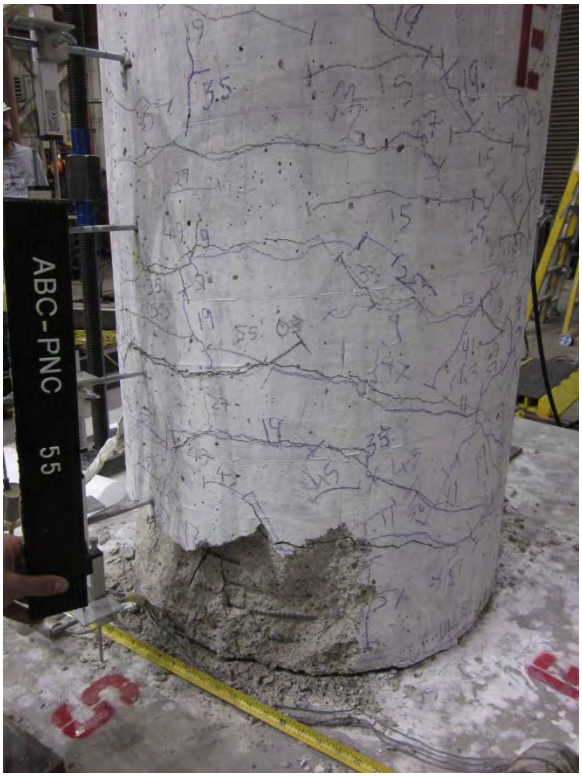

(a) PNC

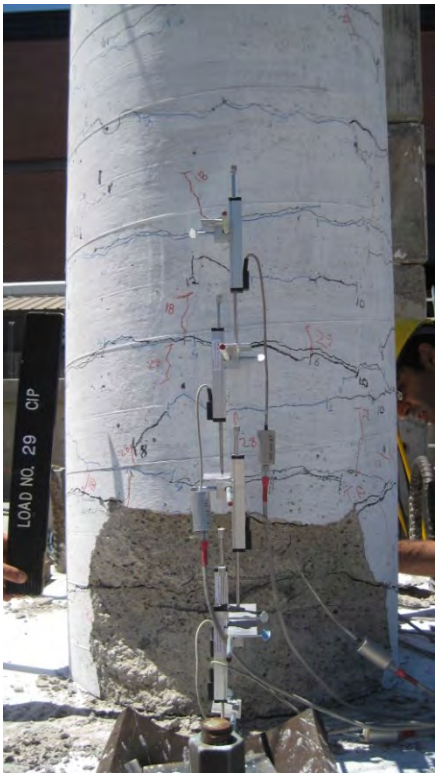

(b) CIP

Figure A.7- PNC and CIP Columns Plastic Hinge Damage after Full Cycles of 4.0% Drift

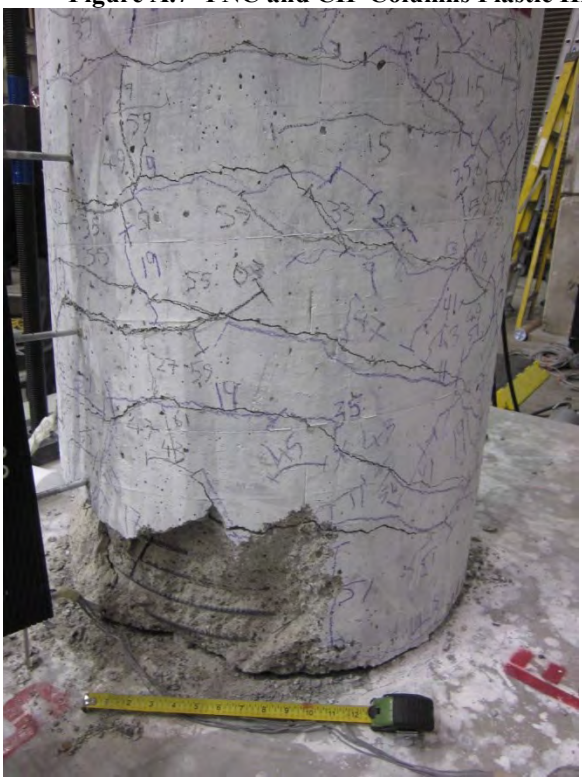

(a) PNC

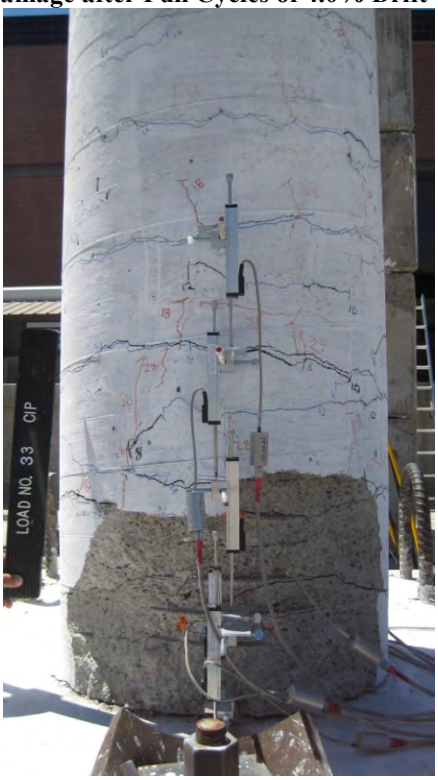

(b) CIP

Figure A.8- PNC and CIP Columns Plastic Hinge Damage after Full Cycles of 5.0% Drift

(a) PNC (b) CIP

Figure A.9- PNC and CIP Columns Plastic Hinge Damage after Full Cycles of 6.0% Drift

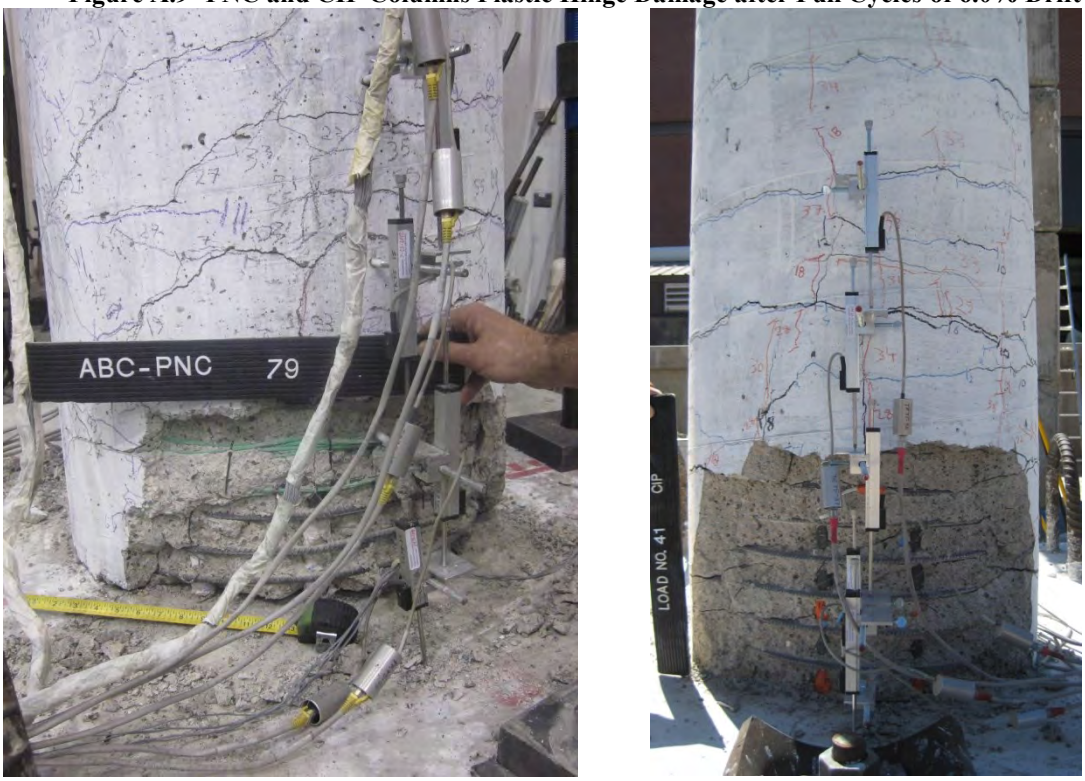

(a) PNC (b) CIP

Figure A.10- PNC and CIP Columns Plastic Hinge Damage after Full Cycles of 8.0% Drift

(a) PNC (b) CIP

Figure A.11- PNC and CIP Columns Plastic Hinge Damage after Full Cycles of 10.0% Drift

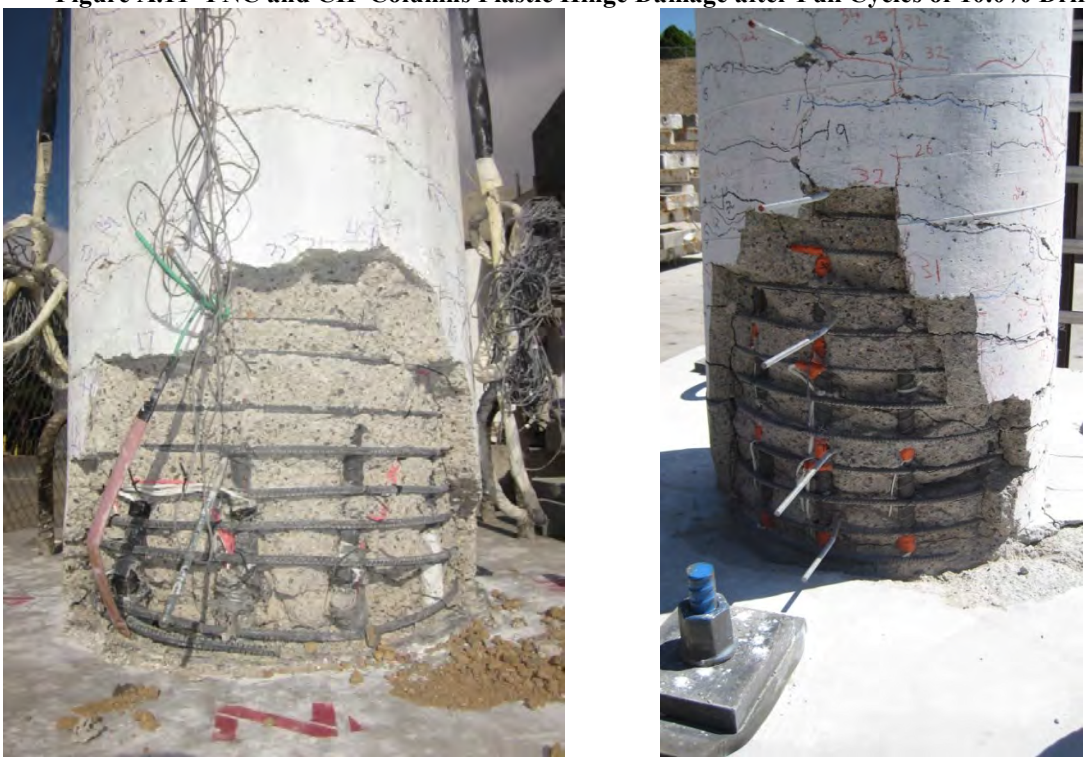

(a) PNC (b) CIP

Figure A.12- PNC and CIP Columns Plastic Hinge Damage after Testing

Appendix B: GCDP, GCDP, and CIP column Models Plastic Hinge Damage

(a) GCDP (b) GCPP (c) CIP

Figure B.1- GCDP, GCPP, and CIP Columns Plastic Hinge Damage after Full Cycles of 0.25% Drift

(a) GCDP (b) GCPP (c) CIP

Figure B.2- GCDP, GCPP, and CIP Columns Plastic Hinge Damage after Full Cycles of 0.5% Drift

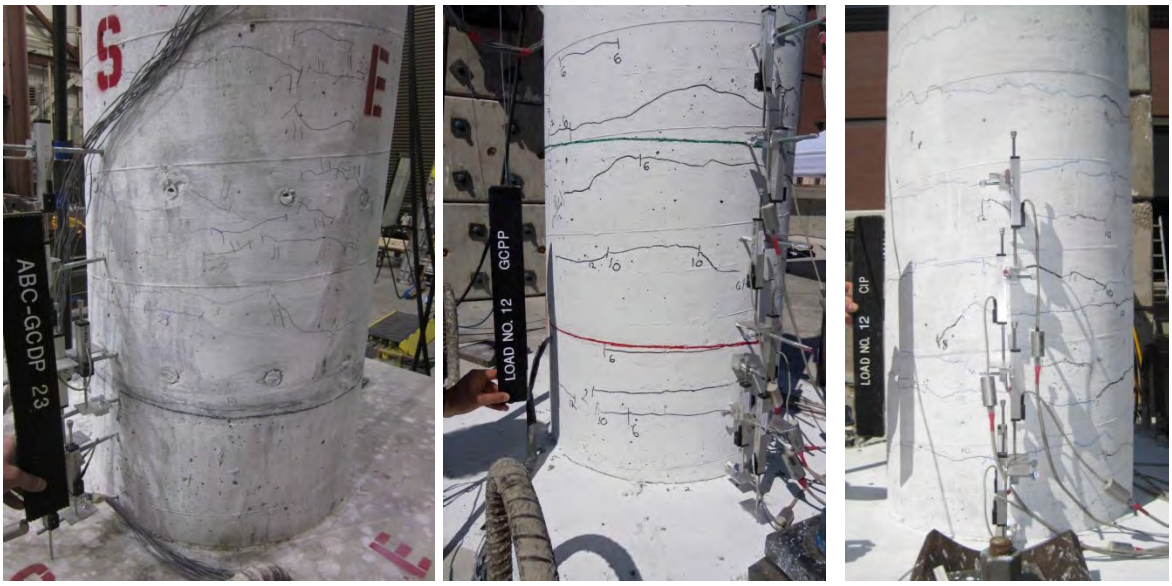

(a) GCDP (b) GCPP (c) CIP

Figure B.3- GCDP, GCPP, and CIP Columns Plastic Hinge Damage after Full Cycles of 0.75% Drift

(a) GCDP (b) GCPP (c) CIP

Figure B.4- GCDP, GCPP, and CIP Columns Plastic Hinge Damage after Full Cycles of 1.0% Drift

(a) GCDP (b) GCPP (c) CIP

Figure B.5- GCDP, GCPP, and CIP Columns Plastic Hinge Damage after Full Cycles of 2.0% Drift

(a) GCDP (b) GCPP (c) CIP

Figure B.6- GCDP, GCPP, and CIP Columns Plastic Hinge Damage after Full Cycles of 3.0% Drift

(a) GCDP (b) GCPP (c) CIP

Figure B.7 GCDP, GCPP, and CIP Columns Plastic Hinge Damage after Full Cycles of 4.0% Drift

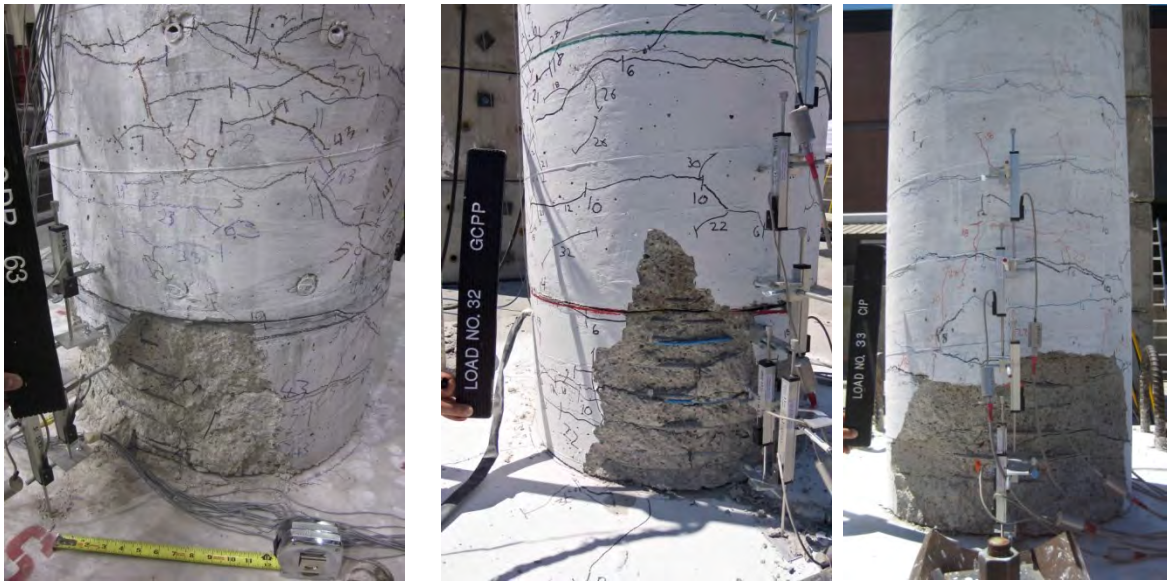

(a) GCDP (b) GCPP (c) CIP

Figure B.8- GCDP, GCPP, and CIP Columns Plastic Hinge Damage after Full Cycles of 5.0% Drift

(a) GCDP (b) GCPP (c) CIP

Figure B.9- GCDP, GCPP, and CIP Columns Plastic Hinge Damage after Full Cycles of 6.0% Drift

(a) GCDP (b) GCPP (c) CIP

Figure B.10- GCDP, GCPP, and CIP Columns Plastic Hinge Damage after Full Cycles of 8.0% Drift

(a) GCDP (b) GCPP (c) CIP

Figure B.11- GCDP, GCPP, and CIP Columns Plastic Hinge Damage after Full Cycles of 10.0% Drift

(a) GCDP (b) GCPP (c) CIP

Figure B.12- GCDP, GCPP, and CIP Columns Plastic Hinge Damage after Testing

Appendix C: HCS, HCNP, and CIP column Models Plastic Hinge Damage

(a) HCS

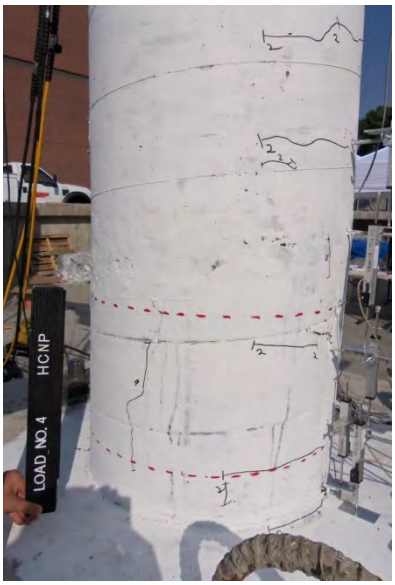

(b) HCNP

(c) CIP

Figure C.1- HCS, HCNP, and CIP Columns Plastic Hinge Damage after Full Cycles of 0.25% Drift

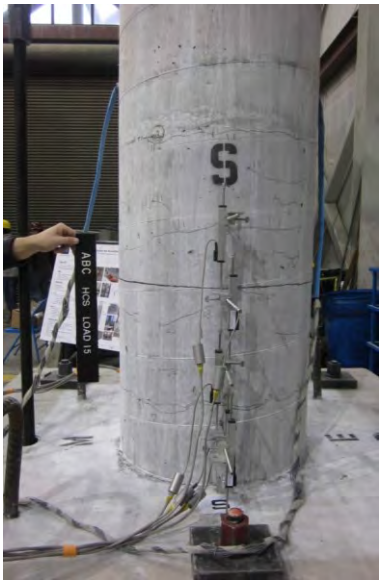

(a) HCS

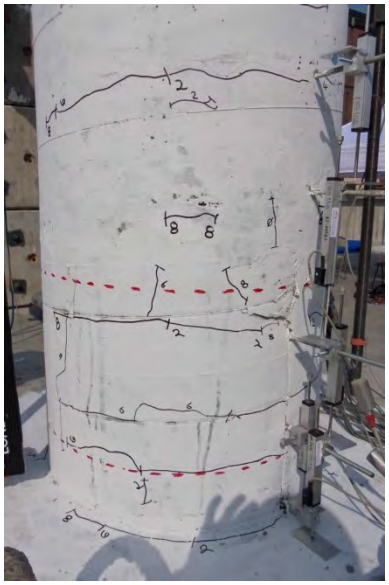

(b) HCNP

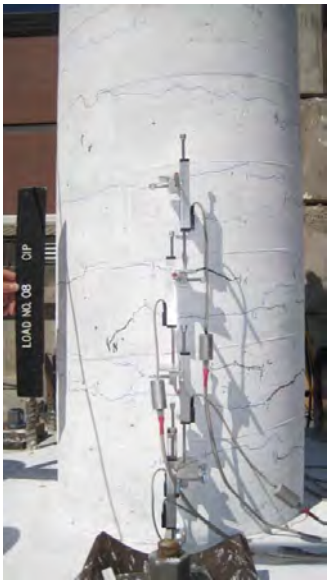

(c) CIP

Figure C.2- HCS, HCNP, and CIP Columns Plastic Hinge Damage after Full Cycles of 0.5% Drift

(a) HCS

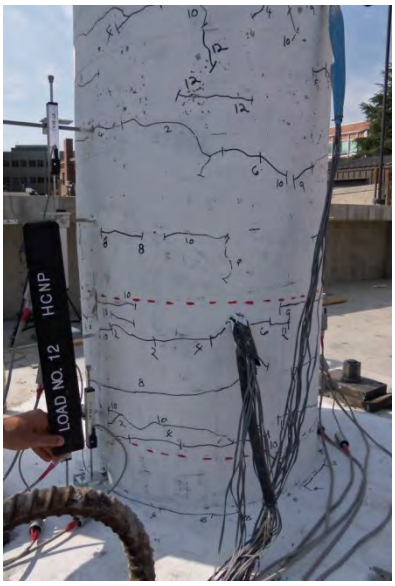

(b) HCNP

(c) CIP

Figure C.3- HCS, HCNP, and CIP Columns Plastic Hinge Damage after Full Cycles of 0.75% Drift

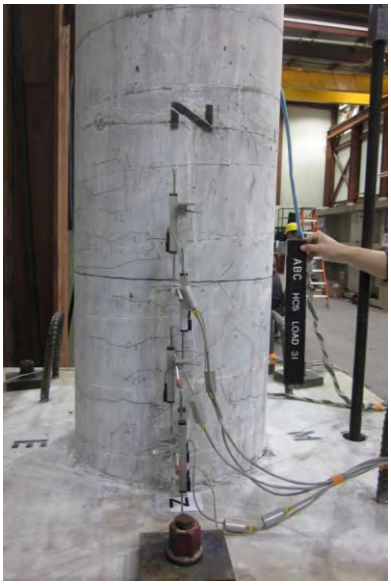

(a) HCS

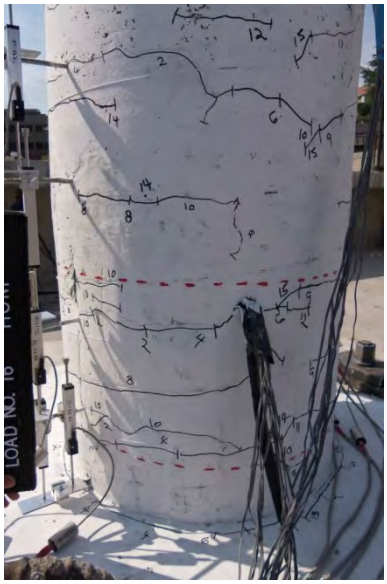

(b) HCNP

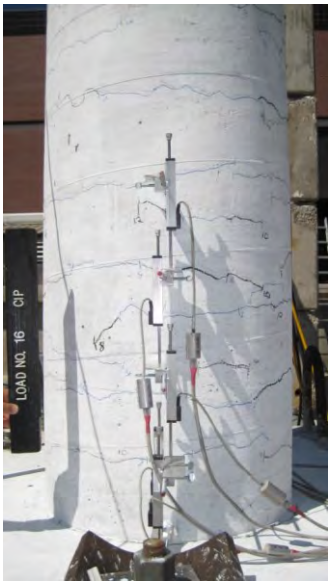

(c) CIP

Figure C.4- HCS, HCNP, and CIP Columns Plastic Hinge Damage after Full Cycles of 1.0% Drift

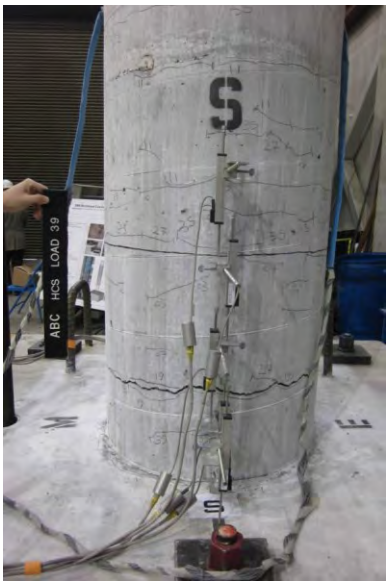

(a) HCS

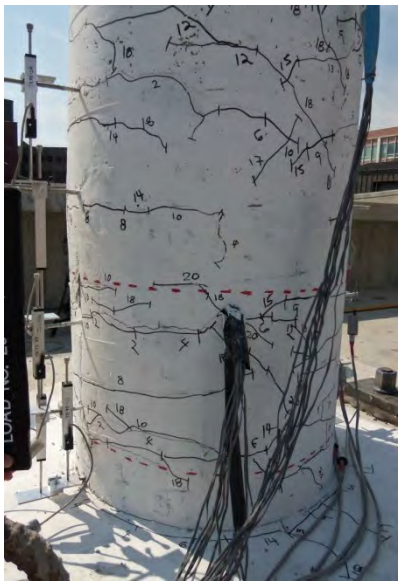

(b) HCNP

(c) CIP

Figure C.5- HCS, HCNP, and CIP Columns Plastic Hinge Damage after Full Cycles of 2.0% Drift

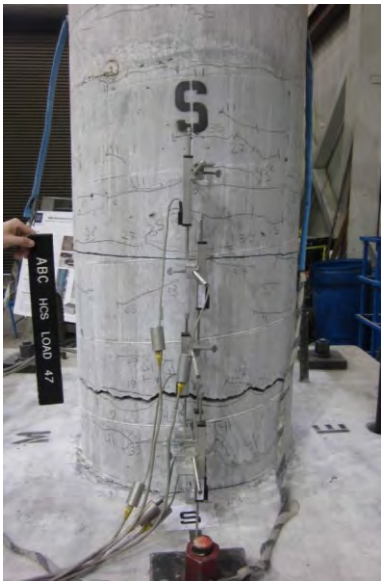

(a) HCS

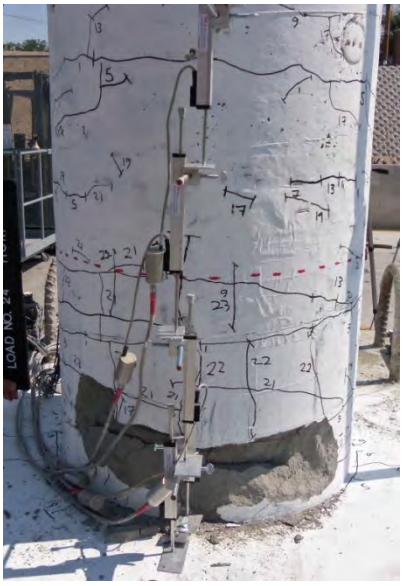

(b) HCNP

(c) CIP

Figure C.6- HCS, HCNP, and CIP Columns Plastic Hinge Damage after Full Cycles of 3.0% Drift

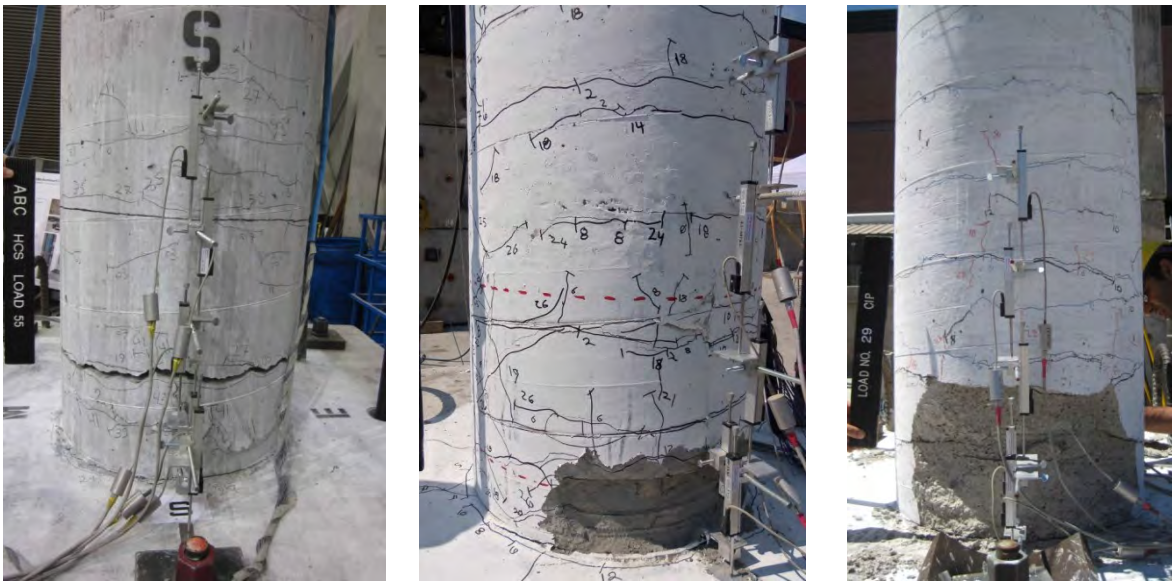

(a) HCS (b) HCNP (c) CIP

Figure C.7 HCS, HCNP, and CIP Columns Plastic Hinge Damage after Full Cycles of 4.0% Drift

(a) HCS (b) HCNP (c) CIP

Figure C.8- HCS, HCNP, and CIP Columns Plastic Hinge Damage after Full Cycles of 5.0% Drift

(a) HCS (b) HCNP (c) CIP

Figure C.9- HCS, HCNP, and CIP Columns Plastic Hinge Damage after Full Cycles of 6.0% Drift

(a) HCS (b) HCNP (c) CIP

Figure C.10- HCS, HCNP, and CIP Columns Plastic Hinge Damage after Full Cycles of 8.0% Drift

(a) HCS (b) HCNP (c) CIP

Figure C.11- HCS, HCNP, and CIP Columns Plastic Hinge Damage after Full Cycles of 10.0% Drift

(a) HCS (b) HCNP (c) CIP

Figure C.12- HCS, HCNP, and CIP Columns Plastic Hinge Damage after Testing

Appendix D: Design Recommendations for Next Generation ABC Bridge Columns

1. Design Recommendations for UHPC-Field Duct Columns Connections

UHPC-filled duct connections are categorized as grouted duct connections (Fig. 1) in which column longitudinal bars are anchored in corrugated ducts placed in adjoining members such as footings and cap beams. UHPC may be incorporated as duct filler instead of normal-strength grout to reduce the embedment length in shallow members. Design recommendations and commentary are presented in this section for these column types.

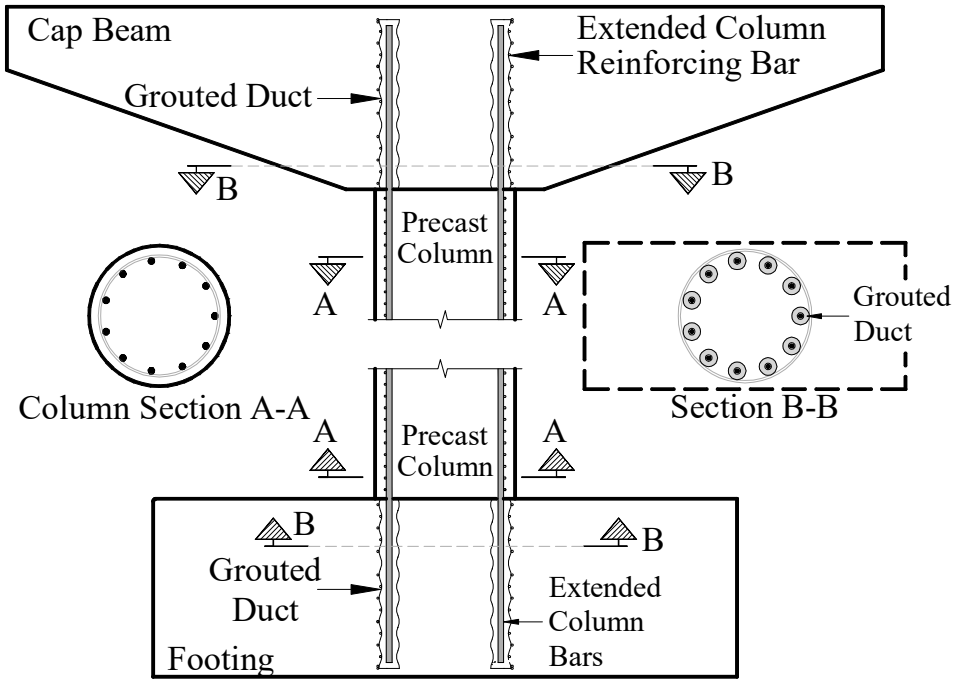

Figure 1- Grouted Duct Connections

Recommendations	Commentary
1.1- UHPC-filled duct columns and adjoining members such as footings and cap beams shall be designed in accordance to a legally adopted bridge code.	**C1.1-** Bridge components are designed according to the AASHTO LRFD (2013) regardless of using UHPC-filled duct connections since these types of connections are emulative of conventional connections.
1.2- Three-day and 28-day compressive strength of UHPC shall not be less than 10000 *psi* (70 *MPa*) and 20000 *psi* (140 *MPa*), respectively.	**C1.2-** ACI Committee 239 (2012) defined UHPC as: "*Concrete that has a minimum specified compressive strength of 150 MPa (22,000 psi) with specified durability, tensile ductility and toughness requirements; fibers are generally included to achieve specified requirements*". Lower strength is allowed in UHPC-filled duct connections because the confining effects of ducts increase the compressive strength beyond the specified strength.
1.3- Only corrugated galvanized strip metal ducts conforming to ASTM A653 shall be used.	**C1.3-** Ducts with other materials such as plastics are not allowed either due to a lack of data, or in the case of plastics, ducts result in lower bond strength.
1.4- Duct diameter (d_d) shall not be less than three column longitudinal bar diameter ($3d_b$).	**C1.4-** Duct diameter shall be sufficiently larger than the anchoring bar diameter for ease of construction and ensuring high bond strength in UHPC-filled duct connections. For bundled bars, this limit shall be based on the equivalent bar diameter resulting in the same total cross section of the bundled bars. The duct diameter minimum limit may be reduced for bundled bars by 10% to avoid large size ducts.
1.5- Duct wall thickness shall not be less than 0.018 *in*. (0.46 *mm*).	**C1.5-** Duct wall thickness affects confinement thus bond strength. Due to a lack of test data, thinner ducts than that specified shall not be used.
1.6- Development length (L_d) of column bars anchored in adjoining members shall be greater than the maximum of Eq. (1)	**C1.6-** Column bars shall be extended to extreme layer of adjoining member reinforcements on the far side to form

Recommendations

and Eq. (2). However, this length shall not be greater than the adjoining member depth less the required cover concrete for those members.

$$L_{d,duct9}=9\frac{d_b}{27d_d\cdot\sqrt{9'_{c9}}} \quad (1)$$

$$L_{d,bar9}=9\frac{d_b}{120\sqrt{9'_{UHPC9}}} \quad (2)$$

1.7- A length of four column longitudinal bar diameter ($4d_b$) above and below the column-footing interface shall be debonded with an appropriate debonding method.

1.8- Duct shall be at least 1 *in*. (25 *mm*) longer than the bar development length. The bottom end of ducts shall be covered.

1.9- Transverse reinforcements similar to column transverse reinforcements shall be provided for duct cage installed in adjoining members.

Commentary

strut-and-tie mechanism to fully transfer the column ultimate loads to those members.

in SI units:

$$L_{d,duct9}=9\frac{d_b}{2.24d_d\cdot\sqrt{9'_{c9}}} \quad (1\text{-SI})$$

$$L_{d,bar9}=9\frac{d_b}{.96\sqrt{9'_{UHPC9}}} \quad (2\text{-SI})$$

C1.7- A deformed bar may be debonded from concrete or UHPC using two layers of duct tape wrapped around the bar. The debonded length in ducts need not be considered in development length of bars in UHPC-filled duct connections (Article 1.6).

C1.8- Galvanized duct caps may be used to cover ducts.

C1.9- Slight increase in cross-sectional dimension of confined concrete is expected.

2. Design Recommendations for Mechanical Grouted Sleeve Bar Splice Columns

Column longitudinal bars and footing dowels are anchored in sleeves then sleeves are filled with a high-strength grout in mechanical grouted bar coupler connections. Location of couplers (Fig. 2) could affect seismic performance of columns due to size of sleeves. Design recommendations and commentary are presented in this section for these column types.

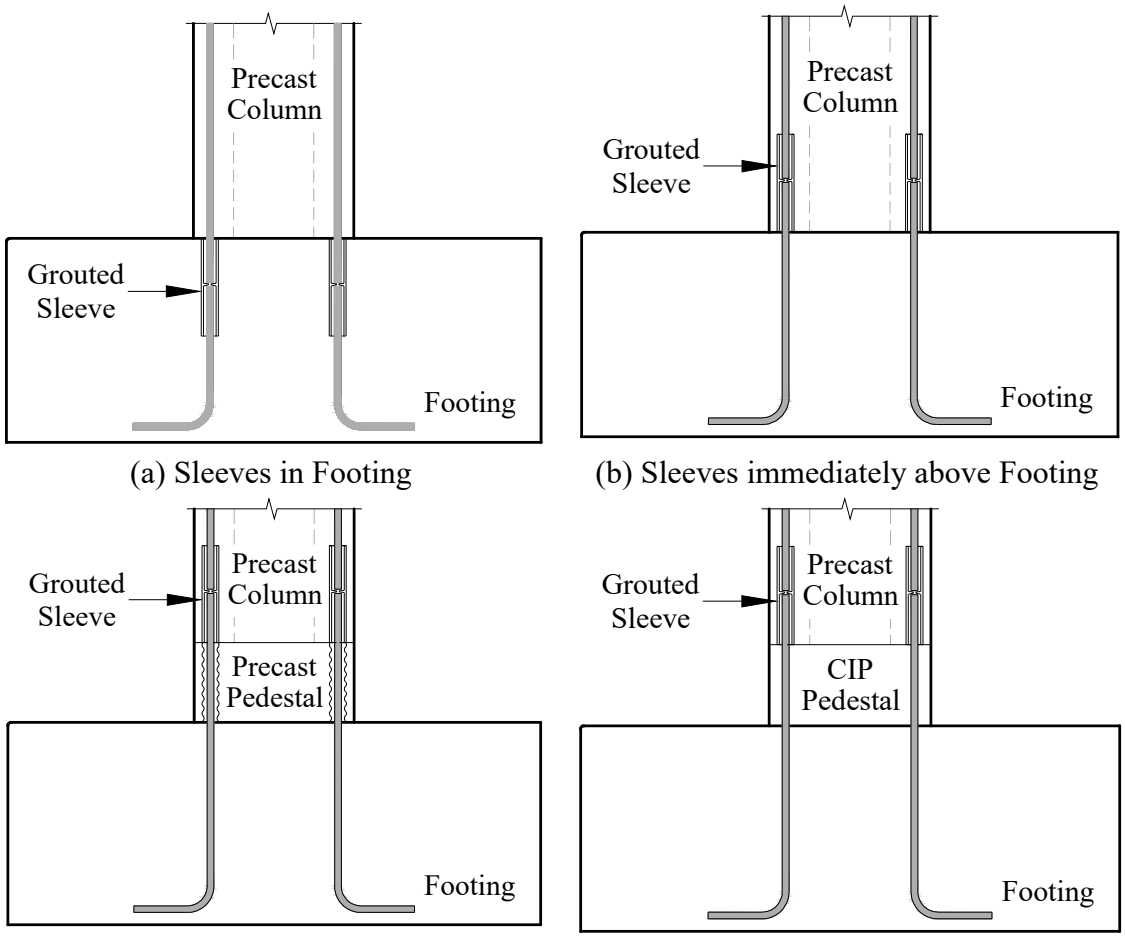

Figure 2- Grouted Couple Connections

Recommendations	Commentary
2.1- Grouted coupler columns and adjoining members such as footings and cap beams shall be designed in accordance to a legally adopted bridge code.	**C2.1-** Bridge components are designed according to the AASHTO LRFD (2013) regardless of using grouted duct coupler connections since these types of connections are emulative of conventional connections.
2.2- Bridge columns shall be constructed in two segments: (1) a cast-in-place pedestal and (2) precast portion.	**C2.2-** Tests have shown improved seismic performance for columns with cast-in-place pedestal over columns with precast pedestal (Tazarv et al, 2013). Thus, only the column configuration shown in Fig. 2d is recommended in high seismic regions.
2.3- Height of pedestal shall not be less than half column diameter (0.5D).	
2.4- Column longitudinal bars shall be debonded from concrete in pedestal area.	**C2.4-** A deformed bar may be debonded from concrete using two layers of duct tape wrapped around the bar.
2.5- Minimum cover concrete requirement of the governing code shall be provided for transverse reinforcement over the sleeves.	
2.6- Transverse reinforcements similar to column transverse reinforcements shall be provided for pedestal and sections with sleeves.	**C2.6-** Slight increase in cross-sectional dimension of confined concrete is expected.

3. Design Recommendations for SMA-Reinforced ECC Columns

Low-damage materials such as engineered cementitious composite (ECC) and shape memory alloy (SMA) may be incorporated in conventional or accelerated bridge construction (Fig. 3). These materials are usually used in plastic hinge of columns to improve the seismic performance over conventional columns. Design recommendations and commentary are presented.

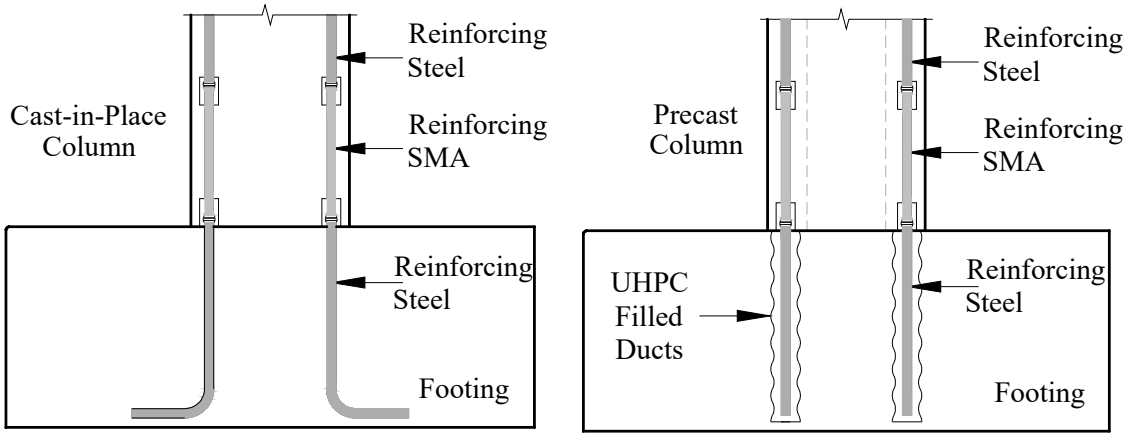

(a) Cast-in-Place SMA Column (b) Precast SMA Column

Figure 3- SMA-Reinforced Columns

Recommendations

3.1- SMA-reinforced columns and connecting members such as footings and cap beams shall be designed in accordance to a legally adopted bridge code.

3.2- Nonlinear material model and mechanical properties and for superelastic NiTi reinforcing SMA shall conform to Fig. 4 and Tables 1 & 2. A symmetric stress-strain material model based on the expected tensile properties shall be permitted for design of SMA-reinforced columns.

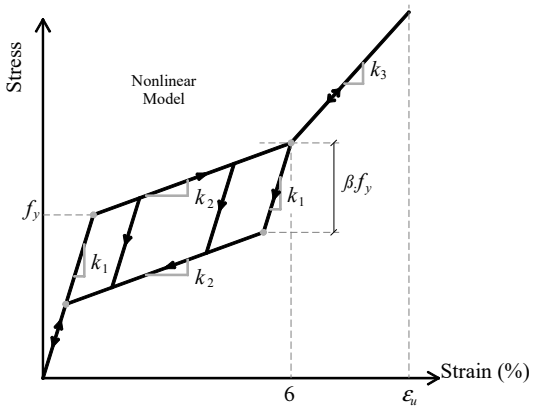

Figure 4- Nonlinear Model for SE SMA

Table 1- Minimum and Expected Tensile NiTi SE SMA Mechanical Properties

Parameter	Minimum*	Expected**
Austenite modulus, k_1	4500 *ksi* (31025 *MPa*)	5500 *ksi* (37900 *MPa*)
Post yield stiffness, k_2	--	250 *ksi* (1725 *MPa*)
Austenite yield strength, f_y	45 *ksi* (310 *MPa*)	55 *ksi* (380 *MPa*)
Lower plateau stress factor, β	0.45	0.65
Recoverable superelastic strain, ε_r	6%	6%
Secondary post-yield stiffness ratio, α	--	0.3
Ultimate strain, ε_u	10%	10%

* To be used in material production
** To be used in seismic design of SMA-reinforced concrete members

Commentary

C3.1- Bridge components are designed according to the AASHTO LRFD (2013).

C3.2- Analytical investigations have shown that a symmetric SMA material model based on the expected tensile properties may be used in lieu of asymmetric model for design of SMA-reinforced bridge columns (Tazarv and Saiidi, 201X).

Reinforcing NiTi SMA bars with lower mechanical properties than the minimum specified in Table 1 shall not be permitted in design and construction.

Recommendations

Commentary

Table 2- Expected Compressive NiTi SE SMA Mechanical Properties

Parameter	Expected
Austenite modulus, k_1	8900 *ksi* (61365 *MPa*)
Post yield stiffness, k_2	1400 *ksi* (9650 *MPa*)
Austenite yield strength, f_y	70 *ksi* (480 *MPa*)
Lower plateau stress factor, β	0.65
Recoverable superelastic strain, ε_r	3%
Secondary post-yield stiffness ratio, α	0.45
Ultimate strain, ε_u	10%

3.3- Incorporation of low-damage materials, SMA and ECC, only over partial length of columns shall be permitted. Length of ECC portion of columns shall not be less than 1.5 column largest cross sectional dimension (1.5D). Length of SMA bars shall not be less than L_p and 75% of column largest cross sectional dimension (0.75D):

$$L_{p9} = 0.08L + 0.15 f_{ye} d_{b9} \geq 0.3 f_{ye} d_{b9} (in, ksi) \quad (9)$$

C3.3- Low-damage materials may be used only in plastic hinge zones to reduce costs.

L_p in SI units:

$$L_{p9} = 0.08L + 0.022 f_{ye} d_{b9} \geq 0.044 f_{ye} d_b \ (mm, MPa) \quad (9)$$

3.4- Reinforcing SMA bars shall be connected to reinforcing steel bars using approved mechanical bar splices. Splicing shall be permitted in critical locations of ductile elements.

C3.4- Couplers shall resist ultimate capacities of SMA and steel bars. Headed reinforcement couplers or threaded couplers may be used.

Current bridge design specifications prohibit bar splicing in plastic hinge zones of columns in high seismic zones. Tests have shown that the seismic performance of columns with headed and threaded couplers incorporated in plastic hinge zones is essentially the same as that of conventional columns (Haber et al., 2014; Saiidi and Wang, 2006; Saiidi, et al., 2009).

Recommendations	Commentary
3.5- Conventional and accelerated construction shall be permitted for SMA-reinforced columns. UHPC-filled duct connections conforming to section 1 shall be permitted for accelerated construction.	**C3.5-** When using UHPC-filled duct connections, SMA bars above the column-footing interface need not be debonded since SMA bars are plain with low bond strength.

4. Notations

d_b: Nominal diameter of longitudinal reinforcing steel bar (*in, mm*)
d_d: Inner diameter of duct (*in, mm*)
D: Column largest cross sectional dimension (*in, mm*)
f_s: Bar stress (*psi, MPa*); 1.5f_y or f_u whichever is greater
f'_c: Compressive strength of concrete surrounding the duct (*psi, MPa*)
f'_{UHPC}: Compressive strength of UHPC in the duct (*psi, MPa*)
f_{ye}: Expected yield stress for longitudinal reinforcing steel bar (*ksi, MPa*)
L: Member length from the point of maximum moment to the point of contra-flexure (*in, mm*)
L_d: Development length for un-hooked deformed bar in UHPC-filled duct connection (*in, mm*)
L_p: Equivalent analytical plastic hinge length (*in, mm*)
$L_{d,duct}$: Bar development length based on duct bond strength (*in, mm*)
$L_{d,bar}$: Bar development length based on bar bond strength (*in, mm*)

5. References

AASHTO. (2013). "AASHTO LRFD Bridge Design Specification," Washington, DC: American Association of State Highway and Transportation Officials.

ACI Committee 239. (2012). "Ultra-High Performance Concrete," ACI Fall Convention, Toronto, Ontario, Canada.

ASTM A653/A653M-11. (2011). "Standard Specification for Steel Sheet, Zinc-Coated (Galvanized) or Zinc-Iron Alloy-Coated (Galvannealed) by the Hot-Dip Process," West Conshohocken, PA, 14 pp.

Brenes, F.J., Wood, S.L. and Kreger, M.E. (2006). "Anchorage Requirements for Grouted Vertical-Duct Connectors in Precast Bent Cap Systems," *FHWA/TX-06/0-4176-1*, Center for Transportation Research, University of Texas at Austin.

Haber, Z.B., Saiidi, M.S. and Sanders, D.H. (2014). "Seismic Performance of Precast Columns with Mechanically Spliced Column-footing Connections," *ACI Structural Journal*, Vol. 111, No. 3, pp. 639-650.

Saiidi, M.S. and Wang H. (2006). "Exploratory Study of Seismic Response of Concrete Columns with Shape Memory Alloys Reinforcement," *ACI Structural Journal*, Vol. 103, No. 3, 436-443.

Saiidi, M.S., O'Brien, M. and Sadrossadat-Zadeh, M. (2009). "Cyclic Response of Concrete Bridge Columns Using Superelastic Nitinol and Bendable Concrete," *ACI Structural Journal*, Vol. 106, No. 1, pp. 69-77.

Tazarv, M., Haber, Z.B., and Saiidi, M.S. (2013). "Precast Column Connections for Accelerated Bridge Construction in High Seismic Regions," *Proceedings of 2013 PCI Convention and National Bridge Conference*, Grapevine, USA, Paper No. 58, 12 pp.

Tazarv, M. and Saiidi, M.S. (201X). "Reinforcing NiTi Superelastic SMA for Concrete Structures," Submitted to *Journal of Structural Engineering, ASCE*.

List of CCEER Publications

Report No.	Publication
CCEER-84-1	Saiidi, M., and R. Lawver, "User's Manual for LZAK-C64, A Computer Program to Implement the Q-Model on Commodore 64," Civil Engineering Department, Report No. CCEER-84-1, University of Nevada, Reno, January 1984.
CCEER-84-1 Reprint	Douglas, B., Norris, G., Saiidi, M., Dodd, L., Richardson, J. and Reid, W., "Simple Bridge Models for Earthquakes and Test Data," Civil Engineering Department, Report No. CCEER-84-1 Reprint, University of Nevada, Reno, January 1984.
CCEER-84-2	Douglas, B. and T. Iwasaki, "Proceedings of the First USA-Japan Bridge Engineering Workshop," held at the Public Works Research Institute, Tsukuba, Japan, Civil Engineering Department, Report No. CCEER-84-2, University of Nevada, Reno, April 1984.
CCEER-84-3	Saiidi, M., J. Hart, and B. Douglas, "Inelastic Static and Dynamic Analysis of Short R/C Bridges Subjected to Lateral Loads," Civil Engineering Department, Report No. CCEER-84-3, University of Nevada, Reno, July 1984.
CCEER-84-4	Douglas, B., "A Proposed Plan for a National Bridge Engineering Laboratory," Civil Engineering Department, Report No. CCEER-84-4, University of Nevada, Reno, December 1984.
CCEER-85-1	Norris, G. and P. Abdollaholiaee, "Laterally Loaded Pile Response: Studies with the Strain Wedge Model," Civil Engineering Department, Report No. CCEER-85-1, University of Nevada, Reno, April 1985.
CCEER-86-1	Ghusn, G. and M. Saiidi, "A Simple Hysteretic Element for Biaxial Bending of R/C in NEABS-86," Civil Engineering Department, Report No. CCEER-86-1, University of Nevada, Reno, July 1986.
CCEER-86-2	Saiidi, M., R. Lawver, and J. Hart, "User's Manual of ISADAB and SIBA, Computer Programs for Nonlinear Transverse Analysis of Highway Bridges Subjected to Static and Dynamic Lateral Loads," Civil Engineering Department, Report No. CCEER-86-2, University of Nevada, Reno, September 1986.
CCEER-87-1	Siddharthan, R., "Dynamic Effective Stress Response of Surface and Embedded Footings in Sand," Civil Engineering Department, Report No. CCEER-86-2, University of Nevada, Reno, June 1987.
CCEER-87-2	Norris, G. and R. Sack, "Lateral and Rotational Stiffness of Pile Groups for Seismic Analysis of Highway Bridges," Civil Engineering Department, Report No. CCEER-87-2, University of Nevada, Reno, June 1987.
CCEER-88-1	Orie, J. and M. Saiidi, "A Preliminary Study of One-Way Reinforced Concrete Pier Hinges Subjected to Shear and Flexure," Civil Engineering Department, Report No. CCEER-88-1, University of Nevada, Reno, January 1988.
CCEER-88-2	Orie, D., M. Saiidi, and B. Douglas, "A Micro-CAD System for Seismic Design of Regular Highway Bridges," Civil Engineering Department, Report No. CCEER-88-2, University of Nevada, Reno, June 1988.

CCEER-88-3 Orie, D. and M. Saiidi, "User's Manual for Micro-SARB, a Microcomputer Program for Seismic Analysis of Regular Highway Bridges," Civil Engineering Department, Report No. CCEER-88-3, University of Nevada, Reno, October 1988.

CCEER-89-1 Douglas, B., M. Saiidi, R. Hayes, and G. Holcomb, "A Comprehensive Study of the Loads and Pressures Exerted on Wall Forms by the Placement of Concrete," Civil Engineering Department, Report No. CCEER-89-1, University of Nevada, Reno, February 1989.

CCEER-89-2 Richardson, J. and B. Douglas, "Dynamic Response Analysis of the Dominion Road Bridge Test Data," Civil Engineering Department, Report No. CCEER-89-2, University of Nevada, Reno, March 1989.

CCEER-89-2 Vrontinos, S., M. Saiidi, and B. Douglas, "A Simple Model to Predict the Ultimate Response of R/C Beams with Concrete Overlays," Civil Engineering Department, Report NO. CCEER-89-2, University of Nevada, Reno, June 1989.

CCEER-89-3 Ebrahimpour, A. and P. Jagadish, "Statistical Modeling of Bridge Traffic Loads - A Case Study," Civil Engineering Department, Report No. CCEER-89-3, University of Nevada, Reno, December 1989.

CCEER-89-4 Shields, J. and M. Saiidi, "Direct Field Measurement of Prestress Losses in Box Girder Bridges," Civil Engineering Department, Report No. CCEER-89-4, University of Nevada, Reno, December 1989.

CCEER-90-1 Saiidi, M., E. Maragakis, G. Ghusn, Y. Jiang, and D. Schwartz, "Survey and Evaluation of Nevada's Transportation Infrastructure, Task 7.2 - Highway Bridges, Final Report," Civil Engineering Department, Report No. CCEER 90-1, University of Nevada, Reno, October 1990.

CCEER-90-2 Abdel-Ghaffar, S., E. Maragakis, and M. Saiidi, "Analysis of the Response of Reinforced Concrete Structures During the Whittier Earthquake 1987," Civil Engineering Department, Report No. CCEER 90-2, University of Nevada, Reno, October 1990.

CCEER-91-1 Saiidi, M., E. Hwang, E. Maragakis, and B. Douglas, "Dynamic Testing and the Analysis of the Flamingo Road Interchange," Civil Engineering Department, Report No. CCEER-91-1, University of Nevada, Reno, February 1991.

CCEER-91-2 Norris, G., R. Siddharthan, Z. Zafir, S. Abdel-Ghaffar, and P. Gowda, "Soil-Foundation-Structure Behavior at the Oakland Outer Harbor Wharf," Civil Engineering Department, Report No. CCEER-91-2, University of Nevada, Reno, July 1991.

CCEER-91-3 Norris, G., "Seismic Lateral and Rotational Pile Foundation Stiffnesses at Cypress," Civil Engineering Department, Report No. CCEER-91-3, University of Nevada, Reno, August 1991.

CCEER-91-4 O'Connor, D. and M. Saiidi, "A Study of Protective Overlays for Highway Bridge Decks in Nevada, with Emphasis on Polyester-Styrene Polymer Concrete," Civil Engineering Department, Report No. CCEER-91-4, University of Nevada, Reno, October 1991.

CCEER-91-5 O'Connor, D.N. and M. Saiidi, "Laboratory Studies of Polyester-Styrene Polymer Concrete Engineering Properties," Civil Engineering Department, Report No. CCEER-91-5, University of Nevada, Reno, November 1991.

CCEER-92-1 Straw, D.L. and M. Saiidi, "Scale Model Testing of One-Way Reinforced Concrete Pier Hinges Subject to Combined Axial Force, Shear and Flexure," edited by D.N. O'Connor, Civil Engineering Department, Report No. CCEER-92-1, University of Nevada, Reno, March 1992.

CCEER-92-2 Wehbe, N., M. Saiidi, and F. Gordaninejad, "Basic Behavior of Composite Sections Made of Concrete Slabs and Graphite Epoxy Beams," Civil Engineering Department, Report No. CCEER-92-2, University of Nevada, Reno, August 1992.

CCEER-92-3 Saiidi, M. and E. Hutchens, "A Study of Prestress Changes in A Post-Tensioned Bridge During the First 30 Months," Civil Engineering Department, Report No. CCEER-92-3, University of Nevada, Reno, April 1992.

CCEER-92-4 Saiidi, M., B. Douglas, S. Feng, E. Hwang, and E. Maragakis, "Effects of Axial Force on Frequency of Prestressed Concrete Bridges," Civil Engineering Department, Report No. CCEER-92-4, University of Nevada, Reno, August 1992.

CCEER-92-5 Siddharthan, R., and Z. Zafir, "Response of Layered Deposits to Traveling Surface Pressure Waves," Civil Engineering Department, Report No. CCEER-92-5, University of Nevada, Reno, September 1992.

CCEER-92-6 Norris, G., and Z. Zafir, "Liquefaction and Residual Strength of Loose Sands from Drained Triaxial Tests," Civil Engineering Department, Report No. CCEER-92-6, University of Nevada, Reno, September 1992.

CCEER-92-6-A Norris, G., Siddharthan, R., Zafir, Z. and Madhu, R. "Liquefaction and Residual Strength of Sands from Drained Triaxial Tests," Civil Engineering Department, Report No. CCEER-92-6-A, University of Nevada, Reno, September 1992.

CCEER-92-7 Douglas, B., "Some Thoughts Regarding the Improvement of the University of Nevada, Reno's National Academic Standing," Civil Engineering Department, Report No. CCEER-92-7, University of Nevada, Reno, September 1992.

CCEER-92-8 Saiidi, M., E. Maragakis, and S. Feng, "An Evaluation of the Current Caltrans Seismic Restrainer Design Method," Civil Engineering Department, Report No. CCEER-92-8, University of Nevada, Reno, October 1992.

CCEER-92-9 O'Connor, D., M. Saiidi, and E. Maragakis, "Effect of Hinge Restrainers on the Response of the Madrone Drive Undercrossing During the Loma Prieta Earthquake," Civil Engineering Department, Report No. CCEER-92-9, University of Nevada, Reno, February 1993.

CCEER-92-10 O'Connor, D., and M. Saiidi, "Laboratory Studies of Polyester Concrete: Compressive Strength at Elevated Temperatures and Following Temperature Cycling, Bond Strength to Portland Cement Concrete, and Modulus of Elasticity," Civil Engineering Department, Report No. CCEER-92-10, University of Nevada, Reno, February 1993.

CCEER-92-11 Wehbe, N., M. Saiidi, and D. O'Connor, "Economic Impact of Passage of Spent Fuel Traffic on Two Bridges in Northeast Nevada," Civil Engineering Department, Report No. CCEER-92-11, University of Nevada, Reno, December 1992.

CCEER-93-1 Jiang, Y., and M. Saiidi, "Behavior, Design, and Retrofit of Reinforced Concrete One-way Bridge Column Hinges," edited by D. O'Connor, Civil Engineering Department, Report No. CCEER-93-1, University of Nevada, Reno, March 1993.

CCEER-93-2 Abdel-Ghaffar, S., E. Maragakis, and M. Saiidi, "Evaluation of the Response of the Aptos Creek Bridge During the 1989 Loma Prieta Earthquake," Civil Engineering Department, Report No. CCEER-93-2, University of Nevada, Reno, June 1993.

CCEER-93-3 Sanders, D.H., B.M. Douglas, and T.L. Martin, "Seismic Retrofit Prioritization of Nevada Bridges," Civil Engineering Department, Report No. CCEER-93-3, University of Nevada, Reno, July 1993.

CCEER-93-4 Abdel-Ghaffar, S., E. Maragakis, and M. Saiidi, "Performance of Hinge Restrainers in the Huntington Avenue Overhead During the 1989 Loma Prieta Earthquake," Civil Engineering Department, Report No. CCEER-93-4, University of Nevada, Reno, June 1993 (in final preparation).

CCEER-93-5 Maragakis, E., M. Saiidi, S. Feng, and L. Flournoy, "Effects of Hinge Restrainers on the Response of the San Gregorio Bridge during the Loma Prieta Earthquake," (in final preparation) Civil Engineering Department, Report No. CCEER-93-5, University of Nevada, Reno.

CCEER-93-6 Saiidi, M., E. Maragakis, S. Abdel-Ghaffar, S. Feng, and D. O'Connor, "Response of Bridge Hinge Restrainers during Earthquakes -Field Performance, Analysis, and Design," Civil Engineering Department, Report No. CCEER-93-6, University of Nevada, Reno, May 1993.

CCEER-93-7 Wehbe, N., Saiidi, M., Maragakis, E., and Sanders, D., "Adequacy of Three Highway Structures in Southern Nevada for Spent Fuel Transportation," Civil Engineering Department, Report No. CCEER-93-7, University of Nevada, Reno, August 1993.

CCEER-93-8 Roybal, J., Sanders, D.H., and Maragakis, E., "Vulnerability Assessment of Masonry in the Reno-Carson City Urban Corridor," Civil Engineering Department, Report No. CCEER-93-8, University of Nevada, Reno, May 1993.

CCEER-93-9 Zafir, Z. and Siddharthan, R., "MOVLOAD: A Program to Determine the Behavior of Nonlinear Horizontally Layered Medium Under Moving Load," Civil Engineering Department, Report No. CCEER-93-9, University of Nevada, Reno, August 1993.

CCEER-93-10 O'Connor, D.N., Saiidi, M., and Maragakis, E.A., "A Study of Bridge Column Seismic Damage Susceptibility at the Interstate 80/U.S. 395 Interchange in Reno, Nevada," Civil Engineering Department, Report No. CCEER-93-10, University of Nevada, Reno, October 1993.

CCEER-94-1 Maragakis, E., B. Douglas, and E. Abdelwahed, "Preliminary Dynamic Analysis of a Railroad Bridge," Report CCEER-94-1, January 1994.

CCEER-94-2 Douglas, B.M., Maragakis, E.A., and Feng, S., "Stiffness Evaluation of Pile Foundation of Cazenovia Creek Overpass," Civil Engineering Department, Report No. CCEER-94-2, University of Nevada, Reno, March 1994.

CCEER-94-3 Douglas, B.M., Maragakis, E.A., and Feng, S., "Summary of Pretest Analysis of Cazenovia Creek Bridge," Civil Engineering Department, Report No. CCEER-94-3, University of Nevada, Reno, April 1994.

CCEER-94-4 Norris, G.M., Madhu, R., Valceschini, R., and Ashour, M., "Liquefaction and Residual Strength of Loose Sands from Drained Triaxial Tests," Report 2, Vol. 1&2, Civil Engineering Department, Report No. CCEER-94-4, University of Nevada, Reno, August 1994.

CCEER-94-5 Saiidi, M., Hutchens, E., and Gardella, D., "Prestress Losses in a Post-Tensioned R/C Box Girder Bridge in Southern Nevada," Civil Engineering Department, CCEER-94-5, University of Nevada, Reno, August 1994.

CCEER-95-1 Siddharthan, R., El-Gamal, M., and Maragakis, E.A., "Nonlinear Bridge Abutment , Verification, and Design Curves," Civil Engineering Department, CCEER-95-1, University of Nevada, Reno, January 1995.

CCEER-95-2 Ashour, M. and Norris, G., "Liquefaction and Undrained Response Evaluation of Sands from Drained Formulation," Civil Engineering Department, Report No. CCEER-95-2, University of Nevada, Reno, February 1995.

CCEER-95-3 Wehbe, N., Saiidi, M., Sanders, D. and Douglas, B., "Ductility of Rectangular Reinforced Concrete Bridge Columns with Moderate Confinement," Civil Engineering Department, Report No. CCEER-95-3, University of Nevada, Reno, July 1995.

CCEER-95-4 Martin, T.., Saiidi, M. and Sanders, D., "Seismic Retrofit of Column-Pier Cap Connections in Bridges in Northern Nevada," Civil Engineering Department, Report No. CCEER-95-4, University of Nevada, Reno, August 1995.

CCEER-95-5 Darwish, I., Saiidi, M. and Sanders, D., "Experimental Study of Seismic Susceptibility Column-Footing Connections in Bridges in Northern Nevada," Civil Engineering Department, Report No. CCEER-95-5, University of Nevada, Reno, September 1995.

CCEER-95-6 Griffin, G., Saiidi, M. and Maragakis, E., "Nonlinear Seismic Response of Isolated Bridges and Effects of Pier Ductility Demand," Civil Engineering Department, Report No. CCEER-95-6, University of Nevada, Reno, November 1995.

CCEER-95-7 Acharya, S.., Saiidi, M. and Sanders, D., "Seismic Retrofit of Bridge Footings and Column-Footing Connections," Civil Engineering Department, Report No. CCEER-95-7, University of Nevada, Reno, November 1995.

CCEER-95-8 Maragakis, E., Douglas, B., and Sandirasegaram, U., "Full-Scale Field Resonance Tests of a Railway Bridge," A Report to the Association of American Railroads, Civil Engineering Department, Report No. CCEER-95-8, University of Nevada, Reno, December 1995.

CCEER-95-9 Douglas, B., Maragakis, E. and Feng, S., "System Identification Studies on Cazenovia Creek Overpass," Report for the National Center for Earthquake Engineering Research, Civil Engineering Department, Report No. CCEER-95-9, University of Nevada, Reno, October 1995.

CCEER-96-1 El-Gamal, M.E. and Siddharthan, R.V., "Programs to Computer Translational Stiffness of Seat-Type Bridge Abutment," Civil Engineering Department, Report No. CCEER-96-1, University of Nevada, Reno, March 1996.

CCEER-96-2 Labia, Y., Saiidi, M. and Douglas, B., "Evaluation and Repair of Full-Scale Prestressed Concrete Box Girders," A Report to the National Science Foundation, Research Grant CMS-9201908, Civil Engineering Department, Report No. CCEER-96-2, University of Nevada, Reno, May 1996.

CCEER-96-3 Darwish, I., Saiidi, M. and Sanders, D., "Seismic Retrofit of R/C Oblong Tapered Bridge Columns with Inadequate Bar Anchorage in Columns and Footings," A Report to the Nevada Department of Transportation, Civil Engineering Department, Report No. CCEER-96-3, University of Nevada, Reno, May 1996.

CCEER-96-4 Ashour, M., Pilling, R., Norris, G. and Perez, H., "The Prediction of Lateral Load Behavior of Single Piles and Pile Groups Using the Strain Wedge Model," A Report to the California Department of Transportation, Civil Engineering Department, Report No. CCEER-96-4, University of Nevada, Reno, June 1996.

CCEER-97-1-A Rimal, P. and Itani, A. "Sensitivity Analysis of Fatigue Evaluations of Steel Bridges," Center for Earthquake Research, Department of Civil Engineering, University of Nevada, Reno, Nevada Report No. CCEER-97-1-A, September, 1997.

CCEER-97-1-B Maragakis, E., Douglas, B., and Sandirasegaram, U. "Full-Scale Field Resonance Tests of a Railway Bridge," A Report to the Association of American Railroads, Civil Engineering Department, University of Nevada, Reno, May, 1996.

CCEER-97-2 Wehbe, N., Saiidi, M., and D. Sanders, "Effect of Confinement and Flares on the Seismic

Performance of Reinforced Concrete Bridge Columns," Civil Engineering Department, Report No. CCEER-97-2, University of Nevada, Reno, September 1997.

CCEER-97-3 Darwish, I., M. Saiidi, G. Norris, and E. Maragakis, "Determination of In-Situ Footing Stiffness Using Full-Scale Dynamic Field Testing," A Report to the Nevada Department of Transportation, Structural Design Division, Carson City, Nevada, Report No. CCEER-97-3, University of Nevada, Reno, October 1997.

CCEER-97-4-A Itani, A. "Cyclic Behavior of Richmond-San Rafael Tower Links," Center for Civil Engineering Earthquake Research, Department of Civil Engineering, University of Nevada, Reno, Nevada, Report No. CCEER-97-4, August 1997.

CCEER-97-4-B Wehbe, N., and M. Saiidi, "User's Manual for RCMC v. 1.2 : A Computer Program for Moment-Curvature Analysis of Confined and Unconfined Reinforced Concrete Sections," Center for Civil Engineering Earthquake Research, Department of Civil Engineering, University of Nevada, Reno, Nevada, Report No. CCEER-97-4, November, 1997.

CCEER-97-5 Isakovic, T., M. Saiidi, and A. Itani, "Influence of new Bridge Configurations on Seismic Performance," Department of Civil Engineering, University of Nevada, Reno, Report No. CCEER-97-5, September, 1997.

CCEER-98-1 Itani, A., Vesco, T. and Dietrich, A., "Cyclic Behavior of "as Built" Laced Members With End Gusset Plates on the San Francisco Bay Bridge," Center for Civil Engineering Earthquake Research, Department of Civil Engineering, University of Nevada, Reno, Nevada Report No. CCEER-98-1, March, 1998.

CCEER-98-2 G. Norris and M. Ashour, "Liquefaction and Undrained Response Evaluation of Sands from Drained Formulation," Center for Civil Engineering Earthquake Research, Department of Civil Engineering, University of Nevada, Reno, Nevada, Report No. CCEER-98-2, May, 1998.

CCEER-98-3 Qingbin, Chen, B. M. Douglas, E. Maragakis, and I. G. Buckle, "Extraction of Nonlinear Hysteretic Properties of Seismically Isolated Bridges from Quick-Release Field Tests," Center for Civil Engineering Earthquake Research, Department of Civil Engineering, University of Nevada, Reno, Nevada, Report No. CCEER-98-3, June, 1998.

CCEER-98-4 Maragakis, E., B. M. Douglas, and C. Qingbin, "Full-Scale Field Capacity Tests of a Railway Bridge," Center for Civil Engineering Earthquake Research, Department of Civil Engineering, University of Nevada, Reno, Nevada, Report No. CCEER-98-4, June, 1998.

CCEER-98-5 Itani, A., Douglas, B., and Woodgate, J., "Cyclic Behavior of Richmond-San Rafael Retrofitted Tower Leg," Center for Civil Engineering Earthquake Research, Department of Civil Engineering, University of Nevada, Reno. Report No. CCEER-98-5, June 1998

CCEER-98-6 Moore, R., Saiidi, M., and Itani, A., "Seismic Behavior of New Bridges with Skew and Curvature," Center for Civil Engineering Earthquake Research, Department of Civil Engineering, University of Nevada, Reno. Report No. CCEER-98-6, October, 1998.

CCEER-98-7 Itani, A and Dietrich, A, "Cyclic Behavior of Double Gusset Plate Connections," Center for Civil Engineering Earthquake Research, Department of Civil Engineering, University of Nevada, Reno, Nevada, Report No. CCEER-98-5, December, 1998.

CCEER-99-1 Caywood, C., M. Saiidi, and D. Sanders, "Seismic Retrofit of Flared Bridge Columns with Steel Jackets," Civil Engineering Department, University of Nevada, Reno, Report No. CCEER-99-1, February 1999.

CCEER-99-2 Mangoba, N., M. Mayberry, and M. Saiidi, "Prestress Loss in Four Box Girder Bridges in Northern Nevada," Civil Engineering Department, University of Nevada, Reno, Report No. CCEER-99-2, March 1999.

CCEER-99-3 Abo-Shadi, N., M. Saiidi, and D. Sanders, "Seismic Response of Bridge Pier Walls in the Weak Direction," Civil Engineering Department, University of Nevada, Reno, Report No. CCEER-99-3, April 1999.

CCEER-99-4 Buzick, A., and M. Saiidi, "Shear Strength and Shear Fatigue Behavior of Full-Scale Prestressed Concrete Box Girders," Civil Engineering Department, University of Nevada, Reno, Report No. CCEER-99-4, April 1999.

CCEER-99-5 Randall, M., M. Saiidi, E. Maragakis and T. Isakovic, "Restrainer Design Procedures For Multi-Span Simply-Supported Bridges," Civil Engineering Department, University of Nevada, Reno, Report No. CCEER-99-5, April 1999.

CCEER-99-6 Wehbe, N. and M. Saiidi, "User's Manual for RCMC v. 1.2, A Computer Program for Moment-Curvature Analysis of Confined and Unconfined Reinforced Concrete Sections," Civil Engineering Department, University of Nevada, Reno, Report No. CCEER-99-6, May 1999.

CCEER-99-7 Burda, J. and A. Itani, "Studies of Seismic Behavior of Steel Base Plates," Civil Engineering Department, University of Nevada, Reno, Report No. CCEER-99-7, May 1999.

CCEER-99-8 Ashour, M. and G. Norris, "Refinement of the Strain Wedge Model Program," Civil Engineering Department, University of Nevada, Reno, Report No. CCEER-99-8, March 1999.

CCEER-99-9 Dietrich, A., and A. Itani, "Cyclic Behavior of Laced and Perforated Steel Members on the San Francisco-Oakland Bay Bridge," Civil Engineering Department, University, Reno, Report No. CCEER-99-9, December 1999.

CCEER 99-10 Itani, A., A. Dietrich, "Cyclic Behavior of Built Up Steel Members and their Connections," Civil Engineering Department, University of Nevada, Reno, Report No. CCEER-99-10, December 1999.

CCEER 99-10-A Itani, A., E. Maragakis and P. He, "Fatigue Behavior of Riveted Open Deck Railroad Bridge Girders," Civil Engineering Department, University of Nevada, Reno, Report No. CCEER-99-10-A, August 1999.

CCEER 99-11 Itani, A., J. Woodgate, "Axial and Rotational Ductility of Built Up Structural Steel Members," Civil Engineering Department, University of Nevada, Reno, Report No. CCEER-99-11, December 1999.

CCEER-99-12 Sgambelluri, M., Sanders, D.H., and Saiidi, M.S., "Behavior of One-Way Reinforced Concrete Bridge Column Hinges in the Weak Direction," Department of Civil Engineering, University of Nevada, Reno, Report No. CCEER-99-12, December 1999.

CCEER-99-13 Laplace, P., Sanders, D.H., Douglas, B, and Saiidi, M, "Shake Table Testing of Flexure Dominated Reinforced Concrete Bridge Columns", Department of Civil Engineering, University of Nevada, Reno, Report No. CCEER-99-13, December 1999.

CCEER-99-14 Ahmad M. Itani, Jose A. Zepeda, and Elizabeth A. Ware "Cyclic Behavior of Steel Moment Frame Connections for the Moscone Center Expansion," Department of Civil Engineering, University of Nevada, Reno, Report No. CCEER-99-14, December 1999.

CCEER 00-1 Ashour, M., and Norris, G. "Undrained Lateral Pile and Pile Group Response in Saturated Sand," Civil Engineering Department, University of Nevada, Reno, Report No. CCEER-00-1, May 1999. January 2000.

CCEER 00-2 Saiidi, M. and Wehbe, N., "A Comparison of Confinement Requirements in Different Codes for Rectangular, Circular, and Double-Spiral RC Bridge Columns," Civil Engineering Department, University of Nevada, Reno, Report No. CCEER-00-2, January 2000.

CCEER 00-3 McElhaney, B., M. Saiidi, and D. Sanders, "Shake Table Testing of Flared Bridge Columns With Steel Jacket Retrofit," Civil Engineering Department, University of Nevada, Reno, Report No. CCEER-00-3, January 2000.

CCEER 00-4 Martinovic, F., M. Saiidi, D. Sanders, and F. Gordaninejad, "Dynamic Testing of Non-Prismatic Reinforced Concrete Bridge Columns Retrofitted with FRP Jackets," Civil Engineering Department, University of Nevada, Reno, Report No. CCEER-00-4, January 2000.

CCEER 00-5 Itani, A., and M. Saiidi, "Seismic Evaluation of Steel Joints for UCLA Center for Health Science Westwood Replacement Hospital," Civil Engineering Department, University of Nevada, Reno, Report No. CCEER-00-5, February 2000.

CCEER 00-6 Will, J. and D. Sanders, "High Performance Concrete Using Nevada Aggregates," Civil Engineering Department, University of Nevada, Reno, Report No. CCEER-00-6, May 2000.

CCEER 00-7 French, C., and M. Saiidi, "A Comparison of Static and Dynamic Performance of Models of Flared Bridge Columns," Civil Engineering Department, University of Nevada, Reno, Report No. CCEER-00-7, October 2000.

CCEER 00-8 Itani, A., H. Sedarat, "Seismic Analysis of the AISI LRFD Design Example of Steel Highway Bridges," Civil Engineering Department, University of Nevada, Reno, Report No. CCEER 00-08, November 2000.

CCEER 00-9 Moore, J., D. Sanders, and M. Saiidi, "Shake Table Testing of 1960's Two Column Bent with Hinges Bases," Civil Engineering Department, University of Nevada, Reno, Report No. CCEER 00-09, December 2000.

CCEER 00-10 Asthana, M., D. Sanders, and M. Saiidi, "One-Way Reinforced Concrete Bridge Column Hinges in the Weak Direction," Civil Engineering Department, University of Nevada, Reno, Report No. CCEER 00-10, April 2001.

CCEER 01-1 Ah Sha, H., D. Sanders, M. Saiidi, "Early Age Shrinkage and Cracking of Nevada Concrete Bridge Decks," Civil Engineering Department, University of Nevada, Reno, Report No. CCEER 01-01, May 2001.

CCEER 01-2 Ashour, M. and G. Norris, "Pile Group program for Full Material Modeling a Progressive Failure," Civil Engineering Department, University of Nevada, Reno, Report No. CCEER 01-02, July 2001.

CCEER 01-3 Itani, A., C. Lanaud, and P. Dusicka, "Non-Linear Finite Element Analysis of Built-Up Shear Links," Civil Engineering Department, University of Nevada, Reno, Report No. CCEER 01-03, July 2001.

CCEER 01-4 Saiidi, M., J. Mortensen, and F. Martinovic, "Analysis and Retrofit of Fixed Flared Columns with Glass Fiber-Reinforced Plastic Jacketing," Civil Engineering Department, University of Nevada, Reno, Report No. CCEER 01-4, August 2001

CCEER 01-5 Not Published

CCEER 01-6 Laplace, P., D. Sanders, and M. Saiidi, "Experimental Study and Analysis of Retrofitted Flexure and Shear Dominated Circular Reinforced Concrete Bridge Columns Subjected to Shake Table Excitation," Civil Engineering Department, University of Nevada, Reno, Report No. CCEER 01-6, June 2001.

CCEER 01-7 Reppi, F., and D. Sanders, "Removal and Replacement of Cast-in-Place, Post-tensioned, Box Girder Bridge," Civil Engineering Department, University of Nevada, Reno, Report No. CCEER 01-7, December 2001.

CCEER 02-1 Pulido, C., M. Saiidi, D. Sanders, and A. Itani, "Seismic Performance and Retrofitting of Reinforced Concrete Bridge Bents," Civil Engineering Department, University of Nevada, Reno, Report No. CCEER 02-1, January 2002.

CCEER 02-2 Yang, Q., M. Saiidi, H. Wang, and A. Itani, "Influence of Ground Motion Incoherency on Earthquake Response of Multi-Support Structures," Civil Engineering Department, University of Nevada, Reno, Report No. CCEER 02-2, May 2002.

CCEER 02-3 M. Saiidi, B. Gopalakrishnan, E. Reinhardt, and R. Siddharthan, "A Preliminary Study of Shake Table Response of A Two-Column Bridge Bent on Flexible Footings," Civil Engineering Department, University of Nevada, Reno, Report No. CCEER 02-03, June 2002.

CCEER 02-4 Not Published

CCEER 02-5 Banghart, A., Sanders, D., Saiidi, M., "Evaluation of Concrete Mixes for Filling the Steel Arches in the Galena Creek Bridge," Civil Engineering Department, University of Nevada, Reno, Report No. CCEER 02-05, June 2002.

CCEER 02-6 Dusicka, P., Itani, A., Buckle, I. G., "Cyclic Behavior of Shear Links and Tower Shaft Assembly of San Francisco – Oakland Bay Bridge Tower," Civil Engineering Department, University of Nevada, Reno, Report No. CCEER 02-06, July 2002.

CCEER 02-7 Mortensen, J., and M. Saiidi, "A Performance-Based Design Method for Confinement in Circular Columns," Civil Engineering Department, University of Nevada, Reno, Report No. CCEER 02-07, November 2002.

CCEER 03-1 Wehbe, N., and M. Saiidi, "User's manual for SPMC v. 1.0 : A Computer Program for Moment-Curvature Analysis of Reinforced Concrete Sections with Interlocking Spirals," Center for Civil Engineering Earthquake Research, Department of Civil Engineering, University of Nevada, Reno, Nevada, Report No. CCEER-03-1, May, 2003.

CCEER 03-2 Wehbe, N., and M. Saiidi, "User's manual for RCMC v. 2.0 : A Computer Program for Moment-Curvature Analysis of Confined and Unconfined Reinforced Concrete Sections," Center for Civil Engineering Earthquake Research, Department of Civil Engineering, University of Nevada, Reno, Nevada, Report No. CCEER-03-2, June, 2003.

CCEER 03-3 Nada, H., D. Sanders, and M. Saiidi, "Seismic Performance of RC Bridge Frames with Architectural-Flared Columns," Civil Engineering Department, University of Nevada, Reno, Report No. CCEER 03-3, January 2003.

CCEER 03-4 Reinhardt, E., M. Saiidi, and R. Siddharthan, "Seismic Performance of a CFRP/ Concrete Bridge Bent on Flexible Footings," Civil Engineering Department, University of Nevada, Reno, Report No. CCEER 03-4, August 2003.

CCEER 03-5 Johnson, N., M. Saiidi, A. Itani, and S. Ladkany, "Seismic Retrofit of Octagonal Columns with Pedestal and One-Way Hinge at the Base," Center for Civil Engineering Earthquake Research, Department of Civil Engineering, University of Nevada, Reno, Nevada, and Report No. CCEER-03-5, August 2003.

CCEER 03-6 Mortensen, C., M. Saiidi, and S. Ladkany, "Creep and Shrinkage Losses in Highly Variable Climates," Center for Civil Engineering Earthquake Research, Department of Civil Engineering, University of Nevada, Reno, Report No. CCEER-03-6, September 2003.

CCEER 03- 7 Ayoub, C., M. Saiidi, and A. Itani, "A Study of Shape-Memory-Alloy-Reinforced Beams and Cubes," Center for Civil Engineering Earthquake Research, Department of Civil Engineering, University of Nevada, Reno, Nevada, Report No. CCEER-03-7, October 2003.

CCEER 03-8 Chandane, S., D. Sanders, and M. Saiidi, "Static and Dynamic Performance of RC Bridge Bents with Architectural-Flared Columns," Center for Civil Engineering Earthquake Research, Department of Civil Engineering, University of Nevada, Reno, Nevada, Report No. CCEER-03-8, November 2003.

CCEER 04-1 Olaegbe, C., and Saiidi, M., "Effect of Loading History on Shake Table Performance of A Two-Column Bent with Infill Wall," Center for Civil Engineering Earthquake Research, Department of Civil Engineering, University of Nevada, Reno, Nevada, Report No. CCEER-04-1, January 2004.

CCEER 04-2 Johnson, R., Maragakis, E., Saiidi, M., and DesRoches, R., "Experimental Evaluation of Seismic Performance of SMA Bridge Restrainers," Center for Civil Engineering Earthquake Research, Department of Civil Engineering, University of Nevada, Reno, Nevada, Report No. CCEER-04-2, February 2004.

CCEER 04-3 Moustafa, K., Sanders, D., and Saiidi, M., "Impact of Aspect Ratio on Two-Column Bent Seismic Performance," Center for Civil Engineering Earthquake Research, Department of Civil Engineering, University of Nevada, Reno, Nevada, Report No. CCEER-04-3, February 2004.

CCEER 04-4 Maragakis, E., Saiidi, M., Sanchez-Camargo, F., and Elfass, S., "Seismic Performance of Bridge Restrainers At In-Span Hinges," Center for Civil Engineering Earthquake Research, Department of Civil Engineering, University of Nevada, Reno, Nevada, Report No. CCEER-04-4, March 2004.

CCEER 04-5 Ashour, M., Norris, G. and Elfass, S., "Analysis of Laterally Loaded Long or Intermediate Drilled Shafts of Small or Large Diameter in Layered Soil," Center for Civil Engineering Earthquake Research, Department of Civil Engineering, University of Nevada, Reno, Nevada, Report No. CCEER-04-5, June 2004.

CCEER 04-6 Correal, J., Saiidi, M. and Sanders, D., "Seismic Performance of RC Bridge Columns Reinforced with Two Interlocking Spirals," Center for Civil Engineering Earthquake Research, Department of Civil Engineering, University of Nevada, Reno, Nevada, Report No. CCEER-04-6, August 2004.

CCEER 04-7 Dusicka, P., Itani, A. and Buckle, I., "Cyclic Response and Low Cycle Fatigue Characteristics of Plate Steels," Center for Civil Engineering Earthquake Research, Department of Civil Engineering, University of Nevada, Reno, Nevada, Report No. CCEER-04-7, November 2004.

CCEER 04-8 Dusicka, P., Itani, A. and Buckle, I., "Built-up Shear Links as Energy Dissipaters for Seismic Protection of Bridges," Center for Civil Engineering Earthquake Research, Department of Civil Engineering, University of Nevada, Reno, Nevada, Report No. CCEER-04-8, November 2004.

CCEER 04-9 Sureshkumar, K., Saiidi, S., Itani, A. and Ladkany, S., "Seismic Retrofit of Two-Column Bents with Diamond Shape Columns," Center for Civil Engineering Earthquake Research, Department of Civil Engineering, University of Nevada, Reno, Nevada, Report No. CCEER-04-9, November 2004.

CCEER 05-1 Wang, H. and Saiidi, S., "A Study of RC Columns with Shape Memory Alloy and Engineered Cementitious Composites," Center for Civil Engineering Earthquake Research, Department of Civil Engineering, University of Nevada, Reno, Nevada, Report No. CCEER-05-1, January 2005.

CCEER 05-2 Johnson, R., Saiidi, S. and Maragakis, E., "A Study of Fiber Reinforced Plastics for Seismic Bridge Restrainers," Center for Civil Engineering Earthquake Research, Department of Civil Engineering, University of Nevada, Reno, Nevada, Report No. CCEER-05-2, January 2005.

CCEER 05-3 Carden, L.P., Itani, A.M., Buckle, I.G, "Seismic Load Path in Steel Girder Bridge Superstructures," Center for Civil Engineering Earthquake Research, Department of Civil Engineering, University of Nevada, Reno, Nevada, Report No. CCEER-05-3, January 2005.

CCEER 05-4 Carden, L.P., Itani, A.M., Buckle, I.G, "Seismic Performance of Steel Girder Bridge Superstructures with Ductile End Cross Frames and Seismic Isolation," Center for Civil Engineering Earthquake Research, Department of Civil Engineering, University of Nevada, Reno, Nevada, Report No. CCEER-05-4, January 2005.

CCEER 05-5 Goodwin, E., Maragakis, M., Itani, A. and Luo, S., "Experimental Evaluation of the Seismic Performance of Hospital Piping Subassemblies," Center for Civil Engineering Earthquake Research, Department of Civil Engineering, University of Nevada, Reno, Nevada, Report No. CCEER-05-5, February 2005.

CCEER 05-6 Zadeh M. S., Saiidi, S, Itani, A. and Ladkany, S., "Seismic Vulnerability Evaluation and Retrofit Design of Las Vegas Downtown Viaduct," Center for Civil Engineering Earthquake Research, Department of Civil Engineering, University of Nevada, Reno, Nevada, Report No. CCEER-05-6, February 2005.

CCEER 05-7 Phan, V., Saiidi, S. and Anderson, J., "Near Fault (Near Field) Ground Motion Effects on Reinforced Concrete Bridge Columns," Center for Civil Engineering Earthquake Research, Department of Civil Engineering, University of Nevada, Reno, Nevada, Report No. CCEER-05-7, August 2005.

CCEER 05-8 Carden, L., Itani, A. and Laplace, P., "Performance of Steel Props at the UNR Fire Science Academy subjected to Repeated Fire," Center for Civil Engineering Earthquake Research, Department of Civil Engineering, University of Nevada, Reno, Nevada, Report No. CCEER-05-8, August 2005.

CCEER 05-9 Yamashita, R. and Sanders, D., "Shake Table Testing and an Analytical Study of Unbonded Prestressed Hollow Concrete Column Constructed with Precast Segments," Center for Civil Engineering Earthquake Research, Department of Civil Engineering, University of Nevada, Reno, Nevada, Report No. CCEER-05-9, August 2005.

CCEER 05-10 Not Published

CCEER 05-11 Carden, L., Itani., A., and Peckan, G., "Recommendations for the Design of Beams and Posts in Bridge Falsework," Center for Civil Engineering Earthquake Research, Department of Civil Engineering, University of Nevada, Reno, Nevada, Report No. CCEER-05-11, October 2005.

CCEER 06-01 Cheng, Z., Saiidi, M., and Sanders, D., "Development of a Seismic Design Method for Reinforced Concrete Two-Way Bridge Column Hinges," Center for Civil Engineering Earthquake Research, Department of Civil Engineering, University of Nevada, Reno, Nevada, Report No. CCEER-06-01, February 2006.

CCEER 06-02 Johnson, N., Saiidi, M., and Sanders, D., "Large-Scale Experimental and Analytical Studies of a Two-Span Reinforced Concrete Bridge System," Center for Civil Engineering Earthquake Research, Department of Civil Engineering, University of Nevada, Reno, Nevada, Report No. CCEER-06-02, March 2006.

CCEER 06-03 Saiidi, M., Ghasemi, H. and Tiras, A., "Seismic Design and Retrofit of Highway Bridges," Proceedings, Second US-Turkey Workshop, Center for Civil Engineering Earthquake Research, Department of Civil Engineering, University of Nevada, Reno, Nevada, Report No. CCEER-06-03, May 2006.

CCEER 07-01 O'Brien, M., Saiidi, M. and Sadrossadat-Zadeh, M., "A Study of Concrete Bridge Columns Using Innovative Materials Subjected to Cyclic Loading," Center for Civil Engineering Earthquake Research, Department of Civil Engineering, University of Nevada, Reno, Nevada, Report No. CCEER-07-01, January 2007.

CCEER 07-02 Sadrossadat-Zadeh, M. and Saiidi, M., "Effect of Strain rate on Stress-Strain Properties and Yield Propagation in Steel Reinforcing Bars," Center for Civil Engineering Earthquake Research, Department of Civil Engineering, University of Nevada, Reno, Nevada, Report No. CCEER-07-02, January 2007.

CCEER 07-03 Sadrossadat-Zadeh, M. and Saiidi, M., "Analytical Study of NEESR-SG 4-Span Bridge Model Using OpenSees," Center for Civil Engineering Earthquake Research, Department of Civil Engineering, University of Nevada, Reno, Nevada, Report No. CCEER-07-03, January 2007.

CCEER 07-04 Nelson, R., Saiidi, M. and Zadeh, S., "Experimental Evaluation of Performance of Conventional Bridge Systems," Center for Civil Engineering Earthquake Research, Department of Civil Engineering, University of Nevada, Reno, Nevada, Report No. CCEER-07-04, October 2007.

CCEER 07-05 Bahen, N. and Sanders, D., "Strut-and-Tie Modeling for Disturbed Regions in Structural Concrete Members with Emphasis on Deep Beams," Center for Civil Engineering Earthquake Research, Department of Civil Engineering, University of Nevada, Reno, Nevada, Report No. CCEER-07-05, December 2007.

CCEER 07-06 Choi, H., Saiidi, M. and Somerville, P., "Effects of Near-Fault Ground Motion and Fault-Rupture on the Seismic Response of Reinforced Concrete Bridges," Center for Civil Engineering Earthquake Research, Department of Civil Engineering, University of Nevada, Reno, Nevada, Report No. CCEER-07-06, December 2007.

CCEER 07-07 Ashour M. and Norris, G., "Report and User Manual on Strain Wedge Model Computer Program for Files and Large Diameter Shafts with LRFD Procedure," Center for Civil Engineering Earthquake Research, Department of Civil Engineering, University of Nevada, Reno, Nevada, Report No. CCEER-07-07, October 2007.

CCEER 08-01 Doyle, K. and Saiidi, M., "Seismic Response of Telescopic Pipe Pin Connections," Center for Civil Engineering Earthquake Research, Department of Civil Engineering, University of Nevada, Reno, Nevada, Report No. CCEER-08-01, February 2008.

CCEER 08-02 Taylor, M. and Sanders, D., "Seismic Time History Analysis and Instrumentation of the Galena Creek Bridge," Center for Civil Engineering Earthquake Research, Department of Civil Engineering, University of Nevada, Reno, Nevada, Report No. CCEER-08-02, April 2008.

CCEER 08-03 Abdel-Mohti, A. and Pekcan, G., "Seismic Response Assessment and Recommendations for the Design of Skewed Post-Tensioned Concrete Box-Girder Highway Bridges," Center for Civil Engineering Earthquake Research, Department of Civil and Environmental Engineering, University of Nevada, Reno, Nevada, Report No. CCEER-08-03, September 2008.

CCEER 08-04 Saiidi, M., Ghasemi, H. and Hook, J., "Long Term Bridge Performance Monitoring, Assessment & Management," Proceedings, FHWA/NSF Workshop on Future Directions," Center for Civil Engineering Earthquake Research, Department of Civil and Environmental Engineering, University of Nevada, Reno, Nevada, Report No. CCEER 08-04, September 2008.

CCEER 09-01 Brown, A., and Saiidi, M., "Investigation of Near-Fault Ground Motion Effects on Substandard Bridge Columns and Bents," Center for Civil Engineering Earthquake Research, Department of Civil and Environmental Engineering, University of Nevada, Reno, Nevada, Report No. CCEER-09-01, July 2009.

CCEER 09-02 Linke, C., Pekcan, G., and Itani, A., "Detailing of Seismically Resilient Special Truss Moment Frames," Center for Civil Engineering Earthquake Research, Department of Civil and Environmental Engineering, University of Nevada, Reno, Nevada, Report No. CCEER-09-02, August 2009.

CCEER 09-03 Hillis, D., and Saiidi, M., "Design, Construction, and Nonlinear Dynamic Analysis of Three Bridge Bents Used in a Bridge System Test," Center for Civil Engineering Earthquake Research, Department of Civil and Environmental Engineering, University of Nevada, Reno, Nevada, Report No. CCEER-09-03, August 2009.

CCEER 09-04 Bahrami, H., Itani, A., and Buckle, I., "Guidelines for the Seismic Design of Ductile End Cross Frames in Steel Girder Bridge Superstructures," Center for Civil Engineering Earthquake Research, Department of Civil and Environmental Engineering, University of Nevada, Reno, Nevada, Report No. CCEER-09-04, September 2009.

CCEER 10-01 Zaghi, A. E., and Saiidi, M., "Seismic Design of Pipe-Pin Connections in Concrete Bridges," Center for Civil Engineering Earthquake Research, Department of Civil and Environmental Engineering, University of Nevada, Reno, Nevada, Report No. CCEER-10-01, January 2010.

CCEER 10-02 Pooranampillai, S., Elfass, S., and Norris, G., "Laboratory Study to Assess Load Capacity Increase of Drilled Shafts through Post Grouting," Center for Civil Engineering Earthquake Research, Department of Civil and Environmental Engineering, University of Nevada, Reno, Nevada, Report No. CCEER-10-02, January 2010.

CCEER 10-03 Itani, A., Grubb, M., and Monzon, E, "Proposed Seismic Provisions and Commentary for Steel Plate Girder Superstructures," Center for Civil Engineering Earthquake Research, Department of Civil and Environmental Engineering, University of Nevada, Reno, Nevada, Report No. CCEER-10-03, June 2010.

CCEER 10-04 Cruz-Noguez, C., Saiidi, M., "Experimental and Analytical Seismic Studies of a Four-Span Bridge System with Innovative Materials," Center for Civil Engineering Earthquake Research, Department of Civil and Environmental Engineering, University of Nevada, Reno, Nevada, Report No. CCEER-10-04, September 2010.

CCEER 10-05 Vosooghi, A., Saiidi, M., "Post-Earthquake Evaluation and Emergency Repair of Damaged RC Bridge Columns Using CFRP Materials," Center for Civil Engineering Earthquake Research, Department of Civil and Environmental Engineering, University of Nevada, Reno, Nevada, Report No. CCEER-10-05, September 2010.

CCEER 10-06 Ayoub, M., Sanders, D., "Testing of Pile Extension Connections to Slab Bridges," Center for Civil Engineering Earthquake Research, Department of Civil and Environmental Engineering, University of Nevada, Reno, Nevada, Report No. CCEER-10-06, October 2010.

CCEER 10-07 Builes-Mejia, J. C. and Itani, A., "Stability of Bridge Column Rebar Cages during Construction," Center for Civil Engineering Earthquake Research, Department of Civil and Environmental Engineering, University of Nevada, Reno, Nevada, Report No. CCEER-10-07, November 2010.

CCEER 10-08 Monzon, E.V., "Seismic Performance of Steel Plate Girder Bridges with Integral Abutments," Center for Civil Engineering Earthquake Research, Department of Civil and Environmental Engineering, University of Nevada, Reno, Nevada, Report No. CCEER-10-08, November 2010.

CCEER 11-01 Motaref, S., Saiidi, M., and Sanders, D., "Seismic Response of Precast Bridge Columns with Energy Dissipating Joints," Center for Civil Engineering Earthquake Research, Department of Civil and Environmental Engineering, University of Nevada, Reno, Nevada, Report No. CCEER-11-01, May 2011.

CCEER 11-02 Harrison, N. and Sanders, D., "Preliminary Seismic Analysis and Design of Reinforced Concrete Bridge Columns for Curved Bridge Experiments," Center for Civil Engineering Earthquake Research, Department of Civil and Environmental Engineering, University of Nevada, Reno, Nevada, Report No. CCEER-11-02, May 2011.

CCEER 11-03 Vallejera, J. and Sanders, D., "Instrumentation and Monitoring the Galena Creek Bridge," Center for Civil Engineering Earthquake Research, Department of Civil and Environmental Engineering, University of Nevada, Reno, Nevada, Report No. CCEER-11-03, September 2011.

CCEER 11-04 Levi, M., Sanders, D., and Buckle, I., "Seismic Response of Columns in Horizontally Curved Bridges," Center for Civil Engineering Earthquake Research, Department of Civil and Environmental Engineering, University of Nevada, Reno, Nevada, Report No. CCEER-11-04, December 2011.

CCEER 12-01 Saiidi, M., "NSF International Workshop on Bridges of the Future – Wide Spread Implementation of Innovation," Center for Civil Engineering Earthquake Research, Department of Civil and Environmental Engineering, University of Nevada, Reno, Nevada, Report No. CCEER-12-01, January 2012.

CCEER 12-02 Larkin, A.S., Sanders, D., and Saiidi, M., "Unbonded Prestressed Columns for Earthquake Resistance," Center for Civil Engineering Earthquake Research, Department of Civil and Environmental Engineering, University of Nevada, Reno, Nevada, Report No. CCEER-12-02, January 2012.

CCEER 12-03 Arias-Acosta, J. G., Sanders, D., "Seismic Performance of Circular and Interlocking Spirals RC Bridge Columns under Bidirectional Shake Table Loading Part 1," Center for Civil Engineering Earthquake Research, Department of Civil and Environmental Engineering, University of Nevada, Reno, Nevada, Report No. CCEER-12-03, September 2012.

CCEER 12-04 Cukrov, M.E., Sanders, D., "Seismic Performance of Prestressed Pile-To-Bent Cap Connections," Center for Civil Engineering Earthquake Research, Department of Civil and Environmental Engineering, University of Nevada, Reno, Nevada, Report No. CCEER-12-04, September 2012.

CCEER 13-01 Carr, T. and Sanders, D., "Instrumentation and Dynamic Characterization of the Galena Creek Bridge," Center for Civil Engineering Earthquake Research, Department of Civil and Environmental Engineering, University of Nevada, Reno, Nevada, Report No. CCEER-13-01, January 2013.

CCEER 13-02 Vosooghi, A. and Buckle, I., "Evaluation of the Performance of a Conventional Four-Span Bridge During Shake Table Tests," Center for Civil Engineering Earthquake Research, Department of Civil and Environmental Engineering, University of Nevada, Reno, Nevada, Report No. CCEER-13-02, January 2013.

CCEER 13-03 Amirihormozaki, E. and Pekcan, G., "Analytical Fragility Curves for Horizontally Curved Steel Girder Highway Bridges," Center for Civil Engineering Earthquake Research, Department of Civil and Environmental Engineering, University of Nevada, Reno, Nevada, Report No. CCEER-13-03, February 2013.

CCEER 13-04 Almer, K. and Sanders, D., "Longitudinal Seismic Performance of Precast Bridge Girders Integrally Connected to a Cast-in-Place Bentcap," Center for Civil Engineering Earthquake Research, Department of Civil and Environmental Engineering, University of Nevada, Reno, Nevada, Report No. CCEER-13-04, April 2013.

CCEER 13-05 Monzon, E.V., Itani, A.I., and Buckle, I.G., "Seismic Modeling and Analysis of Curved Steel Plate Girder Bridges," Center for Civil Engineering Earthquake Research, Department of Civil and Environmental Engineering, University of Nevada, Reno, Nevada, Report No. CCEER-13-05, April 2013.

CCEER 13-06 Monzon, E.V., Buckle, I.G., and Itani, A.I., "Seismic Performance of Curved Steel Plate Girder Bridges with Seismic Isolation," Center for Civil Engineering Earthquake Research, Department of Civil and Environmental Engineering, University of Nevada, Reno, Nevada, Report No. CCEER-13-06, April 2013.

CCEER 13-07 Monzon, E.V., Buckle, I.G., and Itani, A.I., "Seismic Response of Isolated Bridge Superstructure to Incoherent Ground Motions," Center for Civil Engineering Earthquake Research, Department of Civil and Environmental Engineering, University of Nevada, Reno, Nevada, Report No. CCEER-13-07, April 2013.

CCEER 13-08 Haber, Z.B., Saiidi, M.S., and Sanders, D.H., "Precast Column-Footing Connections for Accelerated Bridge Construction in Seismic Zones," Center for Civil Engineering Earthquake Research, Department of Civil and Environmental Engineering, University of Nevada, Reno, Nevada, Report No. CCEER-13-08, April 2013.

CCEER 13-09 Ryan, K.L., Coria, C.B., and Dao, N.D., "Large Scale Earthquake Simulation of a Hybrid Lead Rubber Isolation System Designed under Nuclear Seismicity Considerations," Center for Civil Engineering Earthquake Research, Department of Civil and Environmental Engineering, University of Nevada, Reno, Nevada, Report No. CCEER-13-09, April 2013.

CCEER 13-10 Wibowo, H., Sanford, D.M., Buckle, I.G., and Sanders, D.H., "The Effect of Live Load on the Seismic Response of Bridges," Center for Civil Engineering Earthquake Research, Department of Civil and Environmental Engineering, University of Nevada, Reno, Nevada, Report No. CCEER-13-10, May 2013.

CCEER 13-11 Sanford, D.M., Wibowo, H., Buckle, I.G., and Sanders, D.H., "Preliminary Experimental Study on the Effect of Live Load on the Seismic Response of Highway Bridges," Center for Civil Engineering Earthquake Research, Department of Civil and Environmental Engineering, University of Nevada, Reno, Nevada, Report No. CCEER-13-11, May 2013.

CCEER 13-12 Saad, A.S., Sanders, D.H., and Buckle, I.G., "Assessment of Foundation Rocking Behavior in Reducing the Seismic Demand on Horizontally Curved Bridges," Center for Civil Engineering Earthquake Research, Department of Civil and Environmental Engineering, University of Nevada, Reno, Nevada, Report No. CCEER-13-12, June 2013.

CCEER 13-13 Ardakani, S.M.S. and Saiidi, M.S., "Design of Reinforced Concrete Bridge Columns for Near-Fault Earthquakes," Center for Civil Engineering Earthquake Research, Department of Civil and Environmental Engineering, University of Nevada, Reno, Nevada, Report No. CCEER-13-13, July 2013.

CCEER 13-14 Wei, C. and Buckle, I., "Seismic Analysis and Response of Highway Bridges with Hybrid Isolation," Center for Civil Engineering Earthquake Research, Department of Civil and Environmental Engineering, University of Nevada, Reno, Nevada, Report No. CCEER-13-14, August 2013.

CCEER 13-15 Wibowo, H., Buckle, I.G., and Sanders, D.H., "Experimental and Analytical Investigations on the Effects of Live Load on the Seismic Performance of a Highway Bridge," Center for Civil Engineering Earthquake Research, Department of Civil and Environmental Engineering, University of Nevada, Reno, Nevada, Report No. CCEER-13-15, August 2013.

CCEER 13-16 Itani, A.M., Monzon, E.V., Grubb, M., and Amirihormozaki, E. "Seismic Design and Nonlinear Evaluation of Steel I-Girder Bridges with Ductile End Cross-Frames," Center for Civil Engineering Earthquake Research, Department of Civil and Environmental Engineering, University of Nevada, Reno, Nevada, Report No. CCEER-13-16, September 2013.

CCEER 13-17 Kavianipour, F. and Saiidi, M.S., "Experimental and Analytical Seismic Studies of a Four-span Bridge System with Composite Piers," Center for Civil Engineering Earthquake Research, Department of Civil and Environmental Engineering, University of Nevada, Reno, Nevada, Report No. CCEER-13-17, September 2013.

CCEER 13-18 Mohebbi, A., Ryan, K., and Sanders, D., "Seismic Response of a Highway Bridge with Structural Fuses for Seismic Protection of Piers," Center for Civil Engineering Earthquake Research, Department of Civil and Environmental Engineering, University of Nevada, Reno, Nevada, Report No. CCEER-13-18, December 2013.

CCEER 13-19 Guzman Pujols, Jean C., Ryan, K.L., "Development of Generalized Fragility Functions for Seismic Induced Content Disruption," Center for Civil Engineering Earthquake Research, Department of Civil and Environmental Engineering, University of Nevada, Reno, Nevada, Report No. CCEER-13-19, December 2013.

CCEER 14-01 Salem, M. M. A., Pekcan, G., and Itani, A., "Seismic Response Control Of Structures Using Semi-Active and Passive Variable Stiffness Devices," Center for Civil Engineering Earthquake Research, Department of Civil and Environmental Engineering, University of Nevada, Reno, Nevada, Report No. CCEER-14-01, May 2014.

CCEER 14-02 Saini, A. and Saiidi, M., "Performance-Based Probabilistic Damage Control Approach for Seismic Design of Bridge Columns," Center For Civil Engineering Earthquake Research, Department Of Civil and Environmental Engineering, University of Nevada, Reno, Nevada, Report No. CCEER-14-02, May 2014.

CCEER 14-03 Saini, A. and Saiidi, M., "Post Earthquake Damage Repair of Various Reinforced Concrete Bridge Components," Center For Civil Engineering Earthquake Research, Department Of Civil and Environmental Engineering, University of Nevada, Reno, Nevada, Report No. CCEER-14-03, May 2014.

CCEER 14-04 Monzon, E.V., Itani, A.M., and Grubb, M.A., "Nonlinear Evaluation of the Proposed Seismic Design Procedure for Steel Bridges with Ductile End Cross Frames," Center For Civil Engineering Earthquake Research, Department Of Civil and Environmental Engineering, University of Nevada, Reno, Nevada, Report No. CCEER-14-04, July 2014.

CCEER 14-05 Nakashoji, B. and Saiidi, M.S., "Seismic Performance of Square Nickel-Titanium Reinforced ECC Columns with Headed Couplers," Center For Civil Engineering Earthquake Research, Department Of Civil and Environmental Engineering, University of Nevada, Reno, Nevada, Report No. CCEER-14-05, July 2014.

CCEER 14-06 Tazarv, M. and Saiidi, M.S., "Next Generation of Bridge Columns for Accelerated Bridge Construction in High Seismic Zones," Center For Civil Engineering Earthquake Research, Department Of Civil and Environmental Engineering, University of Nevada, Reno, Nevada, Report No. CCEER-14-06, August 2014.